ANNEX IV

GRANT NO. DE-FG22-89BC14444

1990-1991 ANNUAL REPORT

# RELATING TO FOSSIL ENERGY RESOURCE CHARACTERIZATION, RESEARCH, TECHNOLOGY DEVELOPMENT, AND TECHNOLOGY TRANSFER

between the

UNITED STATE DEPARTMENT OF ENERGY
and
THE STATE OF TEXAS

on

# OIL RECOVERY ENHANCEMENT FROM FRACTURED, LOW PERMEABILITY RESERVOIRS

submitted by

TEXAS A&M UNIVERSITY

Principal Investigator

S. W. POSTON

OIL RECOVERY ENHANCEMENT FROM FRACTURED, LOW PERMEABILITY RESERVOIRS

Contract No. DE-FG07-89BC14444

Texas A&M University
College Station, TX.

Contract Date: June 13, 1989
Anticipated Completion: Sept. 1, 1992
Goverment Award: $256,000
(Current Year)

Principal Investigator:
S. Poston

Project Manager
E.B. Nuckles
Metairie Site Office

Reporting Period: 10/01/90 - 09/31/91

## DISCLAIMER

LIST OF CONTENTS

## 6. LIST OF FIGURES

### 6.1 Subtask 1: Interpreting and Predicting Natural Fractures

6.1.1 Geological Studies

6.1.2 Geophysical Studies

6.1.2.1 Estimation of Fracture Orientations from Shear-Wave Splitting in the Lost Hills VSP



### 6.2 Subtask 2: Relating Recovery to Well-log Signatures

6.2.1 Geological Studies

immature zone, >40 ohm-m in the storage (accumulation) zone, and 10 to 40 ohm-m in the migration (reservoir) zone.

F 2 Residual water saturation in cores ($S_w$) as a function of true resistivity ($R_t$) in the Austin Chalk. Average resistivities of approximately 9 to 40 ohm-m define the potential reservoir sections which have 45% to 75% water saturation. Points denote mean values for the cored intervals; bars show the standard deviation of measurements. From Hinds and Berg (1990).

F 3 Well logs and fluid saturations in a vertical core of the Austin Chalk from the Pearsall field, Dimmitt County, Texas. The highly resistive zone in the lower Austin represents a storage zone of high oil saturation.

F 4 An area of Austin Chalk production in part of the Pearsall field, South Texas, showing locations of 5 vertical holes (7, 8, 10, 11, and 12) and 2 horizontal wells (9 and 13; HBL = bottom-hole location.) All wells were completed in the lower Austin Chalk. Fracture trends are inferred from seismic interpretation.

F 5 Inverse relationship between initial potential (bbl/day) and resistivity-ft ($R_t$ - h) for the perforated intervals of Austin Chalk. Well 12 was abandoned after producing less than 1000 bbl of oil.

6.2.2 Petroleum Engineering Studies

6.2.2.1 A Theory of Modeling Naturally Fractured Reservoirs

F 1 Some Common Types of Reservoir Heterogeneities
F 2 Scale of Fractured Medium

6.3 Subtask 3: Development of the EOR Imbibition Process

6.3.1 Laboratory Displacement Studies

F 1 Visual Imbibition cell
F 2 Imbibition by Circulation at Elevated Temperatures and Pressures
F 3 Laboratory Setup
F 4 Carbon Dioxide Solubility Curve
F 5 Arrangement for Precise Volumetric Measurements
F 6 Imbibition Comparison, 125 md Sandstone Core # 4
F 7 Imbibition Comparison, 389 md Sandstone Core # 2
F 8 Changes in Permeability and Oil Recovery in Sandstone Cores
F 9 Imbibition Comparison, 8.6 md Limestone Core # 5
F 10 Imbibition Comparison, 12.3 md Limestone Core # 12
F 11 Increase in Permeability in Limestone Cores
F 12 Reduction in Interfacial Tension
F 13 Effect of Temperature on Recovery
F 14 Effect of Carbonated Brine Concentration on Recovery

6.3.2 MRI Studies

F 1 Shapes of cores and blocks used for imbibition experiments and models. [8]
F 2 Typical production curve for imbibition. [22]
F 3 One dimensional imbibition process
F 4 Different models used in Aronofsky's studies

F 36 Oil saturation changes as a functiuon of time. Carbonated water was used
F 37 Carbonated water imbibition. a: Initial conditions, b: Displacement of oil from simulated fracture, c-k: Continued imbibition process, l: Conditions at the end of imbibition
F 38 Carbonated water imbibition. a: Initial conditions, b: After imbibition conditions, and c: After pressure depletion
F 39 Cumulative oil production obtained by imbibition of carbonated water
F 40 Profiles taken at initial conditions, at the end of the imbibition period that was allowed, and after the expansion of the $CO_2$ dissolved into the imbibed water. Sample A3 and reference sample 5 were used, see Tables 3 and 4
F 41 Profiles taken after the first, second, and third gas expansion. As a reference to the initial conditions see the previous figure
F 42 Profiles showing conditions at different stages relative to the initial conditions. Subtraction of profiles from the original conditions profile allowed to observe the movement of oil relative to its original position
F 43 Profiles showing conditions at different stages relative to the plain imbibition period allowed. Subtraction of profiles allowed to observe the movement of oil relative to a given condition, end of imbibition in this case
F 44 Cyclic carbonated water imbibition. a: Initial conditions, b: Displacement of oil from simulated fracture, c: Conditions at end of imbibition allowed, d: Conditions after first pressure depletion, e: Final conditions
F 45 Cyclic carbonated water imbibition. a: Initial conditions, b: Final conditions
F 46 Cumulative oil production obtained by imbibition of carbonated water. A cyclic imbibition and pressure depletion method was applied
F 47 Comparison of cumulative oil production using pure and carbonated water

6.3.3 CT Studies

F 1 Core I8 Scan 521
F 2 Core I8 Scan 522
F 3 Core I8 Scan 523
F 4 Core I8 Scan 524
F 5 Core I8 Scan 525
F 6 Core I8 Scan 526
F 7 Core I8 Scan 527
F 8 Core I8 Scan 528
F 9 Core I8 Scan 529
F 10 Core I8 Scan 530
F 11 Core I8 Scan 532
F 12 Core I8 Scan 533
F 13 Core I8 Scan 534
F 14 Core I8 Scan 535
F 15 Core I8 Scan 536
F 16 Core I8 Scan 537
F 17 Core I8 Scan 538
F 18 Core I8 Scan 539
F 19 Core I8 Scan 540
F 20 Core I8 Scan 541
F 21 Core I8 Scan 543
F 22 Core I8 Scan 544

6.3.4 Image Analysis

6.4 Subtask 4: Mathematical Modeling

F 1 Calculated and Laboratory Oil Recovery Performance (M = 1.0, Rate = 0.000787 STB/D)
F 2 Calculated Fracture Water Saturation Profile (M = 1.0, Lamda = 120, Rate = 0.000787 STB/D)
F 3 Effect of Viscosity Ratio on Fracture Water Saturation Profiles (Lamda = 120, Rate = 0.000787 STB/D)
F 4 Calculated Oil Recovery Performance (M = 1.0, Rate = 30 STB/D, Lamda = 0.01)
F 5 Calculated Water Saturation Profiles (M = 1.0, Rate = 30 STB/D, Lamda = 0.01)
F 6 Calculated Matrix Water Saturation Profiles (M = 1.0, Rate = 30 STB/D, Lamda = 0.01)
F 7 An idealized model of naturally fractured porous medium
F 8 The Jacobian matrix equation for oil pressure
F 9 Pressure Profiles in the Matrix and Fracture Systems

6.5 Subtask 5: Field Tests

F 1 Solubility of carbon dioxide in water, as a function of pressure and temperature.
F 2 Amount of carbon dioxide retained in solution as a function of water salinity.
F 3 Comparison of cumulative oil production due to unadulterated and carbonated water imbibition.

## 7. LIST OF TABLES

7.3 Subtask 3: Development of the EOR Imbibition Process



7.4 Subtask 4: Mathematical Modeling



7.5 Subtask 5: Field Tests

# 8. APPENDIX

8.1 Controls on Fracture Development, Spacing, and Geometry in the Austin Chalk.

8.2 Predicting Fracture Connectivity and Intensity Within the Austin Chalk from Outcrop Fracture Maps and Scanline Data.

# 1. ABSTRACT

Joint funding by the Department of Energy and the State of Texas has permitted a three year, multi-disciplinary investigation to enhance oil recovery from a dual porosity, fractured, low matrix permeability oil reservoir to be initiated. The Austin Chalk producing horizon trending thru the median of Texas has been identified as the candidate for analysis.

Ultimate primary recovery of oil from the Austin Chalk is very low because of two major technological problems.

- The commercial oil producing rate is based on the wellbore encountering a significant number of natural fractures. The prediction of the location and frequency of natural fractures at any particular region in the subsurface is problematical at this time, unless extensive and expensive seismic work is conducted.
- A major portion of the oil remains in the low permeability matrix blocks after depletion because there are no methods currently available to the industry to mobilize this bypassed oil.

The following multi-faceted study is aimed to develop new methods to increase oil and gas recovery from the Austin Chalk producing trend. These methods may involve new geological and geophysical interpretation methods, improved ways to study production decline curves or the application of a new enhanced oil recovery technique.

The efforts for the second year may be summarized as one of coalescing the initial concepts developed during the initial phase to more in depth analyses.

## 2.1 Subtask 1: Interpreting and Predicting Natural Fractures

### 2.1.1 Geological Studies

Detailed maps of the fracture traces on bedding planes in the mapped Austin Chalk outcrops were prepared. The maps showed the organized trends of the fracture development and hierarchical nature within the complete fracture system. These efforts were very useful to the development of a representative set of production decline type curves particular to a dual fracture-matrix flow system. Work for the next year will translate these efforts to subsurface interpretation.

### 2.1.2 Geophysical Studies

VSP data has been obtained for estimating fracture orientations from shear-wave splitting. Several programs had to be written to facilitate analysis of the data. Good progress had been achieved in fracture imaging.

## 2.2 Subtask 2: Relating Recovery to Well-Log Signatures

### 2.2.1 Geological Studies

Well-log response in Austin Chalk wells has been shown to be a reliable indicator of organic maturity. Work conducted during the previous year has been to digitize well logs in order to calculate average resistivity of producing zones and to correlate resistivity with production decline characteristics. These studies are still preliminary in nature, and it is still early to derive any significant conclusions.

### 2.2.2 Petroleum Engineering Studies

Additional production decline data were digitized to provide other interpretation examples for the dual permeability-matrix flow type curves developed during the first year. Darcy's law was modified in an attempt to account for the non-homogeneous internal structure of a fractured medium and the permeability contrast between the fractures and the matrix blocks. Work is continuing on this subject.

## 2.3 Subtask 3: Development of the EOR Imbibition Process

### 2.3.1 Laboratory Displacement Studies

Displacement studies were continued from the efforts of the previous year with the development and fabrication of a high pressure-high temperature core holder. Increased temperature was found to accelerate and increase oil recovery by the carbonated water-imbibition process.

### 2.3.2 MRI Studies

Image scanning studies have shown the carbonated water imbibition displacement process accelerates and increases recovery of oils which do not have appreciable asphaltenes. Experimental work conducted in a core saturated with an oil containing asphaltenes were halted because of pore blocking by ashphaltene deposition.

A study of recovery by cyclic carbonated water imbibition followed by reducing the pressure below the bubble point of the $CO_2$-water solution indicated the possibility of a new enhanced recovery method. Additional work is being conducted in this area.

### 2.3.3 CT Studies

Equipment has been constructed and tested which will allow long term imbibition studies to be conducted on 1 md core sample with the CT scanner.

Extent and arrangement of miro-fractures in Austin Chalk horizontal cores was mapped with CT scanning techniques. The degree of interconnection of the micro-fractures was easily visualized.

### 2.3.4 Image Analysis

Efforts continued during the year to upgrade our image processing capabilities. Additional memory was purchased in order to be able to process significant image arrays. We are currently able to visualize 2-D images in 3-D representations.

## 2.4 Subtask 4: Mathematical Modeling

Both the semi-analytical and numerical models for studying the imbibition flooding method have been developed. Model testing is continuing.

## 2.5 Subtask 5: Field Test

Two operators amenable to conducting a carbonated water flood test on an Austin Chalk have been identified. We are still evaluating the ability of their crude to not form asphaltene residue in the presence of $CO_2$.

# 2. EXECUTIVE SUMMARY

## 2.1 Subtask 1: Interpreting and Predicting Natural Fractures

### 2.1.1 Geological Studies

Characterization of Fractures in Outcrop

The field phase of this work is completed. Fracture orientations and spacings have been mapped relative to four major structural types found in outcrops along the Austin Chalk trend from Del Rio/Uvalde through San Antonio and Waco to Dallas (Figures 1 and 2).

Fracture maps

As part of the field work, detailed maps were made of fracture traces on bedding planes in the Austin Chalk at scales of 1:12 to 1:48. These maps were analyzed in detail during the 2nd year of this contract in part using undergraduates for data collection. Data on fracture length, orientation, and connectivity are presented in Wiltschko et al, (1991 and see Appendix 2, herein). Results confirm fracture spacing data collected at 14 field localities along scanlines placed on vertical outcrops.

Intact block geometry

Data from fracture maps at the Lehigh Quarry near Waco show that the bearing or long axes of intact blocks are bimodally distributed and are parallel to the orthogonal fracture patters in this ares where grabens parallel to the Balcones Fault Zone tend are cut by grabens at right-angles to that trend.

Fractal geometry

Data on fracture aerial density (parallel to bedding) from the fracture maps can be generalized by fractal geometry. While this work is not yet complete, it is clear that the fractures indeed are fractal (with an average fractal dimension (D) of 2.29 and range from 2.19 to 2.54) and with D independent of the orientations of the grids used to calculate D.

Fracture (vein) fillings

Veins in the Austin Chalk are partially or completely filled with calcite and a mixed-layer, smectite-illite clay. The details of our analysis of the vein fillings are to be found on pages 6 to 15 of the field guide for the AAPG field guide ( Corbett et al 1991b, herein Appendix 1). Comparison of vein geochemistry (clay abundance, trace elements and stable isotopic data [$O^{18}$ and $C^{13}$] with that of the host rock indicated extra-formational pore fluids, probably at abnormally high fluid pressure, were introduced into the chalk through natural hydraulic fractures, probably from the underlying Eagleford shale.

Fractures in cores of Austin Chalk

Through the kind cooperation of Pinnacle Oil Co. and the Exxon Corp., cores were examined from the vertical segment through the Austin Chalk of the Gise No. 1 well to determine the morphology and the nature of the fractures . Calcite-filled fractures, oriented normal to bedding were the most conspicuous fractures in the cores. At least one very clean and planar natural fracture was encountered (Figure 6a). Also significant and confirmatory of observations on outcrop are fractures that terminate in zones where the clay/organic content of the chalk increases (Figure 6b).

TABLE 1 - FACTORS CONTROLLING FRACTURES IN THE AUSTIN CHALK

Components of the Study

| A | B | C | D |
|---|---|---|---|
| Structural Stratigraphy of of the Austin Chalk | Characterization of Fractures in Outcrops Austin Chalk | Extrapolation of Fracture Data from Outcrops into the Subsurface | Relationship Between Brittle Rock Strength and Fracture Abundance in the Austin Chalk |
| Sponsor: Clayton W. Williams Oil Co. | Sponsor: DOE Contr. No. DE-FG07-89BC14444 $19,600 remaining in third year | Sponsor: Two proposals submitted for State Funds with data supplied by Schlumberger Well Services and their clients. Proposals pending for $24,456 and $59,723 | Sponsor: This proposal |
| Results:(1) Strength of chalk dependent primarily upon porosity and smectite clay content. (2) Atco and Big House members of the Austin Chalk are Chalk and most likely to contain abundant fractures in the subsurface. | Results: (1) Orientation of tectonic fractures characterized for open folds, drape folds, listric normal faults and graben-in-graben structures. (2) Data obtained from 1:12 to 1:48 maps of fractured horizontal surfaces and from horizontal scanlines on surfaces. (3) Data on fracture orientation, length, connectivity and spacing are in hand for five localities. (4) Correlations among compressive fracture strength, tensile strength, Young's Modulus and distortional strain energy suggest that rock fracturability can be predicted from sonic logs. | Approach: Correlate outcrop fracture data (in hand, column B) with fracture spacing and orientation data in the horizontal segments of boreholes drilled into the Austin Chalk as detected primarily with Schlumberger's Formation MicroScanner System. | Approach: Based on encouraging correlations (column B) it is proposed to: (1) Determine the sonic velocity and thereby Young's Modulus for a variety of Austin Chalk specimens. (2) Experimentally deform these same cylindrical specimens in the brittle regime and correlate fracture strength with Young's Modulus, and fracture strength with distortional strain enrgy. (3) Map induced ractures and their surface areas visually (using stereological principles) or with Magnetic Resonance Imagery and correlate this measure of fracture abundance with strength and Young's Modulus. (4) If correlations are positive and strong then there would be a sound basis for using sonic logs to identify potentially highly fractured units (beds) within the Austin Chalk or other potential fractured reservoirs. |
| Publication: Corbett et al, 1987. | Publications: Corbett et al, 1991a, 1991b, and Wiltschko et al, 1991 | | |

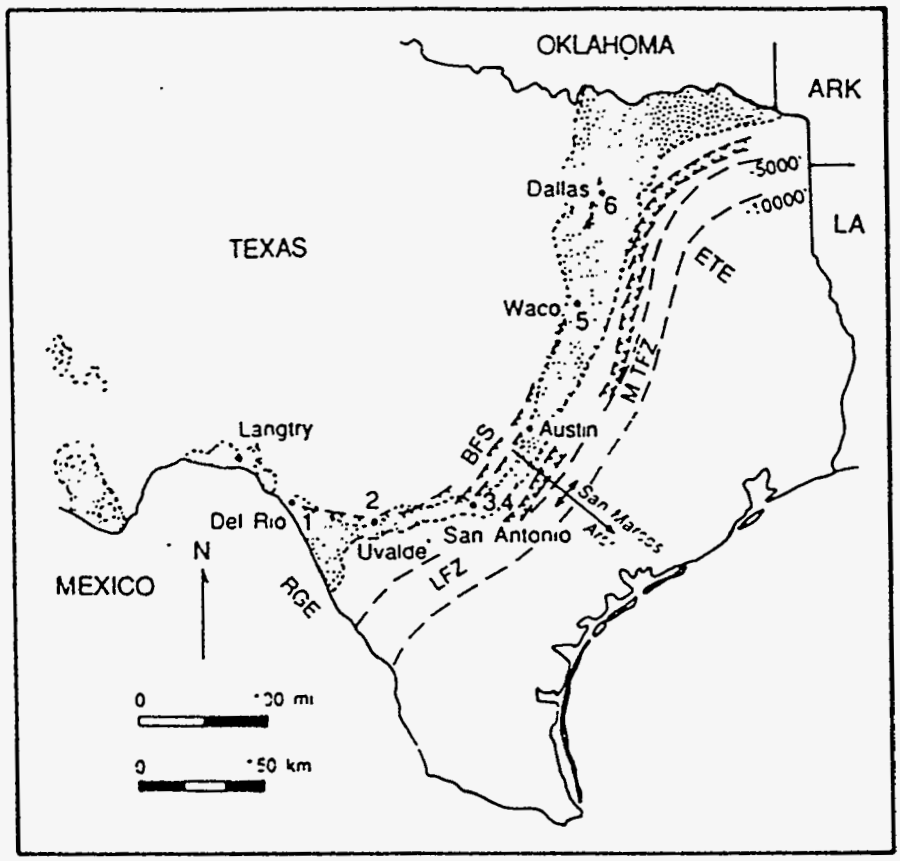


Figure 1. Location Map of Texas showing Austin Chalk outcrop trend with sample locations shown as open circles. Abbreviations: BFS = Balcones fault zone, LFZ = Luling fault zone, M-TFZ = Mexia-Talco fault zone, ETE= East Te;xas embayment, RGR = Rio Grande embayment. Sursurface structure contours (C.I. = 5000 ft) are on top of Austin Chalk. From Corbett et al (1987; reused with permission of the AAPG.

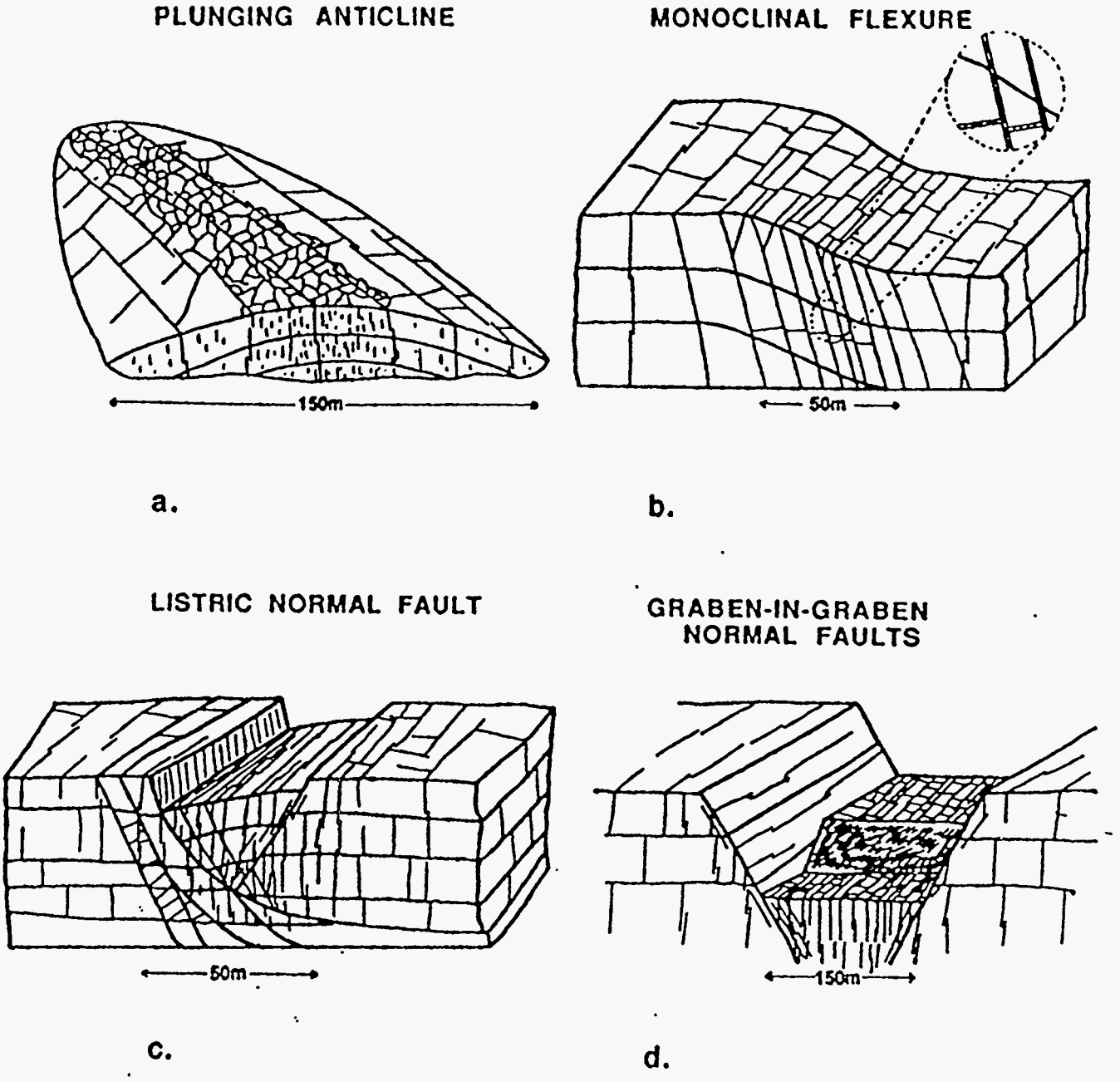


Figure 2. Schematic illustrations of four structural types and associated fractures found in outcrop along the Austin Chalk trend.

Extrapolation of outcrop data into the subsurface

The key question in using data from outcrops to predict or model potential or known naturally fractured reservoirs at depth deals with the degree to which outcrop data on fracture orientation, spacing, width, connectivity, bed-containment, relation to structural types, etc. can be extrapolated. Plans are being made to attack this critical problem with the aid of Schlumberger's Formation Microscanner data from the horizontal segments of wells drilled along the Austin Chalk trend.

Prediction of rock fracturability in the brittle regime

Within a given stratigraphic unit is it possible to determine from standard logs which intervals are most likely to be fractured in the subsurface. Accordingly, the hypotheses we wish to evaluate are: Young's Modulus (YM) correlates strongly with rock strength, and rock strength correlates with fracture abundance upon failure in the brittle regime. If these are true, then sonic and density logs might provide direct measures of rock strength in the brittle regime and hence of the fracturability of the rock, with the strongest rock being the most highly fractured upon deformation.

Work performed on Annex IV (Table 1, column B) and that published previously (Corbett et al, 1987) have provided encouragement to pursue evaluation of the above stated hypothesis. We need to add YM (from sonic velocity measurements) and strength data to the database for the Austin Chalk. We also need to improve quantification of fracture surface area induced in experimental deformed specimens as the measure of fracture abundance. While some work on this topic will be possible during the third year of this effort, funds for determination of the sonic velocities and for use of the XRAY CT imaging will require additional funding. Accordingly, an unsolicited proposal on this topic has been submitted to DOE/OBES.

Technology transfer

We have given special emphasis to communicate our results to industrial representatives. To date results have been presented in 3 publications (Corbett et al, 1991a, 1991b, and Wiltschko et al, 1991), on 1 AAPG field trip, and in 5 presentations with a 6th scheduled for October. In addition, Dr. Kevin P. Corbett had joined the Marathon Oil Co. and is actively involved in the exploration for naturally fractured reservoirs for that company.

### 2.1.2 Geophysical Studies

Estimation of Fracture Orientations from Shear-Wave Splitting in the Lost Hills VSP

During the past year we have concentrated our efforts on processing nine-component data from a Vertical Seismic Profile (VSP). The data used were donated by Mobil Research and Development Corporation, Dallas, TX through Mr. Cliff M. Edwards, their Manager of Geophysics Research.

We have written programs which allow us to: 1) stack the VSP data, 2) reorient the signals from down-hole geophones (using direction information provided by gyroscopes in the down-hole tool containing the three-component geophones), 3) edit and filter the individual traces, 4) generate signals for in-line and cross-line sources (from the original sources which were oriented at 45° with respect to the vertical), 5) rotate the source and geophone signals into the principal-axes orientations for the anisotropic, fractured medium and 6) determine the orientations of subsurface fractures based on the orientations of the principal axes. The results of this work are given in the accompanying report.

We are continuing our study of imaging fractures. The above results are part of

that study. We plan to analyze the nine-component data from Mobil Corporation to perform the fracture imaging and/or detection. We plan to use the surface data (sources and geophones both on the surface) to perform the fracture imaging and detection.

We will also be continuing work on the VSP data set because we have found that errors in the fracture orientations (inferred from the rotation of the data into the principal axes) are introduced because of imbalances in the sources (i.e., the individual sources are not of equal strength) and because of inconsistent geophone coupling. We are presenting the preliminary results of our work at the 61st Annual International Meeting of the Society of Exploration Geophysicists (SEG) which will be held on November 10-14, 1991 in Houston, TX. The title of the presentation is: 'The Effect of Source Imbalances on the Determination of Fracture Orientation From VSP Data," by Sangmoon Choi and Anthony F. Gangi.

The investigation of the seismic parameters was completed in the first year. The spacing of sources and sensors, the frequency response of sources and sensors, the energy of sources and the noise in the sensors were investigated. The effects of summing pulses in seismic arrays was the subject of an M.S. thesis (The Impulse and Wavelet Responses of Seismic Arrays, M.A. Benson, Dept. of Geophysics, TAMU, Dec., 1989) and of a presentation made at the 59th Annual International Meeting of the Society of Exploration Geophysicists held in Dallas, Texas Oct. 29-Nov. 2, 1989 (Paper No. S.A. 3.1: "Wavelet Response of Seismic Arrays"). The results of this study show the degradation in signal-to-noise ratio and resolution (due to loss of high-frequency energy) that results when pulses are not combined exactly in phase (i.e., coherently). While the results are given in terms of array responses, they are equally applicable to any seismic-processing operation (such as imaging) which involves the summation (or combination) of multiple seismic records or traces.

Good progress was made on fracture imaging during 1989-1990. Three seismic data sets were obtained. One was found to have poor signal-to-noise ratio and was discarded. The second data set had adequate signal-to-noise ratio and it was processed to improve its resolution by increasing the high-frequency content. The results of this work is the subject of an M.S. thesis by Eric Hudgens (Analysis of Vertical Resolution of Seismic Signals Associated with a Reservoir; Dept. of Geophysics, TAMU, Dec., 1991).

A third data set was acquired from Mobil Oil Company in 1990. This is a "nine-component" data set. This data set consists of three, orthogonal, displacement components from each of three, orthogonal, vector sources. These data consist of a Vertical Seismic Profile (VSP) survey and a seismic profile. The VSP data have been read into the computer and were processed to improve, as much as possible, the high-frequency content and resolution of the data. The data was "rotated" into the principal axes of the anisotropy existing in the test area (the test area was the Lost Hills Field in Kern County, California). Anisotropy in the horizontal plane is due to vertical fractures; vertical fractures are expected to be the dominant natural fractures in most oil fields (reservoirs). The analysis and interpretation of these data is the subject of a Ph.D. dissertation by Sangmoon Choi, a graduate student in the Geophysics Department of Texas A&M University (TAMU).

Work has begun on investigating seismic-wave-scattering mechanisms; however, little progress has been made to date and it is expected greater progress will be achieved in the coming year. Greater effort has been spent during the past year on fracture imaging than was anticipated. This effort was at the expense of effort on fracture scattering mechanisms. Also, the funded level of effort by the Principal Investigator was less than anticipated when the original proposal was written. The major part of his effort has been directed to supervising the graduate students working on the project.

Future research plans include continued processing of the "nine-component" seismic data set to determine the orientation of the principal axes of the fracture-induced

anisotropy and to image or detect fractures. In addition, mechanisms of wave scattering by fractures will be investigated.

## 2.2 Subtask 2: Relating Recovery to Well-log Signatures

### 2.2.1 Geological Studies

Well-log response in the Austin Chalk is a reliable indicator of organic maturity and of the reservoir zone, as established by previous studies (Hinds and Berg, 1990). Current work will establish the relationship of well-log response to productivity. Over 50 logs have been digitized in order to calculate average resistivity of producing zones and to correlate resistivity with production decline characteristics. In addition, two new cores of the Chalk have been examined to determine the nature of microfactures and their relation to organic content and to oil saturation in the rock matrix. Preliminary interpretation of log response and oil production indicates that average resistivities on the order 10 to 40 ohm-m characterize the reservoir zones of higher productivity. In contrast, resistivities greater than 40 ohm-m indicate that the mature petroleum is retained within the rock matrix, and that the zone has lower productivity.

### 2.2.2 Petroleum Engineering Studies

An attempt to improve the modeling of naturally fractured reservoirs is described. A modified Darcy's Law is proposed to take into account the non-homogeneous internal structure of a fractured medium and the high permeability contrast between the fractures and the matrix blocks. The resulting governing partial differential equation (PDE) by using the proposed flow equation is hyperbolic, instead of the conventional parabolic, type of equation possessing a wavelike solution. The primary advantage of the proposed approach is that only one flow field (for each phase) with build-in consideration of the non-homogeneous internal structure is required. The build-in feature in turn eliminates the uncertainty of the fluid interchanging term in the conventional concepts.

## 2.3 Subtask 3: Development of the EOR Imbibition Process

### 2.3.1 Laboratory Displacement Studies

Laboratory work to study imbibition processes comprised two phases. During the first phase imbibition tests were conducted at room temperature and atmospheric pressure. A visual imbibition cell was developed for this purpose.

The results of the first phase of the experiments have shown that the inclusion of $C0_2$ into the imbibed brine improves both the imbibition rate and the recovery efficiency. One percent (by weight) carbonated brine solution recovered an additional 15% of OOIP from a 9 md limestone core during 72 hours of imbibition.

The second phase of the experimental work, in progress now, is aimed to conduct imbibition experiments at higher temperatures and pressures. The effects of different concentrations of carbonated brine on imbibition rate and recovery efficiency are also being investigated.

A high pressure core holder has been developed and set inside the temperature regulated in-house built oven to conduct water imbibition experiments at higher temperatures and pressures. Water imbibition is conducted by circulating brine across one face of the core at a very slow rate. The system pressure is maintained by a back pressure regulator installed on the outlet line.

Partial results of the second phase of the experiments have shown further improvement in recovery. More experiments are being conducted to quantify these results.

The major factors affecting the increased recovery appear to be the increase in oil mobility due to reduction in viscosity, swelling of oil due to $C0_2$ dissolution, the introduction of a gas phase that acts as solution-gas drive, increased injectivity due to acidic nature of carbonated brine and the reduction of interfacial tension. These effects are more pronounced at higher temperatures and with higher concentrations of carbon dioxide. Higher temperature helps to decrease oil viscosity. Higher concentrations of carbon dioxide yielded improved recoveries due to enhanced solution-gas drive effects. Both parameters add more energy to the system but temperature increase has its limitations in field applications governed by the specific reservoir conditions.

### 2.3.2 MRI Studies

Conventional secondarty methods cannot be applied to fractured reservoirs because injected fluids channel though the fractures bypassing oil trapped in the matrix blocks. Water imbibition is an spontaneous mechanism that could be applied. The process exchanges oil inside the rock matrix for surrounding water filling the fractures. However, the process is very time dependent.

Oil distribution inside carbonated rock samples, and the effects of introducing $CO_2$ into the water being imbibed were studied using Magnetic Resonance Imaging or MRI. Oil saturation profiles and longitudinal images along rock sample were used to monitor water imbibition.

Different cases were studies: (1) Imbibition of unadulterated water; (2) Imbibition of $CO_2$ - enriched water; and (3) Cyclic $CO_2$ - enriched water imbibition and pressure depletion.

Introduction of $CO_2$ into the water being imbibed showed improvements in oil recovery rates during early times of the process. Pressure depletion caused expansion of gas dissolved into the imbibed water. Expansion of the gas probed to cause a substantial oil increase production.

Oil recovery by $CO_2$ - enriched water imbibition and pressure depletion were combined to develop a cyclic method that integrated the beneficial effects encountered at early times and gas expansion caused by pressure depletion. The cyclic method reduced recovery time to nearly one third of the time needed to produce similar amounts of oil by pure water imbibition.

### 2.3.3 CT Studies

Enhanced oil recovery from matrix blocks using $C0_2$ enriched brine in an imbibition process is being examined. The imbibition process objectives have been to design, construct, and test equipment for monitoring long term imbibition experiments using micro darcy matrix blocks. Actual reservoir rock will be used in these experiments, which should provide data to verify existing experimental results using simulated reservoir rocks. An effort is in progress to determine lengths and distributions of microfractures in the matrix blocks of naturally fractured reservoirs. A number of cores have been scanned and analyzed. A larger sample population is necessary for scanning. Several avenues are being pursued to provide this larger sample population.

### 2.3.4 Image Analysis

In recent years a lot of research has been made to improve the methods for

quantitative spectral analysis of NMR data. This need arose out of the fact that the classical treatment of Fourier transformation for obtaining spectra from signals recorded during an NMR experiment might be distorted due to widely different signal intensities, non-linear phase, partly overlapping signals etc. Linear Prediction and Maximum Entropy methods have given encouraging results. Presently we are working to design and develop an integrated simulator which would analyze the NMR data obtained from the laboratory experiments, by employing various processing methods. These methods in conjunction with Fourier transform spectra would enable us to draw more confident conclusions. This would also help to bypass some potential problems, inherent to Fourier transform spectral analysis technique.

### 2.4 Subtask 4: Mathematical Modeling

The purpose of this research is to develop mathematical a model to describe the imbibition recovery of a carbonated waterflood in naturally-fractured porous media. The mathematical modeling effort is divided into two parts. The first part deals with the development of analytical models for a parametric study of laboratory imbibition waterflood performance. The second part deals with the development of a compositional numerical simulator for field scale, carbonated-water imbibition flood in fractured reservoirs.

In this study, nonlinear integro-differential equation presented by de Swaan for plain waterflood has been modified in order to get the solution without the simplifying assumptions made by de Swaan and Kazemi et al. A new iterative semi-analytical technique was developed to solve the aforementioned nonlinear integro-differential equation. The solution method was improved using the Stehfest algorithm to invert from the Laplace domain to real domain. The effect of viscosity ratio was significant in determining the flood performance.

For the numerical simulation part a dual-porosity compositional simulator has been developed. The developed simulator is being tested with several hypothetical test cases presented in the literature.

### 2.5 Subtask 5: Field Test

A major producing operator has decided to test the usefullness of including $CO_2$ in a water injection treatment.

# 3. INTRODUCTION

## 3.1 Subtask 1: Interpreting and Predicting Natural Fractures

### 3.1.1 Geological Studies

During the last few years the technology for drilling horizontal boreholes has swept the petroleum industry and made possible new or revitalized oil booms in a number of states, but principally in Texas (Austin chalk), Montana (Bakken shale) and Alaska (Prudoe Bay, Permo-Triassic clastics), Utah (Cane Creek clastics) and Colorado (Niobrara limestone,and Mesaverde tight gas sands). In fact, the annual growth rate of horizontal drilling is nearly 300% in the US and close to 250% worldwide (Fritz et al., 1991, p. 34). Perhaps the most spectacular results have been experienced in the Austin Chalk trend (Figure 1a, b) where, as of September 1990, 261 horizontal boreholes had been drilled with productivities up to 5 times that of vertical wells and with initial potentials of as much as 5500 BOPD (IBID, p. 26, 33).

The primary purpose of horizontal drilling so far has been to intersect natural fracture systems in which the hydrocarbons abide and which are primarily oriented perpendicular to the sedimentary bedding. That is, in nearly flat-lying strata the fractures are vertical and thus are poorly sampled by conventional vertical boreholes. The chances of intersecting such fractures with a horizontal borehole are vastly greater, especially since it is now possible to control the azimuthal direction of the horizontal borehole and the depth of the horizontal segment of the hole so as to target beds within a 20-foot interval.

The minimum number of essential elements that must be predicted for a successful well in formations such as the Austin chalk are the (1) orientation of the best developed fracture sets relative to local and regional structure [so that horizontal segment of borehole can be directed perpendicular to the best developed fracture set], (2) fracture spacing (density or intensity), (3) fracture width, length and height and corresponding connectivity [with item 2 can serve as the basis of predicting productivity of the fracture system], and (4) stratigraphic intervals within the formation that are apt to be the most fractured [with the realization that horizontal boreholes can be targeted reliably to be drilled into 20'-thick stratigraphic intervals].

Accordingly, Subtask 1 is designed to gain insight into each of the 4 items listed above. While it is focussed on the Austin Chalk as an accessible, sight-specific example, the study also is generic and deals with the exploration of low permeability, naturally fractured petroleum reservoirs, and thus is national and world-wide in application. The overall scope of the effort is laid-out in Table 1. The current study currently is the best funded and the most advanced, which is important as it serves as the basis for further work.

### 3.1.2 Geophysical Studies

#### 3.1.2.1 Estimation of Fracture Orientations from Shear-Wave Splitting in the Lost Hills VSP

Shear-Wave Splitting

When shear waves propagate through an anisotropic medium, they split into shear-wave components which are oriented in the 'fast' and 'slow' directions. This splitting behavior is illustrated in Figure 1 where we show horizontally polarized shear waves travelling in the vertical direction in an anisotropic elastic medium having vertical fractures. Because of the vertical fractures, shear waves oriented with their motions

parallel to the faces of the fractures will have a high speed (fast waves) while those with their motions oriented perpendicular to the fracture faces will have a lower speed (slow waves). If the vertical extent of the fractures (that is, the thickness of the fractured layer) is sufficiently large, the fast and slow s-waves will be separated in time. The time separation will equal the layer thickness times the difference in the 'slownesses' (that is, the inverse of the wave speed) of the slow and fast waves.

This separation into the two components is called birefringence. From Figure 1 it can be seen that only the slow wave will be detected on a geophone oriented perpendicular to the fracture faces (i.e., oriented in the 'slow' direction) while only the fast wave will be detected on a horizontal geophone oriented parallel to the fracture faces (i.e., oriented in the 'fast' direction).

In Figure 1 the source orientation is at some angle to the 'fast' and 'slow' directions; consequently, both 'fast' and 'slow' waves are generated (as shown in the figure). If the source is oriented only in the 'fast' (or 'slow') direction, then only a 'fast' (or 'slow') wave will be generated. Then the 'fast' geophone will detect the 'fast' wave and there will be no signal detected on the 'slow' geophone (and vice versa when only the 'slow' wave is generated). Thus, for sources oriented in either the 'fast' or 'slow' directions, a hodogram (generated by taking the vector sum of the signals from the 'fast' and 'slow' geophones) will show rectilinear motion. This will be illustrated in greater detail later.

The 'fast' and 'slow' orientations (and the vertical direction) constitute the principal axes for this anisotropic medium. The orientation of the (horizontal) principal axes can be determined by finding those directions for the sources and geophones where there is no motion on the 'fast' (or 'slow') geophone when the source is oriented in the 'slow' (or 'fast') direction. The geophone (and source) pairs must be kept mutually perpendicular (because the principal axes of the most anisotropic elastic medium are orthogonal) and each geophone must be oriented parallel to one of the source directions.

In an isotropic medium, there would be no motion on the horizontal geophone which is perpendicular to a horizontal source. This is consistent with sources and geophones (in an anisotropic medium) oriented along the principal axes because, for an isotropic medium, the principal axes can have any orientation. That is, an indication of an anisotropic medium is the detection of shear waves on geophones oriented perpendicular to the sources.

Data Acquisition

The data used to study the fracture orientation using shear-wave splitting were donated by Mobil Research and Development Corporation, Dallas, TX through their Manager of Geophysics Research, Mr. Cliff M. Edwards. The data are a nine-component data set; that is, data from three-component geophones for sources oriented in three orthogonal directions. The data set consists of a Vertical Seismic Profile (VSP) where the sources were on the surface and the geophones in a well (at depths between 3600 and 7700 ft.) and a nine-component surface profile. In this study, only the VSP data set was used. The data were obtained from the Truman Fee Well in the southeast end of the Lost Hills Field, Kern County, CA (see Figure 2).

The data were obtained at 100-ft depth intervals for depths between and including 3600 and 7700 ft. The source location was approximately 500-ft west and 150-ft south of the well head. A plan view of the source and well-head locations are shown in Figure 3. Also indicated in the figure is the deviation of the well bore with depth. The deviation increases monotonically with depth to a maximum deviation of about 80-ft north and 130-ft west of the well head. The in-line direction (that is, the direction from the source to the well head) is approximately N73°E. The cross-line direction is perpendicular to the in-line direction and it is N17°W.

The seismic source is a truck-mounted air gun (Bolt Omni-Pulse). The air gun is in a vertical plane oriented either in the in-line or cross-line direction and is directed at 45° with respect to the vertical. The source is moved in the vertical plane by 90° and fired again while the truck is in the same position. Vertical, in-line and cross-line sources are generated from these sources by adding (to get the vertical source) and subtracting (to get the horizontal in-line and/or cross-line source) the signals from these ('left' and 'right') sources (see Figure 4).

The data acquisition parameters used in obtaining the data are given in Figure 5. Multiple firings ('pops') of the air gun were used for each depth to improve the signal-to-noise ratio. Larger numbers of pops were used at the greater depths to compensate for the spherical spreading and attenuation of the wave with depth.

10 Hz (Oyo Corp.) geophones were used and the data were sampled every 2 milliseconds for a record length of 4 sec. Gyroscope data were also recorded at each position in the well so that the 3-component geophones could be properly 'oriented' by combining their signals. In addition, a 3-component geophone was placed next to the baseplate of the source and its output recorded to detect changes in the source signals.

Preprocessing

The steps taken in the preprocessing operation are shown in Figure 6. After reading the data from the tapes into the computer, the traces were edited to eliminate bad traces. The multiple pops for each level were added together (stacked) and the signals for the horizontal (in-line or cross-line) and vertical (downward) sources were generated by subtracting and adding the traces for the 'left' and 'right' sources, respectively, as indicated earlier.

The results of performing these operations for the horizontal components (the x and y phones) are shown in Figure 7. We start the data traces at 1600 ms where the direct s-waves begin. The p-waves occur at earlier times in the traces and are not shown here because the s-waves are those used to determine the fracture orientation. In Figure 7 we see that the first-arrival, s-wave waveforms are variable both in amplitude and time. Also, there are signals on all four components (the signals in the x and y phones for the in-line and cross-line sources). This would be expected if the geophones are not oriented parallel and perpendicular to the source directions. The geophone can be oriented using the gyro data recorded for each geophone position.

The results obtained after 'gyro rotation' are shown in Figure 8. Note now the smooth variation of the first-arrival signals with depth. However, also note that the cross-diagonal components (the signals from the cross-line receiver for the in-line source, and vice versa) are not zero as would be expected if the medium were isotropic and laterally homogeneous. While some of the cross-diagonal signals may be due to scattering from heterogeneities, the major part of these signals is due to the anisotropy introduced by vertical fractures.

Hodograms generated using the in-line and cross-line geophone signals of Figure 8 are shown in Figure 9 for the in-line and cross-line sources. The same hodograms would be generated using the x- and y-phone signals of Figure 7. The hodograms are generated by the locus of the end of the vector (in the horizontal plane) obtained by the vector addition of the signals from the in-line and cross-line geophones. If the medium was isotropic, the hodograms would show rectilinear motion in the source direction only. The motions for the cross-line source, in particular, are strongly non-rectilinear and neither hodogram is oriented in the direction of its source. This is a clear indication that anisotropy may exist.

## 3.2 Subtask 2: Relating Recovery to Well-log Signatures

### 3.2.1 Geological Studies

The Austin Chalk is both a source rock for petroleum and a fractured reservoir. Average resistivity of the Austin Chalk is a reliable indicator of organic maturity and can be correlated with water saturation of the rock matrix (Hinds and Berg, 1990). Furthermore, it appears that reservoir zones can be identified by log response, and it is possible that productivity also can be related in a general way to the average resistivity of the reservoir section. Therefore, well logs, production data, and cores have been collected to interpret the relationship of log response and oil production.

### 3.2.2 Petroleum Engineering Studies

#### 3.2.2.1 A Theory of Modeling Naturally Fractured Reservoirs

A naturally fractured reservoir has two major features. First, a fractured medium is comprised of two types of sub-medium, fracture and matrix blocks. The properties associated with each sub-medium are quite different. Second, the internal structure (e.g., fracture-matrix geometry, connectivity, ...) is quite complex. In most times, such an internal structure is non-homogeneous. The above two features impose great difficulties (and also present a challenge) in the modeling of a naturally fractured reservoir.

In Figure 1, several common types of reservoir heterogeneity involving at least two sub-media are presented. Major direction of heterogeneity (vertical, lateral or combination) and major fluid flow direction (parallel, series or combination) are also identified. Both reservoir heterogeneity and fluid flow directions referred are macroscopic sense instead of microscopic (pore-grain) scale. Some examples/nomenclatures appearing in the subsurface engineering literature (petroleum, geophysics, geology, civil, soil, ...) are also given. For the same comparative scale, the bottom figure of Figure 1 is far more complex than the others as internal structure is considered.

The first model concerning naturally fractured reservoirs is Barenblatt's[1,2] overlapping-continuum (dual-porosity) theory. The essence of Barenblatt's theory is that both fracture and matrix sub-media are treated as continua. Two fluid pressures, corresponding to the fluid in the fracture and that in the matrix blocks, at each mathematical point (space and time) are proposed. The fracture and matrix pressure fields are then superimposed (overlapped) and are coupled by a fluid interchanging (crossflow) term. No specific fracture-matrix geometries are assumed since the intended model scale is relatively large such that the fracture-matrix geometries lose their identities after imposing the overlapping-continuum assumption.

The existence of dual-porosity (i.e., fracture and matrix) is physically correct for a naturally fractured reservoir. Actually, all the heterogeneity types shown in Figure 1 qualify "dual-porosity" in a very loose sense, i.e., involve at least two different porosities (and hence permeabilities). Two major conceptual difficulties/doubts, however, arises from Barenblatt's fundamental overlapping-continuum concept:

1. It is difficult to visualize two pressures at each point; and
2. The permeability required to calculate flow rate is difficult to define since two pressure fields are overlapped.

The first conceptual difficulty is the result of treating the fracture and matrix blocks as overlapped continua. The assumption of overlapping-continuum has been used (but seldom stated explicitly) in continuum-based multiphase fluid flow problems. In this connection, an equivalent statement to the first conceptual difficulty is that can we treat

both fracture and matrix blocks as continua. The answer depends on the distribution of the fracture-matrix blocks and the scale of the problem interested. The more uniform the distribution of the fracture-matrix blocks, the smaller the matrix blocks and the larger the scale of the problem domain, the more valid the overlapping-continuum assumption. It should be mentioned that this conceptual difficulty may be minor if one considers that the difference between the two "overlapped" pressures will disappear after certain transient time.

The second difficulty always exists. For example, should the permeability of one sub-medium be defined "independently" or "dependently" of the existence of the other sub-medium. (A typical example of permeability "dependency" is the relative permeability concept in the multiphase fluid flow problem.) Actually, how to "correctly" define all the properties attached to each sub-medium (which is to be overlapped with the other) is difficult. The same difficulties will be carried over and even enlarged as multiphase (or multicomponent) flow involving more complex mechanisms is considered. For example, should the relative permeability curves of the sub-media be independent or dependent of each other. In other words, how to "overlap" two (fracture and matrix blocks) relative permeability curves assuming they can be specified individually.

Barenblatt[1,2] further simplified his dual-porosity theory by neglecting the storage capability of the fractures and the macroscopic permeability of the matrix blocks. Warren and Root[3] made similar simplification except the storage capability of the fractures are retained. It turns out that these simplified theories[1-3] relaxed, more or less, the difficulties addressed above, however, not completely.

Two works, Refs. 4 and 5, attempted to refine Barenblatt's dual-porosity theory with emphasis on the fluid interchanging term. Wijesinghe and Culham[4] derived a generalized theory to relax the steady-type interporosity flow assumed by Barenblatt.[1,2] Chen *et al.*[5] further simplified the theory of Ref. 4 and proposed an analytical transient interporosity model. Since the main framework of Refs. 4 and 5 is based on Barenblatt's overlapping-continuum concept, the inherent two difficulties addressed earlier are still remained.

There is another type of dual-porosity model which does not invoke the overlapping-continuum concept, however, requires exact specification of fracture-matrix geometry (i.e., inner structure).[6,7] By specifying the exact inner structure of a fractured medium, which is the most uncertain part in modeling, the problem essentially becomes not only tractable but also, in most cases, solvable. This is especially true for the modeling of fluid interchanging term. Specifically, the inner structure of a fractured medium is represented by certain simple repetitive patterns such as layered, cubic or spherical matrix blocks isolated by the fractures. In other words, the inner structure is assumed to be homogeneous. The major difficulty of such exact geometry models is that the assumed fracture-matrix geometry may not be consistent with field observations. Furthermore, macroscopic matrix permeability is neglected unless layered fracture-matrix structure is assumed (see third figure of Figure 1).[6-8] It should be emphasized that the second difficulty encountered in the Barenblatt's theory may also exist in this type of model if the fracture-matrix geometry is a "mixture" type. An example of the "mixture" type is cubic or spherical matrix blocks isolated by fractures and are distributed over the entire flow domain.

Another dual-porosity model which is worth mentioning is the "dead-end" pore volume concept proposed by Fatt[9] in 1959. Barenblatt's simplified dual-porosity,[1,2] Warren and Root's[3] and exact fracture-matrix geometry models[6,7] conceptually are the same as Fatt's[9] "dead-end" concept since neglecting the macroscopic matrix permeability

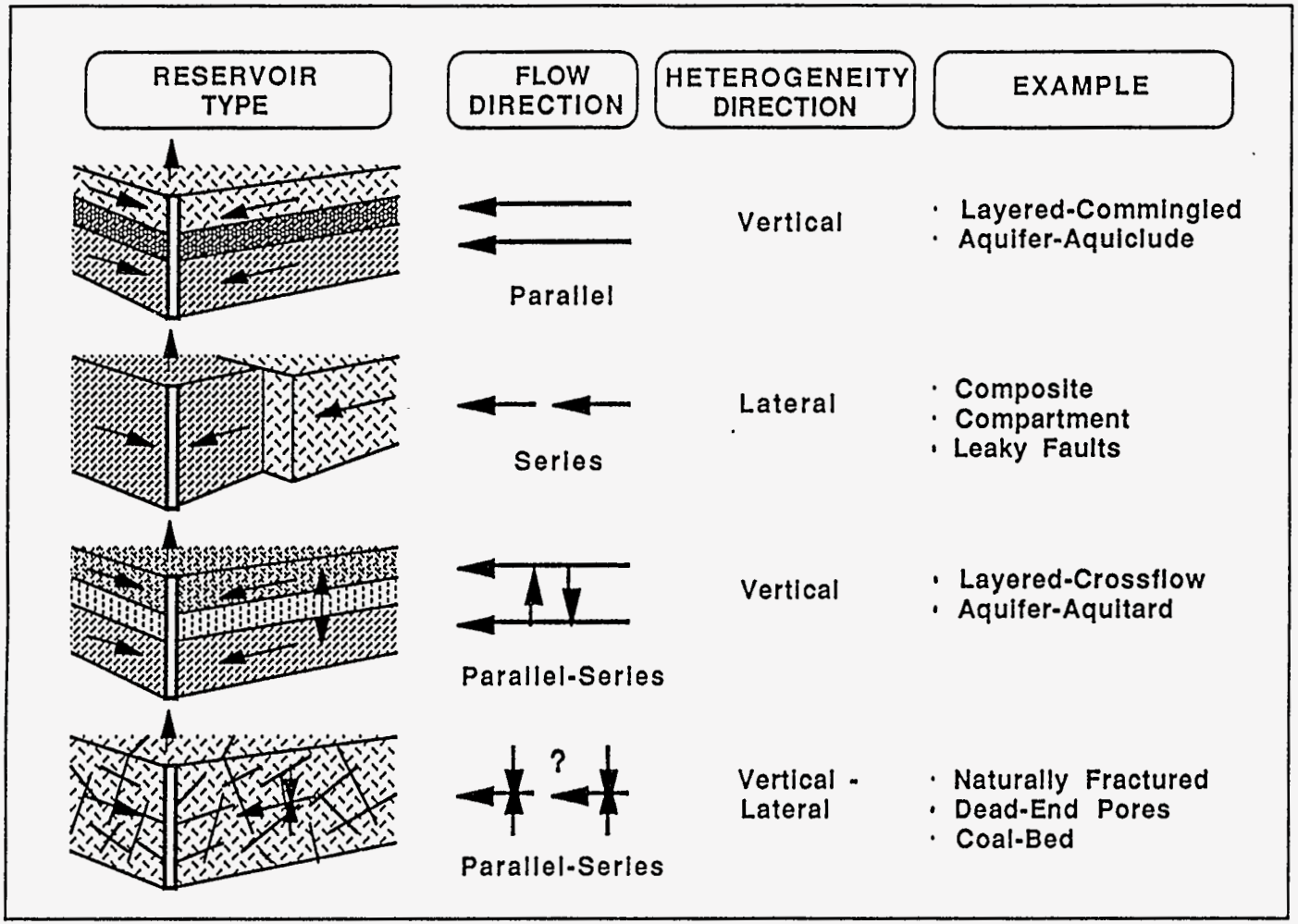


Fig. 1 - Some Common Types of Reservoir Heterogeneity.

is equivalent to stating that the matrix blocks are the dead end pores. Indeed, the experimental results presented in Ref. 9 showed all the characteristics of a typical dual-porosity behavior. Fatt[9] also pointed out the conditions under which a source term is required to be included in the governing differential equation.

Both overlapping-continuum and exact fracture-matrix geometry models involve a fracture-matrix fluid interchanging term. A common and logical issue is that how to "correctly" describe this fluid interchanging term. Theoretically, the answer for this argument is simply how detailed the reservoir description is. In practice, however, a "correct" modeling of fluid interchanging term, actually the entire problem, is either prohibitive or infeasible due to the uncertainty in the internal structure.

Since the introduction of the dual-porosity concept, most research efforts concerning naturally fractured reservoirs follow, more or less, along the line of the above reviewed fundamental concepts. In this study, a quite different concept is explored to relax certain difficulties discussed earlier. Specifically, the proposed concept has the following features: (1) single pressure field (per phase) at each point; (2) no explicit fracture-matrix geometry is assumed; (3) no fluid interchanging term. In view of the above three features, a compromise is more or less made between the existing concepts reviewed earlier.

## 3.3 Subtask 3: Development of the EOR Imbibition Process

### 3.3.1 Laboratory Displacement Studies

Many techniques have been investigated in the laboratory and the field for improving oil recovery. The most common techniques used to produce from the reservoirs to yield maximum recovery include water injection, steam injection, in-situ combustion, chemical flooding and caustic injection. Currently, however, due to its wide applicability, there is a great deal of interest in carbon dioxide ($CO_2$) for the recovery of both light and heavy oils.

Several mechanisms play a role when the carbon dioxide gas flooding method is used to increase oil recovery. These mechanisms are dependent on reservoir temperature, displacement pressure and the properties of the reservoir rock and the crude oil.[1] $CO_2$ has many therapeutic effects which enhance oil recovery. $CO_2$ lowers oil viscosity, adds gas into solution for oil swelling, provides an additional gas drive, initiates potential miscibility and reduces interfacial tension.

Conventional EOR methods cannot be employed to solve the inherent recovery problems in low permeability, naturally fractured reservoirs. Oil production from such reservoirs tends to be only from the oil accumulated in the natural fractures.[2] A large amount of oil is left in the matrix after primary production has been exhausted. The largest fractured reservoirs in Texas are low permeability, naturally fractured limestone reservoirs, such as the Austin Chalk. The extensive interconnected fracturing prevents using traditional flooding methods because of channeling of the injection fluids along the fracture planes.

$CO_2$ gas injection (huff 'n' puff) has been successfully applied in various types of reservoirs. The injection may initiate oil displacement by a number of mechanisms. $CO_2$ miscibility with oil is a function of pressure. It is not usually miscible with reservoir oil upon initial contact, but it may create a miscible front similar to the composition of the lean gas. $CO_2$ displacement may resemble an enriched gas drive process depending on reservoir conditions. It has also been useful in heavy oil reservoirs where thermal methods may not be applied.

The proposed solution is a method applicable to low permeability, fractured reservoirs that can increase oil production. The water imbibition rate can be increased

by using carbonated brine in place of water. Carbonated brine imbibition will also increase the recovery efficiency by displacing immovable oil. Therefore, oil production can be increased substantially by improving the imbibition rate and the recovery efficiency by using carbonated brine. The aim of the experimental work is to blend both, $CO_2$ injection and water imbibition methods and acquire a technique suitable for enhancing oil recovery from low permeability, fractured reservoirs.

$CO_2$ beneficially affects various properties which result in enhancing oil recovery and recovery rate. The interactions of $CO_2$ with oil, rock and brine are reviewed below:

Swelling of Oil

$CO_2$ is highly soluble in hydrocarbon oils, which depends upon the saturation pressure, reservoir temperature and composition of the crude oil. Johnson *et al.*[3] MacFarlane *et al.*[4] and Breston *et al.*[5](1954) reported up to 35 % increase in Bradford crude oil volume when $CO_2$ was transferred from carbonated water into the oil phase. Miller and Jones[6] (1981) reported that for 17 °API crude oil, over 700 SCF of $CO_2$ was dissolved in one barrel of oil, which yielded 10 to 30 % increase in volume. Swelling is important because the residual oil left in the reservoir after flooding is inversely proportional to the swelling factor; i. e, the greater the swelling, the less stock tank oil will be abandoned in the reservoir.

Viscosity Reduction

A large reduction in the viscosity occurs when $CO_2$ gas is dissolved into a crude oil. This reduction can yield viscosities one-tenth to one-hundredth of the original viscosity. The reduction in viscosity is important because it can profoundly affect recovery efficiency in tight matrix reservoirs where oil mobility is a problem. Miller and Jones[6] (1981) noted a large percentage reduction occurred in the viscosity of more viscous crudes. The viscosity of the more viscous crude was reduced from 120 cp to 10 cp (a twelvefold decrease) while the viscosity of the less viscous crude was reduced from 18 cp to 6 cp (a threefold decrease) at a saturation pressure of 1,000 psia. The viscosity reduction and its effect on mobility ratio are more significant in medium and heavy oils and not as large in low viscosity oils. Similar effects for higher viscosity crudes (> 20 cp) has also been reported by Holm[7] (1963) and de Nevers[8] (1966).

Solution Gas Drive

$CO_2$ injection causes an increase in the reservoir pressure and may create a miscible front. Gas comes out of the solution which acts as an additional reservoir energy when pressure drops after the termination of the injection phase of a flood. This mechanism of blowdown recovery is similar to solution gas drive during the normal production depletion of an oil field. Holm and Josendal[9] (1979) have shown that up to 18.6% of oil in place can be recovered by $CO_2$ solution gas drive, while Wang and Locke[10] (1980) found blowdown recoveries from 4.73 to 8.55% for a Drake mineral oil system.

Increased Injectivity

$CO_2$-water mixtures are slightly acidic and react accordingly with the formation matrix. Carbonic acid stabilizes clays in shales due to a reduction in pH:

$$CO_2 + H_2O \rightarrow H_2CO_3$$

Injectivity is improved by partially dissolving the reservoir rock according to the following reactions in carbonates:

$$H_2CO_3 + CaCO_3 \rightarrow Ca(HCO_3)_2$$

and

$$H_2CO_3 + MgCO_3 \rightarrow Mg(HCO_3)_2$$

The produced bicarbonates are quite soluble in water, which may cause a permeability increase by dissolving the matrix in carbonate rocks. Flooding a core sample of calcareous rock with carbonated water resulted in a threefold increase in permeability after injecting forty pore volumes.[11] Additional work has been completed by Ross et al.[12] (1982) on North sea calcareous sandstones.

The dissolution of carbonate materials may free unreacted reservoir fines to flow and later to plug down-stream pore channels and may cause reduction in injectivity. Plugging due to the precipitation of calcium sulfate or asphaltenes may also offset any injectivity gains by the reaction of carbonate materials, causing a reduction in permeability. Similar results have been reported by Sayyegh et al.[13](1990) after conducting experiments on Pembina Cardiam, Alberta, sandstone cores.

Reduction in Interfacial Tension and Capillary Retention

A reduction in the interfacial tension between water and oil leads to better mobilization efficiency. The reduction of capillary retention of oil on rock face has been reported by Grape, S.G.[2] (1990) and others. His observations indicated that carbonated water reduced interfacial tension and the acidic nature of the water beneficially altered the rock wettability, by making the cores more water wet and yielding increased recovery.

### 3.3.2 MRI Studies

Austin Chalk and Spraberry trends of Texas are composed of dual porosity producing systems. Reservoirs in these trends show one or more fracture systems, and at least one set of low permeability matrix blocks. This type of reservoir presents a major problem for enhanced oil production. Secondary oil production comes mainly from the fractures. Large amounts of oil are left in the matrix when oil is produced from the fractures system. If a conventional secondary recovery method is attempted, the injected fluids tends to follow the fractures or high permeability avenues, bypassing large amounts of oil trapped in the matrix. Oil trapped inside the matrix blocks is produced only by water imbibition.

Water imbibition is a spontaneous process that interchanges oil inside the rock matrix with surrounding water that fills the fractures. This interchange of fluids depends on several parameters: rock porosity and permeability, wettability of the reservoir, interfacial tension between the reservoir fluids, etc. Time is also an important parameter because water imbibition is a very time dependent process.

$CO_2$- enriched water imbibition flooding has been suggested as a method to accelerate production rates and to improve ultimate recovery from fractured reservoirs. This method is based on several theoretical considerations. Preliminary studies of the method show improvements in production and recovery. [1] Although the method has shown excellent results in small rock samples, more detailed studies are always needed.

The present research project investigated the applicability of $CO_2$- enriched water imbibition to improve oil production from fractured reservoir.

Magnetic Resonance Imaging, MRI, was used to study movement of oil and water inside rock samples during imbibition. A new core holder had to be developed in order to apply MRI techniques. Conventional high pressure core holders made of stainless steel could not be used because magnetic signals are blocked by the metal. Fiberglass tubing was used as the main body of the new vessel. The new MRI core holder was successfully used to monitor imbibition at a maximum working pressure of 2000 psi.

MRI requires that Deuterium Oxide, $D_2O$, be used in place of distilled water. $D_2O$ and $H_20$ have the same properties for the purposes of this study. $D_2O$ was mixed with $CO_2$ at different pressures to obtain different concentrations. The maximum mixing pressure used was 500 psi. Solubility of $CO_2$ was assumed to follow a theoretical curve presented by Wiebe.

Limestone samples of one inch in diameter and three inches in length were used. Porosities ranged from 25.4 to 26.6 percent and permeabilities from 11.7 to 13.9 md. kerosene was used as the oil phase. Irreducible water saturation was reached with oil saturation ranging from 33.6 to 46.0 percent.

Relatively small rock samples combined with little changes in oil saturation prevented an accurate measurement of the effluent . Proton profiles were used to monitor oil saturation along the core sample. Changes in these profiles allowed a very accurate measurement of the oil being produced. Cumulative oil production curves were acquired by subtracting proton profiles to obtain the amount of oil produced at a given time.

Cumulative oil production curves obtained using the method previously described have shown oil production and ultimate oil recovery improvements.

### 3.3.3 CT Studies

Distribution of microfractures in the matrix blocks of naturally fractured reservoirs is an important parameter necessary for accurate model development. Investigation of this important parameter heretofore has only been possible through destructive testing of the representative sample. The use of CAT scans to study representative samples is an essential tool in the mapping of microfracture distribution.

$CO_2$ enriched imbibition, using imaging techniques, has been previously studied by other investigators. However, these studies have all used representative rocks because of extended experiment durations with actual samples. Use of CAT scans to study this process with actual specimens is possible and will allow verification of short term experimental results.

### 3.3.4 Image Analysis

Nuclear Magnetic Resonance (NMR) has long been used in the oil industry as a research tool for the measurement of petrophysical properties such as porosity, fluid saturation, permeability etc. NMR imaging(MRI) adds the extra feature of the possibility of three-dimensional visualization of two miscible fluids in the porous media.

MRI experiments were conducted on limestone samples of one inch in diameter and three inch in length to study movement of oil and water inside the rock sample during

imbibitions. $D_2O$ was used in place of distilled water, so that the net signal intensity was a function of hydrocarbons present in the core sample. The MRI experiments showed oil production and ultimate oil recovery improvements. These experiments are being run again with a different sequence of spins to obtain $T_1$ measurements. These measurements would help us in quantifying MRI results. The prinipal parameter under investigation is oil saturation. If we are to achieve our objective then obtaining on ly the global $T_1$ would not serve our purpose. At this stage we are trying to obtain $T_1$s for different slices of the sample and deduce oil saturation profiles based upon these local $T_1$s. The experiments are under way so no data is available at this stage to furnish results. However, different spectral analysis techniques are being studied to draw confident results. This is because $T_1$ measurements are local and therefore very much susceptible to noise. For this reason Fourier transform alone cannot be trusted to obtain NMR spectral parameters.

In recent years new quantitative methods for analyzing the NMR data have been introduced. This review is focused on the applicability of these methods and some potential problem in drawing conclusions based upon one of these, while disregarding the others.

The primary goal of a spectroscopic experiment is to obtain an estimate of the frequency response function of a certain molecular system. In the continuous wave NMR experiment this is done directly by recording the output while the frequency of the rf field (or the strength of the **Bo** field ) is varied slowly. In the case of rf pulse approach, the impulse response F(t) (i.e. the free induction decay (FID)) is monitored as a function of the time t, and the frequency response function s(v) is calculated by applying the identity:

$$s(v) = \int_{-\infty}^{\infty} f(t)\exp(-i2\pi vt)dt$$

Thus the frequency response function is the Fourier transform of the impulse response. However, since f(t) is sampled for a finite period of time, only the Discrete Fourier transform (DFT) can be obtained, i.e.

$$S\left(\frac{m}{N.\Delta t}\right) = \sum_{k=0}^{N-1} F(\Delta t.k)\exp(-i2\pi mk/N)$$

t being the sample interval and N the number of sampled points.

If the relaxation process can be considered to be a first order process, the theoretical response will be a sum of decaying exponentials:

$$f(t) = \sum_{j=1}^{p} I_j \exp((i2\pi v_j - R_{2j})t + \varnothing_j)$$

where $I_j$ is the amplitude of the j'th response, vj the chemical shift, $R_{2j}$ the transverse relaxation rate, and $\varnothing_j$ the phase.

3.4 Subtask 4: Mathematical Modeling

Many analytical and numerical mathematical models for fluid flow in fractured reservoirs were presented by several authors.[1-8] de Swaan presented an analytical model to describe the water displacing oil process in a fracture surrounded by matrix blocks using a integro-differential equation. In order to linearize the nonlinear equation, fractional flow of water is equal to the water saturation at the same spatial point was assumed. Kazemi et al [2] improved the analytical solution technique over that presented by de Swaan and attempted to get the solution with numerical method as well. The good match was obtained by both solution methods.

The first compositional simulator was presented by Peng et al. [8] The dual-porosity approach was used. Implicit in pressure and explicit in saturation (IMPES) method was applied.

In this study, the analytical solution technique was improved over that presented by de Swaan and Kazemi et al in solving nonlinear integro-differential equation. Due to the limitations associated with the analytical modeling and the complex oil recovery mechanism involved in carbonated waterflooding in fractured porous media, numerical modeling is necessary to describe the such oil recovery mechanism effectively.

## 3.5 Subtask 5: Field Tests

Field test are being designed and implemented. Field test must be conducted to develop the practical merits of the new enhanced oil recovery concept. Results of the tests will be included in future reports.

# 4. DISCUSSION OF RESEARCH

## 4.1 Subtask 1: Interpreting and Predicting Natural Fractures

### 4.1.1 Geological Studies

Characterization of fractures in outcrop

The field phase of this work is completed. Fracture orientations and spacings have been mapped relative to four major structural types found in outcrops along the Austin Chalk trend from Del Rio/Uvalde through San Antonio and Waco to Dallas (Figure 1 and 2). Included in this database are information on fracture spacing from 14 horizontal scanlines placed along vertical outcrops of the chalk at various angles to the regional and local structural trend ( Figure 3 and 4). In addition 6 detailed maps of fracture traces on bedding planes were prepared (e.g., Figure 3). A paper on part on this phase of the work and was presented at the Austin Chalk Exploration Symposium sponsored by the South Texas Geological Society, February 24 - 26, 1991 and the corresponding paper was published as part of those proceedings (Corbett et al, 1991a). This work was also presented in our First Annual Report for the current contract.

Fracture maps

As part of the field work, detailed maps were made of fracture traces on bedding planes in the Austin Chalk at scales of 1:12 to 1:48 (e.g., Figure 3). These maps were analyzed in detail during this 2nd year of this contract. The map data on fracture length, orientation, and connectivity are presented in Wiltschko et al, (1991 and see Appendix 2, herein). Typical results are as follows: At Tequesquite Creek (30 miles SE of Del Rio), major fracture sets are oriented N50°E and N30°W. These sets bound and drain randomly oriented smaller largely curved fractures (Figure 3). Fracture spacing is negatively exponential with >95% of the fractures spaced less than 15-inches apart. Accordingly, data from the detailed fracture maps of fracture traces on bedding planes confirms similar data acquired along horizontal scan lines placed on vertical outcrops at fourteen locations along the outcrop trend (Figure 4a,b).

The number of fracture intersections or connections per foot (average of about 5 intersections per foot) are nearly randomly distributed, i.e., fracture intersections are independent of fracture orientation. At San Antonio, Old Alamo Quarry, the point is illustrated that fracture intersections decrease as the strength of the orientation of a single major fracture set increases. In this quarry intersections are down to 1.4 per foot in areas where the fracture-set orientation is well ordered. Fracture spacing also is wider there with only about 50% of the fractures spaced less than 15-inches apart. At Waco, where two well-ordered orthogonal fracture sets are developed (see Figure 2, graben-in-graben structure), the fracture density is up, average of 6 per foot and the fracture intersections are independent of fracture orientation.

Fractal geometry

The fracture maps were analyzed further to deter-mine if the fractures could be generalized by fractal geometry and what the orientation of intact blocks, bounded by fractures, might be in a complex pattern such as found in the "graben-within-graben" geometry at Waco. While this work is not yet complete, it is clear that the fractures indeed are fractal (with an average D = 2.29 and range from 2.19 to 2.54) and that the long axes of intact blocks at the Leigh Quarry in Waco are bimodally oriented with peaks orthogonal to one another just as suggested by the overall fracture pattern reflecting the 90°-crossed grabens( Figure 2).

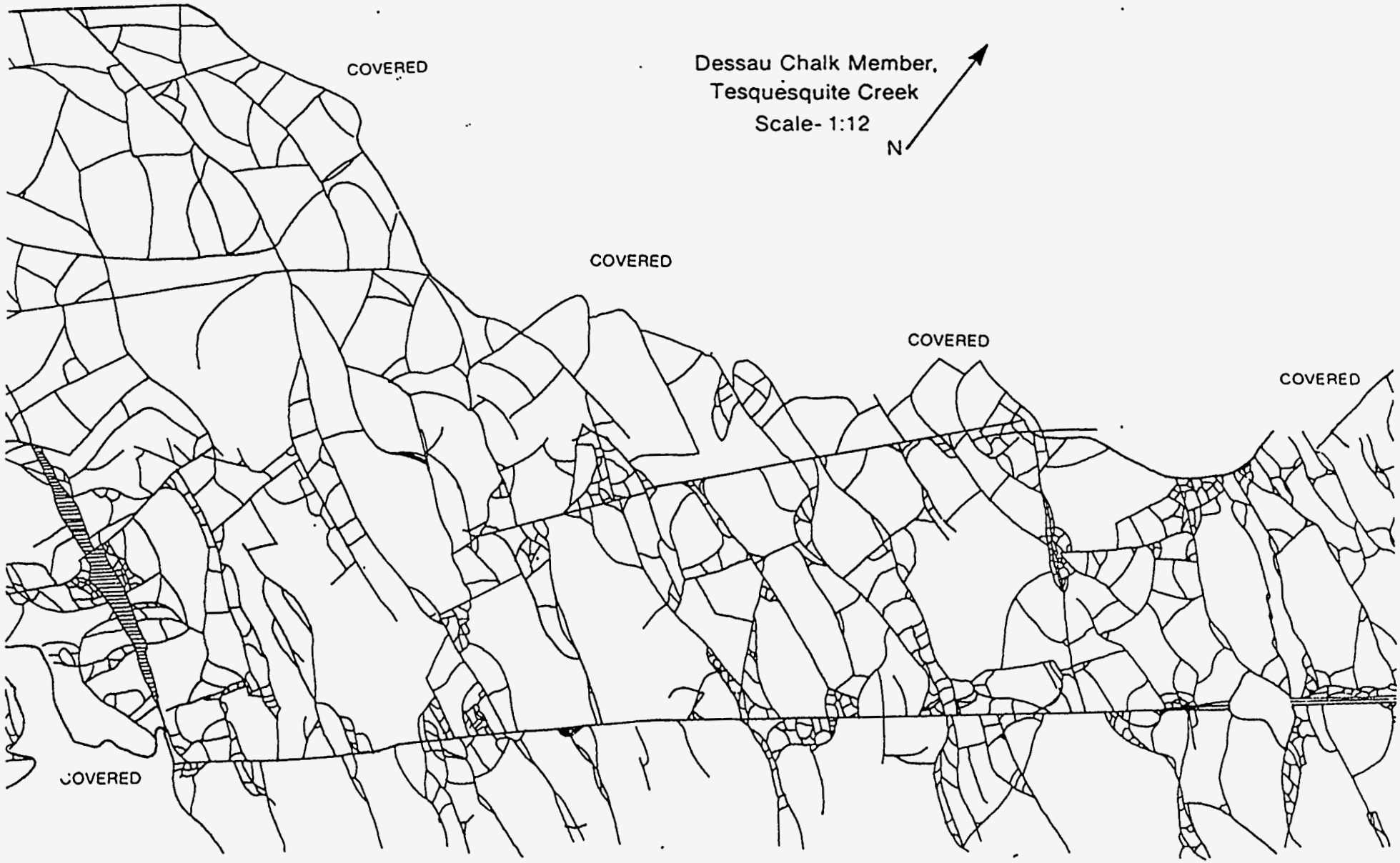


Figure 3. Example of detailed map of fracture traces on bedding plane in the Dessau Chalk Member at Tesquesquite Creek, some 30 miles SE of Del Rio, Texas. Scale of map is 1 : 12. Note sets of master fractures oriented NE-SW and a second set oriented NW-SE. Other smaller fractures tend to be curved and randomly oriented.

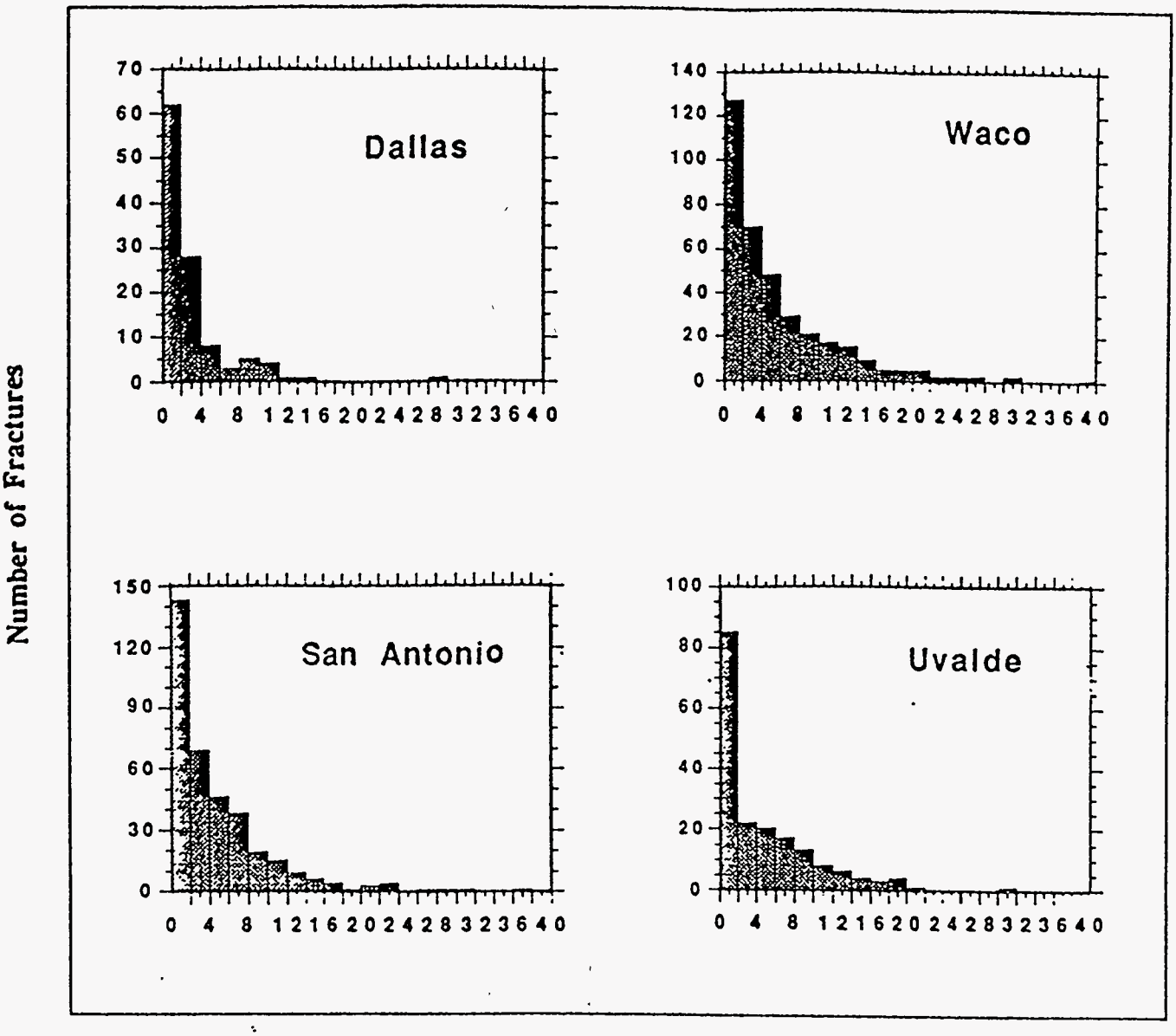


Figure 4a. Plots show fracture spacing data from all fourteen scanlines at the four localities sampled. . Scanlines are placed on vertical outcrops of the chalk and run parallel to bedding and along azimuths inclined at various angles to the local and regional structure. The vast majority of the fractures are spaced less than 15-inches apart and the overall distribution is negatively exponential.

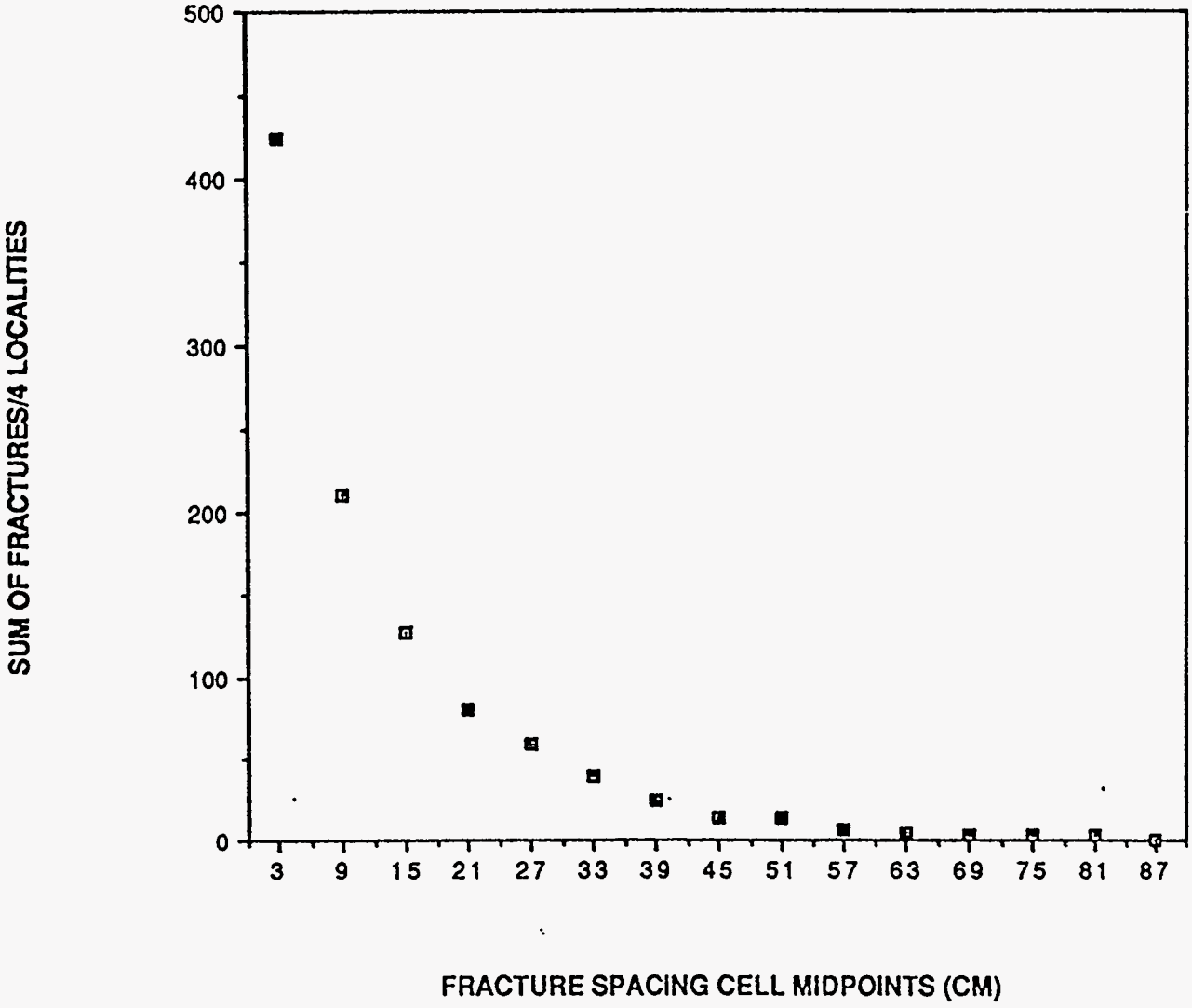


Figure 4b. Compilation of all data in Figure 4a .

Fracture (vein) fillings

Veins in the Austin Chalk are partially or completely filled with calcite and a mixed-lay, smectite-illite clay. Commonly the clay minerals were deposited first on the walls of the fracture and subsequently overgrown by subhedral calcite crystals. "Crack-seal" textures observed commonly suggest multiple fracture episodes. The details of our analysis of the vein fillings are to be found on pages 6 to 15 of the field guide for the AAPG field guide ( Corbett et al 1991b, herein Appendix 1). Comparison of vein geochemistry (clay abundance, trace elements and stable isotopic data [$O^{18}$ and $C^{13}$] with that of the host rock indicated extra-formational pore fluids, probably at abnormally high fluid pressure, were introducted into the chalk through natural hydraulic fractures, probably from the underlying Eagleford shale. Calcite crystals precipitated from these waters contain fluid inclusions suggesting hydrothermal temperatures between 150 and 200°C. The combination of high temperature and introduction of extra-formational waters, leads to the hypothesis that the chalk was under a state of low differential stress, but generally near failure. Increasing the pore fluid pressure had the effect of decreasing all principal stresses and leaving the differenital stress unchanged. This change in stress state produced failure and promoted nature hydraulic fracture. The most likely source for the fluid was compaction (dewatering) of the underlying Eagleford shale. We envision a hydrodynamic system where fluid expelled by compacton of the shale flows up-dip, along the shale/chalk interface until it encounters comparatively high permeability zones in the overlying chalk. The fluid invades the chalk at these zones and eventually reaches a pressure sufficient to produce fracturing ( Corbett et al, 1991b, p. 12-13). Photomicrographs of calcite/clay vein fillings in small fault zones clearly show evidence of considerable dilatancy during faulting and fracturing (Figure 5). This dilatancy (volume increase) would be the site of low presssure and suck fluids into the zone of deformation.

Fractures in cores of Austin Chalk

Through the kind cooperation of Pinnacle Oil Co. and the Exxon Corp., cores were examined from the vertical segment through the Austin Chalk of the Gise No. 1 borehole to determine the morphology and abundance of fractures. Calcite filled fractures, oriented normal to bedding were the most conspicuous fractures in the cores. At least one very clean and planar natural fracture was encountered (Figure 6a). Also significant and confirmatory of observations on outcrop is the development of fractures that terminate in zones where the clay content of the chalk increases ( Figure 6b). The demonstration of bed-containment of fractures in the subsurface is highly significant as the locations horizontally and vertically where marl/shale breaks occur within the section are reasonable well known. For example, horizontal drilling schemes need to bring into consideration fracture-bed-containment where marls and shale breaks are abundant, because vertical communication is apt to be poor in such stratigraphic intervals. During the forthcoming third year of effort, time will be devoted to the examination of fractures in cores with a view toward the extrapolation problem mentioned below. Collections obtain from industry and those already in the core repository of the Bureau of Economic Geology in Austin will be utilized for this purpose.

Extrapolation of outcrop data into the subsurface

The key question in using data from outcrops to predict or model potential or known naturally fractured reservoirs at depth deals with the degree to which outcrop data on fracture orientation, spacing, width, connectivity, bed-containment, relation to structural types, etc. can be extrapolated. For example, while the orientation of major fractures relative to local and regional structure might be extrapolated with some confidence, what of fracture spacing? Is the fracture spacing on outcrop closer than that existant in the subsurface because stress relaxation and weathering processes at the outcrop

Figure 5. Photomicrograph of intense fracturing and subsequent calcite and clay infilling in a small fault zone in the Austin Chalk from a core at 8974 ft in the Petromark Conway No. 1 well, Kurtin Field, Brazos County, Texas. Fault zone has an overall left-lateral shear sense. Bold arrows indicate an epoxy-filled parting that occurred upon handling the core and preparing the thin section. Difference in grain sizes of calcite (see open arrow where grain size is coarse) suggests more than one period of mineralization. Note that the very closely spaced fractures are encased in "pods" or shear domains bounded by left-lateral shear surfaces. Scale bar equals 0.5 cm. Sample courtesy of Dr. R. R. Berg, Dept. of Geology, Texas A&M University.

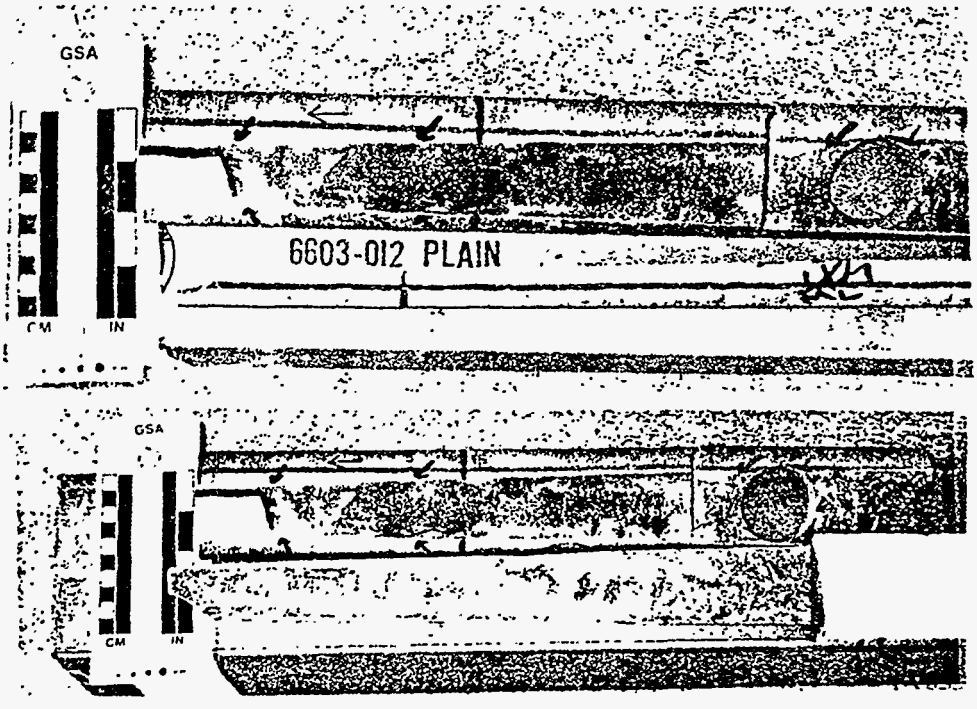


Figure 6a. Photograph of a planar, clean natural fracture in the Gise No. 1 core, Pearsall Field. Fracture extends for at least 3 feet in the vertical direction (normal to bedding). This vertical core was supplied by the Pinnacle Oil Co. and the Exxon Corp.

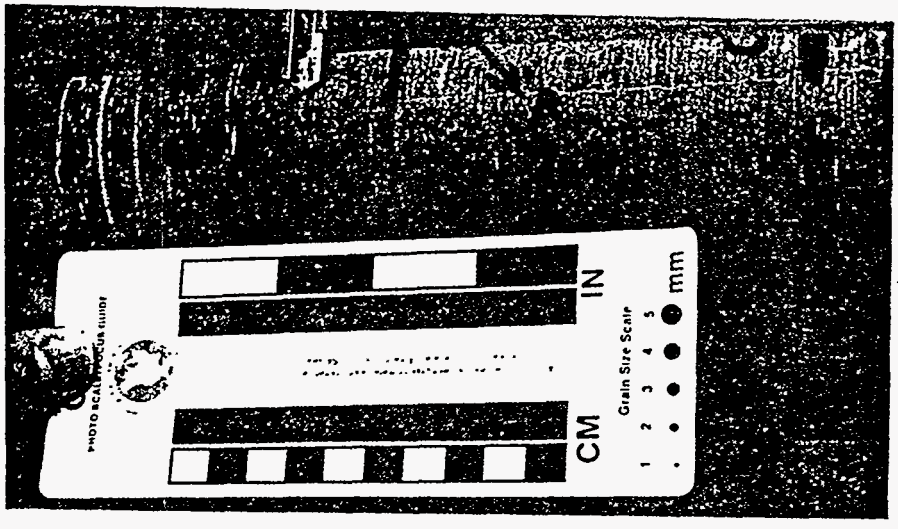


Figure 6b. Photograph of a calcite-filled fracture ( arrows) also from the Gise No. 1 well, shows fracture terminates in darker part of the core where there is an increase in shale and organic matter. Fracture actually terminates at tip of pointed razor.

enhance fracture development? Similarly, what of fracture width or fracture containment within chalk beds relative to marl/shale breaks (above).

The answer to these questions requires direct study of fractures in the subsurface and correlation of those observations with outcrop data already in hand. In addition to direct observation of natural fractures in cores, Schlumberger's Formation Microscanner Survey (FMS) tool provides just the information requisite for this study. The FMS yields a detailed record of fractures, bedding planes, and faults that transect the borehole. Particularly when the survey is run in the horizontal segments of boreholes, the survey provides direct information on fracture orientation, width, and spacing for the bed(s) inwhich the borehole was drilled. Accordingly, contact has been made with Mr. Tom Fett of Schlumberger Well Services who has generously agreed to participate in this study by (a) training Dr. Friedman and his student(s) on the analysis of FMS data, (b) installing their software programs on Sun workstations in our Geophysics Department so that the analyses can be conducted on campus, and (c) working with their clients to provide us with FMS data from a number of horizontal boreholes drilling along the Austin trend.

Proposals to fund this work have been written and submitted to the Center for Energy and Mineral Resources at Texas A&M University and to the Coordinating Board of the State of Texas to compete in their Advance Technology Program. Funds on this DOE Annex IV are not sufficient to pursue this phase of the work to completion.

Prediction of rock fracturability in the brittle regime

Within a given stratigraphic unit is it possible to determine from standard logs which intervals are most likely to be fractured in the subsurface. Accordingly, the hypotheses we wish to evaluate are: Young's Modulus (YM) correlates strongly with rock strength, and rock strength correlates with fracture abundance,upon failure in the brittle regime.

Earlier work on the mechanical stratigraphy of the Austin chalk (Corbett et al, 1987, see Table 1, column A) indicates that the upper (Big House Chalk) and lower (Atco Chalk) massive chalk members are the most fractured stratigraphic intervals in outcrop. This point is in agreement with the empirical evidence from drilling. Moreover, Corbett et al (1987) found that in the brittle regime (i.e., low effective confining pressure) rock fracturability is largely a function of increasing strength which increases with decreasing porosity and decreasing clay (smectite) content. In fact, experimental rock deformation studies show that as little as 4% clay will decrease the strength 30 to 42% compared to specimens with no clay.

Work performed on Annex IV (Table 1, column B) has provided encouragement to pursue evaluation of the above stated hypothesis. Data in the literature indicate for a number of rock types that (a) there is a strong correlation coefficient (R) of 0.94 between Young's Modulus (YM) and compressive strength (Bieniawski, 1984, see Figure 7, herein) and (b) a similarly strong correlation (R = 0.93) exists between YM and tensile strength (Kreck, et al, 1974, see Figure 8 herein). Moreover, preliminary data for the Austin Chalk from samples obtained from two sets of cores from the Pearsall Field, show a correlation (R=0.67) between YM and compressive strength (Figure 9) and a reasonable correlation (R = 0.65) between normalized fracture length (length of induced fractures as observed at the circumference of the deformed right-circular cylinderal specimens) and distortional strain energy (area under the stress strain curve) for specimens of Austin chalk (Figure 10a). The hypotheses to be tested here are shown schematically in Figure 10b.

Clearly, what remains to fully test the above stated hypotheses is to add YM (from sonic velocity measurements) and strength data to the database for the Austin Chalk. We also need to improve quantification of fracture surface area induced in experimental deformed specimens as the measure of fracture abundance. We propose to evaluate the use of XRAY CT imaging in this regard (Figure 11) and to compare the CT data with the results from disking specimens, making direct optical measurements of the fractures and

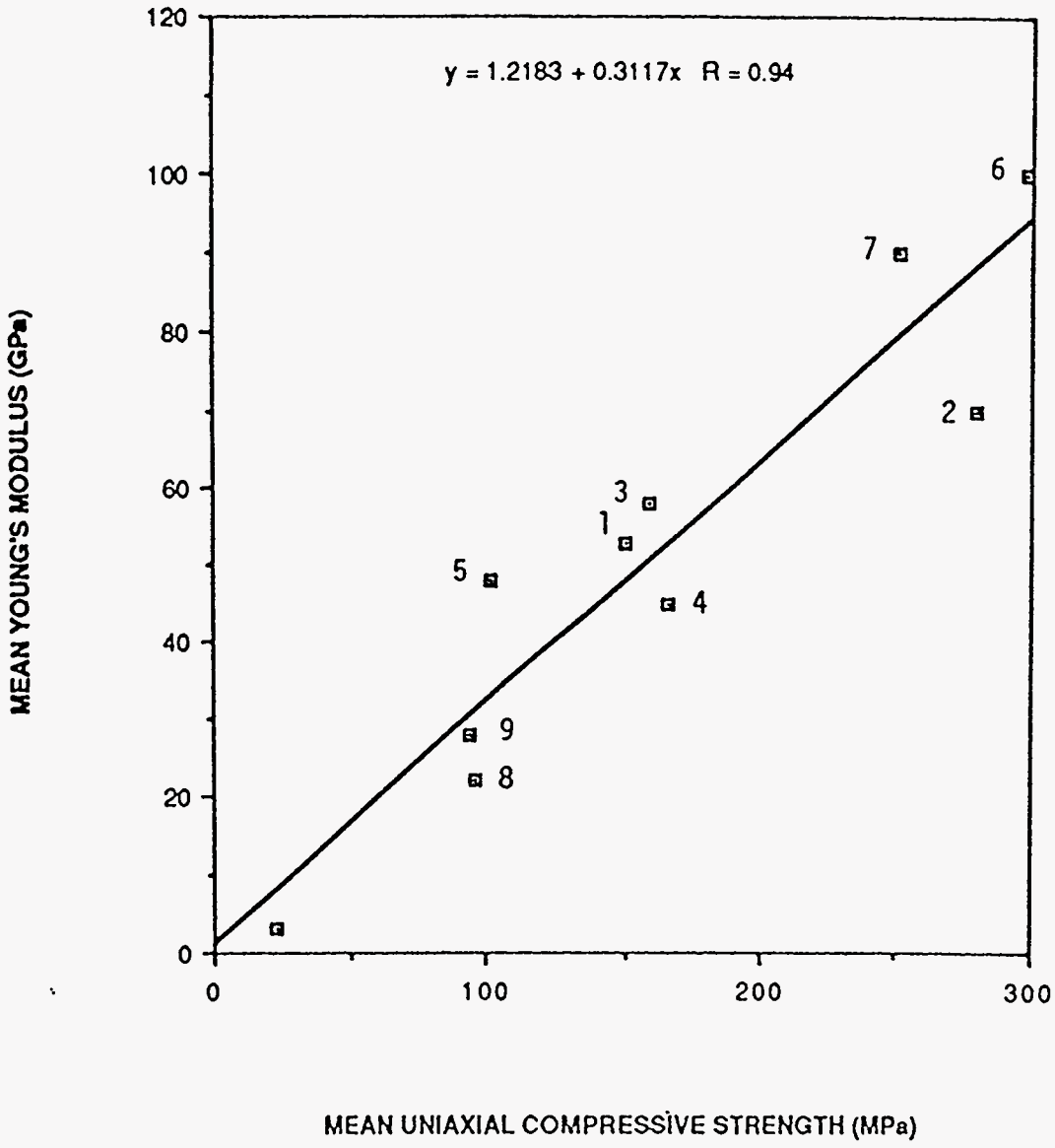


Figure 7. Data show relationship abetwen mean uniaxial compressive strengths and mean Young's Modulus for 10 rock types (after Bieniawski 1984, Table 5.4). Rock types are as follows:

1 - basalt, 2 - dolerite, 3- gneiss, 4- granite , 5 - limestone, 6-norite, 7 - quartzite, 8 - sandstone, 9 - shale, 10 - coal.

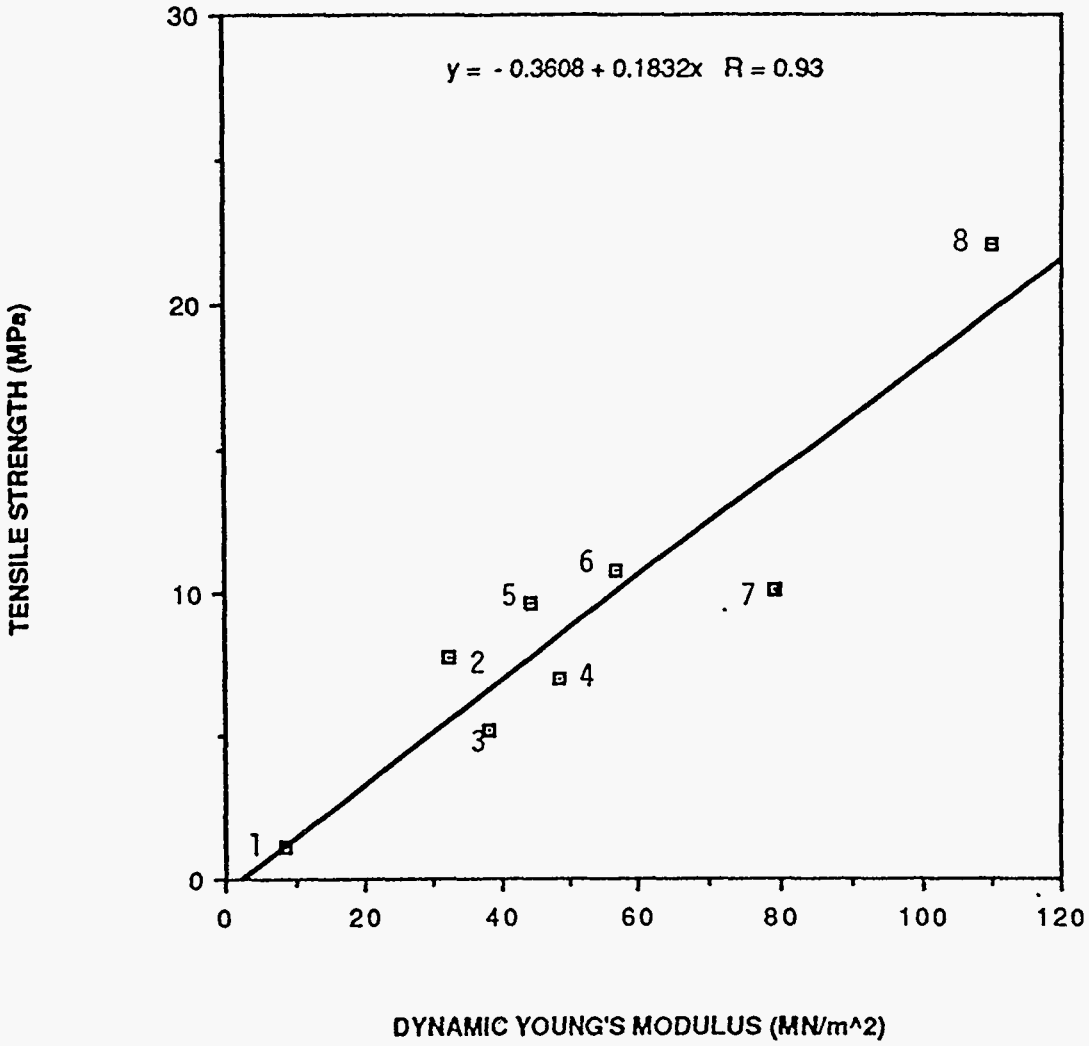


Figure 8. Plot shows strong correlation between the tensile strength of a variety of rock types and their corresponding dynamic Young's Modulus (data from Kreck et al, 1974). Rocks are: 1 - Berea sandstone, 2 - Barre granite, 3 - Salem limestone, 4 - granodiorite, 5 - Westerly granite, 6 - Sioux quartzite, 7 - Tennessee marble, 8 - Dresser basalt.

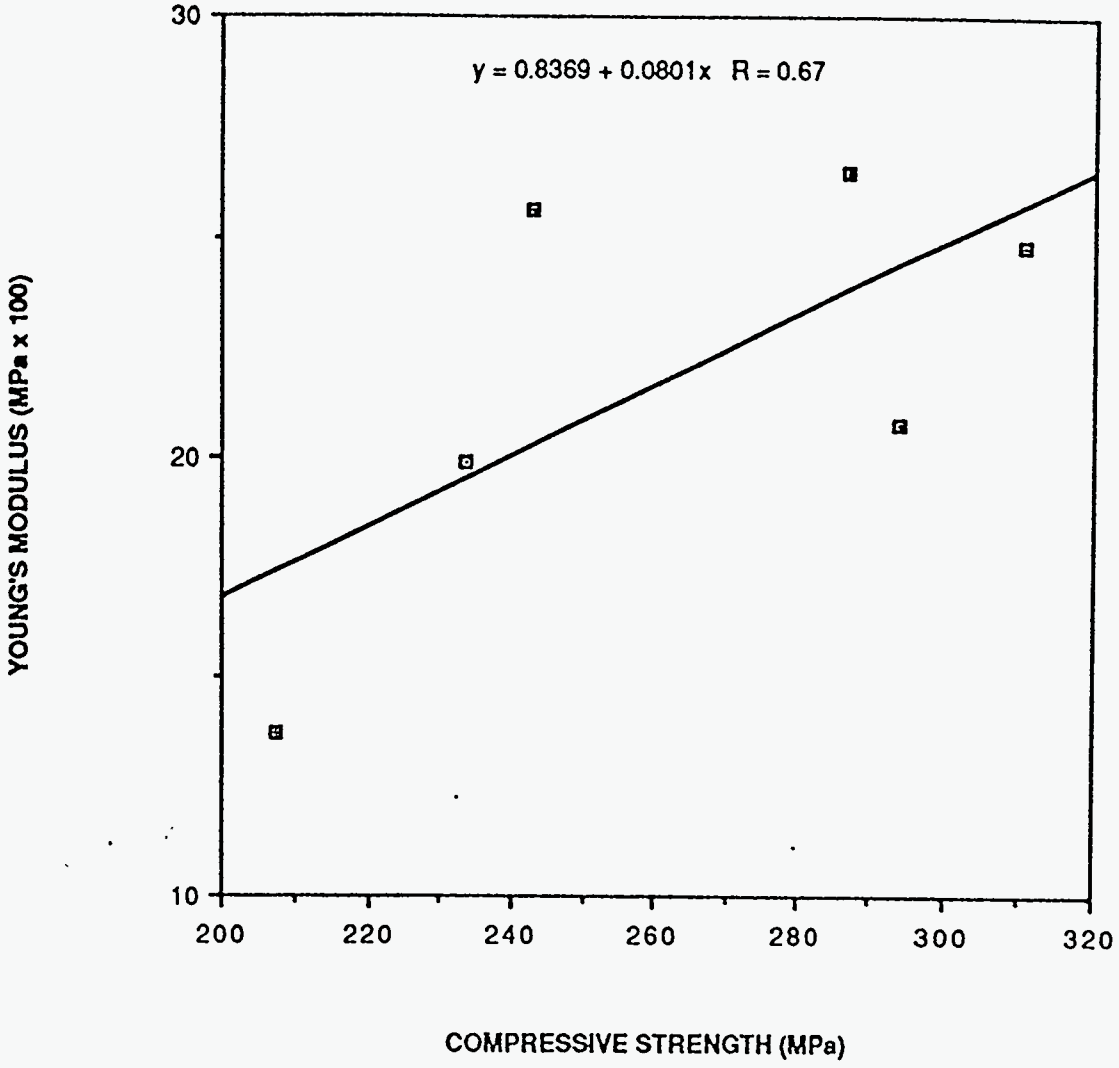


Figure 9 . Plot shows relationship between the static Young's Modulus and compressive strength (at 17 MPa confining pressure) for six specimens of Austin Chalk, three each from the Exxon Hildebrand No. 1 and the Pinnacle/Gise No. 1, Pearsall, Field, S. Texas. Data courtesy of Mr. Dave Becker, Exxon Corp, Corpus Christi as obtained by Mr. Jack N. Maqouirk, Center for Tectonophysics, Texas A&M University.

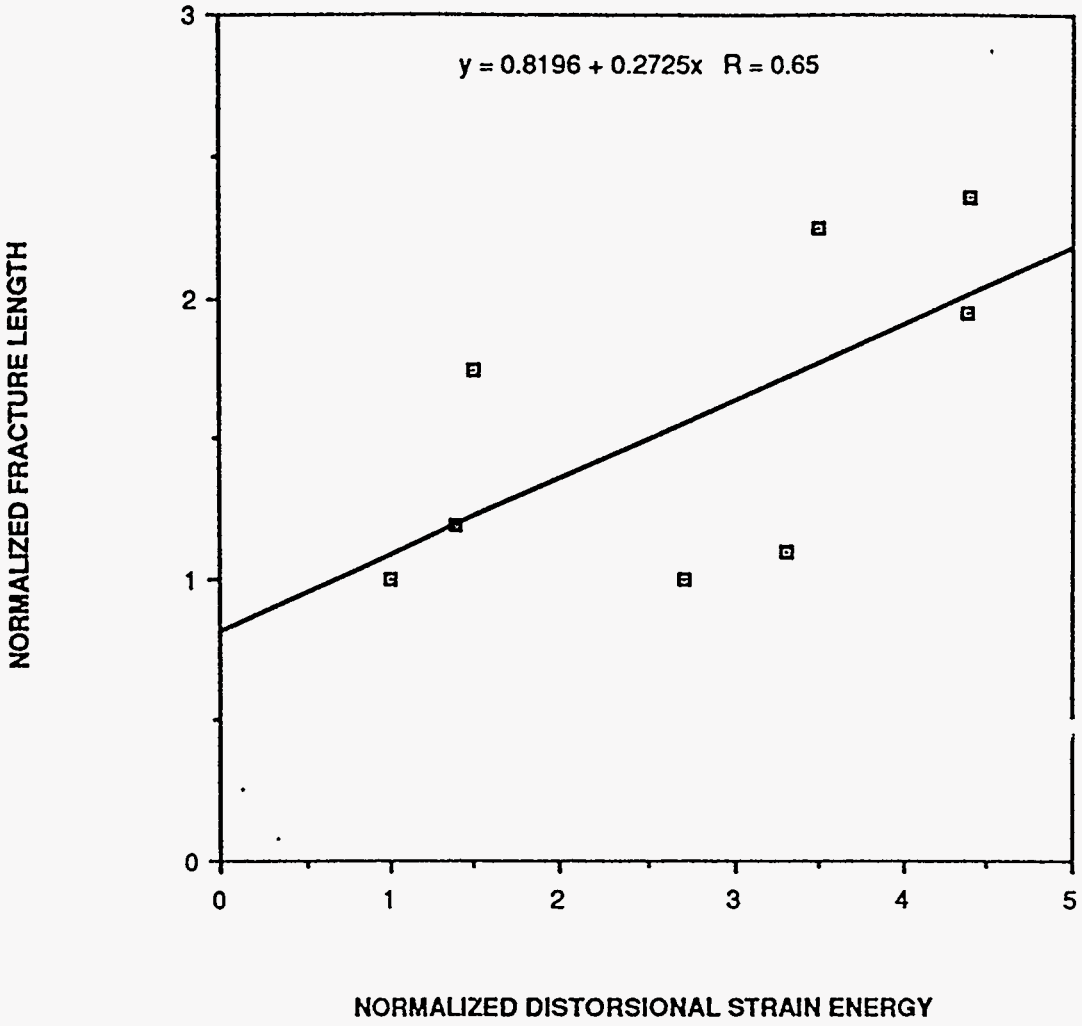


Figure 10a. Plot of normalized fracture length and the corresponding distorsional strain energy for six specimens of Austin Chalk experimentally deformed in the brittle regime by Corbett et al (1987). Fracture length is defined as the total length of fracture traces as observed at the periphery of the deformed cylindrical specimens (initially 10-cm long and 5-cm in diameter). Distorsional strain energy is the area under the stress/strain curve for each specimen from the origin to the point of failure initiation. Normalization is with respect to the smallest fracture length and the smallest strain energy among the six specimens.

in the Brittle Regime

1. Rock strengths increase with:

   a. Increasing quartz and feldspar in siliceous rocks

   b. Increasing dolomite in carbonate rocks

   c. Decreasing grain size

   d. Decreasing porosity

2. Fracture Abundance Increases with Rock Strength

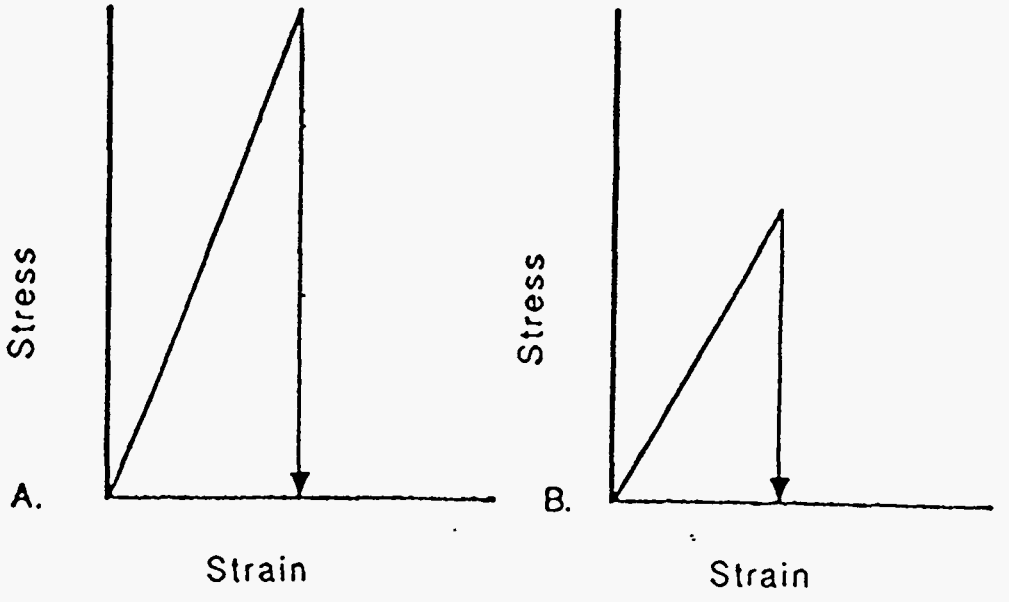


Figure 10b. Explanation of working hypothesis. In the stress/strain data above, panel A represents the brittle failure of a stronger rock and one of greater Young's Modulus (YM) than panel B. The area under each stress/strain curve is the distorsional strain energy, which upon failure is used to create fracture surface in the rock. This area (potential energy) increases as YM and strength increase. Accordingly, the rock with the greater strength and higher YM will contain, upon failure, more fracture surface area per unit volume, i.e., greater fracture abundance. This hypothesis holds only when failure occurs in the brittle regime.

using stereological principles to recover fracture surface area per unit volume (Underwood, 1970). While some work on this topic will be possible during the third year of this effort, funds for determination of the sonic velocities and for use of the XRAY CT imaging will require additional funding. That is why an unsolicited proposal on this topic has been submitted to DOE/OBES.

Technology transfer

We have given special emphasis to communicate our results to industrial representatives. To date results have been presented in 3 publications (Corbett et al, 1991a, 1991b, and Wiltschko et al, 1991), on 1 AAPG field trip, and in 5 presentations, with a 6th presentation scheduled for October, 1991. These include presentations for the Corpus Christi Geological Society (January, 1991), the Austin Chalk Exploration Symposium sponsored by the South Texas Geological Society, San Antonio (February 1991), the Advanced Short Course in Petroleum Geology, sponsored by the University of Tulsa (February 1991), at two symposia sponsored by Oryx (March and April, 1991), on Field Trip No. 4, Dallas Geological Society, held just before the Annual Meeting of the AAPG, Dallas, April 1991, at an on-campus seminar for DOE, State of Texas and representatives from major oil companies (August, 1991), and at the forthcoming October meeting of the Gulf Coast Association of Geological Societies, Houston. In addition, Dr. Kevin P. Corbett had joined the Marathon Oil Co. and is actively involved in the exploration for naturally fractured reservoirs for that company.

Significance of Results

Referring again to Table 1, one sees that the ongoing work while important in itself is a stepping stone to two additional subtasks (Table 1. columns C and D) that are essential to the final goals of the effort., i.e. to predict in some detail the fracture orientation, spacing, connectivity and intact block sizes of the naturally fractured reservoir at depth.

The field phase of our work is completed with information promulgated on the geometry and location of fractures relative to structural types, and on fracture spacing, fracture connectivity and length. These data and our collection of color slides of the corresponding outcrops have given operators along the trend new ideas for exploration drilling and a means of conceptualizing the naturally-fractured chalk reservoirs at depth. Moreover, the recognition (through clay/calcite geochemistry and geothermometry) of the interplay between the fracturing in the chalk and the dewatering of the compacting underlying Eagleford shale provides a new hypothesis for the timing and location of fracturing in the chalk. Once we develope a better understanding of the degree of extrapolation from outcrop to subsurface
there is every expectation that these conceptual models will be converted to quantitative ones that will permit forward modeling, i.e., characterization of the naturally fractured reservoir prior to or early in the history of drilling.

Our approach definitely utilizes the Austin Chalk and its geological framework as a site-specific case. At the same time, however, the approach, which relies on sound rock mechanics principles and cautious extrapolations, equally is generic. As such it is ameanable to application to the exploration and production for petroleum reservoirs in other naturally-fractured low permeability rocks of which there are many nationally and internationally.

Figure 11. Photos show XRAY CT imagery of fractures in an experimentally deformed specimen of Austin Chalk. Specimen remains intact throughout the analysis as only xenon gas is injected into the pores and fractures to affect the image. Cylindrical specimen is 10-cm long and 5-cm in diameter. Whole core image in (a) shows major fractures intersecting the specimen near its mid-point. Circular cross-sections (b - f) show traces of the main fractures in a series of sections along the 10-cm axis of the specimen. Sections (b and f) are near the ends of the specimen, sections (c and e) are about at the 1/3rd and 2/3rds points along the axis, and (d) is at its mid-point where the fractures are closest together. Notice that the fractures are far apart in (b and f) and closer together in the other three sections. In all sections the fractures stike NE if N is located at the top of the page. Courtesy of Mr. Mark Fineout, graduate student, Department of Petroleum Engineering.

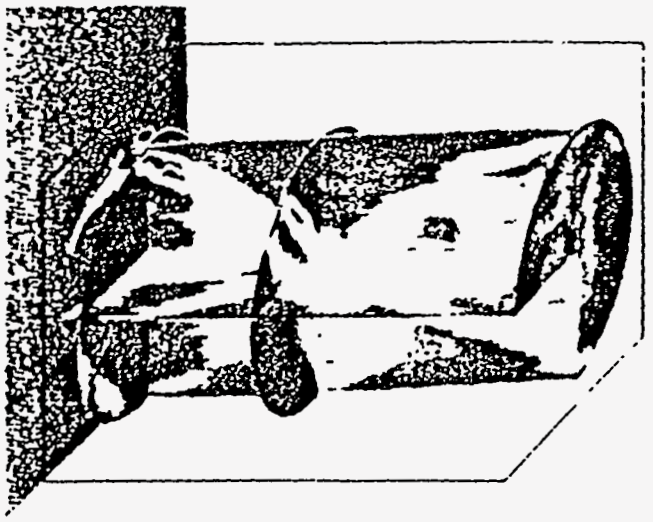

d

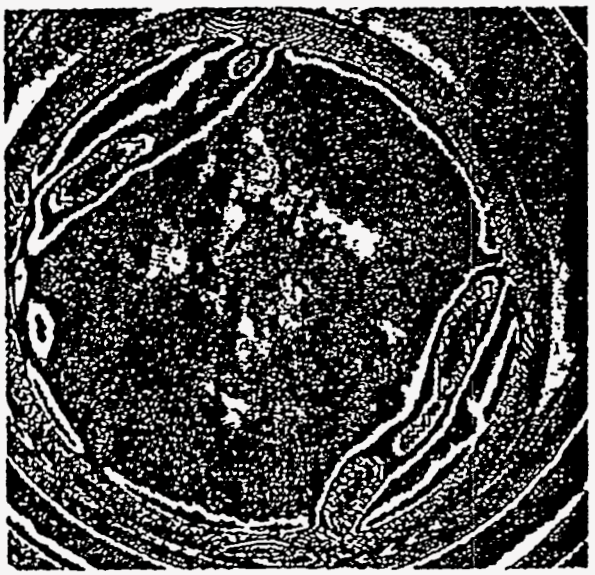

e

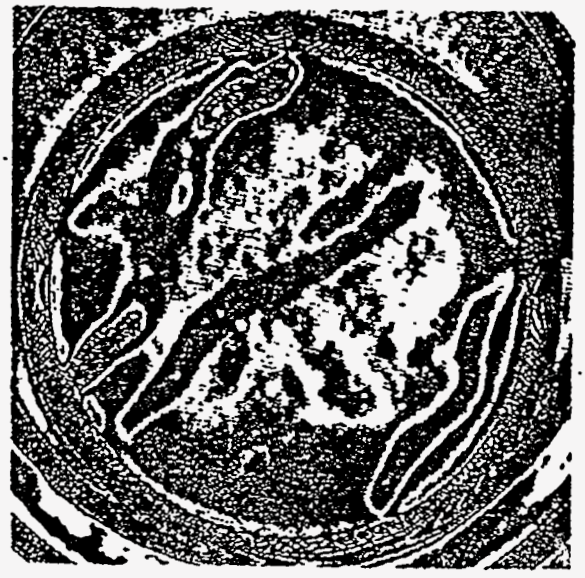

f

4.1.2 Geophysical Studies

4.1.2.1 Estimation of Fracture Orientations from Shear-Wave Splitting in the Lost Hills VSP

Method

The method used to determine the directions of the fractures (i.e., the principal axes for the anisotropy) is to rotate the four horizontal components of the signals into the principal directions. When the signals have been properly rotated, the cross-diagonal terms will be zero or, at least, minimized.

The recorded (matrix) displacement field can be expressed as

$$\mathbf{U}(t,z) = \begin{bmatrix} U_{II}(t,z) & U_{IC}(t,z) \\ U_{CI}(t,z) & U_{CC}(t,z) \end{bmatrix}$$

where $U_{II}(t,z)$, $U_{IC}(t,z)$, $U_{CI}(t,z)$ and $U_{CC}(t,z)$ are: 1) the in-line geophone component for the in-line source, 2) the cross-line component for the in-line source, 3) the in-line component for the cross-line source and 4) the cross-line component for the cross-line source, respectively. The (matrix) displacement field $\mathbf{U}'(t,z;\theta)$, obtained after rotating both the sources and receivers through the angle $\theta$ counterclockwise, is given by

$$\mathbf{U}'(t,z;\theta) = \mathbf{R}(\theta)\ \mathbf{U}(t,z)\ \mathbf{R}^{-1}(\theta)$$

where

$$\mathbf{R}(\theta) = \begin{bmatrix} \cos\theta & \sin\theta \\ -\sin\theta & \cos\theta \end{bmatrix}$$

is the unitary rotation matrix which rotates a vector through an angle of $\theta$.

For the natural polarization directions (or principal axes coordinates), the energy contained in the off-diagonal terms of $\mathbf{U}'(t,z;\theta)$ should be zero (minimized):

$$\mathbf{U}'(t,z;\theta) = \begin{bmatrix} U'_{FF}(t,z;\theta) & U'_{FS}(t,z;\theta) \\ U'_{SF}(t,z;\theta) & U'_{SS}(t,z;\theta) \end{bmatrix};$$

that is, $U'_{FS}(t,z;\theta)$ and $U'_{SF}(t,z;\theta)$ should both be zero or, at least, minimal (where F and S represent the Fast and Slow directions, respectively).

Reslults

The fracture orientations are determined by maximizing the ratio of the energy (in 200-msec windows; shown by the solid lines in Figure 8) in the rotated, 'in-line, in-line' and 'in-line, cross-line' components (i.e., minimizing the ratio of $\Sigma[U'^2_{IC}(t,z;\theta)/ U'^2_{II}(t,z;\theta)]$ over that window). These orientations are shown as a solid line in Figure 10 for depths between 3600 to 7700 ft. The angles obtained by maximizing the ratio $\Sigma[U'^2_{CC}(t,z;\theta)/ U'^2_{CI}(t,z;\theta)]$ are shown as the dashed line in Figure 10. The asterisks on the depth axes indicate those depths for which the source location was changed. There is

no strong correlation between the movement of the source truck and the variations in the determined fracture orientations. However, there are some small (less than 15°) variations in the fracture orientation angle with depth which we will discuss later. The measured fracture orientation is fairly constant with depth and is approximately N45°E. This is the inferred direction for the fracture planes.

Effects of Source Imbalance

In Figure 11 we show the energy ratio of the diagonal terms of the rotated displacement matrix; that is, the ratio of the energy (in the 200-msec window) in the inferred fast direction to that in the inferred slow direction (and vice versa). The energy ratio is fairly constant (it varies between one and three) for all depths except 5000 and 7100 ft. where large deviations occur. These are also the depths for which there are large deviations in the fracture orientation in Figure 10. Looking at the seismic data in Figure 8, we see that the amplitudes for the in-line source are small for the 5000-ft depth compared to the other depths while the traces (signals) of 7100 ft for the in-line source are nosier than the other traces. We concluded that the differences (imbalance) in the in-line and cross-line sources for the 5000-ft depth was the source of the large variability in the orientation determined at that depth. Upon equalizing the source strengths for 5000 ft (by increasing the signal level in both the in-line and cross-line components for the in-line source), the variation of the fracture orientation decreased substantially. Similar equalizations were performed for the traces corresponding to the other depths. The results for the fracture orientations after source balancing are shown in Figure 12. Note, the variability in the fracture orientation is considerably decreased by the simple balancing procedure. The large variation persists for 7100-ft depth because of the the noise in the in-line-source traces. The resulting 'average' fracture orientation is about N45°E.

The time delay between the fast-fast component and the slow-slow component (after source balancing) for all depths is shown in Figure 13. The average time delay is about 40 msec and is relatively constant with depth (if anything, there appears to be a slight decrease in the time delay with depth which would require that the fast and slow directions interchange with depth, a highly unlikely situation). Given that the sampling interval is 2 msec and that the frequency content in the signal peaks at about 10 Hz (i.e., a period of 100 msec - see Figure 8 or 14), a variability of $\pm 4$ msec in the time delay is not unreasonable or unexpected.

The matrix of displacements $\mathbf{U}'(t,z;\theta)$ in the natural coordinates (principal axes) is shown in Figure 14. The fast-fast and slow-slow (or diagonal) components are clearly larger than the fast-slow and slow-fast (or cross-diagonal) terms. The 200-msec windows used to determine the principal directions are also shown (starting at 1600-1800 msec at 3600 ft and ending at 2800-3000 msec at 7700 ft.). The energy in those windows on the cross-diagonal traces is clearly less than that in the same windows on the diagonal traces. However, the energy is still not zero and appears to be about 10% or less of the energy in the diagonal traces. We believe this residual energy is due to imbalances in the geophone couplings as well as the imbalances in the source strengths.

The hodograms obtained for the rotated matrix of displacements, $\mathbf{U}'(t,z;\theta)$, at selected depths is shown in Figure 15. The displacements are not only more rectilinear than those shown in Figure 9, they also are better aligned with the orientation of the sources. As in Figure 9, the hodograms are quite similar with depth, but now the motions for the 'fast' source are predominantly on the 'fast' geophone while the motions for the 'slow' source are predominantly on the 'slow' geophone. While the motions are fairly rectilinear – certainly more rectilinear than those shown in Figure 9 – there still are relatively large components in the cross directions. Again, we believe these 'large' cross

components are due to source and geophone imbalances. We plan to try to eliminate them by compensating for or equalizing these imbalances.

Conclusions

The conclusions we can draw from the results of this study are:

1) the orientation of the fractures in the Lost Hills Fields of Kern County, CA is approximately N45°E. The strike of these fractures parallel the strike of the San Andreas Fault in that region and the origin of these fractures is most likely related to the stress field which generated the fault;

2) the bulk of the fractures is above 3600 ft and there is no significant fracturing below 3600 ft as inferred from the fact that there is little change in the time delay between the fast and the slow s-waves below that depth and

3) the lack of perfectly rectilinear motion for the hodograms from sources oriented along the principal axes (and/or the existence of energy on the cross-diagonal components) is due to imbalances in the source strengths and the geophone couplings. These imbalances lead to significant deviations in the determination of the fracture orientations. Methods for eliminating these imbalances are being investigated presently.

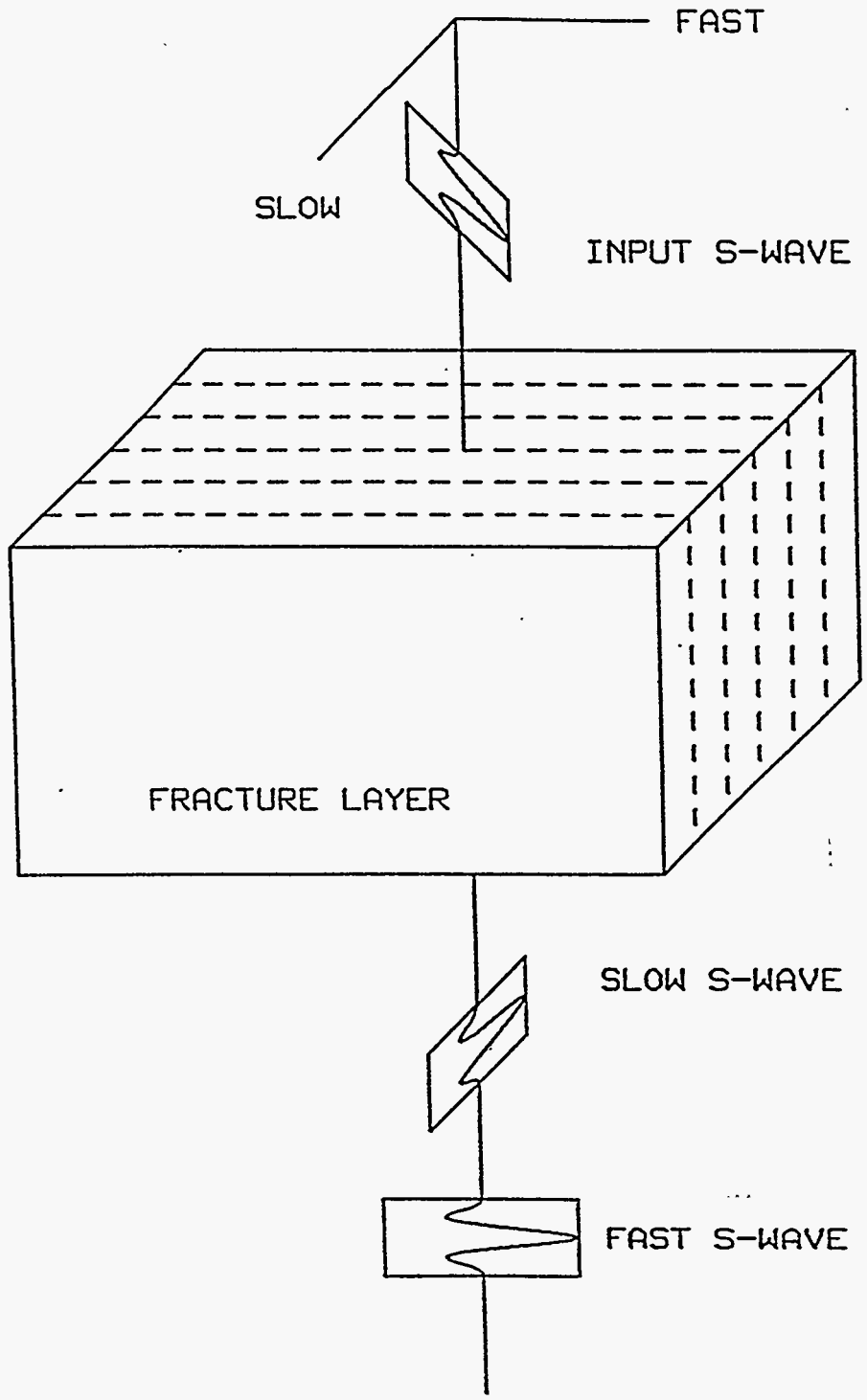


Figure 1. Shear-wave splitting and repolarization after passing through a fractured layer.

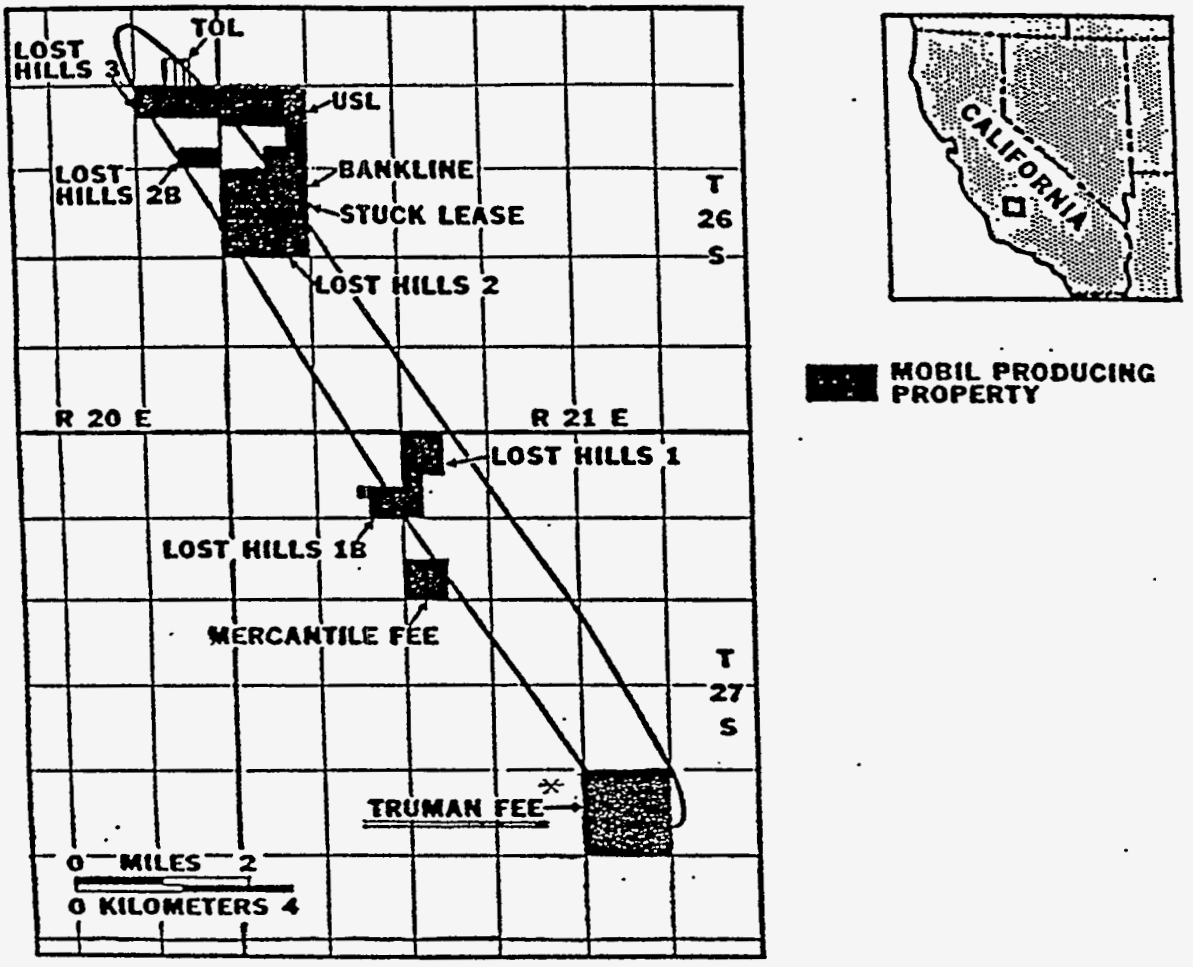


Figure 2. Location map for the Lost Hills VSP data set.

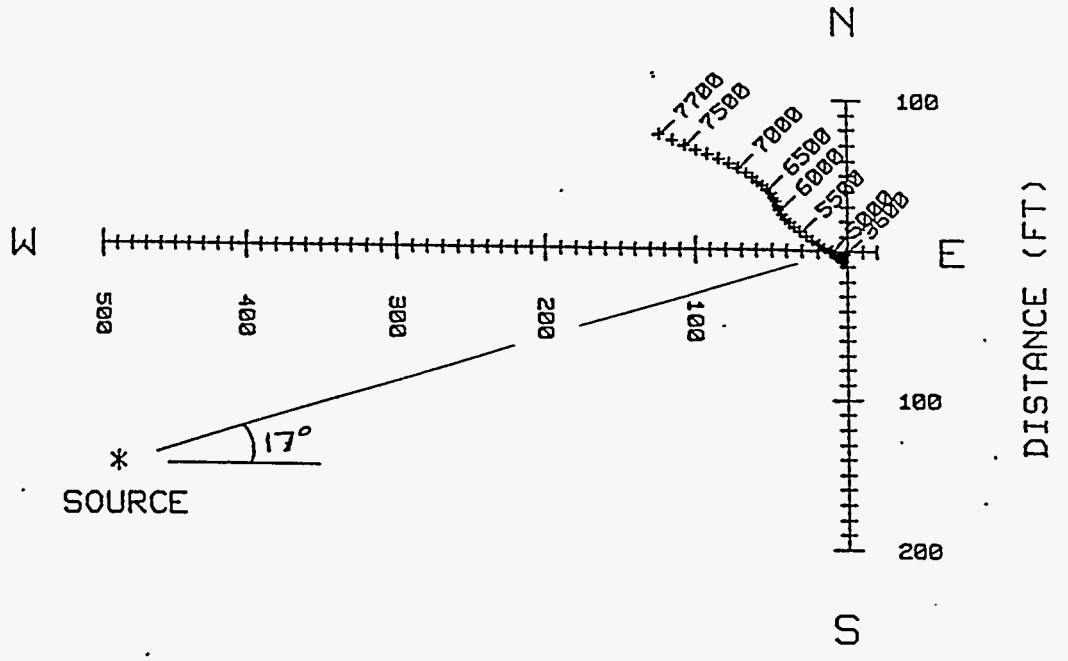


Figure 3. Location map (plan view) for the source and the well head. The pluses show the bore-hole deviation with depth.

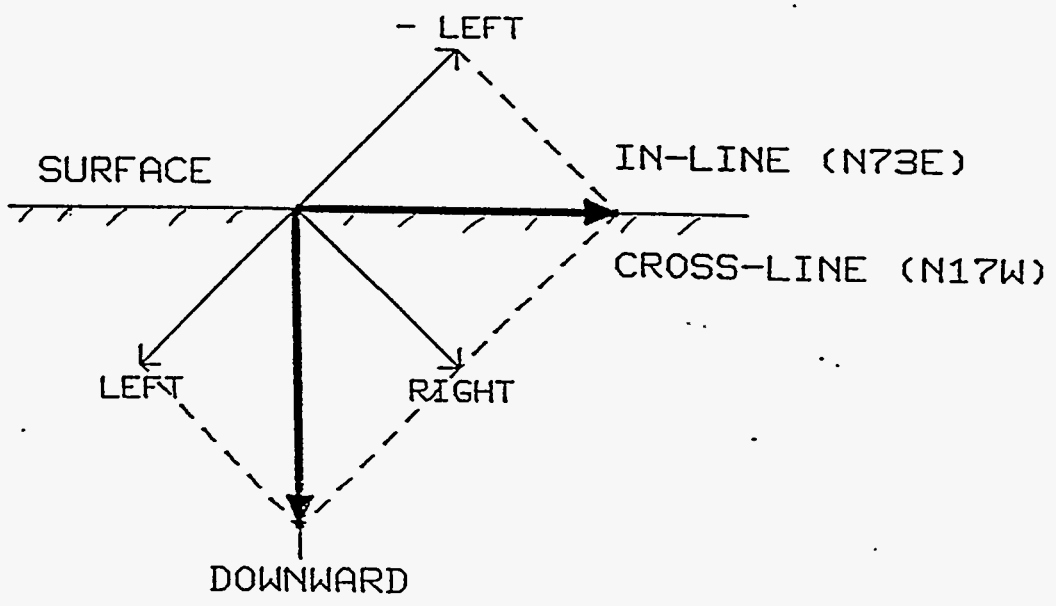


Figure 4. A schematic diagram (vertical section) of the 'right and 'left sources. The resulting vertical (downward) source is obtained by vector addition and the resulting horizontal (in-line or cross-line) source is obtained by vector subtraction of these two sources.

# LOST HILLS VSP DATA SET

- DATA ACQUISITION PARAMETERS

  SOURCE : BOLT OMNIPULSE

  RECEIVER : 10 HZ OYO GEOPHONES

  SAMPLING INTERVAL : 2 MS

  RECORDING LENGTH : 4000 MS

  RECORDING DEPTH INTERVAL : 100 FT

  RECORDING DEPTH : 3600 - 7700 FT

- NUMBER OF POPS

  3600 - 4300 FT : 8

  4400 - 4900 FT : 10

  5000 - 5300 FT : 12

  5400 - 6900 FT : 20

  7000 - 7700 FT : 30

- GYRO DATA RECORDED

- THREE-COMPONENT SURFACE GEOPHONE NEXT TO THE BASEPLATE OF THE SOURCE

Figure 5. Data acquisition parameters used in acquiring the Lost Hills VSP data.

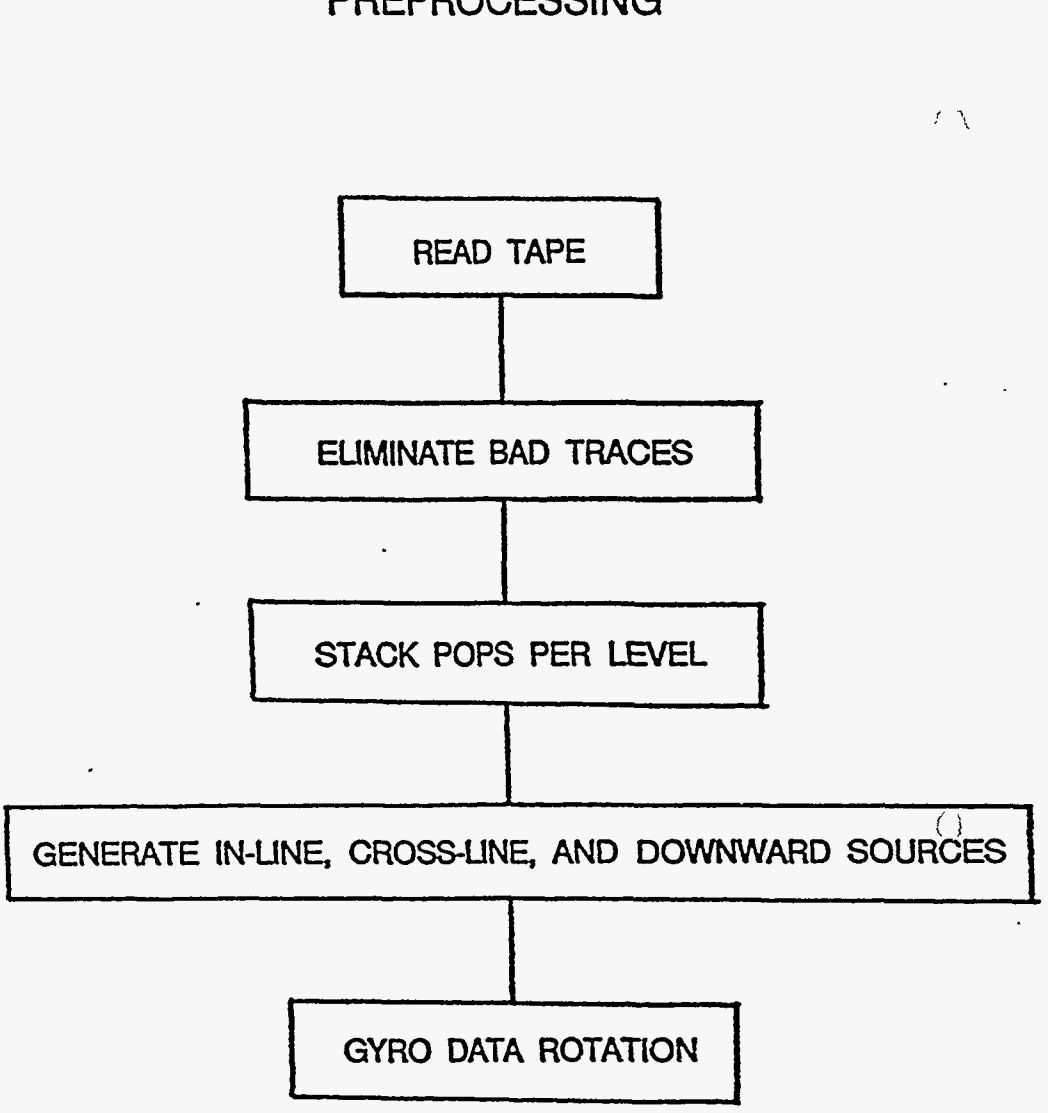


Figure 6. The steps taken in the preprocessing operation on the VSP data set.

VSP BEFORE GYRO ROTATION

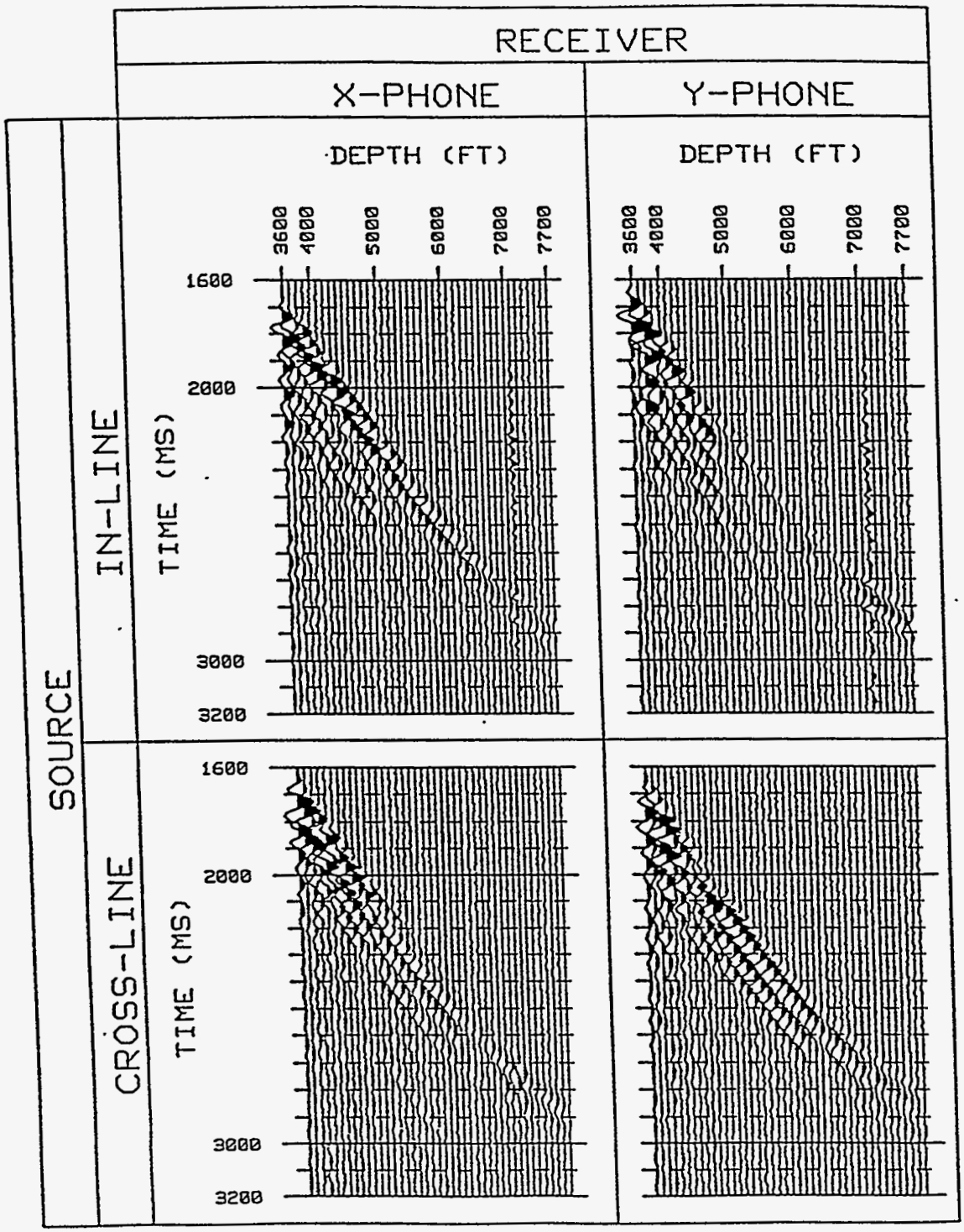


Figure 7. The edited and stacked traces for the four horizontal components of motion (in-line and cross-line sources; x- and y-oriented geophones; before gyro rotation).

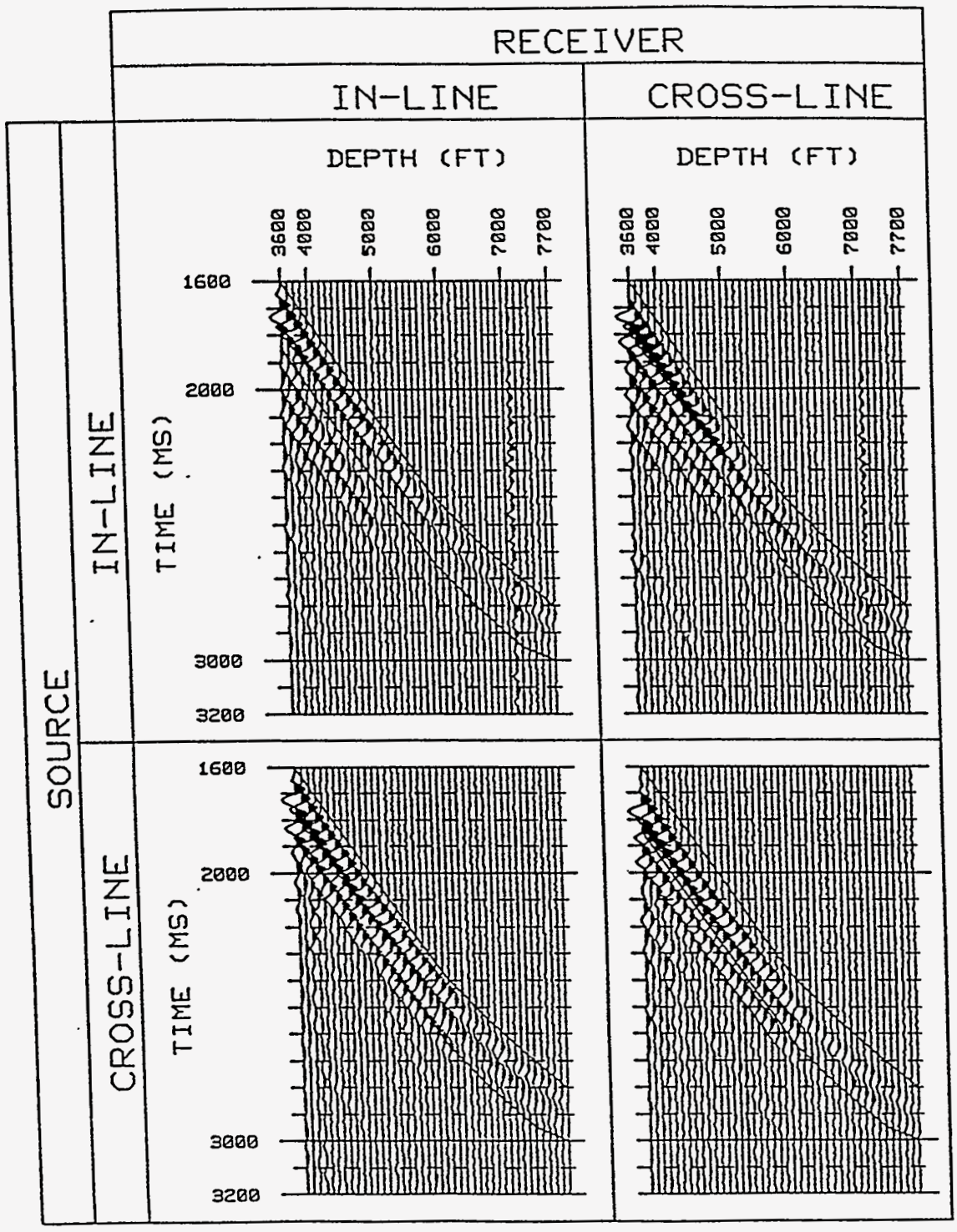


Figure 8. The four horizontal components of motion after gyro rotation (in-line and cross-line sources and geophones).

# HODOGRAM AFTER GYRO ROTATION

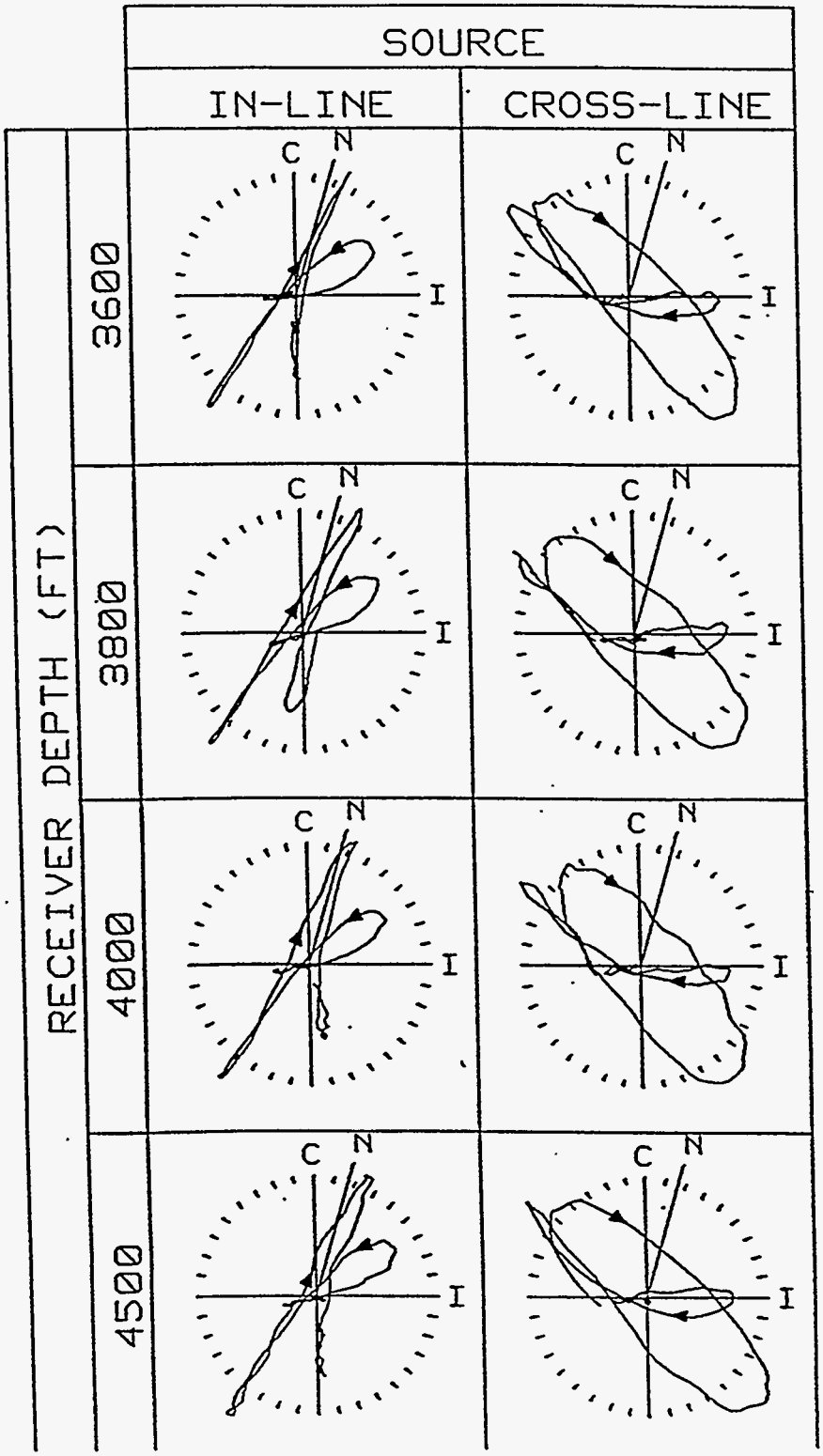


Figure 9. Hodograms generated from the gyro-rotated horizontal components (left column: in-line source; right column: cross-line source) for geophones at depths of 3600, 3800, 4000 and 4500 ft).

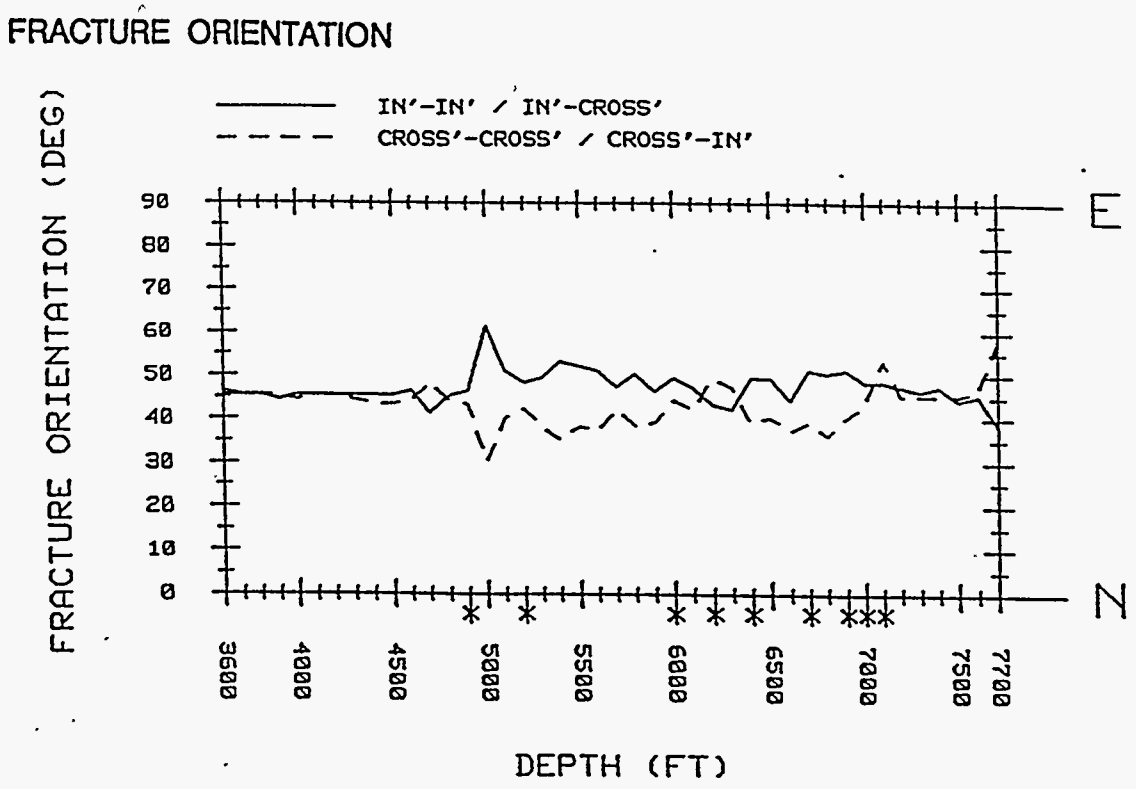


Figure 10. Fracture orientations determined by maximizing the ratio of the 'diagonal' to 'cross-diagonal' energies (or minimizing the inverse ratio) for all depths between 3600 and 7700 ft. (before source balancing). The asterisks indicate those depths for which the source location was changed.

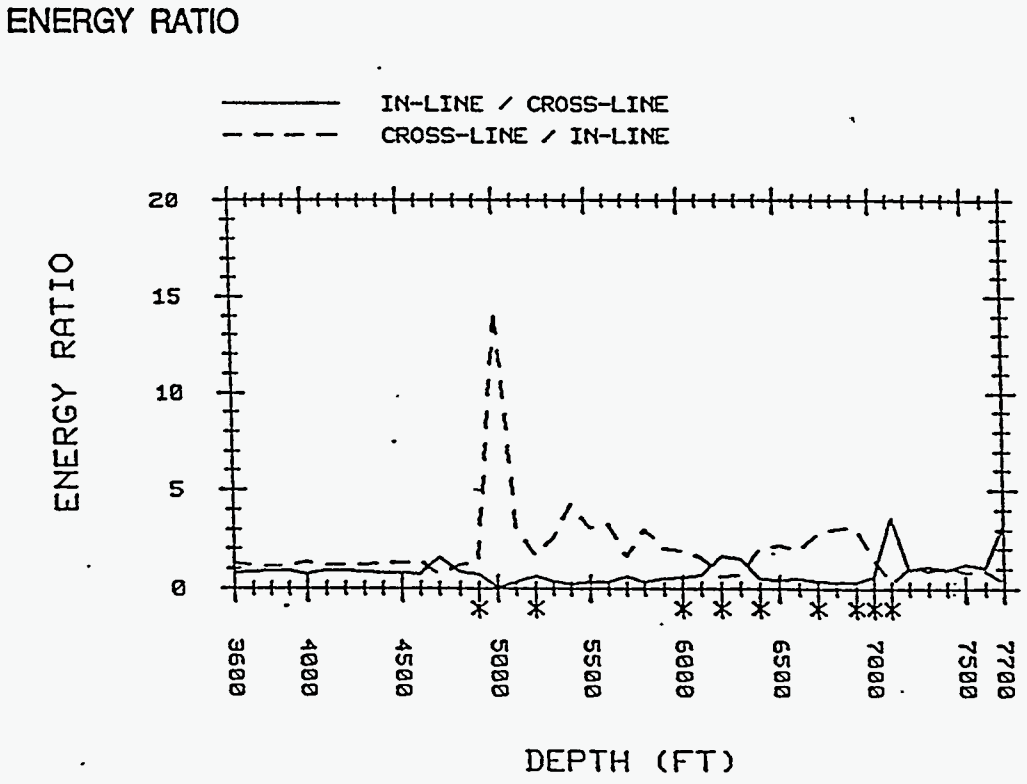


Figure 11. The ratio of the 'diagonal' energies (in the 200-msec window) as a function of depth. The asterisks indicate those depths for which the source location was changed.

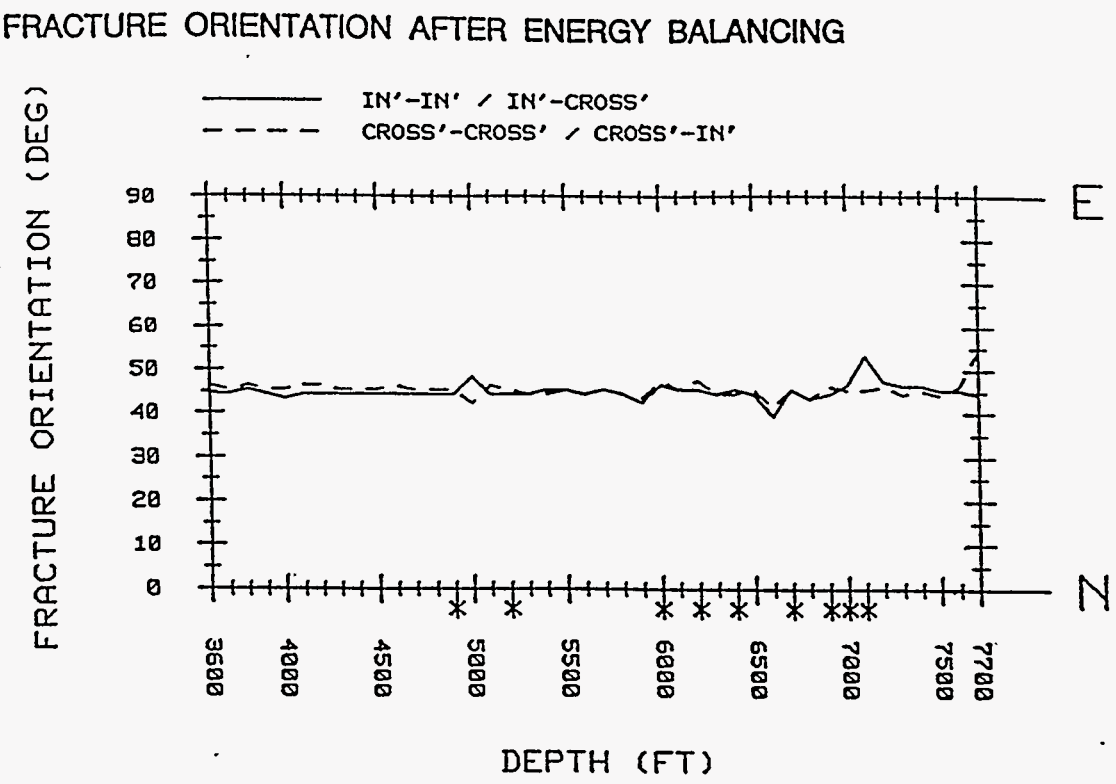


Figure 12. Fracture orientations determined after source (energy) balancing. (Cf. Figure 10.)

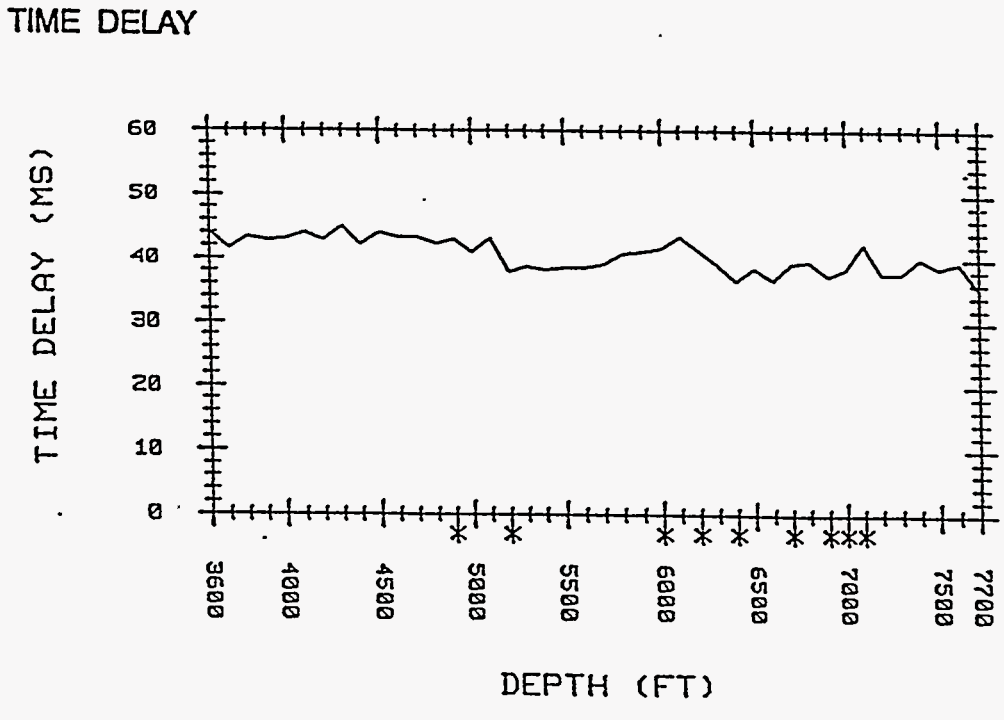


Figure 13. The time delay between the fast s-wave and the slow s-wave (after source balancing).

VSP IN NATURAL COORDINATE FRAME

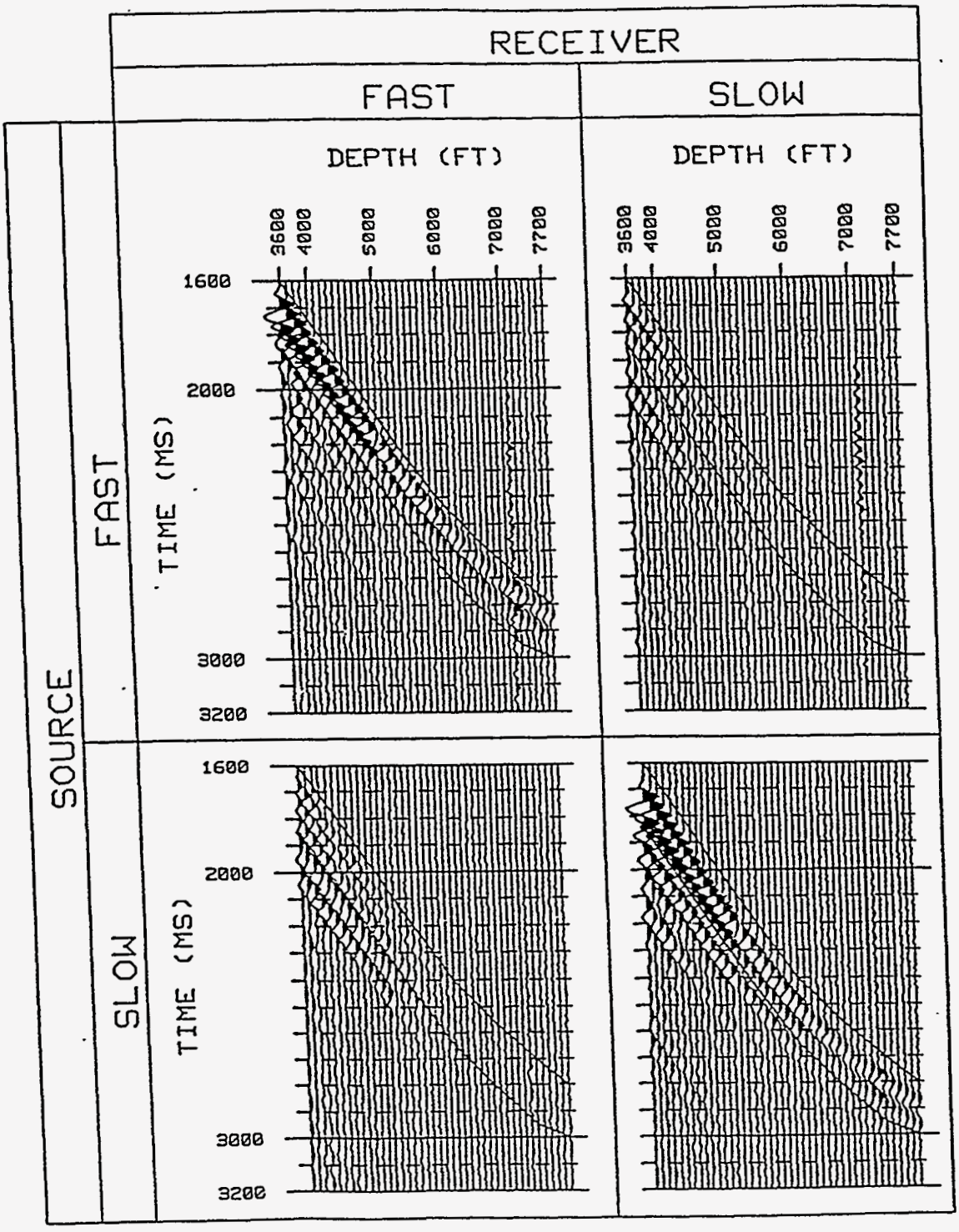


Figure 14. The four horizontal components of the VSP after rotation into the principal-axes coordinate system. (cf. Figure 8).

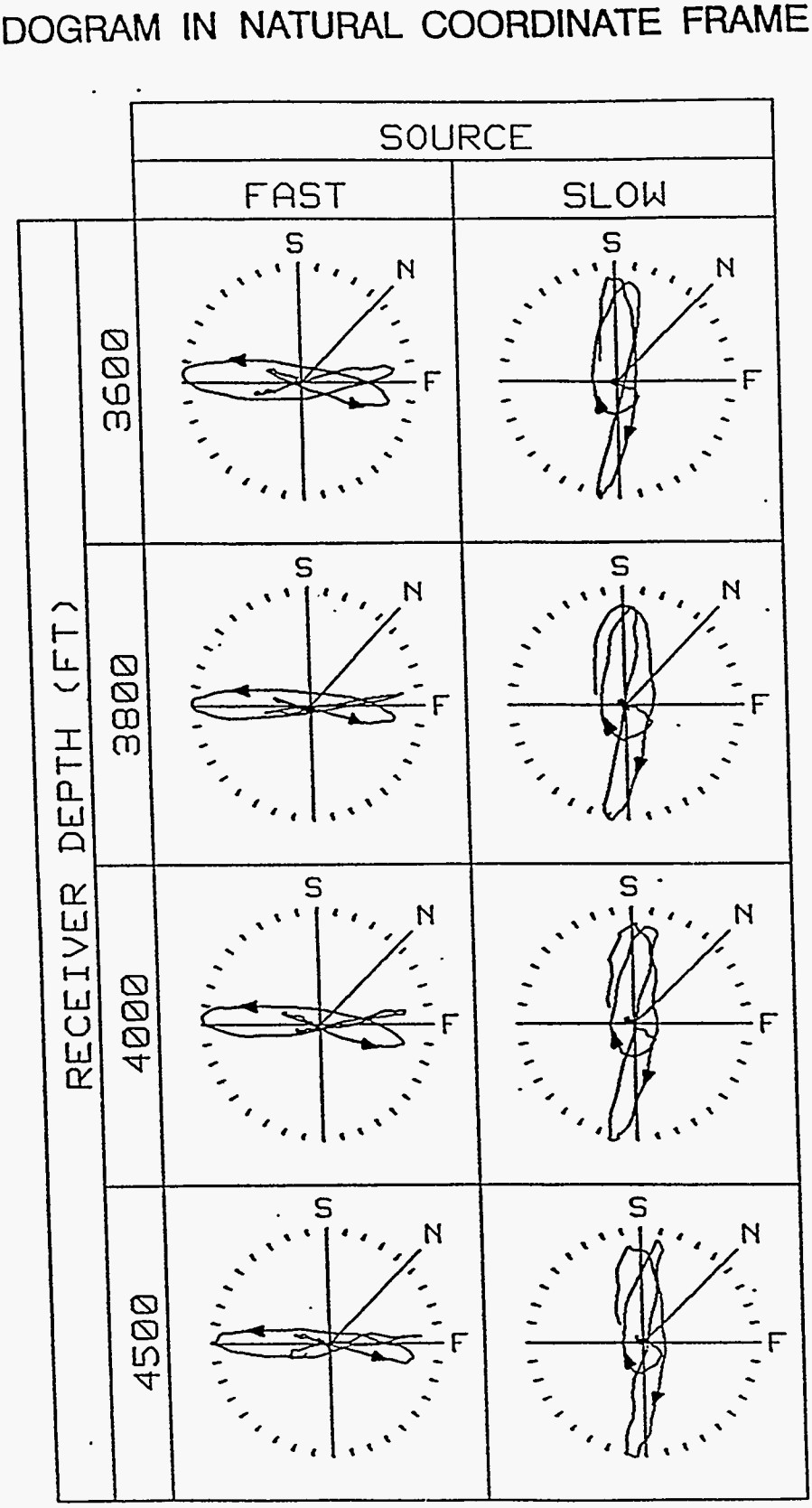


Figure 15. Hodograms generated from the horizontal components when the sources are rotated to the principal (fast and slow) axes. (Cf. Figure 9).

## 4.2 Subtask 2: Relating Recovery to Well-log Signatures

### 4.2.1 Geological Studies

The resistivity response to zones of organic maturity is explained by fluid saturations in the rock matrix. Oil generation in the Austin Chalk begins at 6000 ft and 85°C according to geochemical studies (Grabowski, 1984; Hunt and McNichol, 1984). The immature zone above 6000 ft has essentially no oil saturation and about 90% water saturation (Figure 1). The mature zone is divided into an upper storage zone and a lower migration zone. The storage zone from 6000 to 7000 ft contains greater than 60% oil saturation and 40% or less of water saturation. The migration zone below 7000 ft contains 20% oil saturation and 60 water saturation.

When oil generation begins, bitumen is retained in the rock matrix of the storage zone because permeabilities are less than 0.01 md. There is little fluid loss in core recovery, and under subsurface conditions the matrix holds nearly all of the generated petroleum. As oil generation continues, the expansion of oil and gas resulted in microfactures by which the petroleum escaped from the matrix to nearby tectonic fractures. Consequently, the migration zone contains less oil and more water. The difference in water saturations between the storage and migration zones suggests that approximately 40% of the oil has migrated whereas about 20% remains in the matrix under subsurface conditions. The matrix oil has been lost in core recovery and is interpreted to be moveable oil in the subsurface (Figure 1). Thus the migration zone is the reservoir interval which contains, on the average, about 40% of the generated oil in tectonic fractures and 20% in the matrix.

#### 4.2.1.1 Resistivity and Saturation

The average resistivity recorded in well logs directly reflects the water saturation (Figure 2) (Hinds and Berg, 1990). The immature zone has average resistivities of less than 10 ohm-m; the storage (or accumulation) zone has resistivities greater than 40 ohm-m; and the migration zone has resistivities in the intermediate range of 10 to 40 ohm-m. Consequently, from resistivity logs it is possible to estimate the water saturation of a given interval and to predict whether the generated oil is largely retained in the matrix or has migrated to tectonic fractures from which the oil can be produced.

The storage and migration zones are not controlled by depth alone but depend on the quantity of petroleum which has been generated. Beds which contain a large amount of organic material generate larger amounts of petroleum at an early stage, and migration takes place near 7000 ft. On the other had, beds which contain smaller amounts of organic material generate lesser amounts of petroleum, and migration takes place at somewhat greater depths. Therefore, the storage and migration of oil depends largely on organic richness.

#### 4.2.1.2 Primary Migration

The primary migration of oil from the low-permeability matrix to open tectonic fractures takes place by means of microscale fractures formed during oil generation. The microfractures have been observed in cores of the Austin Chalk from the Pearsall field, Dimmitt County, South Texas. A vertical core from 6800 to 7100 ft was recovered in the Proco Gise 1 well (Figure 3). The lower part of the cored section is highly resistive and has an average oil saturation of about 60%. This section represents a storage zone of non-producible oil. No tectonic fractures were found in the core, and no production test was made of the section. Subsequently, a horizontal hole was drilled in the middle Austin

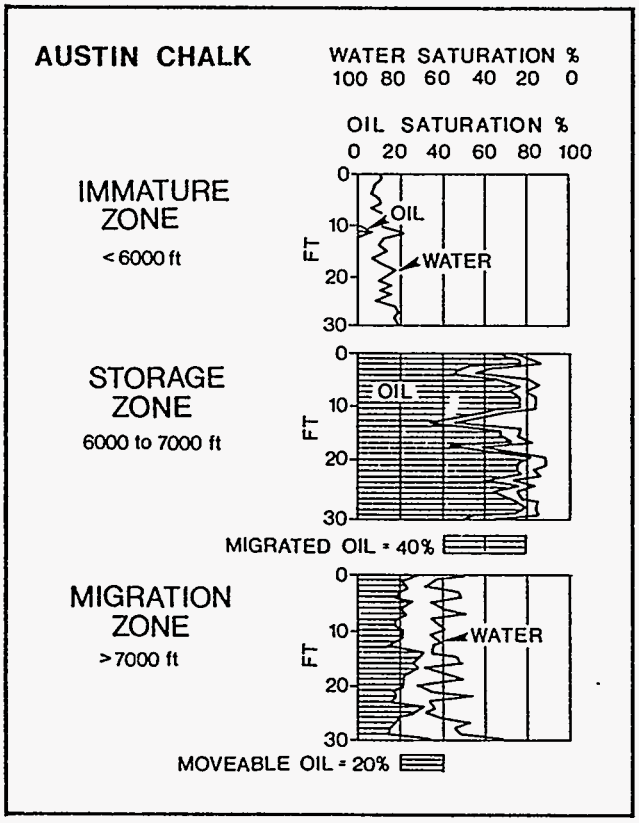
AUSTIN CHALK
WATER SATURATION %
100 80 60 40 20 0
OIL SATURATION %
0 20 40 60 80 100
IMMATURE ZONE
< 6000 ft
OIL
WATER
FT
0
10
20
30
STORAGE ZONE
6000 to 7000 ft
OIL
MIGRATED OIL = 40%
MIGRATION ZONE
> 7000 ft
WATER
MOVEABLE OIL = 20%

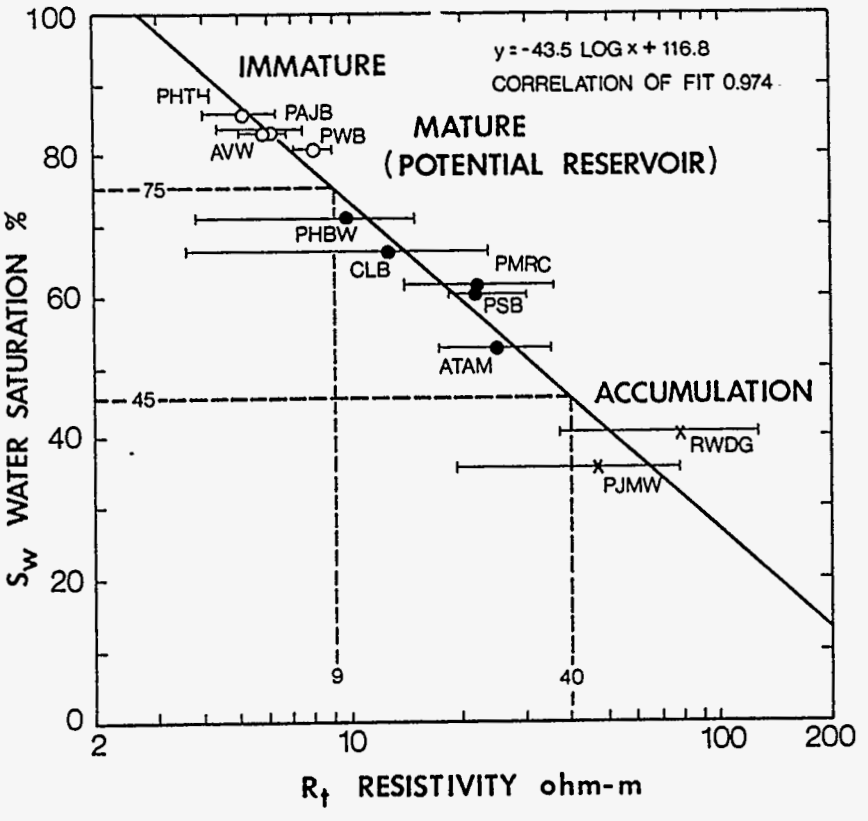
y = -43.5 LOG x + 116.8
CORRELATION OF FIT 0.974
IMMATURE
MATURE
(POTENTIAL RESERVOIR)
ACCUMULATION
PHTH
PAJB
AVW
PWB
PHBW
CLB
PMRC
PSB
ATAM
RWDG
PJMW
75
45
9
40
100
80
60
40
20
0
2
10
100
200
$S_w$ WATER SATURATION %
$R_t$ RESISTIVITY ohm-m

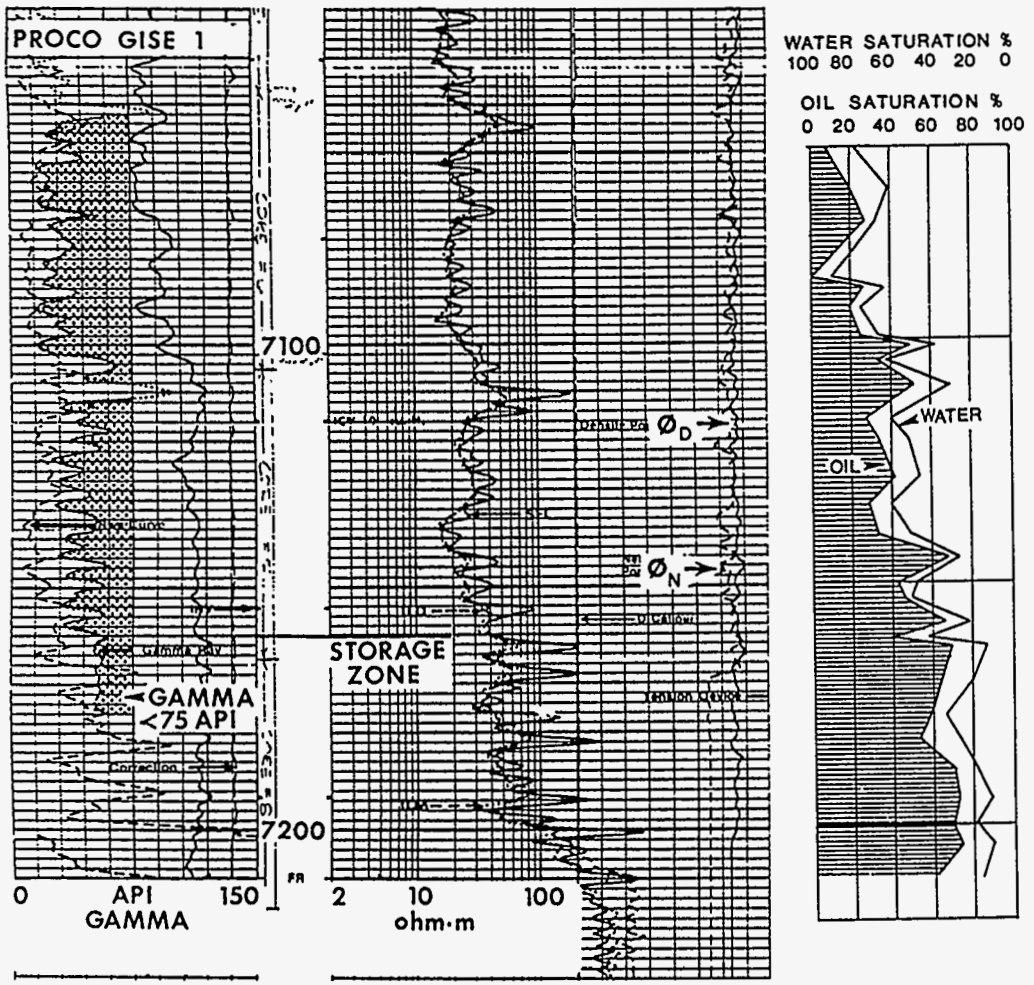
PROCO GISE 1
7100
7200
GAMMA
<75 API
STORAGE
ZONE
$\phi_D$
$\phi_N$
0
API
GAMMA
150
2
10
ohm·m
100
WATER SATURATION %
100 80 60 40 20 0
OIL SATURATION %
0 20 40 60 80 100
WATER
OIL

Chalk, at a depth of about 6900 ft, and oil was produced at a low rate. Apparently, no tectonic fractures were present to provide an economic reservoir at this location.

Microfractures were abundant at many levels in the core. The microfactures are parallel to bedding, have widths on the scale of micrometers (um), and appear to be dissolution seams. Truncated fossil fragments at the margins are primary evidence for dissolution. The microfactures are filled with a matrix of organic material, clay, pyrite, and other insolubles. Oil is present in discontinuous laminae within the matrix and suggests that the dissolution seams could provide the path for primary migration of oil. A geochemical analysis will be made of selected samples in the storage interval to determine the maturity of organic matter and its relation to oil generation, saturation, and well-log response.

4.2.1.3 Aplication of Production

The correlation of resistivity and fluid saturation (Figure 2) suggests that resistivity also may be related to productivity. For example, true resistivity may reflect the relative amount of oil that has migrated from the rock matrix to tectonic fractures. High resistivity would indicate that oil is retained in the matrix whereas lower resistivity would suggest that most of the oil has migrated and now resides in nearby fractures where it is readily producible.

In order to test this hypothesis, a producing area in Pearsall field was selected for an initial study (Sanford, 1990). The lease contains 6 wells and 1 dry hole (Figure 4). Wells 7, 8, 10, and 11 were vertical holes drilled and completed at an earlier date. Well 9 was a short-radius horizontal well, and well 13 was a long-reach horizontal well. Well 12 was a vertical hole that was plugged and abandoned after producing less than 1000 bbl of oil. Significant recoveries were reported for all of the other oil wells, and cumulative production ranged from 16,000 to 174,000 bbl per well during variable periods of a few months to more that 3 years.

Initial potentials for the wells show an inverse relationship with the average resistivities through the perforated intervals (Figure 5). The resistivities are expressed as the product of average resistivity ($R_t$) times the height of the performated section (h). The productive sections are in the lower part of the Austin and have nearly the same thickness of from 80 to 90 ft.

Well 7 had the highest initial potential of 402 bbl/day and the lowest $R_th$ value of 2900 ohm-m-ft. Wells 11, 8, and 9 have successively lower potentials with increasing values of $R_th$. Well 12 had the lowest potential of 18 bbl/day and the highest $R_th$ of 6000 ohm-m-ft. The interpretation of this relationship is that the section in well 12 retains a high saturation of matrix oil whereas in the other wells larger and varibable amounts of oil have been expelled to tectonic fractures. This conclusion assumes that the amounts of oil generated were essentially the same for all sections of the lower Austin.

In the example area (Figure 4) there is no correlation between cumulative production and resistivity. The reason for this may be that the transmissivity of fractures encountered at the several locations are greatly different, and oil produced over a long period reflects the characteristics of the fractures rather than the amount of oil expelled from the matrix.

The results of the initial production study strongly suggest that well-log response can be related to productivity. Data has been gathered on more than 50 wells in the Giddings field, Burleson County, Texas, including well logs, completion histories, and oil production. The well logs have been digitized, and average values of resistivity have been calculated through the producing intervals. Production decline curves will be interpreted to allocate production to fractures and matrix, and productivity of wells will be related to log response.

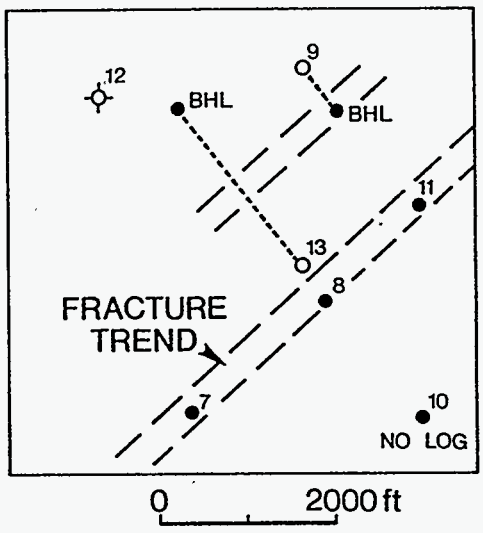
12
BHL
9
BHL
11
13
8
FRACTURE
TREND
7
10
NO LOG
0
2000 ft

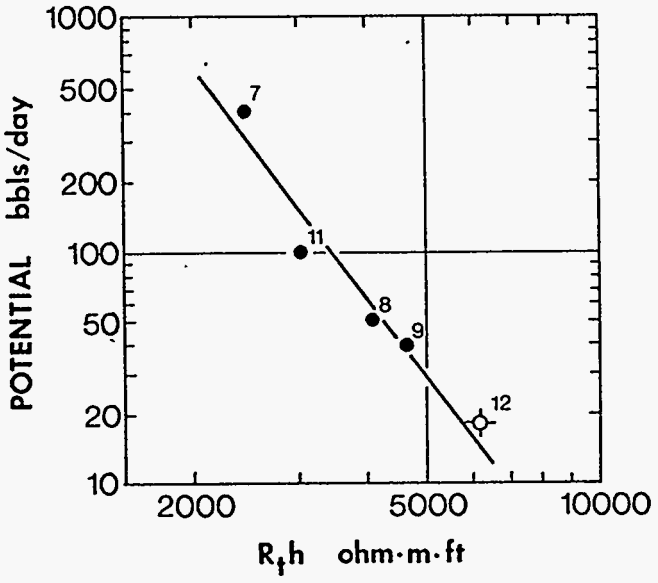
1000
500
200
100
50
20
10
POTENTIAL bbls/day
7
11
8
9
12
2000
5000
10000
$R_t h$ ohm·m·ft

#### 4.2.1.4 Conclusions

It is concluded that the response of resistivity logs is a reliable indicator of organic maturity in the Austin Chalk and that the resistivity response is largely dependent on the oil saturation in the matrix. Therefore, the productivity of wells also may be reflected in log response and may be an aid in prediction of well performance in producing areas and in the evaluation of undrilled areas. Furthermore the interpretation of microscale dissolution features in cores may shed light on the important problem of primary migration from source rock to reservoir.

### 4.2.2 Petroleum Engineering Studies

#### 4.2.2.1 A Theory of Modeling Naturally Fractured Reservoirs

Theoretical Considerations

To accomplish the model features specified in the Introduction, the strategy taken here is to modify the conventional linear constitutive Darcy's Law expressed in terms of Darcy's velocity (flow rate per unit surface) as

$$\mathbf{v}(\mathbf{x},t) = -\frac{k}{\mu}\nabla p(\mathbf{x},t), \tag{1}$$

such that the resulting flow equation has some kind build-in dual-medium characteristics. (In Eq. 1, $\mathbf{v}$, $p$, $k$, $\mu$, $\mathbf{x}$, and $t$ are Darcy's velocity vector, pressure, permeability, viscosity, position vector and time, respectively.) Such a modified flow equation is then combined with the continuity equation, which is independent of the type of flow law, and can be expressed in a form as (without source and sink)

$$-\nabla\cdot\mathbf{v}(\mathbf{x},t) = \phi c_t \frac{\partial p(\mathbf{x},t)}{\partial t}, \tag{2}$$

to obtain the governing partial differential equation (PDE) of the pressure field (or flow field). ($\phi$ and $c_t$ are porosity and total compressibility, respectively.) Note that isothermal equation of state (pressure-density relationship), $c = (1/\rho)d\rho/dp$, has been incorporated in Eq. 2. Thus, only one pressure field (per phase) is considered and avoids the ambiguity of two pressure fields of Barenblatt's theory.[1,2] Furthermore, no explicit fracture-matrix fluid interchanging term and exact internal structure are assumed. Of course, the developed flow equation must be such that it will merge with conventional theory as limiting cases are considered.

As in simplified dual-porosity theories,[1-3] the primary flow path is assumed to be the fracture network. Two major features are to be incorporated into the Darcy's Law. First, the interference of the flow path (in the fracture network) by the matrix blocks. Second, the large permeability contrast between fracture and matrix media. A heuristic development to accomplish the specified goals is presented next.

Consider a scale which is large enough to identify two types of media, fracture and matrix, but still small enough such that only two fracture-matrix interfaces can be seen (see Fig. 2a). For a first approximation, we may assume the relationship between the flux and pressure drop between point "-" and "+" (see Fig. 2a) is governed by a linear relationship, i.e,

$$\frac{dp_m}{dx} = \frac{p_m^+ - p_m^-}{L}, \tag{3}$$

The relationship shown by Eq. 3 is equivalent to a steady-state type flow between point "-" and "+." At the boundaries (i.e., interface of fracture and matrix block), the pressure and flux continuities require that

$$p_m^+ = p_f^+ \; ; \; p_m^- = p_f^- , \tag{4a}$$

and

$$\frac{k_m}{\mu_m}\frac{dp_m^+}{dx} = \frac{k_f}{\mu_f}\frac{dp_f^+}{dx} \; ; \; \frac{k_m}{\mu_m}\frac{dp_m^-}{dx} = \frac{k_f}{\mu_f}\frac{dp_f^-}{dx}. \tag{4b}$$

Since the flux is assumed to be independent of space in Eq. 3, Eq. 4b can be written as

$$\frac{k_m}{\mu_m}\frac{dp_m^+}{dx} = \frac{k_f}{\mu_f}\frac{dp_f^+}{dx} = \frac{k_m}{\mu_m}\frac{dp_m^-}{dx} = \frac{k_f}{\mu_f}\frac{dp_f^-}{dx}. \tag{4c}$$

Equation 3 is more appropriate in terms of fracture pressure since the macroscopic flow field is to be represented by the flow in the fracture network. Using the conditions of Eqs. 4a and 4c, Eq. 3 becomes

$$p_f^+ - p_f^- = \frac{(k/\mu)_f}{(k/\mu)_m} L \frac{dp_f^-}{dx}. \tag{5}$$

If we choose to fix the fracture pressure at point "+", $p_f^+$, and use it as a reference pressure. Then Eq. 5 can be written as

$$p_f^* = -\frac{(k/\mu)_f}{(k/\mu)_m} L \frac{dp_f^*}{dx}, \tag{6}$$

where $p_f^* = p_f^+ - p_f^-$.

Equation 6 is the desired first relationship describing the interference of fracture flow path by the matrix blocks. This interference (or resistance) is in terms of a permeability ratio and certain dimension of matrix block. In this connection, the above concept is similar to the skin concept in well testing theory.

Since the permeability of fracture is much larger than that of matrix blocks. We may assume the flow in the fracture at the neighborhood of interface is governed by a storage controlled process at the scale shown by Fig. 2a. Then, from a material balance consideration, we have

$$q_f = q_m^- - c_f V_f \frac{dp_f^-}{dt}, \tag{7a}$$

$$= A\frac{k_m}{\mu_m}\frac{dp_m^-}{dx} - c_f V_f \frac{dp_f^-}{dt}, \tag{7b}$$

$$\frac{k_m}{\mu_m}\frac{dp_m^+}{dx} = \frac{k_f}{\mu_f}\frac{dp_f^+}{dx} = \frac{k_m}{\mu_m}\frac{dp_m^-}{dx} = \frac{k_f}{\mu_f}\frac{dp_f^-}{dx}. \tag{4c}$$

Equation 3 is more appropriate in terms of fracture pressure since the macroscopic flow field is to be represented by the flow in the fracture network. Using the conditions of Eqs. 4a and 4c, Eq. 3 becomes

$$p_f^+ - p_f^- = \frac{(k/\mu)_f}{(k/\mu)_m} L \frac{dp_f^-}{dx}. \tag{5}$$

If we choose to fix the fracture pressure at point "+", $p_f^+$, and use it as a reference pressure. Then Eq. 5 can be written as

$$p_f^* = -\frac{(k/\mu)_f}{(k/\mu)_m} L \frac{dp_f^*}{dx}, \tag{6}$$

where $p_f^* = p_f^+ - p_f^-$.

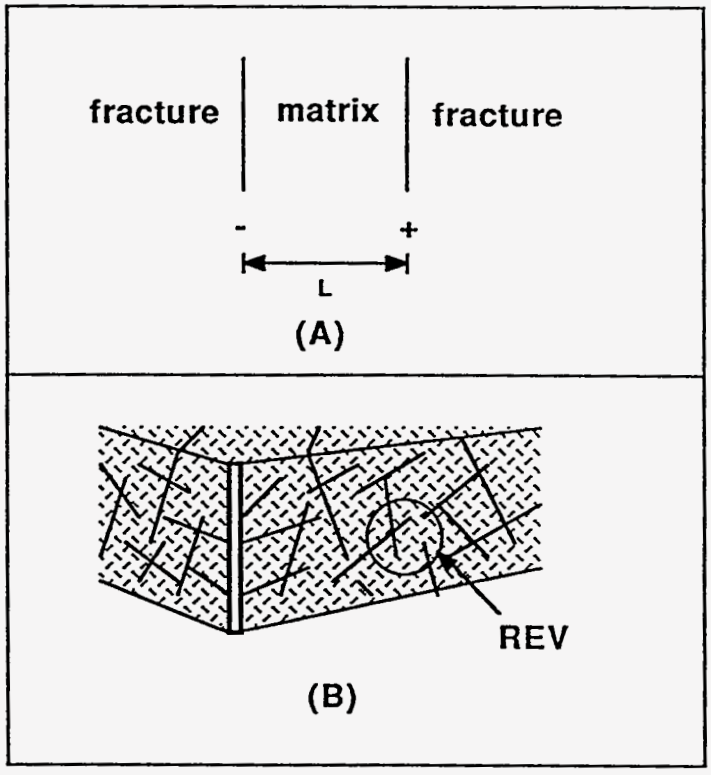


Fig. 2 - Scale of Fractured Medium.

Fig. 2 - Scale of Fractured Medium.

where $A$ is the cross-sectional area normal to flow; $c_f$ is the fluid compressibility in the fracture; and $V_f$ is the fracture volume associated with the element shown in Fig. 2a. Using Eq. 4, Eq. 7 is expressed in terms of fracture pressure as

$$q_f = - A \frac{k_f}{\mu_f} \frac{\partial p_f^*}{\partial x} + c_f V_f \frac{\partial p_f^*}{\partial t}, \tag{8}$$

Equation 8 is the desired second relationship taking into account the fact that the fracture permeability is much higher than that of matrix blocks. Note that the concept applied in Eq. 7 is the same as the wellbore storage phenomenon in well testing theory.

Taking derivative of Eq. 6 with respect to time,

$$\frac{\partial p_f^*}{\partial t} = -\frac{(k/\mu)_f}{(k/\mu)_m} L \frac{\partial^2 p_f^*}{\partial t \partial x}, \tag{9a}$$

$$= -\frac{L/A}{(k/\mu)_m} \frac{\partial q_f^*}{\partial t}, \tag{9b}$$

and combining with Eq. 8, we have

$$q_f = -A \frac{k_f}{\mu_f} \frac{\partial p_f^*}{\partial x} - \frac{L c_f V_f}{A(k/\mu)_m} \frac{\partial q_f^*}{\partial t}, \tag{10}$$

Eq. 10 is the desired flow equation which include the build-in features of resistance of matrix blocks and high permeability of fractures at the scale shown by Fig. 2a.

Now if we consider a scale much larger than that shown by Fig. 2a but still small as compared with the entire flow field considered (see Fig. 2b). At this scale, a representative volume element (REV)[10] may include several fractures and matrix blocks. In other words, the volume associated with the $p_f^*$ will be shrunk into a point as the scale considered now is much larger than that shown in Fig. 2a. We may postulate that the flow equation is represented by Eq. 10 at any point for the scale shown by Fig. 2b such that only one pressure field needs to be considered. With this hypothesis in mind and for the purpose of a general presentation followed, we may generalize Eq. 10 in terms of velocity vector as

$$\mathbf{v}(\mathbf{x},t) = -\frac{k}{\mu} \nabla p(\mathbf{x},t) - t_c \frac{\partial \mathbf{v}(\mathbf{x},t)}{\partial t}, \tag{11a}$$

where

$$t_c = \frac{\phi_f c_f l_c^2}{\sigma (k/\mu)_m}, \tag{11b}$$

$$\sigma = (A/V_b)\, l_c, \tag{11c}$$

$$\phi_f = V_f/V_b, \tag{11d}$$

and $L$ term used earlier is replaced by $l_c$. $l_c$ is defined as an average characteristic length of matrix blocks and the subscripts of $f$ and $m$ are retained only in the definition of $t_c$ (Eq. 11b). The term $t_c$ which involves a "mixed" diffusivity, $(k/\mu)_m/(\phi_f c_f)$, has the same dimension as time and is termed "characteristic time." $\phi_f$, Eq. 11d, is the fracture volume to bulk volume ratio. $\sigma$, Eq. 11c, is the surface area to bulk volume ratio normalized by the average characteristics length of the matrix block ($l_c$) and is dimensionless. Both $\sigma$ and $\phi_f$ serve as "scale factors" as the scale of Fig. 2a is passed to that of Fig. 2b. Gravity effect is neglected in the above development but can be incorporated. The mobility, $k/\mu$, represents a average value of the whole REV which include fracture and matrix blocks.

Again, the extra term describing the rate of change of velocity (second term of Eq. 11a) is to take into account the non-homogeneity of the internal structure of a fractured

medium. If the average characteristic dimension of the matrix block goes to zero, i.e., $l_c \rightarrow 0$ and hence $t_c \rightarrow 0$, then the second term of Eq. 11a describing the rate of change of flux vanishes. The proposed flow equation (Eq. 11a) thus is reduced to the conventional Darcy's Law shown by Eq. 1. Physically, this is equivalent to a non-interfered flow field. Therefore, $t_c$ determines the importance of the rate of change of flux (relative to the flux).

Under steady-state condition (i.e., time-independent), $\partial \mathbf{v}/\partial t = 0$ and Eq. 11 is also reduced to the conventional Darcy's Law even when $t_c \neq 0$. Neglecting the fracture volume, $\phi_f$, or compressibility, $c_f$, is equivalent to setting $t_c = 0$. Such a situation is not allowed in this theory based on the argument of Eqs. 7 and 8. $t_c$ is proportional to $1/(k/\mu)_m$ which represents a resistance term imposed by the matrix blocks. The upper bound of the $(k/\mu)_m$ value should be $(k/\mu)_f$. Equation 11 also can be represented by an integral form and will be discussed later.

Governing PDE

As mentioned earlier, only one pressure field is to be considered. The flow equation is assumed to be represented by Eq. 11. In other words, the flux term in Eq. 2 will be represented by Eq. 11.

Differentiating the modified Darcy's Law Eq. 11a,

$$\nabla \cdot \mathbf{v}(\mathbf{x},t) = -\frac{k}{\mu}\nabla^2 p(\mathbf{x},t) - t_c \frac{\partial}{\partial t}\nabla \cdot \mathbf{v}(\mathbf{x},t), \tag{12a}$$

and combining with Eq. 2, we have

$$-\phi c_t \frac{\partial p(\mathbf{x},t)}{\partial t} = -\frac{k}{\mu}\nabla^2 p(\mathbf{x},t) + \phi c_t t_c \frac{\partial^2 p(\mathbf{x},t)}{\partial t^2}, \tag{12b}$$

where constant properties are assumed. Rearrange Eq. 12b, we obtain

$$\nabla^2 p(\mathbf{x},t) = \frac{1}{\eta}\frac{\partial p(\mathbf{x},t)}{\partial t} + \frac{t_c}{\eta}\frac{\partial^2 p(\mathbf{x},t)}{\partial t^2}, \tag{13}$$

where $\eta$ $[= k/(\phi\mu c_t)]$ is the diffusivity of a fractured porous medium. Equation 13 is the governing pressure field PDE and is in a form of the telegraph equation without leakage (e.g., see Ref. 11, p. 91). Note that the term $t_c/\eta$ in Eqs. 13 and 15 has dimensions of reciprocal velocity squared. Again, if the characteristic time is zero, $t_c = 0$, Eq. 13 is reduced to the familiar parabolic diffusion type equation. For finite value of $t_c$, it is shown in Appendix A that the pressure behavior of Eq. 13 follows wave (i.e., zero $\partial p/\partial t$ term in Eq. 13) and diffusion equation at early and late time, respectively. The time range, evidently, is controlled by the magnitude of $t_c$. The feature that the late time behavior is governed by a diffusion equation is consistent with all the published naturally fractured models.[1-7] (All the models predict that the pressure response differs from that of an equivalent homogeneous medium only under non-steady state conditions.)

Equation 13 is also satisfied if the velocity, instead of pressure, is the dependent variable. Taking derivative of Eq. 11 with respect to time

$$\frac{\partial \mathbf{v}(\mathbf{x},t)}{\partial t} = -\frac{k}{\mu}\nabla\frac{\partial p(\mathbf{x},t)}{\partial t} - t_c \frac{\partial^2 \mathbf{v}(\mathbf{x},t)}{\partial t^2}, \tag{14}$$

and then eliminating $\partial p/\partial t$ with the aid of Eq. 2, we have

$$\nabla^2 \mathbf{v}(\mathbf{x},t) = \frac{1}{\eta}\frac{\partial \mathbf{v}(\mathbf{x},t)}{\partial t} + \frac{t_c}{\eta}\frac{\partial^2 \mathbf{v}(\mathbf{x},t)}{\partial t^2} . \tag{15}$$

Equation 15 the governing velocity field PDE.

Analogy With Heat Conduction Theory

It turns out that the modified Darcy's Law shown by Eq. 11 has the same form as the relaxation heat flux model proposed in heat conduction theory (e.g., see Luikov[12]) The relaxation heat flux model is a generalized Fourier's Law taking into account the finite heat propagation speed. The "characteristic time" ($t_c$, Eq. 11) corresponds to the "relaxation time" used in the generalized Fourier's Law.[12] (The finite heat propagation speed is inversely proportional to the square of the relaxation time.[12]) A casual comparison, however, reveals different physical meaning between these two "times."

The differential form of Eq. 11 also can be represented by an integrodifferential form. Since Eq. 11 is a first-order linear differential equation, an analytical solution can be obtained (e.g., Laplace transform technique) with the following initial condition

$$\mathbf{v}(\mathbf{x},t) = \mathbf{v}_i(\mathbf{x}) ; \; t = 0. \tag{16}$$

The solution of Eqs. 11 and 16 is a convolution type integral as

$$\mathbf{v}(\mathbf{x},t) = \mathbf{v}_i(\mathbf{x})\, exp(-t/t_c) - \frac{k}{\mu t_c}\int_0^t \nabla p(\mathbf{x},\tau)\, exp[-(t-\tau)/t_c]\, d\tau, \tag{17}$$

where the kernel (memory) function is an exponential decay type. Equation 17 indicates that the flux depends on the past history of pressure gradient, i.e., non-local in time. It is interesting to note that Eq. 17 is in a form of the generalized Fourier's Law proposed by Swenson[13] in relation to heat conduction theory. Swenson[13] also showed that by appropriate choice of the memory type of the kernel function, the resulting governing PDE may be in a form of parabolic diffusion, hyperbolic wave or telegraph type equation.

Substituting Eq. 17 into Eq. 2, the following integrodifferential equation is obtained

$$\int_0^t \nabla^2 p(\mathbf{x},\tau)\, exp[-(t-\tau)/t_c]\, d\tau = \frac{t_c}{\eta}\frac{\partial p(\mathbf{x},t)}{\partial t} + \frac{t_c}{k/\mu}\nabla\cdot\mathbf{v}_i(\mathbf{x})\, exp(-t/t_c) . \tag{18}$$

Note that Eq. 18 simply is an integral representation of Eq. 13 with initial flux condition of Eq. 16 been incorporated. This can be checked by taking a time derivative of Eq. 18,

$$\frac{\partial}{\partial t}\int_0^t \nabla^2 p(\mathbf{x},\tau)\, exp[-(t-\tau)/t_c]\, d\tau = \frac{t_c}{\eta}\frac{\partial^2 p(\mathbf{x},t)}{\partial t^2} - \frac{1}{k/\mu}\nabla\cdot\mathbf{v}_i(\mathbf{x})\, exp(-t/t_c) , \tag{19}$$

evaluating the time derivative of the integral at the left-hand-side of Eq. 19 by Leibnitz's rule, and then applying the relationship of Eq. 18, Eq. 13 is recovered as expected.

Comparison With Non-Darcy Flow Theory

The modified Darcy's Law, Eq. 11, is in a form different from the Forchheimer type equations related to non-Darcy flow. Forchheimer type equations are generally represented by a polynomial form in terms of velocity (e.g., p. 66, Ref. 10).

Polubarinova-Kochina[14] also investigated the validity of Darcy's Law and heuristically derived a flow equation which is worth of discussion. Equation 11.4 of Ref. 14 (p. 23), in terms of the notations used here, is the same as Eq. 11a except $t_c$ is replaced by $t_{ck}$ defined as

$$t_{ck} = \frac{k}{\mu}\frac{\rho}{\phi}, \tag{20}$$

where $\rho$ is fluid density and gravity term is dropped for simplicity. Polubarinova-Kochina[14] derived Eq. 11a (with $t_c$ replaced by $t_{ck}$) from microscopic Navier-Stokes equation (see also Hubbert[15]) by neglecting the convective acceleration terms (i.e., $\mathbf{v}\cdot\nabla\mathbf{v}$) and applying Darcy's macroscopic resistance forces (i.e., loss of energy) for fluid flow along the tortuous flow path. He further concluded that the value of $t_{ck}$ is small such that the local acceleration term involving $\partial\mathbf{v}/\partial t$ also can be neglected for all practical purposes. Thus, Darcy's Law can be considered as an empirical equivalent of the Navier-Stokes equation with low fluid velocities. It should be emphasized that Polubarinova-Kochina's[14] equation is based on a homogeneous medium (statistically uniform pore structure) with a scale much less than the intended scale of Eq. 11. The point we try to make is that digressions from Darcy's Law in a form of Eq. 11 (and hence Eq. 13, see also Foster *et al.*[16]) is already possible even for homogeneous porous media.

The telegraph equation shown by Eq. 13 or 15 also appeared in the studies of dispersion phenomenon of porous media. Scheidegger,[17] followed Goldstein's[18] random-walk model approach, derived a telegraph equation by including the autocorrelation effect of the tracer movement. The autocorrelation is the correlation between the directions that a particle possesses at time $t$ and at time $t+\Delta t$. Equation 8.2.3.38 of Ref. 16, in moving coordinates $(\mathbf{x}',t)$ where $\mathbf{x}' = \mathbf{x} - (\mathbf{v}/\phi)t$, is

$$\nabla^2\psi(\mathbf{x}',t) = \frac{1}{D}\frac{\partial\psi(\mathbf{x}',t)}{\partial t} + \frac{t_a}{D}\frac{\partial^2\psi(\mathbf{x}',t)}{\partial t^2}, \tag{21a}$$

where $t_a$ is the autocorrelation time in a form of

$$t_a = \frac{\mu d}{\beta\nabla p}, \tag{21b}$$

$\psi$ and $D$ are probability function (similar to Green's function) and macroscopic dispersion coefficient, respectively. $d$ is particle "walking" distance. $\beta$ depends on the geometry of the flow channel and play the same role as permeability. ($\nabla p$ and $\mu$ are defined as before.) Both $d$ and $\beta$ are microscopic quantities whereas $D$ is a macroscopic quantity. The autocorrelation time, $t_a$, is related to the correlation function, $R(t)$, by

$$R(t) = \exp(-t/t_a). \tag{22}$$

Comparing Eq. 13 (and Eq. 11) with Eq. 21 indicates certain similarity between them. The physical meaning of the characteristic time defined here ($t_c$, Eq. 11b) is more similar to the Scheidegger's[17] autocorrelation time ($t_a$, Eq. 21b) than to the Polubarinova-Kochina's[14] characteristic time ($t_{ck}$, Eq. 20). Also note that the exponential type correlation function shown by Eq. 22 corresponds to the memory (kernel) function indicated in Eq. 17.

## Discussion

It is well known that the concept of Darcy's Law is always associated with a porous volume, i.e., in a macroscopically and statistically correct nature. The Darcy velocity actually is a fictitious velocity averaged over a cross section of a porous medium rather than a true velocity in the pore. Above implies that the nature of the permeability associated with the Darcy's Law and the validity of Darcy's Law depend on the volume interested (or defined). In this connection, our approach using a modified Darcy's Law (Eq. 11) which takes into account the coexistence of fracture and matrix media with highly contrast properties is intuitively correct. As in Barenblatt's[1,2] dual-continuum theory, the scale intended for Eq. 11 is sufficient large to encompass two distinct types of media. As can be seen from the derivation of Eq. 11, the Darcy's Law is still assumed to be valid if only one type of porous medium is considered. Therefore, we may say that the modified Darcy's Law is built up from the Darcy's Law. The modified Darcy's Law in field units is presented in Appendix B.

The approach taken here is different from that used by Barenblatt's[1,2] dual-continuum theory. However, a casual examination of the solutions presented by Barenblatt[1,2] and that of the telegraph or wave type equations reveal certain similarities. This is probably due to that steady-type equation (Eq. 3) is used in developing the modified Darcy's Law here and also is used in Barenblatt's[1,2] fluid interchanging term. We also note that by neglecting the terms with order greater than two (i.e., $>2$) in any dual-continuum PDE[1,2,4,5] (e.g., Eq. 8 of Ref. 1) results in a form similar to Eq. 13. The exact relationship, however, is immediately clear and is not identified yet.

## Conclusion

An approach using a modified Darcy's Law to model the naturally fractured reservoirs is proposed. Derivation of the modified Darcy's Law is "sketched" in this note. The resulting governing PDE using the modified Darcy's Law is a hyperbolic type equation. The development is highly heuristic. Justification from sound fundamental theory is required. Also, the relationship between the proposed model and Barenblatt's needs to be identified.

## Nomenclature

$A$ = area, ft$^2$
$B_o$ = formation volume factor, reservoir volume/standard volume
$c$ = compressibility, 1/psi
$c_t$ = total compressibility in the formation, 1/psi
$c_f$ = fluid compressibility in the fracture, 1/psi
$D$ = dispersion coefficient
$k$ = permeability, md
$l_c$ = characteristic length of matrix block, ft
$L$ = length, ft
$p$ = pressure, psi
$q$ = flow rate, ft$^3$/day
$\mathbf{q}$ = flow rate vector, ft$^3$/day
$t$ = time, day

$t_a$ = autocorrelation time, Eq. 21b
$t_c$ = characteristic time, Eq. 11b
$t_{ck}$ = characteristic time, Eq. 20
$\mathbf{v}$ = velocity vector, ft/day
$V_b$ = bulk volume, $ft^3$
$V_f$ = fracture volume, $ft^3$
$\mathbf{x}$ = position vector, ft
$\mathbf{x}'$ = moving position vector, ft
$\psi$ = distribution function
$\eta$ = $k/(\phi\mu c_t)$, diffusivity of porous medium
$\mu$ = viscosity, cp
$\phi$ = porosity, fraction
$\sigma$ = surface/volume ratio, dimensionless
$\nabla$ = del, differential operator on a scalar
$\nabla\cdot$ = divergence, differential operator on a vector
$\nabla^2$ = Laplacian operator

Subscripts
$c$ = characteristic
$f$ = fracture
$m$ = matrix blocks

## 4.3 Subtask 3: Development of the EOR Imbibition Process

### 4.3.1 Laboratory Displacement Studies

#### 4.3.1.1 Laboratory Aparatus and Procedure

The experimental work was divided into two phases. The first phase was to conduct unadultrated brine and carbonated brine imbibition experiments at room temperature and atmospheric pressure. Compare the results of the experiments and to quantify the improvement in recovery and recovery rate. One of the objectives was to determine the dominant recovery mechanisms, observed during the experimental work.

Phase - I

The sequence of laboratory work in the first phase was to prepare, extract and dry the cores and then determine the basic rock properties like air permeability and porosity. Initially cores were set in the core holder with an overburden pressure and were saturated to 100 % brine, by flowing through the core at a very slow rate of 0.3 c.c/min. The overburden pressure was always kept at least 100 psig greater than the flowing pressure. Oil was then flooded through the core, until brine recovery from the out-let end of the core was reduced to a minimum value. Core samples were weighed after every step to confirm volumetric results by mass material balance. The oil saturated core samples were soaked in brine in a visual imbibition cell for standard 72 hours to monitor the imbibition process at predetermined time intervals. The displaced oil was captured in the thin graduated tube of the visual imbibition cell and was measured as a function of time. The visual imbibition cell especially developed for the first phase of imbibition tests is shown in Figure 1.

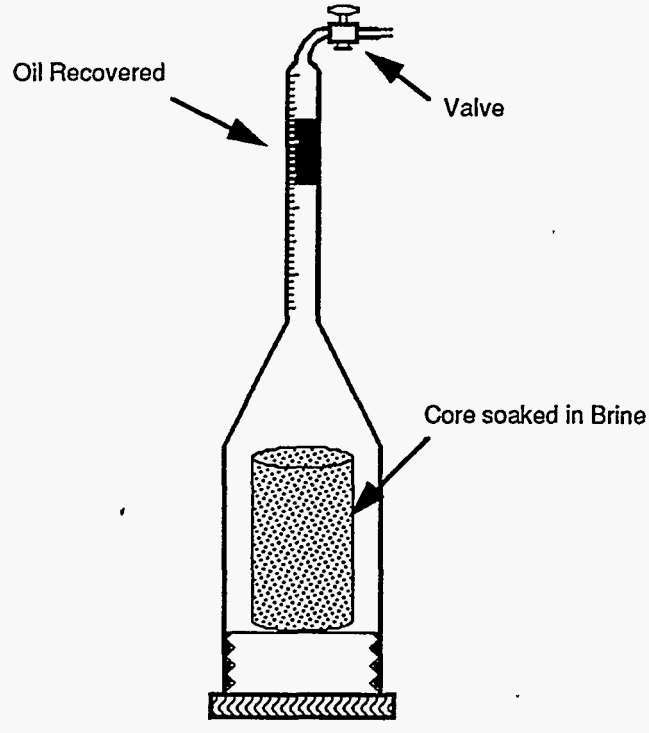


Figure 1 Visual Imbibition Cell

The same procedure was repeated using carbonated brine in place of unadulterated brine to measure oil displacement by carbonated brine imbibition. The data from the two runs was compared to determine any changes in recovery rate or recovery efficiency. Changes in the rock properties after carbonated brine imbibition were also studied. If any change in physical properties was observed in the core sample, the core sample was discarded for any further tests.

The flood brine was distilled water mixed with 10,000 ppm NaCl for all runs. This salt concentration was chosen to be sufficiently high to reduce any possibility of clay interaction and sufficiently low to allow adequate $CO_2$ solubility. The carbonated brine was one percent (by weight) $CO_2$ gas dissolved into 10,000 ppm brine at standard conditions. Kerosene oil was used to conduct all the experiments. Kerosene oil has been selected to avoid the potential of asphaltene precipitation.

Phase - II

The second phase of the experimental work is still in progress. Imbibition experiments are being conducted at higher temperatures and pressures. The visual imbibition glass cell could not be used to conduct experiments at higher temperatures and pressures. A high pressure core holder was developed and set inside the temperature regulated oven to conduct imbibition at higher temperatures and pressures. The core holder has dual fluid taps 3/4 inch apart at inlet face for one inch diameter cores. The oven is a home made, double walled oven built by Celotex insulating sheets. The oil saturated core with irreducible water saturation is placed in the cell. The valve at the outlet face of the core holder is closed and the dual tap at the inlet end is used to conduct imbibition by circulating across one face of the core. The imbibing fluid is introduced through the lower inlet tap at a very slow rate of 0.3 c.c/min. as shown in Figure 2.

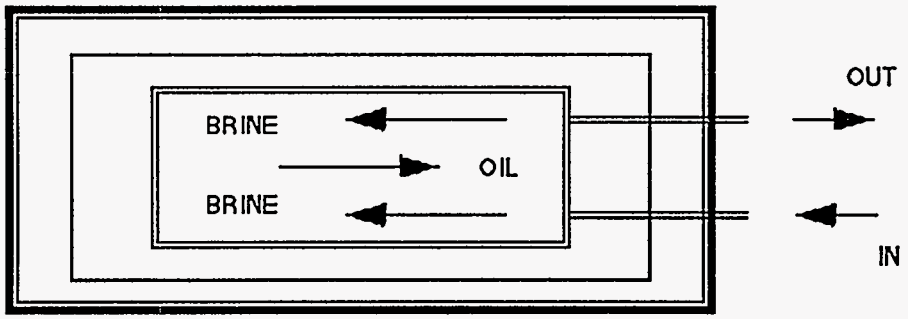


Figure 2 _ Imbibition by circulation across one face of the core at elevated temperature and pressure

The upper fluid tap is connected to a back pressure regulator to control the imbibition pressure and effluent fluids at the inlet face. Different concentrations of carbonated brine will be used for imbibition runs to study the effect on recovery rate and recovery efficiency. The pumps being used for fluids displacement are low volume, high pressure ALCOTT Micromeritics, Model 760 HPLC pumps. An outline of the laboratory setup for the second phase is illustrated in Figure 3.

Different concentrations of carbonated brine solutions have been achieved in the laboratory by dissolving different percentages of $CO_2$ in 10,000 ppm brine at room temperature and higher pressures using $CO_2$ solubility data of Dodds et al.[14] A typical carbon dioxide solubility cure at 70 $^oF$ temperature is shown in Figure 4. Solubility of $CO_2$ in water is directly proportional to the carbonization pressure and is inversely proportional

to the temperature. Solubility of CO decreases as the specific gravity of the water increases due to dissolved salts.

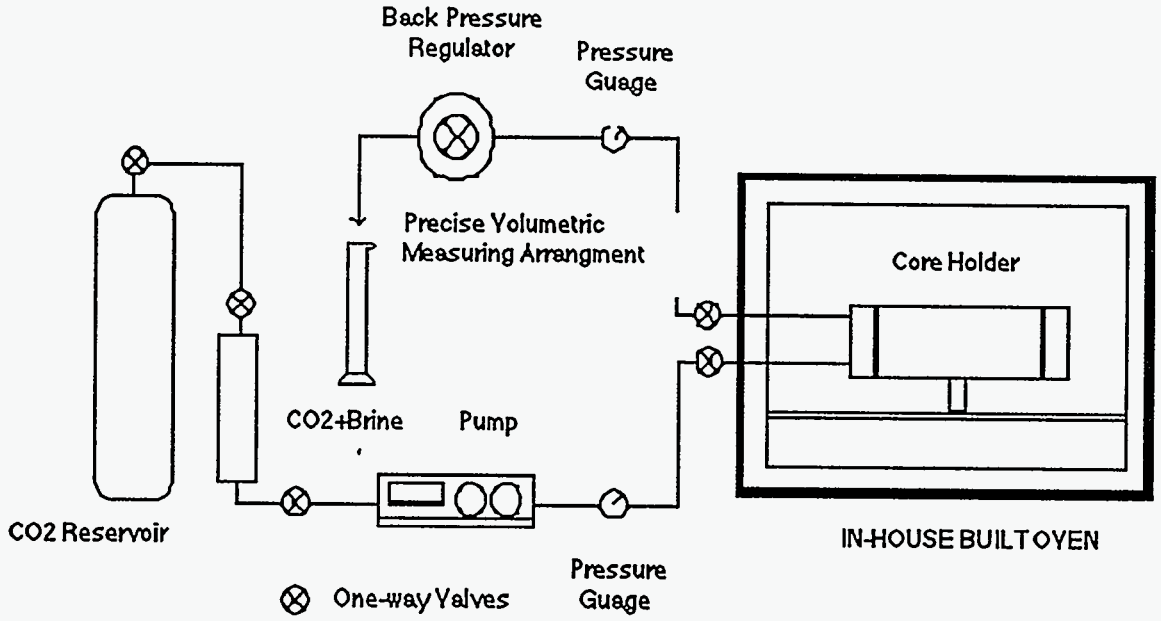


Figure 3 Outline of the laboratory setup for PHASE - II

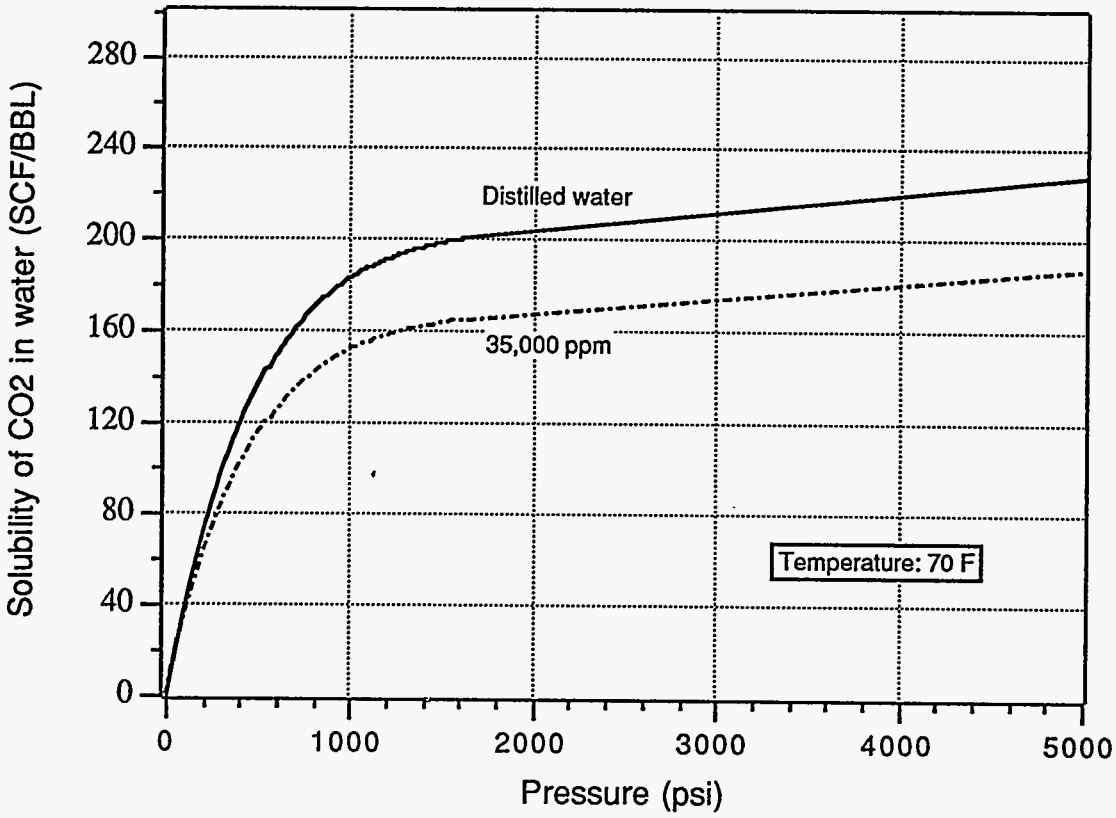


Figure 4 Carbon dioxide solubility curve at 70 $^{o}$F

High degree of precision and accuracy was required in measurements of the fluids because of the extremely small pore volumes of the cores. The average pore volume of the cores is about 5 c.c. and OOIP is of the order of 3 to 4 c.c. The accuracy in measurements have been achieved by collecting the effluent flow in a 6 mm diameter graduated glass tube connected to the bottom of a large bottle with a rubber tube as shown in Figure 5. With this arrangement the displaced oil stayed in the fine tube and the brine moved to the large bottle due to the density difference. Very small volumes upto 0.025 c.c. could be measured with ease.

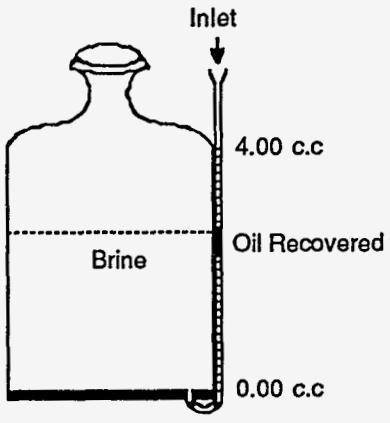


Figure 5 Arrangement for Precise Volumetric Measurements

4.3.1.2 Discussion of Results

Phase - I

The basic data of the sandstone and limestone cores used in the first phase of the imbibition experiments is presented in table 1.

TABLE 1 BASIC DATA FOR SANDSTONE AND LIMESTONE CORES

| SANDSTONES | | | LIMESTONES | | |
|---|---|---|---|---|---|
| Core No. | permeability (md) | porosity (%) | Core No. | permeability (md) | porosity (%) |
| 2 | 389 | 19.5 | 1 | 9.1 | 26 |
| 3 | 107 | 17 | 5 | 8.6 | 22 |
| 4 | 125 | 20 | 7 | 12.3 | 25 |
| 9 | 264 | 22 | 12 | 7.3 | 24 |

Sandstone Cores

Observations from the imbibition runs conducted on sandstone cores gave mixed results. Figure 6 represents comparison of the imbibition runs performed on 125 md,

sandstone core # 4. Neither any improvement in recovery nor any effect on permeability was observed as a result of carbonated brine imbibition.

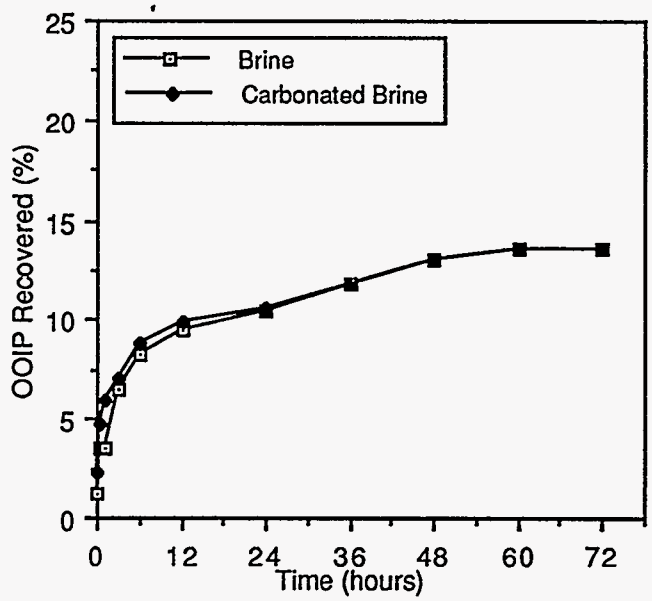


Fig. 6 - Imbibition comparison, 125 md sandstone core # 4

Another 389 md, sandstone core # 2 showed zero recovery when imbibed in unadultrated brine as compared to 9.4 % of OOIP recovery when imbibed in carbonated brine. Figure 7 shows the results of the imbibition experiments conducted on the core.

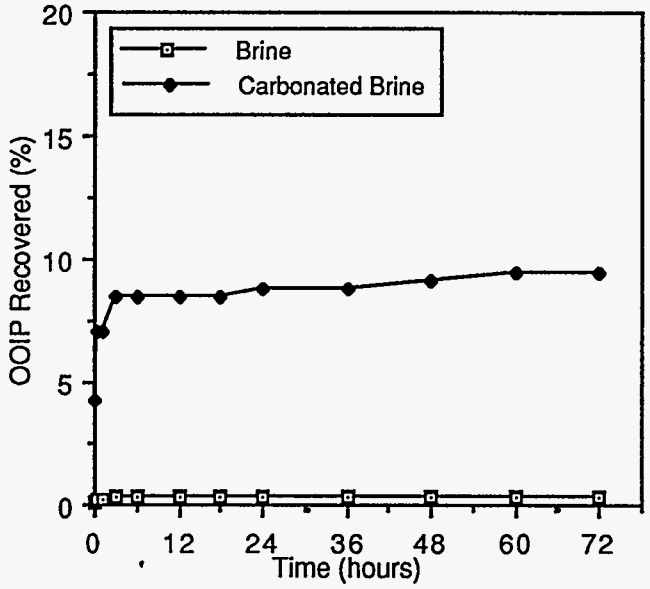


Fig. 7 - Imbibition comparison, 389 md sandstone core # 2

It could be assumed from the results that it was an oil wet sandstone core and carbonated water beneficially affected the wettability of this core. The summary of the effects of carbonated brine imbibition on oil recovery and permeability of the four sandstone cores is presented in Figure 8 below.

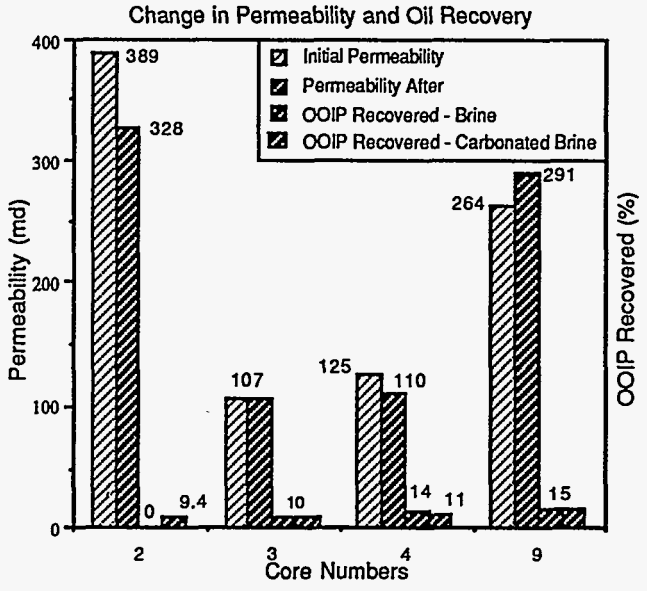


Figure 8 Changes in permeability and oil recovery in sandstone cores

It is obvious that any conclusions based on the results of the experiments conducted, about the sandstone reservoirs behavior to carbonated brine is hard to draw. Sandstone behavior to carbonated brine is highly dependent on the composition of clay minerals present in the rock. Study of depositional environment and detailed mineralogical analysis of sandstone reservoirs is highly desirable. Study of interaction of sandstone reservoirs with carbonated brine have been discussed in papers mentioned in references 13 and 15.

Limestone cores

The limestone cores showed increase in recovery and recovery rate when imbibed by carbonated brine. Figure 9 represents the results of the imbibition experiments conducted on 8.6 md limestone core # 5. Recovery was improved by 26 % and permeability was increased to 10.3 md after carbonated brine imbibition. The vertical dotted line at the end of the carbonated brine curve represents an extra 5 % OOIP recovery induced by blowdown effect when pressure was reduced in the imbibition cell.

Another 12.3 md limestone core # 12 showed recovery improvement by the amount of 18.2 % and permeability increased to 14.8 md. Figure 10 represents the results of the imbibition tests conducted on the core.

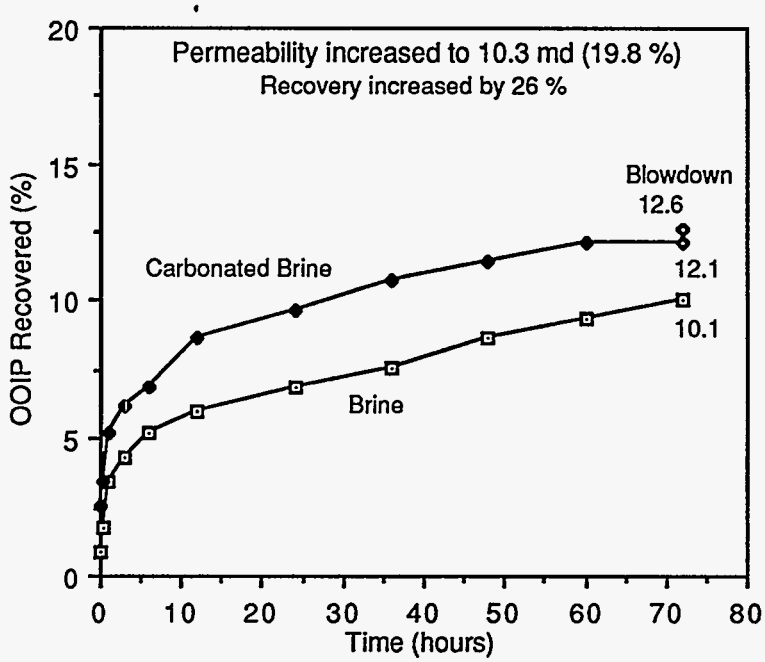


Fig. 9 - Imbibition Comparison, 8.6 md limestone core #5

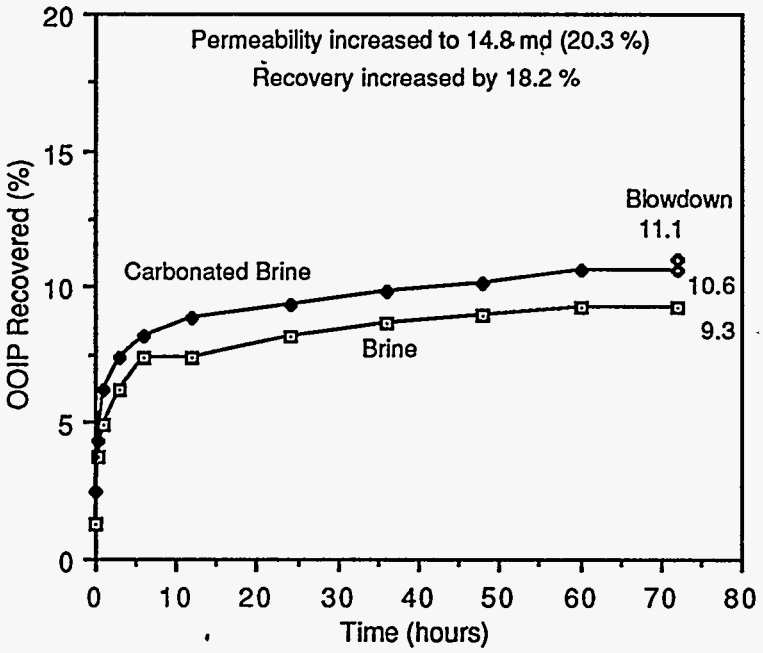


Fig. 10 - Imbibition comparison, 12.3 md limestone core #12

Results of the imbibition run conducted on limestone cores have been summarized in table 2.

TABLE 2 INCREASE IN RECOVERY AND SOLUTION-GAS DRIVE EFFECT IN LIMESTONE CORES

| Core No. | OOIP Recovered (%) | | | Recovery Increased (%) | |
|---|---|---|---|---|---|
| | Brine | Carbonated Brine | Blowdown | Total | Blowdown Effect |
| 1 | 10.2 | 11.8 | 12.2 | 19.6 | 3.9 |
| 5 | 10.1 | 12.1 | 12.6 | 25.7 | 4.9 |
| 7 | 9.3 | 10.6 | 11.1 | 19.4 | 5.4 |
| 12 | 9.6 | 10.5 | 11.1 | 15.7 | 6.3 |

The minimum improvement in recovery at standard conditions is 15 % and the dominant single recovery mechanism observed is the solution-gas drive. Increase in permeability in limestone cores is represented in Figure 11. The minimum permeability increase, more than ten percent, was observed in limestone core # 7.

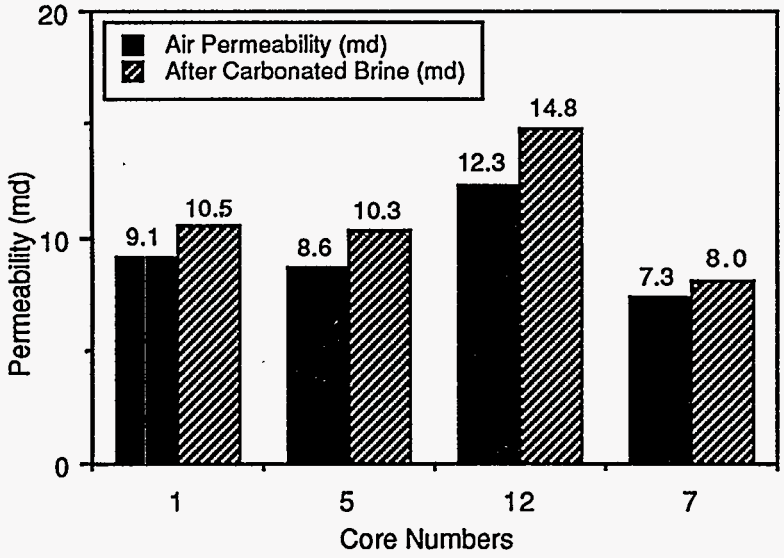


Figure 11 Increase in permeability in limestone cores

One of the dominant factors causing recovery increase is reduction in interfacial tension. This effect was clearly visible in the glass imbibition cell. Oil droplets sticking to the core face showed higher contact angle in unadultrated brine as compared to carbonated brine. This affect is sketched in Figure 12.

Phase - II

Work is in progress in the second phase of the laboratory studies of imbibition flooding. It was decided for this part of the studies to conduct all imbibition experiments using only one limestone rock. Texas Cream Chalk was selected for this purpose because reservoir cores are hard to obtain and this rock is readily available from the outcrop near Austin. The average porosity of the cores cut from the rock is about 24 % and the permeability varies between 7 to 12 md. Results of the experiments conducted so far have indicated that increase in recovery is proportional to increase in temperature and is also proportional to increase in concentration of carbonated brine. A number of experiments

have been conducted on 9 md limestone cores using different concentrations of carbonated brine at 70 °F and 110 °F temperatures.

The comparison of the results of the imbibition experiments conducted for 48 hours at 70 °F and 110 °F temperature and 500 psi pressure using 4 % by weight carbonated brine are shown in Figure 13. Four percent by weight carbonated brine is equivalent to 130 cu ft of $CO_2$ gas dissolved in one barrel of 10,000 ppm brine at standard conditions.

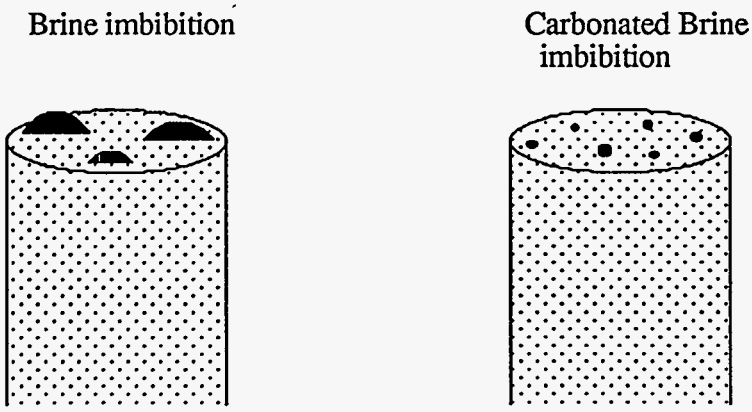


Figure 12 Reduction in interfacial tension

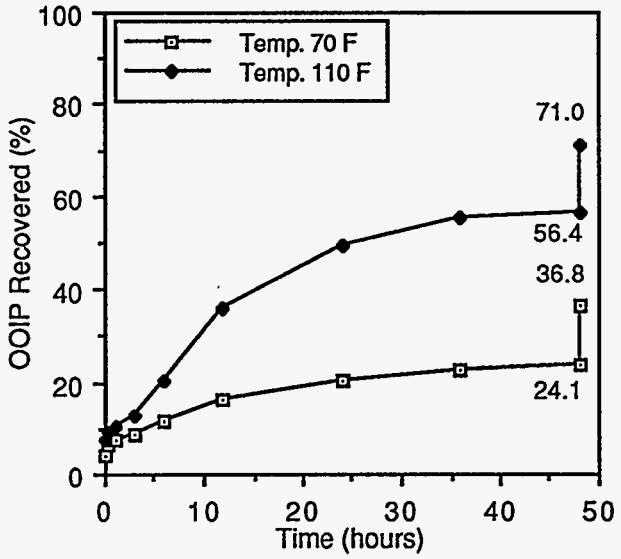


Fig. 13 - Imbibition comparison showing effect of temperature on recovery

At 110 °F an extra 34.2 % of OOIP was recovered compared with the recovery at 70 °F, keeping all the other parameters constant. Blow down process yielded 12.7 % of OOIP at 70 °F and 16.6 % of OOIP at 110 °F, indicating that at higher temperature the solution gas-drive effect is more prominent. Figure 14 shows the effect of change in the

concentration of carbonated brine on the ultimate recovery and recovery rate. Increase in concentration of dissolved $CO_2$ in brine from 2.25 % by weight (85 cu ft/bbl) to 4 % by weight (130 cu ft/bbl) yielded an extra 50.9 % of OOIP. The blow-down effect with 2.25 wt.% of carbonated brine produced an extra 6 % of OOIP whereas with 4 wt.% of carbonated brine the blow-down process yielded an extra 14.6 % of OOIP. These experiments were conducted at 500 psi imbibition pressure and 110 $^{o}$F temperature. Further experiments are being conducted to quantify the results of the imbibition experiments at elevated temperatures and pressures. It is also planned to run imbibition experiments using 5.5 percent by weight carbonated brine which is equivalent to 170 cu ft of CO gas dissolved in one barrel of brine at standard conditions.

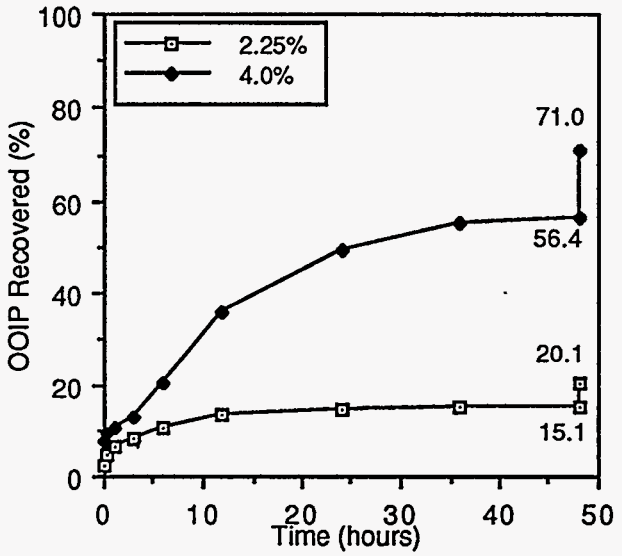

Fig. 14 - Imbibition comparison showing effect of carbonated brine concentration on recovery

Preliminary microscopic studies on the 9 md limestone (Texas cream chalk) have shown no effect of matrix dissolution due to acidic nature of the carbonated brine. It may be due to the fact that the core samples were cut from an outcrop of the rock which has already been long exposed to the atmospheric conditions and clay minerals present may have been altered due to weathering effects.

### 4.3.1.3 Conclusions

Results of the first phase of the experimental work have shown that carbonated brine beneficially effects the recovery.

Phase - I

1. Sandstone cores behavior to carbonated brine is unpredictable. It is more dependent on the depositional environment of the reservoir and clay minerals present at the time of deposition.
2. Limestone cores have shown 15 percent average increase in oil recovery under standard conditions.
3. An average 10 percent increase in permeability was observed in limestone cores.
4. Carbonated brine, being acidic in nature reacts with the rock matrix.

5. Dominant recovery mechanisms observed during the imbibition runs are:
   a - Solution-gas drive effect
   b - Reduction in interfacial tension
6. Reservoir rock composition analysis is vital and primitive to carbonated brine displacement studies.

Phase - II

Results obtained from the partial experimental work conducted in the second phase could be summarized as follow:

1. Development of the laboratory equipment and process to conduct imbibition experiments at elevated temperatures and pressures.
2. Increase in ultimate recovery and recovery rate is proportional to increase in temperature, but this is a limiting factor dependent on the reservoir temperature.
3. Increase in recovery is proportional to the increase in concentration of carbonated brine solution. At higher pressure more $CO_2$ goes into the solution and provides extra energy to the system.
4. Increase in concentration of brine has more prominant effect on recovery improvement than the increase in temperature.
5. Injectivity is also improved at higher pressures as the carbonated brine solution becomes more acidic.

### 4.3.2 MRI Studies

#### 4.3.2.1 Present Status of Imbibition Flooding

Water imbibition by an oil saturated rock is the spontaneous intake of water by the rock. This intake of the wetting phase creates a counterflow of the non-wetting fluid, oil. An exchange of fluids inside the rock is created.

There has been a considerable amount of work published on the imbibition flooding subject. [2-21] Many investigators have tried to determine the parameters that dominate the rate of imbibition and the ultimate oil recovery that can be achieved by this method. The majority of these studies have been performed at low temperatures and pressures. [3-16] Some authors have concentrated on experimental studies while others have focused on mathematical modeling.

Brownscombe and Dyes suggested that imbibition flooding could contribute to oil production from the Spraberry trend of West Texas, [12] in 1952 . This study established the following conditions for applying a successful imbibition flood: (1) the rock has to be preferentially water-wet; (2) the rock surface exposed to imbibition should be as large as possible; and (3) a high oil saturation would greatly benefit the process.

Published studies have been concerned with different conditions under which water imbibition occurs. Geometrical shape and size of the samples, boundary conditions, effects of gravity, type of fluids, and flowing conditions of the fluid surrounding the rock blocks are among the many factors that have been considered. Figure 1 shows several rock shapes used by different authors to study water imbibition flooding.

Imbibition tests have also been used in wettability measurements[22]. These tests consist of immersing a fluid - filled porous media into another fluid and measuring the rate at which the original fluid is being displaced. A typical imbibition curve is shown in Figure 2. The higher the wettability of the porous medium the greater the rate of imbibition. [22] However, the rate of imbibition depends on many factors other than wettability.

Basic Concepts

One dimensional imbibition is described by assuming that a cylindrical piece of porous media is completely surrounded by an impermeable surface except for one end of the cylinder which is designated as the imbibition face. [22] If the porous media is filled with a fluid, the presence of a more wetting fluid against the imbibition face creates a flow of wetting fluid into the porous media, and a counterflow of original fluid from the porous media.

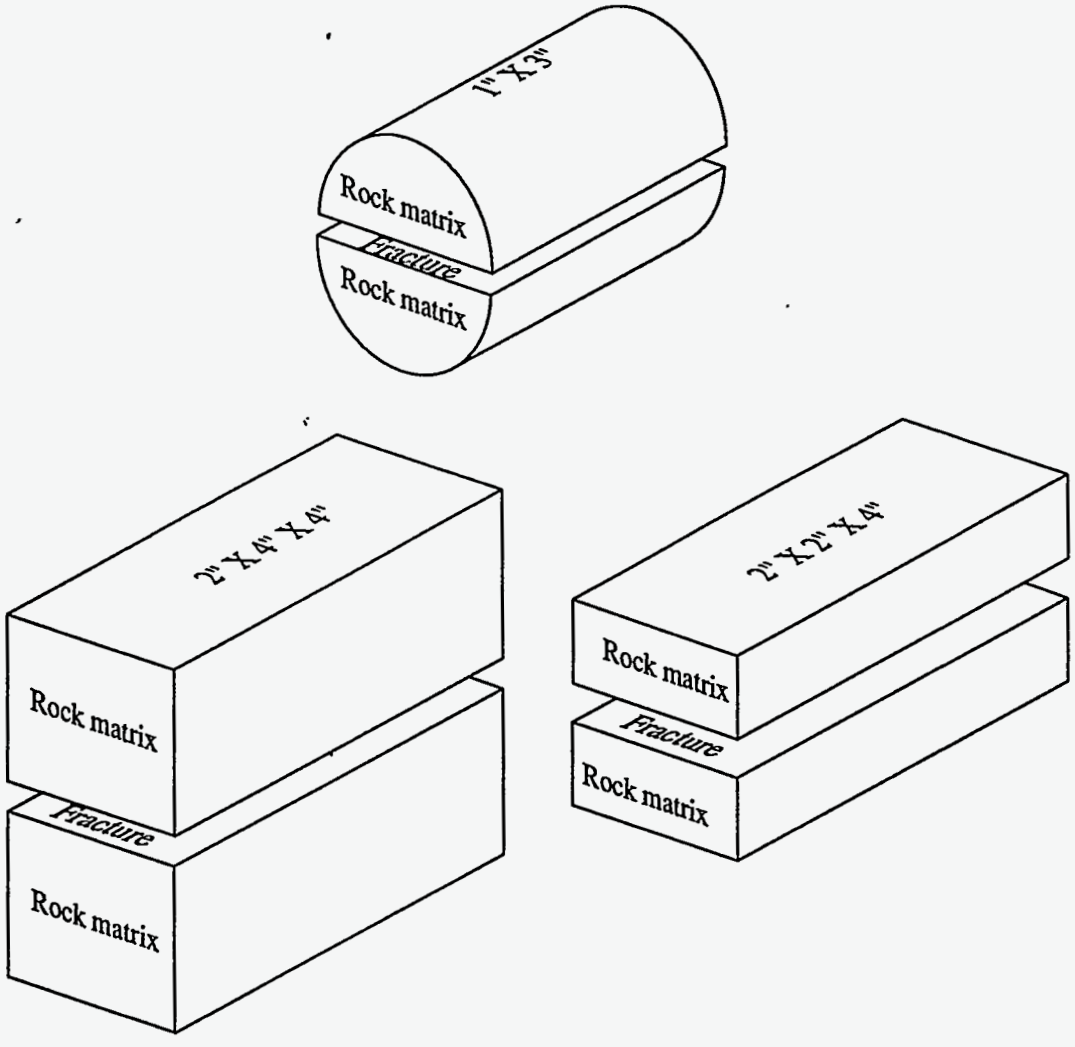


Figure 1 Shapes of cores and blocks used by different authors to study water imbibition flooding. [8]

Imbibition is termed linear whenever the imbibed water moves in one direction only, in the macroscopic scale, see Figure 3. Linear imbibition has been studied by different authors. [2,3,11-13,22-24]

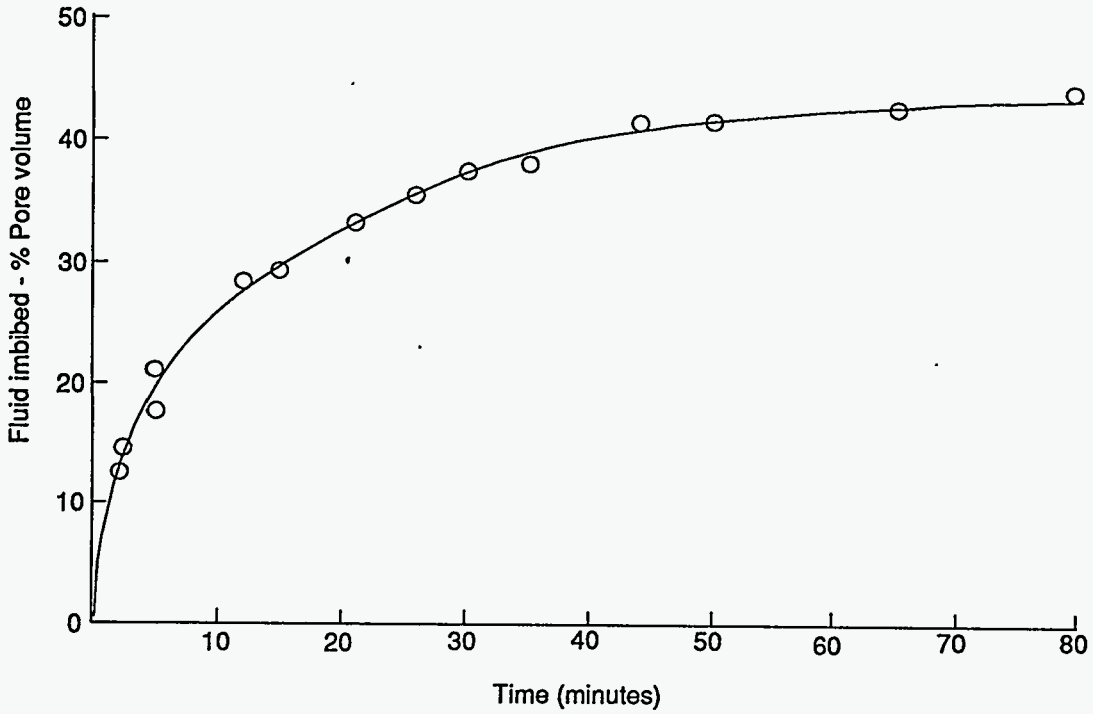


Figure 2 Typical production curve for imbibition. [22]

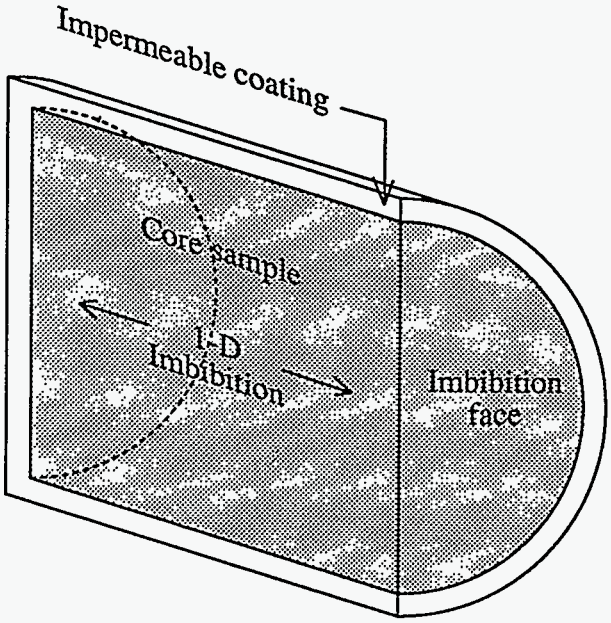


Figure 3 One dimensional imbibition process.

It is assumed that both the flow of wetting fluid (*w*) and the counterflow of original fluid (*n*) are governed by Darcy's law [22]:

$$q_w(x,t) = \frac{k_w(x,t)}{\mu_w} k \frac{\partial p_w(x,t)}{\partial x} \quad (1)$$

$$q_n(x,t) = \frac{k_n(x,t)}{\mu_n} k \frac{\partial p_n(x,t)}{\partial x} \quad (2)$$

Also, the capillary pressure is related to the non-wetting and wetting fluid pressure by the expression:

$$p_c = p_w - p_n \quad (3)$$

Combining the capillary equation with equations 1 and 2, and noting that:

$$q_n(x,t) = - q_w(x,t) \quad (4)$$

Scheidegger[21] obtained the equation that describes the flow rate of non-wetting fluid produced from the imbibing face as a function of time:

$$q_n(0,t) = -k\left[\frac{k_w(0,t)k_n(0,t)}{\mu_w k_n(0,t) + \mu_n k_w(0,t)}\right]\left[\frac{\partial p_c}{\partial x}\right]_{x=0} \quad (5)$$

Leverett's function is expressed as:

$$J(S_w) = \frac{p_c}{\sigma}\sqrt{\frac{k}{\phi}} \quad (6)$$

solving Leverett's expression for capillary pressure[21]:

$$p_c = J(S_w)\sigma\sqrt{\frac{\phi}{k}} \quad (7)$$

The expression of Darcy's law for imbibition flooding was obtained when the expression of capillary pressure shown in equation 7 was introduced [3]:

$$q_n(0,t) = -k\sqrt{\phi}\left[\frac{k_w k_n}{\mu_w k_n + \mu_n k_w}\right]_{x=0}\left[\frac{\partial \sigma}{\partial x}J(S_w) + \sigma\frac{dJ}{ds_w}\frac{\partial S_w}{\partial x}\right]_{x=0} \quad (8)$$

The equation of continuity expresses that:

$$\phi\left(\frac{\partial S_w}{\partial t}\right)_x = -\left(\frac{\partial q_w}{\partial x}\right)_t \quad (9)$$

this equation implies that:

$$\left(\frac{\partial S_w}{\partial x}\right)_t = - \frac{\left(\frac{\partial q_n}{\partial x}\right)_t}{\phi\left(\frac{\partial x}{\partial t}\right)_{S_w}} \qquad (10)$$

Substitution of the previous equation into equation 8 transforms the flow equation into the form [22]:

$$q_n(0,t) = k\left[\frac{k_w k_n}{\mu_w k_n + \mu_n k_w}\right]_{x=0} \left[\sqrt{\phi}\frac{\partial \sigma}{\partial x} J(S_w) - \frac{\sigma}{\sqrt{\phi}} \frac{dJ}{ds_w} \frac{\left(\frac{\partial q_n}{\partial x}\right)_t}{\phi\left(\frac{\partial x}{\partial t}\right)_{S_w}}\right]_{x=0} \qquad (11)$$

Equation 2.11 reveals the importance of several factors: (1) the outflow rate of non-wetting fluid $q_n(0,t)$ varies directly with $\sqrt{k}$; and (2) the term in the first brackets can be written as:

$$\left[\frac{k_w k_n}{\mu_w k_n + \mu_n k_w}\right] = \left[\frac{k_n}{\mu_w (k_n/k_w) + \mu_n}\right] \qquad (12)$$

Scheidegger assumed that the region of porous media in the vicinity of the imbibition face soon acquired high wetting fluid saturation. [22] Therefore, the following equality was considered as a good approximation:

$$\left[\frac{k_w k_n}{\mu_w k_n + \mu_n k_w}\right] = \frac{k_n}{\mu_n} \qquad (13)$$

Therefore, the outflow rate $q_n(0,t)$varies with $1/\mu_n$.

Subsequent Developments

Graham and Richardson

Graham and Richardson also derived an equation that describes the imbibition process [2]:

$$q_o(L,t) = -\sqrt{k\phi} A\sigma f(\theta)\left[\left(\frac{k_{rw} k_{ro}}{\mu_w k_{ro} + \mu_o k_{rw}}\right)\frac{dJ(S_w)}{ds_w}\frac{\partial S_w}{\partial L}\right] \qquad (14)$$

where $f(\theta)$ is a function of contact angle, or a function of wettability, $J(S_w)$ is the Leverett dimensionless capillary pressure, L is the distance from the imbibition face, and t is the time from start of imbibition. They defined the following time scaling term:

$$\sqrt{\frac{k}{\phi}}\sigma f(\theta)/\mu_w \qquad (15)$$

where $f(\theta)$ is a function of contact angle, or wettability.

Graham's equation reveals several facts:

-The oil production rate varies directly with the oil - water interfacial tension, $\sigma$.

-The oil production rate is dependent upon some function of the contact angle, $f(\theta)$.

-The rate of imbibition is a function of the viscosity of oil and water. The rate of water imbibition is inversely proportional to the viscosity, and

-The rate of imbibition is a complicated function of the relative permeability and capillary pressure characteristics of the porous medium.

Graham and Richardson reported that the initial rate of imbibition and the fraction of oil recovered were independent of the sample length. [3] They also reported that the presence of free gas decreased the rate of water imbibition. [3]

Gravity effects are not present in these studies because rock permeabilities are often very low (10 md or less) in fractured reservoirs. Large capillary forces, which drive imbibition flooding, minimize the relative importance of gravity. [13]

Mattax and Kyte

Mattax and Kyte established the basis to scale laboratory results to actual reservoir conditions. [13] The scaling conditions were outlined as follows:

-The shape of the model must be identical to that of the matrix block.

-The reservoir water-to-oil viscosity ratio must be duplicated in the laboratory tests.

-Initial fluid distributions in the reservoir matrix block and the pattern of water movement in the surrounding fractures must be duplicated in the laboratory tests.

-The relative permeability functions must be the same of the matrix block and the laboratory model.

-The capillary pressure functions for the matrix block and the laboratory model must be related by direct proportionality.

When these conditions are satisfied, saturations in the laboratory model will be the same as those in the reservoir matrix block at corresponding times. Corresponding times for the model and the matrix block are related as follows:

$$\left[\frac{tk}{\phi\mu_w L^2}\frac{\partial P_c}{\partial S_w}\right]_{model} = \left[\frac{tk}{\phi\mu_w L^2}\frac{\partial P_c}{\partial S_w}\right]_{\substack{matrix \\ block}} \qquad (16)$$

Using the derivative of the Leverett's function with respect to water saturation:

$$\frac{dJ(S_w)}{dS_w} = \frac{1}{\sigma f(\theta)}\sqrt{\frac{k}{\phi}}\frac{dp_c}{dS_w} \qquad (17)$$

and noting that $dJ(S_w)/dS_w$ and wettability $f(\theta)$ are the same for the model and the reservoir blocks, a dimensionless time scaling factor is found[13]:

$$\left[t\sqrt{\frac{k}{\phi}\frac{\sigma}{\mu_w L^2}}\right]_{model} = \left[t\sqrt{\frac{k}{\phi}\frac{\sigma}{\mu_w L^2}}\right]_{\substack{matrix \\ block}} \quad (18)$$

Mannonn examined the relationship between the rate of water injection through the fractures and the rate of water imbibition. [16] Increase in water injection leads to an increase in oil production, under adequate conditions. Mattax reported that fracture widths above 0.0025 cm have no effect on imbibition. [13]

Aronofsky and Natanson

Iffly concluded, after extensive testing, that only imbibition studies with actual reservoir fluids and rock samples will yield results that can directly be applied to an specific oil field. [17]

Aronofsky and Natanson assumed that oil production from a small volume of porous medium is a continuous monotonic function of time and that it converges to a finite limit. [2] A second basic assumption made was that the properties determining the rate of convergence remain constant during the process. Therefore, the rate of convergence and the limit will remain constant, see Figure 2.

The form of the function of time relative to production from the matrix volume was assumed as follows:

$$R = V_o(t)/V_i(t) \quad (19)$$

$$R = R_\infty(1-e^{\lambda t}) \quad (20)$$

where

$$R_\infty = (1 - S_{orm} - S_{wcm})\phi_m \quad (21)$$

is the limit toward which production converges,

$$R = (S_{wm} - S_{wcm})\phi_m \quad (22)$$

is the recovered fraction of oil originally in place, $\lambda$ is a constant giving the rate of convergence, and $V_i(t)$ is the volume of oil originally in place.

Aronofsky and Natanson [2] considered two cases (1) a single rock block, and (2) a stack of blocks, or a fractured reservoir model, see Figure 4. Recovery from the reservoir is lower than that from a single model element at any time before the production limit is reached, and that the value of the difference at any given time depends uniquely on $\lambda t$ and $R_\infty$. [2]

Extensive waterflood test have shown that the variation of residual oil values is very small in spite of large variations in rock permeability. [2] It has been found that large changes in viscosity and in differential pressure do not affect the value of the residual oil.

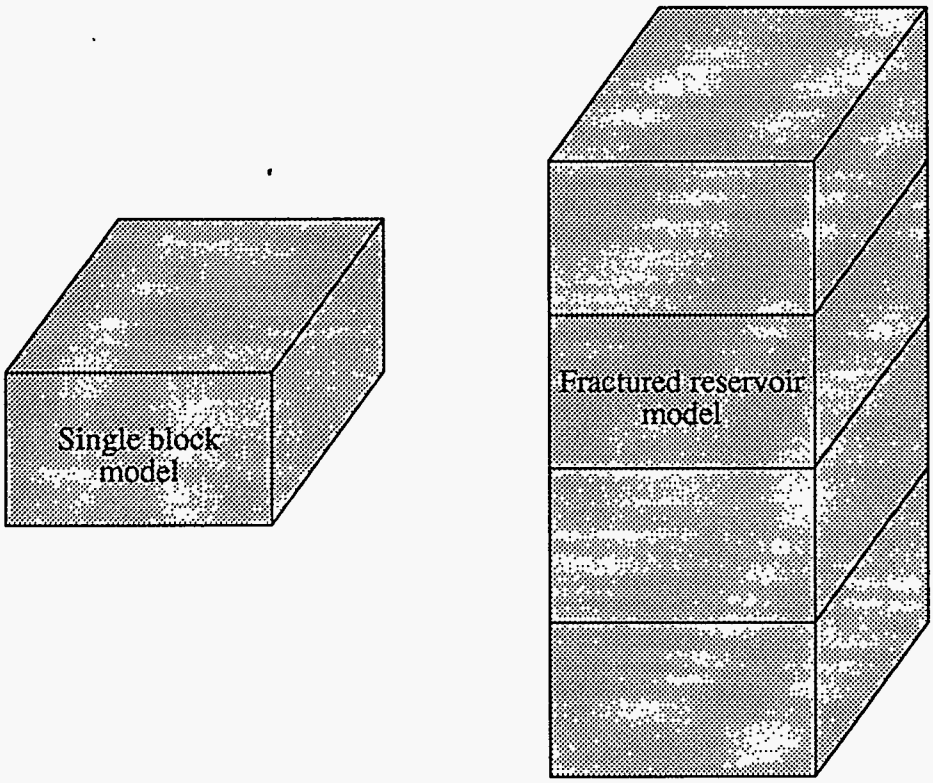


Figure 4 Different models used in Aronofsky's studies.

Kazemi and Gilman

Combining the scaling parameters presented by Mattax and Kyte, [13] and the exponential equation describing oil production due to imbibition introduced by Aronofsky and Natanson, [2] Kazemi and Gilman introduced a dimensionless expression describing the process [11]:

$$R = R_{\infty}(1-e^{\lambda_D t_D}) \tag{23}$$

where

$$t_D = \left(\sqrt{\frac{k}{\phi}}\frac{\sigma}{\mu_w L^2}\right)t$$

and

$$\lambda_D = \left(\sqrt{\frac{\phi}{k}}\frac{\mu_w L^2}{\sigma}\right)\lambda \tag{24}$$

is a dimensionless counterpart of $\lambda$, a constant giving the rate of convergence.

A new shape factor was introduced instead of the characteristic distance L. The shape factor was defined as [11]:

$$\delta = \sum_{s} \frac{A_m}{V_m d} \tag{25}$$

where $V_m$ is the volume of the matrix block, A is the total surface area open to imbibition, and d is the distance from the open surface(s) in a given flow direction to the center of the matrix block. This new factor redefined $t_D$ and $\lambda_D$ as follows:

$$t_D = \left(\sqrt{\frac{k}{\phi}\frac{\sigma\delta}{\mu_w}}\right)t \tag{26}$$

and

$$\lambda_D = \left(\sqrt{\frac{\phi}{k}\frac{\mu_w}{\sigma\delta}}\right)\lambda \tag{27}$$

Kazemi concluded that the exponential recovery constant, $\lambda$, should be considered purely as a curve fitting parameter. Mathematical simulation of the problem was started with the Bucley-Leverett displacement equation. The Buckley-Leverett displacement in a fracture surrounded by matrix rock undergoing imbibition was given by de Swaan as [7]:

$$-u\frac{\partial f_{wf}}{\partial x} = \frac{\partial S_{wf}}{\partial t} + \frac{\lambda R_\infty}{\phi_f}\int_o^t e^{-\lambda(t-\alpha)}\frac{\partial S_{wf}}{\partial \tau}d\tau \tag{28}$$

Study of the equations that describe water imbibition provides an insight into the role of the factors affecting the process.

#### 4.3.2.2 Carbon Dioxide

Carbon dioxide flooding as a method to enhance oil recover is not a new idea. Pirsons suggested injection of $CO_2$ as a mechanism to enhance oil recovery, [25] in 1941.

Whorton and Brownscombe proposed in 1952 that oil recovery could be enhanced using $CO_2$ as an oil displacing mechanism. [26]

McFarlane, et al. concluded that carbonated waterflooding yields additional oil recovery after waterflooding, and that the efficiency of the process is directly proportional to the amount of $CO_2$ dissolved in the water. [27]

Holm found that considerable oil production was obtained by pressure depletion following a carbonated waterflood of a core. [28] An increase in carbonated rocks permeability is also created by a carbonated waterflood. This increase in permeability is proportional to the amount of carbonated water injected through the core. [28]

Menzie and Nielson demonstrated the mechanism of crude oil vaporization and extraction by $CO_2$. [29] Over 50% of a 35° API crude oil was vaporized and extracted by $CO_2$ at 135 °F and 2000 psi.

Kumar and Von Goten found that complete miscibility between $CO_2$ and Woodruff crude oil was not possible in a 45-inch long Berea sandstone core, at 100 °F and 2000 psig. [30]

In 1974 Holm and Josendal concluded that: (1) $CO_2$ is capable of displacing crude oil immiscibly; (2) $CO_2$ is completely miscible with the light hydrocarbons at low temperatures and reservoir pressures; and (3) $CO_2$ is capable of displacing crude oil by multiple contact processes. [31]

Yelling and Metcalfe presented a correlation for predicting the minimum pressure at which $CO_2$ would become miscible with crude oil samples. [32]

A field pilot project in Texas showed that over 50% more oil was produced by the carbonated waterflood than by the conventional waterflood, [33] in 1965 .

The most important mechanisms leading to higher oil recovery are:

-$CO_2$ becomes miscible with water and most crude oils at some pressure.

-$CO_2$ might create swelling of oil.

-$CO_2$ has an acidic effect on calcareous rocks, and

-$CO_2$ creates a gas drive when pressure is depleted below its bubble point.

Carbon dioxide is not miscible with most reservoir oils at low pressures. [34] The solubility of $CO_2$ in crude oils becomes appreciable at pressures above 700 psi. Carbon dioxide becomes miscible with most crude oils at pressures greater than 1400 psi. [31]

The evidence presented by previous authors suggests that the use of carbonated water in water imbibition flooding would accelerate the process and enhance ultimate recovery. It is important to study carbon dioxide properties and its effects on oil and water because $CO_2$ plays an important role in oil recovery by water imbibition flooding.

## Carbon Dioxide Properties

### Gas Compressibility

The perfect gas law expresses the relationship between pressure, temperature, and volume of an ideal gas as:

$$PV = nRT \tag{29}$$

There is no gas that behaves as an ideal gas at all temperatures and pressures. Therefore, the imperfect gas law equation is used for imperfect gases.

$$PV = ZnRT \tag{30}$$

Where Z is the compressibility, or deviation factor. This empirical factor is determined experimentally. The deviation of $CO_2$ from the ideal gas behavior, Z, is given as a function of pressure and temperature.

### Density

Carbon dioxide normally exists as a gas and possibly as a liquid at normal reservoir temperature and pressure. Carbon dioxide is a relatively dense gas with a 50% greater density than air at atmospheric pressure. Carbon dioxide has a much lower compressibility factor at typical reservoir conditions.

$CO_2$ behaves as a vapor with density increasing as pressure increases above the critical temperature. Gas density (lb/ cu ft) can be calculated using the following expression:

$$\rho = \frac{PM}{ZRT} \tag{31}$$

where:

P = pressure, psia,
M = molecular weight ($CO_2$ = 44.01),
Z = gas supercompressibility,
T = temperature, °R,
R = universal gas constant, 10.73.

The Use of $CO_2$ to Increase Oil Recovery

Whorton received the first patent for using $CO_2$ in oil recovery, [26] in 1952. Carbon dioxide was considered a solvent for crude oil. The use of $CO_2$ as an aid to improve oil recovery includes:

-Continuous $CO_2$ gas injection.
-Carbonated water injection.
-$CO_2$ gas or liquid slug followed by water.
-$CO_2$ gas or liquid slug followed by alternate water and $CO_2$ gas injection, and,
-Simultaneous injection of $CO_2$ gas and water.

Carbon dioxide has a critical temperature of 87 °F. This low critical temperature usually prevents most reservoirs from having liquid $CO_2$ present at the sandface.

The majority of mechanisms that take place in imbibition are very similar to those taking place in the previously mentioned conventional methods.

Oil displacement by $CO_2$ injection relies on a number of mechanisms related to the phase behavior of $CO_2$ - crude oil mixtures regardless of how $CO_2$ is injected into the reservoir. The dominant displacement characteristics which are strongly dependent on reservoir temperature, pressure, and crude oil composition, fall into one of the five regions shown in Figure 5:

I Low pressure applications.
II Intermediate pressure, high temperature applications.
III Intermediate pressure, low temperature applications.
IV High pressure applications, and
V High pressure, low temperature (liquid) applications.

The limits that divide regions would vary according to crude oil composition. Heavier crudes will shift these divisions upward.

The present research effort studied imbibition flooding at 2000 psi. Therefore, only mechanisms from intermediate and high pressure, low temperature were be studied.

Low Pressure Applications

The major effects of $CO_2$ injection on oil recovery appear to be induced by the solubility of $CO_2$ in the crude oil. The use of $CO_2$ has several beneficial effects:

-Swelling of crude oil.
-Significant reduction of crude oil viscosity.
-Increases rock permeability, in carbonates, and
-Creates an internal gas drive.

Carbon dioxide diffuses out of the introduced water - $CO_2$ mixture when in contact with the reservoir fluids. As $CO_2$ moves into the reservoir its beneficial effects start acting upon rock and fluid properties.

Swelling of Oil

Carbon dioxide is highly soluble in oils. The solubility depends on saturation pressure, reservoir temperature, and composition of crude oil. [44]

Swelling of crude oil is important for two reasons: (1) the residual oil left in the reservoir after flooding is inversely proportional to the swelling factor; and (2) Swollen oil droplets will tend to force water out of the pore spaces, creating a drainage rather than

imbibition process for water-wet systems. Drainage relative permeability curves are higher than their imbibition counterparts, creating a more favorable oil flow environment at any given saturation conditions.

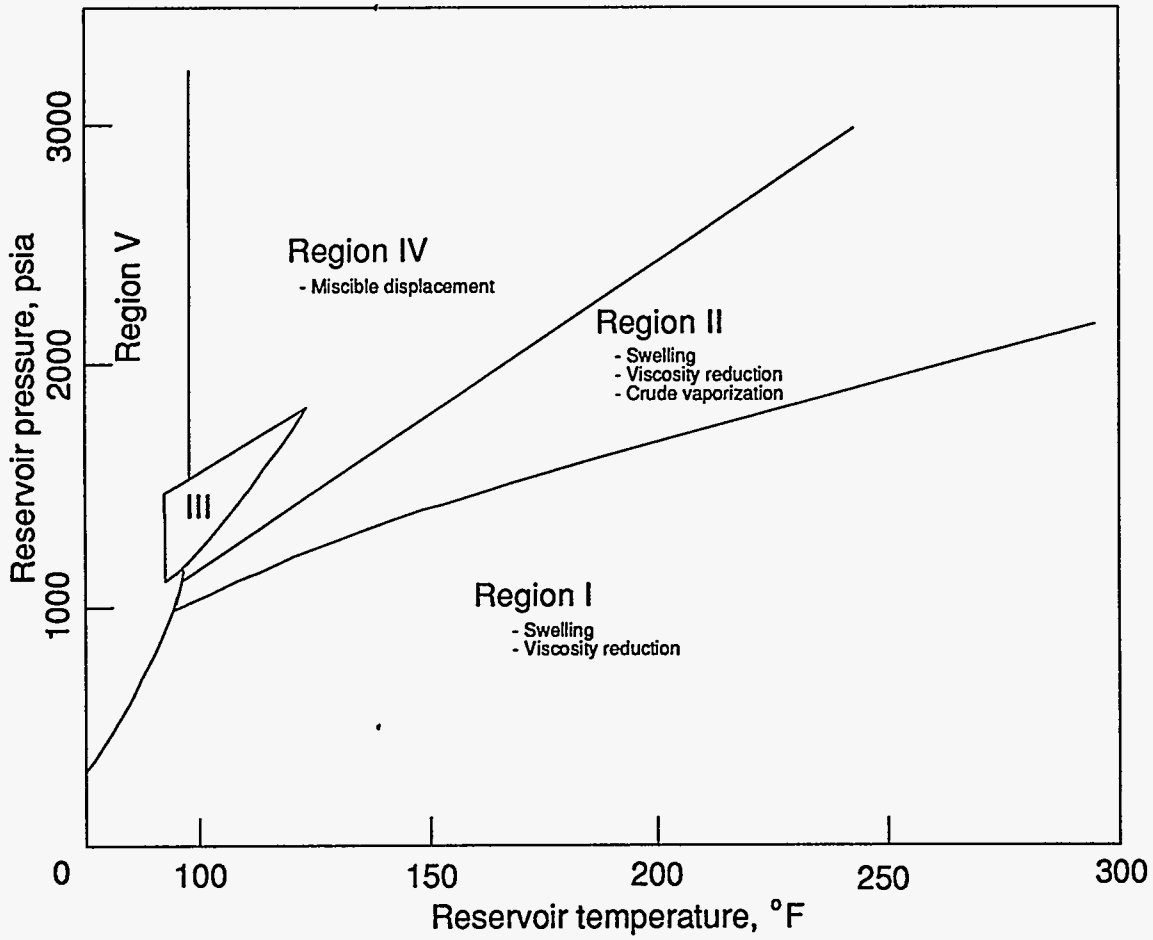


Figure 5 The effect of reservoir temperature and pressure on $CO_2$ injection displacement mechanisms. [43]

Viscosity Reduction

A large reduction in oil viscosity occurs as $CO_2$ saturates the crude. This reduction can yield viscosities one-tenth to one one-hundredth of the original oil viscosity. A large percentage of the reduction occurs in more viscous crudes. The viscosity reduction and its effect on mobility ratio is more significant in medium and heavy crudes. [44]

Increased Rock Permeability

Carbon dioxide mixed with water forms carbonic acid, which might be highly corrosive. Carbon dioxide-water mixtures are slightly acidic and react with the formation matrix. In shales, carbonic acid stabilizes clays due to a reduction in ph:

$$CO_2 + H_2O \longrightarrow H_2CO_3 \qquad (32)$$

Rock permeability is improved by partially dissolving the reservoir rock according to the following equations, in carbonates:

$$H_2CO_3 + CaCO_3 \longrightarrow Ca(HCO_3)_2 \quad (33)$$

$$H_2CO_3 + MgCO_3 \longrightarrow Ca(HCO_3)_2 \quad (34)$$

Figure 6 shows the results of flowing a core sample of calcareous rock with carbonated water and the resulting threefold increase in permeability. [45]

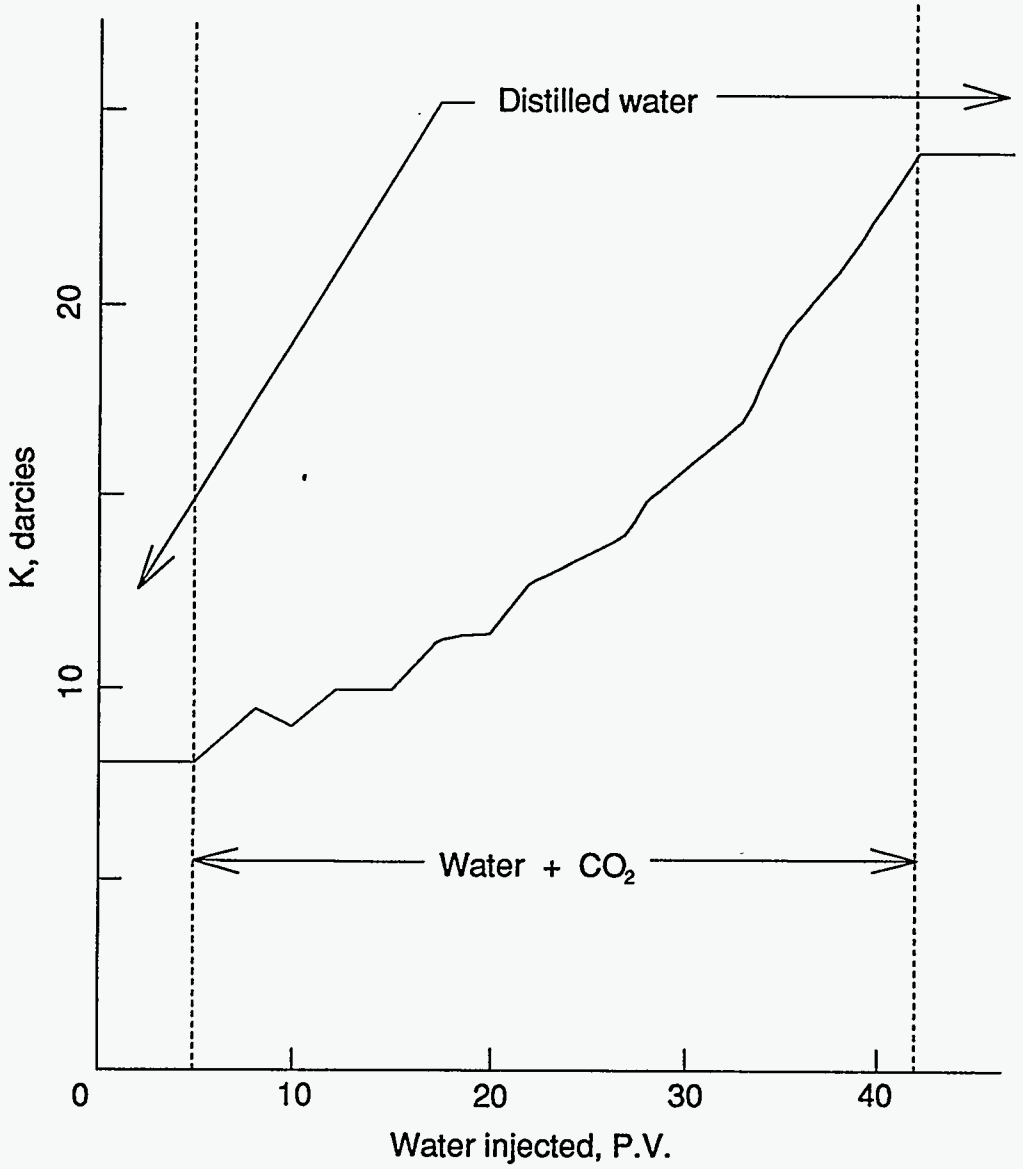


Figure 6 Increase in rock permeability due to $CO_2$. [45]

Solution Gas Drive

After the injection phase of a flood, if the pressure is depleted, gas will come out of solution and continue to drive oil out of the rock matrix. This mechanism of pressure depletion recovery is similar to solution gas drive during the normal production drainage of an oil field.

Carbon dioxide - crude oil solubility, $R_{so}$

Carbon dioxide is highly soluble in oil, making it an attractive immiscible flooding project. Figure 7 shows a solubility correlation. [46] Solubility is expressed as $X_{CO_2}$, the mole fraction of $CO_2$ in a $CO_2$ - oil mixture. For a given saturation pressure, and reservoir temperature, $X_{CO_2}$ can be converted to $R_{so}$ knowing that by definition:

$$R_{so} = \frac{X_{co_2}}{(1-X_{co_2})}\left(\frac{\text{moles } CO_2}{\text{moles oil}}\right) \tag{35}$$

First, convert the moles of $CO_2$ to SCF by multiplying by 379.4 (assuming a standard T and P of 60 °F and 14.7 psia). Then, convert moles of oil to stock tank barrels by: (1) estimating oil molecular weight using Cragoe's estimates [47]:

$$M_o = \frac{6084}{\gamma_o - 5.9} \tag{36}$$

and (2) calculate oil density at standard conditions by the definition:

$$\rho_o = 62.4\left(\frac{141.5}{131.5 + \gamma_o}\right) \tag{37}$$

where

| | | |
|---|---|---|
| $M_o$ | = | molecular weight of stock tank oil, |
| $\gamma_o$ | = | oil gravity, °API, |
| $\rho_o$ | = | stock tank oil density, lb/cu ft. |

Therefore:

$$R_{so} = \frac{\left(X_{co_2}\right)\left(379.4\right)}{\left(1 - X_{co_2}\right)\left(M_{oil}\right)/\left[\left(\rho_o\right)\left(5.615\right)\right]} \tag{38}$$

Care should be taken when using the Simson and Graue correlations. [46] They are empirical fits to make preliminary observations. They should not be used as a substitute for true laboratory measurements when making final predictions.

Intermediate Pressure, High Temperature

Additional production mechanisms come into play under these conditions. Hydrocarbon may be vaporized into the gas phase. $CO_2$ extracts oil in increasing amounts with increasing pressure for a given crude oil and reservoir temperatures. Oil swells only

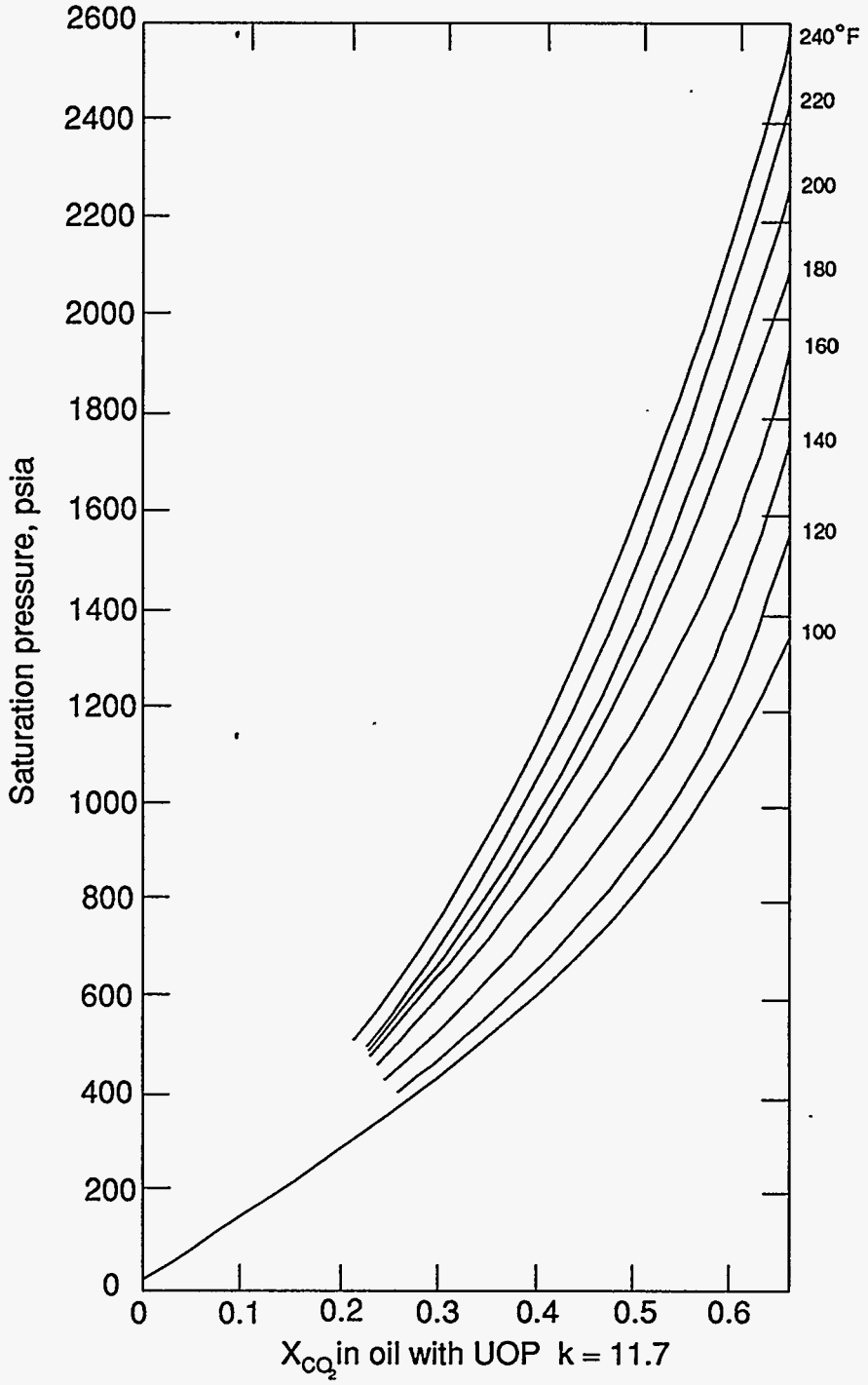


Figure 7 Solubility of $CO_2$ in crude oil as determined by pressure and temperature.[46] Solubility is expressed as $X_{CO_2}$.

to a maximum point. The oil begins to vaporize into a $CO_2$ - rich gas phase after a given pressure.

Vaporization of crude oil is a strong function of pressure and little extraction occurs under 1000 psia saturation pressure. [48] Extraction of liquid hydrocarbons into a $CO_2$ - rich vapor phase occurs when the density of $CO_2$ is at least 0.25 to 0.35 gm/cc. [29]

Intermediate Pressure, Low Temperature

Carbon dioxide may vaporize significant quantities of crude oil so rapidly that multiple - contact miscibility occurs in a very brief period of time, and over a very short reservoir distance, at high reservoir pressures (2000 to 3000 psia). A normal assumption is that $CO_2$ displacement under these conditions obtain instantaneous miscibility; however, because of the high pressure needed, is is doubtful that any field applications of $CO_2$ will involve true first - contact miscibility.

Carbon Dioxide - water solubility, $R_{sw}$

Carbon Dioxide solution in water is proportional to pressure, [49] see Figure 8. An increase in salinity of the reservoir water decreases the gas solubility significantly. A correction factor is needed, see Figure 9 and 10.

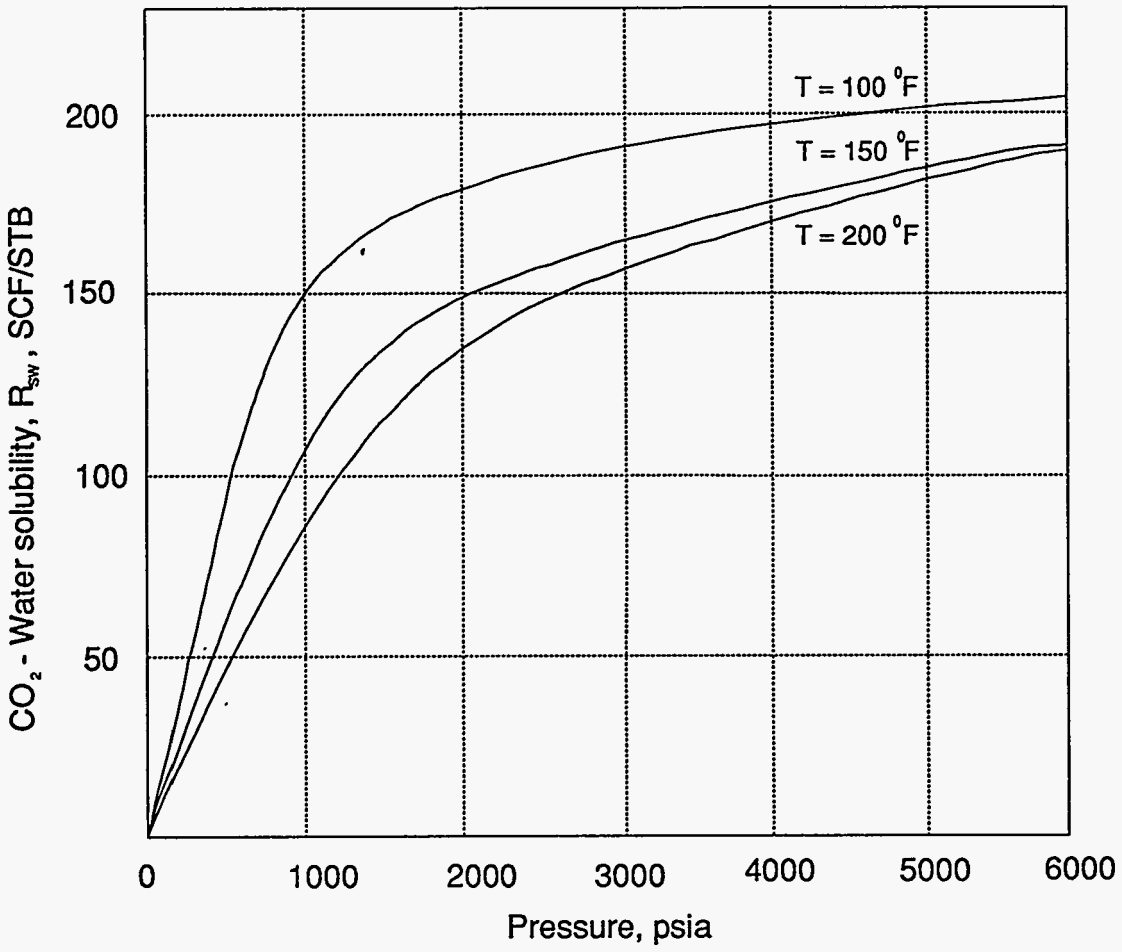


Figure 8 Solubility of $CO_2$ in pure water. [49]

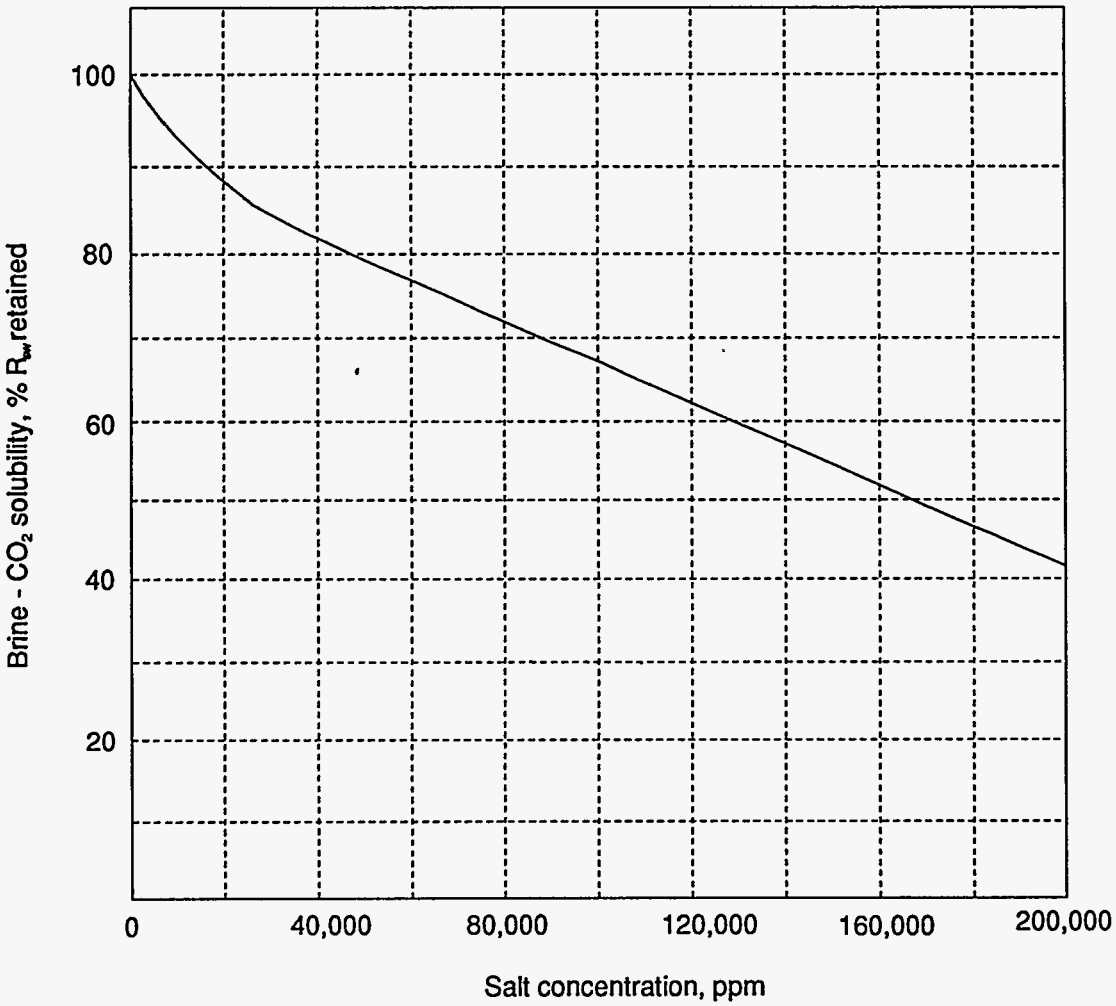


Figure 9 Effect of dissolved salts on the solubility of $CO_2$ in reservoir brines. [50-53]

High Pressure Applications

$CO_2$ may vaporize significant quantities of crude oil so rapidly that multiple - contact miscibility occurs in a very brief period of time, and over a very short reservoir distance, at high pressures (2000 to 3000 psia). Normally it is assumed that $CO_2$ displacements taking place in Region IV type reservoirs, see Figure 5, obtain instantaneous miscibility. First - contact miscibility can be represented on the pressure - composition diagram as an isobar that does not pass through a multiphase region. The reservoir oil (1) and the injected $CO_2$ (2) are miscible in virtually any proportion at the given reservoir pressure and temperature.

First - contact miscibility occurs when a line can be drawn between injected fluid and reservoir oil without passing through the two - phase region. The size of the two-phase envelope shrinks with increasing displacement pressure at a constant reservoir temperature.

Relevant Fluid Properties

Interfacial Tension

Relative permeability curves usually exhibit considerable curvature under immiscible conditions. Residual saturations of the respective phase are also present. As interfacial tension approaches zero, the residual phase saturations decrease, and the relative permeability curves approach straight lines.

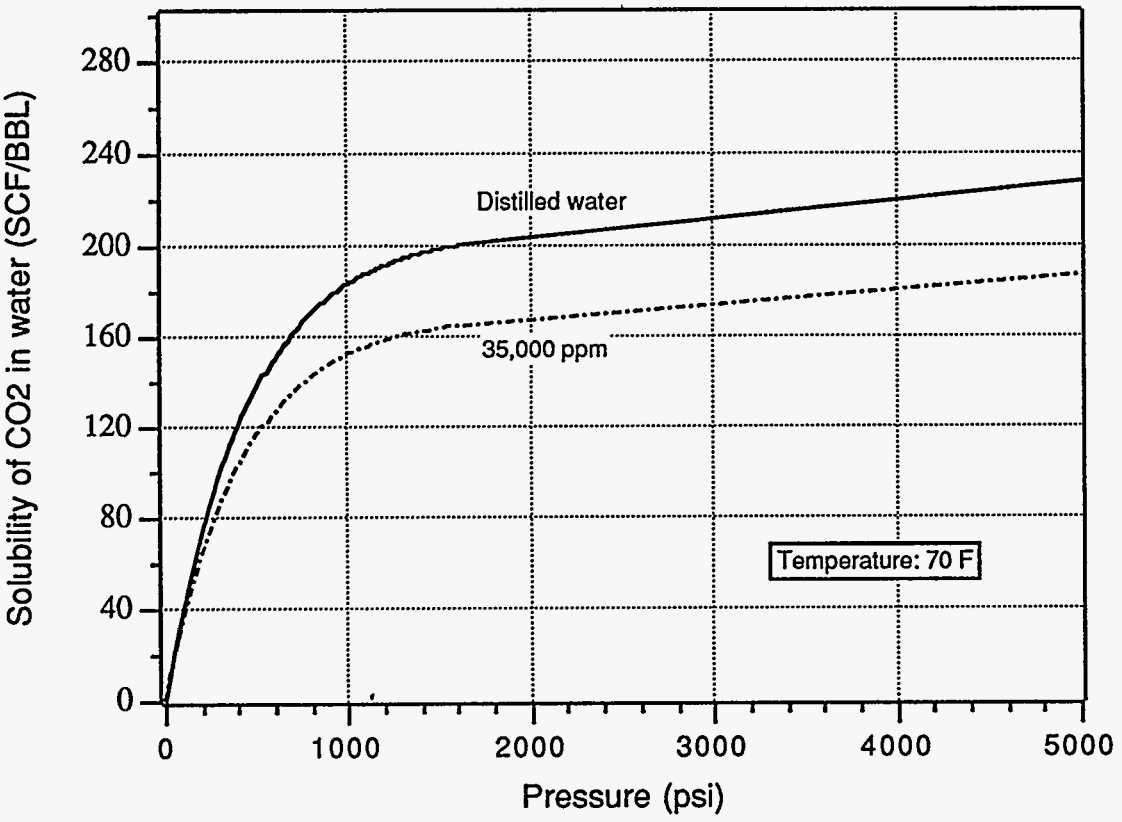


Figure 10 Effect of salinity on $CO_2$ solubility in water.

4.3.2.3 Principles of MRI

Magnetic Resonance Imaging, MRI, was chosen as a method to study water imbibition because the technique presents several advantages: (1) it is a method that does not interfere in any way with the experiments being conducted; (2) allows to monitor oil and water movements inside rock samples; (3) very small changes in oil saturation can be detected; and (4) images on different planes with respect to the sample being studied can be obtained. The images obtained provide useful information about the processes studied, giving a visual conception of the process being studied.

MRI is based on the interaction of nuclei with a strong magnetic field and a radio frequency magnetic field. Certain nuclei spin about their axes, creating tiny magnetic fields. These magnetic fields interact with the strong magnetic field of the spectrometer, which in turn creates two or more energy levels of the nuclei. The magnetic moment for each nuclei is given by:

$$\mu = \gamma h I/2\pi \tag{39}$$

The total magnetization, $\mathbf{M_0}$, is given by:

$$\mathbf{M_o} = N\mathbf{B_o}\gamma^2 h^2(I+1)/3kT(16\pi^2) \tag{40}$$

where:

N = number of nuclei
k = Boltzman's constant
h = Planck's constant
I = spin quantum number
$\mu$ = magnetic moment
$\gamma$ = magnetogiric ration.

The total magnetization is governed by the Bloch equations:

$$dM_z/dt = -(M_z - M_0)/T_1 + \gamma\,(M \times B)z \tag{41}$$

$$dM_x/dt = -M_x/T_2 + \gamma\,(M \times B)_x \tag{42}$$

$$dM_y/dt = -M_y/T_2 + \gamma\,(M \times B)_y \tag{43}$$

Proton profiles that can be obtained using MRI are proportional to oil inside the rock sample because the intensity of the signal obtained is proportional to the number of spins per unit volume. Water and oil give proton responses that are very close. Deuterium oxide was used in place of water to nullify water signals. The only response monitored was obtained from oil within the rock samples.

There are several MRI parameters of particular relevance to the type of experiments conducted during this research effort. In order to apply MRI to an specific oil displacing experiment this parameters have to be adjusted. A brief introduction to the most relevant parameters for this study is given. A detailed study of the subject can be found in the references cited.

Interaction of Nucleus and Magnetic Field

In the absence of any external magnetic field spin-active nucleus spin at random in their atomic or molecular environment but when placed in a strong magnetic field, $\mathbf{B_0}$, these nuclear magnets orient themselves with respect to the direction of the magnetic field.

The interaction of the magnetic moment of a nucleus with an external magnetic field is usually described with a combination of classical and quantum mechanical concepts. Spin-active nuclei can orient themselves in more than one way. For protons there are two possible alignments, either with the field, or against it. MRI techniques perturb these orientation in order to acquire information regarding spin-active nuclei. An external force has to be applied to move the axis away from $\mathbf{B_0}$. This force will change the angle that the axis of rotation makes with $\mathbf{B_0}$.

Slightly more than one-half of the nuclei will orient in one direction along $\mathbf{B_0}$, and slightly fewer than one-half of the nuclei will orient in the opposite direction. The entire collection of magnetic vectors will have a resultant magnetic moment, **M**, called the magnetization, directed along $\mathbf{B_0}$, because there is a slight excess of nuclei oriented in one direction. There is only a tiny population difference between the spin states. A strong

magnetic field, $B_0$, is necessary to create a total magnetic moment, M, large enough to be used in MRI.

MRI flip the resultant magnetic moment and measures the response obtained when the moment comes back to its original position. Necessary torque, in the form of a radio frequency (magnetic field) in a coil, has to be applied to change the orientation of some of the nuclei. The coil is positioned with its axis perpendicular to $B_0$. The transmitter coil is positioned along the x-axis. An alternating current moves through the coil and produces a magnetic field, $B_1$, directed along the x-axis.

The magnitude of the magnetic field varies with time because the current is oscillating with time.

The precessing nuclei experience a torque toward $B_1$. The rotating field accomplishes two things: (1) it causes some of the nuclei to change their orientation, decreasing the magnitude of the magnetization in the z-direction; and (2) the precessing vectors are oriented, forcing the magnetization vector towards the xy-plane. A component in the xy-plane is created.

The component of the magnetization vector in the xy-plane produces a current in the receiver coil in the same way as a generator produces an electric current. The current is then amplified and eventually is displayed as a function of frequency. The receiver does not generate a current until the nuclei begin to relax from the excited state. The relaxation results in a loss of energy that is detected as the magnetic field $B_1$ decays. The magnetic field in turn produces a decaying oscillating current in the receiver coil.

Fourier Transform Spectroscopy

In this type of spectroscopy a high intensity radio frequency pulse is used to excite all the resonance in the range. A signal containing only one frequency is defined as monochromatic. This pulse is sufficient to excite nuclei of different frequencies if the duration of the pulse is correctly chosen. Therefore, a pulse rather than a continuously variable frequency can be used to excite all the nuclei of an isotope in a sample.

A pulse of exactly the right duration and power will move the magnetization vector down to the y-axis, see Figure 11. Pulses of this type, $90^o$ pulses, generate the maximum signal for detection by the receiver, which only detects the component of the magnetization along the y'-axis (x', y', and z' are the axis of a rotating frame introduced to simplify the system). [58] The pulse is a $180^o$ pulse if it is long enough to rotate the magnetization to the z'-axis. The angle between the z'-axis and the rotated magnetization at the conclusion of the pulse is called the flip angle. The flip angle is controlled by intensity of the radio frequency and the duration of the pulse, or pulse width.

The component $M_y$ of the magnetization along the y-axis decreases exponentially as the relaxation occurs. This exponentially decreasing magnetization induces a current in the receiver coil that decays in the same fashion.

Relaxation Mechanisms

The two components of the magnetization can be treated separately. Return of the z-component to its equilibrium value, $M_0$, is known as longitudinal relaxation while the return of $M_{xy}$ to zero is called transverse relaxation. Both processes can be characterized by the time $T_1$, and time $T_2$, respectively, with the Bloch equations, [58] see equations 4.3, 4.4, and 4.5.

Spin-lattice relaxation time, T1, spin-spin relaxation time, T2, and the range of frequencies at which the nuclei resonate, or linewidth, are the most important parameters that concern the petroleum engineer in this type of experiments.

$T_2$ is related to the life time of the signal, [58] for the saturated samples studied was in the order of 10 milliseconds. $T_1$ is the necessary time for the magnetic moment to

recover to its original position after a pulse sequence, [58] for the saturated samples studied was in the order of several hundred milliseconds. Ideally $T_1$ should be as short as possible, and $T_2$ as long as possible. Linewidth is the range at which protons respond to MRI. [58] The linewidth must be as short as possible in order to obtain adequate image resolution

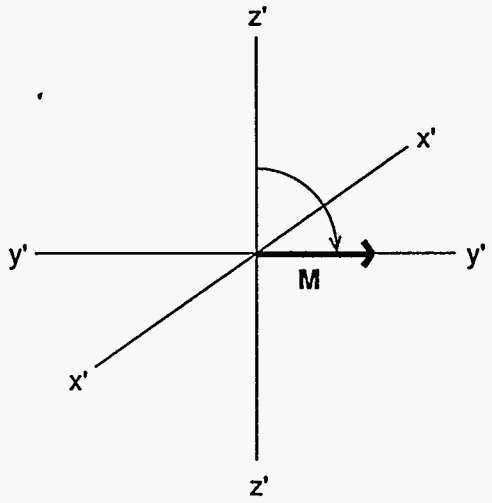


Figure 11 A 90° pulse right after transmitter is turned off.

$T_2 \leq T_1$ because $M_{xy}$ can return to zero before $M_z$ regains its equilibrium value but $M_z$ can never return to equilibrium before $M_{xy}$ becomes zero.

MRI applies a train of radio frequency pulses to perturb the spin system. A pulse sequence often begins with a 90° r.f. pulse. Following pulses depend on the technique to probe the spin system.[58] Recycle time, TR, is the total time for the pulse sequence, see Figure 12. Echo time is defined as the length of time that separates the 90° and 180° pulse, see Figure 12.

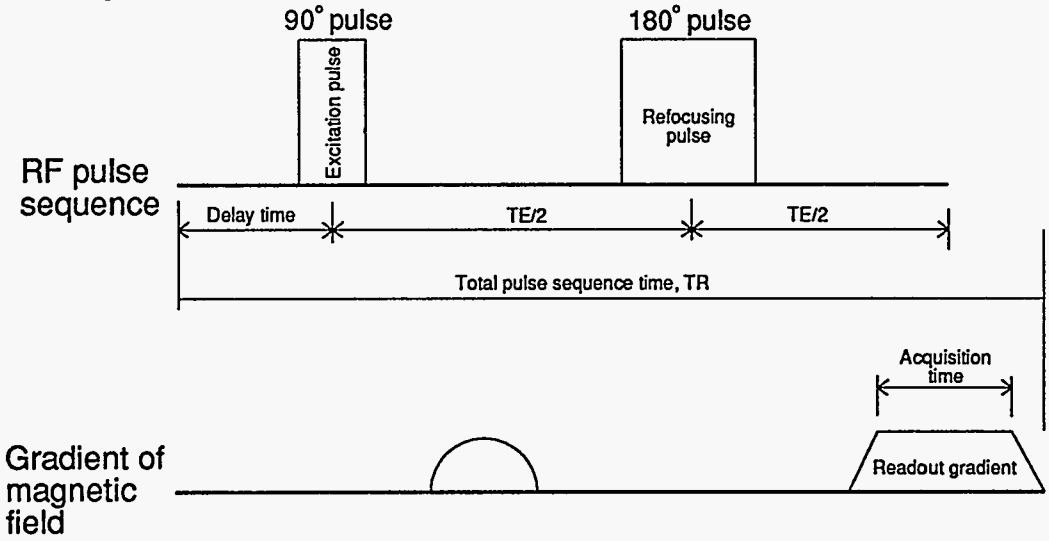


Figure 12 Typical pulse sequence.

Spectrometer frequency refers to the central frequency of the frequency range that made to resonate the protons in the sample at 2 Tesla.

The Spectrometer

Any spectrometer has the following basic components: a source of radiation, a sample compartment, a transmitter-receiver coil, an amplifier, and a recording device. In an MRI spectrometer the source of radiation is a radio frequency transmitter. The sample compartment is an opening where the transmtter-receiver coil is placed surrounding the sample. The transmitter-receiver coil has two functions: (1) transmits the radio frequency power to the sample in order to perturb the spin-state population; and (2) detects the minute radio frequencies emitted by the rotating bulk magnetization of the spins.

The magnetic field is generated by a magnet capable of producing a field of 2 Tesla. The magnet is designed with superconducting materials and cooled to the temperature of liquid helium. One of the most critical conditions of MRI experiments is the presence of a homogeneous magnetic field at the sample. The homogeneous field is created by: (1) varying the current in the shim coils of the magnet until the field is as homogeneous as possible; and (2) carefully controlling the temperature of the environment of the magnet.

Pulse Sequences Used

Two different sequences were used. Longitudinal proton profiles were obtained using the sequence PROFIL.SEQ. Images taken along the longitudinal edge of the sample were obtained using the spin echo sequence IAMNTE.SEQ. Tables 1 and 2 show the sequences used.

| PROFIL.SEQ<br>Hard - Hard Spin echo sequence<br>used for profile bulk measurements | | |
|---|---|---|
| 1 Recycle time (TR) | 2000 | msec |
| 2 180 degree pulse -length | 120 | µsec |
| 3 -power | 100 | % |
| 4 Field of view -observe | 69.44 | mm |
| 5 Echo time (TE) | 8 | msec |
| 6 Spectrometer frequency | 85.548174 | MHz |
| 7 Readout direction (1/2/3, y/z/x) | 2 | |
| 8 Number of Acquisitions | 16 | |
| 9 Readout gradient | 800 | Hz/mm |
| 10 Readout rephasing const. (1.47) | 1.57 | |
| 11 Dephasing pulse width | 1 | msec |

Table 1 MRI sequence used to obtain oil saturation profiles.

| IAMNTE.SEQ<br>Slice selective-90° Hard-180° pulse sequence | | |
|---|---|---|
| 1 Recycle time (TR) | 300 | msec |
| 2 180 degree pulse -length | 120 | µsec |
| 3 -power | 100 | % |
| 4 Slice -thickness (0.25 mm min.) | 5.0 | mm |
| 5 -pulse power (25 min. 90) | 20 | % |
| 6 -offset | 0 | mm |
| 7 Image resolution -phase-encode | 128 | points |
| 4 Field of view -phase-encode | 59.52 | mm |
| 5 -observe | 119.04 | mm |
| 10 Gate trigger 0 off 1 60Hz 2 T2 | 0 | |
| 11 Phase cycle (on/off, 1/0) | 0 | |
| 12 Scan/set - gain (1/0) | 1 | |
| 13 Spectrometer frequency | 85.558580 | MHz |
| 14 Image plane -Transverse/Sagittal/Coronal (1/2/3) | 2 | |
| 15 Readout gradient | 700 | Hz/mm |
| 16 Number of acquisitions (NA) | 16 | |
| 17 Block size (CB) 2*readout res. | 512 | |

Table 2 MRI sequence used to obtain longitudinal images.

4.3.2.4 $CO_2$-Enriched Water Imbibition

Rock Samples

Rock sample preparation

All rock and reference samples used to study imbibition processes were drilled from the same piece of rock, to assure similar characteristics. An outcrop dolomite was used. Rock samples were prepared in two different manners: 1) Rock samples intended as references, and 2) Rock samples for the study of imbibition.

Reference Samples

MRI signals can have slight shifts when different rock samples are placed inside the magnet for analysis. Small shifts occur even when using the same rock sample and fluids. The use of reference rock samples would eliminate the error that these small shifts introduced, and would allow the comparison among different experiments that used the same rock and fluids. Consistency of rock and fluid properties allows this comparison. The use of reference samples also facilitate comparison of proton profiles to obtaining cumulative production curves.

The following procedure was used to prepare reference samples:

-The rock was cut to one inch in diameter cylinders, and a quarter of and inch in length. The total length of the core and the reference sample being studied is restricted by the length of the homogeneous magnetic field. Therefore, short reference samples had to be used.

-A drying period of 24 hours at 120 $^0$F was chosen to eliminate water trapped inside the rock.

-Reference samples were weighted to obtain the dry weight to calculate porosity by the volumetric method.

-The samples were measured to obtain bulk volume.

-A nitrogen permeameter was used to measure permeabilities.

-Saturation of the cores with $D_2O$ followed these measurements. The samples were submerged in $D_2O$ for 24 hours and vacuum was applied until all the air was extracted.

-The saturated weight was measured to calculate porosity. Porosity was calculated using the difference between the dry and saturated weight, and density of the liquid used to saturate the sample, $D_2O$ in this case.

-An oil saturation was obtained by flowing oil through the samples. At least 10 pore volumes were driven through the reference samples to reach the maximum oil saturation possible.

-The samples were weighted again to obtain average oil saturation values.

A method to maintain fluid saturations of the reference samples had to be developed. The reference samples were coated with epoxy to preserve the oil and water saturations attained by the previously described procedure.

Gases expand and contract as a function of pressure. Air trapped inside the core holder would move liquids inside the rock sample as it expands and contracts with small changes in pressure. Therefore it was necessary to evacuate any air trapped inside the samples. A capillary hole was drilled though the reference sample to allow oil to flow through the center of the reference sample in order to evacuate the air trapped between the rock sample and the reference, or the reference sample and the nylon spacers . The core holder was placed in a vertical position for this maneuver. The diameter of the capillary was chosen extremely small because oil filling the capillary would affect the MRI response from the reference samples. Properties of the reference samples used are shown in Tables 3. Table 4 shows some properties of the samples used.

The procedure used to wrap reference samples in epoxy and still be able to pass fluids though their length is as follows:

-A 1/16 of an inch hole was drilled through the completely saturated reference sample.

-The sample was coated with epoxy. The epoxy coating was allowed to dry and setup.

-A 16/1000 of an inch capillary was drilled though the epoxy filling the 1/16 - inch hole drilled in the rock sample, see Figure 13.

| REFERENCE SAMPLES | | | | | | |
|---|---|---|---|---|---|---|
| Reference core | Length (in) | Diameter (in) | Bulk Vol (cc) | $\phi$ (%) | $V_o$ (cc) | $S_o$ (%) |
| 1 | 0.32 | 0.98 | 3.92 | 28.6 | 0.57 | 50.5 |
| 2 | 0.21 | 0.99 | 2.69 | 26.5 | 0.25 | 35.3 |
| 3 | 0.22 | 0.98 | 2.77 | 26.5 | 0.38 | 51.5 |
| 4 | 0.21 | 0.99 | 2.62 | 25.2 | 0.25 | 38.2 |
| 5 | 0.19 | 0.99 | 2.41 | 24.8 | 0.21 | 35.9 |
| 6 | 0.18 | 0.99 | 2.30 | 23.5 | 0.09 | 16.9 |
| 7 | 0.23 | 0.99 | 2.92 | 22.0 | 0.21 | 33.4 |
| 8 | 0.34 | 0.99 | 4.31 | 23.5 | 0.43 | 42.3 |

Table 3 Different rock and saturation properties of the reference core samples 1 through 8. Kerosene oil and unadultered $D_20$ were used to saturate the reference samples.

| ROCK SAMPLES |
|---|

| Core | Length (in) | Diameter (in) | Bulk Vol (cc) | $\phi$ (%) | Vol of oil (cc) | $S_o$ (%) | K md |
|---|---|---|---|---|---|---|---|
| A1 | 3.00 | 0.99 | 37.62 | 26.3 | 4.56 | 46.0 | 11.7 |
| A2 | 3.01 | 0.99 | 37.59 | 26.6 | 3.88 | 38.9 | 13.6 |
| A3 | 3.00 | 0.99 | 37.58 | 26.4 | 3.33 | 33.6 | 12.1 |
| A4 | 3.03 | 0.99 | 37.71 | 25.4 | 3.70 | 38.6 | 13.9 |

Table 4 Different rock and saturation properties of the rock samples used. Kerosene oil and unadultered $D_2O$ were used to saturate the rock samples.

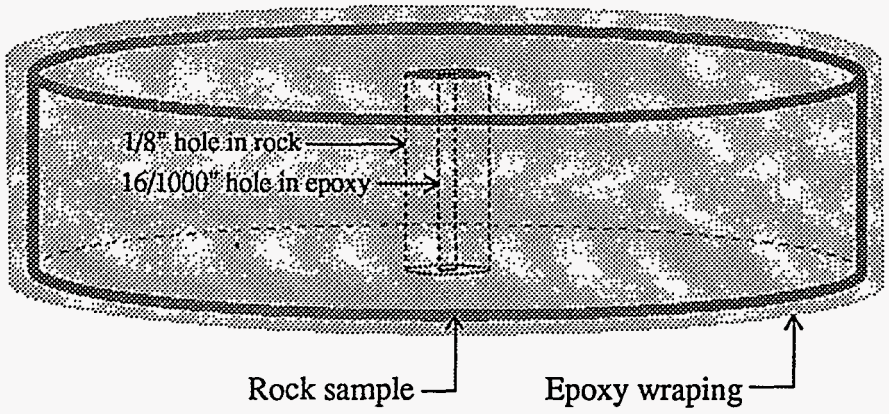


Figure 13 Reference sample placed in epoxy.

Core Samples

All the samples were prepared in the same manner that the reference samples were prepared. Permeability porosity and saturations were measured in all the samples studied. The same procedure used to prepare the reference samples was used to prepare the rock samples for imbibition studies. Epoxy wrapping was not used for the rock samples.

Procedure Used to Study Water Imbibition

Laboratory Equipment

Two ALCOTT 760 HPLC constant flow rate pumps were used. One to maintain overburden pressure, 200 psi, and the other to flow oil through the sample. A conventional low pressure core holder was used to saturate the samples. Ease placing and removing of the samples was the main advantage of using a conventional core holder to saturate the rock and reference samples.

The same type of pumps was used for the imbibition experiments. One pump supplied 2500 psi of overburden pressure, while other was used to drive the different fluids during the flooding phase. A back pressure regulator was also necessary to maintain 2000 psi pressure inside the system at all times.

MRI applications require the use of an unconventional core-holder. A fiber glass core holder was designed, tested and used for this research effort during last year.

Fiber Glass Core Holder

A high pressure, high temperature core holder transparent to x-rays, and magnetic waves was developed. The core holder is composed of a fiberglass body with aluminium end caps. The holder may be constructed to operate with a variety of core sizes and operating CT and MRI scanning conditions. At the present,only one inch in diameter samples are being used in the core holder. The major advantages of the new core holder are its low cost and flexibility of operation.

CT scan and MRI imaging techniques have been proven to permit actual visualization of two phase fluid flow occurring in a core sample. [59-61] Many of these flow studies must be performed at high temperature and pressure. Most fluid flow test are performed in a conventional, stainless steel cylinder with screwed on end caps. All fluid interactions occurring within the core are determined from either liquid effluent measurements or from taps along the axis of the core.

Conventional core holders cannot be used when flow studies are examined with either CT scan or MRI tools because stainless steel obstructs the scanning procedures. An inexpensive core holder that allows the acquisition of data was needed.

Core Holder Description

A new application of an already existing material was sought to solve this problem. The properties of fiberglass tubing were thought to be compatible with the demands of the new CT and MRI techniques.

A 3-inch ID fiberglass tubing, 24 inches long with tapered graphite threads was used as the main body of the core holder. The type of tubing available is designed to seal when the appropriate torque is applied, but when a seal by hand is attempted the designated torque is difficult to apply. Therefore, rubber seats were placed to obtain the desired seal.

The adjusting pieces that actually hold the rock sample inside the tubing shell were made of nylon to avoid any distortion to the signals being taken during an experiment. The end caps were constructed of aluminum because of the low magnetic properties of this metal.

The core holder was tested for working pressures up to 2,000 psi and temperatures up to 250 $^{o}$F. It is designed for one inch cores, but can easily be adapted to handle 1, 1.5, and 2 - inch samples.

MRI and CT images have been taken using the newly constructed tool and did not show any sign of distortion or negative effects.

MRI Tests

A diagram of the system used to run the MRI experiments is shown in Figure 14. The sequence followed to conduct imbibition experiments is as follows:

-The reference and the core samples were placed inside the fiber glass core holder.

-The annular space of the core holder was filled with distilled water. Oil and water signals are very similar, and special techniques have to be used to separate the signals. A neutralizer had to be added to diminish the MRI signal from the water filling the annular space that would otherwise mask the results,. Manganese (II) Chloride, $MnCl_2$ was used.

-An overburden pressure of 300 psi was applied.

-Oil was pumped through the sample to displace any air trapped between the core sample and the reference sample. Care was taken not to exceed the flow rate or the differential pressure previously applied when saturating the sample to maintain previously established fluid saturations. The minimum oil volume needed to displace the trapped air was used in order to preserve fluid saturations.
-When all the air was evacuated, the outlet valve was closed and the fiber glass core holder was placed inside the magnet.
-Oil was used to bring the system pressure up to 2000 psi. The pressure was increased in a stepwise manner. The difference between the overburden pressure and the rock sample pressure was kept to a maximum of 300 psi during the pressure increase. Ultimate overburden pressure was 2500 psi.
-Oil was flowed at 0.3 cc/min to maintain a system pressure of 2000 psi, see Figure 15.
-To initiate the imbibition process, $D_2O$ displaced the oil inside the small reservoir in front of the rock, sample. Figure 15 shows a detailed diagram of the small reservoir used to simulate a reservoir fracture. Proton profiles obtained from MRI were used to monitor the displacing of the oil from the reservoir. This procedure was of assistance to determine the starting time for water imbibition.
-Pressure in the system was maintained at a constant 2000 psi. The flow rate was also maintained constant at 0.3 cc/min across the core face.

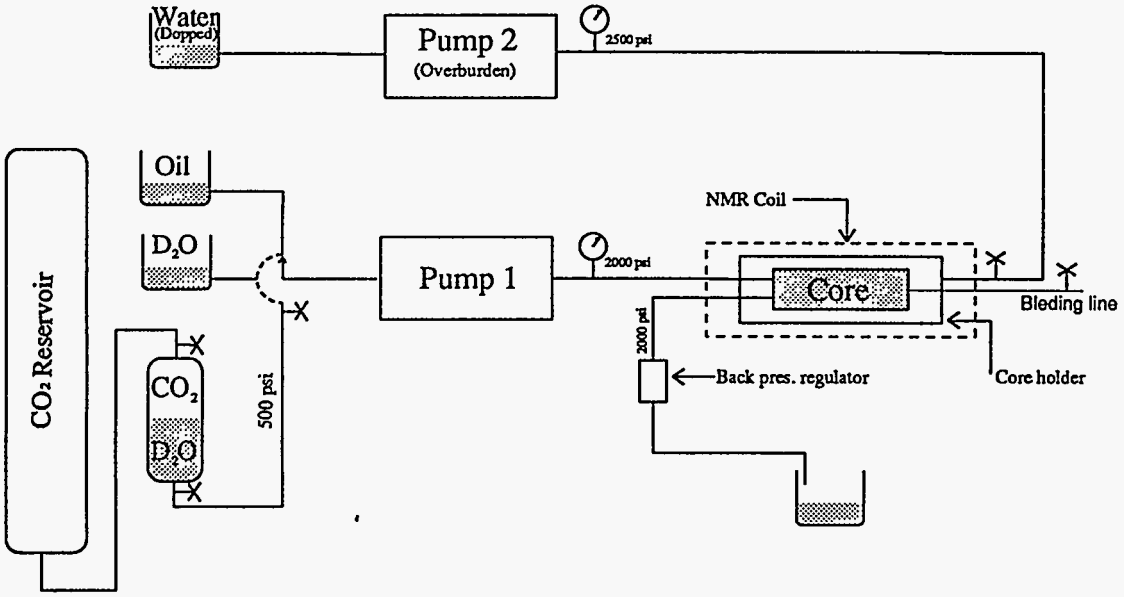


Figure 14 Laboratory diagram of the system used to run MRI imbibition experiments.

Type of Information Obtained

Proton Profiles

Proton profiles were extensively used to monitor the imbibition process. Profiles of samples with different oil saturations were used to confirm the proportionality of the MRI responses to the volume of oil inside the samples. Proton profiles from different sets of reference samples are shown in Figure 16 and 17. The area underneath the response due to each sample was plotted against the weighted volume of oil to verify a linear correlation. The results are shown in Figure 18 and 19. These two sets of MRI responses cannot be assembled together because there is no common sample placed in both sets to serve as a

reference to scale the sets. When sample 5 is disregarded a very good correlation is obtained with an $R^2$ factor of 1.000, see Figure 20.

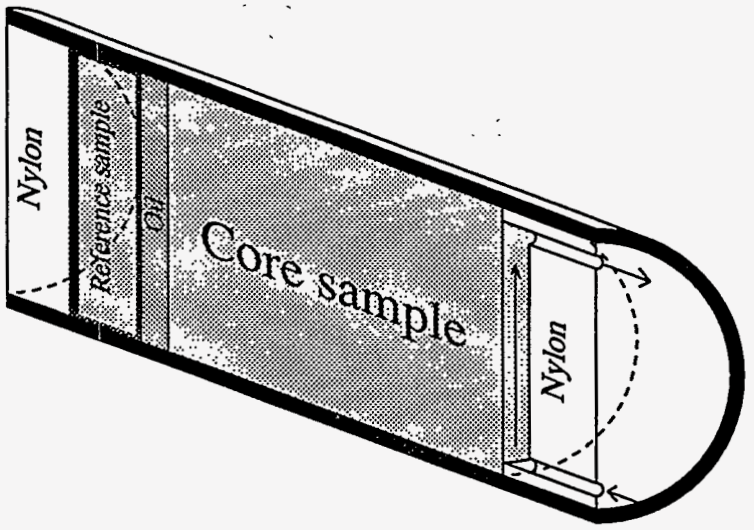


Figure 15 Layout of the core sample and the reference sample inside the fiber glass core holder.

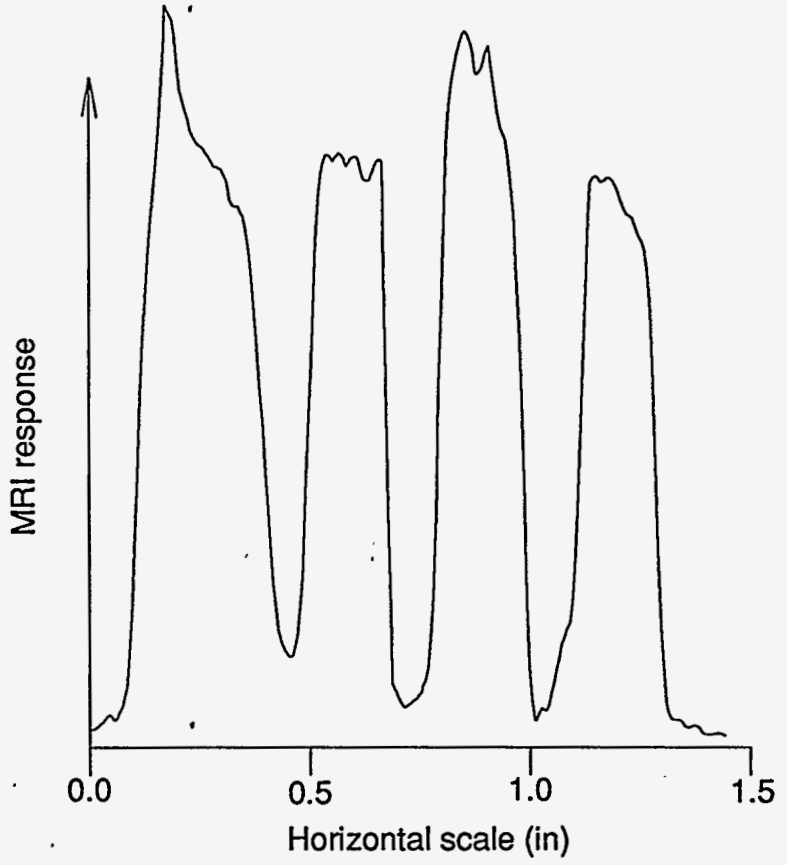


Figure 16 MRI response obtained for reference samples 1,2,3,and 4.

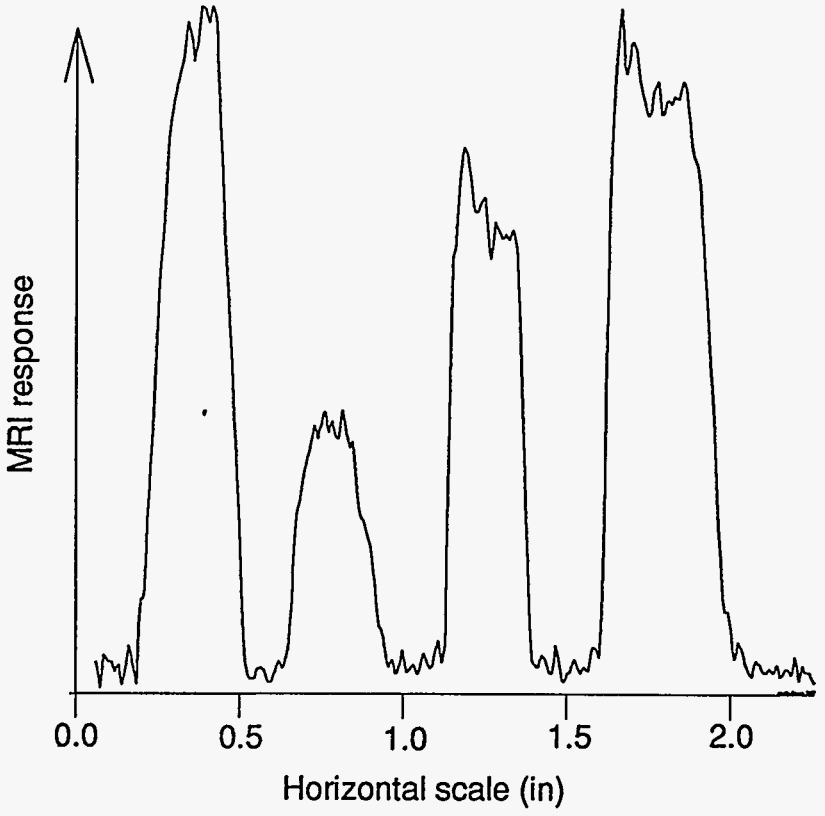


Figure 17 MRI response obtained for reference samples 5,6,7,and 8.

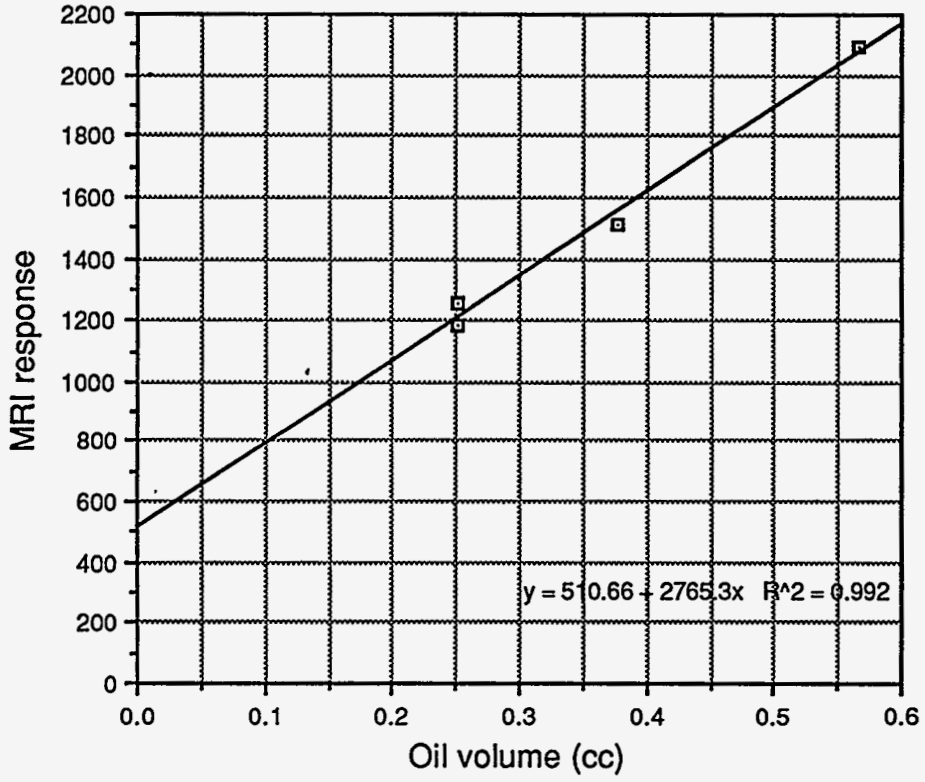


Figure 18 MRI correlation for samples 1,2,3, and 4.

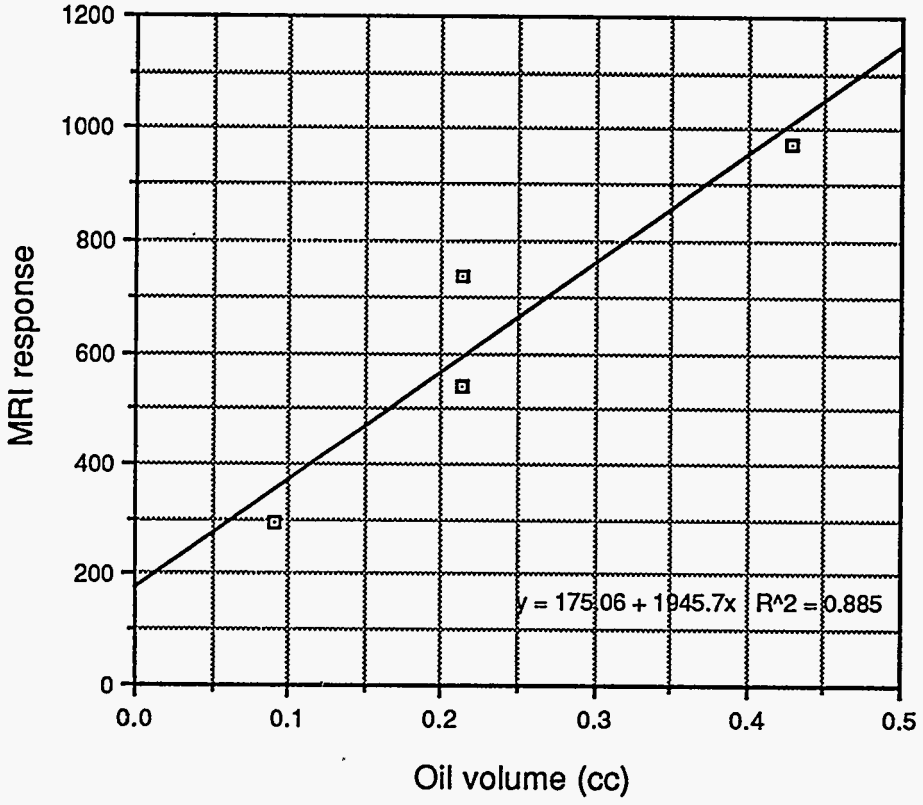


Figure 19 MRI correlation for samples 5,6,7, and 8.

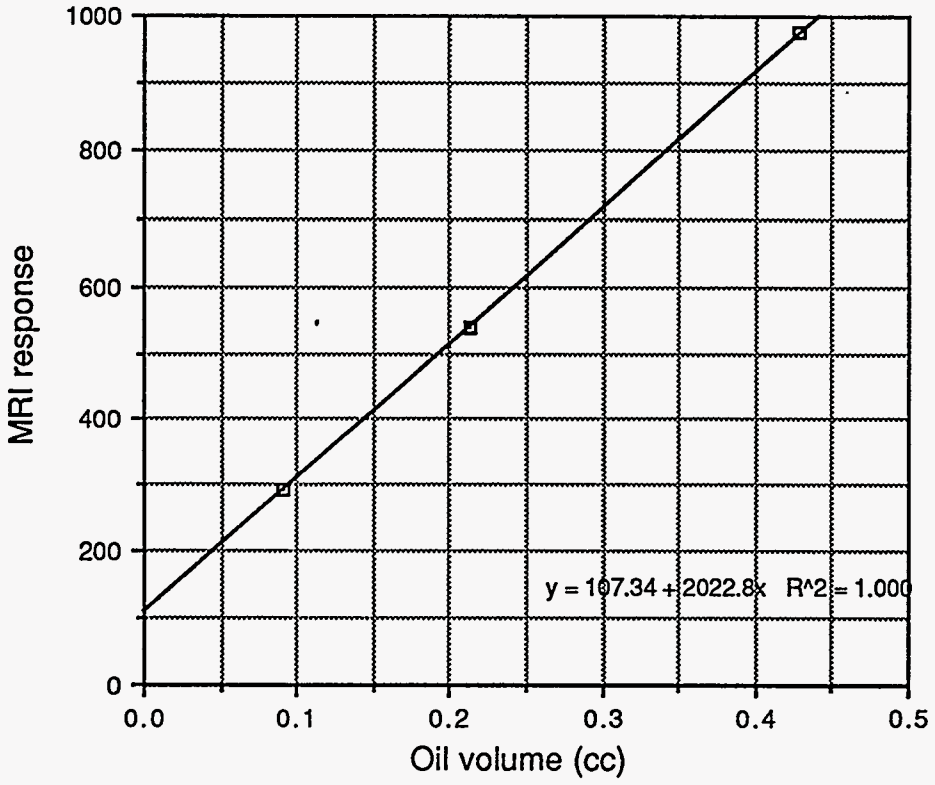


Figure 20 MRI correlation for samples 6,7, and 8.

A typical profile of a reference sample along with the sample used to study the process is shown in Figure 21. The profile was taken before displacing the oil from the small reservoir. This profile shows oil trapped between the reference and the sample, and inside the small reservoir facing the sample. Profiles were taken as often as possible to maintain a good data acquisition in any imbibition curve,or cumulative oil production curve, obtained from the profiles after the imbibition process was initiated.

An outcrop limestone, $D_2O$, and kerosene oil were used. Several runs were conducted with unadulterated $D_2O$ to establish a basic pattern of behavior. Carbonated water was elaborated by dissolving $CO_2$ in $D_2O$ at 500 psi.

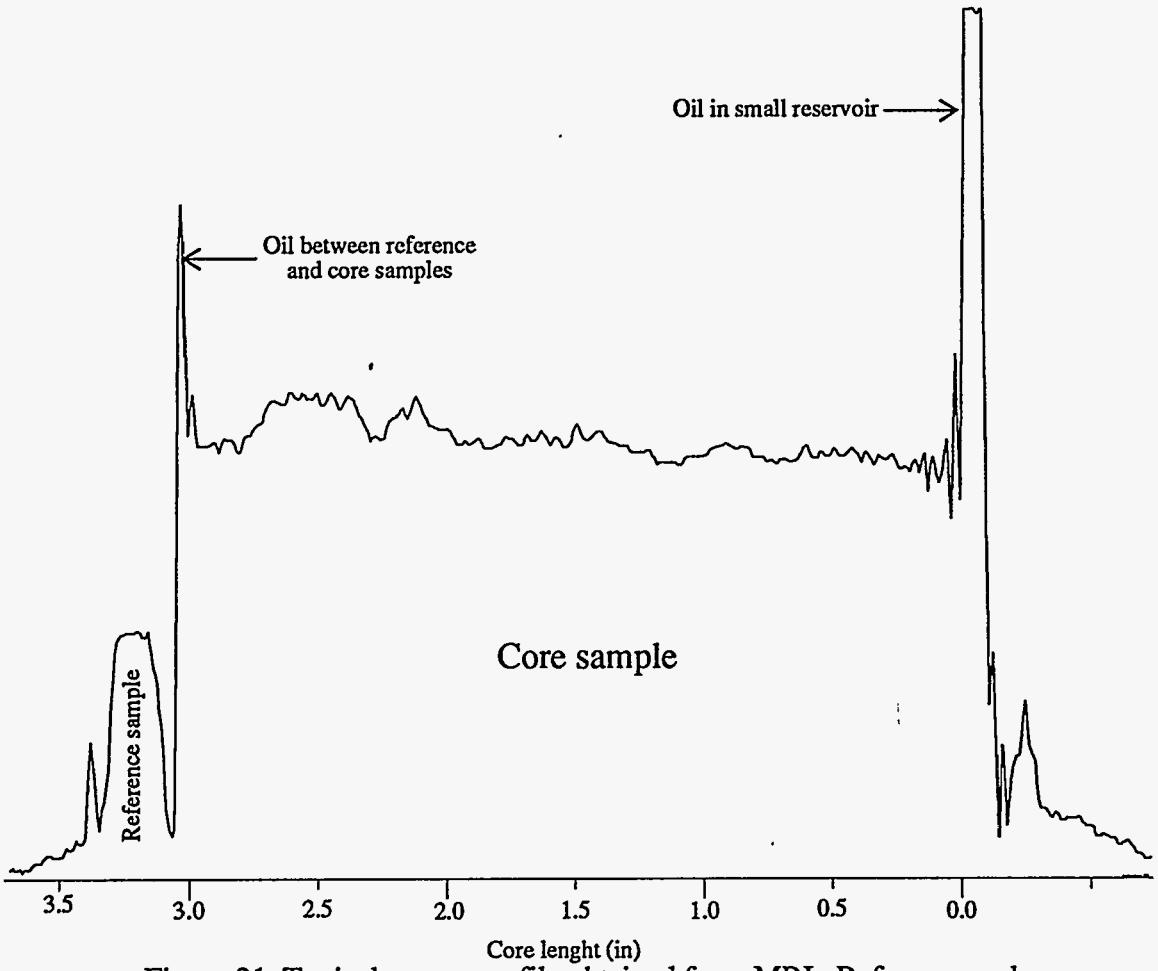


Figure 21 Typical proton profile obtained from MRI. Reference and core samples are clearly identified.

Images

Two dimensional images were also taken. Longitudinal images of the sample were primarily taken to observe oil saturation changes and movement along the main axis of the sample. Fifteen minutes were necessary to acquire each image. Acquisition time was a limiting factor. Some cross sectional images were taken, but not with the frequency desired. Typical images are shown in Figures 22, 23, and 24.

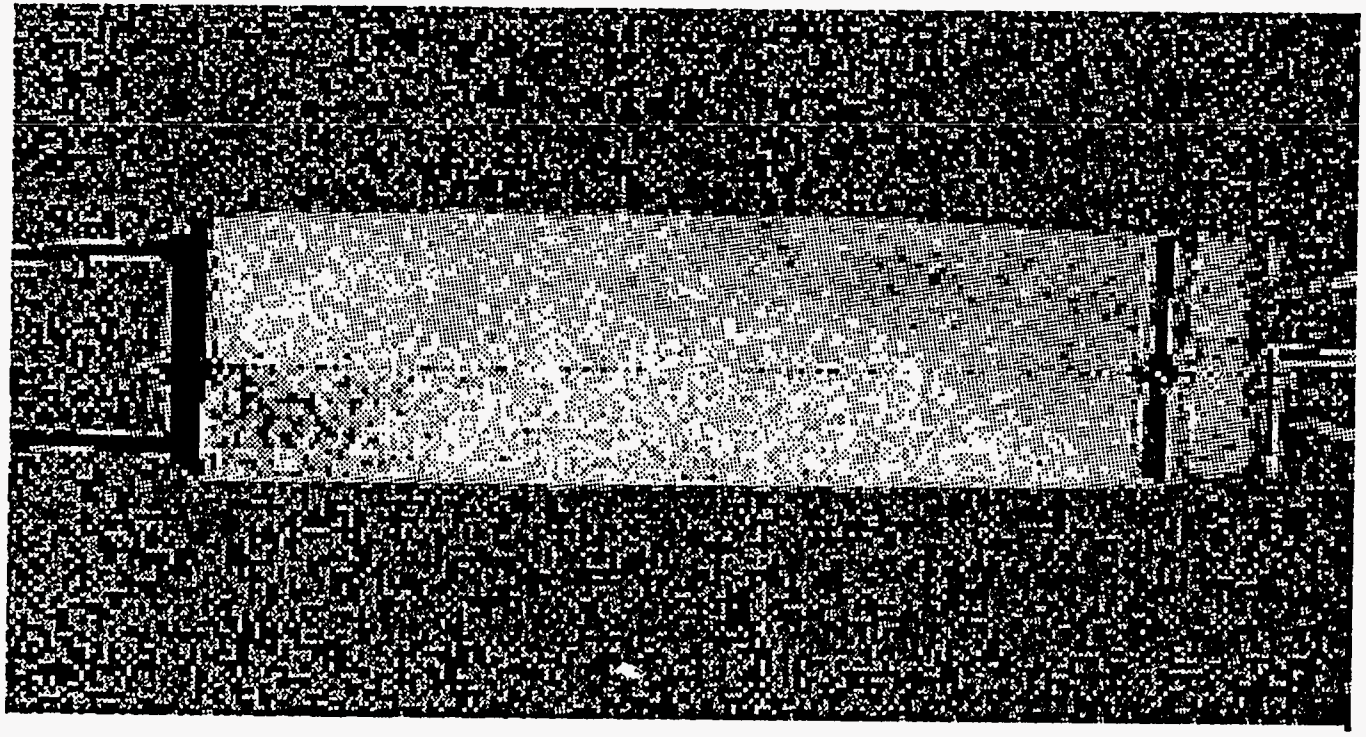

**Figure 22 Longitudinal image taken at initial conditions. Maximum oil saturation was present. The small reservoir filled with oil can be seen at the left of the sample. Tubing can also be seen because of the oil inside.**

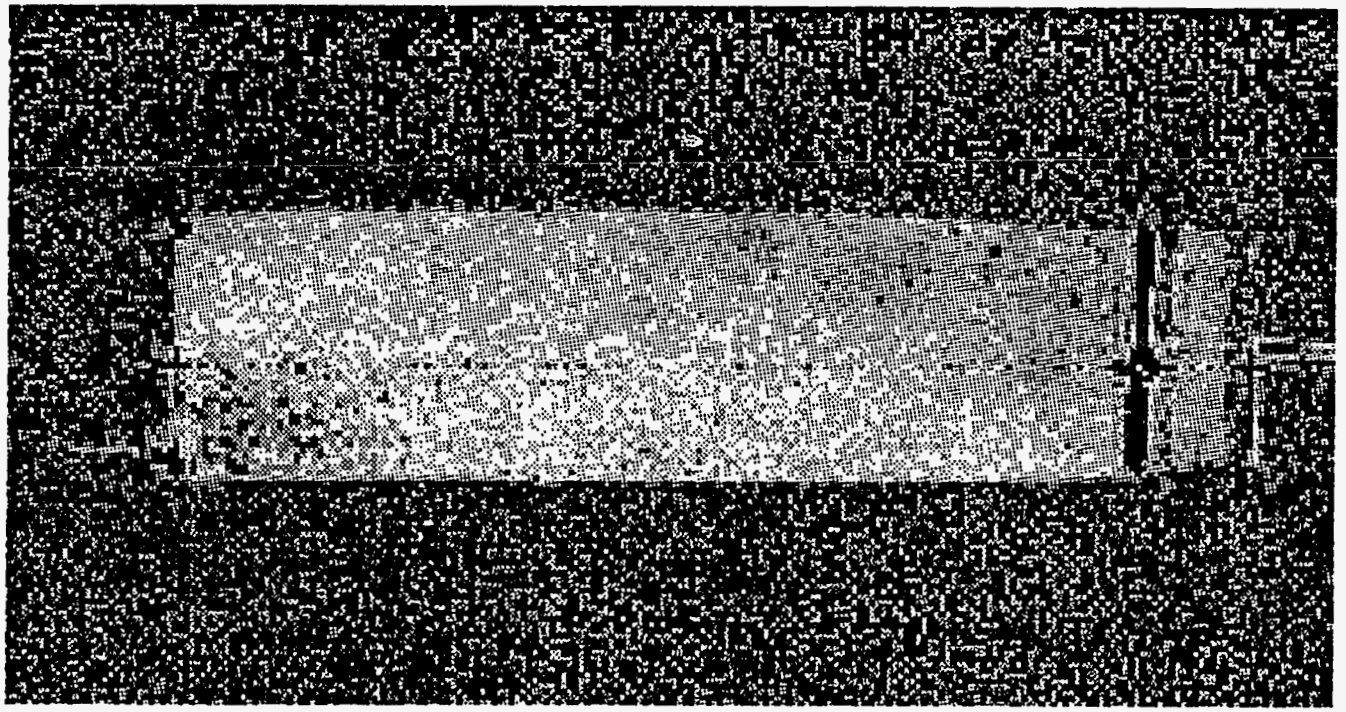

**Figure 23 Logitudinal image taken after the oil filling the simulated fracture had been displaced. Small droplets of oil can be seen adhering to the surface of the rock.**

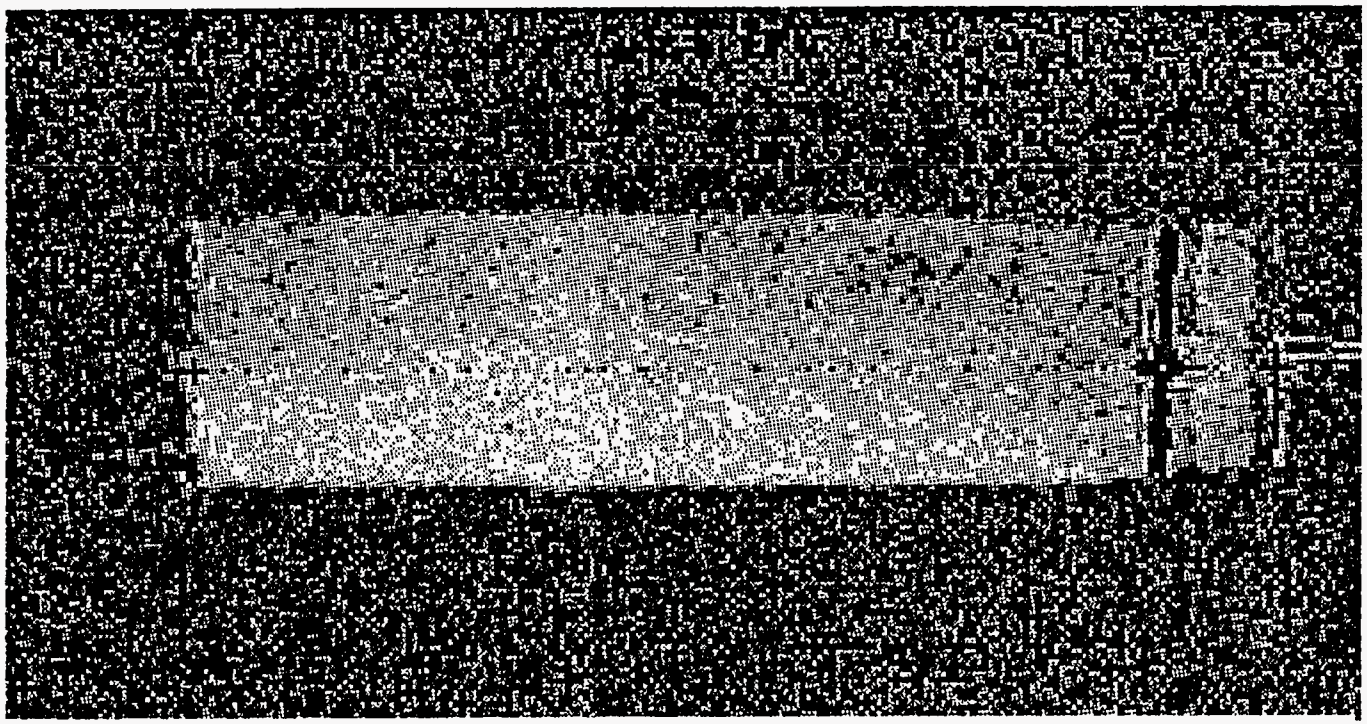

**Figure 24 Longitudinal image taken at final conditions. A change in oil saturation can be observed along the rock sample.**

4.3.2.5 Results Obtained

The use of proton profiles permitted oil saturation changes inside the rock samples to be monitored. Profiles obtained under initial and final conditions of an unadulterated imbibition flood are observed in Figures 25 and 26, respectively. Sample A1 and reference 5 were used, see Tables 3 and 4. The MRI response was translated to the oil volume inside the sample, (BV/L) $\phi$ $S_o$, based on the proportionality previously shown. Small shifts in the MRI response are observed when the profiles are plotted together. All the profiles had to be normalized before any comparison. The reference sample evidenced the small shifting of the signal, see Figure 27.

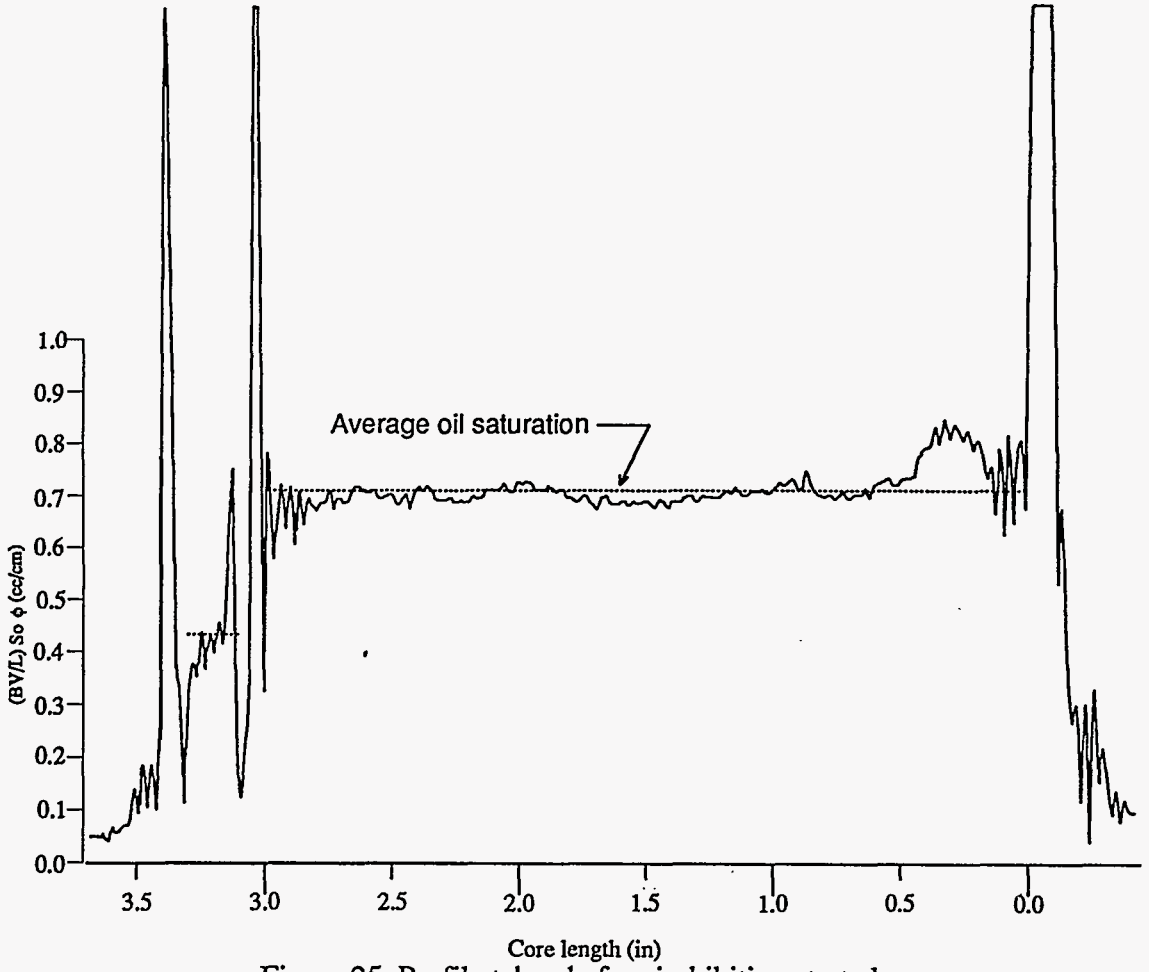


Figure 25 Profile taken before imbibition started.

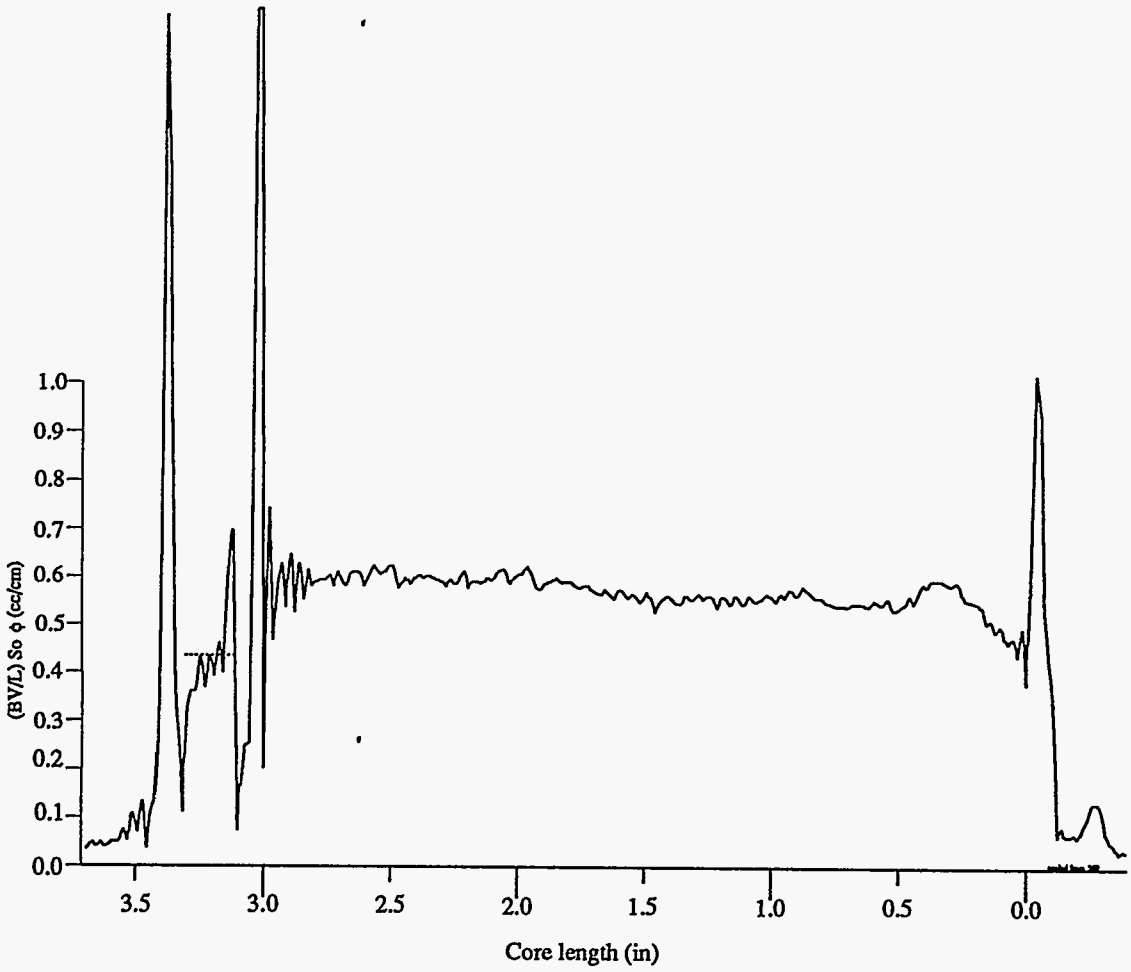


Figure 26 Profile taken 903 minutes after imbibition started.

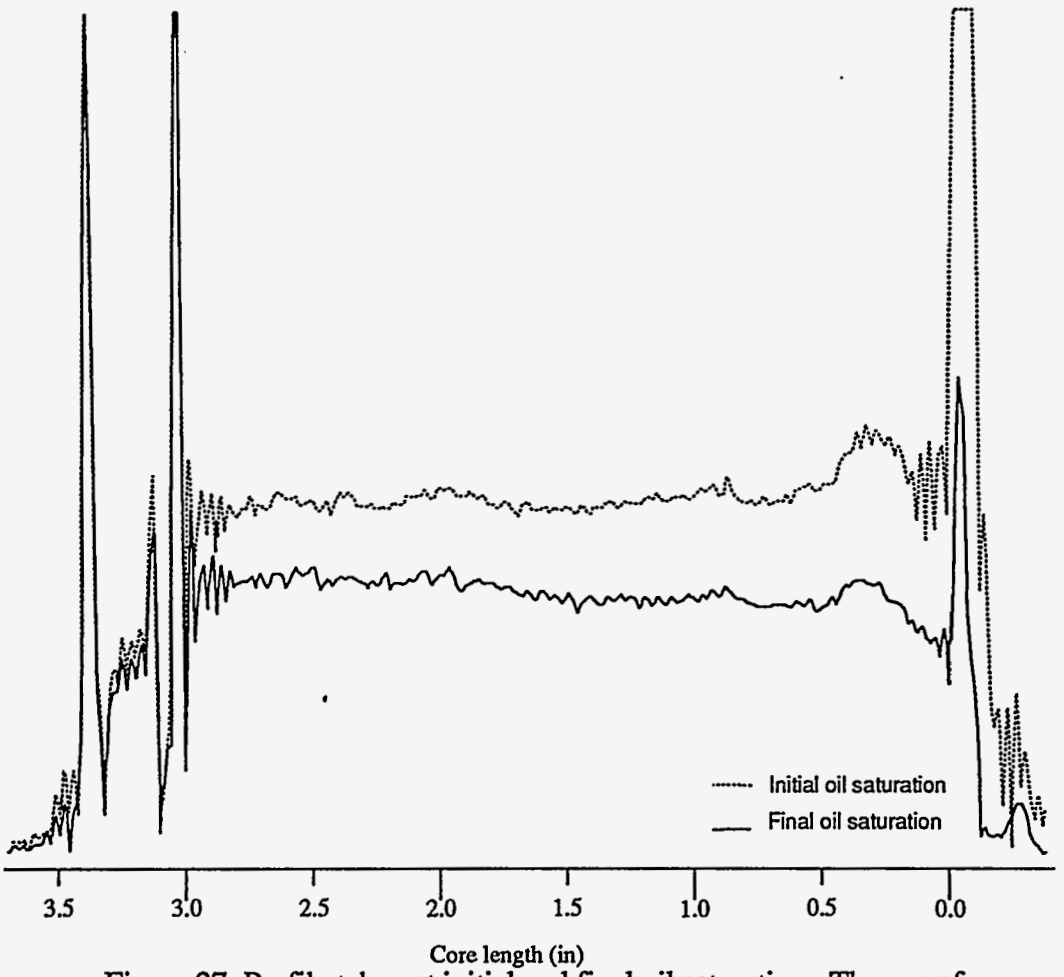


Figure 27 Profile taken at initial and final oil saturation. The use of a reference sample evidenced the small shifting of the signal.

The integral of the signal from the reference sample was used to normalize all the experimental data. The integral of the signal from the reference sample was made equal for all the profiles, $\int_{ref\,i} = \int_{ref}$, to normalize the profiles. The subtraction of profiles allowed to observe the changes in oil saturation as a function of time after normalization.

Subtraction of normalized profiles taken at different times during the imbibition flooding allowed to construct oil saturation profiles that evidenced the displacement of the oil inside the sample by the water front moving into the rock, see Figure 28. Notice that

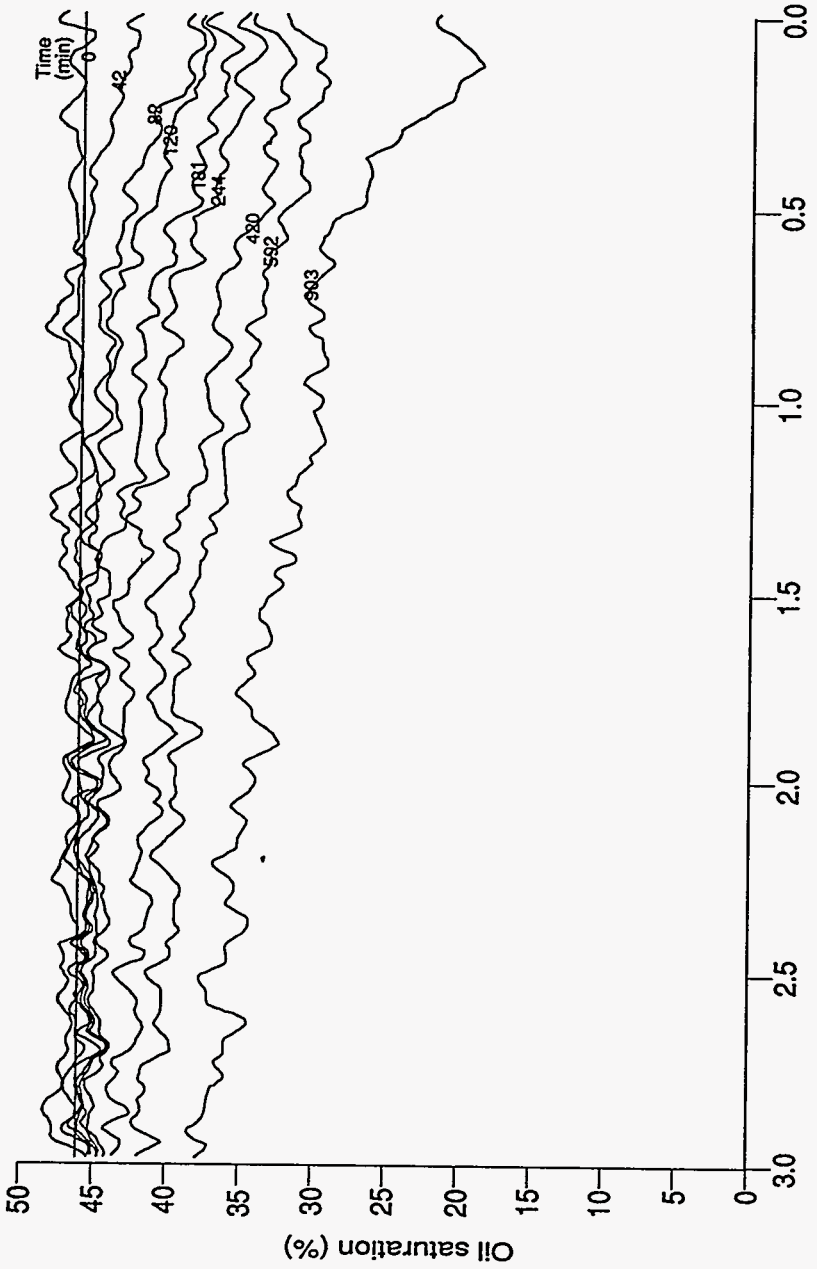


Figure 28 Oil saturation changes as a function of time. Pure water was used.

the oil saturation profiles have a straight line trend. This trend shows that oil being produced comes from the complete length of the sample.

The integral of the signal obtained from the reference sample was also used to obtain the percentage of Original Oil in Place, OOIP, being produced. The approach used to calculate % produced of OOIP is as follows:

The volume of oil inside the core sample, Oil $Vol_{sam}$, can be calculate from:

$$\text{Oil vol}_{sam} = \frac{\int_{sam\,i} \times \text{Oil vol}_{ref}}{\int_{ref}} \tag{44}$$

Notice that Oil $Vol_{sam}$ can be found with this technique because $T_{2\,ref} = T_{2\,sam}$. If they are different a different technique has to be applied. [62] At initial conditions:

$$\text{Oil vol}_{sam\,i} = \frac{\int_{sam\,i} \times \text{Oil vol}_{ref\,i}}{\int_{ref\,i}} \tag{45}$$

Produced % of OOIP can be calculated from:

$$\%\text{ of OOIP} = \left(\frac{\text{Oil vol}_{sam\,i} - \text{Oil vol}_{sam}}{\text{Oil vol}_{sam\,i}}\right) 100 \tag{46}$$

By substituting the expressions of Oil $vol_{sam\,i}$, and Oil $vol_{sam}$ we obtain:

$$\%\text{ of OOIP} = \left[\left(\frac{\int_{sam\,i}}{\int_{ref\,i}} - \frac{\int_{sam}}{\int_{ref}}\right) \Big/ \frac{\int_{sam\,i}}{\int_{ref\,i}}\right] \times 100 \tag{47}$$

After normalization, which means that:

$$\int_{ref\,i} = \int_{ref} \tag{48}$$

$$\%\text{ of OOIP} = \left(\frac{\int_{sam\,i} - \int_{sam}}{\int_{sam\,i}}\right) 100 \tag{49}$$

Figure 29 and 30 show cumulative oil production curves obtained by this method. Only the amount of oil inside the rock sample, without taking into account oil adhering to the rock surface, was measured to calculate the % of OOIP being produced. An MRI profile of initial conditions show a high oil saturation being reached during the first stages of the process. Cumulative OOIP recovered shows a higher recovery rate at early times, see Figure 30. Imaging of the imbibition process confirmed that when a pocket of higher oil saturation is reached by the water being imbibed, oil production rate increased. The opposite is also true, when a lower oil saturation region is encountered, the cumulative oil production curve tends to flatten, see Figure 30. Figure 31 also shows evidence of the phenomenon. Oil saturation is clearly shown as non-uniform along the sample, with higher oil saturation closer to the imbibing face. Therefore, the process is proportional to oil saturation. MRI techniques allow a single experiment to yield, or confirm, significant results.

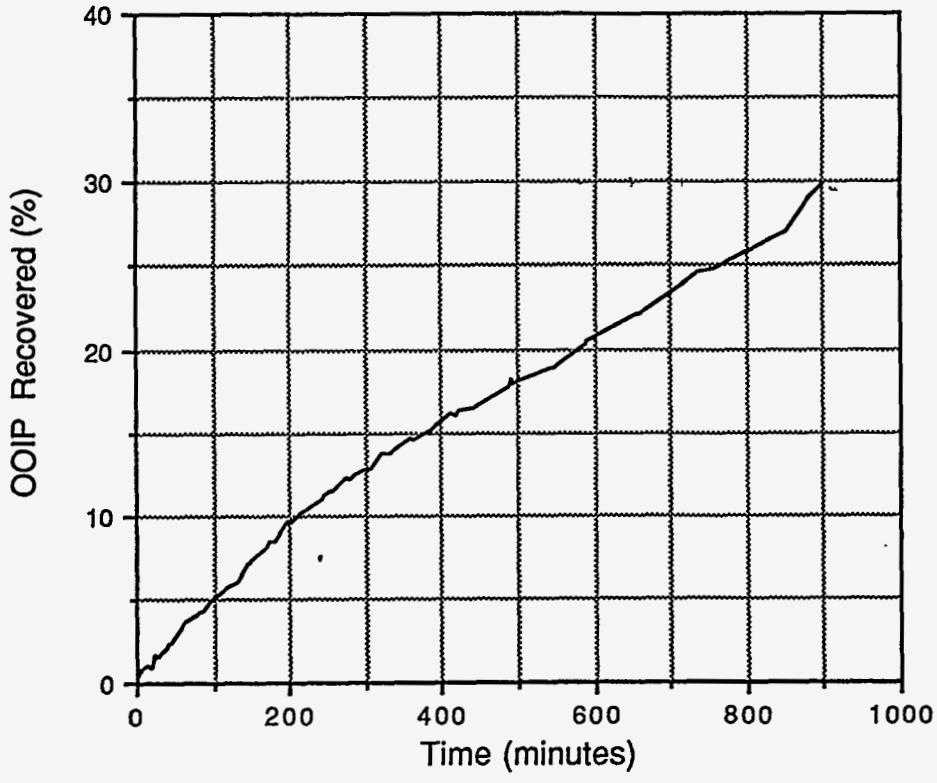


Figure 29 Cumulative oil production obtained by imbibition of pure water. Sample A1 and reference sample 5 were used, see Tables 3 and 4.

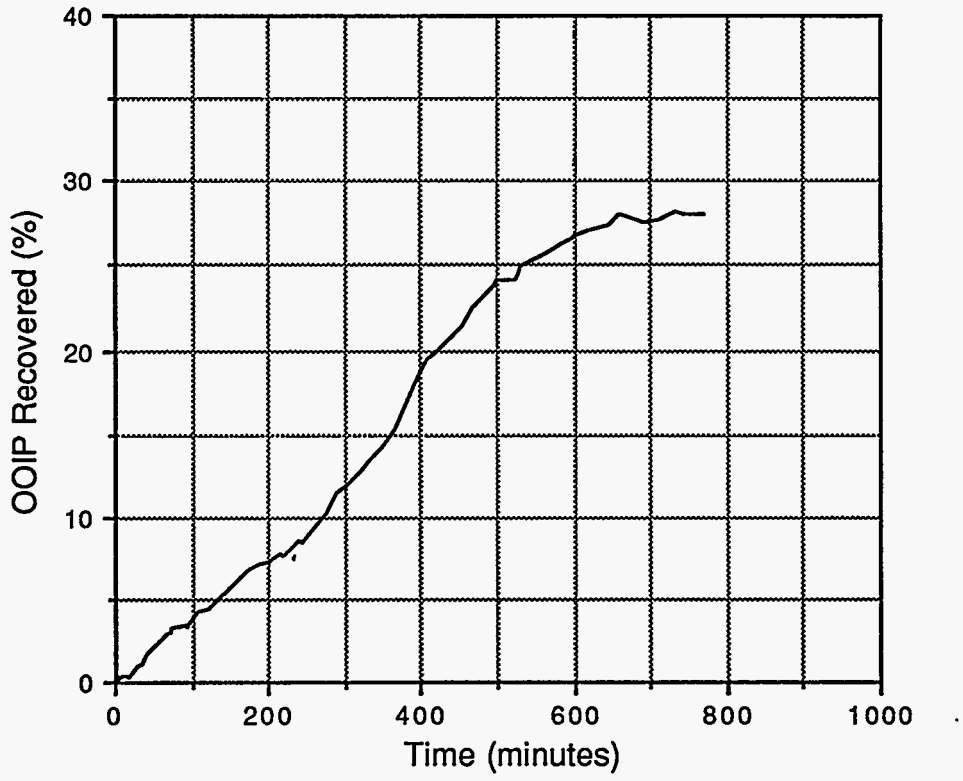


Figure 30 Cumulative oil production obtained by imbibition of pure water. Sample A4 and reference sample 5 were used, see Table 3 and 4.

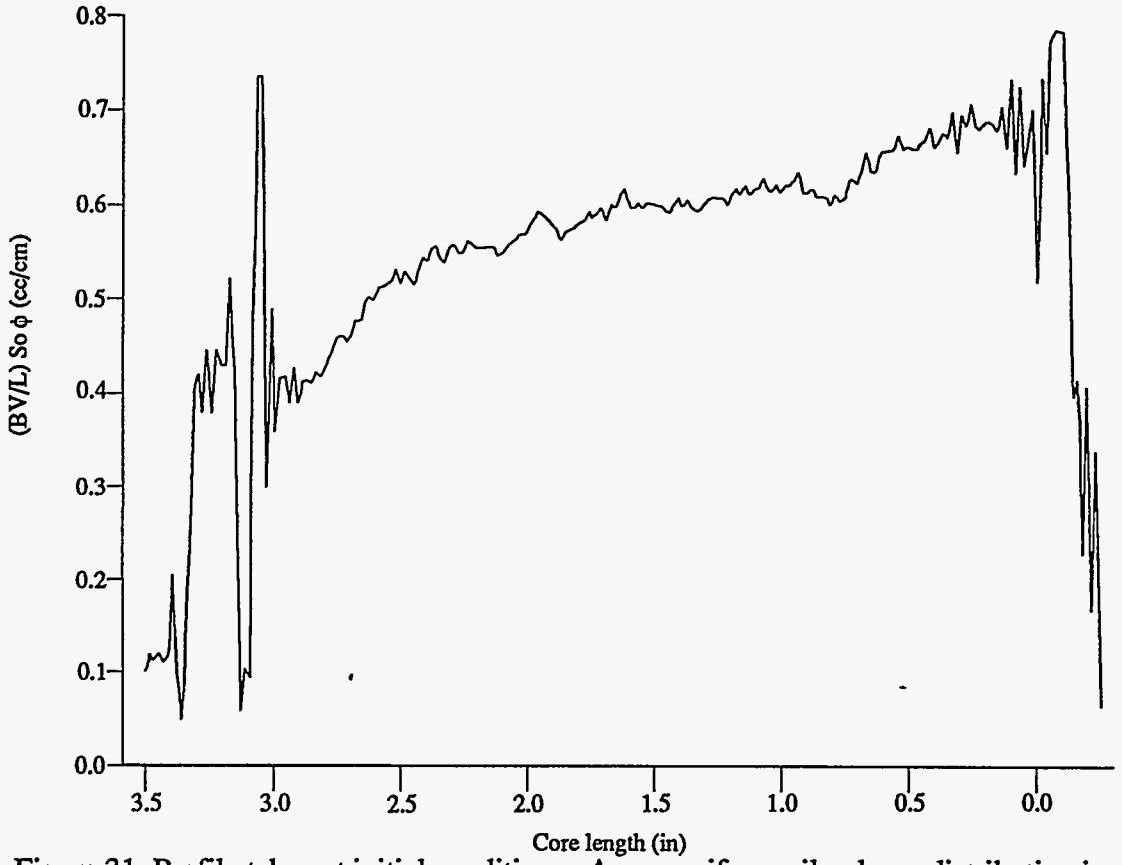


Figure 31 Profile taken at initial conditions. A non-uniform oil volume distribution is shown. A higher oil volume is encountered closer to the imbibing face, to the right hand side of the sample. Sample A4 and reference sample 5 were used for this unadulterated $D_2O$ experiment, see Tables 3 and 4.

Changes in oil saturation were monitored using the same technique when $CO_2$ - enriched water was introduced. Figures 32 and 33 show initial and final oil saturation profiles before and after normalization for a $CO_2$ - enriched water experiment. Notice that the response from the reference sample has been equalized, allowing a true comparison of the profiles.

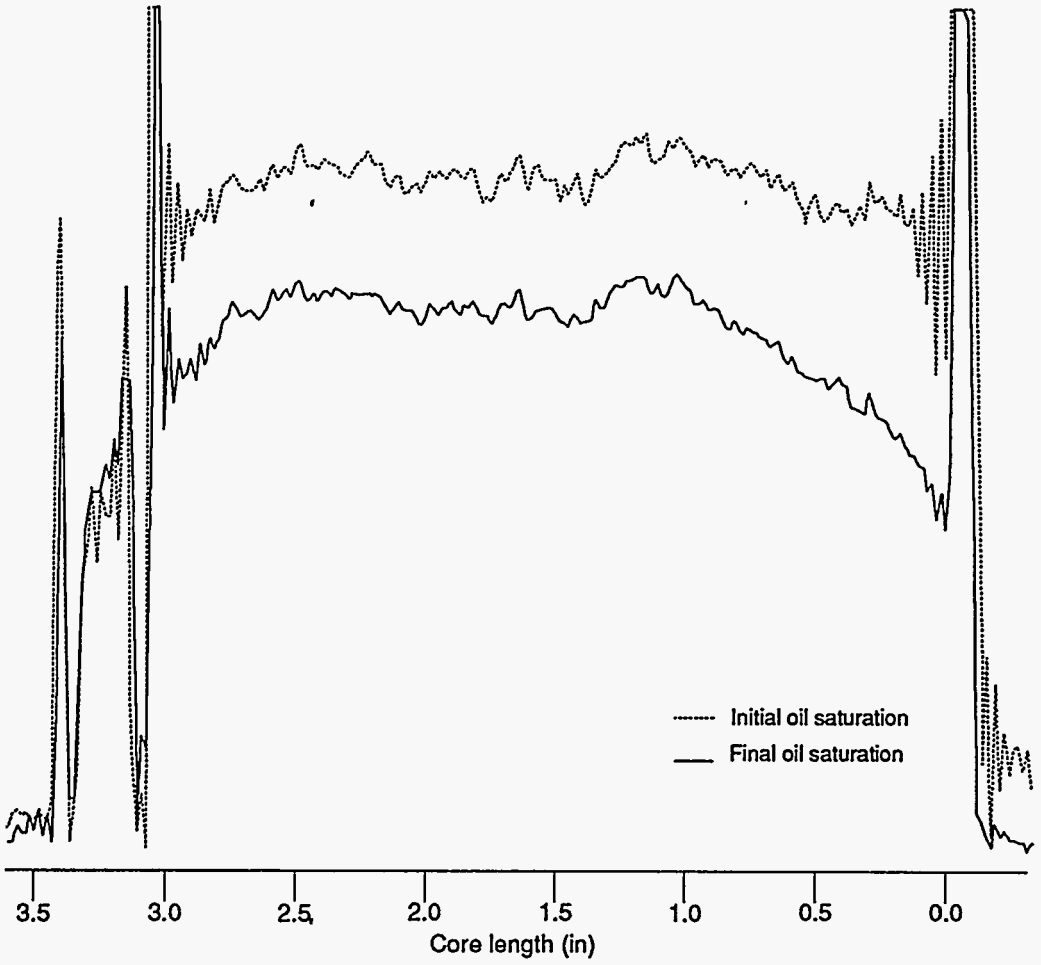


Figure 32 Profile taken at initial and final oil saturation. Again, the use of a reference sample evidenced the shifting of the signal.$CO_2$ - enriched water was used in this case. Sample A2 and reference sample 5 were used, see Tables 3 and 4.

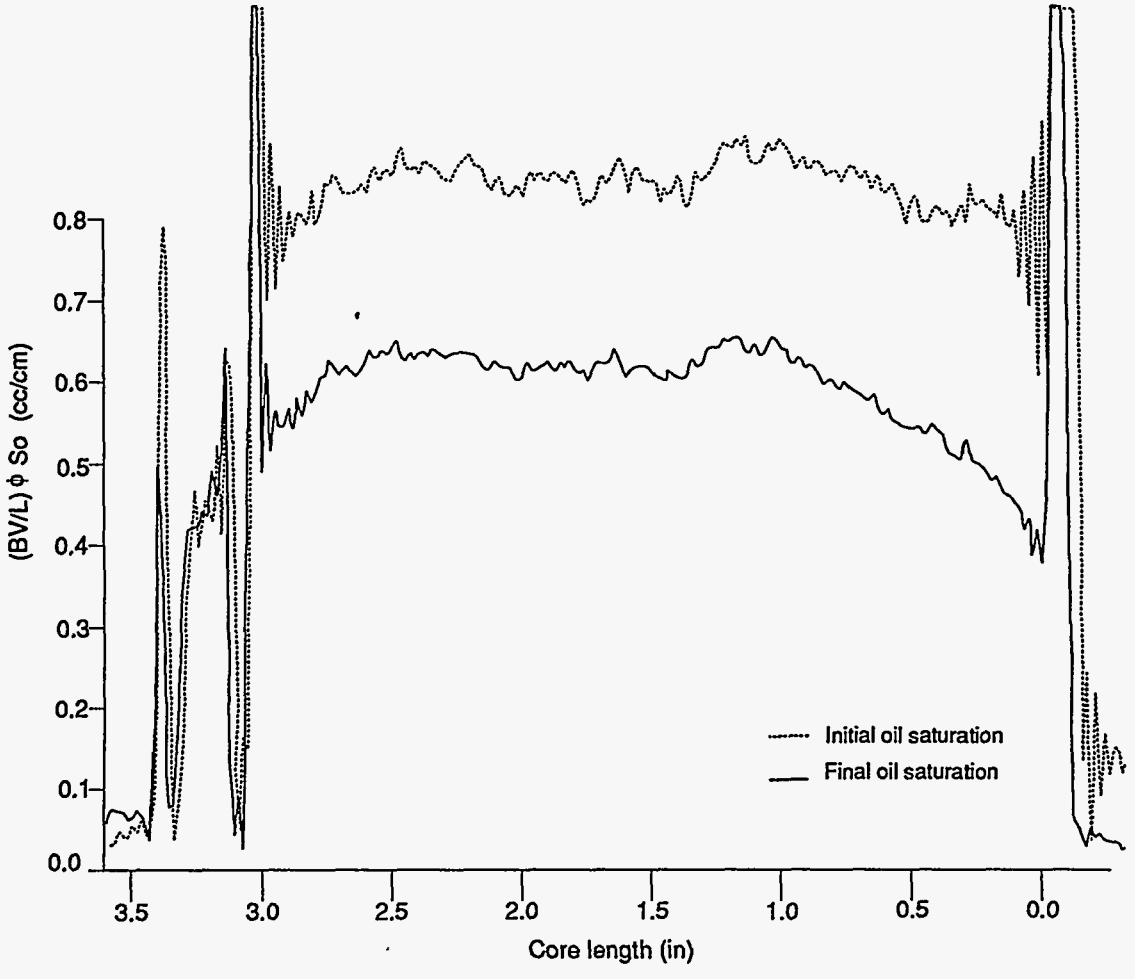


Figure 33 Profile taken at initial and final oil saturation. After normalizing the signal, comparisons of the profiles can be done.

An induced gas drive was attempted for $CO_2$ - enriched water cases. The pressure was dropped bellow the bubble point after the oil production rate became insignificant. The pressure decrease forced the dissolved $CO_2$ to come out of solution. A solution gas drive was created inside the sample. This localized gas drive forced liquids out of the rock, creating a substantial decrease in oil saturation, see Figure 34. A subtraction of the profiles before and after the pressure decrease presents a better description of the fluids movement inside the sample, see Figure 35. Oil was forced out of the rock, but at the same time, a smaller volume of oil was forced inside the sample. On the other hand, a drop of the system pressure caused no effect when unadultered water was being used.

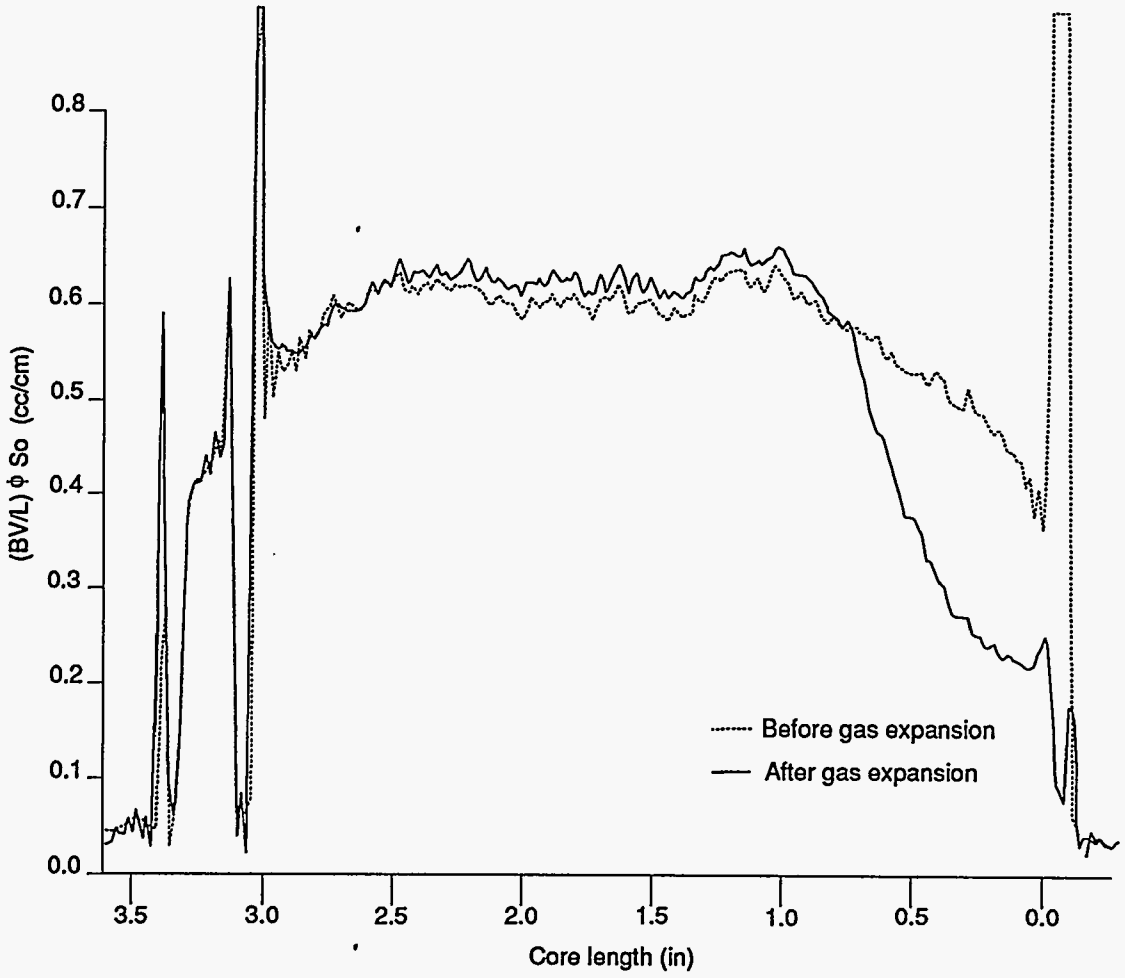


Figure 34 Profile taken before and after the expansion of the $CO_2$ dissolved into the imbibed water.

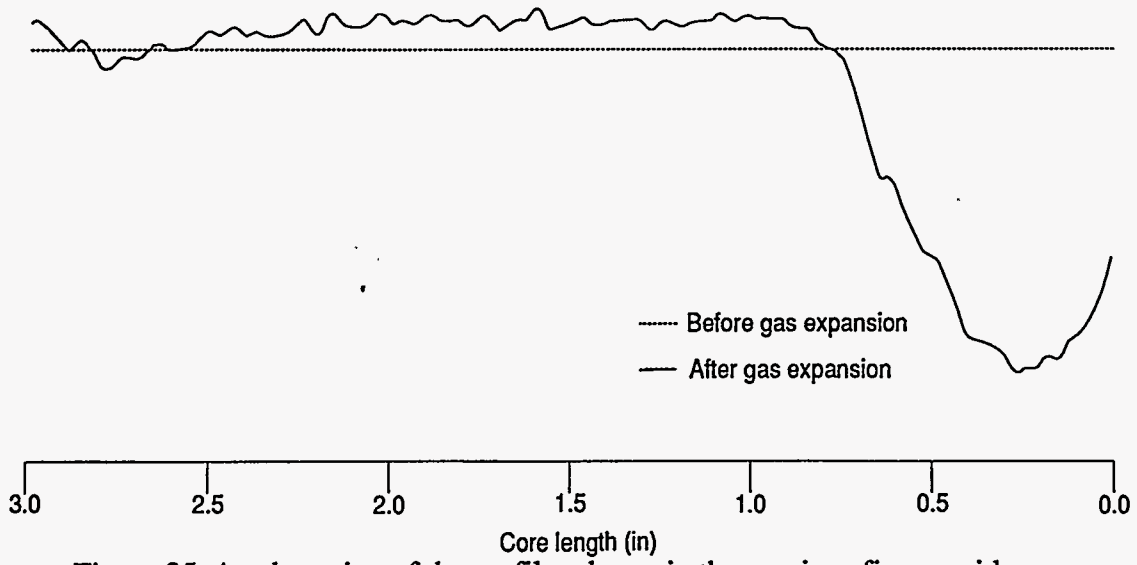


Figure 35 A subtraction of the profiles shown in the previous figure evidences the location of the oil being pushed out by the expansion of the gas.

Oil saturation profiles do not show the straight line trend shown for the case of pure water, see Figure 36. For the $CO_2$ cases a more accentuated decrease in oil saturation closer to the imbibing rock face was observed. It is important to point out the dramatic decrease in oil saturation close to the imbibing face after the gas expansion. The drastic decrease in oil saturation only in a region of the sample reveals that the dissolved gas was not reaching the full length of the rock. This evidence suggests that $CO_2$ was being consumed close to the face of the rock being flooded. Chemical reaction between the rock matrix and $CO_2$ are believed to be responsible for the occlusion of the $CO_2$ movement.

Figure 37 shows a series of longitudinal images taken during $CO_2$ - enriched water imbibition. Similar time lapses were used to obtain the images. Notice the rapid decrease in oil saturation in the region close to the imbibing face, see Figure 37 a, and b. Figure 38 shows changes obtained at the end of imbibition and after pressure depletion. A significant decrease in oil saturation is observed after the gas drive has forced a substantial amount of oil out of the rock, see Figure 38 b, and c.

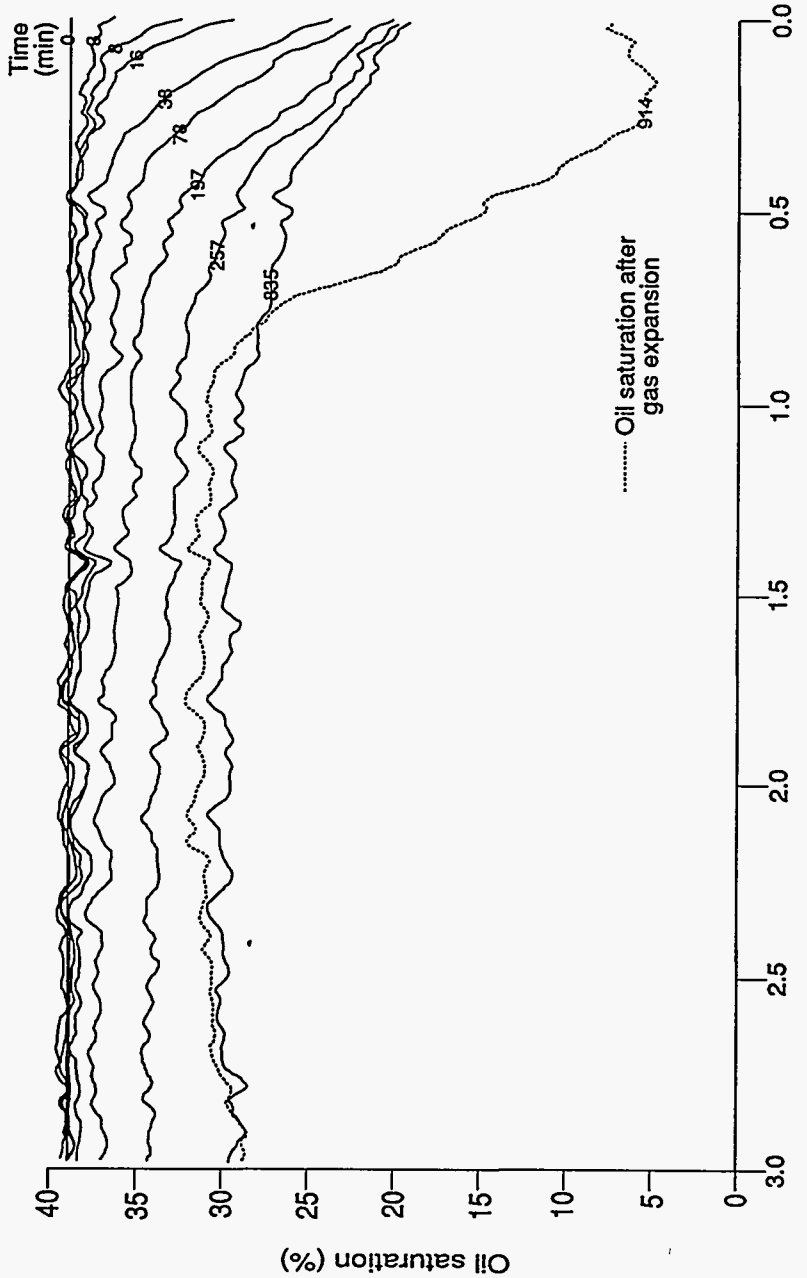


Figure 36 Oil saturation changes as a function of time. Carbonated water was used.

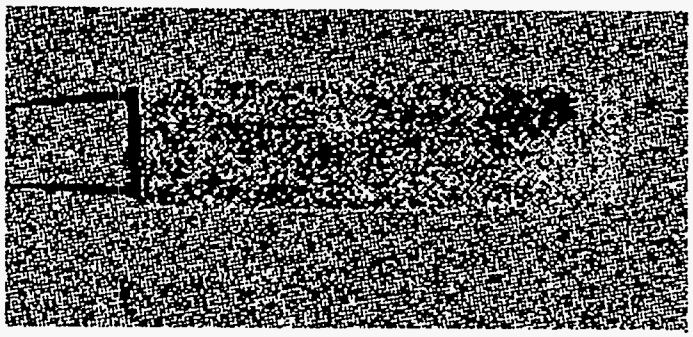

a

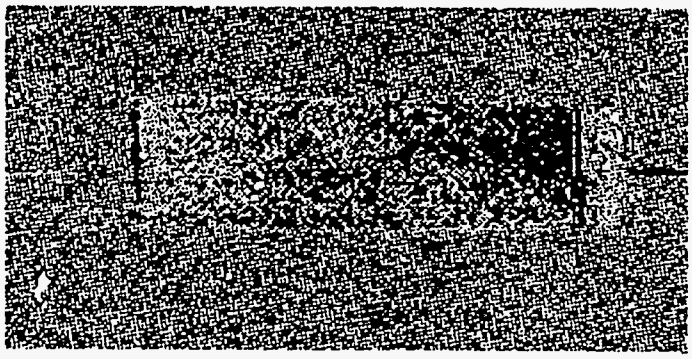

b

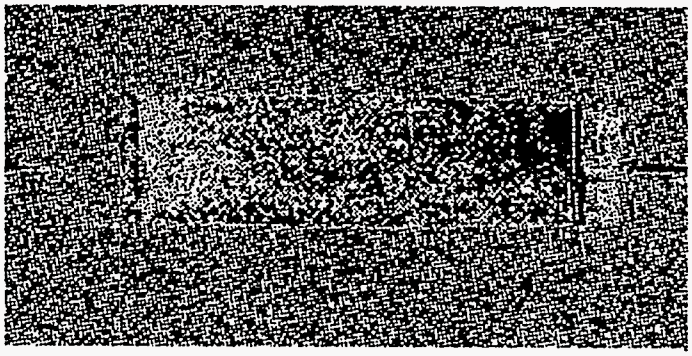

c

**Figure 37 Carbonated water imbibition. a: Initial conditions, b:Displacement of oil from simulated fracture, c - k: Continued imbibition process, l: Conditions at the end of imbibition.**

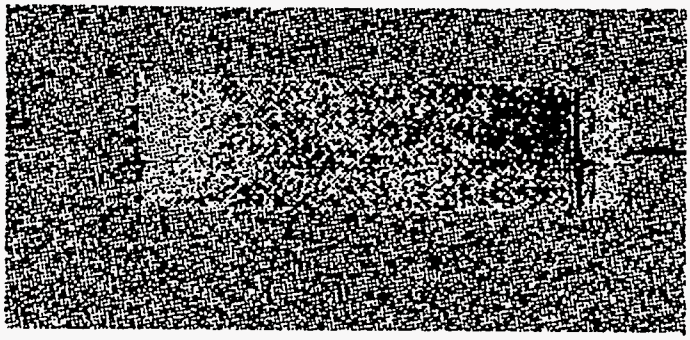

d

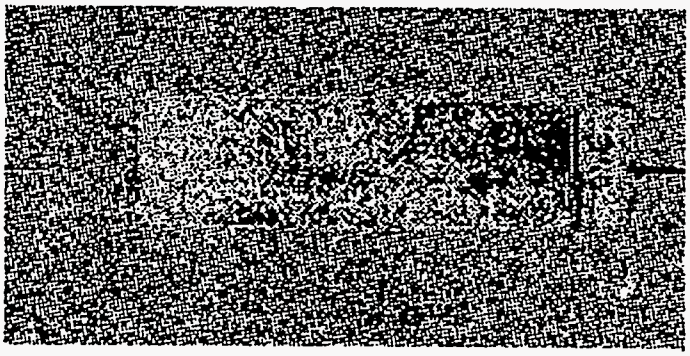

e

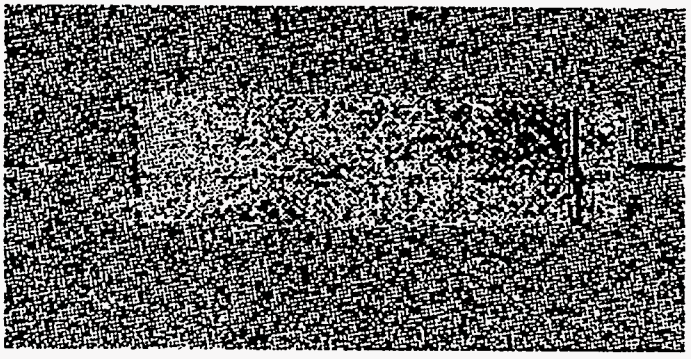

f

**Figure 37 Continued**

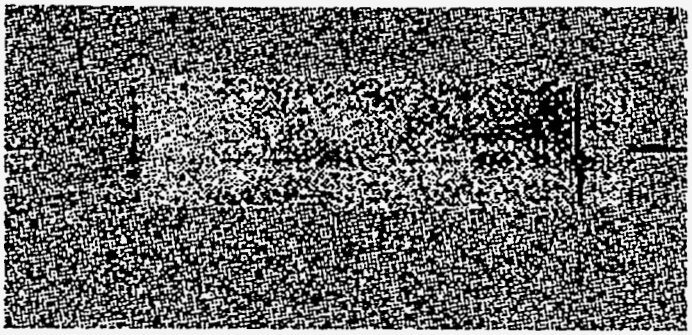

g

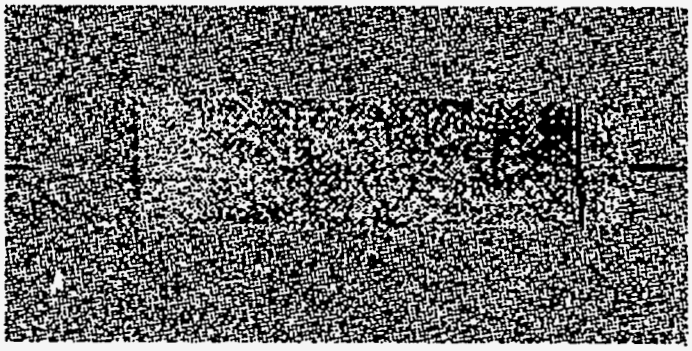

h

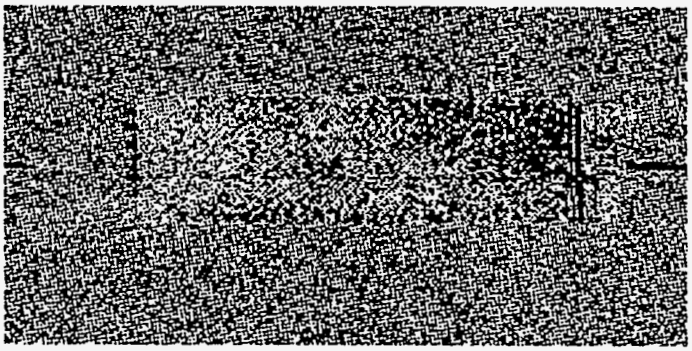

i

**Figure 37 Continued**

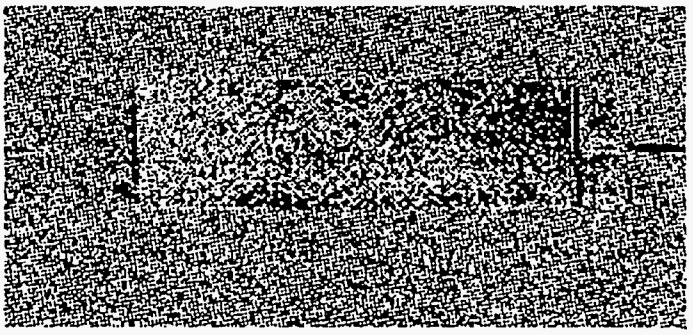

j

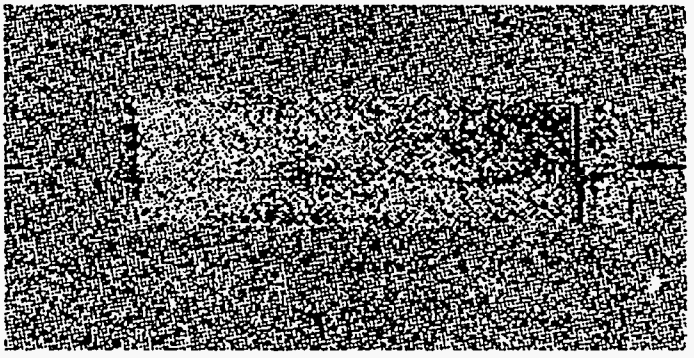

k

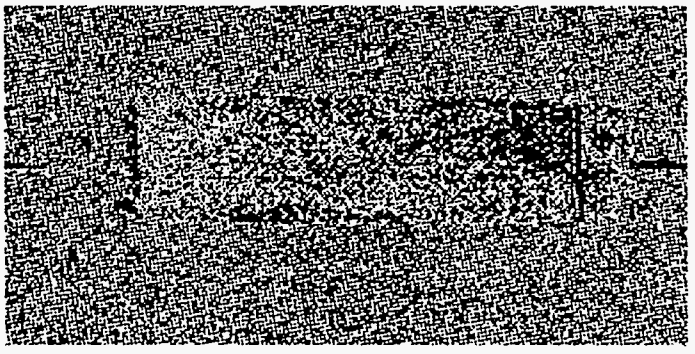

l

**Figure 37 Continued**

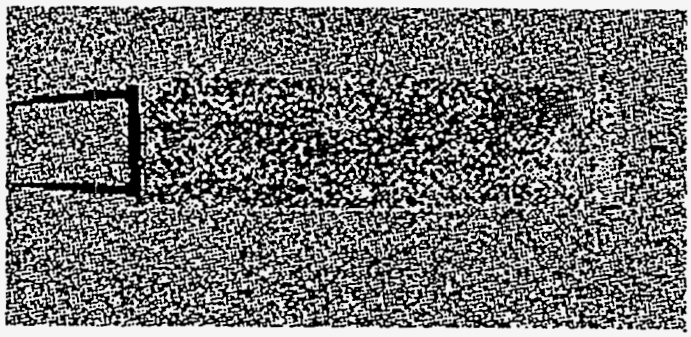

a

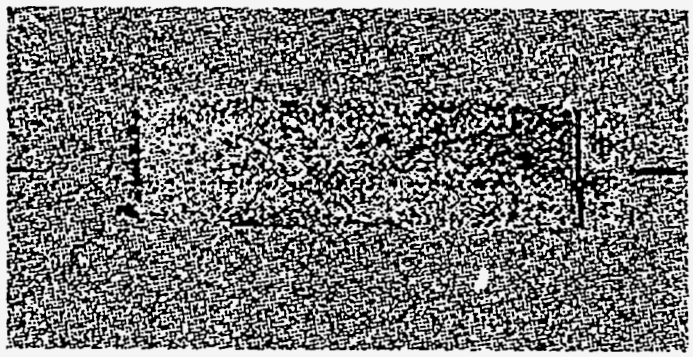

b

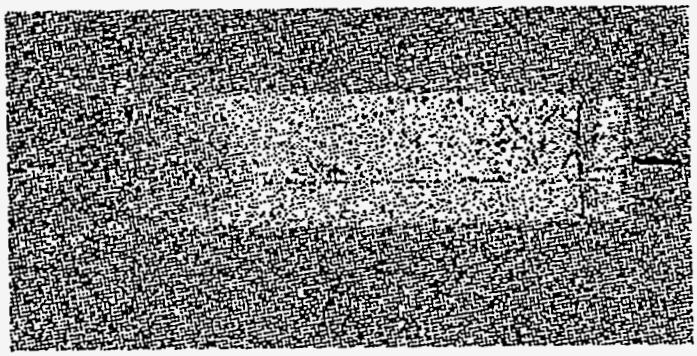

c

**Figure 38 Carbonated water imbibition. a: Initial conditions, b: After imbibition conditions, and c: After pressure depletion.**

Figure 39 shows the cumulative oil production curve obtained when $CO_2$ - enriched water was used. The cumulative production curve was modified. Beneficial effects are noticeable at the beginning of the process, and the typical exponential trend became more obvious. A substantial increase in oil recovery is obtained due to the gas expansion of dissolved gas. There is an excellent agreement between the obtained data and the exponential equation proposed by Aronofsky [2]:

$$R = R_{\infty}(1-e^{\lambda t}) \tag{50}$$

but only for early times. After a period of time the experimental data deviate from their expected values, see Figure 39. Aronofsky's theory is based on the assumption that all rock and fluid properties remain constant. Therefore, an increase in rock permeability is believed to cause the disagreement. The presence of $CO_2$ in carbonated cores is believed to produced an increase in rock permeability but the increase in permeability was noticeable only after a period of about eight hours, when the laboratory data departs from the exponential diagram.

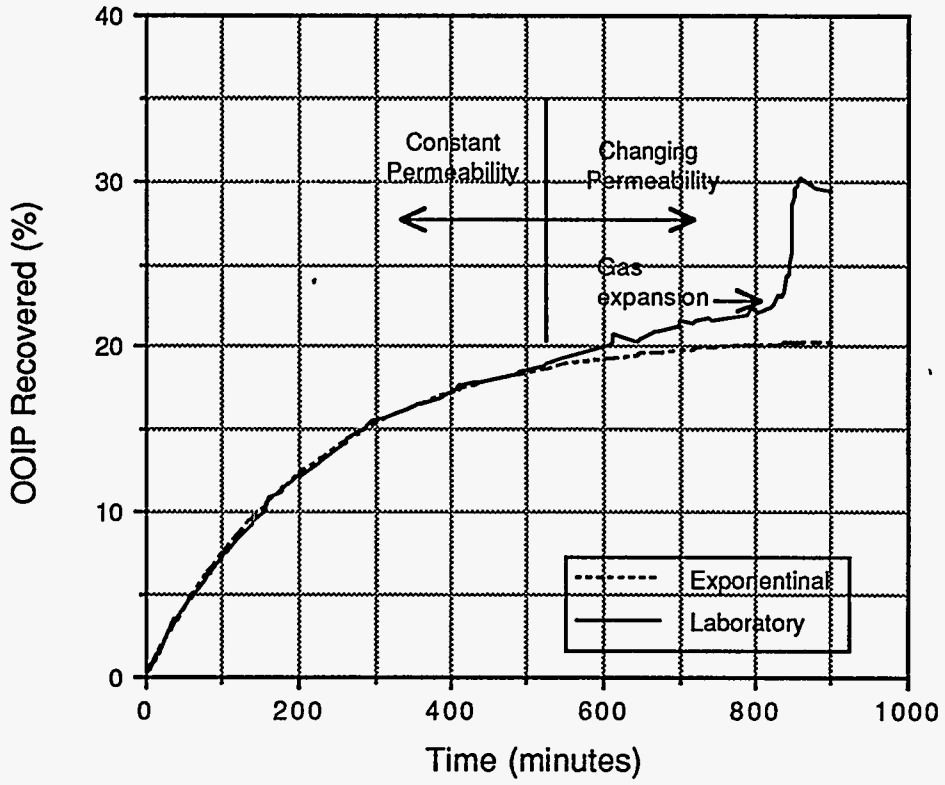


Figure 39 Cumulative oil production obtained by imbibition of carbonated water.

$CO_2$ - enriched water imbibition and the localized gas drive created by the gas expansion were combined into a cyclic sequence that increased oil production rate. A combination of imbibition and pressure pulsing produced a cyclic imbibition type of production. The new method combines two advantages to increase oil production rate: (1) it uses the benefit of imbibition to carry $CO_2$ dissolved in water into the rock sample improving fluid properties during early times of the process; and (2) localized gas drives created when the pore pressure is dropped bellow the bubble point pushes the oil out of the rock sample.

Figure 40 shows oil saturation profiles at initial condition, following a period of $CO_2$ - enriched water imbibition, and after the system pressure was brought under the bubble point. when a gas drive is created. After re-pressurization of the system a period of $CO_2$ - enriched water imbibition was allowed, this period yielded no oil production. No differential pressure was instituted. A cycle of re-pressurization and pressure drop bellow the bubble point was repeated three times. An oil decrease due to these cycles is shown in Figure 41. Subtraction of profiles allowed a more explicit interpretation of the profiles, Figure 42 shows oil saturation changes relative to the initial conditions. Note that imbibition of $CO_2$ - enriched water produced the same curved type of oil saturation profile. Subtraction of profiles also enhanced the fact that an additional oil bank was created, and left inside the rock by the second and third cycles of gas expansion. It appears that the amount of gas evolved in the second and third cycles was not enough to force this oil bank out of the rock sample. If the oil saturation profiles are related to the last condition created by imbibition alone, the same effect is seen for the first cycle, with the difference that the oil bank was driven all the way out, leaving only the last portion inside the sample, see Figure 43.

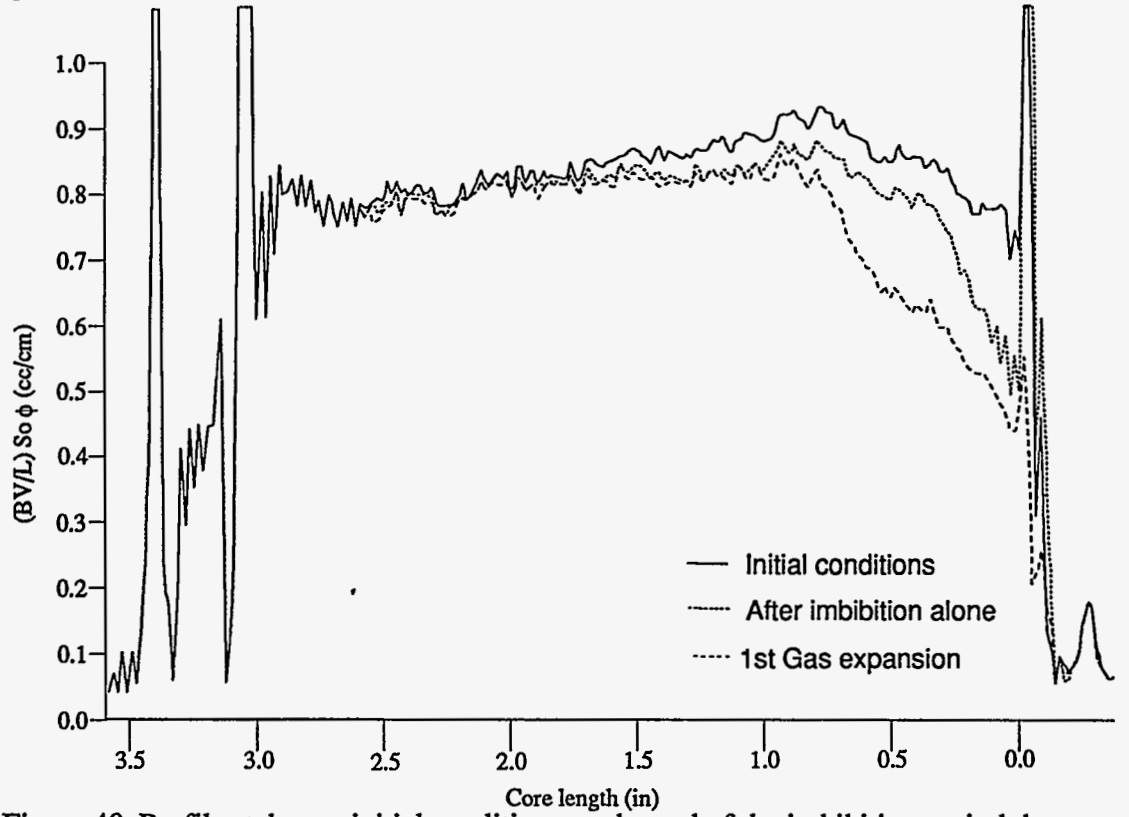


Figure 40 Profiles taken at initial conditions, at the end of the imbibition period that was allowed, and after the expansion of the $CO_2$ dissolved into the imbibed water. Sample A3 and reference sample 5 were used, see Tables 3 and 4.

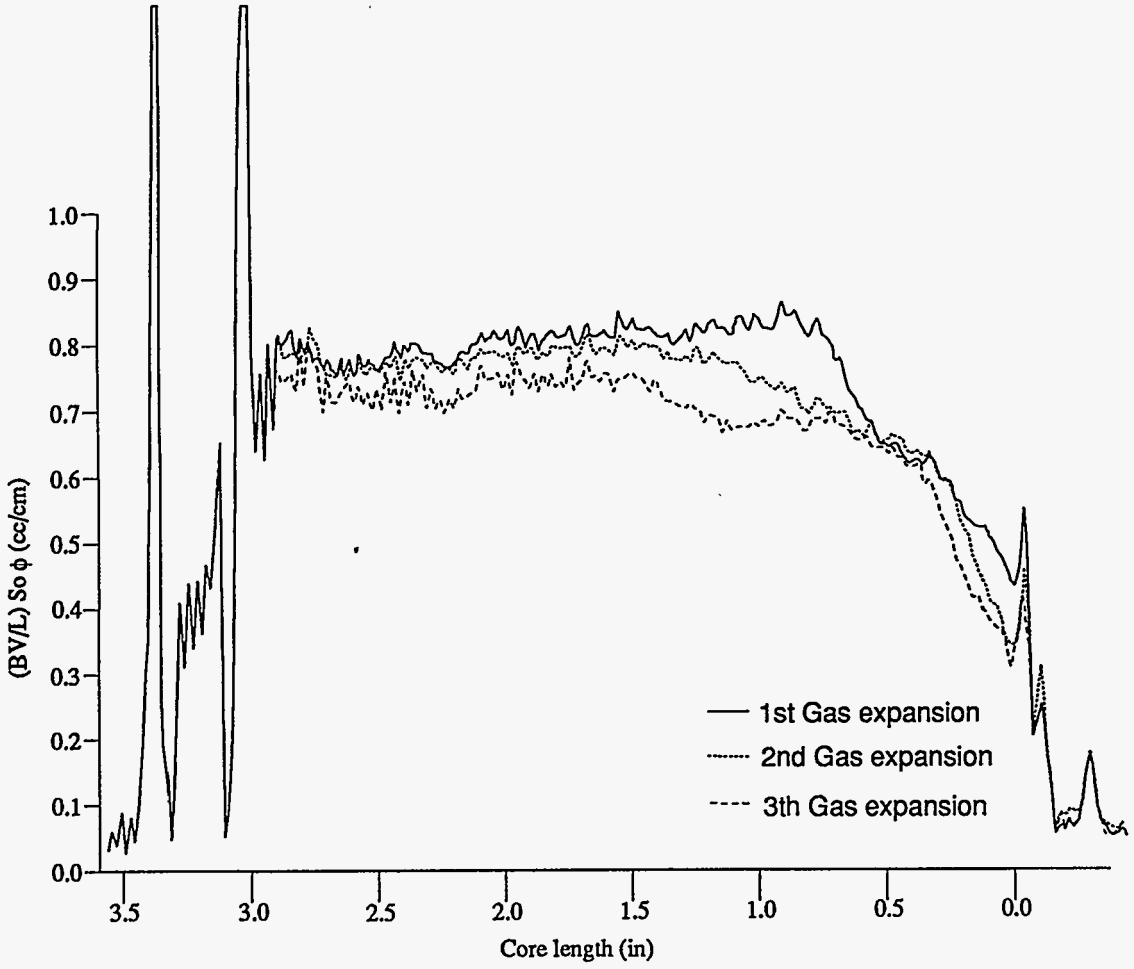


Figure 41 Profiles taken after the fist, second, and third gas expansion. As a reference to the initial conditions see the previous figure.

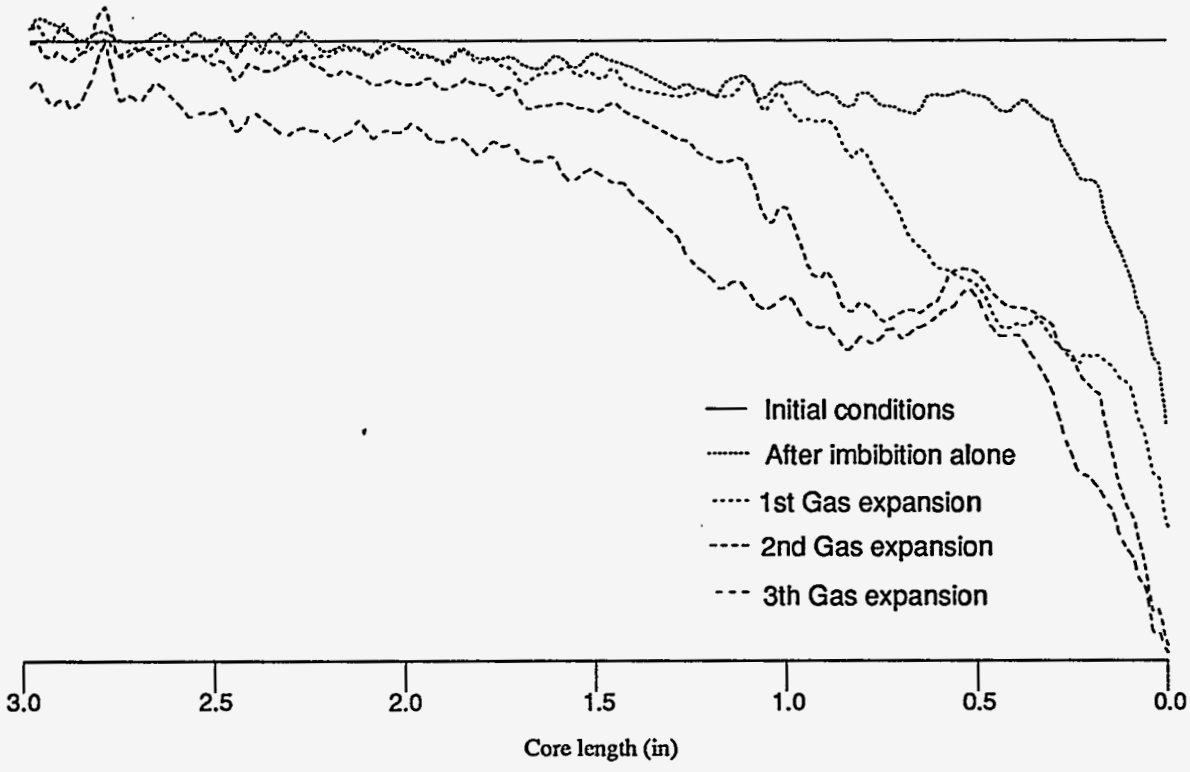


Figure 42 Profiles showing conditions at different stages relative to the initial conditions. Subtraction of profiles from the original conditions profile allowed to observe the movement of oil relative to its original position.

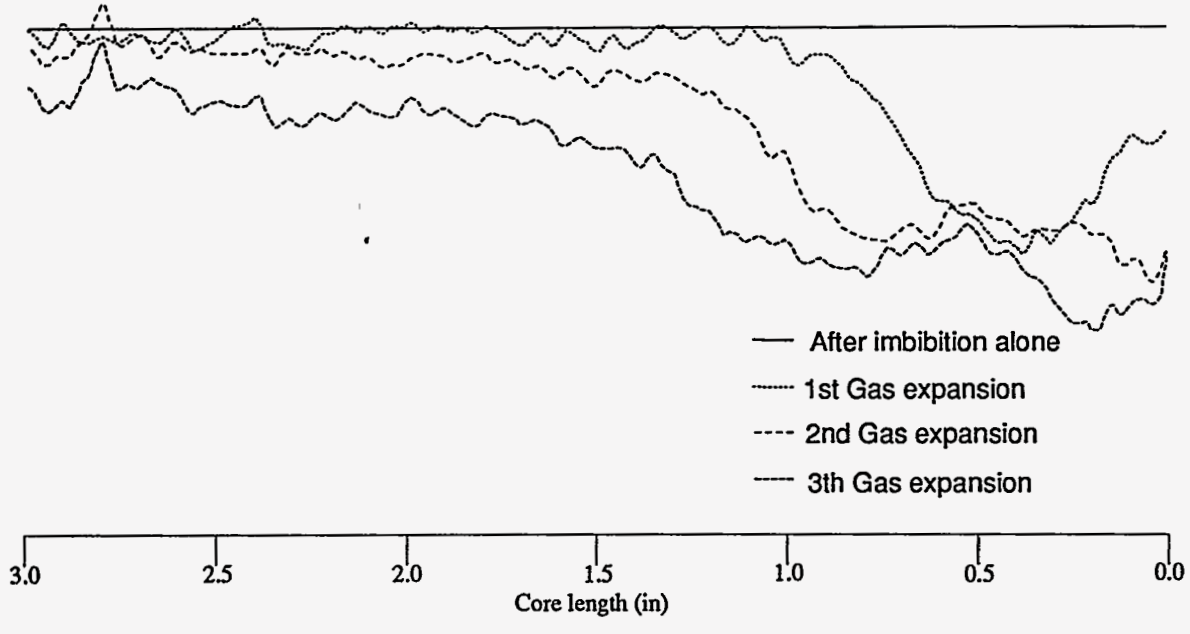


Figure 43 Profiles showing conditions at different stages relative to the plain imbibition period allowed. Subtraction of profiles allowed to observe the movement of oil relative to a given condition, end of imbibition in this case.

Figure 44 is a series of longitudinal images taken at relevant times during the process. Decrease in oil saturation due to pressure depletion is the dominant factor in these images, compare the difference between Figure 44 c and d. Figure 45 shows initial and final conditions of the sample.

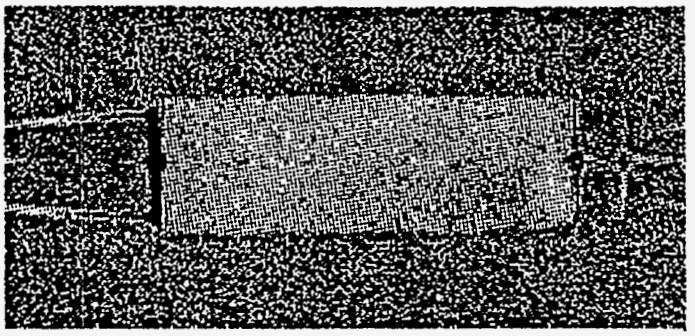

a

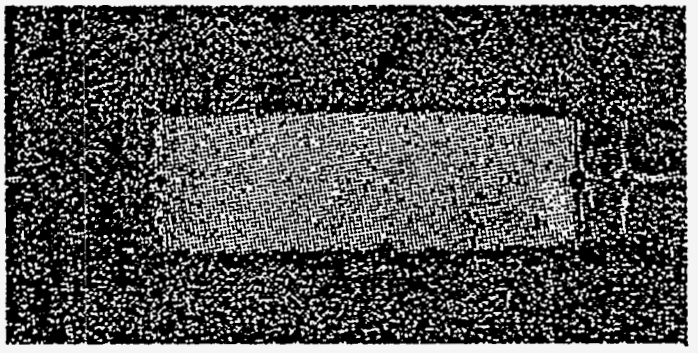

b

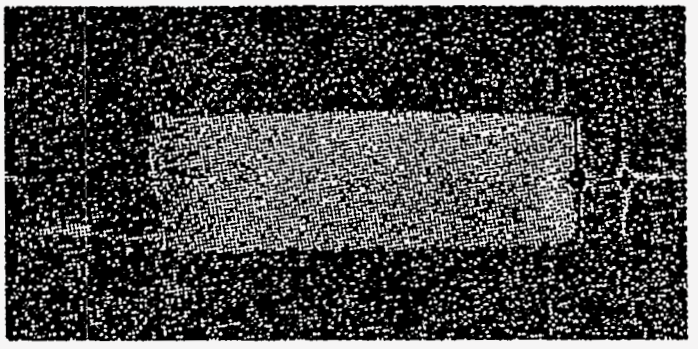

c

**Figure 44 Cyclic carbonated water imbibition. a: Initial conditions, b:Displacement of oil from simulated fracture, c : Conditions at end of imbibition allowed, d: Conditions after first pressure depletion, e: Final conditions**

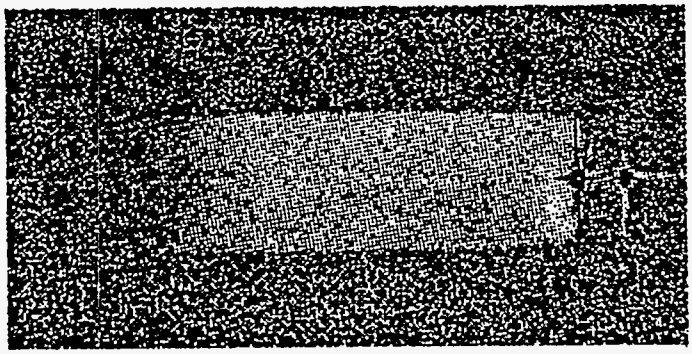

d

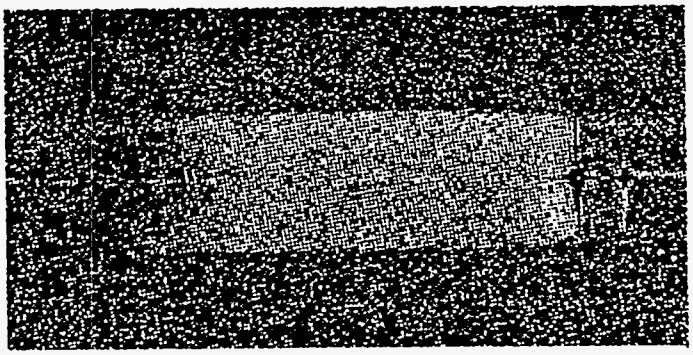

e

**Figure 44 Continued**

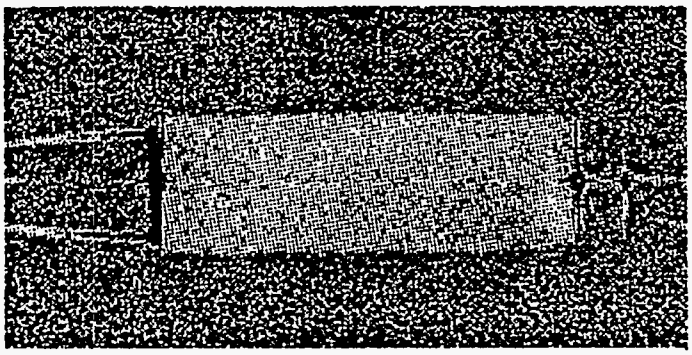

a

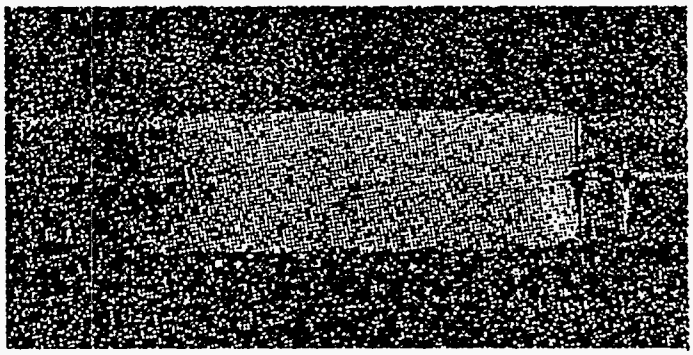

b

**Figure 45 Cyclic carbonated water imbibition. a: Initial conditions, b: Final conditions.**

Figure 46 shows the cumulative oil production curve for the method developed.

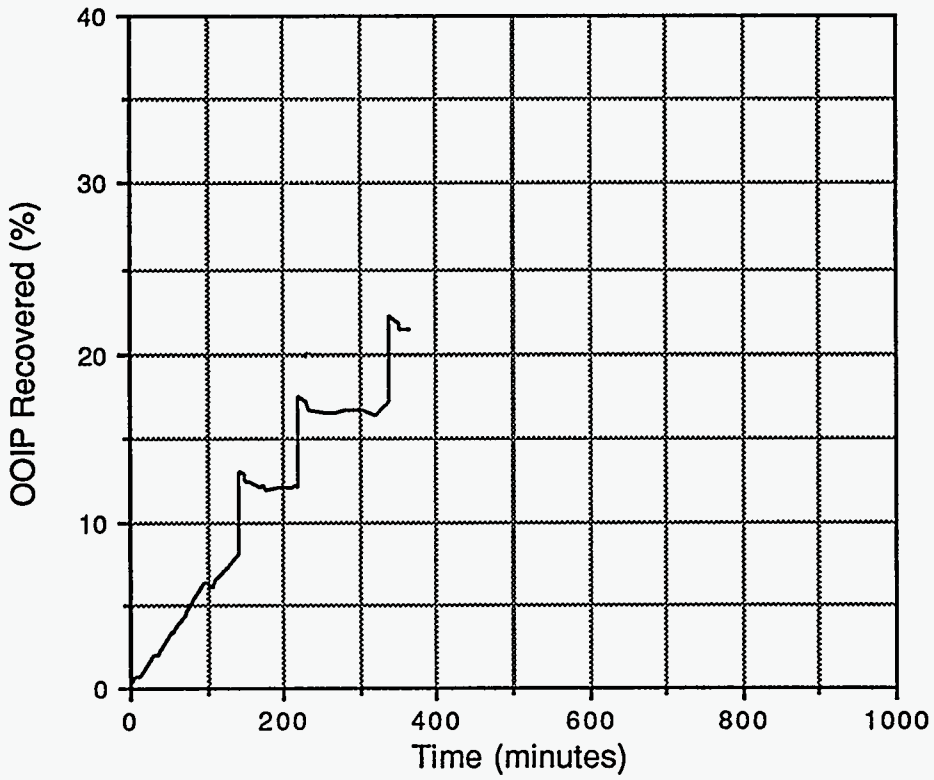


Figure 46 Cumulative oil production obtained by imbibition of carbonated water. A cyclic imbibition and pressure depletion method was applied.

Figure 47 shows a comparison of the cumulative production curves obtained for the different imbibition methods described above. The best oil production rate was yielded by the cyclic method. The inclusion of $CO_2$ yielded benefits during early times of the process but decreased at latter times. The early time increase in oil production is believed to be a product of the change in fluid properties, mainly interfacial tension and viscosities. Changes in rock wettability caused by the inclusion of $CO_2$ are believed to cause the retardation of oil production at latter times. $CO_2$ might reach the rock surface, after crossing a layer of bounded water, in a period of eight hours. Rock wettability may shift from water wet to more oil wet due to this effect. Decreasing oil production rate would be the result of such a change.

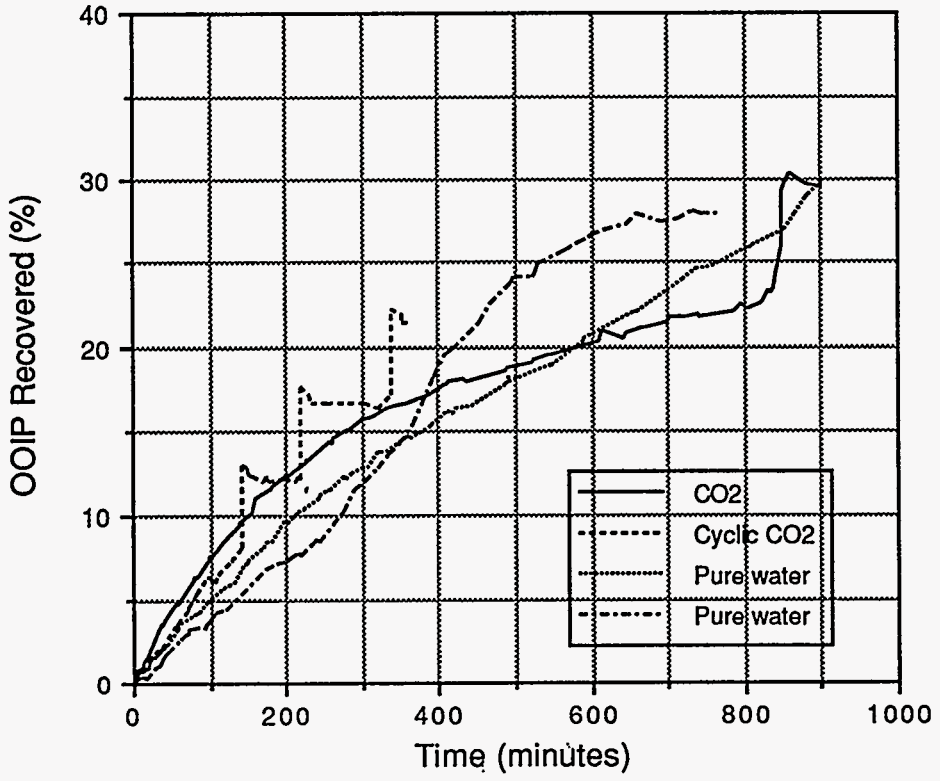


Figure 47 Comparison of cumulative oil production using pure and carbonated water.

### 4.3.2.6 Conclusions

Several conclusions can be derived from the evidence presented in this work:

MRI proved extremely helpful in the study of oil recovery by imbibition flooding. The method permits measuring very small changes in oil saturations along a rock sample.

Uniform oil saturations are generally assumed to be present throughout a core. The use of MRI proved that oil saturation values may vary considerably along a core. Oil saturation as a function of core length was determined for the samples used during this study. Saturation distributions were not only observed but also monitored to study water imbibition flooding.

MRI proton profiles proved that $CO_2$ dissolved in the water being imbibed into the rock sample did not reach the full length of the rock sample. Increase in oil recovery could be accomplished if the full length of the rock sample could be reached by $CO_2$.

MRI profiles have shown that there are significant changes in oil saturation within short distances from the imbibing face. Effects of introducing carbon dioxide into the imbibed water have shown drastic changes in oil saturation along the core. Therefore, not all the core and block shapes previously used by different authors are suitable for this type of study. A short distance from the simulated fracture to the end of the core would yield distorted results.

Evidence presented suggests that $CO_2$ was being consumed close to the rock face, and dissolved into the rock fluids. Oil being produced would carry some of the dissolved $CO_2$ out of the sample preventing it from moving deeper into the sample.

Obstruction of the $CO_2$ moving into the sample prevented complete utilization of its beneficial effects to maximize oil recovery efficiency. A decrease in oil saturation was obtain along the complete core, but the most drastic decrease was observed only close to the face of the rock sample.

Inclusion of $CO_2$ into the imbibed water had beneficial effects at early times of the process. At latter times the most significant effect is the increase in oil production created by a localized gas drive. The gas drive is produced when carbon dioxide dissolved into the imbibed water evolves to its gaseous form due to pressure depletion. Gas expansion significantly contributed to oil recovery.

A combination of $CO_2$ - enriched water imbibition and pressure depletion created a cyclic type of recovery. This method combined the beneficiating effects of $CO_2$ at early times, and the increase in oil production due to the localized gas drive observed after pressure depletion. The time needed to recover similar amounts of oil was reduced to nearly one third of the time required when unadulterated water imbibition was applied. This method exhibited the highest oil production rate.

A drastic increase in oil recovery rate was not the only encouraging result obtained by the developed cyclic method. A significant oil production potential was also determined. An oil bank was driven from inside the sample close to the imbibing face but was not produced. The inclusion of additional $CO_2$ could yield enough gas to drive this oil bank out of the sample, increasing oil production.

Nomenclature

| | | |
|---|---|---|
| A | = | area |
| $\mathbf{B_1}$ | = | secondary magnetic field |
| $\mathbf{B_0}$ | = | external magnetic field |
| BV | = | Bulk volume |
| d | = | distance |
| f | = | fractional flow |
| J | = | Leverett's function |
| k | = | absolute permeability |
| L | = | length |
| M | = | molecular weight |
| **M** | = | total magnetic moment |
| *n* | = | number of moles |
| OOIP | = | Original oil in place |
| p | = | pressure |
| q | = | flow rate |
| R | = | fraction |
| R | = | oil recovery |
| R | = | universal gas constant |
| $R^2$ | = | correlation coefficient squared |
| S | = | saturation |
| T | = | temperature |
| t | = | time |
| $T_1$ | = | spin-latice relaxation time |
| $T_2$ | = | spin-spin relaxation time |
| u | = | interstitial velocity |
| V | = | volume |
| X | = | solubility |

| | | |
|---|---|---|
| x | = | distance |
| x',y',z' | = | axis of rotating frame |
| Z | = | compressibility factor |
| $\int$ | = | integral underneath an MRI signal |
| $\delta$ | = | shape factor |
| $\phi$ | = | porosity |
| $\gamma$ | = | oil gravity |
| $\lambda$ | = | rate of convergence |
| $\mu$ | = | viscosity |
| $\theta$ | = | wetting angle |
| $\rho$ | = | density |
| $\sigma$ | = | interfacial tension |

Subscripts

| | | |
|---|---|---|
| c | = | capillar |
| c | = | connate |
| D | = | dimensionless |
| f | = | fracture |
| i | = | initial |
| m | = | matrix |
| n | = | non-wetting phase |
| o | = | oil |
| r | = | irreducible |
| ref | = | reference |
| s | = | solubility |
| sam | = | sample |
| w | = | water |
| w | = | wetting phase |
| $\infty$ | = | infinite time |

### 4.3.3 CT Studies

#### 4.3.3.1 $CO_2$ Enriched Imbibition in Austin Chalk

Computer Aided Tomography (CAT) scanning of the imbibition process is an ideal application for this technology. Traditional studies of the imbibition process consist of measurement of fluid recoveries over time. This type of investigation is not very satisfactory because the change in distribution of fluids within the rock are not obtained. Fluid distribution is very important when modeling the imbibition process in very heterogeneous media such as Austin Chalk. CAT scan can supply not only fluid distributions but also saturation changes over time within the core.

The imbibition process in Austin Chalk is modeled using the theory that fractures, which predominantly influence flow, is the path that carries water to the matrix block. An assumption is made that the majority of production is from fracture flow. Imbibition into the matrix block will then displace matrix oil which can greatly enhance recoveries. To model the insitu process of imbibition in the lab, a special core holder has been developed. The core is confined in a standard Hassler sleeve and is isolated with flow in and out of

only one end of the core. A recess which is not in contact with the core face conducts flow of the imbibing water and carries off produced oil through two holes along the recess perimeter. This has proven to provide satisfactory fracture simulation.

$CO_2$ enriched imbibition, using imaging techniques, has been previously studied by other investigators. However, these studies have all used representative rocks because of extended experiment durations with actual samples. Use of CAT scans to study this process with actual specimens is possible and will allow verification of short term experimental results. Studies to date have been performed using MRI to provide core saturations and fluid distributions over time. Results show that the imbibition process augmented by $CO_2$, does increase recovery over non-augmented imbibition. However, all studies have been conducted on surrogate rock because actual imbibition times using reservoir rock are beyond normal experimental durations.

With projected experiment times of three months duration, use of actual reservoir rocks with permeability in the micro darcy range provides a challenge. MRI is unsuitable because the magnet can only be dedicated to a single experiment at a time. Removing and repositioning the core holder each day for imaging will not allow as accurate a duplication of results as would be preferred.

The solution is the use of the CAT scanner. A linear motion table translates along the **z** axis for scanning. Because of this, several experiments may be placed upon the table, with each being scanned in turn. Repeatability is excellent and whole core scans can be performed on a daily basis to monitor the imbibition.process. Images are then processed to provide changes in saturations.

Development of saturations on the CAT scanner requires a set of four arrays for each spatial slice. The initial array required is one of a dry core, which is the bulk volume. The second required is an array of the wetting phase, in this case water. Maximum oil saturation is the third, and the fourth is the daily scan which monitors the progress of imbibition. By subtraction of these arrays; bulk volume from brine saturated, maximum oil saturated from this array, and then the daily scan from either of the previous two provides information on the advance of imbibition.

Among work planned is the investigation of $CO_2$ as an enhancement in the imbibition process. Experiments will be conducted on both Austin Chalk over a long time duration at very low rates. Experiment duration is expected to be one to two weeks. During this time, full core scans will be made daily. Image analysis will then be conducted to determine the advancement of the imbibition process. The large amount of data generated should provide great detail about the imbibition process and issues that effect micro models in the lab, such as gravity segregation.

Actual experimental work in long term imbibition has just begun. Equipment to monitor the process for the experimental duration has been developed and tested however. Pressures and volumes are fully instrumented, and instrumentation is registered on a chart recorder.

A normal experimental progression is planned. Initial imbibition experiments should be performed with a normal brine without $CO_2$ enrichment. After establishment of experimental parity, experimentation with imbibition enhanced by $CO_2$ will commence.

#### 4.3.3.2 Visualization of Fractures in Austin Chalk

Because fracture flow is thought to dominate flow in Austin Chalk, models of fracture size and distribution are of great importance to development and management of production from the trend. The use of CAT scanning has proven a significant tool to advance model theory in fracture magnitude and distribution.

The mapping of microfractures using nondestructive techniques is presently unique to the research effort here. An attempt is being made to determine average fracture length,

distribution of microfractures, and the relationship between interconnected and discontinuous microfractures. The subjects for these studies have been cores from Austin Chalk horizontal well.

Imaging of fractures is the only method available that has the capacity to study microfractures nondestructively. The CAT scanner has been chosen because of the superior resolution afforded when imaging. The resolution available is 256 x 256 pixels which can be focused to a five inch square area for a four inch diameter core. With the focal area of 127 x 127 mm and a pixel saturation of 256 x 256, this gives a theoretical minimum fracture imaging capability of 0.5 mm. Actual fracture imaging capability has proven to be about 1 mm, however. This is due to difficulty with pattern recognition necessary to identify microfractures below the 1 mm minimum. Resolution on the **z** axis is 7 mm. A scan overlap has been chosen using a slice width of 4 mm. It has been found that this slice width is the minimum practically possible with the equipment now in use. Good results have been achieved with this compromise, however. The **x - y** axis microfracture resolution is then, 1 mm and the **z** axis resolution is 4 mm. It would be suspected that the **z** axis resolution would not be sufficient. Horizontal well are oriented normal to the fracture system however, and experimental evidence has shown most fractures to be normal to the **z** axis.

Cores are prepared for scanning by placing the subject into a low vacuum core holder. The core is then subjected to evacuation at ultra low vacuum pressures for a period of up to one week. Scanning of the subject is then initiated. After the initial scan with the core evacuated, xenon gas is introduced into the core holder at low pressure (15 psig). The core is then rescanned using the same **z** axis locations.

Xenon gas has an atomic weight of 131 and air an molecular weight of 29. Because of the difference in weights, xenon has an x-ray attenuation approximately four and a half times that of air. This by itself provides enhanced imaging of fractures, but as will be shown also has additional benefits.

Each scan is simply an 3 dimensional array, which is composed of 256 **x - y** dimension elements, and is one element thick in the **z** direction. By subtraction of two arrays, a third array may be generated containing new information. In this case, subtraction of the initial scan of the evacuated core from the xenon filled core produces an image of only micro fractures that have continuity. By comparison with an unmanipulated scan, the distribution of continuous and discontinuous microfractures can be determined. Discontinuous microfractures are apparent in the original scans, but disappear in the subtracted image.

The image collection for each slice can then be printed, with a scaling factor calculated between the actual size of the core and the size of the image. Using this scaling factor, it is a simple procedure to use a linear map distance recorder to calculate the actual microfracture lengths.

The experimental procedures used here are relatively simple in concept. After initial start up problems were solved, experiments have been fairly error free. The experimental turn around time is approximately two weeks. Image analysis of the experimental results is more complicated, however. With approximately two hundred megabytes of data generated for each foot of core, it can be seen that image analysis of the data is machine and also operator intensive. This can extend total results turn around to a one month period.

Data from a number of scans have been processed. Microfractures have been mapped. It is felt, however that the number of cores (five) that have been scanned is to small to be a representative population. Data analysis has proven that a large number of micro fractures evident are not interconnected. The cores are relatively homogeneous, but small amounts of higher permeability areas are evident, which have good interconnectivity. Statistical analysis of fracture extension and orientation is under investigation.

Images of a small segment of a horizontal core have been included as an example. The subject is core I8, and images begin at scan 521 which is the end of the core (Figure 1), and extend 88 millimeters into the core to scan 544 (Figure 22). Black boxes have been placed around fractures. Continuity can be observed from scan to scan. Resolution in these reproductions is not as high as is possible for analysis purposes. Images for analysis are 8 bit ,which can be represented by a 256 color spectrum. Output to a 1 bit monochrome printer for duplication purposed requires that a color image be first represented in grey scale, and then dithered to produce a printable image. This causes a considerable image degradation. Fractures evident in color analysis are also evident in the degraded 1 bit images, however. Fractures around the perimeter of the core are possibly induced, while internal fractures are most probably native.

Because of large number of cores that are needed to form a representative population, an effort is underway to secure more. Major operators in the Chalk trend have pledged their cooperation in this effort. Coring is a relatively rare occurrence with most wells, and consequentially the sample population is not great. There is however, a number of cores that have been promised for the experimental work in progress. One of the greatest advantages to this experimental technique, is that it is nondestructive in nature, and therefore, the core may be returned to the donor intact.

The Austin Chalk outcrops in Texas, from Dallas to Del Rio. Because creation of microfractures in the Chalk was bed contained, it is felt that surface samples should provide comparable results to the core studies presently under way. The readily available nature of this sample population can provide further data toward microfracture mapping.

Experiments have been conducted on specimens from surface outcrops with fractures mechanically induced by axial loading. These samples were provided by the Dept. of Geophysics. The samples were then scanned to determine the ratio of length of internal fractures to those that were easily measured on the core surface. Development of a mathematical model by the Dept. of Geophysics to predict this relationship is on going.

Existing data from scans of mechanically fractured core samples and horizontal cores will be analyzed in conjunction with the Dept. of Geophysics. A larger set of mechanically fractured core samples is available. These cores when scanned will provide a larger data set for model development and prediction.

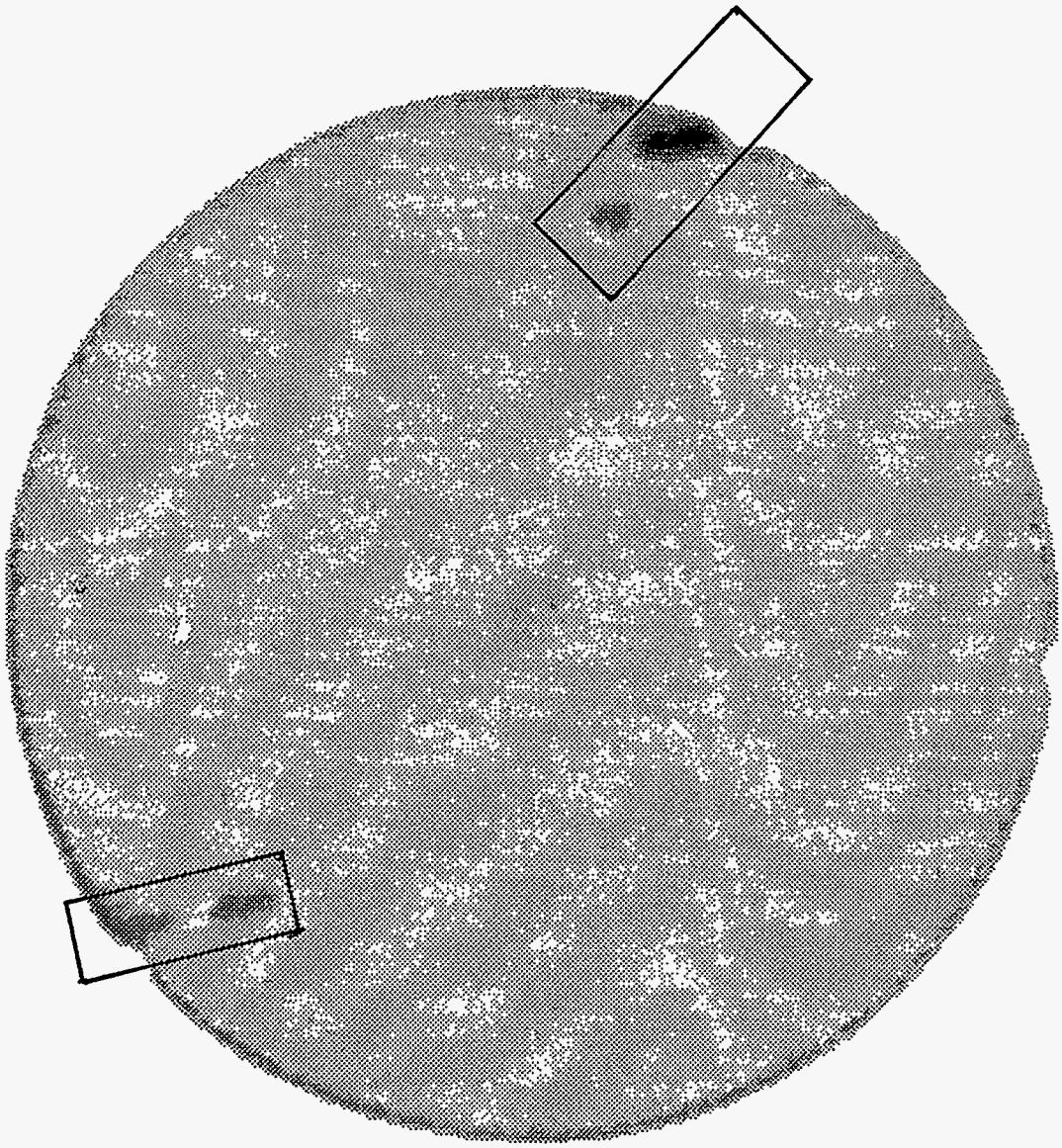

Figure 1
Core I8 Scan 521

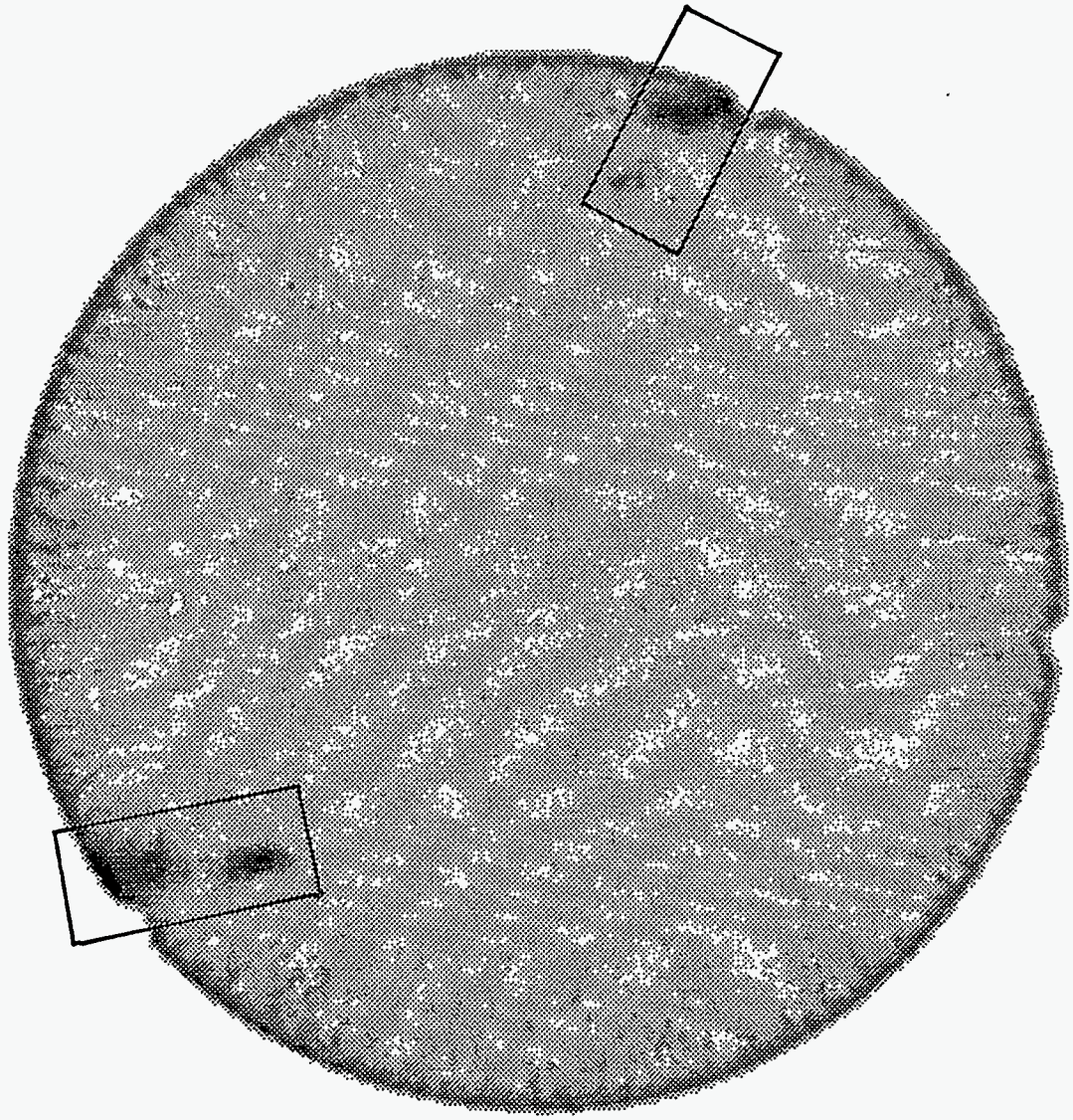

Figure 2
Core I8 Scan 522

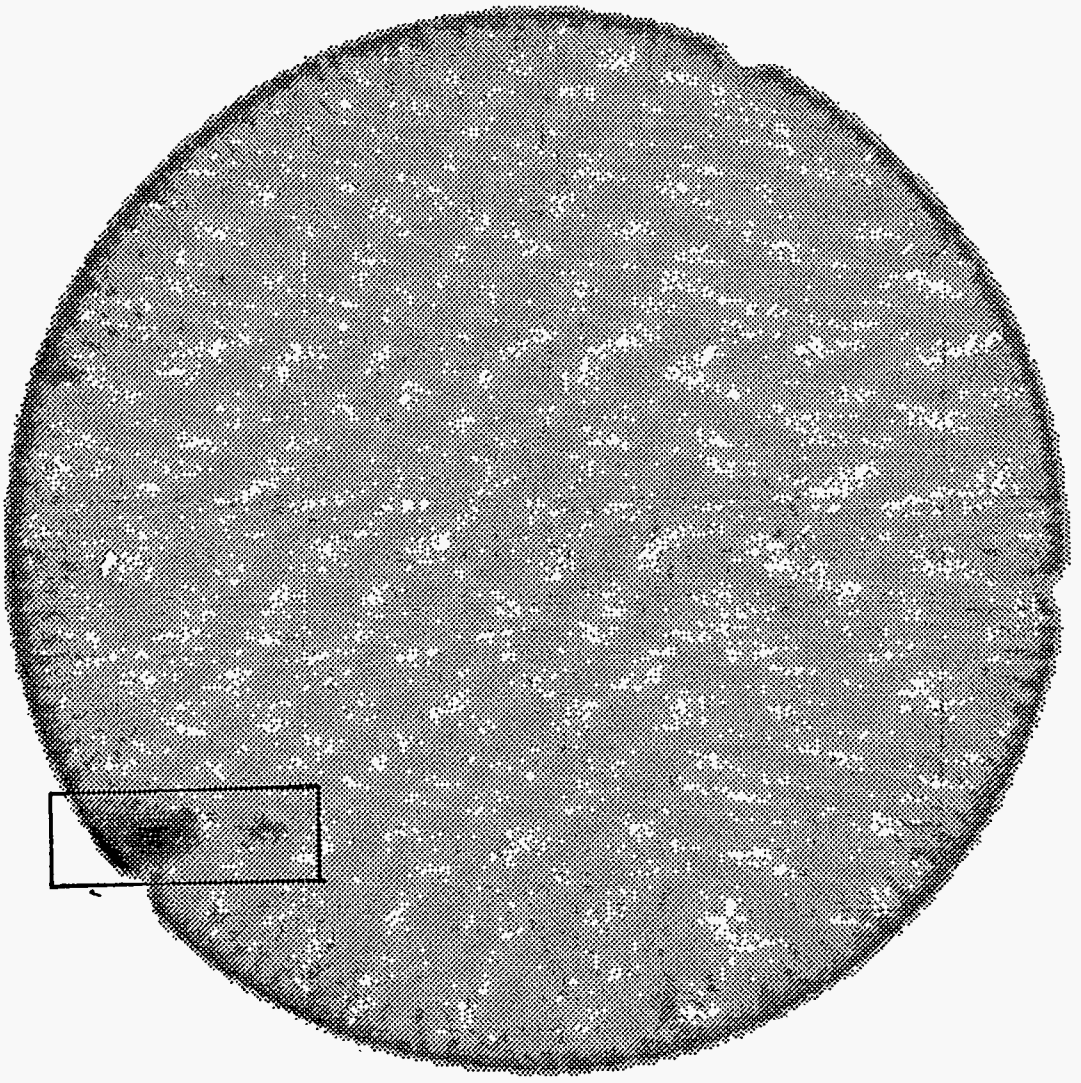

Figure 3
Core I8 Scan 523

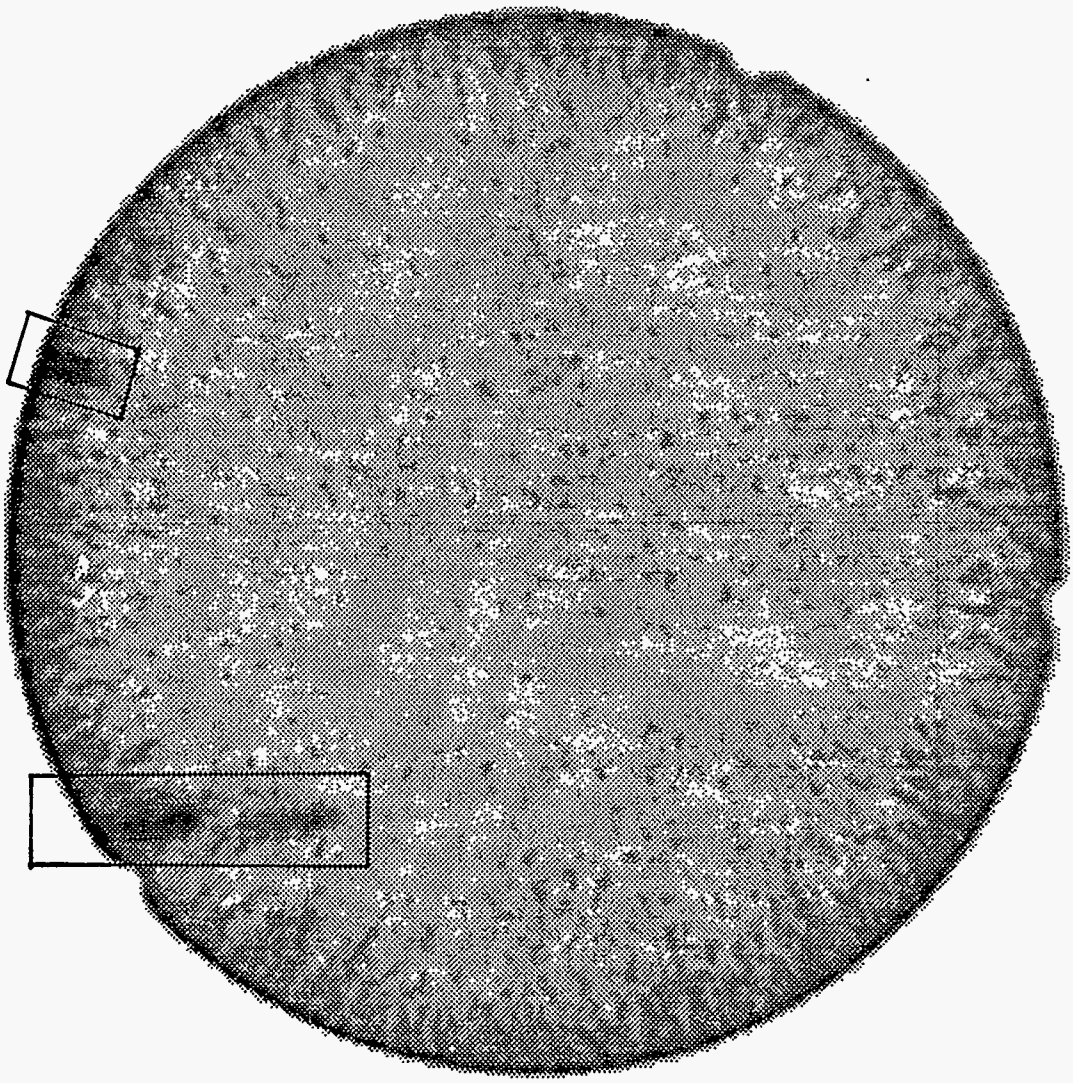

Figure 4
Core I8 Scan 524

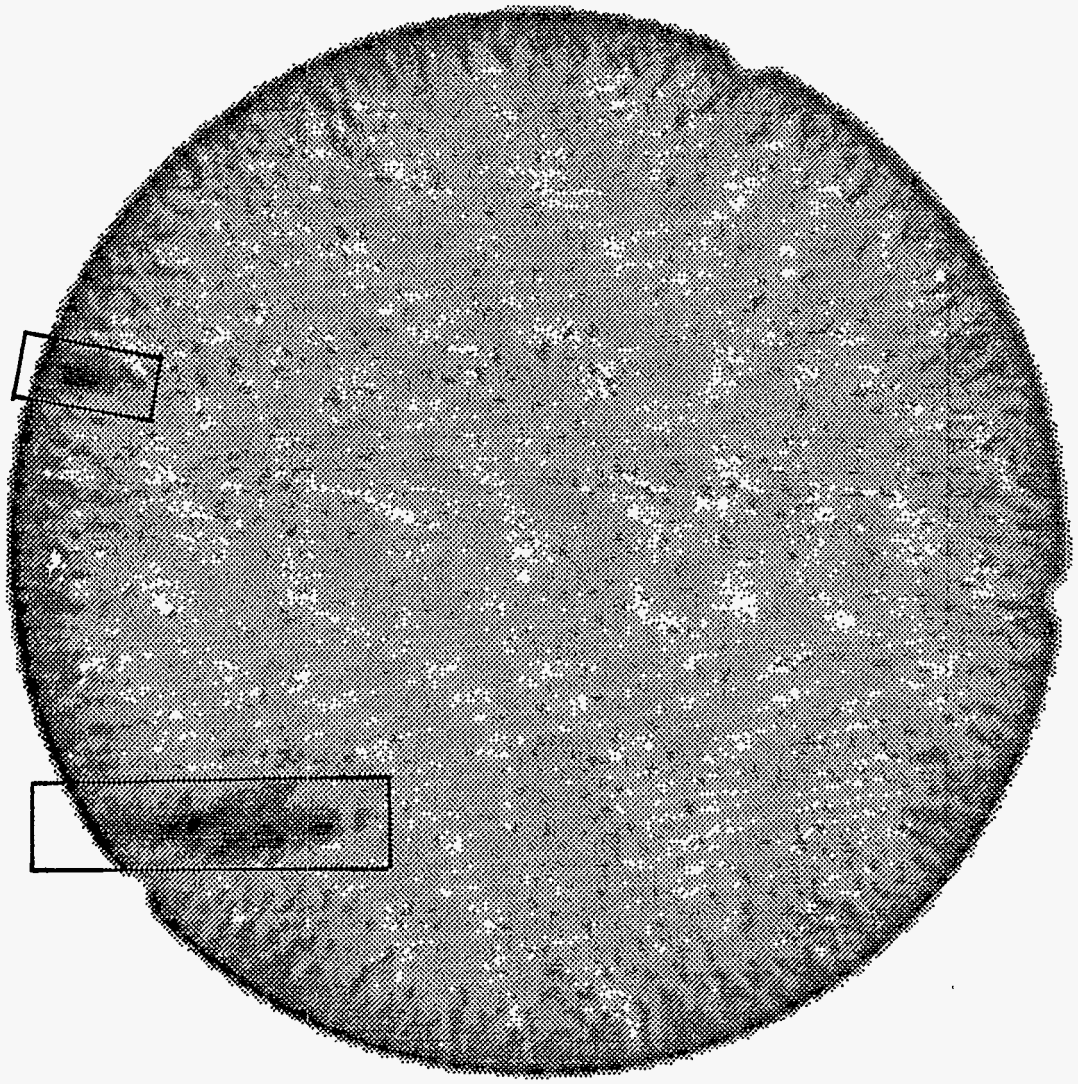

Figure 5
Core I8 Scan 525

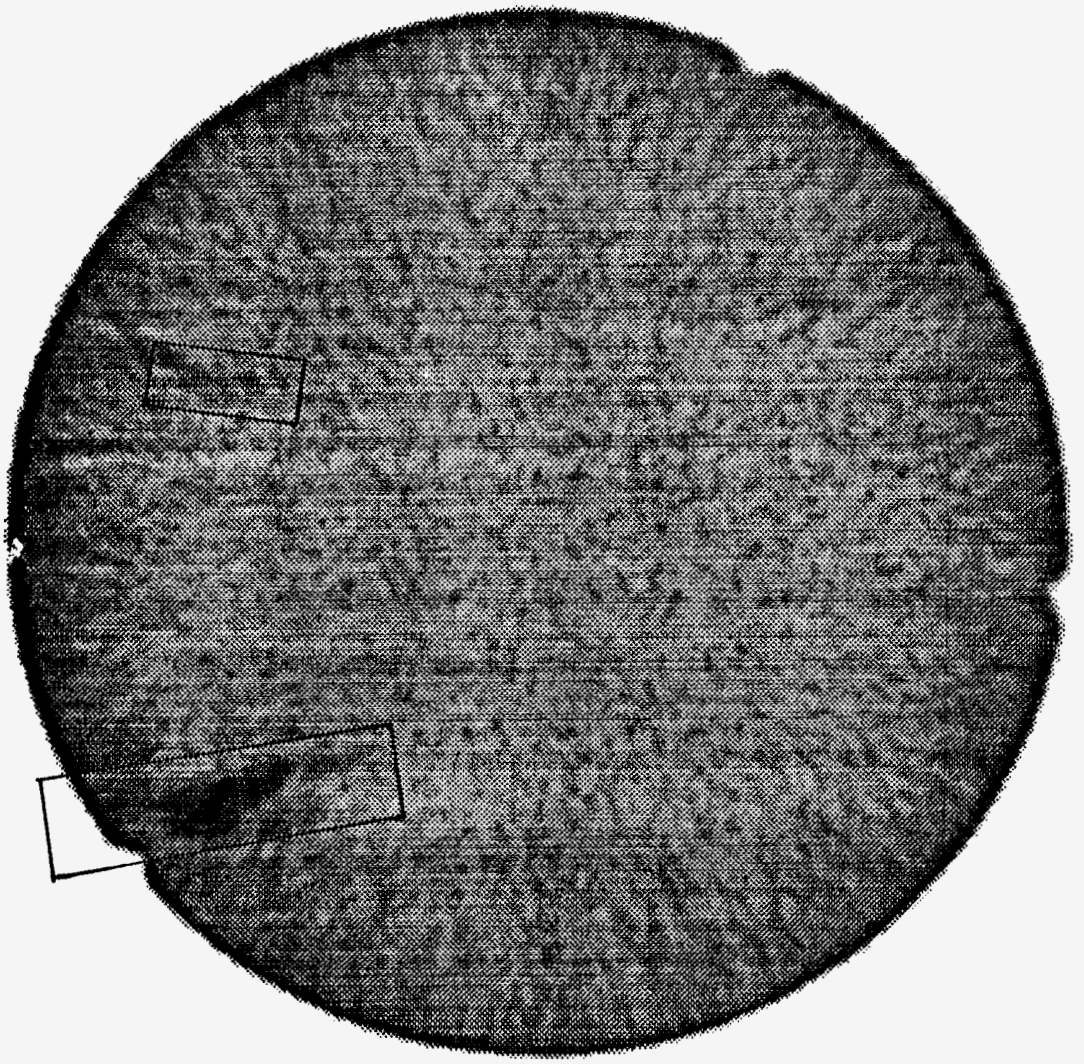

Figure 6
Core I8 Scan 526

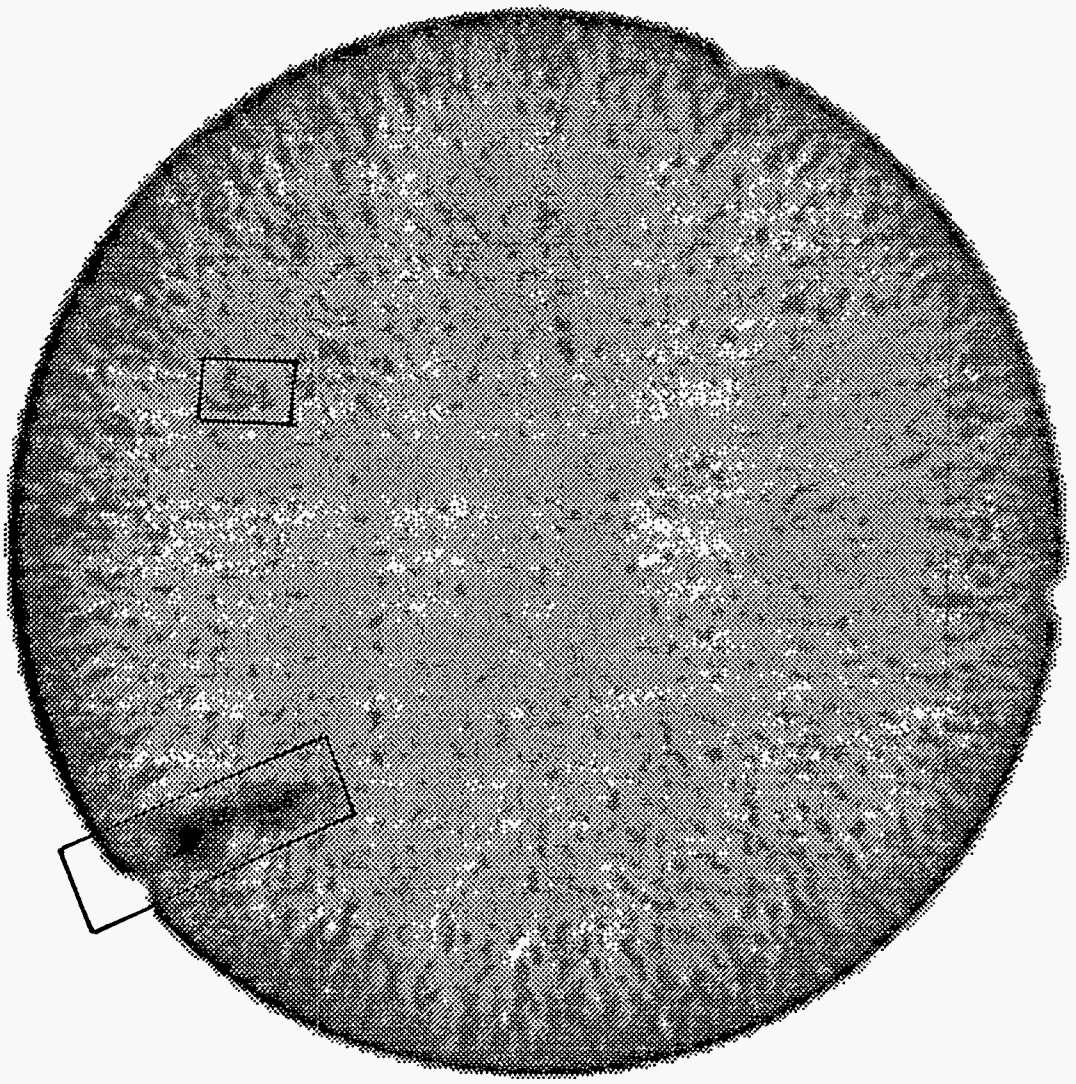

Figure 7
Core I8 Scan 527

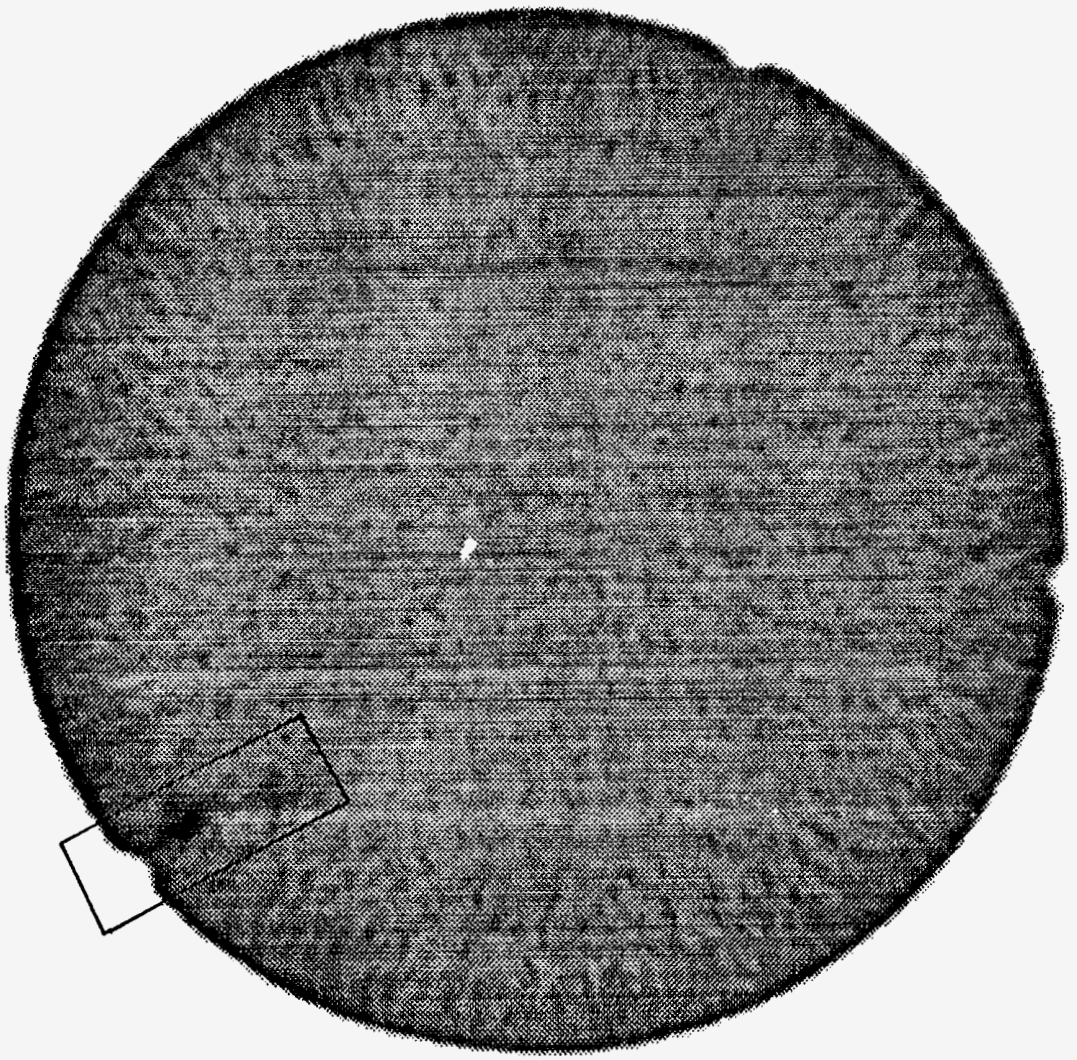

Figure 8
Core I8 Scan 528

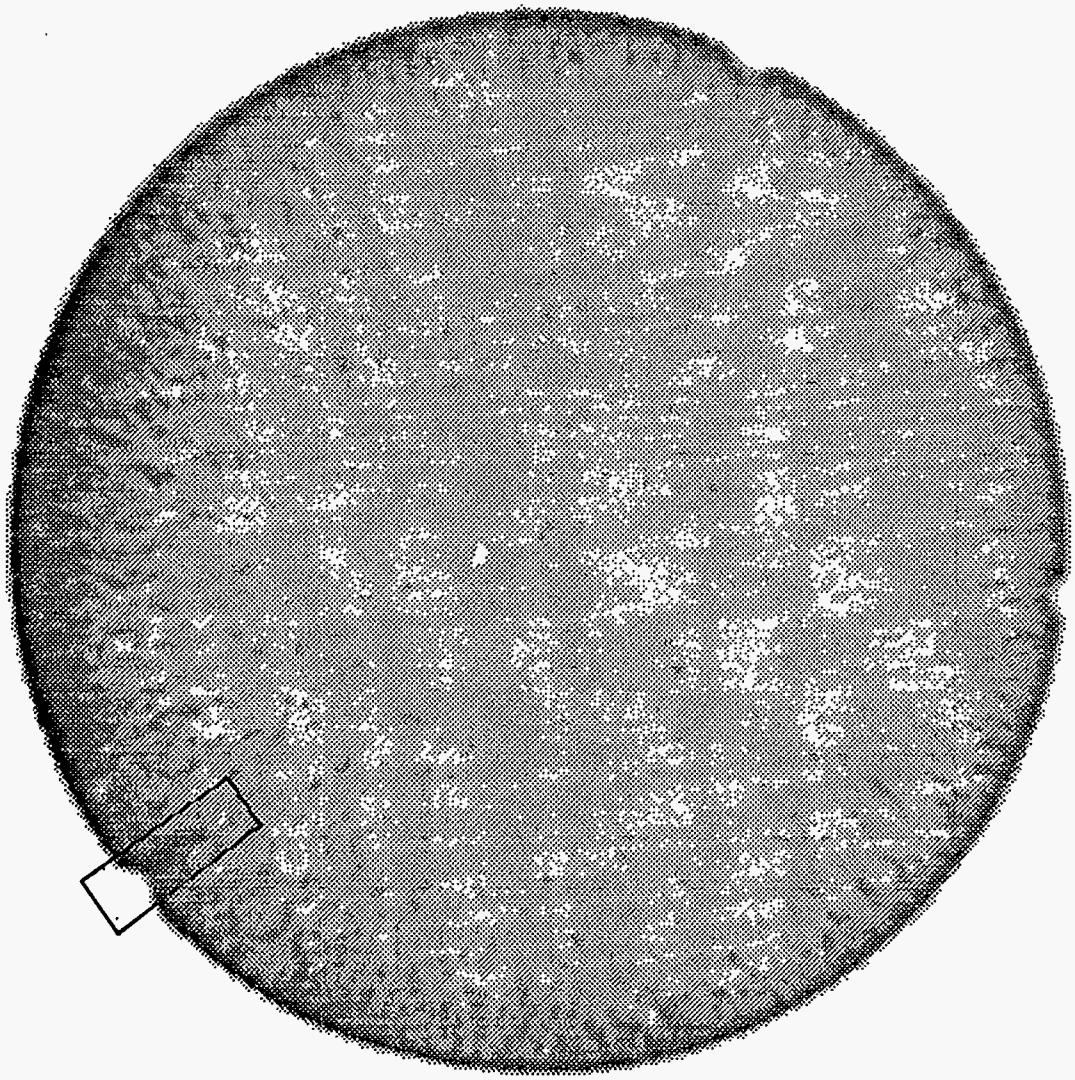

Figure 9
Core I8 Scan 529

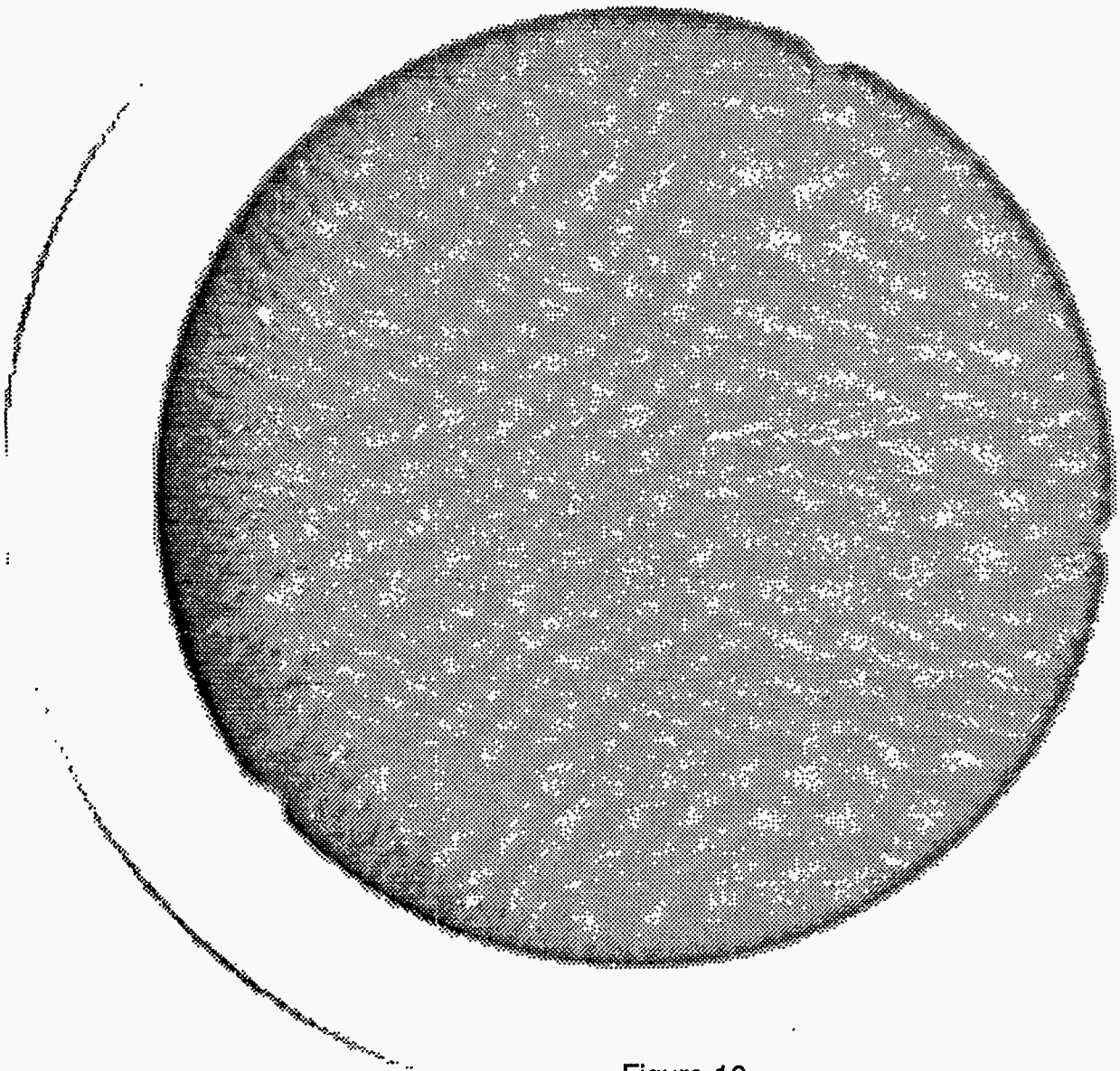

Figure 10
Core I8 Scan 530

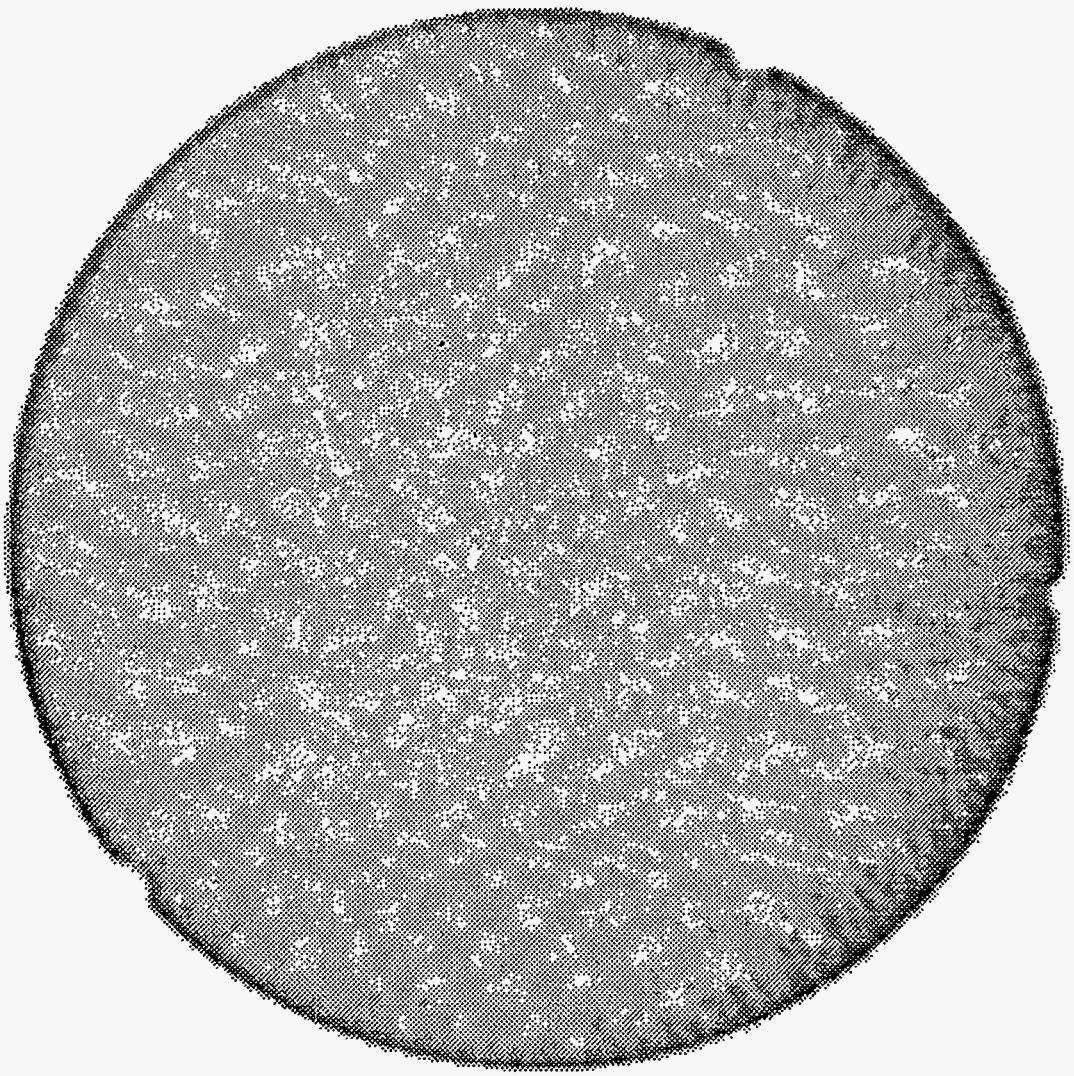

Figure 11
Core I8 Scan 532

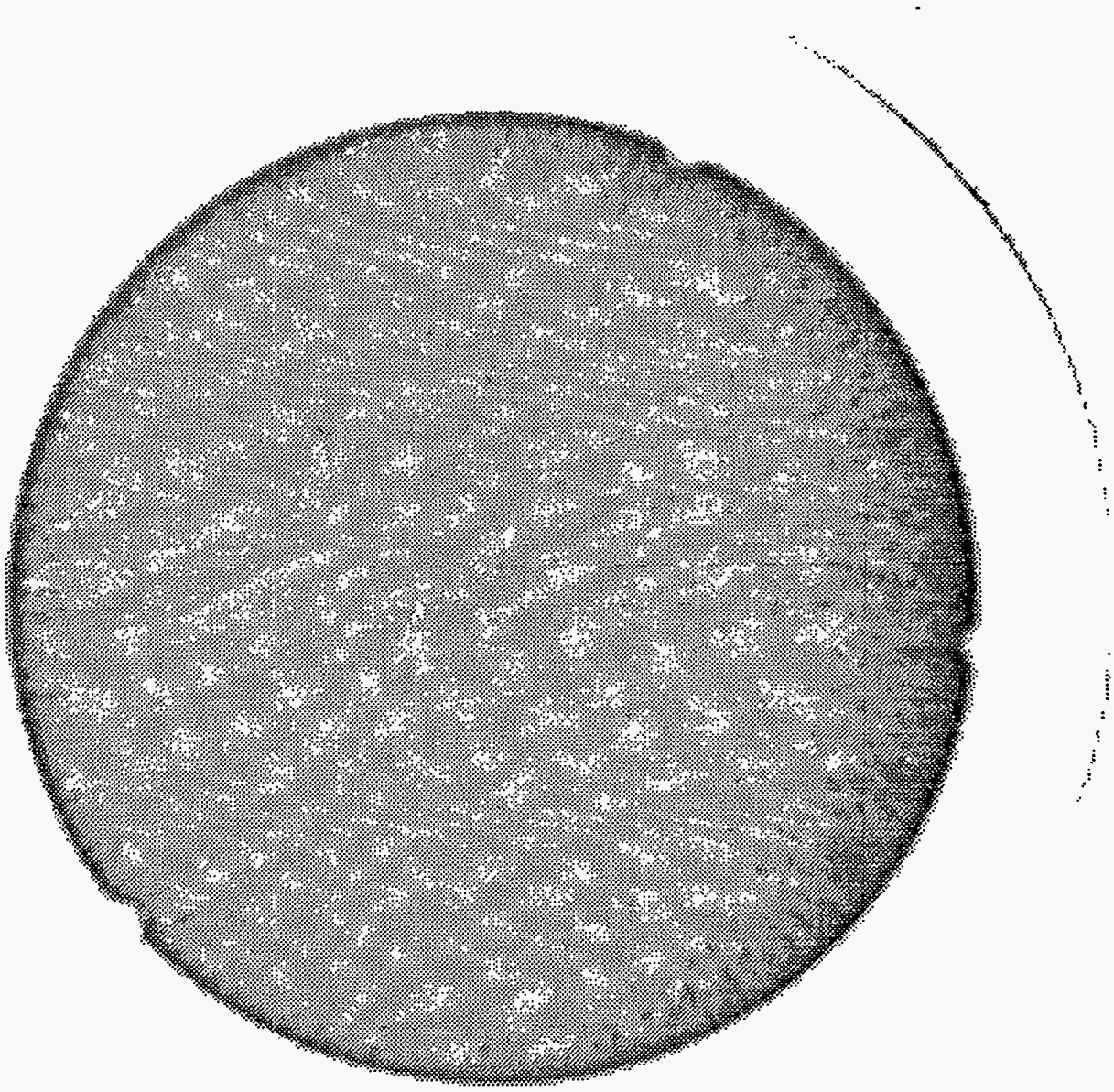

Figure 12
Core I8 Scan 533

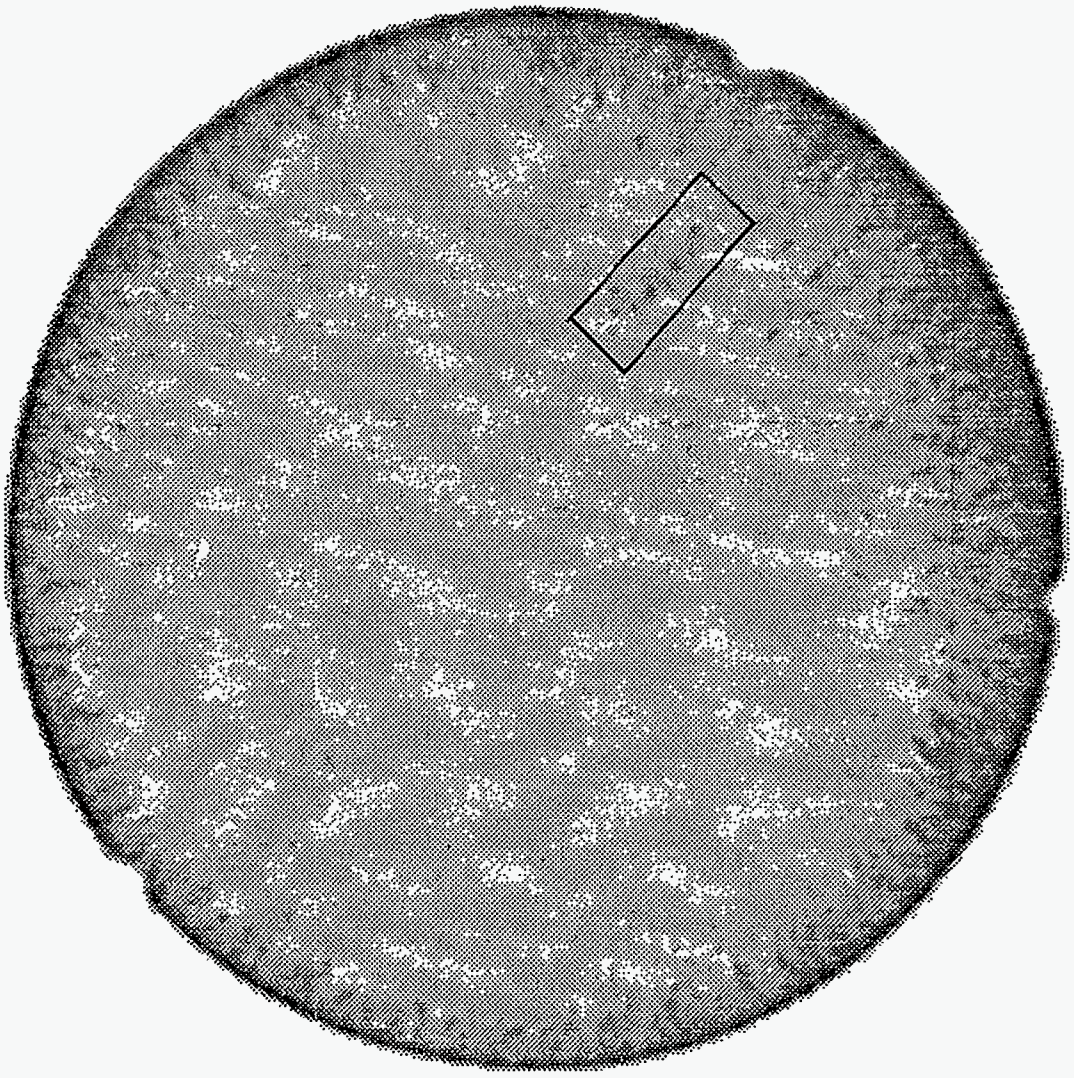

Figure 13
Core I8 Scan 534

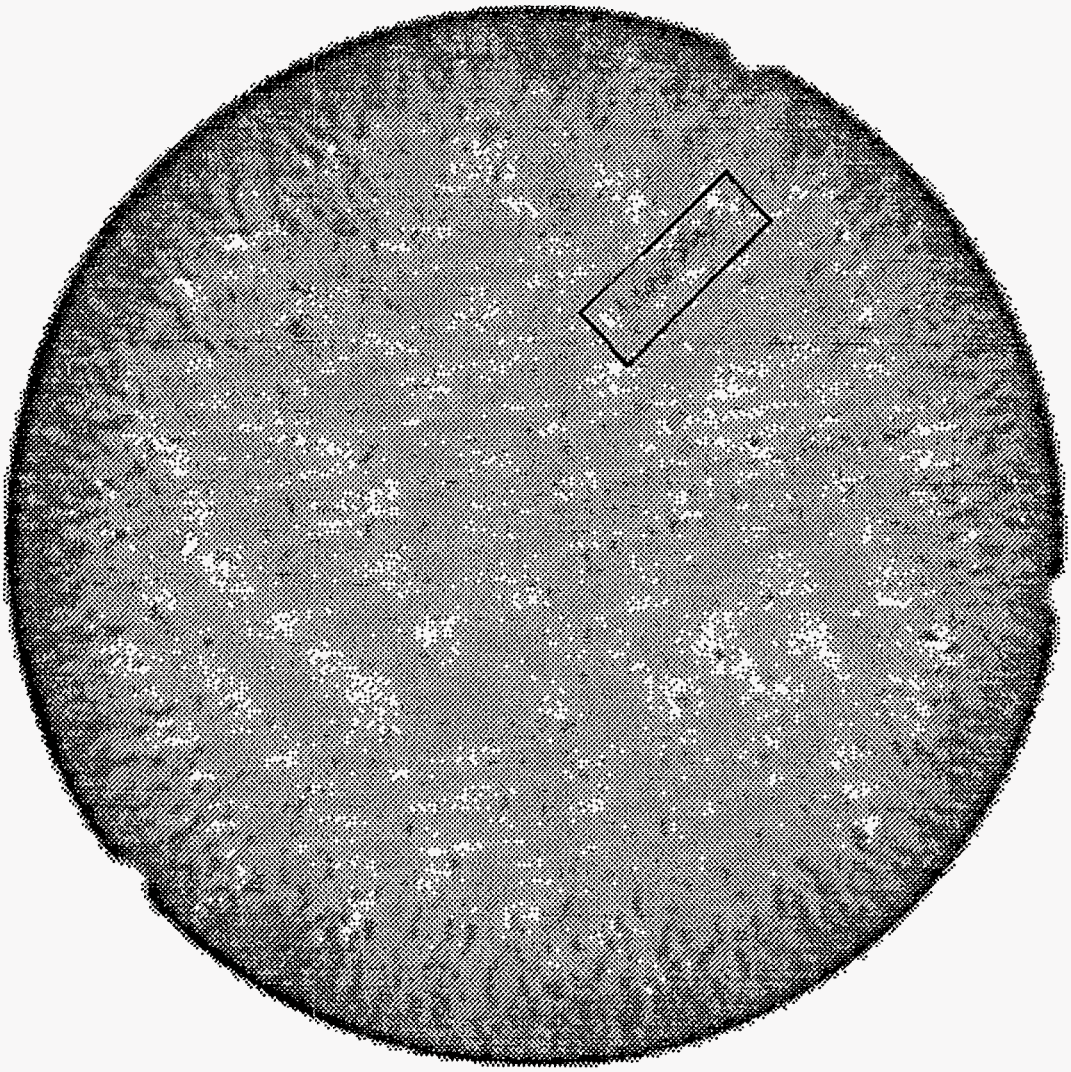

Figure 14
Core I8 Scan 535

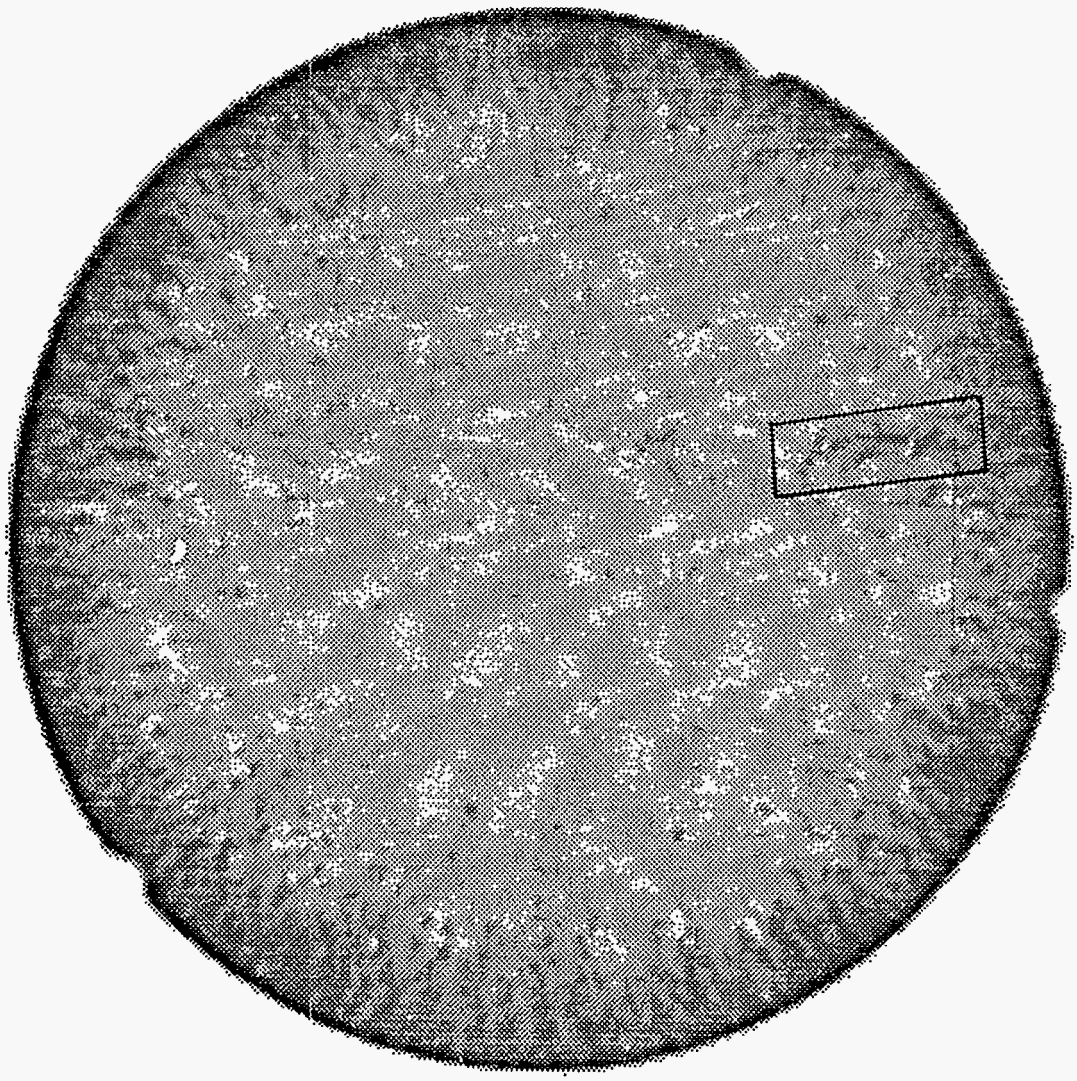

Figure 15
Core I8 Scan 536

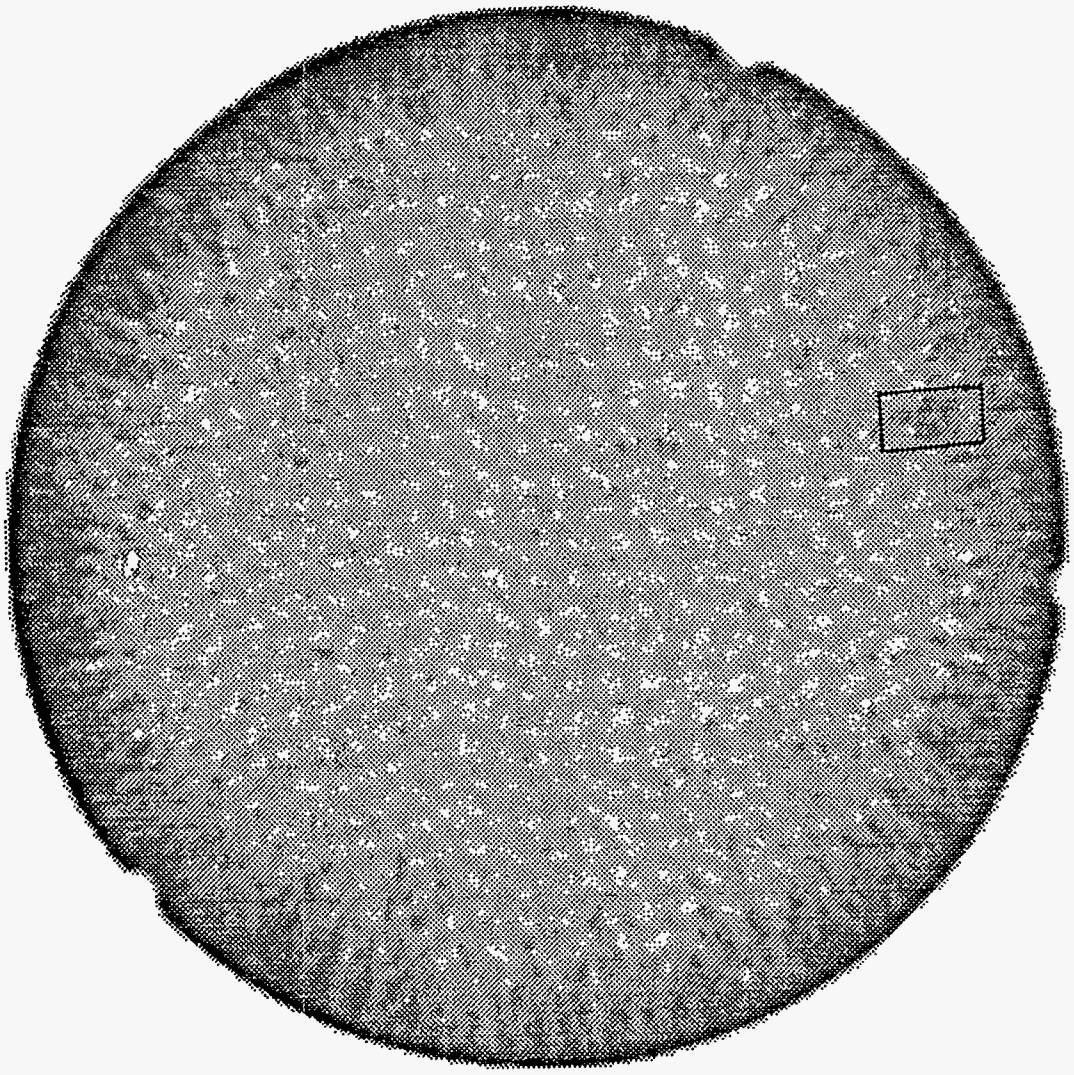

Figure 16
Core I8 Scan 537

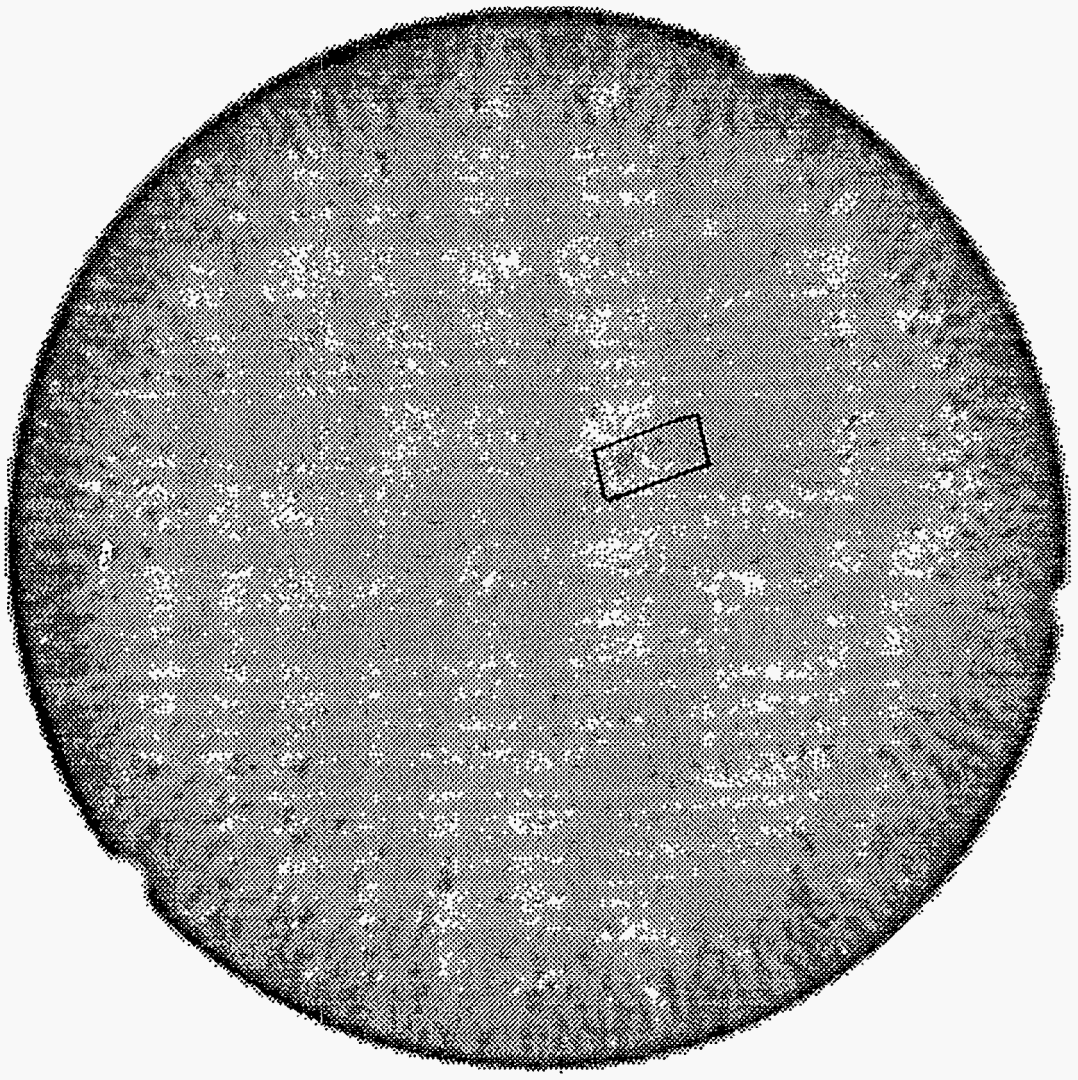

Figure 17
Core I8 Scan 538

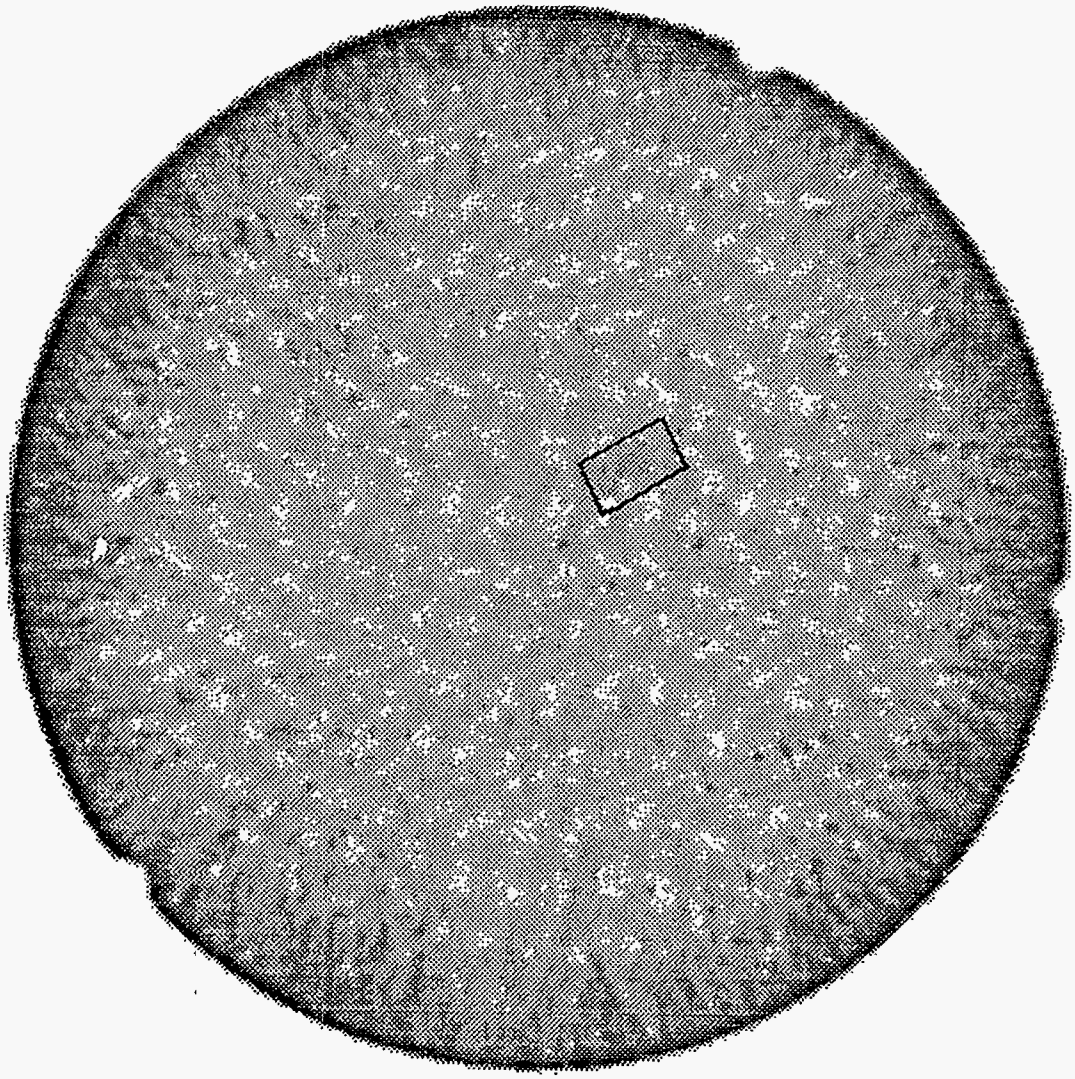

Figure 18
Core I8 Scan 539

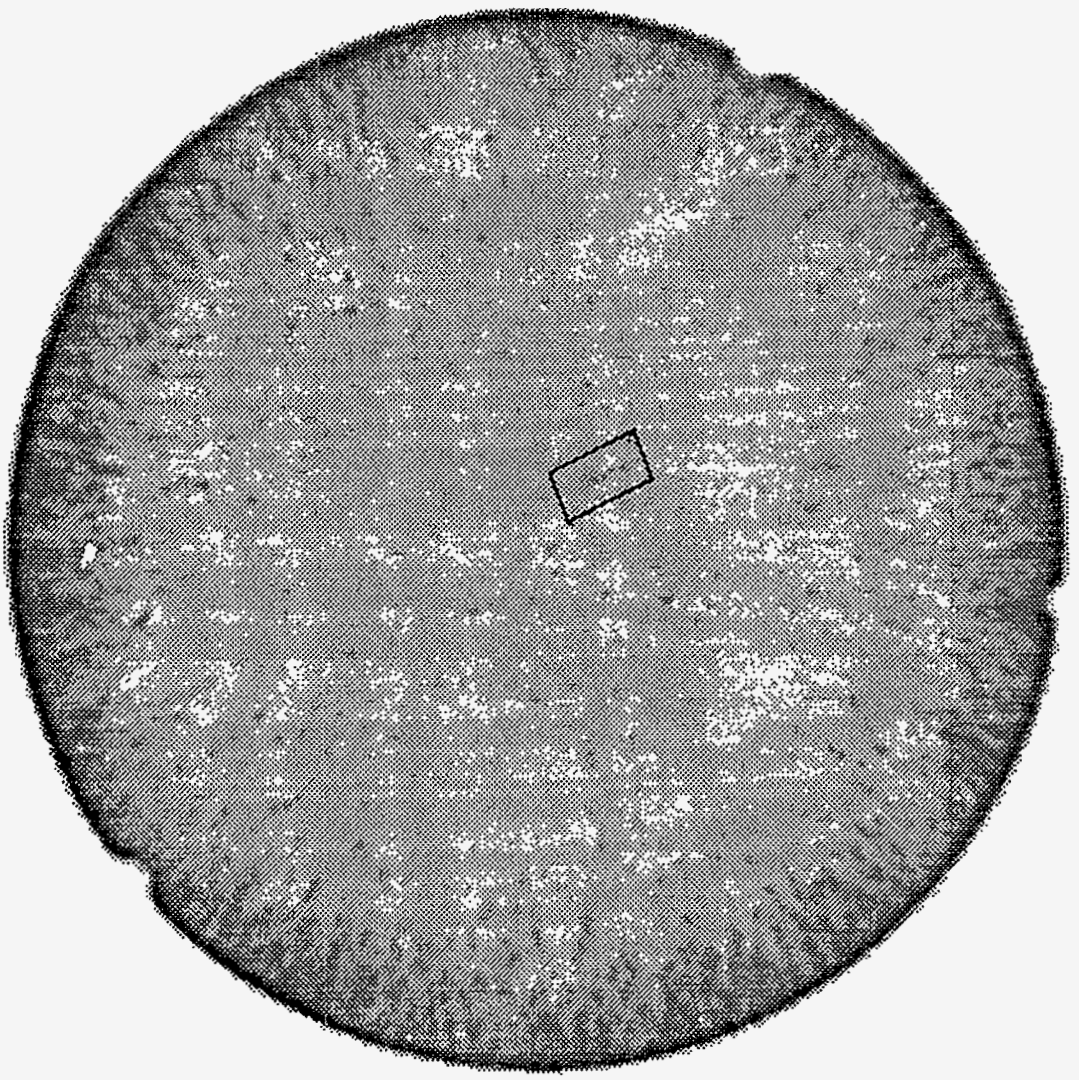

Figure 19
Core I8 Scan 540

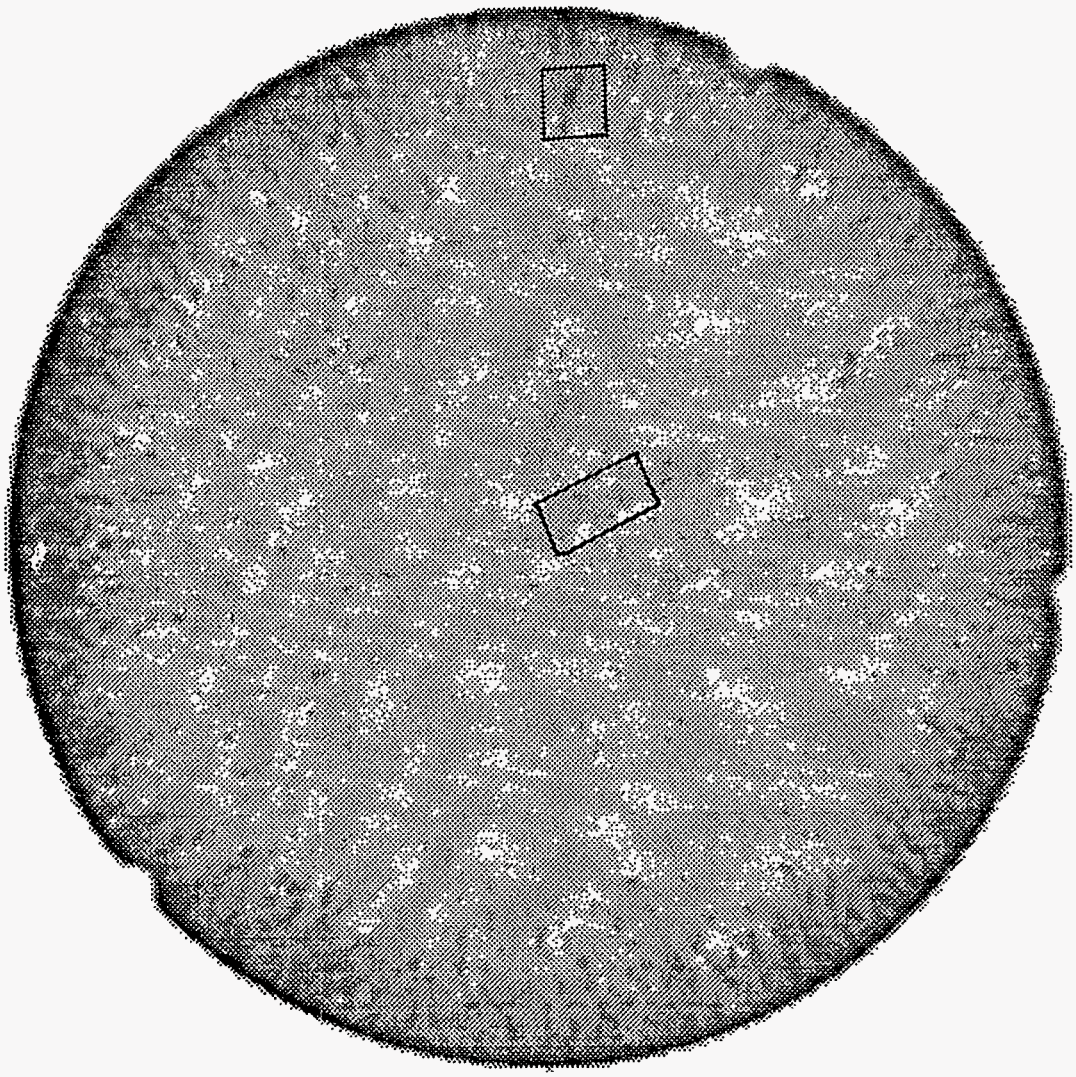

Figure 20
Core I8 Scan 541

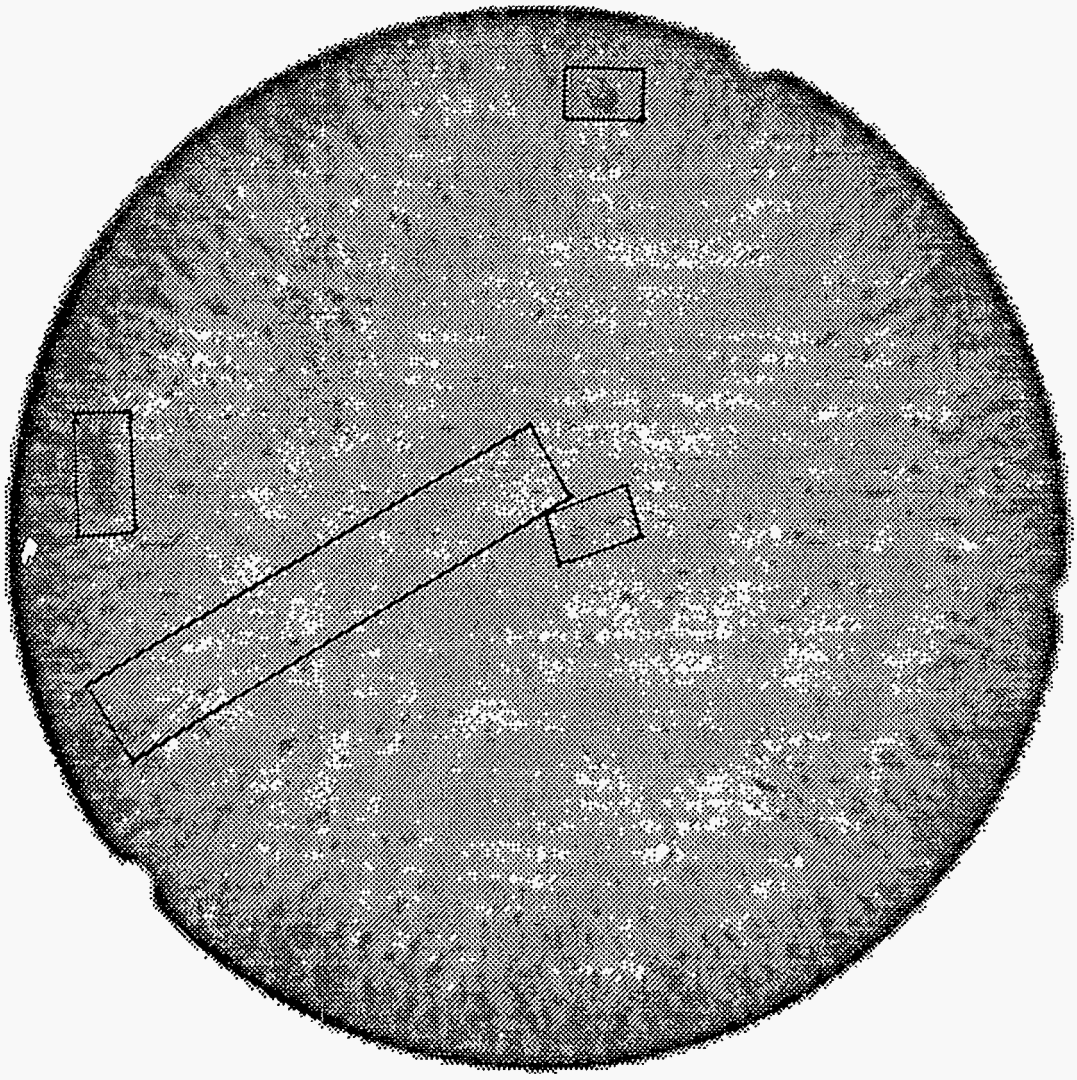

Figure 21
Core I8 Scan 543

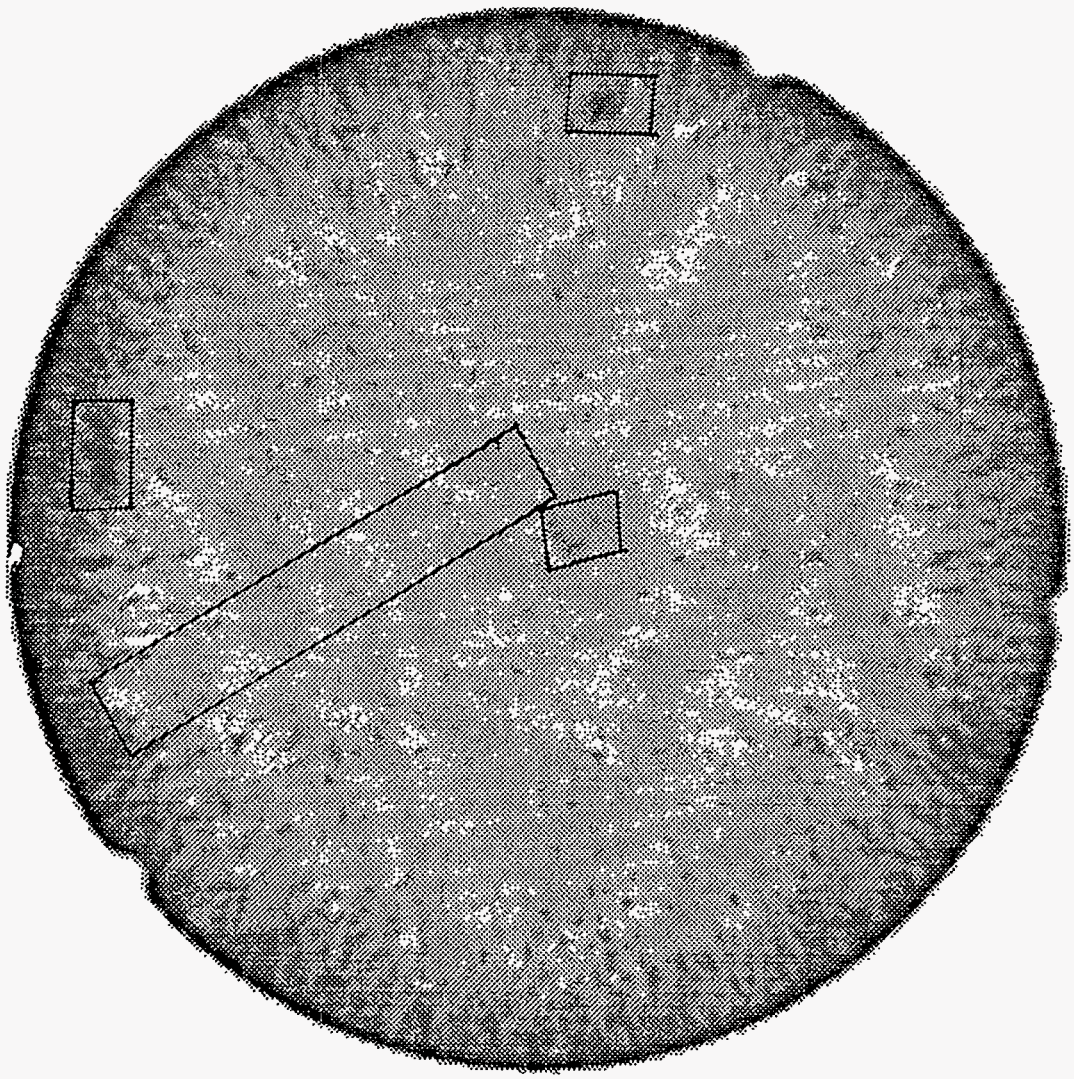

Figure 22
Core I8 Scan 544

### 4.3.4 Image Analysis

#### 4.3.4.1 Fourier Transform Spectroscopy

For obvious reasons, the Fourier transform is extensively used in most forms of magnetic resonance spectroscopy as a fast and convenient way of obtaining spectra from signals recorded in the time domain. However, this approach is less than ideal when instruemental shortcomings or time considerations compel one to acquire distorted or incomplete signals . In such cases the desired spectrum cannot be obtained simply by taking the Fourier transform of the data. If one wanted a spectrum of narrow lines from a truncated free induction decay, Fourier transformation would give either lines broadened by apodization or distorted by "sinc wiggles". Similarly, it is difficult to obtain a spectrum with lines of natural width from data recorded in an inhomogeneous field.

Most of the spectral analysis data that we obtain for our on-going research is through laboratory experiments. For such an ideal environment, perhaps the Fourier transform might be a reasonable choice . But assuming that everything possible has been done to optimize the quality of the detected signal, the only solution to the above mentioned problems is to employ a data processing method that takes into account the instruemental distortions and the fact that the part of the signal might be missing. Or we should always validate the Fourier transform spectrum by correlating it with the spectrums obtained from alternative data processing methods. Some of these alternative methods -- their advantages and disadvantages -- are discussed briefly in the following section.

#### 4.3.4.2 Least Square Method

Several examples of least squares analyses of the discrete Fourier transform NMR spectrum have appeared in the literature. In 1988 Abildgaard *et al* concluded that a detailed and reliable quantitative desription of Fourier transform NMR spectra can be obtained by employing least squares (LSQ) curve fit to the data. This is true even in the case of non-ideal spectra, i.e. spectra distorted by aliasing, truncation errors, widely different signal intensities and relaxation rates, non-linear phase distortions, and partly overlapping signals. The procedure they desribed allows the maximum possible information to be retrieved from the experimental data and in the case of a truncated FID it provides more spectral information than can be obtained by Fourier transformation alone.

The only serious drawback of the LSQ estimator is that a set of reasonable initial values of the spectral parameters is required. In the case of complicated spectra with many overlapping resonances, this requirement cannot be fulfilled.

#### 4.3.4.3 Linear Prediction Estimator

The LSQ method as appeared in the literature was applied in the frequency domain. The linear prediction method, on the other hand, is usually applied in the time domain.

The basic aim of the linear prediction approach is to estimate the frequencies, vj , and relaxation rates, R2j directly from the free induction decay, under the assumption of f(t) calculated. The intensities, Ij , and phases, $\varnothing_j$, are finally determined by a linear LSQ calculation.

When a free induction decay given by f(t) is sampled at regularly spaced intervals, the resulting discrete function

$$F_k = F(\Delta t.k) = \sum_{j=1}^{p} I_j \exp(i\varnothing_j)\exp((i2\pi v_j - R_{2j})\Delta t.k) + w_k$$

has the following property

$$(F_k - w_k) = \sum_{m=1}^{p} b_m (F_{k+m} - w_{k+m})$$

Here bm is the m'th backward prediction coefficient, and wk is the noise contribution connected with the measured value Fk. If the bm's are known, the frequencies, vj , and the relaxation rates R2j, can be calculated from the p complex roots, cj , of the characteristic polynomial

$$P(z) = z^p - \sum_{m=1}^{p} b_m z^{p-m}$$

The biggest advantage of Linear Prediction method is that no pre-knowledge of the spectral parameters is necessary and therefore this method can be used as an efficient sub-optimum alternative in cases where an LSQ calculation is not feasible.

4.3.4.4 Maximum Entropy Method

Of the alternative data processing methods so far applied to magnetic resonance, that which has generated most debate is the maximum entropy method in the form proposed by Gull and Daniell(2). In principle this method is supposed of finding the spectrum, F(w), which both maximizes a suitably defined entropy, *S*, and is consistent with the observed time-domain data, *dt*, . The latter constraint is usually expressed in terms of a $\chi^2$ parameter of the form

$$\chi^2 = \sum_t | d_t - D_t | / \sigma_t^2$$

where Dt is the time-domain signal predicted by F(w), $\sigma_t$ is the statistical uncertainty in *dt*, and the summation runs over the available time-domain data points. The spectrum is judged to be consistent with the data when $\chi^2$ has some particular value, usually equal to the number of recorded data points, P. The problem is then to find the spectrum that maximizes $S - \lambda\chi^2$ , where $\lambda$ is a Lagrange multiplier such that $\chi^2$ equals P. Known instruemental distortions can be included in the calculation of Dt from F(w), which may or may not involve Fourier transformation. In this way artifacts due to missing data and instruemental imperfections should appear in F(w).

4.3.4.5 Final Remarks

It is our intent to design and develop an integrated simulator which could analyze the NMR data obtained from laboratory experiments, using different processing methods desribed above. This effort would help us in drawing more confident conclusions regarding our spectrum analysis. Correlating the Fourier spectrum with the spectrums

obtained from other methods would also help in bypassing potential problems, inherent to Fourier transformation method.

4.4 Subtask 4: Mathematical Modeling

4.4.1 Analytical Modeling

4.4 Subtask 4: Mathematical Modeling

4.4.1 - Analytical Modeling

4.4.1.1 Governing Equations

The following differential-integral equation developed by de Swaan[1] is solved to analyze the laboratory[2] imbibition waterflood performance:

$$-u_f \frac{\partial f_{wf}}{\partial x} = \frac{\partial S_{wf}}{\partial t} + \frac{\lambda R_\infty}{\phi_f} \int_0^t e^{-\lambda(t-\tau)} \frac{\partial S_{wf}}{\partial \tau} d\tau \quad \ldots\ldots\ldots\ldots\ldots\ldots (1)$$

(Explanation of symbols and references is at the end of this section)

the initial condition is

$$S_{wf}(x,0) = 0 \quad \ldots\ldots\ldots\ldots\ldots\ldots\ldots\ldots\ldots\ldots\ldots\ldots (2)$$

the boundary conditions is

$$S_{wf}(0,t) = 1.0 \quad \ldots\ldots\ldots\ldots\ldots\ldots\ldots\ldots\ldots\ldots\ldots\ldots (3)$$

The following differential-integral equation is developed for the matrix system similar to that proposed by Davis and Hill[3]:

$$0 = \frac{\partial S_{wm}}{\partial t} - \frac{\lambda R_\infty}{\phi_m} \int_0^t e^{-\lambda(t-\tau)} \frac{\partial S_{wf}}{\partial \tau} d\tau \quad \ldots\ldots\ldots\ldots\ldots\ldots (4)$$

the initial condition is

$$S_{wm}(x,o) = S_{wmirr} \quad \ldots\ldots\ldots\ldots\ldots\ldots\ldots\ldots\ldots\ldots (5)$$

4.4.1.2 Nonlinear Iterative Solution Technique

It is difficult to obtain the solution for the nonlinear differential-integral equation, Equation (1). While an analytical approach is out of question, the numerical method is plagued by numerical instability. de Swaan[1] and Kazemi, et al[2] linearized the integro-differential equation by assuming the water fractional flow in the fracture is equal to the corresponding water saturation in the fracture. Davis and Hill[3] linearized the equation by assuming the water fractional flow equal to the ratio of water saturation and the water-oil viscosity ratio. By means of the linearizations, the authors obtained the analytical solutions.

We attempt to solve the nonlinear integro-differential equation by an iterative semi-analytical technique without the simplifying assumptions made by de Swaan,[1] and the Davis and Hill[3] . The fractional flow gradient in Equation (1) is factored as follows:

$$-u_f\left(\frac{df_{wf}}{dS_{wf}}\right)\frac{\partial S_{wf}}{\partial x} = \frac{\partial S_{wf}}{\partial t} + \frac{\lambda R_\infty}{\phi_f}\int_0^t e^{-\lambda(t-\tau)}\frac{\partial S_{wf}}{\partial \tau}\,d\tau \qquad \ldots\ldots\ldots\ldots (6)$$

For convenience of illustrating the iterative nonlinear solution procedure, the water fractional flow in the fracture and its derivative with respect to the water saturation are expressed as below:

$$f_{wf} = \frac{1}{1 + \frac{k_o \mu_w}{k_w \mu_o}} \qquad \ldots\ldots\ldots\ldots\ldots\ldots\ldots\ldots\ldots\ldots\ldots\ldots\ldots\ldots\ldots\ldots (7)$$

$$k_w = S_w \qquad \ldots\ldots\ldots\ldots\ldots\ldots\ldots\ldots\ldots\ldots\ldots\ldots\ldots\ldots\ldots\ldots (8)$$

$$k_o = 1 - S_w \qquad \ldots\ldots\ldots\ldots\ldots\ldots\ldots\ldots\ldots\ldots\ldots\ldots\ldots\ldots\ldots\ldots (9)$$

$$\frac{df_{wf}}{dS_{wf}} = \frac{M}{[1 + (M-1)S_{wf}]^2} \qquad \ldots\ldots\ldots\ldots\ldots\ldots\ldots\ldots\ldots\ldots\ldots\ldots\ldots\ldots (10)$$

$$M = \frac{\mu_o}{\mu_w} \qquad \ldots\ldots\ldots\ldots\ldots\ldots\ldots\ldots\ldots\ldots\ldots\ldots\ldots\ldots\ldots\ldots (11)$$

For a particular time step the coefficient of the saturation gradient term in Equation (6) is calculated using the saturation at the beginning of the time step and the solution to the equation at a specified location is obtained by Laplace transformation. In Laplace domain, Equation (6) is transformed as

$$-uf'_w \frac{d\widetilde{S_{wf}}}{dx} = s\left(1 + \frac{\alpha}{s+\lambda}\right)\widetilde{S_{wf}} \qquad \ldots\ldots\ldots\ldots\ldots\ldots\ldots\ldots\ldots\ldots\ldots\ldots\ldots\ldots (12)$$

Solving Equation (12) in the Laplace domain with the boundary condition gives,

$$\widetilde{S_{wf}} = e^{-\alpha s}\left(\frac{1}{s}e^{\frac{\alpha\lambda s}{s+\lambda}}\right) \qquad \ldots\ldots\ldots\ldots\ldots\ldots\ldots\ldots\ldots\ldots\ldots\ldots\ldots\ldots (13)$$

The Laplace transform of the saturation is inverted to obtain the real time saturation by using the Stehfest algorithm. For each time step the procedure is iterated using the updated saturation until the saturation difference between iterations converges to within a given tolerance.

Solution to the equation provides a saturation profile in the fracture as a function of time. The saturation history at the outlet is used to calculate the fractional flow of oil and water, thereby, the water cut and oil production rate. Once the saturation in the fracture is calculated, the water saturation in the matrix system can be calculated using Equations (4) and (5).

4.4.1.3 Analysis of Imbibition Waterflood Performances

The nonlinear solution technique is used to analyze the Kazemi et al[2] laboratory imbibition waterflood data. Table 1 lists the laboratory test conditions.

TABLE 1 - A LABORATORY TEST DATA[2]

| | | | |
|---|---|---|---|
| L | = 0.355 ft | $\phi_m$ | = 0.1744 |
| A | = 0.02713 $ft^2$ | $\phi_f$ | = 0.0014 |
| $\mu_o$ | = 1.0 cp | $S_{wcm}$ | = 0.43 |
| $\mu_w$ | = 1.0 cp | $S_{orm}$ | = 0.34 |
| $\lambda$ | = 30, 50, 500 $day^{-1}$ | q | = 0.000787 STB/D |

Figure 1 shows the the comparison of pore volume oil recovery obtained from the laboratory test and from the semi-analytical solution. As shown in this figure, as the value of LAMDA increases, the calculated oil recovery agrees better with the laboratory oil recovery, and a very good match was obtained with the value of LAMDA equal to 120. An adjustment of the value of LAMDA is necessary to match the laboratory data.

Figure 3 shows the effect of mobility ratio on the saturation distribution in the fracture. As the viscosity ratio decreases below one, a sharp shock front appeared to exist in the fracture system. An increase in viscosity ratio results in a large trailing phase production.

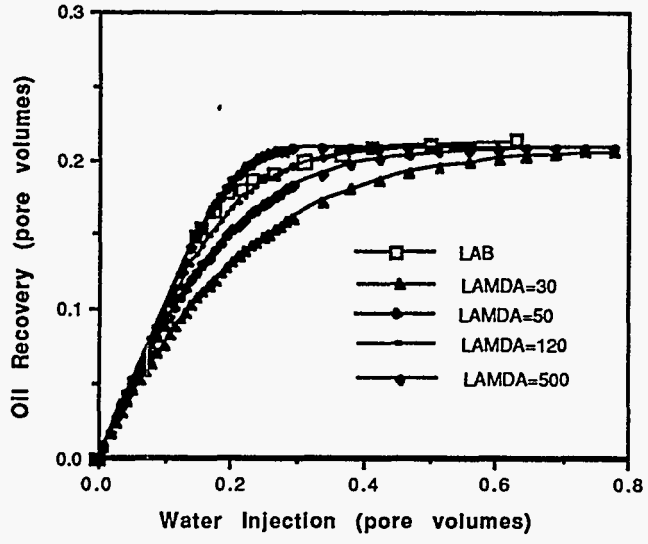


**Fig. 1 - Calculated and laboratory oil recovery performance (M = 1.0, Rate = 0.000787 STB/D)**

Figure 2 shows the calculated water saturation distribution in the fracture at different time steps. For unit viscosity ratio a sharp water front does not appear to exist in the fracture system.

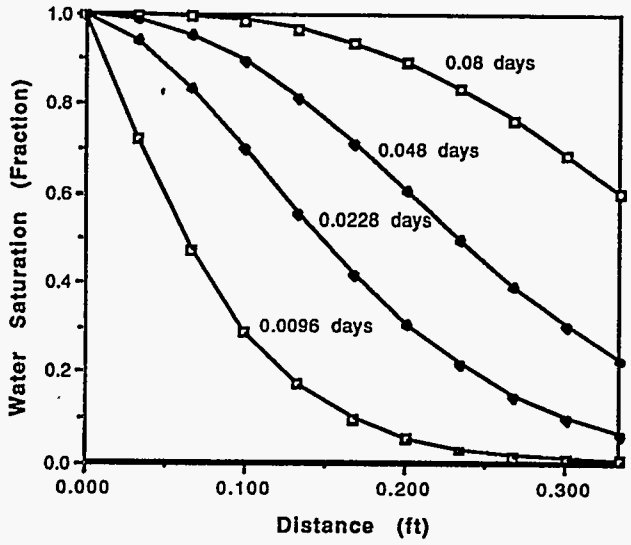


**Fig. 2 - Calculated fracture water saturation profile (M=1.0, Lamda=120, Rate=0.000787 STB/D)**

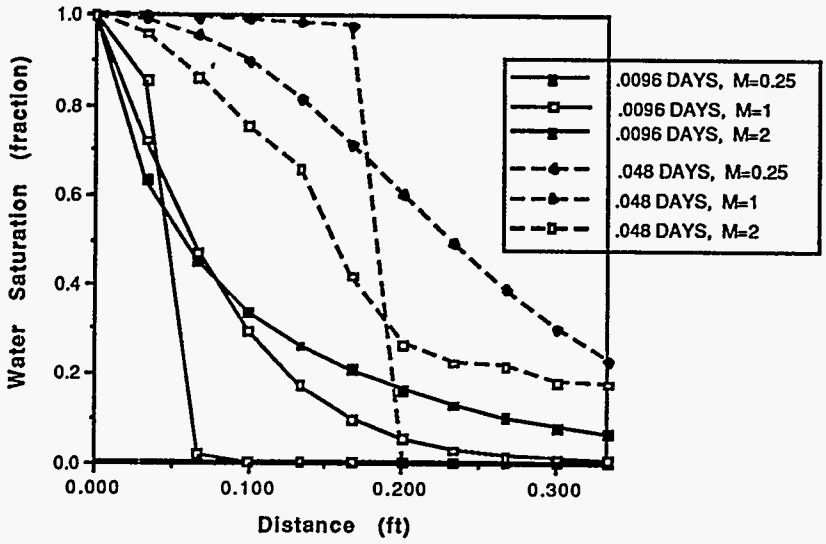


**Fig. 3 - Effect of viscosity ratio on fracture water saturation profiles (Lamda=120, Rate=0.000787 STB/D)**

A hypothetical field case[2] is also analyzed using the semi-analytical model. The conditions of the field hypothetical case are listed in Table 2.

TABLE 2 - A HYPOTHETICAL FIELD CASE DATA[2]

| | | | |
|---|---|---|---|
| L | = 1,000 ft | $\phi_m$ | = 0.16 |
| A | = 1,000 $ft^2$ | $\phi_f$ | = 0.001 |
| $\mu_o$ | = 1.0 cp | $S_{wcm}$ | = 0.25 |
| $\mu_w$ | = 1.0 cp | $S_{orm}$ | = 0.25 |
| $\lambda$ | = 0.01 $day^{-1}$ | q | = 30 STB/D |

Figure 4 shows the oil recovery in pore volumes calculated using the semi-analytical model. Figure 5 shows the water saturation distributions in the fracture at different time steps. Figure 6 shows the water saturation distributions in the matrix system.

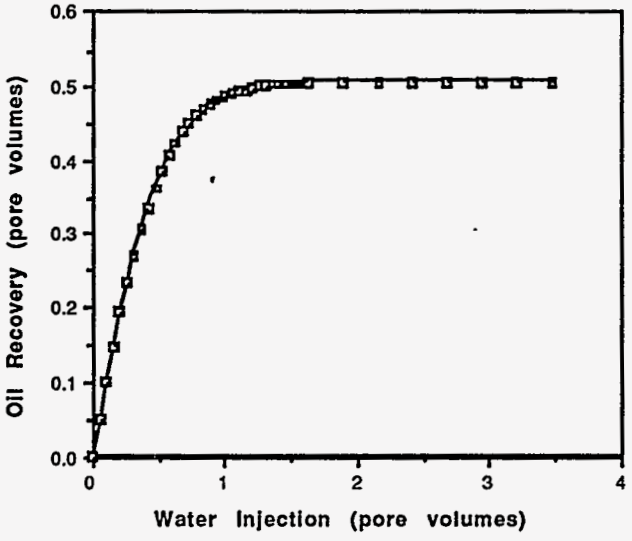


**Fig. 4 - Calculated oil recovery performance (M=1, rate=30 STB/D, Lamda=0.01)**

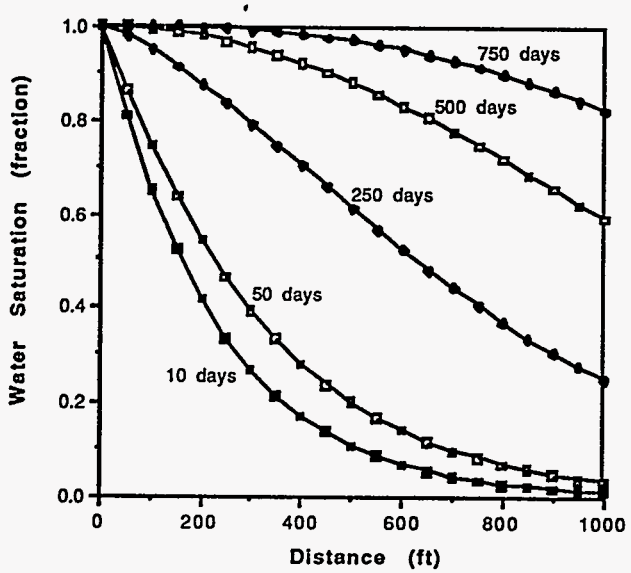


**Fig. 5 - Calculated water saturation profiles (M=1.0, Rate=30 STB/D, Lamda=0.01)**

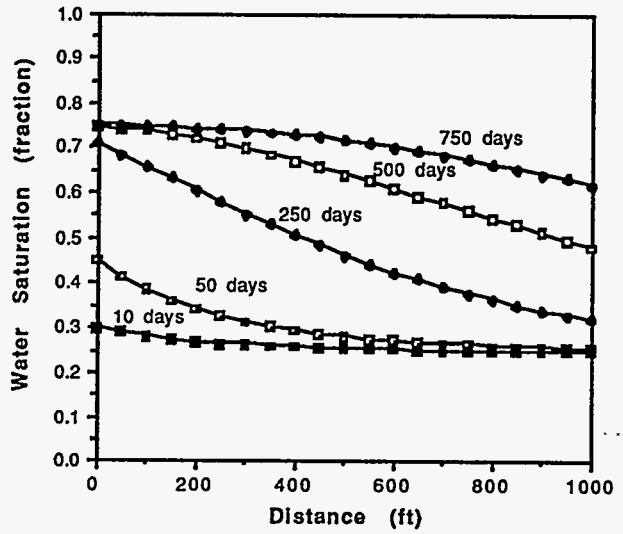


**Fig. 6 - Calculated matrix water saturation profiles (M=1.0, Rate=30 STB/D, Lamda=0.01)**

### 4.4.1.4 Limitations of the Nonlineart Iterative Aproach

The technique has a limited applicable range of viscosity ratio. Results of this study indicated that the viscosity ratio is limited to the range between 0.25 and 2.0. Results of initial sensitivity study also indicated that the results are very sensitive to the variation in

injection rate. Further investigation on the limitations is in order. Because of these limitations, a compositional numerical modelling will be needed to provide reasonable mathematical solutions.

### 4.4.2 Numerical Modeling

The limitations associated with the analytical modeling of $CO_2$-enriched waterflood in a naturally-fractured reservoir necessitate the use of numerical compositional simulation approach. To simulate a naturally-fractured reservoir, the dual-porosity approach is the most widely used in the literature.[2-8] The first compositional simulation using the dual-porosity approach was presented by Peng et al.[8]

The modification of our existing compositional single-porosity simulator for a dual-porosity compositional simulator is completed. Testing, debugging and validation of the model process has begun to test the new developed simulator with hypothetical test cases.

Matrix system equations were added to the single-porosity simulator to incorporate the both fracture and matrix systems as a dual-porosity simulator. Tested the fracture and matrix systems separately with the two sets of rock and fluid properties, the equations for the matrix and fracture fluid transfer are added to the single-porosity system simulator.

An idealization of a naturally fractured porous medium can be represented by a simplifying model as shown in Figure 7. The matrix system and fracture system are superimposed for the naturally fractured porous medium with their average rock and fluid properties.

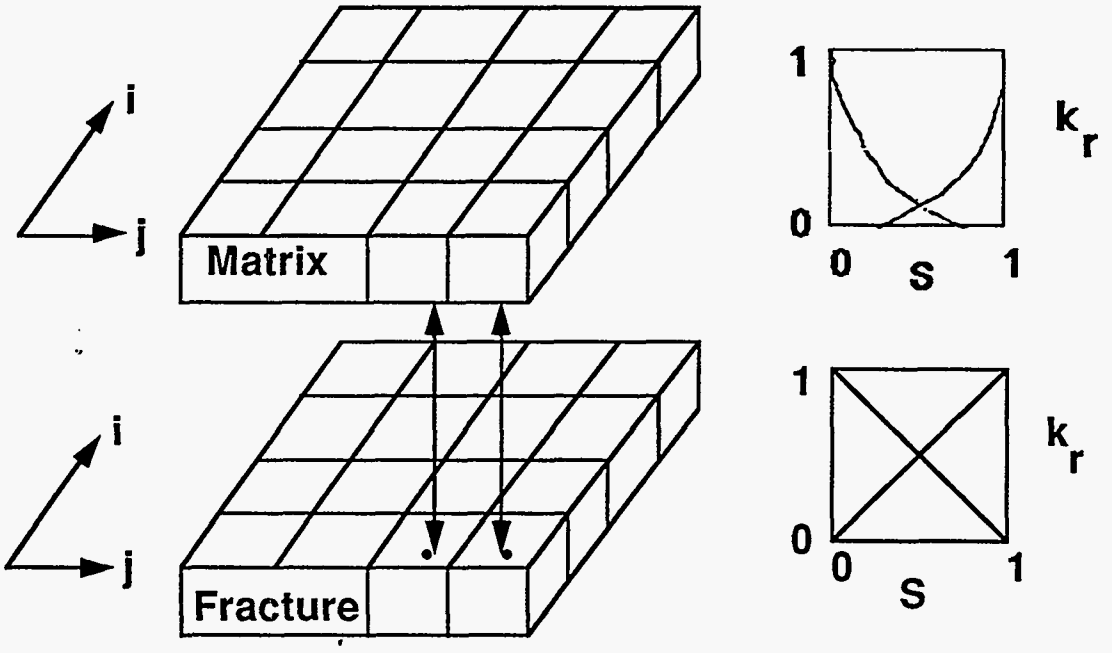


Fig. - 7 An idealized model of naturally fractured porous medium

### 4.4.2.1 Governing Equations for Naturally Fractured Reservoirs

The differential material-balance equations for component 'l' can be written as follows:

for the fracture system:

$$\nabla.\left[\frac{k\,k_{ro}\rho_o}{\mu_o}x_{o,l}(\nabla p_o-\gamma_o\nabla D)+\frac{k\,k_{rg}\rho_g}{\mu_g}y_{g,l}(\nabla p_g-\gamma_g\nabla D)+\frac{k\,k_{rw}\rho_w}{\mu_w}w_{w,l}(\nabla p_w-\gamma_w\nabla D)\right]_f$$
$$+F_s\left[\frac{k_{ma}\,k_{ro}\rho_o}{\mu_o}x_{o,l}(p_{o,ma}-p_{o,f})+\frac{k_{ma}\,k_{rg}\rho_g}{\mu_g}y_{g,l}(p_{g,ma}-p_{g,f})+\frac{k_{ma}\,k_{rw}\rho_w}{\mu_w}w_{w,l}(p_{w,ma}-p_{w,f})\right]$$
$$+\left[x_{o,l}\rho_o q_o+y_g\rho_g q_q+w_{w,l}\rho_w q_w\right]_f$$
$$=\frac{\delta}{\delta t}\left[\phi(x_{o,l}\rho_o S_o+y_{g,l}\rho_g S_g+w_{w,l}\rho_w S_w)\right]_f \quad \ldots\ldots\ldots\ldots\ldots\ldots\ldots\ldots (14)$$

the second term represents the matrix and fracture fluid transfer.

For the matrix system:

$$-F_s\left[\frac{k_{ma}\,k_{ro}\rho_o}{\mu_o}x_{o,l}(p_{o,ma}-p_{o,f})+\frac{k_{ma}\,k_{rg}\rho_g}{\mu_g}y_{g,l}(p_{g,ma}-p_{g,f})+\frac{k_{ma}\,k_{rw}\rho_w}{\mu_w}w_{w,l}(p_{w,ma}-p_{w,f})\right]$$
$$=\frac{\delta}{\delta t}\left[\phi(x_{o,l}\rho_o S_o+y_{g,l}\rho_g S_g+w_{w,l}\rho_w S_w)\right]_{ma} \quad \ldots\ldots\ldots\ldots\ldots\ldots\ldots\ldots (15)$$

### 4.4.2.2 Finite Difference Solutions

The following mass-balance finite difference equations for each phase can be developed for the fracture and matrix systems after applying the following constraints to the Eqs. (14) and (15).

$$\sum_{l=1}^{n_{c+1}} x_{o,l}=1 \qquad \sum_{l=1}^{n_{c+1}} y_{g,l}=1 \qquad \sum_{l=1}^{n_{c+1}} w_{w,l}=1 \quad \ldots\ldots\ldots\ldots\ldots\ldots (16)$$

For the fracture system (Flow is assumed left to right in 'X' direction) :

$$F(p,X,\text{in } i)=0.00633T_{i-\frac{1}{2}}\frac{k_{rp_{i-1}}}{\mu_{p_{i-1}}}\rho_{p_{i-1}}\left[p_{p,f_{i-1}}-p_{p,f_i}-\gamma_p\Delta D\right]\Delta X_i\Delta Y_i\Delta Z_i \quad \ldots\ldots\ldots (17)$$

$$F(p,X,\text{out } i)=0.00633T_{i+\frac{1}{2}}\frac{k_{rp_i}}{\mu_{p_i}}\rho_{p_i}\left[p_{p,f_i}-p_{p,f_{i+1}}-\gamma_p\Delta D\right]\Delta X_i\Delta Y_i\Delta Z_i \quad \ldots\ldots\ldots (18)$$

Then for the fracture grid block (i,j,k), the total mass balance between the neighboring fracture grid blocks and fracture/matrix fluid transfer can be expressed as :

Flow in - Flow out = Accumulation

$$\text{L.H.S} = \begin{array}{l} F(p,X,\text{in i}) - F(p,X,\text{out i}) \\ F(p,Y,\text{in i}) - F(p,Y,\text{out i}) \\ F(p,Z,\text{in i}) - F(p,Z,\text{out i}) \\ + F_s k_{ma} V_b \dfrac{k_{rp_{usmaf}}}{\mu_{p_{usmaf}}} \rho_{p_{usmaf}} \left[ p_{p_{ma,i}} - p_{p_{f,i}} \right] \end{array} \quad \ldots\ldots\ldots\ldots\ldots\ldots (19)$$

$$\text{Accumulation} = \frac{V_b}{\Delta t}\left[\phi(\rho_o S_o + \rho_g S_g + \rho_w S_w)^{n+1} - \phi(\rho_o S_o + \rho_g S_g + \rho_w S_w)^{n}\right]_f \quad \ldots \quad (20)$$

The transmissibility terms in Eqs. (17) and (18) are defined as :

$$T_{i-\frac{1}{2}} = 0.00632827 \frac{1}{\Delta X_i}\left[\frac{1}{\frac{\Delta X_{i-1}}{k_{i-1}} + \frac{\Delta X_i}{k_i}}\right] \quad \ldots\ldots\ldots\ldots\ldots\ldots\ldots\ldots (21)$$

$$T_{i+\frac{1}{2}} = 0.00632827 \frac{1}{\Delta X_i}\left[\frac{1}{\frac{\Delta X_i}{k_i} + \frac{\Delta X_{i+1}}{k_{i+1}}}\right] \quad \ldots\ldots\ldots\ldots\ldots\ldots\ldots\ldots (22)$$

For the matrix system:

$$F(p,X,ma) = - F_s k_{ma} V_b \frac{k_{rp_{usmaf}}}{\mu_{p_{usmaf}}} \rho_{p_{usmaf}} \left[ p_{p_{ma,i}} - p_{p_{f,i}} \right] \quad \ldots\ldots\ldots\ldots\ldots\ldots (23)$$

$$\text{Accumulation} = \frac{V_b}{\Delta t}\left[\phi(\rho_o S_o + \rho_g S_g + \rho_w S_w)^{n+1} - \phi(\rho_o S_o + \rho_g S_g + \rho_w S_w)^{n}\right]_{ma} \quad . \quad (24)$$

Symmetric flow coefficients for oil phase can be defined as follows:

$$a_{oE} = T_{i+\frac{1}{2}}\left(\frac{k_{ro_i}\rho_{o_i}}{\mu_{o_i}}\right)^n \qquad a_{oS} = T_{j-\frac{1}{2}}\left(\frac{k_{ro_{j-1}}\rho_{o_{j-1}}}{\mu_{o_{j-1}}}\right)^n \qquad a_{oW} = T_{i-\frac{1}{2}}\left(\frac{k_{ro_{i-1}}\rho_{o_{i-1}}}{\mu_{o_{i-1}}}\right)^n$$

$$a_{oN} = T_{j+\frac{1}{2}}\left(\frac{k_{ro_j}\rho_{o_j}}{\mu_{o_j}}\right)^n \qquad a_{oB} = T_{k-\frac{1}{2}}\left(\frac{k_{ro_{k-1}}\rho_{o_{k-1}}}{\mu_{o_{k-1}}}\right)^n \qquad a_{oT} = T_{k+\frac{1}{2}}\left(\frac{k_{ro_k}\rho_{o_k}}{\mu_{o_k}}\right)^n \quad (25)$$

Similarly, symmetric flow coefficients for gas and water are defined. The coefficients for matrix/fracture fluid transfer are defined as follows:

for oil :

$$a_{to} = F_s k_{ma} V_b \left(\frac{k_{ro_i}\rho_{o_i}}{\mu_{o_i}}\right)_{usmaf} \quad \ldots\ldots\ldots\ldots\ldots\ldots\ldots\ldots\ldots\ldots (26)$$

for water :

$$a_{tw}=F_s k_{ma} V_b \left(\frac{k'_{rw_i}\rho_{w_i}}{\mu_{w_i}}\right)_{usmaf} \quad \ldots\ldots\ldots\ldots\ldots\ldots\ldots\ldots\ldots\ldots\ldots\ldots (27)$$

for gas :

$$a_{tg}=F_s k_{ma} V_b \left(\frac{k_{rg_i}\rho_{g_i}}{\mu_{g_i}}\right)_{usmaf} \quad \ldots\ldots\ldots\ldots\ldots\ldots\ldots\ldots\ldots\ldots\ldots\ldots (28)$$

where subscript 'usmaf' represents as upstream matrix or fracture.

4.4.2.3 The Jacobian Matrix Formulation with Residuals 'r'

The residual '$r_{i,j,k}$' at each iteration level can be defined as :

$$r^v_{i,j,k} = \left[\text{Flow in}_{i,j,k} - \text{Flow out}\right]^v - \text{Accumulation}^v_{i,j,k} \quad \ldots\ldots\ldots\ldots\ldots\ldots (29)$$

for fracture system:

$$\begin{aligned}
r^v_{i,j,k} = {} & a_{oW}\left[p^{n+1}_{of_{i-1}} - p^{n+1}_{of_i} - \gamma^n_o \Delta D\right] - a_{oE}\left[p^{n+1}_{of_i} - p^{n+1}_{of_{i+1}} - \gamma^n_o \Delta D\right] + a_{oS}\left[p^{n+1}_{of_{j-1}} - p^{n+1}_{of_j} - \gamma^n_o \Delta D\right] \\
& - a_{oN}\left[p^{n+1}_{of_j} - p^{n+1}_{of_{j+1}} - \gamma^n_o \Delta D\right] + a_{oB}\left[p^{n+1}_{of_{k-1}} - p^{n+1}_{of_k} - \gamma^n_o \Delta D\right] - a_{oT}\left[p^{n+1}_{of_k} - p^{n+1}_{of_{k+1}} - \gamma^n_o \Delta D\right] \\
& + a_{gW}\left[p^{n+1}_{gf_{i-1}} - p^{n+1}_{gf_i} - \gamma^n_g \Delta D\right] - a_{gE}\left[p^{n+1}_{gf_{j-1}} - p^{n+1}_{gf_j} - \gamma^n_g \Delta D\right] + a_{gS}\left[p^{n+1}_{gf_{j-1}} - p^{n+1}_{gf_j} - \gamma^n_g \Delta D\right] \\
& - a_{gN}\left[p^{n+1}_{gf_j} - p^{n+1}_{gf_{j+1}} - \gamma^n_g \Delta D\right] + a_{gB}\left[p^{n+1}_{gf_{k-1}} - p^{n+1}_{gf_k} - \gamma^n_g \Delta D\right] - a_{gT}\left[p^{n+1}_{gf_k} - p^{n+1}_{gf_{k+1}} - \gamma^n_g \Delta D\right] \\
& + a_{wW}\left[p^{n+1}_{wf_{i-1}} - p^{n+1}_{wf_i} - \gamma^n_w \Delta D\right] - a_{wE}\left[p^{n+1}_{wf_i} - p^{n+1}_{wf_{i+1}} - \gamma^n_w \Delta D\right] + a_{wS}\left[p^{n+1}_{wf_{j-1}} - p^{n+1}_{wf_j} - \gamma^n_w \Delta D\right] \\
& - a_{wN}\left[p^{n+1}_{wf_j} - p^{n+1}_{wf_{j+1}} - \gamma^n_w \Delta D\right] + a_{wB}\left[p^{n+1}_{wf_{k-1}} - p^{n+1}_{wf_k} - \gamma^n_w \Delta D\right] + a_{wT}\left[p^{n+1}_{wf_k} - p^{n+1}_{wf_{k+1}} - \gamma^n_w \Delta D\right] \\
& - \frac{V_b}{\Delta t}\left[\phi(\rho_o S_o + \rho_g S_g + \rho_w S_w)^{n+1} - \phi(\rho_o S_o + \rho_g S_g + \rho_w S_w)^n\right] \\
& + a_{to}\left(p_{o,ma_i} - p_{o,f_i}\right) + a_{tg}\left(p_{g,ma_i} - p_{g,f_i}\right) + a_{tw}\left(p_{w,ma_i} - p_{w,f_i}\right) \quad \ldots\ldots\ldots\ldots\ldots\ldots (30)
\end{aligned}$$

For matrix system :

$$r^v_{i,j,k_{ma}} = -a_{to}\left[p^{n+1}_{oma_i} - p^{n+1}_{of_i}\right] - a_{tg}\left[p^{n+1}_{gma_i} - p^{n+1}_{gf_i}\right] - a_{tw}\left[p^{n+1}_{wma_i} - p^{n+1}_{wf_i}\right] \quad \ldots\ldots\ldots\ldots (31)$$

In order to construct a Jacobian matrix, presented in Fig. 8, the pressure difference between the two time level is determined by differentiating the above residual equations for the fracture and matrix systems with respect to each grid block after converting the pressures of water and gas to the oil pressure using the appropriate capillary pressure values.

$$(p_g - p_o) = P_{cog}, \qquad (p_o - p_w) = P_{cow} \quad \ldots\ldots\ldots\ldots\ldots\ldots\ldots\ldots\ldots\ldots (32)$$

$$A^v(p_o^{v+1} - p_o^v) = r^v, \qquad A^v = \frac{-r^v}{dp} \quad \ldots\ldots\ldots\ldots\ldots\ldots\ldots\ldots\ldots\ldots (33)$$

The coefficients of Jacobian Matrix for fracture and matrix systems are defined as follows:

for fracture system:

$$\frac{\delta r^{v}_{f_{ijk}}}{\delta p_{o,f_{i-1}}} = a^{n}_{oW} + a^{n}_{gW} + a^{n}_{wW} = C \quad \ldots\ldots (34)$$

$$\frac{\delta r^{v}_{f_{ijk}}}{\delta p_{o,f_{j-1}}} = a^{n}_{oS} + a^{n}_{gS} + a^{n}_{wS} = B \quad \ldots\ldots (35)$$

$$\frac{\delta r^{v}_{f_{ijk}}}{\delta p_{o,f_{k-1}}} = a^{n}_{oB} + a^{n}_{gB} + a^{n}_{wB} = E \quad \ldots\ldots (36)$$

$$\begin{aligned}\frac{\partial r^{v}_{f_{ijk}}}{dp_{o,f_{ijk}}} = & -a^{n}_{oW} - a^{n}_{gW} - a^{n}_{wW} - a^{n}_{oS} - a^{n}_{gS} - a^{n}_{wS} - a^{n}_{oB} - a^{n}_{gB} - a^{n}_{wB} \\ & - a^{n}_{oE} - a^{n}_{gE} - a^{n}_{wE} - a^{n}_{oN} - a^{n}_{gN} - a^{n}_{wN} - a^{n}_{oT} - a^{n}_{gT} - a^{n}_{wT} \\ & - \frac{V_b}{\Delta t}\frac{\delta}{\delta p_{of_{ijk}}}\left[\phi(\rho_o S_o + \rho_g S_g + \rho_w S_w)\right] \\ & + \left(\frac{\delta(q_o \rho_o)}{\delta p_{of_{ijk}}}\right) + \left(\frac{\delta(q_g \rho_g)}{\delta p_{gf_{ijk}}}\right) + \left(\frac{\delta(q_w \rho_w)}{\delta p_{wf_{ijk}}}\right) \\ & = D \text{ (center diagonal term)} \quad \ldots\ldots (37)\end{aligned}$$

$$\frac{\delta r^{v}_{f_{ijk}}}{\delta p_{o,f_{i+1}}} = a^{n}_{oE} + a^{n}_{gE} + a^{n}_{wE} = G \quad \ldots\ldots (38)$$

$$\frac{\delta r^{v}_{f_{ijk}}}{\delta p_{o,f_{j+1}}} = a^{n}_{oN} + a^{n}_{gN} + a^{n}_{wN} = F \quad \ldots\ldots (39)$$

$$\frac{\delta r^{v}_{f_{ijk}}}{\delta p_{o,f_{k+1}}} = a^{n}_{oT} + a^{n}_{gT} + a^{n}_{wT} = A \quad \ldots\ldots (40)$$

$$\frac{\delta r^{v}_{f_{ijk}}}{\delta p_{o,ma_{ijk}}} = a^{n}_{to} + a^{n}_{tg} + a^{n}_{tw} = H \quad \ldots\ldots (41)$$

for matrix system:

$$\frac{\delta r^{v}_{ma_{ijk}}}{\delta p_{o,f_{ijk}}} = a^{n}_{to} + a^{n}_{tg} + a^{n}_{tw} = I \quad \ldots\ldots (42)$$

$$\frac{\delta r^{v}_{ma_{ijk}}}{\delta p_{o,ma_{ijk}}} = - a^{n}_{to} - a^{n}_{tg} - a^{n}_{tw} - \frac{V_b}{\Delta t}\frac{\delta}{\delta p_{o,ma_{ijk}}}\left[\phi(\rho_o S_o + \rho_g S_g + \rho_w S_w)\right] = J \quad \ldots\ldots (43)$$

The subscripts 'f' and 'ma' refers as fracture and matrix system respectively. The coefficient 'a' represents the symmetric flow coefficients in 3-D for 3 phases. The developed Jacobian matrix is solved in determining oil pressure implicitly, and then saturation and composition are determined explicitly.

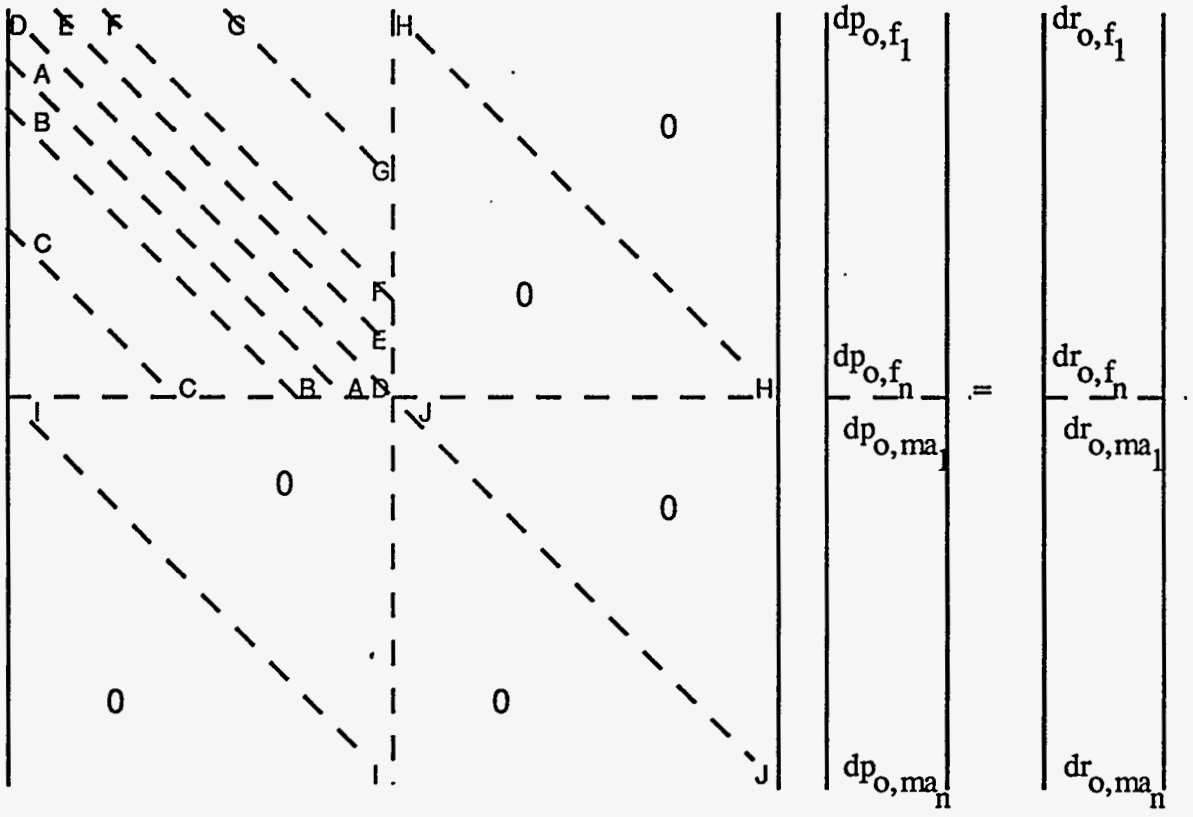


Fig. 8 - The Jacobian matrix equation for oil pressure

4.4.2.4 A Test Case for the Fracture and Matrix System

The following hypothetical test case presented in Table 3 was formulated to run the simulator for the fracture and matrix system independently. All relevant data are taken from SPE Test Case Number 5 [9] except the relative permeability data for the fracture system is taken as $K_{rw}=S_w$. A single block tank type model was used. The pressure profile for each system is presented in Fig. 9.

TABLE 3 - A HYPOTHETICAL FIELD CASE DATA FOR NUMERICAL SIMULATION

Length (X direction) = 500 ft
Length (Y direction) = 500 ft
Length (Z direction) = 20 ft
Initial water saturation= 0.2
Initial gas saturation = 0.0

Matrix System

porosity = 0.3
permeability = 500 md

Fracture System

porosity = 0.05
permeability = 5000 md

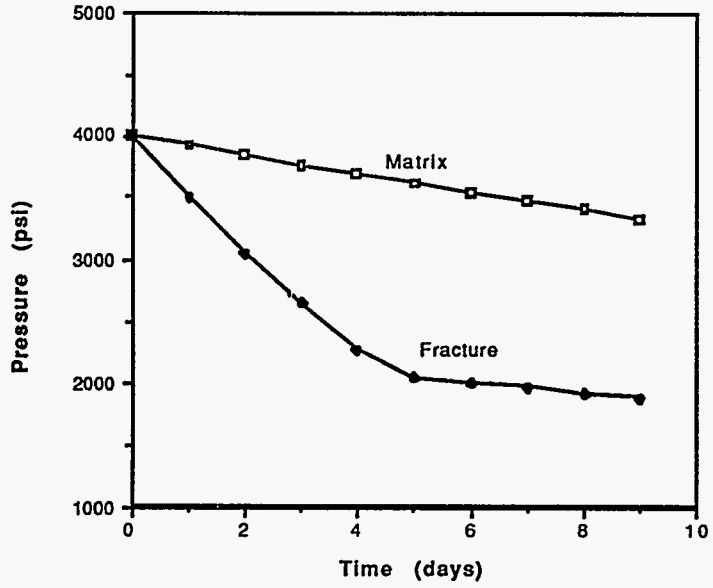


**Fig. 9 - Pressure profiles in the matrix and fracture systems**

Nomenclature

| | | |
|---|---|---|
| a | = | symmetric flow coefficient, [md-lbmole/($ft^5$-cp)] |
| A | = | total surface area exposed to imbibition, [$L^2$] |
| D | = | depth, [ft] |
| e | = | 2.7182 |
| f | = | fractional flow, [fraction] |
| F | = | flow of component 'l' in phase 'p', [lb mole/Day] |
| $F_S$ | = | shape factor, [1/($ft^2$)] |

| | | |
|---|---|---|
| $k$ | = | absolute permeability, md, $[L^2]$ |
| $k_r$ | = | relative permeability, [fraction] |
| $L$ | = | length of a block in a direction, [L] |
| $M$ | = | viscosity ratio, [fraction] |
| $n$ | = | number |
| $n$ | = | time step index |
| $p$ | = | pressure, [psi] |
| $q$ | = | volumetric flow rate, $[L^3/t]$ |
| $r$ | = | residual between two time steps, [lb mole/day] |
| $R$ | = | imbibition recovery, [pore volumes] |
| $R_\infty$ | = | maximum imbibition recovery, [pore volumes] |
| $s$ | = | parameter in Laplace space |
| $S$ | = | saturation of a phase , [fraction] |
| $t$ | = | time, [t] |
| $T$ | = | geometrical transmissibility, $[md/ft^2]$ |
| $u$ | = | flow velocity, [L/t] |
| $V$ | = | volume, $[L^3]$ |
| $w$ | = | mole fraction of a component in an aqueous phase |
| $x$ | = | lineal dimension, [L] |
| $x$ | = | mole fraction in of a component in liquid hydrocarbon phase |
| $y$ | = | mole fraction of a component in gaseous phase |
| $\Delta(X,Y,Z)$ | = | dimension of a grid block, [ft] |
| $\alpha$ | = | $\lambda R_\infty/\phi f$, $[t^{-1}]$ |
| $\lambda$ | = | reciprocal of time required to produce 63% of recoverable oil in place, $[t^{-1}]$ |
| $\mu$ | = | viscosity, [M/Lt] |
| $\phi$ | = | porosity, [fraction] |
| $\tau$ | = | Integration parameter for time dependent terms, [t] |
| $\rho$ | = | molar density of phase 'p', [lb mole/RCF] |
| $\gamma_p$ | = | gravity gradient for a phase 'p', [psi/ft] |

Superscripts

| | | |
|---|---|---|
| $n$ | = | old time level |
| $n+1$ | = | new time level |
| $v$ | = | iteration level index |
| $b$ | = | bulk volume $[L^3]$ |
| $B$ | = | bottom of the block |
| $c$ | = | component |
| cog | = | oil/gas capillary pressure |
| cow | = | oil/water capillary pressure |
| cm | = | connate water saturation in matrix |
| $E$ | = | east side of the block |
| $f$ | = | fracture |
| $g$ | = | gas |
| $i,j,k$ | = | a grid block index in X, Y and Z direction |
| $l$ | = | an index for a component |
| ma | = | matrix |

| | | |
|---|---|---|
| N | = | north side of the block |
| o | = | oil |
| orm | = | irreducible oil saturation in the matrix |
| p | = | phase |
| rp | = | relative permeability for phase 'p' |
| S | = | south side of the block |
| T | = | top of the block |
| tg | = | fracture/matrix transfer term for gas |
| to | = | fracture/matrix transfer term for oil |
| tw | = | fracture/matrix transfer term for water |
| w | = | water |
| W | = | west side of the block |
| usmaf | = | upstream matrix/fracture |

## 4.5 Subtask 5: Field Tests

### 4.5.1 Recomendations to Implement a Pilot $CO_2$-Enriched Water Imbibition Flood in an Austin Chalk Well

An idealized fracture-matrix geometry is assumed since a detailed description of the reservoir is not presently available. The following conditions are assumed in order to approximate an initial design for the proposed pilot test:

1. The fractures and matrix block pattern is repetitive throughout the fractured reservoir.
2. Outcrop studies indicate that the following geometry could represent an Austin Chalk reservoir: Matrix blocks of about 4 X 4 X 4 ft and a system of macro-fractures 0.8 mm wide. The system of micro-fractures 0.1 mm wide [1,2] that exists within the matrix blocks was assumed to be equivalent to a single macro-fracture across each block and parallel to the regional fracture trend.
3. From log analysis in the Bagget lease in Zavala and Dimmit counties, the producing interval was assumed to be 80 ft thick.
4. Movable oil saturation in the matrix blocks, after primary recovery, was assumed to be 45%. Laboratory experiments have shown an additional oil recovery due to carbonated water imbibition of 15% of OOIP.
5. Laboratory experiments indicate that oil droplets adhere to the rock surface, in the fracture system, after primary production.
6. A gaseous phase is present in the fracture system. Dissolved gas drive is assumed to be the primary production mechanism.
7. The average depth of the reservoir, in the area of interest, is 5,500 ft with a BHT of 170 $^{o}$F.
8. Representative reservoir matrix rock, fluid characteristics, and laboratory rock and fluid properties are shown in table I. Laboratory characteristics were needed to scale the obtained results to reservoir a reservoir scale.

Several considerations have to be done in order to duplicate the beneficial effects of a carbonated water imbibition flooding seen in repeated laboratory experiments using Austin Chalk crude.

#### 4.5.1.1 Surface rock area

Water imbibition is directly proportional to the contact area between the rock and water. In order to maximize the process, the contact area has to be as large as possible. Imbibing area is proportional to the stimulated fracture volume which in turn is proportional to the injected water volume. This consideration suggest that the largest possible volume of carbonated water be injected. An injection, soaking, and subsequent production method would have an imbibing area that decreases as oil comes out of the matrix block and fills the fractures system. After the initial injection of carbonated water, injection of small volumes of water, or carbonated water through one well and production of water and crude through adjacent wells would help to maintain imbibing area to a maximum value by sweeping produced oil.

#### 4.5.1.2 Initial Gaseous Phase Saturation

Previous cyclic water injection projects[4] have shown that a gas saturation after primary production can be very detrimental to imbibition flooding. In the field, the increase

in pressure during water injection apparently could cause the gas in the matrix blocks to go back in solution into the remaining oil, while a water drive would force oil adhering to the surface of the blocks into the rock matrix. This mechanism would create a shell of high water saturation close to the surface of the blocks. The reduced relative permeability of the oil phase in this shell next to the fracture faces greatly slows the rate of oil production by water imbibition.

Early injection of carbonated water combined with a disappearing gaseous phase inside the rock blocks, due to increasing pressure, would help to place dissolved carbon dioxide deep into the matrix blocks. The initial injection of carbonated water would transform a negative scenario into a very positive situation that would accelerate oil production.

#### 4.5.1.3 Amount of $CO_2$, Injection Pressure

Laboratory experiments have shown that oil recovery is proportional to the amount of $CO_2$ dissolved into the imbibed water. Solubility of $CO_2$ into water is a direct function of pressure, see Figure 1. The increase of solubility is greatest at low pressures. At high pressure values the solubility becomes approximately a linear function of pressure. Carbon dioxide solubility in water is also a function of temperature and salinity. Increases in temperature will decrease the solubility. The amount of $CO_2$ dissolved in water will remain constant from a surface mixing pressure of 650 psi at surface temperature, to a bottom hole pressure and temperature of 3000 psi and 170 $^{o}$F respectively, see Figure 1. The ability to increase and maintain an elevated reservoir pressure (3,000 psi) is a key factor of the process. The mentioned 650 psi is the maximum mixing pressure that would not create a free $CO_2$ phase under stabilized bottom hole conditions. A gaseous free $CO_2$ phase would be detrimental under reservoir conditions.

#### 4.5.1.4 Volume of Carbonated Water to be Injected

Detailed reservoir, rock, and fluid information would allow a mass balance calculation of the carbonated water volume needed to re-pressurize the reservoir. In order to maintain injected carbon dioxide in solution, reservoir pressure has to be kept at the designated constant bottom hole pressure. A large enough volume of carbonated water has to be injected to achieve this objective. When more information becomes available an estimate of the required volume to increase and maintain reservoir pressure could be performed.

#### 4.5.1.5 Water Salinity

The ability of water to carry carbon dioxide into the reservoir is reduced by an increasing salinity, see Figure 2. The use of fresh water would reduce the volume of water needed to carry a similar amount of carbon dioxide into the reservoir.

#### 4.5.1.6 Intervals of Injection

Horizontal wells produce from different fracture systems encountered by the borehole. Therefore, injection through a single fracture system would stimulate only a fraction of the potential producing matrix blocks. Selective injection would ensure carbonated water injection through the majority of the fracture systems.

4.5.1.7 Oil production Expected

If dissolved gas drive is assumed to be the primary production mechanism, water imbibition would be non-existent or very limited. The observance of some water production could indicate that water imbibition had taken place at a small scale. A partial matrix support of production could be caused by limited water imbibition.

Oil recovery due to carbonated water imbibition flooding would come from two different sources: (1) Oil being produced from the matrix itself, and (2) Oil removed from the fracture system due to the localized gas drive when the system pressure is dropped below the mixing pressure. A gaseous phase coming out of the matrix would remove small droplets adhering to the surface of the rock.

Oil production due to carbonated water imbibition:

Oil production due to carbonated water imbibition could be calculated scaling laboratory results. Laboratory experiments have shown a cumulative oil production of about 15% of OOIP, see Figure 3. The observed laboratory recovery translates to about 630 Bbl/acre (standard conditions) under the reservoir geometry assumed.

Oil production due to the fractures cleaning:

When the system pressure is released, carbon dioxide evolves to its gaseous form. This localized gas drive forces some oil out of the rock matrix. In addition, the gas production from inside of the rock matrix will initiate production of crude already out of the rock matrix but adhered to the rock surface. Laboratory experiments have shown a decrease in the amount of crude oil adhering to the rock surface from 6.5 to 3.9 $cm^3$ of crude / 100 $cm^2$ of imbibing area. The amount of adhering oil traduces to a total of 1,062 Bbl of crude/acre of reservoir.

Total oil production:

Simple addition of the methods presented yield a total oil production of 1,692 Bbl/acre, see Table II.

Calculated fracture storage capacity is 1634 Bbl/acre. Therefore, a total production of 90,000 Bbl of crude would occupy and area of 55 acres, with a drainage radius of 873 ft, disregarding compressibility effects and assuming there is no significant matrix support of production.

4.5.1.8 Time Required for Maximum Oil Production

The following equation can be used to scale model time to reservoir time:

$$\left[ t \sqrt{\frac{k}{\phi}} \frac{\sigma}{\mu_w L^2} \right]_{model} = \left[ t \sqrt{\frac{k}{\phi}} \frac{\sigma}{\mu_w L^2} \right]_{reservoir}$$

Values of rock and fluid properties previously mentioned would be considered to be representative of the laboratory and reservoir systems. Solving the previous expression for $t_{reservoir}$ the following equation is obtained:

$$t_{reservoir} = t_{model} \frac{\left[\sqrt{\frac{k}{\phi}} \frac{\sigma}{\mu_w L^2}\right]_{model}}{\left[\sqrt{\frac{k}{\phi}} \frac{\sigma}{\mu_w L^2}\right]_{reservoir}}$$

Substituting the assumed values into this equation, an equivalent reservoir to model time is obtained:

$$t_{reservoir} = t_{model} * 52.84$$

This is the time required to reach equivalent oil saturation conditions. The observed $t_{model}$ to achieve maximum oil recovery has been about 48 hrs. Therefore, time needed to achieve maximum oil recovery $t_{reservoir}$ = 106 days.

| | Matrix k (md) | Matrix $\phi$ (%) | Int. tension $\sigma$ (dyne/cm) | Imb. depth L (in) |
|---|---|---|---|---|
| Reservoir | 0.002 | 3 | 15 | 3 |
| Laboratory | 10 | 26 | 33 | 3 |

Table I. Rock and fluid properties.

| | | | Production | | | |
|---|---|---|---|---|---|---|
| Productive interval (ft) | Initial oil sat. Swi (%) | additional recovery (%) | Matrix imbibition (Bbl/acre) | Fracture cleaning (Bbl/acre) | Total (Bbl/acre) | Required time (days) |
| 80 | 45 | 15 | 630 | 1062 | 1692 | 106 |

Table II. Oil production.

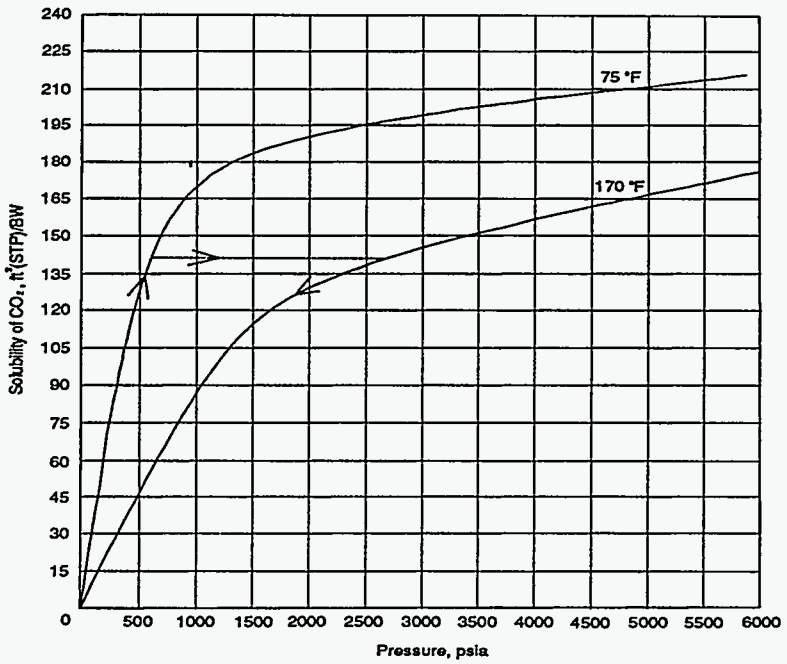


Figure 1. Solubility of carbon dioxide in water, as a function of pressure and temperature.

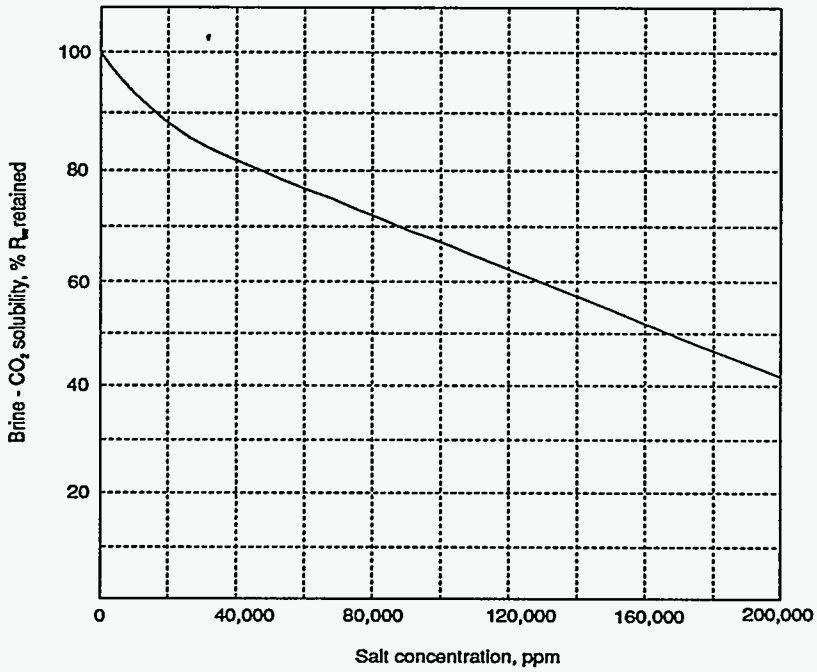


Figure 2. Amount of carbon dioxide retained in solution , as a function of water salinity.

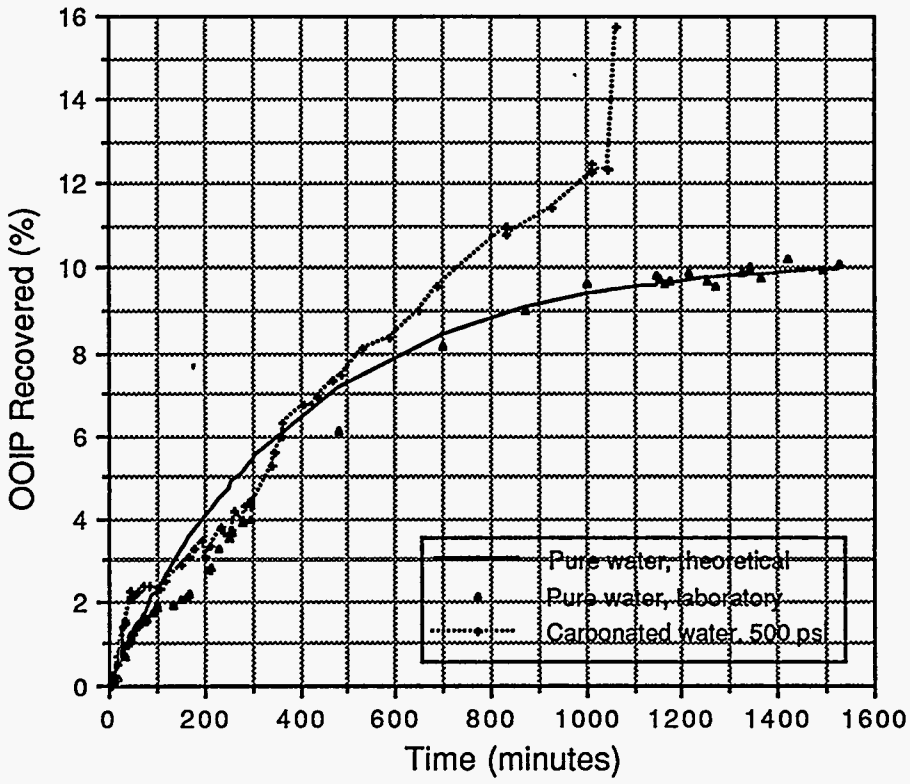


Figure 3. Comparison of cumulative oil production due to unadulterated and carbonated water imbibition.

## 5. REFERENCES

### 5.1 Subtask 1: Interpreting and Predicting Natural Fractures

#### 5.1.1 Geological Studies


1 Bieniawski, Z.T., 1984, *Rock Mechanics Design in Mining and Tunneling*, A. A. Balkema Publishers, Rotterdam and Boston, 272 p.

2 Corbett, Kevin, Friedman, M., and Spang, J., 1987, Fracture development and mechanical stratigraphy of Austin chalk, Texas. *Am. Assoc. Petroleum Geol. Bulletin,* v. 71, p. 17-28.

3 Corbett, K.P., Friedman, M., Wiltschko, D.V., Hung, J., 1991a, Characteristics of natural fractures in the Austin chalk outcrop trend, p. 3 - 11 *in*, Stewart Chuber, Ed., *Proc. South Texas Geological Society Symposium on the Austin Chalk,* Feb. 25, 26, San Antonio, Tx., 131 p.

4 Corbett, K.P., Friedman, M., Wiltschko, D. V.,and Hung, J.H., 1991b, Controls on fracture development, spacing, and geometry in the Austin Chalk formation, Central Texas: Considerations for Exploration and Production: *Dallas Geological Soc. Field Trip No. 4,* AAPG Ann. Conv., Dallas, Tx, April 1991, 49p.

5 Fritz, R.D., Horn, M.K., and Joshi, S. D., 1991, Geological Aspects of horizontal drilling, *American Assoc. Petroleum Geologists, Cont. Ed. Course Note Series No.* 33, 563p.

6 Kreck, W.W., Henderson, F. A., and Hjelmstad, K.E., 1974, A standard rock suite for rapid excavation research, U. S. Bureau of Mines, R.I. 7865, 29p.

7 Underwood, E. E., 1970, *Quantitative Stereology*, Addison-Wesley, Reading, Mass.

8 Wiltschko, D. V., Corbett, K. P., Friedman, Mel, and Hung, Jih-Hao, in press, Predicting fracture connectivity and intensity within the Austin Chalk from outcrop fracture maps and scanline data, *Gulf Coast Association of Geol. Socs.*


#### 5.1.2 Geophysical Studies

##### 5.1.2.1 Estimation of Fracture Orientations from Shear-Wave Splitting in the Lost Hills VSP

### 5.2 Subtask 2: Relating Recovery to Well-log Signatures

#### 5.2.1 Geological Studies


1 Grabowski, G.J., Jr., 1984, Generation and migration of hydrocarbons in Upper Cretaceous Austin Chalk, south-central Texas, in J.G. Palacas, editor, Petroleum geochemistry and source-rock potential of carbonate rocks: AAPG Studies in Geology 18, p. 97-115.

2 Hinds, G.S., and R.R. Berg, 1990, Estimating organic maturity from well logs, Upper Cretaceous Austin Chalk, Texas Gulf Coast: Gulf Coast Association of Geological Societies Transactions, v. 40, p. 295-300.

3 Hunt, J.M., and A.P. McNichol, 1984, The Cretaceous Austin Chalk of South Texas - a petroleum source rock, in J.G. Palacas, editor, Petroleum

geochemistry and source-rock potential of carbonate rocks: AAPG Studies in Geology 18, p. 117-125.

4 Sanford , J.R., 1990, Well productivity in the Austin Chalk: Master of Engineering Report, Texas A&M University.

5.2.2 Petroleum Engineering Studies

5.2.2.1 A Theory of Modeling Naturally Fractured Reservoirs

1 Barenblatt, G.I. and Zheltov, Yu.P.: "Fundamental Equations of Filtration of Homogeneous Liquids in Fissured Rocks," *Soviet Physics - Doklady* (1960) **5**, 522-25; (English Translated from *Doklady Akademii Nauk SSSR* (1960) **132**(3) 545-48.)

2 Barenblatt, G.I., Zheltov, Iu.P. and Kochina, I.N.: "Basic Concepts in the Theory of Seepage of Homogeneous Liquids in Fissured Rocks (Strata)," *PMM* (1960) **24**(5) 1286-303; (English Translated from *Priklad. Mat. Mekh.* (1960) **24**(5) 852-64; *J. App. Math. and Mech., USSR*)

3 Warren, J.E. and Root, P.J.: "The Behavior of Naturally Fractured Reservoirs," *SPEJ* (Sept. 1963) 245-55; *Trans.*, AIME, **228**.

4 Wijesinghe, A.M. and Culham, W.E.: "Single-Well Pressure Testing Solutions for Naturally Fractured Reservoirs With Arbitrary Fracture Connectivity," paper SPE 13055 presented at the 1984 Annual Technical Conference and Exhibition, Houston, TX, Sept. 16-19.

5 Chen, H.Y., Poston, S.W. and Raghavan, R.: "The Well Response in a Naturally Fractured Reservoir: Arbitrary Fracture Connectivity and Unsteady Fluid Transfer," paper SPE 20566 presented at the 1990 Annual Technical Conference and Exhibition, New Orleans, LA, Sept. 23-26.

6 Kazemi, H.: "Pressure Transient Analysis of Naturally Fractured Reservoirs with Uniform Fracture Distribution," *SPEJ* (Dec. 1969) 451-58.

7 de Swaan, O.A.: "Analytic Solutions for Determining Naturally Fractured Reservoir Properties by Well Testing," *SPEJ* (June 1976) 117-22; *Trans.*, AIME, **261**.

8 Bourdet, D.: "Pressure Behavior of Layered Reservoirs With Crossflow," paper SPE 13628 presented at the 1985 California Regional Meeting, Bakersfield, CA, March 27-29.

9 Fatt, I.: "A Demonstration of The Effect of "Dead-End" Volume On Pressure Transient in Porous Media," *Trans.*, AIME, (1959) **216**, 449-453.

10 Bear, J.: *Hydraulics of Groundwater*, McGraw-Hill, New York (1979) 28-31.

11 Sneddon, I.N.: *Elements of Partial Differential Equations*, McGraw-Hill Book Co. Inc., New York (1957) 90-92.

12 Luikov, A.V.: *Analytical Heat Diffusion Theory*, Academic Press, New York and London (1968) 9-12.

13 Swenson, R.J.: "Generalized Heat Conduction Equation," *Am. J. Phys.* (Jan. 1978) **46**(1) 76-77.

14 Polubarinova-Kochina, P. Ya: *Theory of Ground Water Movement* (in Russian), Gostekhizdat, Moscow, 1952; English translated by De Wiest, R.J.M., Princeton University Press, Princeton, New Jersey (1962) 17-23.

15 Hubbert, M.K.: "Darcy's Law and the Field Equations of the Flow of Underground Fluids," *Trans.*, AIME (1956) **207**, 222-39.

16 Foster, W.R., McMillen, J.M. and Odeh, A.S.: "The Equations of Motion of Fluids in Porous Media: I. Propagation Velocity of Pressure Pulses," *SPEJ* (Dec. 1967) 333-341; *Trans.*, AIME (1956) **240**.
17 Scheidegger, A.E.: *The Physics of Flow Through Porous Media*, 3rd Ed., University of Toronto Press, Toronto (1974) 198-205.
18 Goldstein, S: "On Diffusion by Discontinuous Movements, and on the Telegraph Equation," *Quart. J. Mech. Appl. Math.* (1951) **4**, Pt. 2, 129-156.

## 5.3 Subtask 3: Development of the EOR Imbibition Process

### 5.3.1 Laboratory Displacement Studies

1 Klins, Mark A.: "Carbon Dioxide Flooding - Basic mechanisms and project design," IHRDC, Boston, MA (1984)
2 Grape, S.G.: "Imbibition Flooding With $CO_2$-Enriched Water": A M.S. Thesis in Petroleum Engineering, Texas A & M University. (Aug. 1990)
3 Johnson, W.E., MacFarlane, R.M. and Breston, J.N.: "Changes in Physical Properties of Bradford Crude Oil When Contacted With Carbon Dioxide and Carbonated Water - Part I," Producers Monthly (Nov. 1952) pp:16-22.
4 MacFarlane, R.M., Breston, J.N. and Neil, D.C.: "Oil Recovery From Cores When Flooded With Carbonated Water and Liquid $CO_2$ - Part II," Producers Monthly (Nov. 1952) pp: 23-35.
5 Breston, J.N. and MacFarlane, R.M.: "The Effects of a Number of Variables on Oil Recovery From Cores When Flooded With Carbonated Water and Liquid $CO_2$ - Part III," Producers Monthly (Nov. 1952) pp: 36-45.
6 Miller, J.A. and Jones, R.A.: "A Laboratory Study to Determine Physical Characteristics of Heavy Oil After $CO_2$ Saturation," paper SPE 9789 presented at the 2nd. Joint SPE / DOE Symposium on EOR, Tulsa, April 5-8, 1981.
7 Holm, L.W.: "$CO_2$ Requirements in $CO_2$ Slug and Carbonated Water-Oil Recovery Processes," Producers Monthly (Sep. 1963) pp: 6-28.
8 de Nevers, N.: "Carbonated Waterflooding," World Oil (Sep.1966) PP: 93-96.
9 Holm, L.W. and Josendal, V.A.: "Mechanism of Oil Displacement by Carbon Dioxide," J. Pet. Tech. (Dec. 1974) pp:1427-1438.
10 Wang, G.C. and Locke, C.D.: "A Laboratory Study of the Effects of $CO_2$ Injection Sequence on Tertiary Oil Recovery," SPEJ (Aug. 1980) pp: 278-280.
11 Latil, M.: "Enhanced Oil Recovery," Gulf Publishing, Houston. (1980)
12 Ross, G.D., Todd, A.C., Tweddie, J.A. and Will, A.G.S.: "The Dissolution Effects of $CO_2$-Brine Systems on the Permeability of U.K. and North Sea Calcareous Sandstones," paper SPE 10685 presented at the 3rd. Joint SPE/DOE Symposium on EOR, Tulsa, April 4-7, 1982.
13 Sayegh, S.G., Krause, F.F., Girard, M. and DeBree, C.: "Rock / Fluid Interactions of Carbonated Brines in a Sandstone Reservoir; Pembina Cardium, Alberta, Canada," SPE Formation Evaluation, (Dec. 1990) pp: 399-405.

14 Dodds, W.S., et al.: "$CO_2$ Solubility in Water," Chem. Eng. Data Series 1,Gas Jour., (Oct. 8, 1962).

15 Bowker, K.A. and Shuler, P.J.: "Carbon Dioxide Injection and Resultant Alteration of the Weber Sandstone, Rangely Field, Colorado," The American Association of Petroleum Geologists Bulletin, v 75, No. 9 (Sep.1991) pp: 1489-1499.

5.3.2 MRI Studies

1 Grape, Steve G.: *Imbibition Flooding with $CO_2$ - Enriched Water*, MS thesis, Texas A&M University, College Station, TX (1990)

2 Aronofsky, J.S., Masse, L., and Natanson, S.G.: "A Model for the Mechanism of Oil Recovery from a Porous Matrix Due to Water Invasion in Fractured Cores," *Trans.*, AIME (1958) **213**, 17-19.

3 Graham, J.W., and Richardson, J.G.: "Theory and Application of Imbibition Phenomena in Recovery of Oil," *Trans.*, AIME (1959) **216**, 377-381.

4 Blair, P.M.: "Calculation of Oil Displacement by Countercurrent Water Imbibition," paper SPE 1475-G presented at the 1960 SPE Fourth Biannual Secondary Recovery Symposium, Wichita Falls, TX, May 2-3.

5 Braester, C.: "Simultaneous Flow of Immiscible Liquids through Porous Fissured Media," *SPEJ* (Aug. 1972) 297-305.

6 Kleppe, J., and Morse, R.A.: "Oil Production from Fractured Reservoirs by Water Displacement," paper SPE 5084 presented at the 1974 SPE-AIME Annual Fall Technical Conference and Exhibition, Houston, TX, October 6-9.

7 DeSwaan, A.: "Theory of Waterflooding in Fractured Reservoirs", *SPEJ* (April 1978) 117-122.

8 Kazemi, H., and Merril, L.S.: "Numerical Simulation of Water Imbibition in Fractured Cores," *SPEJ* (June 1979) 175-181.

9 Davis, G.B., and Hill, J.M.: "Some Theoretical Aspects of Oil Recovery from Fractured Reservoirs," *Trans., I. Chem. E.* (1982) **60**, 352-358.

10 Sonier. F., Souillard, P., and Blaskovich, F.T.: "Numerical Simulation of Naturally Fractured Reservoirs," *SPERE* (Nov. 1988) 1114-1122.

11 Kazemi, H., Gilman, J.R., and El-Sharkaway, A.M.: "Analytical and Numerical Solution of Oil Recovery from Fractured Reservoirs Using Empirical Transfer Functions," paper SPE 19849 presented at the 1989 SPE Annual Technical Conference and Exhibition, San Antonio, TX, Oct. 8-11.

12 Brownscombe, E.R., and Dyes, A.B.: "Water-Imbibition Displacement... Can it Release Reluctant Spraberry Oil?," *Oil and Gas J.* (Nov. 17, 1952) 264-265.

13 Mattax, C.C., and Kyte, J.R.: "Imbibition Oil Recovery from Fractured, Water-Drive Reservoirs," *JPT* (June 1962) 177-184.

14 Parsons, R.W., and Cheney, P.R.: "Imbibition Model Studies on Water-Wet Carbonated Rocks," *SPEJ* (March 1966) 26-34.

15 Kyte, J.R.: "A Centrifuge Method to Predict Matrix-Block Recovery in Fractured Reservoirs," *SPEJ* (June 1970) 164-70.

16 Mannon, R.W., and Chilingar, G.V.: "Experiments on Effect of Water Injection Rate on Imbibition Rate in Fractured Reservoirs," paper SPE 4101 presented at the 1972-AIME Annual Fall Meeting, San Antonio, TX, Oct. 8-11.

17 Iffly, R., Rousselet, D.C., and Vermeulen, J.L.: "Fundamental Study of Imbibition in Fissured Oil Fields," paper SPE 4102 presented at the 1972 SPE-AIME Annual Fall Meeting, San Antonio, TX, Oct. 8-11.

18 Lefebvre du Prey, E.F.: "Gravity and Capillary Effects on the Matrix Imbibition in Fissured Reservoirs," *SPEJ* (June 1978) 195-206.

19 Keijzer, P.P.M., and DeVries, A.S.: "Imbibition of Surfactant Solutions," paper SPE/DOE 20222 presented at the 1990 SPE/DOE Symposium on Enhanced Oil Recovery, Tulsa, Oklahoma, April 22-25.

20 Ghedan, S.G., and Poettmannn, F.H.: "Oil Recovery from Fractured Reservoirs Through Imbibition by Water and Polymer Flooding," paper SPE/DOE 20244 presented at the 1990 SPE/DOE Symposium on Enhanced Oil Recovery, Tulsa, Oklahoma, April 22-25.

21 Cuiecl, L.E., Bourbiaux, B., and Kalaydjian, F.: "Imbibition in Low-Permeability Porous Media: Understanding and Improvement of Oil Recovery," paper SPE/DOE 20259 presented at the 1990 SPE/DOE Symposium on Enhanced Oil Recovery, Tulsa, Oklahoma, April 22-25.

22 Scheidegger, A.E.: *The Physics of Flow Through Porous Media*, The Macmillan Co., New York, N.Y. (1960)

23 Baker, W.J.: "Flow in Fissured Formations," *Proc.*, Fourth World Pet. Cong. (1955) Sec. II, 379.

24 Birks, J.: "Recovery of Oil from Fissured Limestone Formations," *Proc.*,Fourth World Pet. Cong. (1955) Sec. II, 425.

25 Pirson, S. J.: "Tertiary Recovery of Oil," Paper presented before the Central Appalachian Section, AIME (June 26, 1941)

26 Whorton, L. P., Brownscombe, E. R., and Dyes, A. B.: "A Method for Producing Oil By Means of Carbon Dioxide," U.S. Patent No 2,623,596 (1952).

27 MacFarlane, R. M., Breston, J. N., and Neil, D. C.: "Oil Recovery from cores When flooded with Carbonated Water and Liquid Gas," *Producers Monthly* (Nov. 1952) **17**, 23-25.

28 Holm, L. W.: "Carbon Dioxide Solvent Flooding for Increasing Oil Recovery," *Trans.*, AIME (1959) **216**, 225.

29 Menzie, D. E., and Nielsen, R. F.: "A Study of the Vaporization of Crude Oil By Carbon Dioxide Repressuring, " *Trans.*, AIME (1963) **228**, 1247.

30 Kumar, N., and Von Gonten, W. D.: "An Investigation of Oil Recovery by Injecting $CO_2$ and LPG Mixtures", Preprint SPE 4581, AIME.

31 Holm, L, W., and Josendal, V. A.: "Mechanism of Oil Displacement by Carbon Dioxide," *Trans.*, AIME (1974) 1427.

32 Yelling, W. F., and Metcalfe, R. S.: "Determination and Prediction of $CO_2$ Minimum Miscibility Pressures", *JPT* (Jan. 1980) 160-168.

33 Holm, L. W., and O'Brien, L. J.: "Carbon Dioxide Test at the Mead-Strawb Field," *JPT* (April 1971) 23, 431.

34 Partovi, R. N.: "Experimental study of Oil Recovery from Porous Material by Means of Carbon Dioxide Flooding", PhD Dissertation, Texas A&M University, College Station, TX (1968).

35 Reamer, H. H., olds, R. H., Sage, B. H., and Lacey, W. N.: "Phase Equilibria in Hydrocarbon Systems," *J. Ind. Eng. Chem.* (Jan 1944) 15-17.

36 Stalkup, F. I., Jr.: *Miscible Displacement*, Monograph Series, SPE, Dallas (1983) **8**, 137-158.

37 Unruh, C. H., and Katz, D. L.: "Gas Hydrates pf Carbon Dioxide - Methane Mixtures," *Trans.*, AIME (1949) **186** 83-86.

38 Robinson, D.B., and Mehta, B. R.: "Hydrates in the Propane - Carbon Dioxide - Water System," *JCPT* (Jan.-March 1971) **33.**

39 Holm, L. W., and Josendal, V. A.: "Effect of Oil Composition on Miscible - Type Displacement by Carbon Dioxide, " *SPEJ* (Feb. 1982) 87-98.

40 Vukalovich, M. P., and Altunin, V. V.: *Thermophysical Properties of Carbon Dioxide*, Collet's Ltd., London (1968)

41 Goodrich, J. H.: "Review and Analysis of Past and Ongoing Carbon Dioxide Injection Field Test," paper SPE/DOE 8832 presented at the First Joint DOE/SPE Symposium on Enhanced Oil Recovery, Tulsa, April 20-23, 1980.

42 Carr, N. L., Kobayashi, R., and Burrows, D. B.:"Viscosity of Hydrocarbon Gases under Pressure," *Trans.*, AIME (1954) **201**, 264-272.

43 Klins, M. A.: *Carbon Dioxide Flooding, Basic Mechanisms and Project Design*, Internal Human Resources Development Corporation, Boston, MA (1984).

44 Miller, J. A., and Jones, R. A.: "A Laboratory Study to Determine Physical Characteristics of Heavy Oil after $CO_2$ Saturation," paper SPE 9789 presented at the 2nd Joint SPE/DOE Symposium on Enhanced Oil Recovery, Tulsa, April 5-8, 1981.

45 Latil, M.: *Enhanced Oil Recovery*, Gulf Publishing, Houston, TX (1980).

46 Simon, R., and Graue, D. J.:"Generalized Correlations for Prediction Solubility, Swelling and Viscosity Behavior of $CO_2$ - Crude Systems," *JPT* (Jan. 1965) 102-106.

47 Cragoe, C. E.: *Thermodynamic Properties of Petroleum Product*, Monograph 10 Bureau of Mines, Washington, D.C. (1957) **1.**

48 Menzie, D. E., and Nielsen, R. F.: "A Study of the Vaporization of Crude Oil By Carbon Dioxide Repressuring, " *JPT* (Nov. 1963) 1247.

49 Dodds, W. S., Stutzman, L. F., and Sollami, B. J.: "Carbon Dioxide Solubility in Water," *J. Ind. and Eng. Chem.* (1956) **1**, 92-95

50 Holm, L. W.: "$CO_2$ Requirements in $CO_2$ Slug and Carbonated Water - Oil Recovery Processes," *Producers Monthly* (Sept. 1963) 6-28.

51 Crawford, H. R., Neill, G. H., Bucy, B. J., and Crawford, P. B.: "Carbon Dioxide - A Multipurpose Additive for Effective Well Stimulation," *JPT* (March 1963) 237-242.

52 Johnson, W. E. MacFarlane, R. M., and Breston, J. N.: "Changes in Physical Properties of Bradford Crude Oil When Contacted with $CO_2$ and Carbonated Water," *Producers Monthly* (Nov. 1952) 16.

53 Martin, J. W.: "Additional Oil Production through Flooding with Carbonated Water," *Producers Monthly* (July 1951) 18-23.

54 David, A.: "Asphaltene Flocculation During Solvent Stimulation of Heavy Oils," paper 47nd presented at the 71st National Meeting of American Institute of Chemical Engineers, Dallas, Feb. 20-23, 1972.

55 Simon, R., Rosman, A., and Zana, E.: "Phase - Behavior Properties of $CO_2$ - Reservoir Oil Systems," *SPEJ* (Feb, 1978) 20-26.

56 Bardon, C., and Longeron, D. G.: "Influence of Very Low Interfacial Tensions on Relative Permeability," *SPEJ* (Oct. 1980) 391-401.

57 Yoder, Claude H., and Schaeffer, Charles D.:*Introduction to Multinuclear NMR*, The Benjamin/Cummings Publishing Company, Menlo Park, California (1987)

58 Homans, S.W.: *A Dictionary of Concepts in NMR*, Oxford University Press, New York, NY (1989)

59 H.J. Vinegar, "X-RAY CT and NMR Imaging of Rocks", *JPT* (March 1986) 755-60.

60 H.J. Vinegar, and S.L. Wellington, "Tomographic Imaging of three-phase *flow experiments", Rev. Sci. Instrum.* (1987) **58**, No. 1, 1-15.

61 W.A. Edelstein, H.J. Vinegar, P.B. Roemer, and O.M. Mueller, "NMR Imaging for Core Analysis", paper SPE 18272 presented at the Annual Technical Conference and Exhibition, Houston, TX, Oct. 1988.

62 C. T. Chang, J. W. Robinson, and C. M. Edwards, "An Agarose Gel Reference Standard For Use In MRI Determination of Porosity and Fluid Saturations in Porous Media", *Engineering Imaging Laboratory Research Report 90-01*, Texas A&M University, College Station, TX, Feb. 1991.

5.3.3 CT Studies

5.3.4 Image Analysis

1 Stephenson, D.S. "Maximum Entropy Approach to NMR Data", *Prog. NMR Spectroscopy,* Vol. 20, 515 (1988).

2 Gull, S.F. and Daniell, G.J., *Nature(London)* Vol. 272, 686(1978)

3 Daniell, G.J. and Hore, P.J. "Maximum Entropy and NMR-- A New Approach", *Jour. of Mag. Resonance,* Vol. 84, 515 (1989).

4 Chan, S.O. and Comisarow , M.B. , *Journ. of Mag. Resonance* Vol. 54, 201 (1983).

5 Abildgaard, F. and Gesmar, H. "Least Squares Fit to Fourier transform spectrum", *Journ. of Mag. Resonance* Vol. 79, 78 (1988).

6 Brigham, E.O., "The Fourier Transform", Prentice-Hall Inc. Englewood Cliffs, NJ(1974).

7 Andrew, R.E. "NMR Imaging", *Acc. Chem. Res.* , Vol. 16, 114(1983).

8 Pople, J.A. and Shneider, W.G. ,"High Resolution Nuclear Magnetic Resonance", McGraw-Hill: New York, 1969.

9 Gesmar, H., Led, J.J. and Abildgaard, F. "Spectral Analysis of NMR Data", *Prog. in NMR Spec.* Vol. 22, 255(1990).

10 Perez, J. "MRI study of Imbibition Flooding using Carbonated Water", Dissertation, Texas A&M University, 1991.

5.4 Subtask 4: Mathematical Modeling

1 de Swaan, A.: "Theory of Waterflooding in Fractured Reservoirs," *SPEJ* (April 1978) 117-22.

2 Kazemi, H., Gilman, J.R. and El-Sharkaway, A.M.: "Analytical and Numerical Solution of Oil Recovery from Fractured Reservoirs Using Empirical Transfer Functions," paper SPE 19849 presented at the 1989 SPE Annual Technical Conference and Exhibition, San Antonio, Texas, Oct. 8-11.

3 Davis, G.B. and Hill, J.M.: "Some Theoretical Aspects of Oil Recovery from fractured Reservoirs," Transactions of Institution of Chemical Engineers (1982) v. 60, 352-358.

4 Warren, J.E. and Root, P.J. : "The Behavior of Naturally Fractured Reservoirs," *Soc. Pet. Eng. J.* (Sept. 1963) 245-255, *Trans.*, AIME, vol.228.

5 Kazemi, H., Merril, L.S. JR., Porterfield, K.L. and Zeman, P.R. : "Numerical Simulation of Water-Oil Flow in Naturally Fractured Reservoirs," *Soc. Pet. Eng.* J. (Dec. 1976) 317-326.

6 Thomas, L.K., Dixon, T.N. and Pierson, R.G.: "Fractured Reservoir Simulation," *Soc. Pet. Eng. J.* (Feb. 1983) 42-54, SPE Reprint Series 20, 221-233.

7 Sonier, F., Souillard, P. and Blaskovich, F.T.: "Numerical Simulation of Naturally Fractured Reservoirs," *SPERE* (Nov. 1988) 1114-1122.

8 Peng, C.P., Yanosik, J.L. and Stephenson, R.E. : "A Generalized Compositional Model for Naturally Fractured Reservoirs," *SPERE* (May, 1990) 221-226.

9 Killough, J.E. and Kossack, C.A.: "Fifth Comparative Solution Project: Evaluation of Miscible Flood Simulator," Paper SPE 16000 presented at the Ninth SPE Symposium on Reservoir Simulation, San Antonio, Texas, February 1-4, 1987.

5.5 Subtask 5: Field Tests

1 Corbett, K.P.: "Structural Stratigraphy of the Austin Chalk,"; Ms thesis, Texas A&M University, College Station, TX (1982).

2 Stearns, D.W., 1968, Certain Aspects of Fracture in Naturally Deformed Rocks: in NSF Advanced Science Seminar in Rock Mechanics, R.E. Riecker, ed., Sp. Rept. Air Force Cambridge Research Laboratories, Bedford, Mass., pp. 97-118.

3 Poston, S. W.: "Oil Recovery Enhancement from Fractured, Low Permeability Reservoirs," Annual report, Grant No. DE-FG22-89BC14444, U.S. DOE (Sept. 1990)

4 Elkins, L.F., Skov, A.M., and Gould, R.C.: "Progress Report on Sproberry Waterflood Reservoir Performance, Well Stimulation and Water Treating and Handling," *JPT* (Sept. 1068) 1039-1049.

# Controls on Fracture Development, Spacing, and Geometry in the Austin Chalk

## Formation, Central Texas: Considerations for Exploration and Production

DIAMOND JUBILEE AAPG APRIL 7-10, 1991 DALLAS

Annual Convention


Field Trip Leaders:

Kevin P. Corbett
Melvin Friedman
David V. Wiltschko
Jih Hao Hung


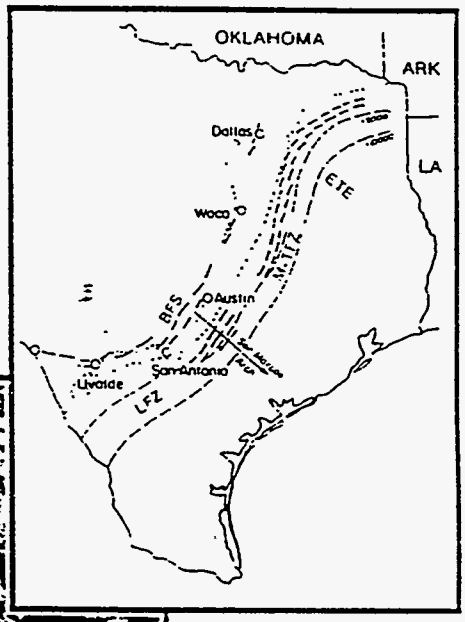


Dallas Geological Society
Field Trip #4
April 6-7, 1991

# Controls on Fracture Development, Spacing, and Geometry in the Austin Chalk Formation, Central Texas: Considerations for Exploration and Production

Guidebook
DGS Field Trip # 4

April 6-7 1991

American Association of Petroleum Geologists
1991 Annual Convention

Field Trip Leaders:


Kevin Corbett
Marathon Oil Company
Petroleum Technology Center
P. O. Box 269
Littleton, Colorado 80160

Melvin Friedman
Center for Tectonophysics and
Department of Geology
Texas A&M University
College Station, Texas 77843

David V. Wiltschko
Center for Tectonophysics and
Department of Geology
Texas A&M University
College Station, Texas 77843

Jih Hao Hung
Center for Tectonophysics and
Department of Geology
Texas A&M University
College Station, Texas 77843


1991 AAPG Annual Convention Field Trip Chairman:
Robert T. Clarke, Mobil Research and Development Corporation

This guidebook for DGS Field Trip #4, Controls on Fracture Development, Spacing, and Geometry in the Austin Chalk Formation, Central Texas: Considerations for Exploration and Production, was prepared for the American Association of Petroleum Geologists Annual Convention held in Dallas, Texas, from April 7-10, 1991.

The guidebook is available for purchase at $10.00 (+ $1.00 postage) from:

The Dallas Geological Society
One Energy Square, Suite 170
Dallas, Texas 75206



ISBN 1-879325-19-5

# Contents

# Controls on Fracture Development, Spacing, and Geometry in the Austin Chalk Formation, Central Texas: Considerations for Exploration and Production

Kevin P. Corbett
Melvin Friedman
David V. Wiltschko
Jih Hao Hung

## Introduction

Horizontal drilling has made fractured reservoirs attractive exploration targets. The Austin Chalk Formation, as a consequence of this new technology, has been one of the most extensively pursued exploration targets in the continental United States for the last several years, particularly in the number of production wells drilled in the Pearsall and Giddings fields, Texas. In spite of the advantages horizontal drilling offers for enhancing initial and total production, successful operations still are predicated on the location of zones of high fracture intensity and a high density of fracture intersections. Often, these zones are not directly detectable from seismic surveys. Consequently, the most viable strategy for success to date has been to offset highly productive wells along strike. Accordingly, the purpose of this field trip is to observe fractures in outcrops of the Austin Chalk with a view towards providing conceptual models of fracture development and corresponding data for extrapolation into the subsurface.

In order to enhance predictability of these high fracture intensity regions in the subsurface, we investigated the outcrop trend of the chalk to identify the tectonic environments where high fracture intensities are found. We used two techniques to assess the characteristics of the fracture systems. First, we measured the length, spacing, and orientation of fractures along scan lines on vertical quarry walls. Second, we made detailed maps of the fracture systems as exposed on bedding surfaces, at scales ranging from 1:12 to 1:48. We paid particular attention to investigating domains comparable in style, character, and size to currently producing subsurface structural settings. Accordingly, these well exposed and extensively studied outcrop structures can then serve as direct corollaries in identifying exploration targets and in improving the siting and geometry of production boreholes.

We have identified four tectonic environments and associated structural settings possessing statistically higher fracture intensities and more

long *master* fractures, which are one of the principal controls on increasing effective drainage area (Corbett and others, 1991). Additionally, we have statistically characterized the general form of the distribution of several fracture parameters including spacing, length and orientation.

Our studies also indicate that at least two discrete episodes of fracturing have occurred. The earliest of these episodes is apparently attributable to the development of abnormally high pore fluid pressure in the chalk. Several lines of evidence, including fluid inclusion trapping temperatures, trace element abundances, the stable isotope characteristics of vein filling calcite, and an order of magnitude increase in smectite clay in veins compared to chalk matrix, leads us to identify this first fracturing episode as a natural hydrofracture event. The hydrofractures influenced the location of major structures produced during the second fracture episode, and to a degree have determined the location of faults and master fractures during this second event. We believe it is essential to understand the genetic development of the composite fracture system in order to formulate a complete fracture model.

On this field trip we will inspect three of the four tectonic environments we have identified along the outcrop trend, a listric normal fault system, a monoclinal flexure, and a graben-in-graben normal fault system. The fourth environment, an anticline, is located near Del Rio in southwest Texas, making a visit to this locality impractical. At each location there will be ample opportunity to inspect the spatial, geometric, and temporal properties of the fracture systems. We will discuss facets of the stress state, at the time of formation, which can be discerned from fracture surface morphology and fracture interactions. We will also review the statistical properties of the fracture systems for each specific locality, and the geochemical and mineralogical aspects of the hydrofracture veins.

The field guide is divided intc two sections. In the first section we present general observations, properties, and attributes of the fracture systems, discuss the development of the hydrofractures and present a conceptual model for their formation. In this section we also discuss the statistical analysis of the fracture data, and general aspects of fracture mechanics. In the second section we present the specific details of the outcrops we will inspect. Particularly salient aspects of each outcrop are identified, and our interpretations of the origin and evolution of these specific examples are put forth for discussion. Since we feel that these localities are likely candidates as analogue models for producing structures, we are vitally interested in eliciting your observations, interpretations, and conclusions so that we may test, refine, and where necessary redefine our current hypotheses.

We trust you will find the trip intellectually stimulating and beneficial to you in your own exploration and production efforts in the Austin Chalk and other fractured reservoirs. We look forward to the opportunity to interact with a diverse group of active explorationists and broaden our understanding of natural fracture systems.

# Geologic Setting

The regional geologic setting, sedimentology, diagenesis, and stratigraphy of the Austin Chalk Formation has been established by other workers and references to the pertinent literature are provided in Corbett and others 1987. Here we summarize those aspects of the regional geology and tectonics pertinent to the outcrops we will visit.

The Austin Chalk crops out throughout Texas, from Red River County in the northeast to Val Verde County in the southwest (Figure 1). Both the surface and subsurface trends follow the form of the Gulf Coast miogeocline. In central Texas the outcrop belt is coincident with the Balcones fault system. This fault system parallels the structural grain of the Paleozoic Ouachita deformed belt, which is exposed to the northwest in the Llano uplift and Texas Hill Country. It may be inferred, but cannot be proved, that the location and trend of the Balcones system is the result of an existing weak zone in the underlying Ouachita basement rocks. Regardless of any basement control, the general style of faults in the Balcones system indicates that they formed in response to down-to-the-coast extension of the sedimentary prism. In this respect, they are

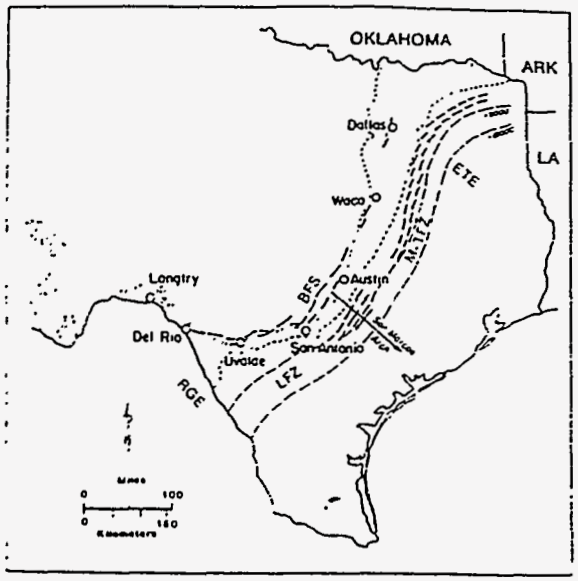


Figure 1. Geographic reference map showing Upper Cretaceous outcrop (stippled), subsurface structural contours on the top of the Austin Chalk (dashed lines), The Balcones fault system (BFS), Luling fault zone (LFZ), Mexia-Talco fault zone (M-TFZ),and the Rio Grande and east Texas embayments (RGE, ETE) of the Gulf Coast miogeocline (reproduced by permission from Corbett and others, 1987).

similar to other, younger faults in the Gulf Coast region. The age of Balcones system faulting is not tightly constrained, as no cross-cutting stratigraphic relationships have been preserved. All sediments younger than Cretaceous and older than Quaternary have been removed by erosion. Therefore, the age is established by analogy with the tectonically similar, subsurface, Luling, Mexia, and Talco fault zones (Figure 1). These zones affect rocks as young as Oligocene but apparently do not offset Miocene strata (Weaks, 1945).

As a consequence of Balcones system faulting, exposures of the chalk are more extensive than other formations. Nevertheless, natural exposures are limited, confined primarily to stream beds. The best exposures occur in cement quarries in Dallas, Waco, and San Antonio. In particular, these quarries afford the only opportunity to examine fractures, faults, and related structures on the bedding surface, and in two approximately vertical and orthogonal profile planes. While nowhere are all three surfaces directly linked, they do provide a composite, three-dimensional view of the fracture systems.

Durham (1957) studied the chalk in the Austin area and erected a stratigraphic section composed of one formal member, the Atco Chalk Member, and six informal ones. Subsequently, Pessagno measured and formally described chalk sections from southwest Texas, Waco, and Dallas (Figure 2). All quarries except the Longhorn Quarry in San Antonio are within the basal Atco Chalk Member (Dravis,1979; Cloud, 1975). The Longhorn Quarry exposes middle and upper Austin Chalk on either side of a large displacement Balcones system fault (Cloud, 1975). The contact with the underlying Eagleford Shale is not exposed in the San Antonio quarries. At the Waco and Dallas quarries the contact and underlying shale are exposed. Subsurface stratigraphy can be correlated with the outcrop section based on gross lithologic similarity, as reflected in electric log response (Figure 2; Corbett and others, 1987; 1991).

The Atco Chalk Member is composed of rhythmically bedded chalk-marl sequences. The chalk beds generally range from 0.5 to 2 m thick and are separated by marls ranging from 0.5 to 15 cm thick. The thickness of intervening marl beds increases from San Antonio north, attaining a maximum in the Dallas area. The thickening of intervening marls coincides with a concurrent thickening of the basal Atco Chalk Member. Both circumstances are a consequence of the original depositional setting. At the time of chalk deposition the San Marcos Arch (Figure 1), a subsurface extension of the Llano uplift, formed a topographic high (Murray, 1961; Young, 1963). Chalk strata, particularly the basal Atco Chalk Member, are thinned across this depositional high and thicken both to the northeast and southwest, where deposition was in the deeper-water basinal settings of the Rio Grande and East Texas embayments. The increase in marl thickness is likewise a result of variation in depositional setting, from shallow shelf on the San Marcos Arch to more basinal away from the arch.

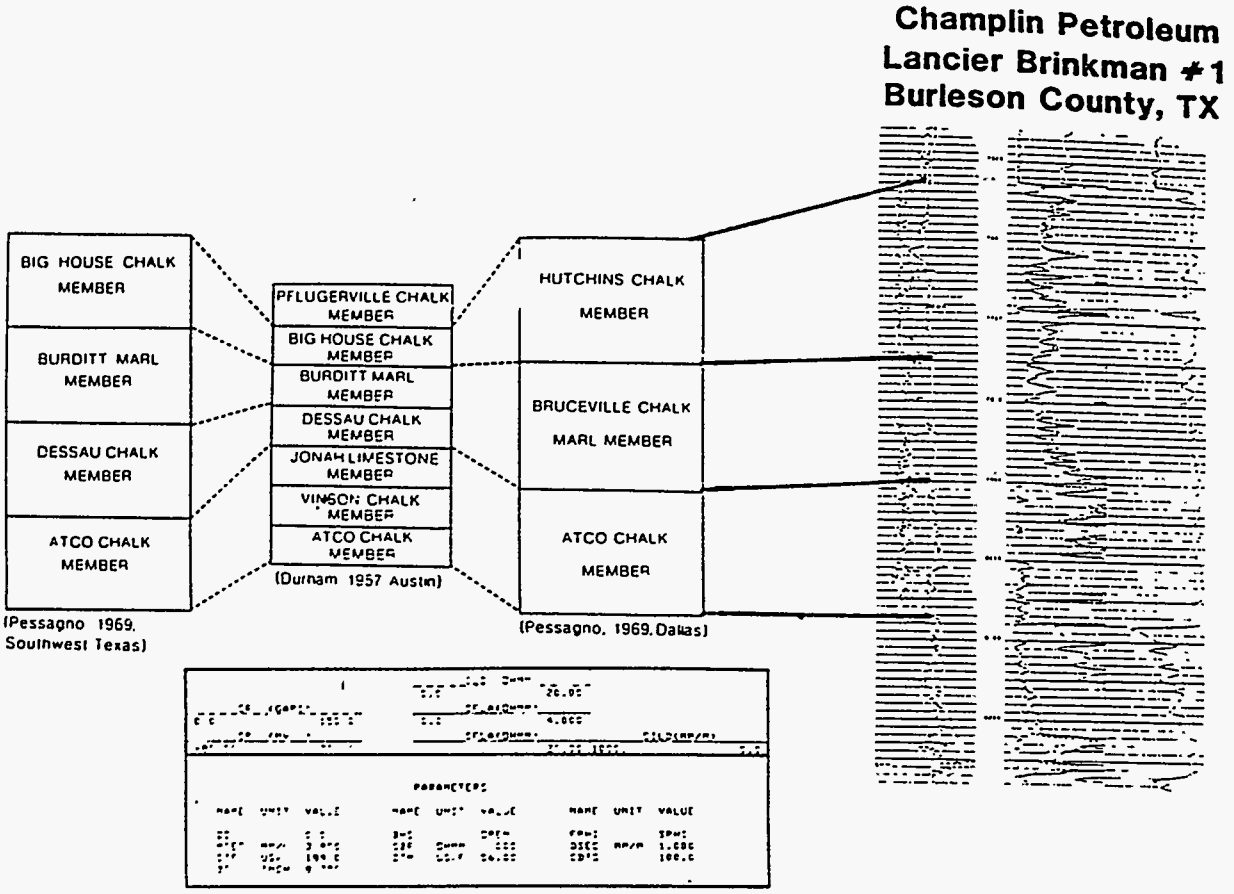


Figure 2. Correlation of outcrop and subsurface stratigraphic sections for the Austin Chalk (adapted from Corbett and others, 1987).

The mineralogy of the Atco Chalk Member is relatively uniform. It ranges from 85% to 91% calcite, with quartz and clay minerals representing the only significant minor components (Corbett, 1982; Corbett and others, 1987). Quartz occurs primarily as microscopic, euhedral crystals ranging from 5 μm to 10 μm in size. Clay minerals occur as large amorphous masses ranging from 30 μm to 80 μm in size. These accessory phases most likely were derived from syn-depositional volcanic ash, as discrete ash layers are found higher in the formation, and contemporaneous eruptive centers have been identified (Lonsdale, 1927). Diagenesis of the Atco Chalk Member is relatively mild in central Texas, showing a moderate increase in overgrowth cement from Dallas south to San Antonio (Cloud, 1975). Scanning electron microscopy reveals only minor dissolution of the fragmented coccolith tests which compose the bulk of the rock matrix (Cloud, 1975; Dravis, 1979). Dravis (1979) inferred that fresh water diagenesis dominated the central Texas outcrop belt, based primarily on the removal of aragonite macrofossil material. Alternatively, Cloud (1975) argued for early burial diagenesis, based on texture and stable oxygen and carbon isotope compositions. Our textural observations and geochemistry (Corbett, 1982; and this study) support Cloud's interpretation.

It has been proposed that the Austin Chalk may be a self sourcing reservoir ( Grabowski, 1984; Hunt and McNichols, 1984; Hinds and Berg, 1990). According to this theory fracturing accompanies oil maturation and is related to high pore fluid pressures generated by hydrocarbon expulsion. Considering the variability in oils recovered from the Austin Chalk throughout the productive subsurface trend, it seems unlikely that this mechanism is universally responsible for fracturing and oil formation. Perhaps detailed source rock - oil comparisons can establish the validity and applicability of this hypothesis.

# General Fracture Characteristics

## Fractures

Fracture nomenclature is controversial and in a state of flux. Workers in the fields of rock mechanics, structural geology, petroleum engineering, and civil engineering do not attach the same meaning to a particular term, or may use different terms to refer to one feature or process (Engelder, 1987; Pollard and Segall; 1987; Pollard and Aydin, 1988). Therefore, to avoid ambiguity we define the terminology used in this report in the short discussion which follows. Diagrammatic representations of the fracture and fault types are shown in Figure 3.

A fracture is any planar discontinuity in a rock mass produced by brittle failure. The failure process may have been aided, enhanced, or accelerated by chemical reactions with the pore fluids, but is fundamentally a result of mechanical breakdown of rock mass integrity. A simple extension fracture forms perpendicular to the direction of the least principal compressive stress. It represent a discrete failure event in both space and time. A joint is a composite surface resulting from the coalescence of two or more simple extension fractures. These may form during a discrete failure event, but more commonly result

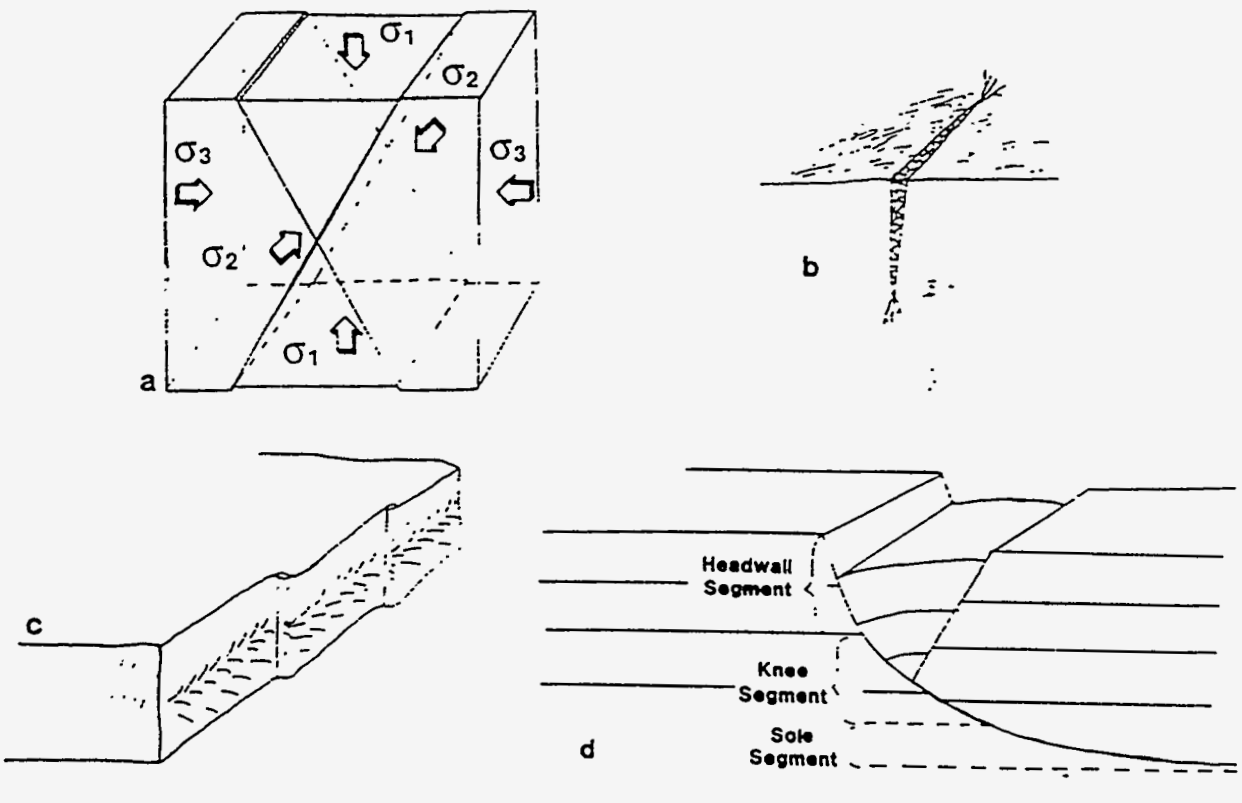


Figure 3. Schematic representations of fracture, vein, joint, and fault characteristics. a) A conjugate set of shear fractures and their relationship to the principal stress directions; $\sigma_1$ greatest, $\sigma_2$ intermediate, and $\sigma_3$ least principal stresses. b) A vein filled extension fracture with horsetail fracture tips. c) A joint composed of three extension fractures each with characteristic hackle and plume structures showing direction of fracture propagation. Note the en-passant fracture tip relationship shown on the bedding surface. d) Characteristic geometry of a listric normal fault with an antithetic fault in the hanging wall.

from progressive failure as evidenced by fracture surface markings and fracture tip interactions (Pollard and Aydin, 1988; Engelder 1985). As such, joints are generally not discrete failure events in either space or time.

Shear fractures are failure surfaces inclined at an angle ranging from 15° to 45° to the maximum compressive stress at the time of failure. They often form conjugate sets (Stearns, 1964; Friedman, 1975), but this is not requisite. Shear fractures are characterized by differential offset of the two rock masses on either side of the fracture surface (ie. they have accommodated shear-displacement), but the magnitude of shear displacement may be too small to observe in the field. In reality, shear fractures and faults describe a continuum in displacement. We distinguish shear fractures as those shear surfaces having a net displacement which is less than 0.1% of the fracture length in the displacement direction. Although in principle this criteria is unambiguous, true fracture length is not always exposed in the field, sometimes rendering distinction between shear fractures and faults impossible. Nevertheless, it is desirable to have a clear working definition for classifying shear fractures.

A vein is any fracture which is partially or completely filled by minerals which crystallized in the opening created by the fracture. Generally, vein minerals precipitate from pore fluids which invade the fracture during or after formation.

Four types of fractures are present in Austin Chalk outcrops. In all cases vein-filled fractures were first to form as indicated by cross-cutting relationships. Simple extension fractures, joints, and shear fractures developed after the vein filled fractures. The origin and relative timing of these latter fractures depends on the tectonic setting in which they are found.

## Faults

We classify those faults, or segments of a fault, where the dip exceeds 50° as high-angle faults. Faults which dip between 30° and 50° are intermediate-angle faults, and those with a dip of 30° or less are shallow-angle faults. Listric faults are characterized by continuous variability in dip angle from a high-angle headwall segment, through an intermediate-angle knee segment to a shallow-angle sole segment. Listric faults result in rotation of hanging wall strata in the vicinity of the headwall and knee segments of the fault (Figure 3).

Listric and high-angle normal faults are the most common fault types. They have produced horst-and-graben and graben-in-graben structures respectively. Each possesses increased fracture intensity and enhanced development of master fractures. The third fault type develops on monoclinal flexures. These faults are sub-parallel to bedding, allowing for extension perpendicular to the fold axes during the early stages of fold growth. Later, high-angle normal faults accommodated continued fold growth.

## Vein systems

Vein filled fractures were the first systematic fracture set to form. They are cross-cut by all other fracture and fault surfaces. Individual veins range from 100 μm to 30 cm in length and from 10 μm to 5 mm in width (Figure 4). They generally occur in en-echelon swarms, with 5 cm to 25 cm wide zones of high vein density separated by barren zones 100 cm to 1 m wide. Fracture tips for the veins frequently exhibit a wispy, horsetail appearance, which indicates low stress concentration at the tip and low deviatoric stress. The vein fill is composed primarily of two phases, calcite and a mixed-layer, smectite-illite clay. The clay minerals were deposited first on the vein walls and subsequently were overgrown by subhedral calcite crystals. Many of the veins exhibit crack-seal texture (Ramsey, 1980), demonstrating multiple fracture episodes.

Several lines of evidence indicate that the most plausible origin for the veins is a series of natural hydrofracture events. Comparison of vein geochemistry with that for the bulk chalk suggests that extra-formational pore fluid was introduced to the chalk. We postulate that introduction of this fluid into the chalk raised the pore fluid pressure triggering fracturing and vein formation.

We determined vein clay mineralogy by analyzing the acid insoluble residue from

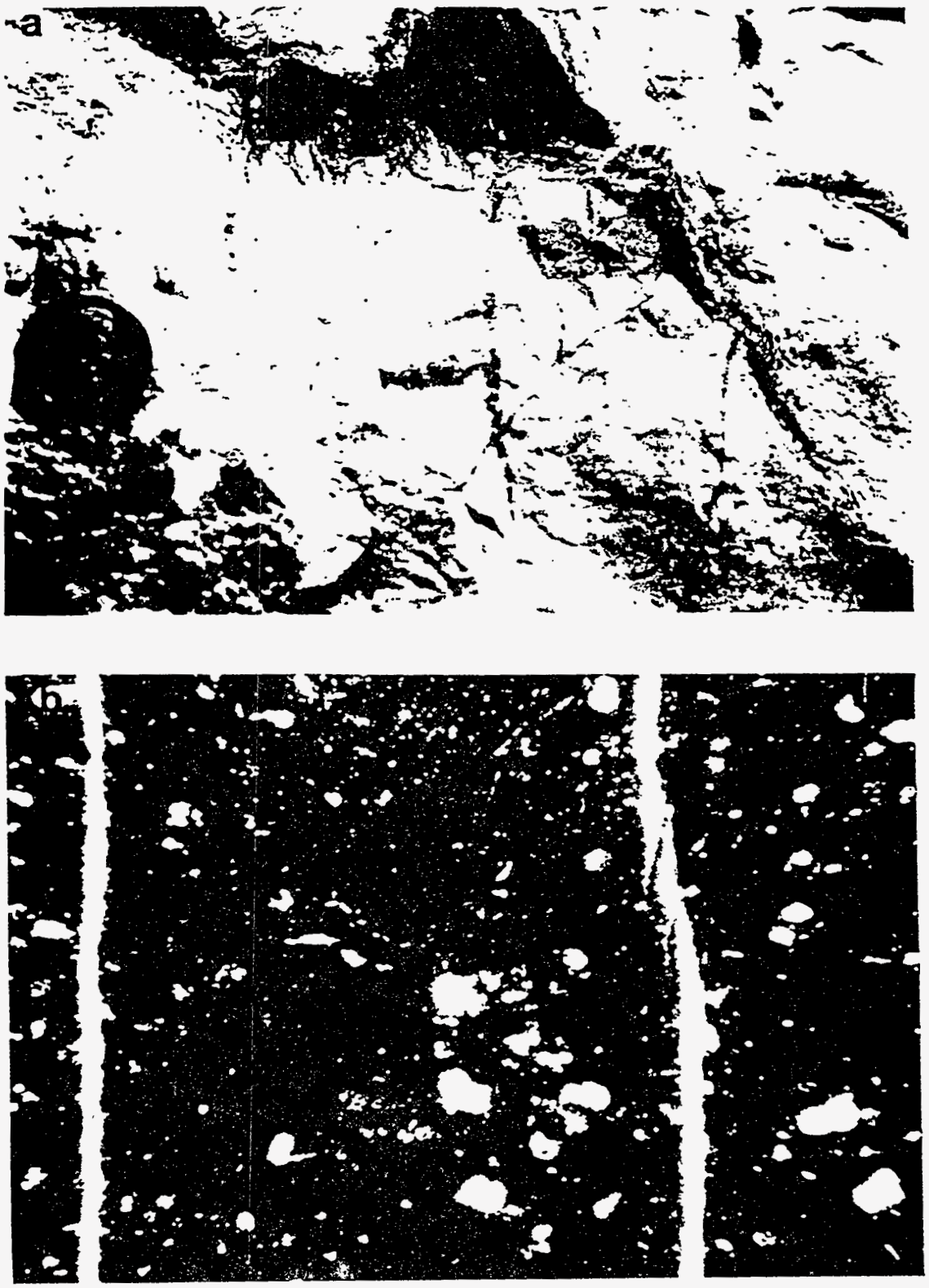


Figure 4. Typical vein characteristics in the basal Atco Chalk Member. a) Vein swarm cut by a small displacement fault; Lafarge quarry, Dallas. b) Thin-section photomicrograph of two parallel vein systems; Old Alamo Quarry, San Antonio. One vein system shows a left-stepping, en-echelon relationship, photo is 1.5 mm wide.

powdered samples on the Cameca SX-50 microprobe at Texas A&M University using a 20 kev, 10 na beam, a 2 μm beam size and count times of thirty seconds for major elements and sixty seconds for the minor elements fluorine and titanium. Trace element abundances for vein calcite were also determined by microprobe analysis using a 10 kev, 20 na beam, with a spot size of 10 μm. Low concentrations for the principal trace elements: strontium, manganese, and iron, necessitated count times of 5.5 minutes while count times of thirty seconds were used for the major and minor elements calcium and magnesium. We established an empirical linear regression relationship between counts per second and concentration for each trace element (Table 1), and used this relationship to recalculate trace element abundances and normalized the total to 100%.

TABLE 1

| ELEMENT | R | n | CPS/0ppm |
|---|---|---|---|
| Sr | 0.919 | 25 | 31.07 |
| Mn | 0.947 | 28 | 43.46 |
| Fe | 0.743 | 26 | 5.06 |

Fluid inclusion measurements were made on a Leitz Ortholux microscope equipped with a heating-cooling stage. Reproducibility for Tm (melt temperature) and Th (homogenization temperature) was ± 0.1° C. Stable isotope analysis of the vein calcite was performed by Dr Ethan Grossman, Texas A&M University. We report all isotopic values as $\delta C^{13}$-$\delta O^{18}$ PDB. We have used the relevant trace element and stable isotope data for bulk chalk samples reported in Cloud (1975) and Dravis (1979) as our basis of comparison.

Clay minerals are much more abundant in veins than they are in the chalk matrix. They constitute 4% to 9% by volume of outcrop chalks (Corbett and others. 1987). Smectite clays, including the proportionate share of mixed layer clays, range between 1% and 4% by volume in the chalk. In veins, clay minerals range from 18% to 25% by volume. They are dominantly mixed-layer smectite-illite with a 2:1 to 3:1 ratio. The interlayer cation for the smectites is most likely Ca, but our separation and analysis technique precludes an unequivocal determination. The location of the clay minerals on vein walls is well illustrated by energy dispersive maps of elemental abundance for a microprobe thin section (Figure 5).

Trace element composition of the vein calcites is distinctly different from that for bulk chalk samples (Figure 6). Most striking is the discrepancy for the large incompatible element strontium, which will preferentially go into solution when calcite dissolves (Veizer, 1983). None of the median values of strontium for the veins overlap the first quartile of either set of bulk samples. All of the veins are depleted in strontium with respect to the bulk samples. This is opposite to the expected outcome if the vein calcite were derived from local chalk dissolution and reprecipitation. Likewise, the veins are depleted in Fe and Mn with respect to the bulk chalk samples, again in contrast with results expected based on a local dissolution-reprecipitation model. No clear trend for the minor element magnesium is apparent, most of the vein samples possess median values between the first and third quartiles for one of the groups of bulk samples. Noteworthy, is the generally much greater variability in magnesium abundance in the veins as compared to the bulk samples. In view of the crack-seal textures this scatter may reflect different degrees of fluid-chalk interaction prior to a specific hydrofracture event.

Stable isotope data for the vein calcite clearly points to an extra-formational source for the veins in the Dallas and Waco areas. These veins are preferentially depleted in $O^{18}$ compared to the bulk chalk samples (Figure 7). In the Del Rio area the vein calcite is slightly depleted in $O^{18}$ and enriched in $C^{13}$ in comparison with the chalk matrix. This is not surprising as the interbedded marls in the Dessau Chalk and Burditt marl members provide a local source for vein forming pore fluids. For the San Antonio area the vein calcite and bulk chalk samples have comparable stable isotope characteristics. Two bulk samples from Cloud (1975) are strongly depleted in $C^{13}$. These samples appear to be anomalous and may indicate contamination. Exclusive of these samples, the vein calcites in San Antonio are compatible in their stable isotope composition with either local derivation or equilibration with the chalk matrix.


Finally, fluid inclusions in the vein calcite suggest derivation from an extra-formational source. Three populations of inclusions may be distinguished based on salinity and homogenization temperature (Figure 8). Textural relationships, including size, shape, and distribution suggests that these are primary inclusions trapped during formation of the vein calcite from pore fluids. For San Antonio two groups of inclusions are evident. One group is in the range 1 to 4 weight percent NaCl, while the second group ranges from 6 to 10 weight percent NaCl. The mean homogenization temperatures are Th=186 °C, and Th=183 °C for each group respectively. For the three Waco measurements the salinities are comparable, but the homogenization temperatures are lower than for San Antonio. Disregarding the one anomalously low value, which we believe is a secondary inclusion formed in the near surface environment, the remaining two Waco measurements yield a mean Th of 134 °C. The homogenization temperatures provide a minimum estimate of the original fluid temperature at the time of trapping. Temperature estimates derived from vitrinite reflectance values for bulk chalk samples are substantially lower than the fluid inclusion temperatures (Table 2). The most straight forward interpretation of this discrepancy is that the fluids from which the vein minerals precipitated were derived from a deeper, hotter source.

The crack-seal texture of many veins and horsetail fracture tips require a pore fluid pressure equivalent to the least principal compressive stress. Furthermore, the crack-seal texture indicates multiple fracturing and vein forming episodes. The vein minerals are almost completely undeformed. No fracturing of vein deposits is evident and mechanical twins in the coarse-grained, sparry calcite are extremely rare. There is no preferred crystallographic fabric orientation of the vein

Figure 5. (at the left). A back-scattered electron image of a dense vein swarm which has been rotated and sheared in a fault zone. Elemental maps of aluminum and silicon demonstrate the concentration of clay minerals along vein walls and on the brittle shear surfaces; Longhorn Quarry, San Antonio.

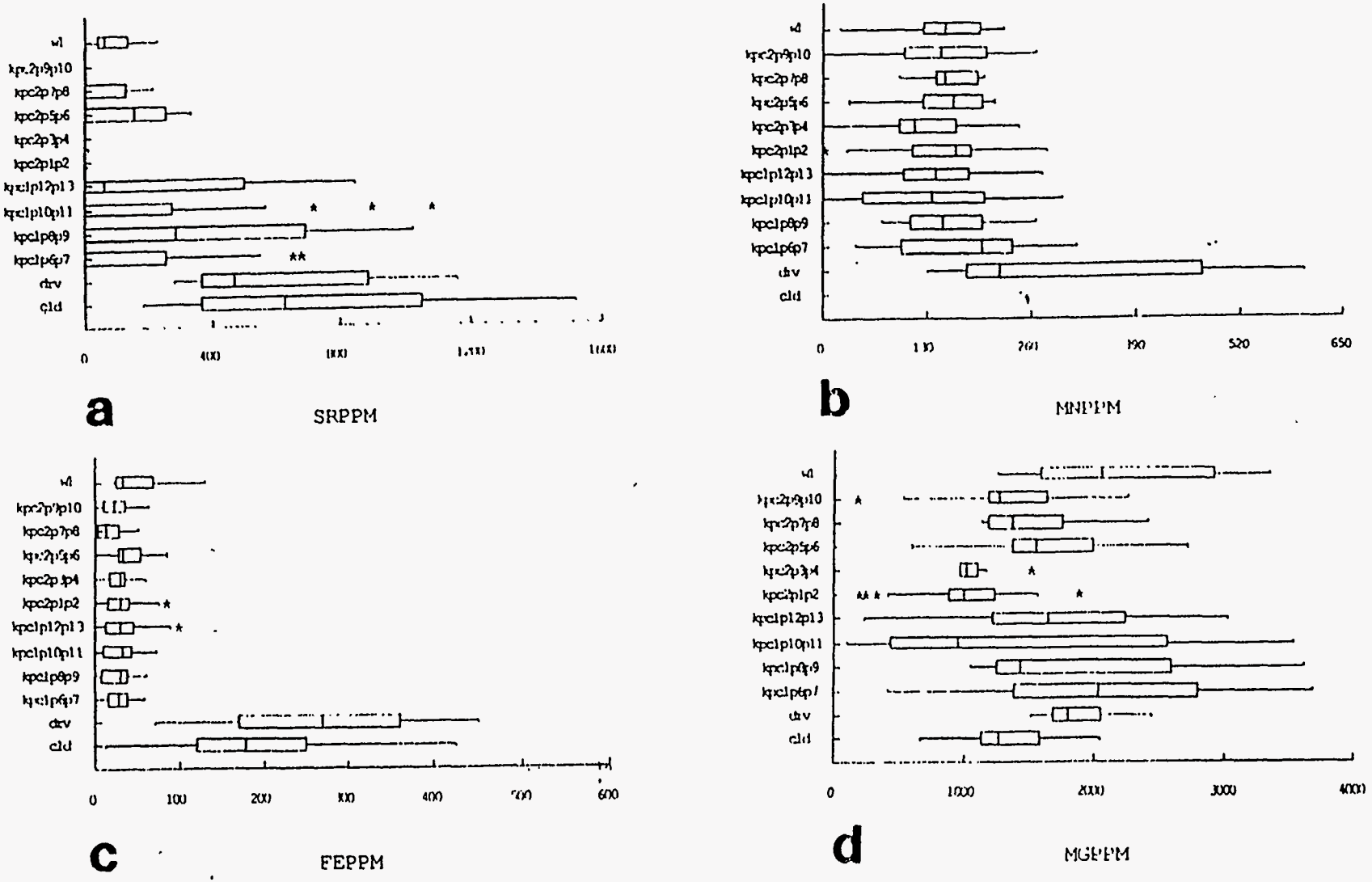


Figure 6. Comparison of minor and trace element compositions between the bulk chalk matrix and vein calcite. Bulk samples are from Dravis (1979) drv, and Cloud (1975) cld. Vein samples kpc1... and kpc2... from Longhorn quarry, San Antonio, w1 from Lehigh quarry, Waco. Box and wiskers plots show the median value for sample population with vertical bar in box, left and right box boundaries delimit the first and third quartiles respectively, whisker ends show boundaries for 5% and 95% of the sample population, outlier values are indicated by an asterisk. a) Veins are strongly depleted in strontium compared to bulk chalk. b) Veins are strongly depleted in manganese with respect to bulk chalk. Cloud (1975) did not measure manganese. c) Veins are strongly depleted in iron with respect to bulk chalk. d) Veins show a much larger scatter in magnesium content than bulk chalk. For further discussion see text.

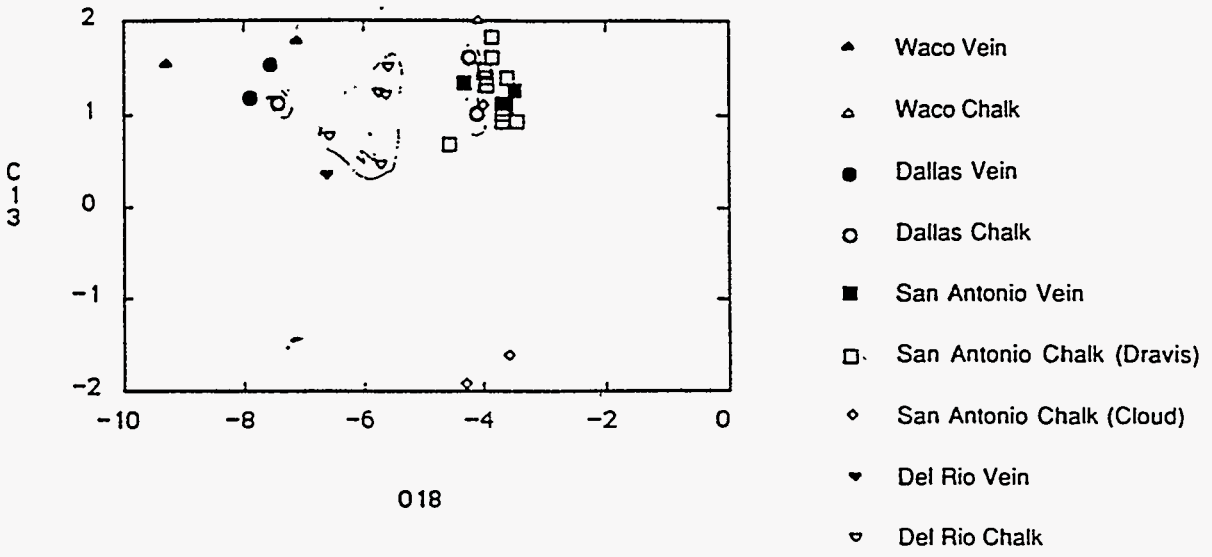


Figure 7. Plot of $\delta O^{18}$ versus $\delta C^{13}$ for bulk chalk and vein calcite, bulk samples are those reported in Cloud (1975) except where noted in the legend.

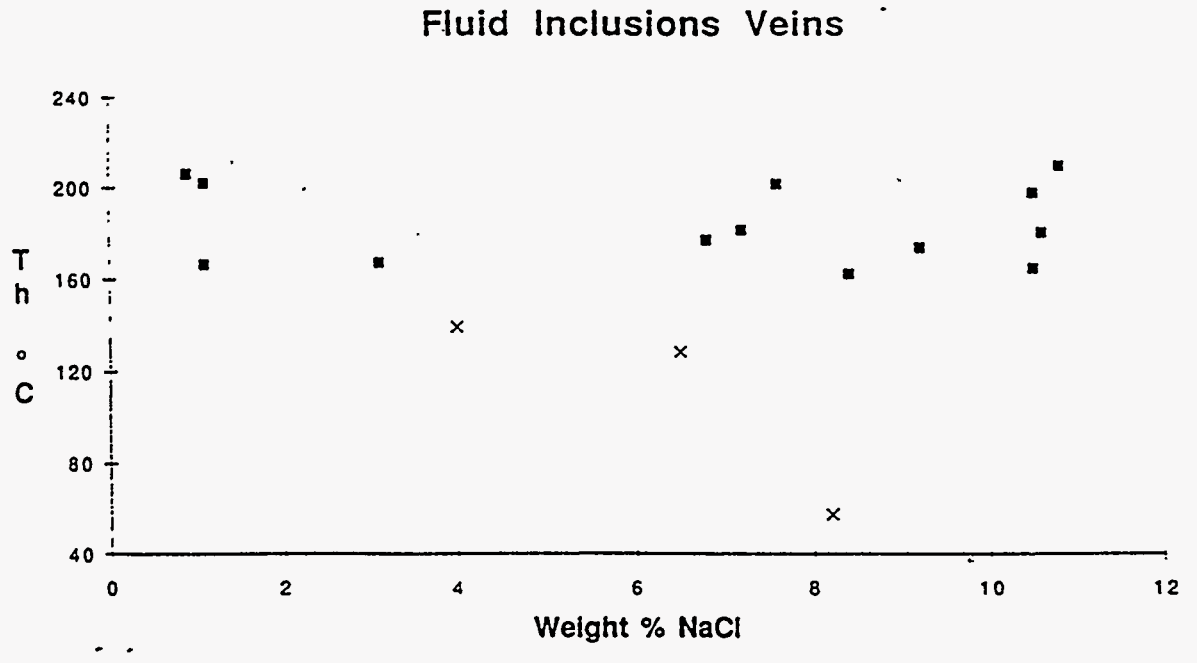


Figure 8. Plot of homogenization temperature (Th) in degrees celsius versus weight percent NaCl for fluid inclusions in vein calcites. Key to symbols: squares, Longhorn quarry, San Antonio; crosses, Lehigh quarry, Waco.

TABLE 2

| SAMPLE NO. & LOCATION | REFLECTANCE | ESTIMATED TEMP. °C |
|---|---|---|
| ZGE Dallas* | 0.71 | 108 |
| ZGI Dallas* | 0.74 | 110 |
| ZEA Dallas* | 0.76 | 111 |
| ZEI Austin* | 0.81 | 118 |
| SAL-1b San Antonio | 0.70 | 107 |
| ZAR Del Rio* | 0.79 | 116 |

* Data from Cloud, 1975. Temperatures calculated using the kinetic model of Burnham and Sweeney (1989).

calcite (Corbett, 1989), in spite of the incorporation of many veins into fault zones. This lack of preferred orientation suggest crystallization occurred under a hydrostatic stress state.

The textural characteristics and virtually all of the geochemical evidence indicates that the vein forming fluids were derived from outside the chalk and from deeper in the basin. These fluids evidently infiltrated the chalk and eventually reached a pressure sufficient to promote fracturing. The increase in pore volume produced by fracturing resulted in the pore fluid pressure returning to a value below that of the least principal stress. Crystallization of the vein minerals, first clays and then calcite, was triggered by the pressure drop. The combination of vein mineral growth and continued infiltration of pore fluid resulted in this scenario being episodically repeated. How this invasion of fluids from below relates to possible self-hydraulic fracturing of the chalk associated with oil maturation is unknown.

## Hypotheses

Our current working hypothesis is that the chalk was under a state of low differential stress, but generally near failure. Increasing the pore fluid pressure had the effect of equivalently reducing all principal stresses, thereby leaving the differential stress unchanged and producing failure (Figure 9).

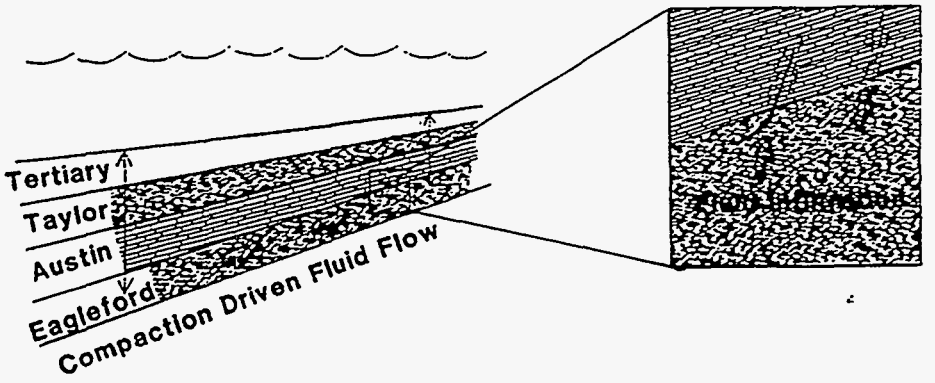


Figure 9. Conceptual model for the generation of high pore fluid pressure and resultant natural hydrofracturing of the Austin Chalk. Pore fluids driven from the Eagleford shale, due to compaction beneath a thick overburden section in the more distal portion of the sedimentary prism, migrated up-dip along the shale, invaded the chalk and produced extension fractures which propagated upwards from the contact. Frequently faults developed concurrent with fracturing.

The large volume of smectite clay in the veins, along with depletion of trace elements and the high fluid inclusion homogenization temperatures for calcite, indicate to us the most likely source for the fluids is dewatering of the underlying Eagleford Shale. We envision a hydrodynamic system where fluid expelled by compaction from the Eagleford Shale flows up-dip, along the shale, until it encounters comparatively high permeability zones in the overlying chalk. The fluid invades the chalk at these zones and eventually reaches a pressure sufficient to produce fracturing (Figure 9). The close relationship between veins and faults poses a chicken-and-egg question, which came first. Certainly, faults would serve as ideal high permeability conduits for pore fluids to invade the chalk. We are inclined to believe, from observations on small faults in a rhythmically bedded chalk-marl sequence in the Burditt Marl Member near Del Rio, that the veins and faults frequently develop simultaneously. As fluid from the shale invades the chalk, the shale experiences local compaction initiating faulting at the chalk-shale bedding surface (Figure 10).

An alternative hypothesis is that relating oil maturation to self-hydrofracturing. This hypothesis is incapable of explaining the foregoing geochemical considerations, particularly the fluid inclusion homogenization temperatures, and thus appears unlikely as a candidate for explaining the outcrop vein systems. However, it may be more viable in describing subsurface fracturing. Both hypotheses need to be tested further. In either case abnormally high pore fluid pressures would be generated, resulting in low effective stresses for both the outcrop and subsurface environments at the time of fracturing. This condition permits extrapolation of outcrop fracture data into the subsurface.

We note that these vein systems are not restricted to the outcrop trend, but are also found in the subsurface (Figure 10). Again they are associated with faults. The vein/fault fabric indicates that the veins were forming during fault displacement. Although we have only identified this one occurrence from the subsurface, we suspect that these veins are commonly developed but go unrecognized, unless a core is obtained and adequately preserved for structural study.

The location of faults, folds, and associated high fracture intensities was evidently controlled by the location of the veins. Two aspects of the vein systems served to localize later deformation. First, the inception of faulting in many cases occurred prior to complete crystallization of the veins. Primary evidence for this is the S-C type fabrics developed in many of the fault zones (Figure 11). This fabric results from rotation of the veins during fault displacement. The latest formed veins demonstrate that the fault zone walls are perpendicular to original vein orientation. Lack of a preferred crystallographic fabric for the calcite crystals in the rotated veins indicates that crystallization followed rotation. Thus, the implication from the S-C fabrics is that the veins had not completely crystallized at the time of faulting, and were at least partially fluid-filled fractures. The veins constituted a location for the initiation of shear failure, the fluid-filled vein swarms being unable to support a shear stress. This first faulting event was ductile in character and did not result in formation of an open fracture networks.

A second important consideration is the veins introduced and concentrated appreciable amounts of smectite clay in the chalk. We previously identified smectite clay as a significant control on rock strength in experimentally deformed chalk samples (Corbett and others, 1987). For those experiments, we noted that increasing smectite content from 0% to .1% by volume was sufficient to decrease chalk strength by a factor of two (Figure 12). Further increases in smectite content continued to decrease chalk strength, but at a reduced rate. The very high concentration of smectite clay in veins as compared to the chalk matrix (Figure 5) resulted in the veins being exceptionally weak elements in the rock mass. As such, the veins again served as macroscopic flaws and initiated failure. All faults show at least two displacement episodes, one during vein formation, as indicated above, and a brittle episode following complete vein crystallization. It is during this second faulting event that the role of smectite clay in the failure process is important. The open fracture networks developed during this second deformation episode. Whether these two events represent a continuum of deformation we do not know. However, their

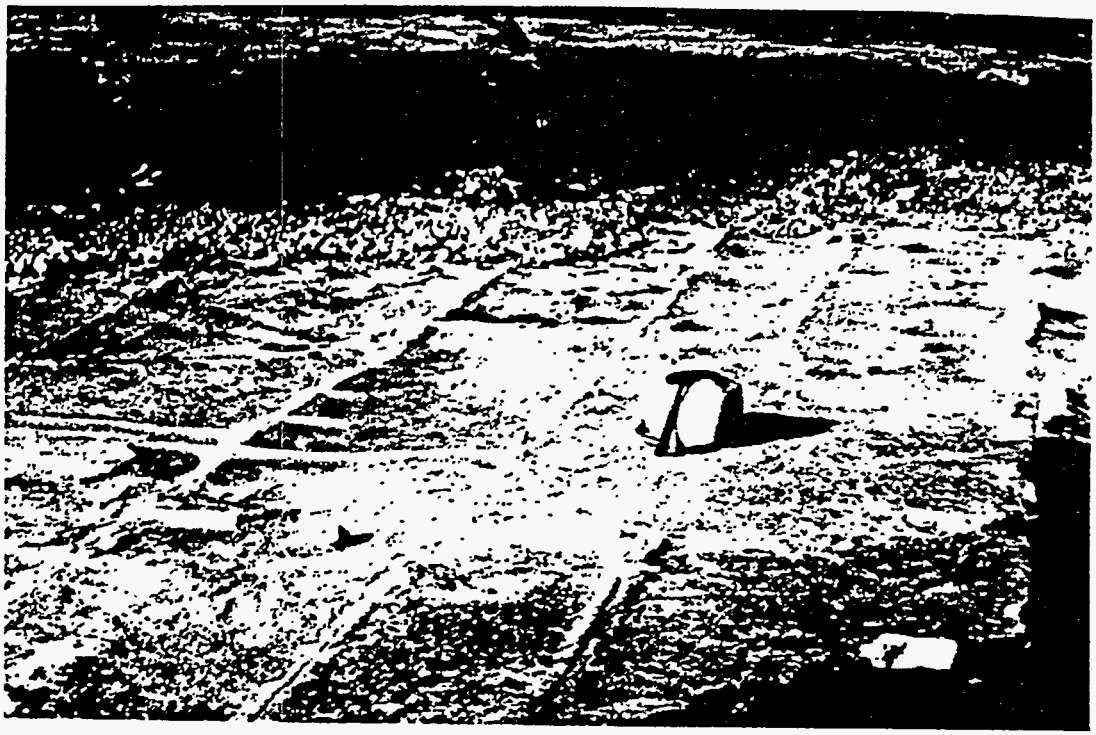

Figure 10. Small displacement faults and natural hydrofractures. a) Systematic set of natural hydrofractures in rhythmic chalk-marl sequence in the Burditt Marl Member of the Austin Chalk at Sycamore Creek, 15 miles southeast of Del Rio. Note the preservation of greater chalk bed thickness adjacent to the fractures. Arrow in 10a shows location of small displacement fault shown in detail in 10b. b) Small displacement fault (2 cm) localized by a vein swarm in 12 cm thick chalk bed. Fault displacement rapidly decreases to 0 in overlying and underlying marl beds.

Figure 10. (continued). c) Thin-section photomicrograph of a small displacement fault localized by and deforming a vein swarm in basal chalk section from the Exxon G. Longenbaugh #1. Sample from -7005 feet, photo is 0.25 mm tall, crossed nicols.

very different character suggests they are discrete and separate events.

## Fracture Statistics

Regardless of the specific structural setting, several characteristics of these later fracture populations are similar. Both fracture length and spacing, measured on scan lines, show a negative exponential distribution (Figure 13). Accordingly, most fractures are small and closely spaced. Smaller fractures show less preferred orientation than larger fractures (Figure 14). Overall, fracture populations from each locality show similar, moderately well-developed preferred orientation. At all localities two orthogonal fracture sets are present (Corbett and others, 1987). The orientation of the master fractures was evidently controlled by the orientation of major faults and folds. The master fractures strike parallel with these structures and generally have dips near vertical.

Master fractures appear in some cases to have periodic spacing. Plots of fracture length versus distance along a scan-line suggest that

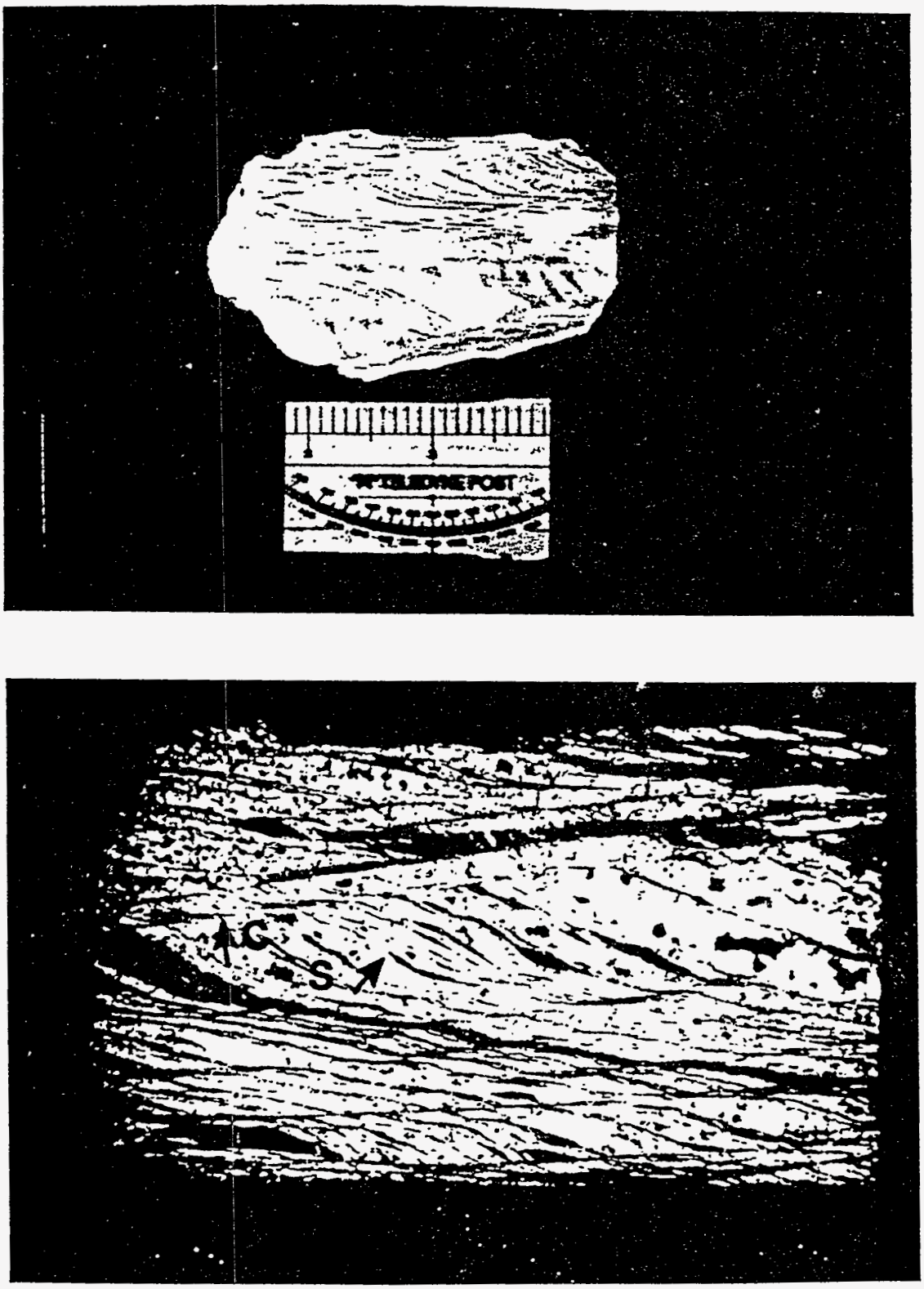


Figure 11. S-C type fabrics developed where veins forming the S-fabric were rotated by fault displacement and later cut by brittle shear surfaces forming the C-fabric. a) Gouge sample from a fault with approximately 2 m of stratigraphic throw, Longhorn quarry, San Antonio. b) Whole thin-section photograph of sample in (a) shows the variability in offset of different vein swarms as indicated by the variability in vein rotation, thin - section is 4 cm wide, crossed nicols.

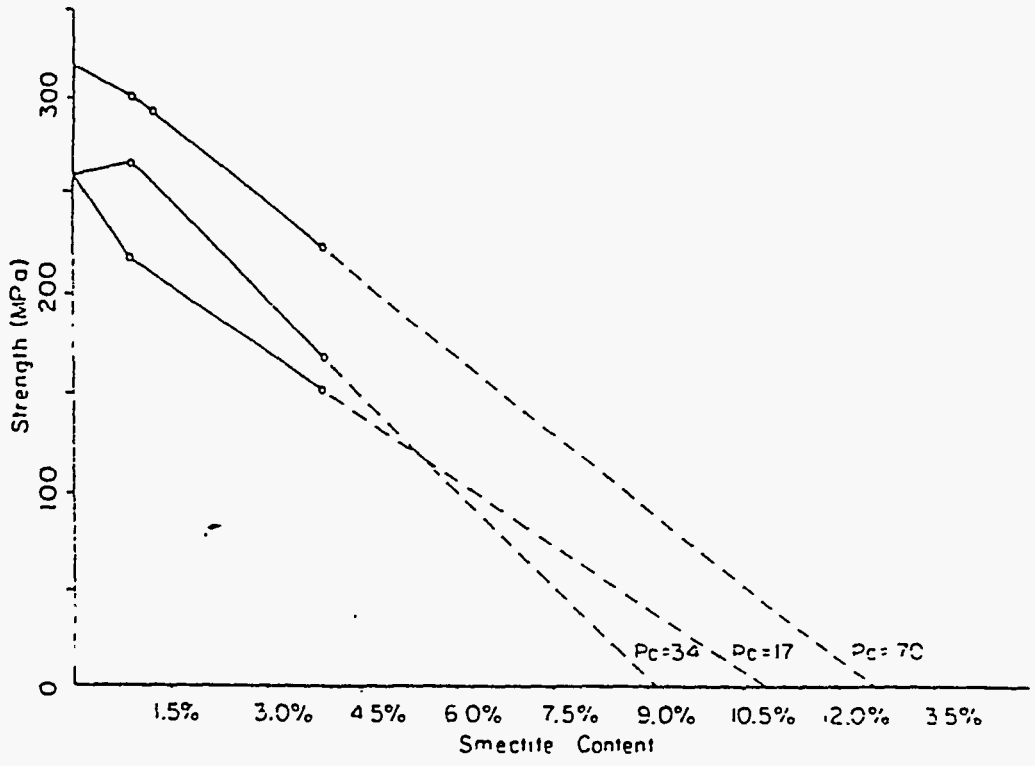


Figure 12. Plot of strength versus smectite content for experimentally deformed samples of the Atco Chalk Member reported in Corbett and others (1987) demonstrates the rapid reduction in strength with increasing smectite content.

the longer fractures recur with a predictable frequency (Figure 15). Indeed, these plots resemble a waveform with fracture length equivalent to amplitude, spacing equivalent to wavelength, and the apparent decrease in fracture length with distance from faults indicating a damping function. Since these data are irregularly spaced they are not amenable to standard methods of time series analysis. We are currently investigating several modeling strategies using non-linear estimation algorithms. Our first goal is to predict fracture length as a function of distance along a scan-line. If we are able to realize this first objective, we will then seek to determine the underlying physical process responsible for the repetition.

## Brittle Fracture Characteristics

Fracture surface features and the interaction of fracture tips indicate the chalk behaved in a very-brittle fashion (Figure 16). Plumose and hackle structures are commonly developed on fracture surfaces. The hackles are generally of high relief indicating a comparatively fast velocity for joint propagation (Pollard and Aydin, 1988). Commonly, fractures initiate and/or terminate at faults, other fractures and bedding surfaces. Shear fractures can be seen to merge into extension fractures. In experimental rock deformation this is associated with very brittle failure (Handin, 1966), especially at very-low effective pressure. Extension fractures commonly show an en-passant relationship, where the stress field at the tip of an existing fracture influenced the trajectory of another fracture propagating towards it. The second fracture tip curves away from the first as it approaches and overlaps it. When it is beyond the influence of the localized stress field associated with the tip of the first fracture, the second fracture tip curves towards the first fracture and merges with it, and vice-versa. The en-passant relationship suggests a relatively low, far-field differential stress, since a large differential stress would negate the small local perturbation produced by the fracture tip. Relative timing for fractures of different orientation, as inferred from cross-cutting relationships, is dependent on specific structural setting. We discuss the cross-

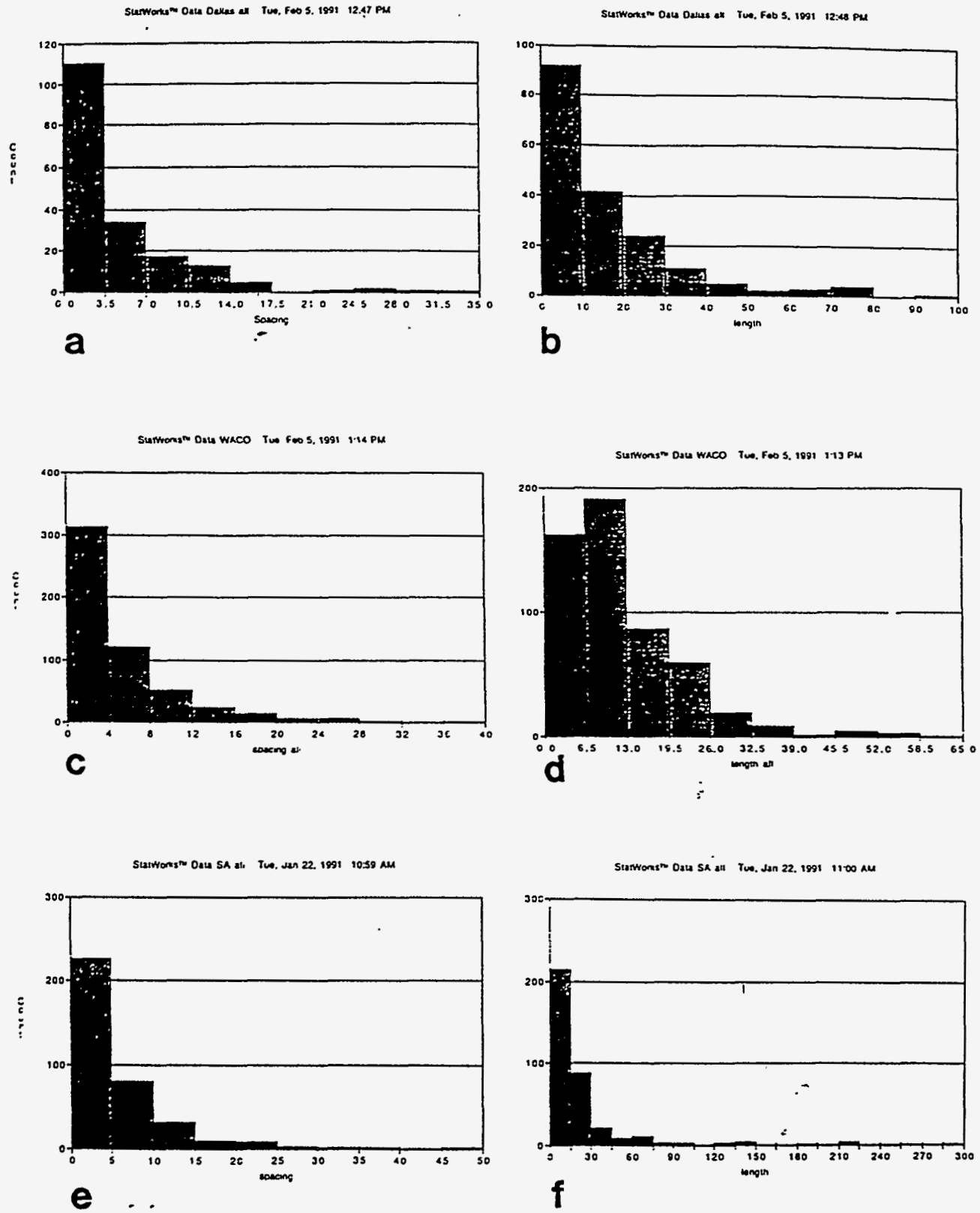


Figure 13. Plots of frequency versus length and spacing (reported in inches) respectively for fracture populations from Dallas (a & b), Waco (c & d), and San Antonio (e & f).

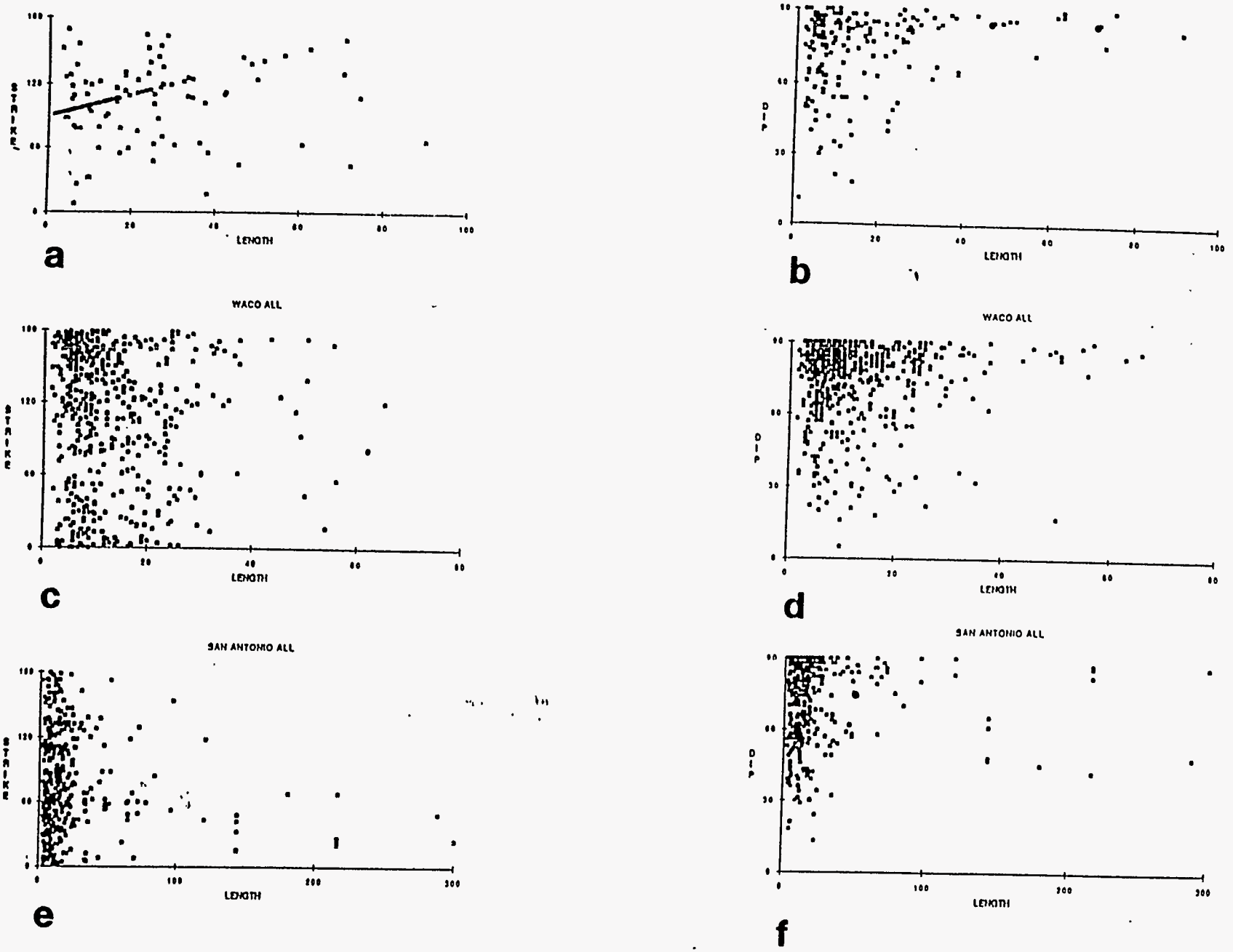


Figure 14. Plots of Strike and dip versus fracture length (reported in inches) for Dallas (a & b), Waco (c & d), and San Antonio (e & f).

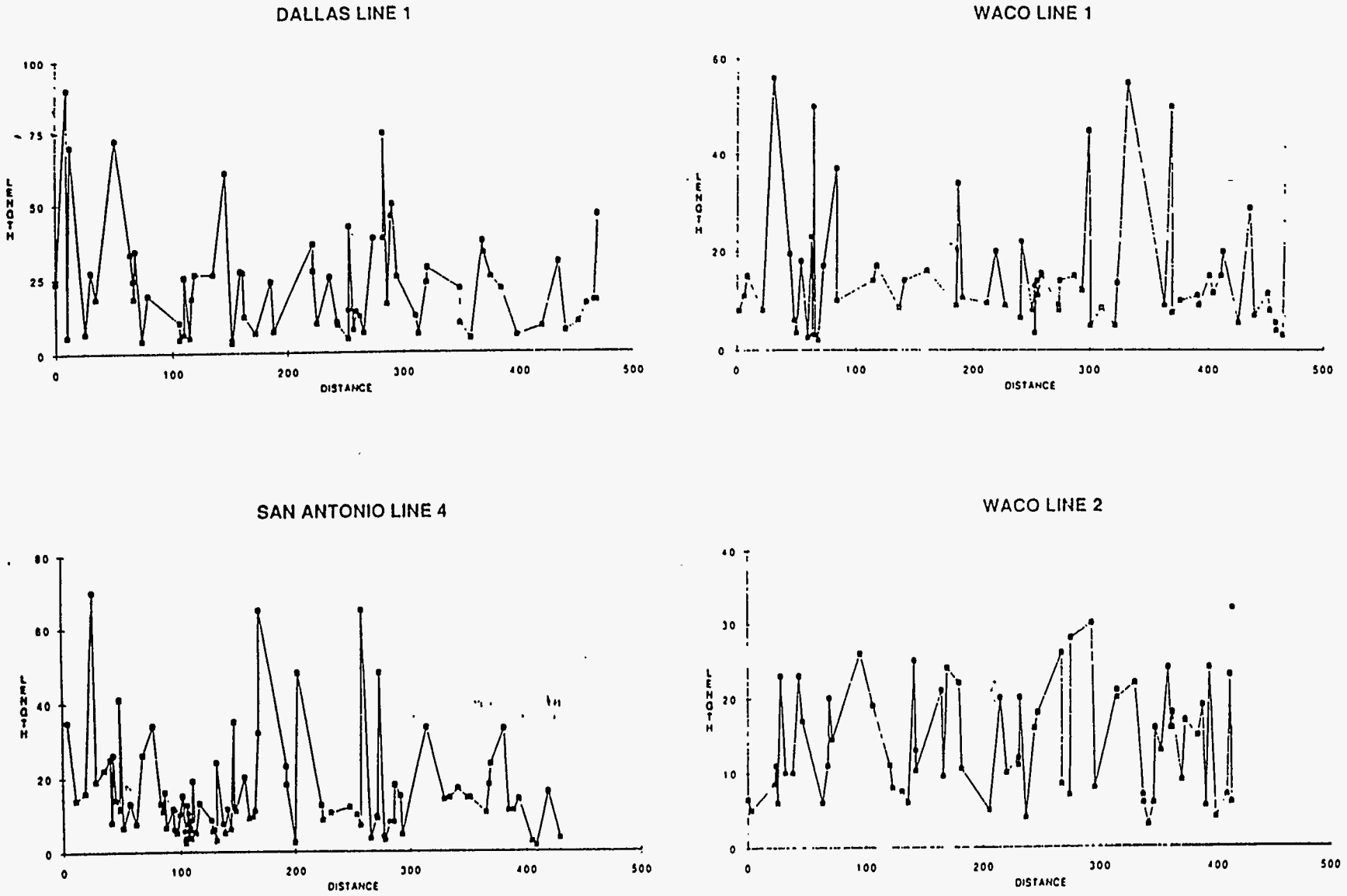


Figure 15. Plots of fracture length (reported in inches) versus cumulative distance along scan-lines tend to have a periodicity which resembles a waveform with a characteristic frequency and amplitude, particulary for the longer master fractures.


Figure 16. Surface features and styles of fracture interaction. a) En-passant juncture of fracture tips for a joint forming fracture set, bedding plane view, Old Alamo Quarry, San Antonio. b) Plume structure and very-coarse hackle marks show horizontal propagation for this vertical, NE trending extension fracture which terminates at a cross-fracture, Old Alamo Quarry, San Antonio.


Figure 16. c) Plumose structure shows this vertical, NE trending fracture propagated vertically, initiated at a shallow-dipping fracture and terminated against another shallow-dipping fracture, Old Alamo Quarry, San Antonio. d) Shear fractures wedging into an extension fracture, bedding plane view, Old Alamo Quarry, San Antonio. Note the banding produced by multiple invasion episodes of oxidizing, vadose zone, groundwater.

cutting relationships with respect to each field locality in the second section of the guide.

## Fractures and fluid flow

Abundant qualitative evidence indicates that fractures are preferred avenues for fluid flow (Figure 17). All of the quarry sites have excavated below the top of the water table. The upper quarry levels were within the vadose zone which is characterized by white to buff colored, bleached, oxidized chalk. Below this zone of alteration the chalk is generally a medium grey color where it is unoxidized. Additionally, pyrite in the alteration zone, in fracture fillings and burrows in the chalk matrix, is almost completely weathered to hematite and limonite. Below the alteration zone pyrite is unaffected. Infiltration of oxidizing vadose zone water, selectively along fractures into the zone of saturation, is evident from the bleached zones surrounding fractures in the zone of saturation. Generally, these alteration halos are symmetric with respect to the fractures. The halos are banded reflecting variation in depth of matrix penetration for specific fluid compositions. Characteristically, three alteration regions can be recognized outward from a fracture. There is an outermost band of buff colored chalk, its outer limit marks the oxidation front, and its inner limit is marked by the limonite front. The middle band is a brown to ochre color due to limonite staining, it lies between the limonite front and the flushed front. The innermost band is a white color and straddles the fracture. The absolute width of these alteration bands is variable at a specific locality and between localities. Numerous factors affected the depth of alteration, including the chemistry of the vadose zone waters, depth below the top of the water table, length of exposure to vadose zone waters, dilution of vadose zone waters within the zone of saturation, and repetition of vadose water invasion. This last effect is demonstrated by numerous concentric alteration bands around some fracture sets.

For petroleum production the following attributes of groundwater flow along and across fractures appear to be significant: (1) Closed, tight fractures, some partially filled with vein minerals, have much higher permeability than the chalk matrix, as evidenced by the alteration bands mantling fractures originally below the water table in the zone of saturation. (2) Very minor differences in fluid density were evidently sufficient to drive fluid flow along the fractures for appreciable distances. Higher density vadose zone waters flowed down fractures for tens of meters into the zone of saturation. (3) Permeability of the chalk matrix perpendicular to fractures appears to be homogeneous based on the symmetry of the oxidation bands mantling the fractures. (4) Depth of matrix penetration is a function of numerous factors, but chemistry of the invading fluids which controls fluid density differences, depth of invasion below the water table, and total time for the invasion process are likely controlling factors. (5) Fracture orientation appears to have little effect on the transmissivity of vadose zone waters into the zone of saturation. (6) Vadose zone alteration extends to greater depth along fault zones and folds, the areas of higher fracture intensity.


Figure 17. Alteration zones produced by invasion of oxidizing, vadose zone groundwater into the zone of saturation. a) Oxidation front (white) and limonite front (dark grey) around an isolated extension fracture in grey chalk, Lafarge quarry, Dallas. b) Selective permeability along fractures is displayed by fracture swarm containig the fracture in (a).

# Description of Field Localities

## Old Alamo Cement Quarry, San Antonio

The old Alamo Cement Quarry is located at the southern end of the city of Alamo Heights, in north suburban San Antonio. The main entrance to the quarry is off Jones-Maltzberger Road near the intersection with Tuxedo Drive. Access to the quarry is restricted, permission to enter should be obtained in advance from the Alamo Cement Company, P.O. Box 34807, San Antonio, Texas 78265. The quarry was abandoned in 1982 and is currently being in-filled and reclaimed. The property is for sale. Thus, the availability of this locality for future study is questionable. You may note with some wonder the proximity of relatively high-priced homes to the quarry rim (Figure 18). It seems certain that pressure from these affluent home owners will influence the future use of this location.

Approximately 75 m of chalk is exposed at this location, all within the basal Atco Chalk Member. The deepest level of the quarry is below the current water table, producing a small pond. The floor of this level is approximately 3 m above the Austin Chalk-Eagleford Shale contact. The chalk is characterized by rhythmic bed sets, intervening marls are generally less than 1.0 cm thick, but range up to 30 cm. Internal structure in the chalk beds is mostly lacking, save for occasional burrows or macro-fossil fragments. The chalk is essentially homogeneous and massive.

One of the primary features of interest at this location are the very-long joints which are well exposed, in profile, in the deepest quarry

Figure 18. Systematic joint set developed at the base of the Atco Chalk section in the Old Alamo Quarry, San Antonio.

level, and in map view on the adjacent quarry floor (Figure 18). The principal structural setting observable here is a listric normal fault system exposed in profile on a north-south trending quarry wall. Additional fracture characteristics well displayed at this location are fracture surface markings, fracture tip interactions, and selective permeability along fractures and the associated alteration bands, and the containment of fractures to individual beds by very thin marl breaks exclusive of the joints and away from faults.

The joints have an average strike of N40E and are vertical. In the dip direction their lengths range from 1 m to more than 4 m, which is the limit of exposure. In the strike direction they have lengths ranging from 1 m to more than 12 m. Spacing between joints varies from 0.2 m to 2.5 m, averaging 1.0 m. Pyrite, clay and sparry calcite vein mineralization is variably present along the joints. The joints have widths of less than 0.1 mm to 4 mm. wider zones are typically filled with vein minerals. Plumose structures on joint faces show that individual fractures originated at bedding surfaces, propagated vertically to the center of an individual bed and then propagated laterally. Individual fractures which comprise the joints range in strike length from 5 cm to 2.5 m, with their dip length equal to or less than the thickness of the bed in which they formed. Fracture tips most commonly display an en-passant relationship in map view, but en-echelon relationships are also present. Fractures with an en-echelon relationship are preferentially left-stepping.

We interpret the vein-filled fractures exposed at higher levels in the quarry as equivalent in age and origin with the fractures which form the large systematic joints. While the vein mineralization is not identical to that in the joints it is similar, and the differences appear related to stratigraphy. Pyrite is not as abundant in higher-level veins, evidently because it was derived primarily from pyritized burrows which are common only near the base of the section. Otherwise, both sets of veins possess equivalent vein mineralogies. Additionally, they have the same orientation, and are the oldest fracture system present. They are invariably cut-off by faults and all other fractures terminate against them.

Of particular interest is the observation that the vein-filled fractures only form a systematic joint set at the base of the formation. We speculate that this may be a consequence of their origin as hydrofractures associated with dewatering of the Eagleford Shale. Near the base of the formation, and the source of the invading fluids, the joints were formed by propagation of fractures upwards into successively higher beds. As distance from the underlying shale increased, the localization of the fluid-pressure differential decreased due to bleed-off into the surrounding chalk matrix. This could result in discontinuous fractures at higher stratigraphic levels controlled by zones of high matrix permeability, rather than continuation of the joint system.

We have made a map at a scale of 1:24 of a portion of the floor of the Alamo quarry in a location about 200 m from the area of the joints and listric fault system (Figure 19). Our purpose was to better characterize the fracture network, especially mutual intersections or fracture connections. Interconnectivity has been shown to be directly related to the hydraulic conductivity of a fracture network. Our goal was to characterize the directional nature of the connectivity and thereby better predict, at least qualitatively, directions of easy fluid flow.

A remarkable aspect of the mapped fractures in this quarry, which are distant from major faults, is the lack of connections. The fracture network is characterized by a strong preferred orientation of fractures and relatively less dispersion than in other quarries to be visited on this trip (Figure 20). Due in part to the good preferred orientation the fractures on this map display, on average, there are only 2 connections per fracture, or 1.4 on a per foot of fracture basis. In addition, there is a greater proportion of "blind" or completely unconnected fractures at this level of exposure than in other quarries we will visit; the percentage of blind fractures is even greater in other parts of the quarry. Similarly, of those that are not blind, nearly 90% have a free end, or fracture tip, unconnected to other fractures; only 7% of all fractures abut other cracks on either end. This connectivity is directional because there is a high preferred orientation to the fractures (Figure 20). However, because a significant portion of the fractures are filled with minerals, it is unclear how directional the

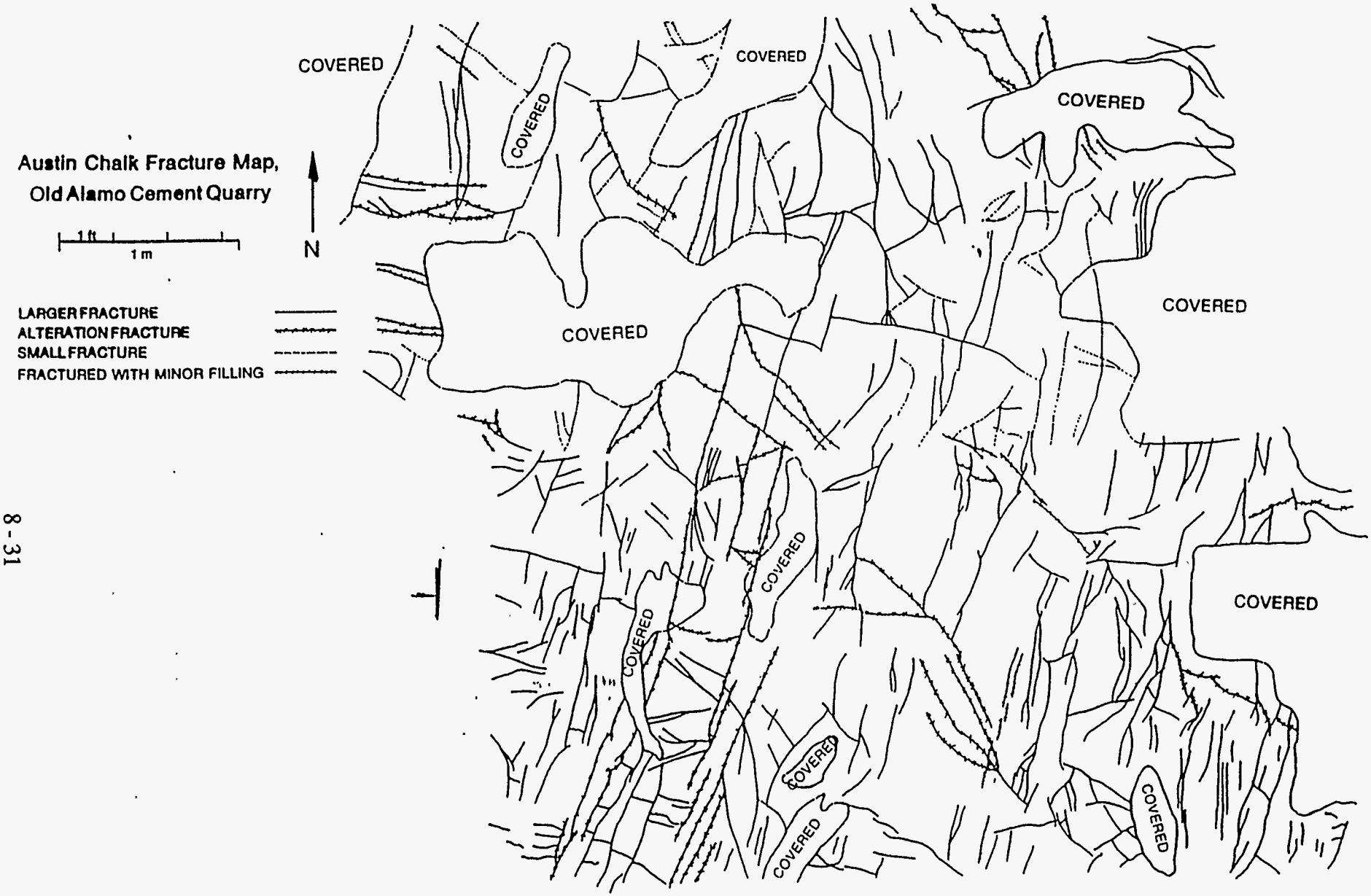


Figure 19. Map of a portion of the quarry floor of the Old Alamo Cement Quarry, San Antonio. The mapping was done at a scale of 1:24. A large percentage of the fractures are altered or filled and isolated from other fractures.

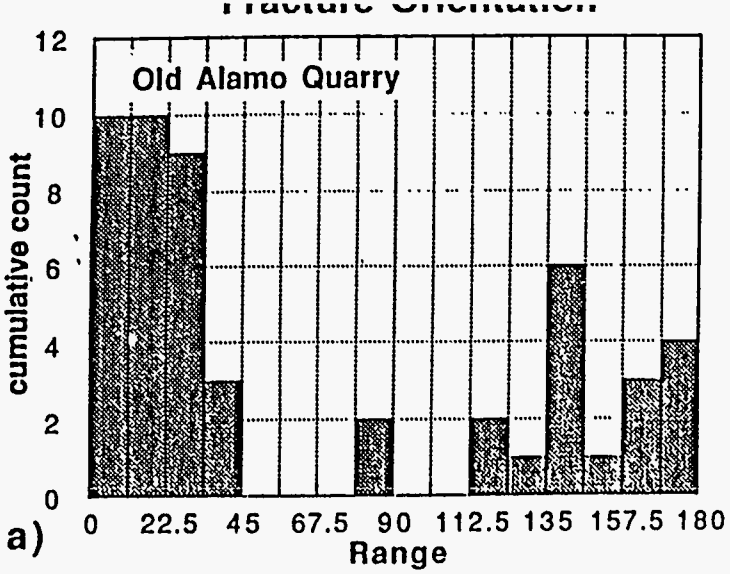


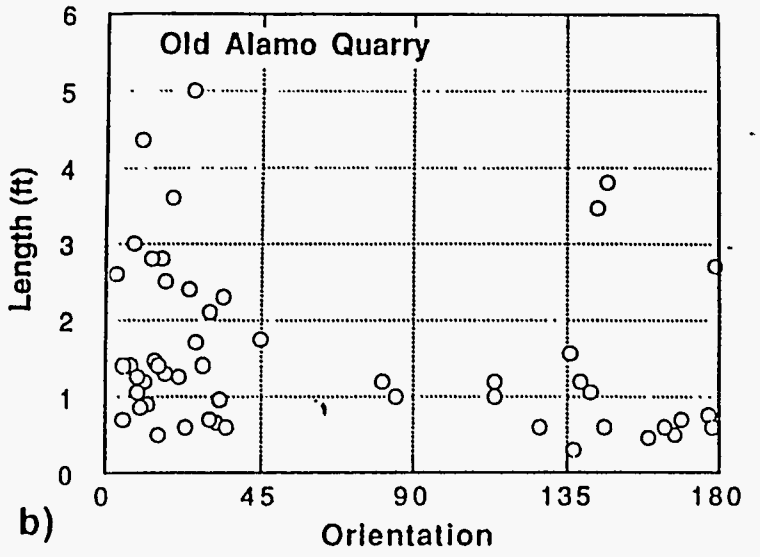


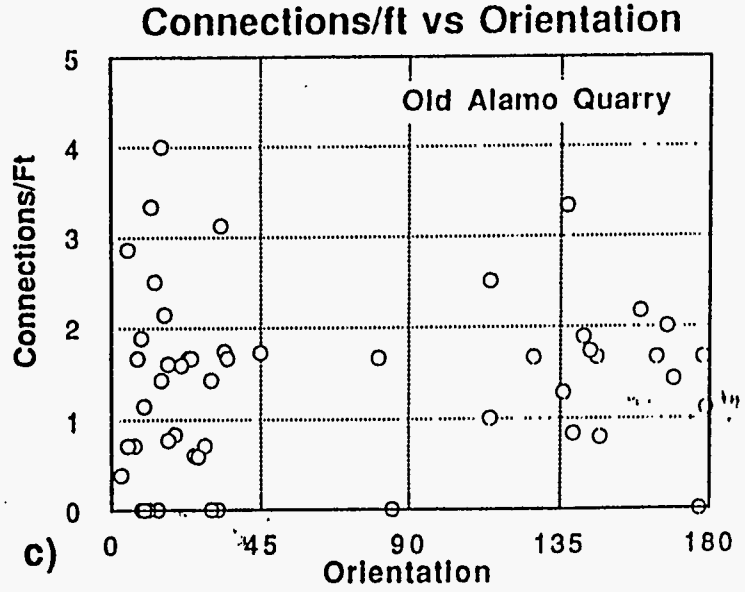


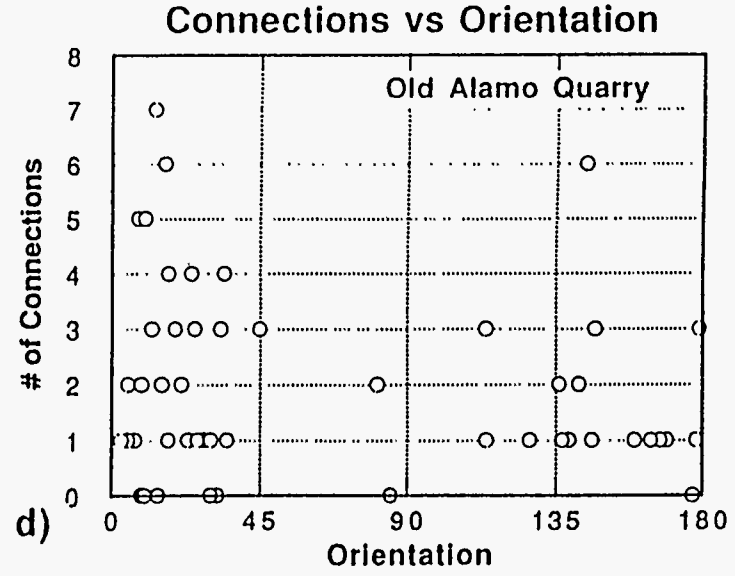


Figure 20. Plots of data from the Old Alamo Quarry map. a) Frequency plot of fracture orientation. One well developed fracture set exists. b) Plot of length versus orientation. The most prevalent set also harbors the longest fractures. c) Fracture connections (or intersections with other fractures) per foot of fracture length versus orientation. The average connections per foot are greater for the well-developed fracture set. d) Number of connections versus orientation. The absolute numbers of connections is greatest for the longest fractures, as is to be expected.

hydraulic conductivity would be at the present time.

Attributes of the joint system which may be important for exploration and production include the following: (1) Our observations suggest that in an extensional environment well-developed systematic joints are restricted to the basal 10 m of the chalk. This may be a consequence of formation by the natural hydrofracture process. (2) Joints are near vertical and strike parallel to the regional structural grain. (3) Joints are partially vein filled and may require stimulation to achieve acceptable permeability and production.

The listric fault system at this location is composed of a main fault which accounts for virtually all of the displacement, several subsidiary faults of minor displacement in both the hanging wall and footwall, and related shear and extension fractures (Figure 21). The main fault has a headwall segment which has a maximum dip of 60°. The knee segment is a displacement transfer zone, where the headwall segment fault dies-out into the hanging wall, with a commensurate increase in displacement on the fault surface which becomes the sole fault segment. The sole segment roots in a 30 cm thick marl interbed in the chalk sequence. Subsidiary footwall faults are all steeply dipping and parallel to the headwall segment of the master fault, they are spaced 1 m to 2 m apart. In contrast, hanging wall subsidiary faults range from steep to shallow dips and are both truncated by and merge with the sole segment of the main fault. Hanging wall subsidiary faults show a systematic increase in spacing with distance from the main fault and are present up to 35 m away from the main fault.The main fault has 10 m of stratigraphic throw. Subsidiary footwall faults, of which there are three, have a total stratigraphic throw of 2.5 m, while the eight subsidiary hanging wall faults have a total stratigraphic throw of 1.8 m. The main and footwall faults are located in a zone of high vein density. They have truncated and rotated earlier formed veins, and been the site of later vein formation. Subsidiary faults in the hanging wall are devoid of vein mineralization.

The main and footwall subsidiary faults have dip lengths in excess of 30 m, the limit of outcrop exposure. Dip length of the hanging

Figure 21. Listric normal fault system and associated fractures. a) View of the entire fault system shows the increased fracture intensity in the hanging wall compared to the footwall. Arrows indicate the headwall and sole segments of the main fault, note 1.5 m tall individual for scale.


Figure 21. (continued). (left). Listric normal fault system and associated fractures. b) Detail of the headwall and knee segments shows antithetic faults, displacement transfer in the knee segment, and small-displacement footwall faults parallel to the headwall segment.

Figure 21. (continued). (below). Listric normal fault system and associated fractures. c) Detail of the sole segment (individual pointing) show faults and shear fractures in the hanging wall are synthetic to the main fault and are spaced progressively farther apart away from the headwall segment.

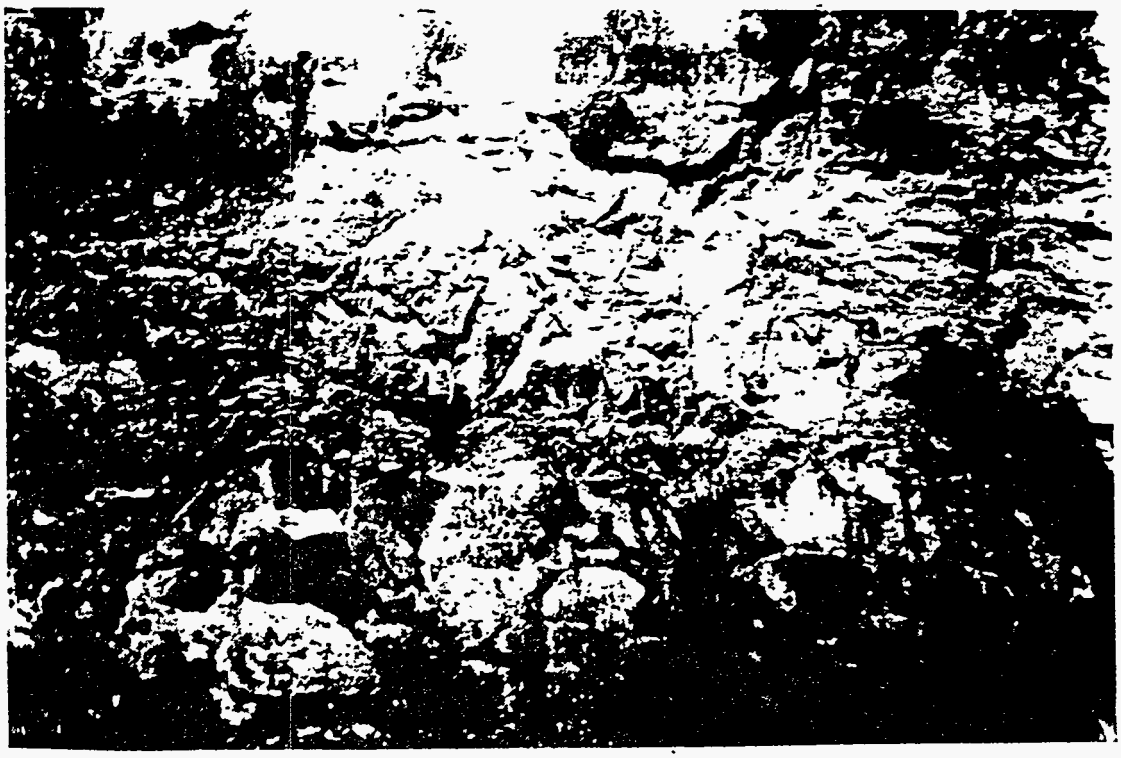

wall faults decreases from 12 m directly adjacent to the main fault to 1.8 m at a distance of 35 m. Both the footwall and hanging wall possess a set of vertical extension fractures, but these fractures are 1.5 times as abundant in the hanging wall as they are in the footwall (Figure 22). Fracture lengths show the same trend as fault length in the hanging wall, while in the footwall the length is generally limited by bed thickness, i.e., the fractures are bed contained. Two sets of shear fractures also are present. The first set is synthetic to the main and subsidiary faults in the hanging wall, and is restricted to the hanging wall. These fractures decrease in abundance, decrease in length, and increase in spacing away from the main fault, against which they truncate. The second set of shear fractures is conjugate to the first and antithetic to the main fault. In contrast with the first set, these fractures are present in both the footwall and hanging wall. They terminate against faults and first set fractures. The fracture and fault relationships are depicted schematically in Figure 23.

The following aspects of listric normal faul systems appear to be viable concerns for exploration and production: (1) Subsidiary footwall faults parallel the high-angle segment of the main listric fault and are within 5 m of the high-angle segment. Fracture intensity away from the subsidiary faults in the footwall decreases rapidly. (2) The hanging wall is more highly fractured than the footwall, and long, through-going, master shear fractures synthetic to the main fault are restricted to the hanging wall. (3) For master fractures, length decreases and spacing increases with distance away from the main listric fault suggesting an optimum horizontal drilling distance may be established.

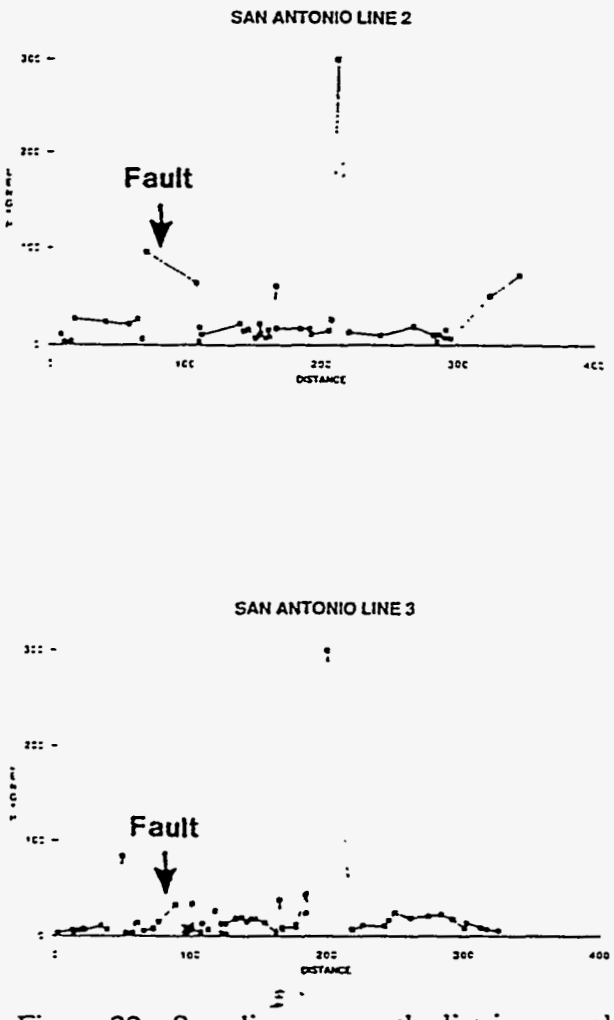


Figure 22. Scan lines across the listric normal fault system shown in Figure 21, main fault is indicated by an arrow. a) 21 in thick chalk bed. b) 43 in thick chalk bed.

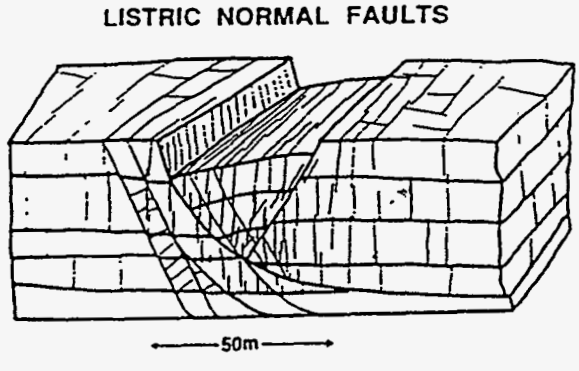


Figure 23. Schematic illustration of a listric fault system.

# Longhorn Cement Quarry, San Antonio

The entrance to the Longhorn Cement Quarry is located off Perrin-Beitel Road near the intersection with Schurtz Road. This quarry also is owned by the Alamo Cement Company, and again entrance is allowed only after obtaining prior permission.

Approximately 15 m of the middle and upper Austin Chalk are exposed at this location (Cloud, 1975). The depth to the underlying Eagleford Shale is not known. In most respects the chalk here is very similar to that exposed in the Old Alamo Quarry. The principal difference is the degree of weathering and oxidation. Since these exposures were much closer to the original land surface, they are more strongly weathered than the outcrop we viewed in the morning.

Two monoclinal flexures and their associated faults, vein systems, and open fracture network are the structures of primary interest at this locality (Figure 24). The best developed S-C fault fabrics occur in the fault zones which have produced these monoclinal folds. Also of interest is a large, high-angle normal fault. Quarrying has resulted in excellent exposure of the slickensided fault surface, and the 10 cm to 15 cm thick, sparry calcite vein material which fills the fault zone.

The monoclines exposed here are NW facing, possess horizontal upper and lower limbs, and a gently dipping (5° to 8°) interlimb between their anticlinal and synclinal hinges. They are near (400 m to 800 m), but not directly adjacent to NW dipping faults of the Balcones system. The total structural relief across these folds, from their upper to lower horizontal limbs, ranges between 5 m and 8 m across a horizontal distance of 50 m.

Four ordered fracture sets are developed in conjunction with these fold structures (Figure 24). The vein filled fractures constitute the first two fracture sets. There are two dominant orientations for these extension fractures, one group (1A) strikes N20E parallel to the trend of the monoclinal folds with dips near vertical, the other group (1B) strikes the same direction but dips range from 10°NW through horizontal to 30° SE. Since these vein-filled fractures are mutually cross-cutting they must have formed simultaneously. The approximately horizontal set indicates that pore fluid pressures were abnormally high and may have approached the overburden pressure (Corbett, 1989). These fractures are variable in dip length ranging from 5 cm to 1 m. The essentially cliff exposure precluded direct determination of the strike length for all fractures associated with these monoclinal folds.

A conjugate set of shear fractures constitutes the second fracture set. They strike N20E and dip from 10° to 30° SE and NW, but exhibit preferential development of SE dipping fractures. They are approximately twice as abundant as their NW dipping counterparts, and have overprinted the earlier formed, shallowly-dipping extension fractures. Frequently, the SE dipping shear fractures have developed into small faults which were localized by both groups of veins (Figure 24). The displacement across these faults is variable, ranging from 1 cm to 30 cm. Their dip length is also highly variable ranging from 1 m to 5 m. These faults apparently accommodated lateral translation during the initial stages of fold growth. They probably allowed for flexural slip in the absence of thick intervening marls or other weak beds which could accommodate nearly horizontal displacement.

Steeply-dipping conjugate shear fractures which cross-cut and offset the faults of the second set constitute the third fracture set. These fractures again strike N20E, but shows unequal development of the two conjugate orientations. Each group in the conjugate set has an average dip of 60°, but NW dipping fractures are roughly twice as abundant as SE dipping fractures. As with the shallowly-dipping conjugate set, the more abundant NW dipping fractures have preferentially developed into small displacement faults. These faults also contain the rotated veins characteristic of the shallowly dipping, second set faults. Offset across these NW dipping faults ranges from 10 cm to 2 m, and in composite they


Figure 24. Monoclinal folds and associated fractures and faults. a) Large Balcones system fault with coarse calcite vein filling and 200 m wide monoclinal flexure in the hanging wall. b) Monoclinal flexure produced by numerous small faults has 8 m of relief across a distance of 50 m. Arrows show the location of highest fracture/fault intensity.

Figure 24. (continued). Monoclinal folds and associated fractures and faults. c) Detailed view of high fracture/fault intensity in the short interlimb of the flexure between the anticlinal and synclinal hinges.

Figure 24. (continued). Monoclinal folds and associated fractures and faults. d) Low-angle fault which allowed for flexural slip during the early stages of fold growth is cut by later high-angle fault which fans-out into a series of four shear fractures.

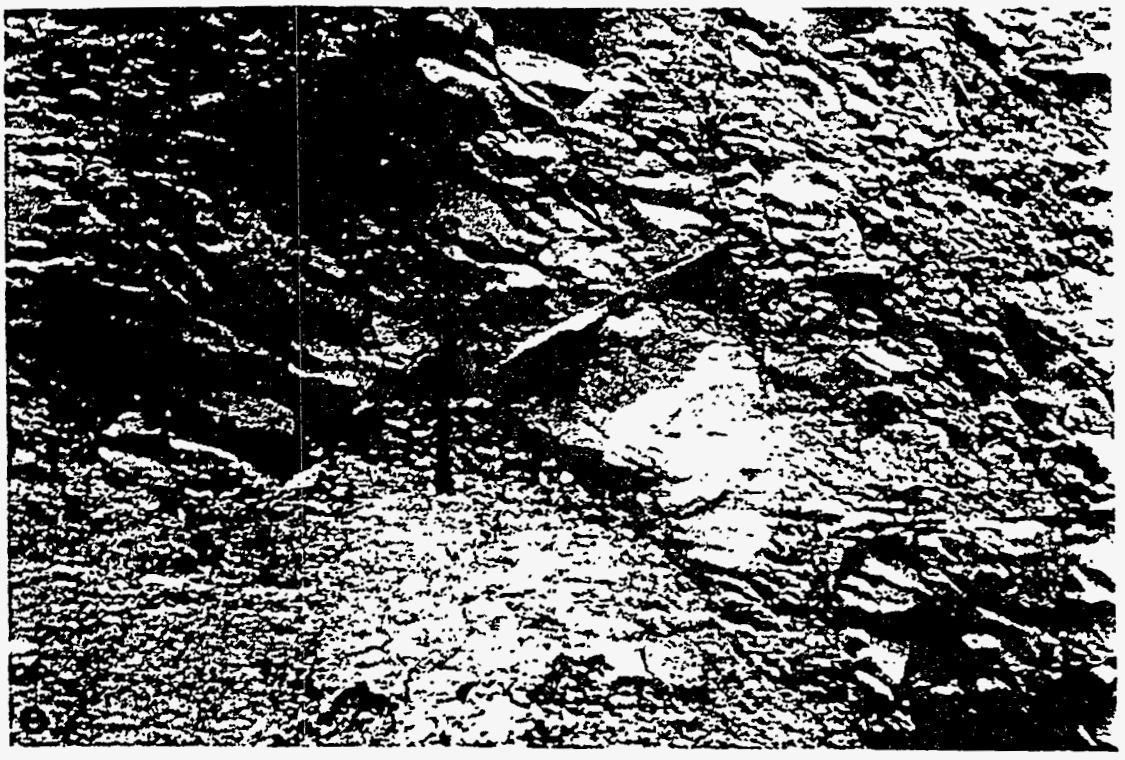

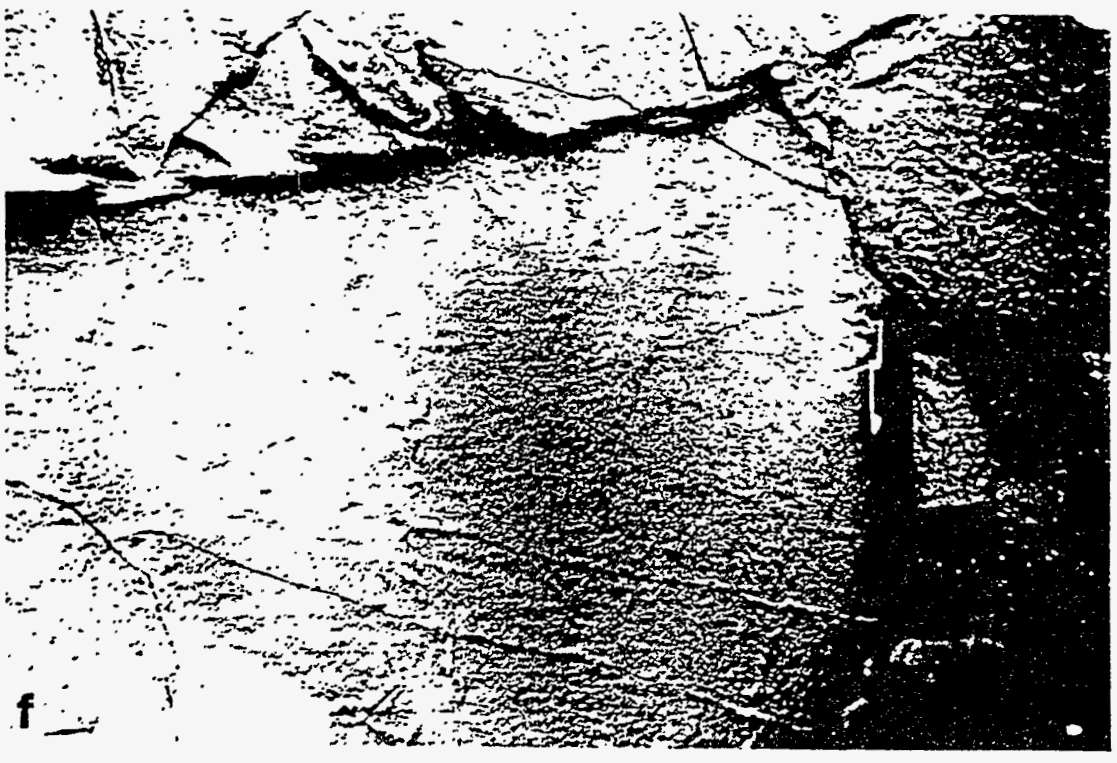

Figure 24. (continued). Monoclinal folds and associated fractures and faults. e) Low-angle fault with resistant weathering, S-C fabric vein gouge is offset by later high-angle faults which merge and also contain S-C fabric vein gouge. f) Conjugate set of low-angle shear fractures.

account for the folding seen at a smaller scale. If these faults were related to fold curvature they should show the highest intensity along the hinges. However, the highest intensity is in the vicinity of the short interlimb. We interpret all three fracture/fault sets as having formed in response to development of the monocline as a drape fold above a buried fault. The fault and fracture distribution on these structures is shown schematically in Figure 25.

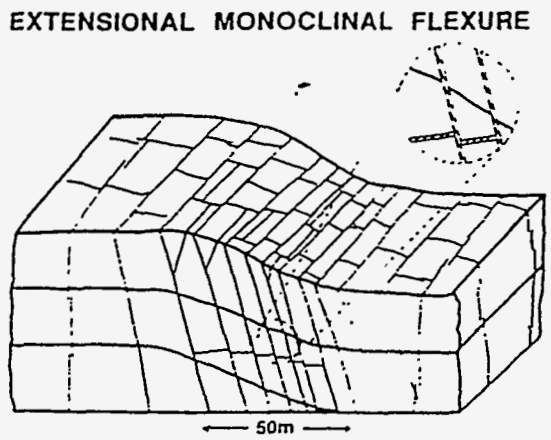


Figure 25. Schematic illustration of monoclinal flexures and associated faults and fractures.

Several observations about the style of fracturing on the monoclines may be relevant to exploration for and production from these structures. (1) The highest fracture intensities are in the interlimb region between the anticlinal and synclinal hinges. (2) Shear fractures and small faults greatly predominate over extension fractures on these folds. Shallowly-dipping shear fractures and small faults are well developed. This suggests that, to optimize borehole-fracture intersections in this structural setting, a shallowly-descending deviated borehole is preferable to a horizontal borehole. (3) Most of the shear fractures and small faults are vein filled, suggesting that stimulation will enhance permeability and well performance.

A major Balcones system fault is exposed in three-dimensions by the quarrying operation. Throw on this fault exceeds the height of the outcrop which is approximately 35 m. The fault zone varies from 10 cm to 30 cm wide and is filled with very-coarse-grained vein calcite. These calcite crystals have grown from the fault-zone walls towards the center and show the dog-tooth crystal habit. Vuggy space remains in the center of the veins, indicating in conjunction with the crystal habit that they grew into open space. The fault zone walls, and vein walls within the fault zone, are prominently striated, demonstrating that at least part of the displacement history post-dates vein formation. Notably, the vein calcites are completely undeformed, even though present in the shear zone during displacement. Footwall strata within 2 m of the fault zone are much more indurated than further away or than hanging wall strata. Evidently footwall strata adjacent to the fault were cemented by the same fluids responsible for vein mineralization. Close inspection reveals numerous, small, isolated veins in these rocks. We believe this fault served as a dewatering conduit for over-pressured fluids from the underlying Eagleford Shale. We infer that this and other major Balcones system faults developed after the monoclinal flexures, because veins were evidently necessary for the formation of the small faults which produced the folds and would be less likely to form if large faults capable of alleviating the over-pressure in the underlying shale were already present. Since hanging wall strata show no rotation towards the fault zone, and the fault plane shows no decrease in dip, it is unlikely that this fault has a listric geometry.

# Lehigh Cement Quarry, Waco

The Lehigh Cement Quarry is located approximately 6 miles west of Woodside off U.S. Highway 84 at 100 Wickson Road, Waco. The quarry is owned by the Lehigh Portland Cement Company, P.O. Box 2576, Waco, Texas 76702-2576. Access to the quarry site is restricted and only available with prior authorization. This quarry site was abandoned in 1987. Consequently, the outcrop here is fresher than in either of the San Antonio quarries.

Approximately 30 m of the Atco Chalk Member is exposed in the quarry. The contact with the underlying Eagleford Shale is exposed at several localities in the main quarry, and extensively exposed in the shale pit. Lehigh Cement quarried the Eagleford Shale for illite clay, which was used as an additive in cement production. The chalk here is characterized by beds ranging from 25 cm to 3 m thick. Marl interbeds are thicker here than in San Antonio, ranging from 4 cm to 0.5 m. Again, the chalk beds are generally homogeneous, lacking in any distinct internal structures.

Among the principal structural features of interest at this locality is a main fault of the Balcones system, its vein/gouge zone, and associated fractures. Unique to this northern portion of the outcrop trend are cross-faults, contained within grabens of the major Balcones system. These cross-faults have resulted in a keystone block geometry within the main graben which we have named a graben-in-graben structure. The final structural setting of interest is a small roll-over anticline in the hanging wall of a small displacement cross-fault. An increased fracture intensity is associated with this fold.

Two large displacement faults of the Balcones system are exposed in this quarry (Figure 26). One is a listric normal fault forming part of the main Balcones system graben, while the other is evidently a high-angle cross-fault. Both fault zones are filled by pyrite, clay, calcite


Figure 26. Graben-in-graben fault systems. a) Listric normal fault of the Balcones fault system forming part of a main graben structure. Fault zone is vein filled.


Figure 26. (continued). Graben-in-graben fault systems. b) Nested graben structure produced by small-displacement cross-faults. c) Close-up of lowest, keystone graben block in (b).

veins, analogous to the veins in faults from the San Antonio area. Numerous, small, spider-web veins are present in both hanging wall and footwall strata bounding these fault zones. Vein density is high within 0.5 m of each fault zone and then rapidly decreases. Fault zone veins contain rhombic, coarse-grained calcite, euhedral pyrite, and amorphous clay masses. Vuggy porosity is preserved in many of these veins. Slickensides are well developed on the fault zone and vein walls, with slip surfaces localized by vein clays. The main Balcones fault strikes N40W, and dips 63NE. Slickensides on this fault have a rake of 78° S. The oblique slip on this fault is probably a consequence of variability in displacement along strike. The large cross-fault strikes N34E, and dips 62NW. Slickensides indicate that displacement was directly down-dip for this fault zone. Although no decrease in fault dip is apparent in outcrop, rotation of hanging wall strata into the fault indicates a listric geometry for the cross-fault. This fault probably soles into the Eagleford Shale which is approximately 10 m to 12 m below the level of exposure.

A series of nested grabens bounded by NE striking cross-faults, part of the graben-in-graben structure, are well exposed at the east end of the quarry (Figure 26). Fracture intensity for beds of comparable thickness is highest in the structurally lowest, most internal graben. Here at Waco, and for the northern portion of the outcrop trend in general, fracture intensity scales reasonably well with bed thickness, thinner beds are more highly fractured than thicker beds in the same structural position (Figure 27). This is a direct consequence of the increased thickness of intervening marl beds. Because of the thicker marls, individual chalk beds behave as independent mechanical units. A corollary of this is that most fractures here are bed contained, they die-out at marl interbeds. The only exception is adjacent to faults.

Three systematic fracture sets are present in these outcrops. As in San Antonio, vein filled extension fractures are the oldest fractures present. We suspect they did not form large through-going joints here because the thicker marl interbeds were effective barriers to widespread fluid infiltration from below. The almost exclusive coincidence of veins and faults here is strong qualitative support for this

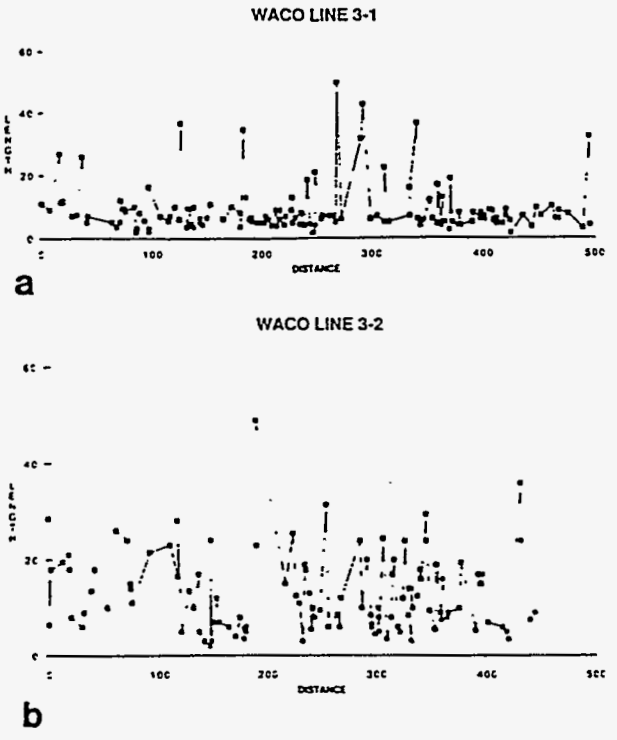


Figure 27. Scan lines in nested graben structure. a) scan line in an 8 in thick chalk bed in the keystone block shown in Figure 26. b) scan line in a 23 in thick chalk bed directly below the bed in (a), separated by a 7 in thick marl.

interpretation. The other two fracture sets evidently formed during faulting. Each of the other fracture sets is represented by shear fractures synthetic to the major faults and a series of related vertical extension fractures. One set is parallel to the principal faults of the Balcones system and strikes N40°W. The other set is parallel with the cross-faults and has an average strike of N50°E. Shear fractures terminate against graben-bounding faults and are almost exclusively restricted to hanging walls. Most shear fractures are within 2 m of a fault. Extension fractures within 3 m of faults transect several beds and terminate against shear fractures or faults. At greater distance from fault zones the shear fractures terminate at bed boundaries. The graben-in-graben structure is shown schematically in Figure 28.

A map of a small portion of the quarry floor was made at a scale of 1:12 about 300 m from the graben-in-graben structure (Figure 29). The map shows similar features to those

HIGH-ANGLE, GRABEN-IN-GRABEN NORMAL FAULTS

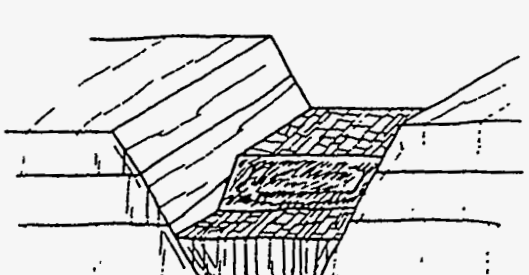


Figure 28. Schematic illustration of the graben-in-graben structure.

described from scan-line data, although there are intriguing differences. Again, the distributions for length and spacing follow a negative exponential law. Also, there is a regularity in spacing among the longest fractures. However, the best developed fracture set and the longest fractures both trend north-south and the next best developed set trends east-west, with much scatter in the latter (Figure 30). Some important aspects of fractures in this map area are: (1) Few of the fractures display free ends (fracture tips); on average 25% of all fractures have a free end. The set that has the most is the N-S set, about one half having a free end. Other orientations are statistically more likely to abut against other fractures. Moreover, all but a few of the fractures on our map are traversed by others, whether their ends are free or not. The mean number of connections per fracture is about 6, although the frequency distribution is skewed toward low values with a high kurtosis. Nevertheless, the number of connections per unit length of fractures is nearly independent of orientation, whereas the most connections are found along fractures oriented N-S (Figure 30). Although we would judge this map area to be highly conductive to fluids if all fractures were open, there would be a petroleum production advantage in intersecting as many N-S fractures as possible due to their increased permeability lengths. (2) There are numerous curved fracture segments, some traversing nearly a right angle bend from a N-S to E-W orientation. It was not possible to determine whether these curved segments represent two fractures of each set joining or whether their junction was a particularly persistent stress concentration from which two fractures propagated during two different fracturing events. It seems implausible, though not impossible, that a single fracture, during one episode of propagation, would traverse such a 90° bend.

A small roll-over anticline is present in the hanging wall of a small listric cross-fault on the west side of the main quarry (Figure 31). Extension fractures fan around this fold and show the highest intensity between the listric fault and crest of the structure (Figure 32). Continuing into the hanging wall away from the fault and crest of the fold the fracture intensity exponentially decreases. A group of relatively evenly-spaced shear fractures, sympathetic to the headwall segment of the fault, are present in the footwall within 5 m of the fault. As with the listric fault system in San Antonio, fracture intensity within the hanging wall is 1.5 times greater than for the footwall. The similarities in the principal features of the fracture systems between this listric fault system and the much larger system in San Antonio, their wide geographic separation, and the differences in stratigraphy, particularly the much thicker marl interbeds here in Waco, suggests that deformation style is scale independent. This implies that smaller structures may serve as accurate models for much larger, productive, subsurface structures.

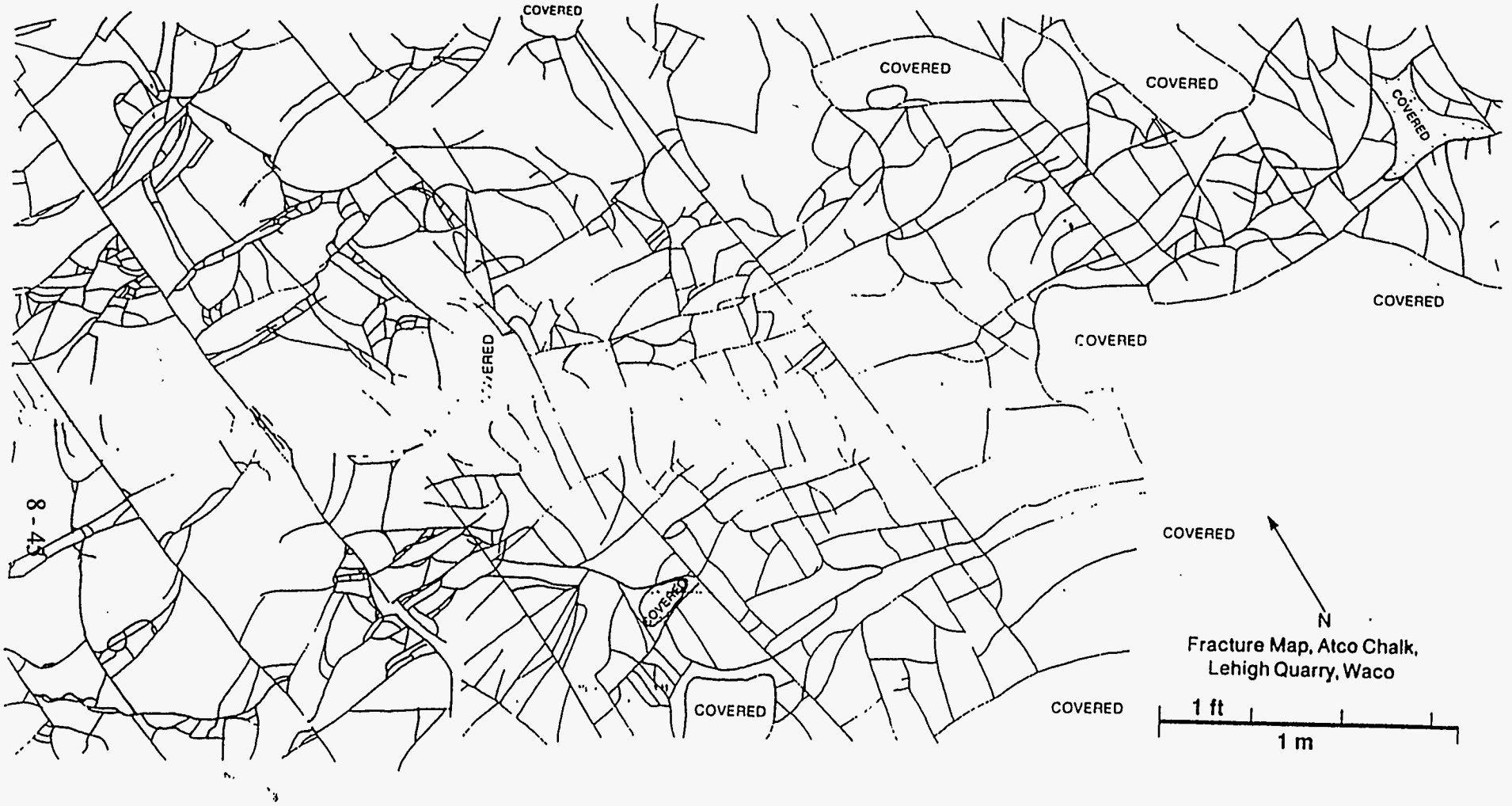


Figure 29. Map of a portion of the quarry floor of the Lehigh Quarry, Waco. The mapping was done at a scale of 1":12. A large percentage of the fractures are curved and the preferred orientation of fractures is less than in San Antonio. Note that the mapped area is about one half that of figure 19.

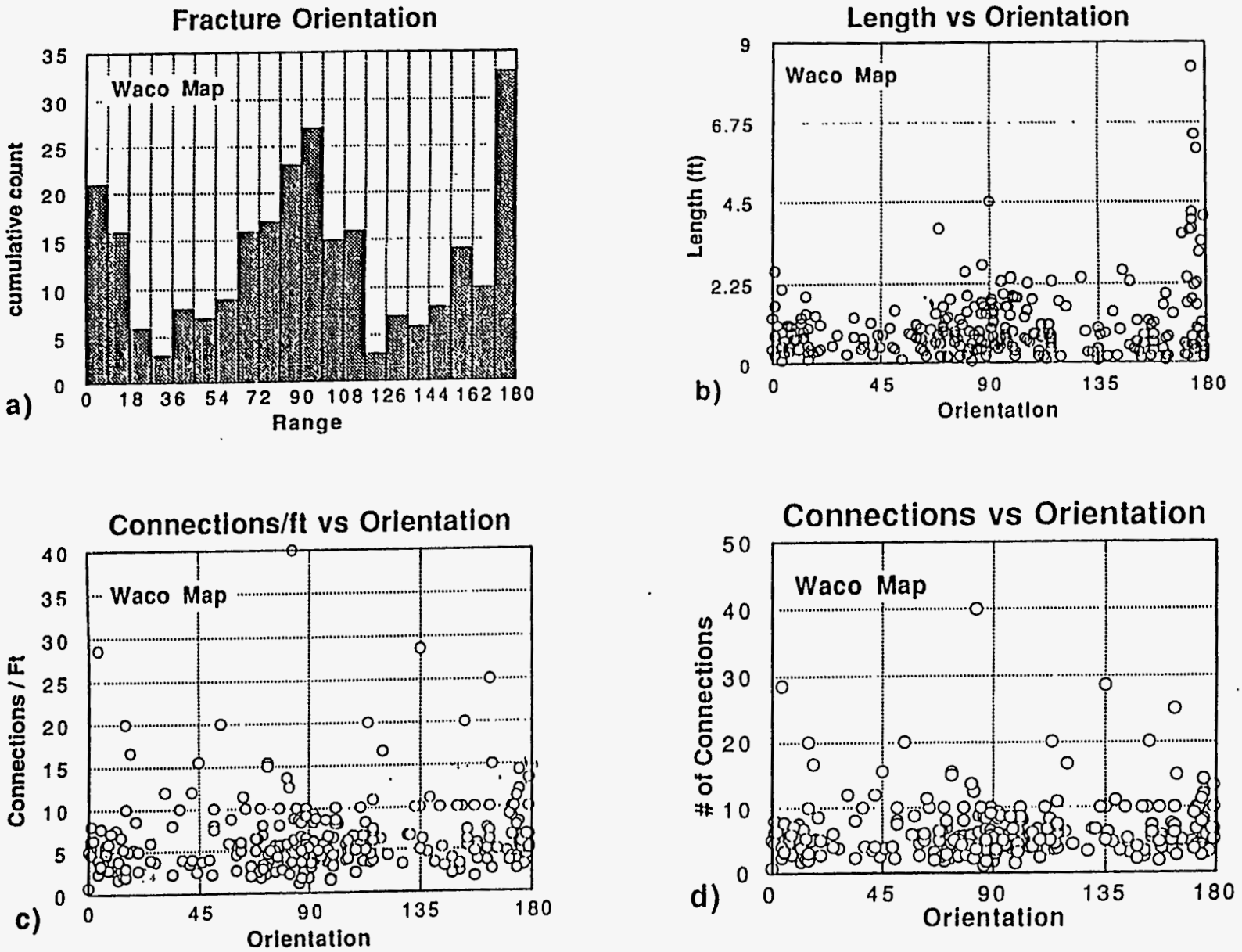


Figure 30. Plots of data from the Lehigh Quarry map. a) Frequency plot of fracture orientation. Two moderately well developed fracture sets exist. b) Plot of length versus orientation. The best defined set (N-S) also harbors the longest fractures. c) Fracture connections (or intersections with other fractures) per foot of fracture length versus orientation. The average connections per foot do not show any particular trend with orientation. d) Number of connections versus orientation. See text.

Figure 31. Small roll-over anticline in the hanging wall of a listric cross-fault.

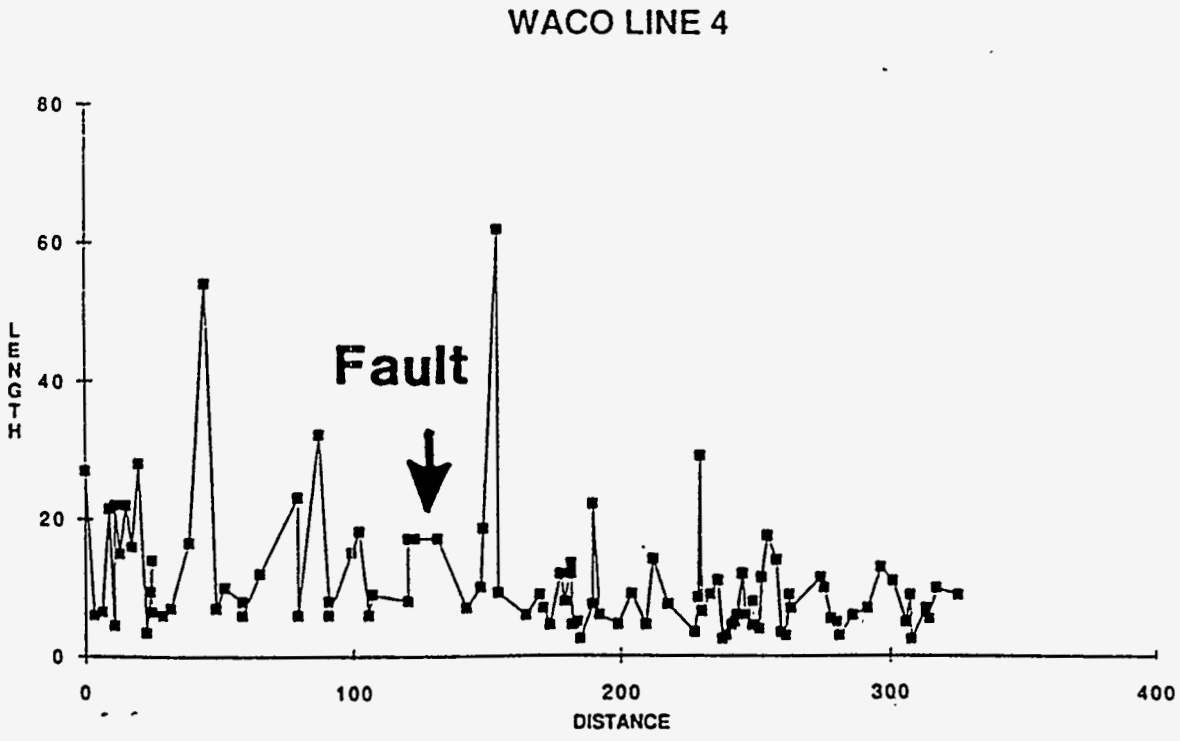


Figure 32. Scan line across the cross-fault and anticline shown in Figure 31. Arrow indicates the location of the cross-fault.

# Lafarge Cement Quarry, Dallas

The Lafarge Cement Quarry is located at 3333 Fort Worth Avenue in Dallas. As with the other quarries, access is only by permission. Requests for entry should be directed to Mr. John S. Wittmayer, Environmental Manager, Lafarge Corporation, P.O. Box 324, Dallas, TX 75221. This quarry was abandoned in 1982. Consequently, the site is extensively overgrown. Due to a change in the style of quarrying from terraced levels to a layback system there are few walls to inspect here.

Approximately 15 m of the basal Atco Chalk Member are exposed in this quarry. The contact with the underlying Eagleford Shale is exposed at scattered locations throughout the pit, and the quarry floor is generally within 1 m of the contact. Chalk bed thickness is more variable here than at the other localities ranging from 30 cm to 4 m. Intervening marls also show a greater variability in thickness ranging from 4 cm to 1.5 m. In general, the marls are thicker here than elsewhere along the central Texas outcrop trend. Again, the chalk beds tend to be homogeneous, lacking any significant internal structure. An interesting stratigraphic oddity is a very high concentration of fossil shark teeth in the top 1 m of the Eagleford Shale.

As a consequence of abandonment and the change in quarrying techniques fractures and fault styles are much more difficult to observe now than when we originally worked in this quarry in 1981. Photographs from our earlier investigations (Figure 33) illustrate that the fault style here is analogous to that in Waco, graben-in-graben structures predominate. Because of less offset on the main faults and cross-faults of the Balcones system, and because of the increase in marl thickness, fracture intensities here are lower than in Waco (Corbett and others, 1987). Even near faults, the thicker marl beds effectively terminate most fractures.

Well exposed at this locality is a vein system captured by later faults (Figure 4). The superposition of faults and veins is particularly compelling because the two surfaces are nearly orthogonal. The fault surfaces have very small displacements, generally only a few centimeters. They are also notably curviplanar, a consequence of being localized by the vein system which did not develop as a simple planar array.

Our quarry floor map (Figure 34) in the Lafarge quarry was made 150 m from faults shown in Figure 4. The fractures in this quarry are remarkable in their lack of preferred orientation, continuing the trend toward more random fracture fabrics from San Antonio, through Waco, to the present locality. Fractures length, spacing and number of connects per fracture show the same negative exponential distribution as in the other quarries. However, except for a moderately abundant N-S set and a moderately long ENE set, few systematics in either length or abundance with respect to orientation are apparent (Figure 35). As with Waco and San Antonio, we do not put much credence in surface-derived values of fracture aperture due to the age of the quarry. Again, similar to Waco, we are struck by the connectedness of the fracture system. On average only 25% or the fractures have a free end. There are 5.3 fracture intersections per fracture or about 4.6 per fracture foot (Figure 35). The abundance of curved fractures is greater in the Dallas quarry, perhaps also reflecting the absence of a strong preferred orientation. The fracture pattern, in map view, suggests a uniform extension in the plane of bedding under low differential stress. We would expect that the fracture system represented here would be highly conductive if all fractures are open, and nondirectional. A horizontal well in any direction would do as well as any other, everything else being equal.

The other primary feature of interest at this site are oxidation halos around fractures in grey chalk which was originally below the water table (Figure 17). Since these have been extensively discussed in the previous section, we will simply reiterate that fractures, even vein-filled, tight ones, are obviously much more permeable than the chalk matrix.



Figure 33. Graben-in-graben fault systems. a) Main Balcones system fault indicated by an arrow truncates a cross-fault. b) Close-up of a cross-fault.

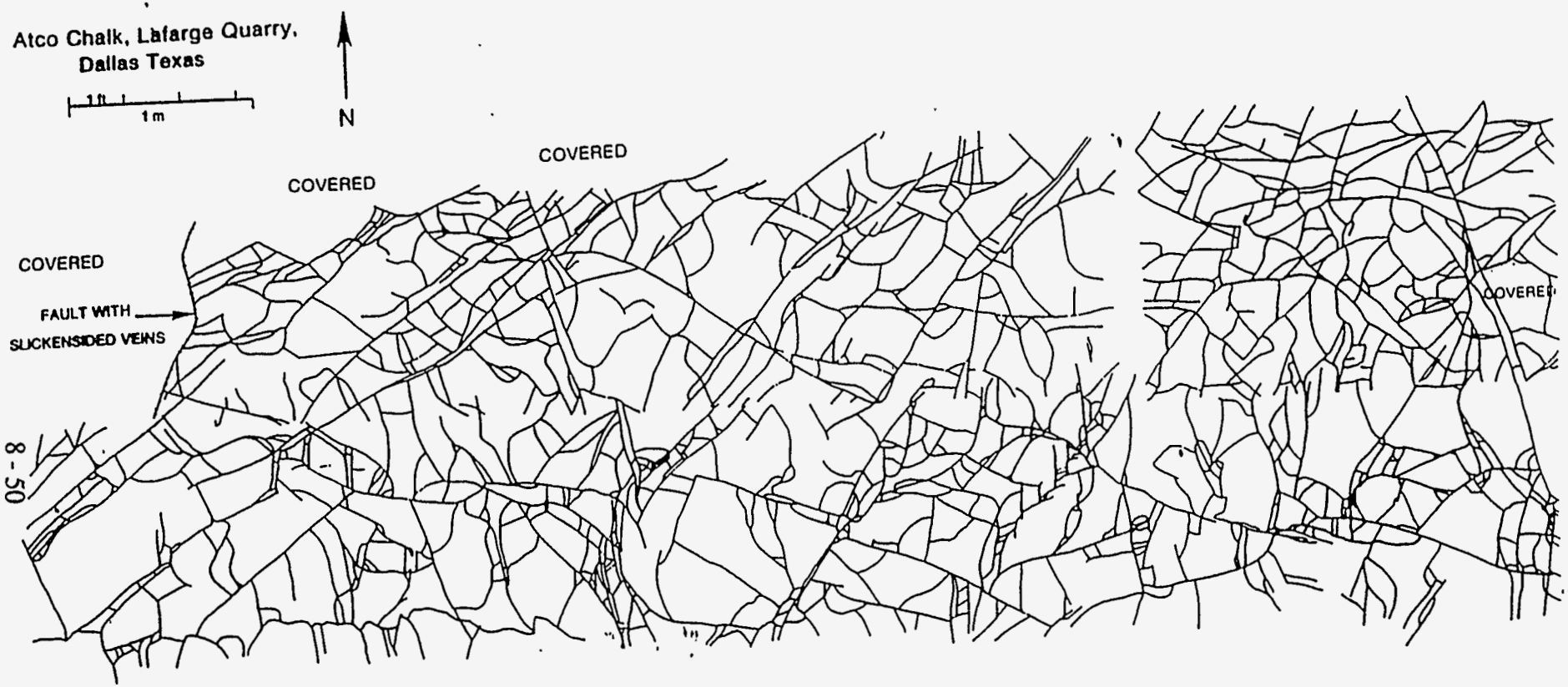


Figure 34. Map of a portion of the quarry floor of the LaFarge Quarry, near Dallas. The mapping was done at a scale of 1:24. The large percentage of curved fractures is similar to that found in Waco.

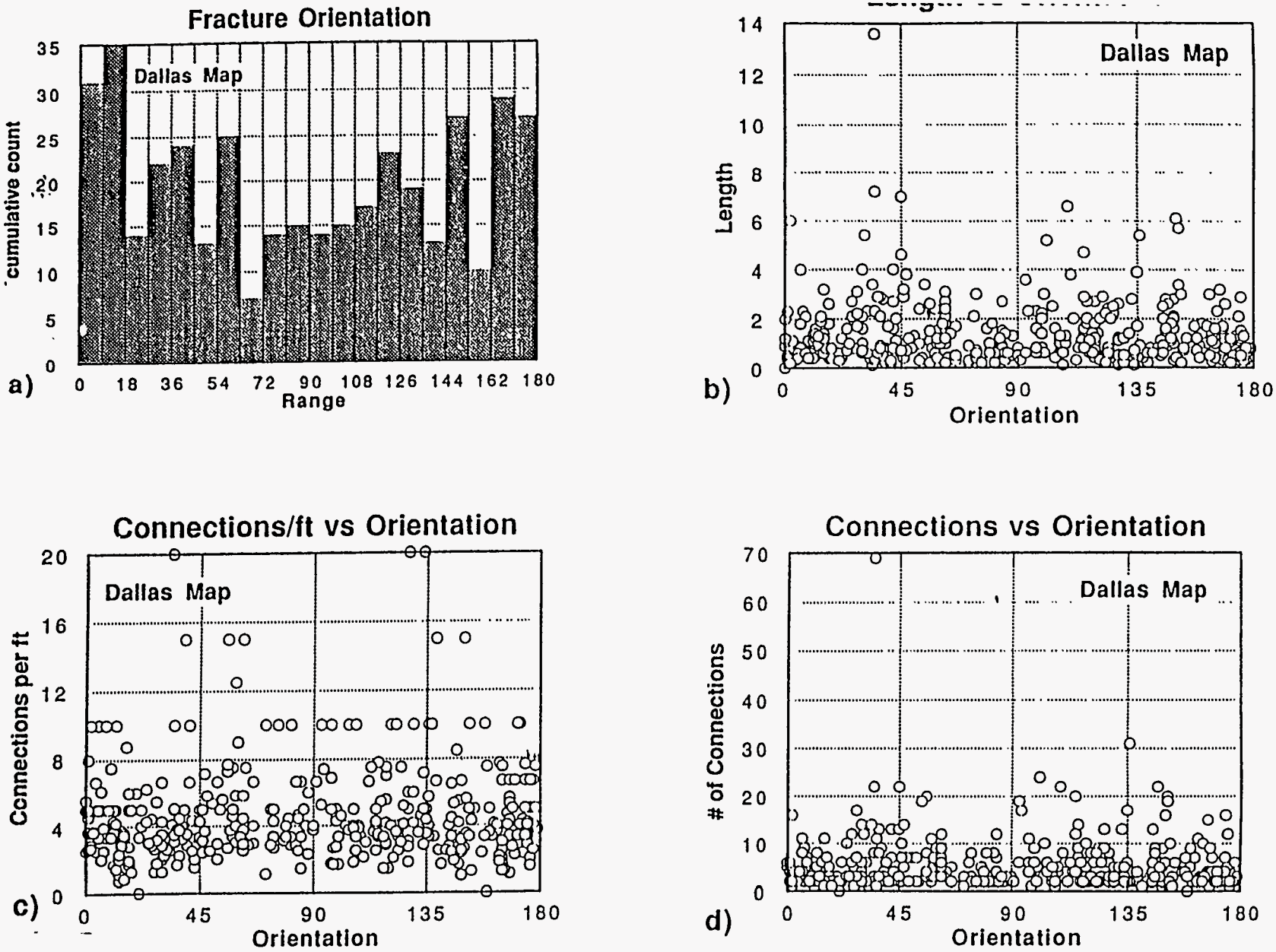


Figure 35. Plots of data from the LaFarge Quarry map. a) Frequency plot of fracture orientation. There is no particular preferred orientation to the fracturing. b) Plot of length versus orientation. c) Fracture connections (or intersections with other fractures) per foot of fracture length versus orientation. d) Number of connections versus orientation. See text for discussion.

# Acknowledgments

Field work was supported by Department of Energy contract No. DE-FG07-89BC14444 and the Center for Energy and Mineral Resources, Texas A&M University, State of Texas. Geochemical work was supported by a Research, Scholarship, and Professional Growth Grant to Corbett from Weber State University, Ogden, Utah and by the Department of Geology, Texas A&M University. We are indebted to Mr. Alan Walsh, Alamo Cement Company, San Antonio; Mr. C. B. Leos, Mr. Charlie Moore, and Mr. Dave Groman Lehigh Portland Cement Company, Waco; and Mr. Jim Melead and Mr. John S. Wittmayer, Lafarge Corporation, Dallas for allowing us repeated access to their respective quarries. Ethan Grossman, Reinauld Guillemette, Will Lamb, John Spang, and Paula Wilson assited with various aspects of geochemical data collection and interpretation. Gerald Drake, Union Pacific Resources Company provided well logs from the Giddings Field. Mike Howell assisted with data collection from fracture maps. We thank all of these individuals for their cooperation and support.

# References

Burnham, A.K., and Sweeney, J.J., 1989, A chemical kinetic model of vitrinite maturation and reflectance: Geochimica et Cosmochemica Acta, v. 53, p. 2649-2657.

Cloud, K.W., 1975, The diagenesis of the Austin Chalk: Master's thesis, University of Texas at Dallas, Dallas, Texas, 70p.

Corbett, K.P., 1982, Structural stratigraphy of the Austin Chalk: Master's thesis, Texas A&M University, College Station, Texas, 111p.

_____, 1989, Natural hydrofracturing and ductile faulting in the Austin Chalk, Texas: American Association of Petroleum Geologists Bulletin, v. 73, p. 346.

Corbett, K.P., Friedman, M., and Spang, J., 1987, Fracture development and mechanical stratigraphy of Austin Chalk, Texas: American Association of Petroleum Geologists Bulletin, v. 71, p. 17-28.

Corbett, K.P., Friedman, M., Wiltschko, D.V., and Hung, J., 1991, Characteristics of natural fractures in the Austin Chalk outcrop trend: in S. Chuber, Ed., *Abstracts and Short Papers, Austin Chalk Exploration Symposium*, South Texas Geological Society, P. 3-11.

Dravis, J.J., 1979, Sedimentology and diagenesis of the Upper Cretaceous Austin Chalk Formation, south Texas and northern Mexico: Ph.D. dissertation, Rice University, Houston, Texas, 513 p.

Durham, C.O., 1957, The Austin Group in central Texas: Ph.D. dissertation, Columbia University, New York, New York, 130 p.

Engelder, T., 1985, Loading paths to joint propogation during a tectonic cycle: an example from the Applachian Plateau, U.S.A.: Journal of Structural Geology, v. 7, p. 459-476.

_____, 1987, Joints and shear fracture in rock: in B.K. Atkinson, Ed., *Fractures Mechanics of Rock*, Academic Press, London, England, p. 27-69.

Friedman, M., 1975, Fractures in rock: Reviews of Geophysics and Space Physics, v. 13, p. 352-358.

Grabowski, G.J., Jr., 1984, Generation and migration of hydrocarbons in Upper Cretaceous Austin Chalk, south-central Texas: in J.G. Palacas, Ed., *Petroleum Geochemistry and Source Rock Potential of Carbonate Rocks*: American Association of Petroleum Geologists, Studies in Geology, v. 18, p. 97-115.

Handin, J., 1966, Strength and ductility: in S.P. Clark, Ed., *Handbook of Physical Constants*, Geological Society of America Memoir 97, p. 223-289.

Hinds, G.S., and Berg, R.R., 1990, Estimating organic maturity from well logs, Upper Cretaceous Austin Chalk, Texas Gulf Coast: Transactions- Gulf Coast Association of Geological Societies, v. XL, p. 1-6.

Hunt, J.M., and McNichol, A.P., 1984, The Cretaceous Austin Chalk of south Texas - a petroleum source rock: in J.G. Palacas, Ed., *Petroleum Geochemistry and Source Rock Potential of Carbonate Rocks*: American Association of Petroleum Geologists, Studies in Geology, v. 18, p. 117-125.

Lonsdale, J.T., 1927, The igneous rocks of the Balcones fault region of Texas: University of Texas Bulletin, No. 2744, 178 p.

Murray, G.E., 1961, *Geology of the Atlantic and Gulf Coast provinces of North America*: Harper Brothers, New York, New York, 692 p.

Pollard, D.D., and Aydin, A., 1988, Progress in understanding jointing over the past century: Geological Society of America Bulletin, v. 100, p. 1181-1204.

Pollard, D.D., and Segall, P., 1987, Theoretical displacements and stresses near fractures in rock, with applications to faults, joints, veins, dikes, and solution surfaces: in B.K. Atkinson, Ed., *Fracture Mechanics of Rock*, Academic Press, London, England, p. 277-349.

Ramsey, J.G., 1980, The crack-seal mechanism of rock deformation: Nature, v. 284, p. 135-139.

Stearns, D.W., 1964, Macrofracture patterns on Teton anticline, northwest Montana: Transactions of the American Geophysical Union, v. 45, p. 107-108.

Veizer, J., 1983, Trace elements and isotopes in sedimentary carbonates: in R.J. Reeder, Ed., *Carbonates: Mineralogy and Chemistry*, Reviews in Mineralogy Volume 11, Mineralogical Society of America, Washington, D.C., p. 265-299.

Weaks, A.W., 1945, Balcones, Luling, and Mexia fault zones in Texas: American Association of Petroleum Geologists Bulletin, v. 29, p. 1733-1737.

Young, K., 1963, Mesozoic history, Llano region: in V.E. Barnes, W.C. Bell, S.E. Clabaugh, P.E. Cloud, Jr., K. Young, and R.V. McGehee, Eds., Field Excursion: geology of the Llano region and Austin area, University of Texas Bureau of Economic Geology Guidebook 5, p. 98-106.

# Predicting Fracture Connectivity and Intensity within the Austin Chalk from Outcrop Fracture Maps and Scanline Data

by

David V. Wiltschko[1], Kevin P. Corbett[2], Mel Friedman[1] and Jih-Hao Hung[1]

submitted to

Gulf Coast Association of Geological Societies

[1] Department of Geology and Center for Tectonophysics, Texas A&M University, College Station, TX 77843-3115.

[2] Marathon Oil Company, Petroleum Technology Center, P. O. Box 269, Littleton, CO 80160.

Wed, Aug 28, 1991

## ABSTRACT

Maps at scales of 1:12 to 1:48 of portions of quarry floors and scanlines along vertical to near vertical outcrop faces in the Austin Chalk reveal the change in fracture intensity, connectivity, length and ordering with respect to orientation along the trend from Del Rio to Dallas. Outcrops with more marl beds and/or a larger total percent smectite clay (Del Rio, Waco, Dallas) display, in general, more random, more closely spaced, and more interconnected fractures. Fractures in the vicinity of San Antonio where smectite clay content is low, by contrast, are, 1) developed into well oriented sets and, 2) more widely spaced, 3) longer and, 4) less interconnected than other areas studied. Several of the fracture patterns mapped indicate that the concept of "fracture set" has only local applicability in the Austin Chalk. Highly curved fractures outside of the San Antonio area and the occurrence of en passant fracture geometry suggest low differential stress at the time of fracturing. Random orientation of all but the longest fractures suggests uniform extension of the Austin Chalk in the horizontal (bedding) plane.

## INTRODUCTION

Naturally fractured reservoirs represent an increasingly important target for petroleum exploration, especially with the advent of horizontal drilling. Optimum success in both exploration and production, however, depend on adequate characterization of the fracture system and associated rock mass permeability as a function of lithology (*e.g.* bed thickness, clay content, percent calcite), rock properties (*e.g.* triaxial compressive strength, porosity, permeability), structural position, and tectonic history. It is impossible to completely characterize fracture networks at depth. Geophysical and petrophysical methods at best yield measures of fracture spacing and aperture, but no information concerning the amount and degree of fracture interconnection or fracture dimensions. Yet fracture connectivity, especially, is crucial to reservoir response (see Long and Witherspoon, 1985).

A simple thought experiment illustrates the kinds and importance of interconnectivity. Consider three different fracture networks (Figure 1). Only relatively straight, long, and isolated fractures occur in the first fracture array (Figure 1a) and as a result the degree of interconnectivity is poor. Depending on the distribution of fracture lengths and how many are intersected by a horizontal well bore, the success in petroleum production could range from good to poor. The fractures would act as fluid conduits, but due to low matrix permeability and possibly great differences in permeability between open fractures and matrix, fluid flow would short circuit through the fractures leaving large regions of the reservoir undrained. Similarly, water flooding would be inefficient, because the water would flow through the open fractures, by-passing mobile oil within blocks between the isolated fractures. Although the dimensions of blocks across subtending fractures is small, the other, parallel-to-the-fracture direction, is large. For the second hypothetical fracture array there are two fractures sets distributed in a spatially heterogeneous fashion (Figure 1b). Both sets on average have equal fracture spacing, but their mean lengths are different due to the poor development of the less abundant set. Drainage of this reservoir would be optimized by intersecting the patches where fractures are interconnected (such as in the left portion of this figure), but even then only a limited portion of the reservoir would be drained. The degree of fracture interconnection in places is high but spatially isolated. In the third situation, nearly all fractures are connected (Figure 1c). Whether the fractures are straight or curved, this situation leads to relatively smaller intact block sizes, higher hydraulic conductivity through the fractures if they are open, and therefore a highly conductive reservoir. In this case the direction of horizontal drilling is immaterial, whereas in the first case the choice of the horizontal drill orientation was critical. A consequence illustrated by these three situations is that prediction of both the degree of innerconnectivity and the spatial variability of the interconnectivity, is

important in understanding the success of draining a fractured, low matrix-permeability reservoir.

We have investigated the Austin Chalk outcrop trend from Dallas to Del Rio (Figure 2) in order to quantify further the characteristics of fracturing, especially interconnectivity. The results reported here amplify and extend earlier studies on fracturing in the Austin Chalk (Corbett, 1982; Corbett *et al.*, 1987, 1991; Reaser and Collins, 1988). We provide new data on fracture length, connectivity, spacing and areal density and the significance of establishing these parameters for accurate reservoir characterization and modelling.

Understanding the fracturing in the Austin Chalk is a particularly timely topic given the current active exploration interest and drilling activity. Successful wells in the Austin Chalk have historically been those where zones of high fracture intensity and presumably zones of high fracture interconnectivity have been found. Production is thought to be predominantly structurally controlled. Although zones of increased fracture productivity are often near faults (*e.g.*, Kuich, 1989), they also are associated with other structures (Stapp, 1977). Our data on the characteristics of fracturing in the Austin Chalk may bear on the occurrence of fractures in the Austin Chalk and the underlying reasons for the variability in production.

The plan of this paper is to, 1) review the regional geology and rock properties of the Austin Chalk, 2) describe the mapped fracture arrays, and 3) present data on the constituent fracture populations.

## REGIONAL GEOLOGY

The regional geology, petrography, diagenesis and sedimentology of the Austin Chalk have been previously summarized (Corbett *et al.*, 1987, and references therein). We give here only a brief review for the purposes of this paper. The Austin Chalk crops out from Oklahoma to the Mexican border, generally trending parallel to the form of the Gulf Coast Basin. Along this trend the Austin Chalk consists of fine-grained carbonates and marls derived from pelagic muds. Typical fossil fragments include coccoliths, planktonic and benthic foraminifera, calcispheres, mollusks, echinoids, and bryozoans. Porosities in outcrop range from 30% in the vicinity of Dallas decreasing southwestwardly to 9% at Langtry (Cloud 1975). Subsurface porosities are less than those found in outcrop (Dravis, 1979). Subsurface matrix permeabilities average less than 0.1 md (Snyder and Craft, 1977).

The stratigraphy of the Austin Chalk is shown in Figure 3, after Corbett *et al.* (1987). Our data from Dallas, Waco, and San Antonio quarries comes from the Atco Chalk member, and the Tequesquite Creek data near Del Rio comes from the Dessau member of the Austin Chalk. Deposition of the Chalk between San Antonio and Austin occurred on a pre-existing high (San Marcos Arch) (Figure 2). Bedding is massive, marl interbeds are not prominent, and the total stratigraphic thickness is reduced in this vicinity. To the southwest and northeast rhythmic bedding appears with marls becoming a large portion of the stratigraphic section (Dravis, 1979). The thickness of the chalk in outcrop varies from a few hundred feet to about 600 feet (about 180 m)(Pessagno, 1969). The thickness generally increases down dip away from the San Marcos Arch reaching a maximum of about 1000 feet (about 300 m) in the Kanes trough in Gonzales and Wilson counties (Holifield, 1982).

The structural setting of the Austin Chalk has been controlled by the Gulf Coast Basin and affected by the Balcones, Luling, Mexia, and Talco fault zones as well as old, inherited, Ouachita fold and thrust belt trends (Weaks, 1945). The major faulting style in outcrop gives rise to horsts and grabens with conjugate normal faults, often listric, dipping to the southeast and northwest (Corbett *et al.*, 1987, 1991). In the Waco and Dallas areas graben within graben structures prevail, monoclinal flexures are present in the San Antonio area as well (Ibid). Movement on all these faults may have begun as early as Late

Cretaceous, although Weeks (1945) reports that major movement occurred along all fault zones during the Late Oligocene or early Miocene. Kuich (1989) found that major motion on faults in the Giddings Field of Burleson and Grimes County was in the Eocene. There is no evidence for a spatial trend in ages as would be expected from fault propagation. Likewise, there is no evidence for episodic fault motion.

## DATA COLLECTION PROCEDURES

### Maps

Suitable sections of a quarry floor were located and cleaned and a map scale selected (1:12, 1:24, or 1:48). Sites were chosen on the basis of completeness of initial exposure and the ability to clean off ruble to expose nearly 100% of a bed surface. Heavy excavation equipment was not used (compare Barton and Hsieh, 1989). Mapping was facilitated by using a gridded mapping square, 4 ft on a side, divided internally by 1 ft marker strings. Depending upon ultimate map size, a base line was established where necessary and the map square moved parallel to this surveyed reference line as mapping progressed. All fractures that could be observed from standing height (about 6 ft or 2m) were mapped. Mineralization and alteration along fractures were noted on the map.

Field maps were compiled and redrafted in the office to both facilitate data collection and allow comparison with our scanline data from vertical quarry faces (Corbett *et al.*, 1991; see below). Lines were drawn on the maps parallel and normal to the major fracture sets and, in some cases, also oblique to the two most prominent fracture sets in order to sample the fracture networks. A fracture which intersected a sampling line was logged as to length, orientation, number of intersections with other fractures (connections), number of free ends, number of ends where the fracture abutted against another fracture, and fracture spacing. Fracture spacing was measured by drawing a perpendicular line from the fracture being logged to the nearest fracture of any orientation in a forward direction. Data on spacing of "sets" were also collected. We did not measure fracture aperture believing this number to be unreliable in surface outcrops (compare Barton and Hsieh, 1989).

Several decisions had to be made during the data collection process in the office. Many of the fractures on our maps, especially in regions away from San Antonio, are highly curved. As a consequence, we developed the following protocols for establishing the parameters outlined above. 1) If a 90° bend in the fracture took place over less than 2 inches (5 cm) of fracture length, then we considered the fracture to be composed of two separate intersecting segments. 2) Otherwise the fracture must have either ended or clearly abutted against another in a "T" intersection for a fracture termination to be recorded.

### Scanlines

We also measured fracture characteristics along scanlines placed on individual beds exposed on vertical to near vertical outcrops. Fractures intersecting the scanline were logged as to length, orientation and spacing. Because these data were collected in the same localities as the quarry floor maps, they provide a view of the third dimension. Scanline data are available for three of our four mapped sites: San Antonio, Waco and Dallas.

### Limitations of the Data

Because our maps were made on two dimensional surfaces, the data extracted from them are limited in several ways. First, the map data provide no information in the third dimension on the length, shape, consistency of orientation or interaction with bedding surfaces of the fractures. Similarly, we cannot predict how the fracture features measured at the surface can be extrapolated into the subsurface based on map data alone. For instance, how many of the fractures seen at the surface formed there, i.e., as a consequence of being at the air/rock interfaces? One indication that not <u>all</u> fractures are near-surface features is the fact that several fracture sets are locally vein filled; these fractures, at least,

were formed in the subsurface and presumably therefore reflect conditions there. Another limitation is that the maps are of finite size. The longest fractures do not end on our maps so that there is a truncation bias in length for long fractures. In a similar way, fractures that could not be seen from standing height were not mapped. As a result there is a non-representation bias for small lengths. While the lack of accurate lengths for the longest fractures may be troublesome, smaller fractures are often unconnected to others and therefore of limited importance hydrologically (Segall and Pollard, 1983). A third limitation of our data is that it is based on maps which represent a miniscule proportion of the outcrop trend of the Austin Chalk. The area of the largest map is 792 $ft^2$ (88 $m^2$). Yet, despite these problems, map data provide views of both fracture connectivity and shape unavailable by other means.

Scanline data, if used with map data, provide a view of the third dimension. However, although rapidly collected, scanline data do not provide information on connectivity where both the fractures and exposures are nearly bed-perpendicular. Fracture measurements along scanlines also have the representativeness uncertainty associated with the map data. However, because, 1) many more fractures can be measured in the same amount of time as it takes to map a representative fracture pavement and, 2) vertical outcrops in our areas are large, the same areal restrictions for maps do not apply to scanlines; longer fractures could be sampled. Maps and scanline data therefore are complementary.

## DESCRIPTION OF FRACTURE PATTERNS

### Tequesquite Creek

We have made fracture maps along Tequesquite Creek, Texas, about 30 miles southeast of Del Rio on Route 277 (No. 1 on Figure 2; Figure 4). The map reported on here was made at a scale of 1:24 in the Dessau Chalk member. There are no surface faults mapped in the vicinity of the stream cut (Figure 4). The area mapped lies on the north limb of a small anticline (Corbett *et al.*, 1991).

The fracturing in Tequesquite Creek is markedly different from any other which we have observed along the trend (Figure 5). The fracture pattern is characterized by a set of long continuous widely spaced fractures of a persistent orientation between which are curved, nearly randomly oriented fractures; the latter appear much like mud cracks. The largest fractures, which generally trend N50E, are subparallel to the southwestern extension of the Balcones fault zone and are parallel to axis of the small anticline (Figures. 2, 6a). Another more abundant group trends N30W (Figure 6b). Like other fracture patterns we see along the Austin Chalk trend, there are few fracture tips exposed. Only 15% of the fractures show tips, the rest being abutments against other fractures. The frequency distributions of the lengths of fractures in either group follow a negative exponential distribution as is found for the lengths (and spacings) of fractures throughout the Austin Chalk (Corbett *et al.*, 1991) and in most other studies of fracture pavements (*e.g.*, Segall and Pollard, 1983; La Pointe and Hudson, 1985; Barton and Larsen, 1985; Barton and Hsieh, 1989). The number of fracture intersections or connections per foot of fracture length are nearly independent of orientation (Figure 6c). On average, fractures display five intersections per foot of fracture length. Fracture spacing is distributed in a negative exponential fashion with truncation at the low end (Figure 7a) . As mentioned before, this truncation is due to the fact that fractures not visible from standing height were not mapped. There is no preferred orientation to fracture spacing at Tequesquite Creek (Figure 7b), *i.e.*, the spacing of fractures versus orientation show no trends on this map, despite the fact that the longest fractures appear to show a regular spacing. Apparently the great majority of fractures are nearly randomly oriented so that the few, albeit long, fractures which are regularly spaced, are a small portion of the population.

The northeast trending set has a mean length of 1.6 ft (0.5 m), whereas the less

persistent but more prevalent northwest set has a mean length of about 1.2 ft (0.4 m). This illustrates the fact that the prominent, and apparently longest set, consists of closely spaced and parallel, yet, multiple fractures.

The two distinct fracturing styles on this map suggests a distinct fracturing mechanism for each. Our current hypothesis is that the long, straight, widely spaced joints occurred early due to local tectonism. The curved, nearly randomly oriented, fracture between the long straight segments occurred second by uniform stretching of the Austin Chalk along the crest of the fold as plunge developed. The evidence for this sequence is that curved fractures abut against the long, straight ones.

Although no data are available at this locality, elsewhere, such as at our Dallas site (see below) the curved, randomly oriented fractures appear to be bedding normal and therefore are not classic "synersis" cracks (Nelson, 1985)

We predict that this fracture system would be highly conductive in the subsurface if, 1) present in substantially the same form as seen in outcrop and, 2) if all fractures are open as well.

**Old Alamo Cement Quarry, San Antonio**

We have made a map at a scale of 1:24 of a portion of the floor of the Old Alamo Cement quarry, in the Alamo Heights portion of San Antonio (No. 3 on Figure 8). The mapped interval is about 13 ft (4 m) above the Austin Chalk-Eagleford Shale contact. Numerous normal faults, generally trending northeast, crop out near our study site. The local structure in the quarry is characterized by listric normal faults (Corbett *et al.*, 1991). Fracturing in the vicinity of San Antonio (Figure 9) is markedly different from that near Del Rio (Figure 5). The most remarkable aspect of the fractures in this quarry at this level of exposure is the lack of intersections among fractures. The fracture network is characterized by a strong fracture preferred orientation, or relatively less dispersion in fracture orientation than elsewhere along the outcrop trend (Figure 10a,b). There is essentially only one fracture set trending N45E, although a few long fractures trend N45W. The longest fractures, as at Tequesquite Creek, are fracture zones. Although the longest fracture zone is more than 30 ft (9.1 m) long, the longest fracture is only about 9 ft ( 2.7 m) long. The mean fracture length in this map is 1.1 ft (0.3 m). Due in part to the good preferred orientation, on average, the fractures on this map display only two connections per fracture, or 1.4 on a per foot of fracture basis (Figure 10c). In addition, there is a greater proportion of unconnected fractures (*i.e.*, fractures with ends completely unconnected to other fractures as viewed in two-dimensions) than in other study sites. Similarly, of those that are not totally blind, nearly 90% have a free or unconnected end, or fracture tip; only 7% abut other cracks at either end. This connectivity is directional because there is a high preferred orientation of the fractures (Figure 10b). However, because a significant portion of the fractures are partially filled with vein minerals, the directional hydraulic conductivity is complex. As in all other sites the fracture spacing is skewed toward small spacings (Figure 11a), following the fracture length distribution that we have reported elsewhere (Corbett *et al.*, 1991).

The most closely spaced fractures trend N45E (Figure 11b). There would be an exploration benefit to drilling normal to the best developed fracture set, especially higher up in the Atco Chalk member where the degree of veining apparently decreases (Corbett *et al.*, 1991).

**Lehigh Cement Quarry, Waco**

A map of a small portion of the floor of the Lehigh Cement Quarry was made at a scale of 1:12. The particular locality mapped is about 10 ft (3m) stratigraphically above the base of the Chalk. An unusual aspect of the regional geology is the occurrence of small north-south trending normal faults north of the quarry (Figure 12). The local structure in

the quarry is graben-in-graben structure (Corbett *et al.*, 1991).

Waco lies between our San Antonio and Dallas sites in ordering of the fracture pattern, San Antonio being the most ordered and Dallas the least. The best developed fracture set containing the longest fracture trends nearly north-south, the next best developed set trends east-west, but with greater scatter in orientation (Figures. 13, 14a,b). The longest fracture on our map is 8.3 ft (2.5 m) long; the mean for all fractures is 1.1 ft (0.3 m).

All but a few of the fractures on our map are intersected by others. The mean number of connections per fracture is about six, although the frequency distribution is skewed toward low values with a high kurtosis. Moreover, the number of connections per unit length of fractures is nearly independent of orientation (Figure 14c). Eleven percent of the fractures display free ends (unconnected fracture tips). The N-S fracture set has the most with about 50% of the fractures exhibiting a free end. Fracture spacing shows a moderately strong association with fracture orientation (Figure 15). Like Tequesquite Creek, there are numerous curved fracture segments in the Waco site, some nearly curving through a right angle bend from a N-S to E-W orientation.

These curved segments may represent either two fractures of each set which joined, or fractures formed at a particularly persistent stress concentration during two different fracturing episodes. It seems implausible, though not impossible, that a single fracture would traverse such a 90° bend, during one episode of applied differential stress where the stress axes are fixed. However, if the greatest and least principal stresses were nearly bed parallel and nearly the same value, changes in the amount of one or the other could change the direction of the maximum principal compressive stress to change markedly with time.

This, too, would result in curved, single fractures.

Although we would judge this map area to be highly conductive to fluids if all fractures were open, there would be an advantage for petroleum production in intersecting as many N-S fractures as possible due to their increased lengths.

### LaFarge Cement Quarry, Dallas

The Lafarge Quarry in Dallas, Texas, was mapped at a scale of 1:24 in an area with few regional outcropping faults (Figure 16).

The fracturing is less regular than that found in the Waco Quarry (Figure 17). Stretching the definition of a fracture set, we can recognize a poorly ordered fracture set trending roughly north-south and a second dispersed set trending east-northeast (Figure 18a, b). The most prevalent set is that which trends nearly north-south, although the set which has fractures of the greatest length is east-northeast, or parallel to the Gulf Coast Basin edge (Figure 18b). The mean length of the east-northeast trending fractures (set 1) is 1.6 ft (0.5 m) on this map, whereas the mean length of the north-southeast, (set 2) is 1.4 ft (0.4m). The most prevalent set of fractures, the north-south set (set 2), has a mean fracture length of 1.1 ft (0.3 m) on the map. There is no preferred orientation to the connectivity vs. orientation plot (Figure 18c). Like the Waco map, few (13%) Dallas fractures show fracture tips and there are few free (unconnected) fractures. There is no appreciable difference among the three fracture sets in their spacing (mean = ~0.3 ft) (Figure 19).

The disorder in the fracture pattern in the Dallas Quarry is shown by, 1) zones of en echelon fracturing as exemplified by the en echelon fracture zone in the bottom middle of the map; 2) "fracture" fans such as shown in the lower right of the map and like the Waco map, many of the fractures turn from one orientation to another through nearly 90°.

## COMPARISON WITH SCANLINE DATA

The scanline data show similar negative exponential distributions for fracture spacing as found from the map data (Figure 20; no scanline data are available from Tequesquite Creek). Most fractures measured along scan lines are more closely spaced than

one foot. Also like the map data, fractures measured along scanlines are longest at San Antonio, although the longest individual fracture was a quarry wall face at our Waco study site (Figure 21c). The scanline data, likewise, displays the same degree of preferred orientation as found among map sites. The fracture pattern from the Old Alamo Cement Quarry, San Antonio, shows the strongest preferred orientation (about N45E) and the LaFarge Cement Quarry, Dallas, the least. The degree of similarity in kind if not degree between the results from maps and scanlines, 1) mutually reinforce the conclusions drawn from both and, 2) provide additional confidence in extrapolating into the subsurface the length and spacing patterns observed on the maps.

## DISCUSSION AND CONCLUSIONS

Fracture spacing, a fundamental control on interconnectivity, is thought to be a function of rock strength and brittleness. Factors that control strength and brittleness are composition, grain size, porosity, bed thickness and tectonic history. Rocks composed primarily of more brittle constituents such as dolomite, quartz, and feldspar have higher fracture intensities (*e.g.* Nelson, 1985, Figure 4-4). Rock strength increases with decreasing porosity as has been shown by Price (1966), Dunn *et al.* (1973), and for the Austin Chalk, by Corbett *et al.* (1987). Corbett *et al.* (1987) show that, in addition to porosity, ultimate strength correlates with the smectite clay content. Brace (1961), Ramez and Mosalamy (1969) among many others show that increased compressive strength correlates with decreasing grain size. Perhaps the best studied relationship between fracture spacing and a lithologic property is that of bed thickness. (Bogdanov, 1947; Harris *et al.*, 1960; Price, 1966; Sowers, 1972; Ladiera and Price, 1981). Sowers (1972) shows that the relationship between fracture intensity and bed thickness can be explained by an interfacial instability between beds giving rise to a regular spacing in stress concentrations. This instability arises due to different elastic properties among beds.

Two other factors must be considered in understanding fracture intensity. One is that some rocks over geological time periods may deform by other processes. For instance, carbonates which contain greater than about 15% clay may deform by pressure solution at a differential stress lower than that for brittle failure (*e.g.*, Marshak and Engelder, 1985). Likewise, it is conceivable that rocks of extremely uniform character may have few stress concentrations at which fractures can initiate. Therefore, one would expect, everything else being equal, that the rocks which are heterogeneous should be more highly fractured. This, in part, is the reason why porosity and smectite clay content control strength, in that higher porosities and larger smectite clay content reflect a greater number flaws or stress concentrations (Friedman, 1976; Pollard and Aydin , 1988). Clearly a number of factors control fracture abundance in rock, *e.g.*, bedding thickness, structural position and proximity to faults, and intrinsic properties that control rock strength such as porosity, grain size, clay contact, etc.

Both porosity and clay content of the chalk in the San Antonio (Old Alamo) quarry are relatively high with respect to other areas along the outcrop trend and the rocks are among the weakest and most ductile (Corbett *et al.*, 1987). In fact, at this study site the fractures are more widely spaced and have the lowest areal density of fracture intersections compared to all other areas studies (Table 1). This correlates with observations of fractures at the Teton Anticline, NW Montana (Sinclair, 1980) where weaker more ductile lithofacies in the Mississippi Madison Group exhibit more ordered fracture orientations. Corbett *et al.* (1987) have found that rocks from Tequesquite Creek have the greatest ultimate strength, lowest porosity and highest smectite clay content of those areas we have studied. As a result, fracture intensity and number of intersections there are on average higher than elsewhere along the trend. The ultimate/fracture strength of the Austin Chalk for samples from Waco ranges from 38.5 MPa (Pc = 10 MPa) to 103 MPa (Pc = 70 MPa) (Wiltschko, unpublished data), *i.e.*, about the same or somewhat weaker than at San Antonio.

Accordingly, we anticipated behavior similar to that at San Antonio, everything else being equal. However, these two areas are very different in their fracture patterns and intensities, suggesting that factors such as bed thickness and structural type and position complicate the laboratory-based strength-intensity relationship. The low strengths for the laboratory samples from our Dallas site are likewise inconsistent with the high intensity of fracturing on our map from there. However, the Dallas map site is on the bed forming the contact with the underlying Eagleford shale and consequently it may be more highly fractured due to the proximity to overpressured fluids (Corbett *et al.*, 1991).

As our data show, fracture spacing in the sense of regular fracture sets or arrays, appears to have limited application in some areas within the Austin Chalk, especially near Del Rio and Dallas. We find that fracture spacing in the Austin Chalk follows a negative exponential distribution when one measures the distance between fractures of any orientation along either a map sampling line or a scanline. One can somewhat arbitrarily identify fracture sets, as we have done, and measure their fracture spacings, ignoring intervening ones. However, this measure ignores the bulk fracture density. Therefore, for units as fractured as the Austin Chalk, and for units lacking, in general, a strong preferred orientation of fracturing as the Austin Chalk, other measures of fracture intensity such as fracture line lengths per area (Table 1), or fractal measures (Mandelbrot, 1983; La Pointe, 1988) may be more appropriate. It is these measures, therefore, that one would correlate with rock strength, composition, bed thickness, and tectonic history in order to produce a predictive tool.

Although it is impossible to clearly separate all of the factors contributing to fracture intensity and style in the Austin Chalk, several observations seem appropriate.

1) The Atco Chalk member in the vicinity of San Antonio is massively bedded (free of marl interbeds). There, too, the fractures are least interconnected and most ordered with respect to orientation.

2) The degree of development of curved, nearly randomly oriented small fractures between major fracture sets increases from San Antonio toward both Dallas and Del Rio as does the percent of intercalated marl beds in the portion of the Austin Chalk we studied.

3) Several modes of origin for the development of curved fractures, as best developed in Dallas and Del Rio, are possible. Curved fractures are generally indicative of a low differential stress (*e.g.*, Olson and Pollard, 1989). We have suggested that the curved fractures are due to uniform stretching in the plane of bedding. Others have proposed the chalk is "self-sourcing", whereby maturation of solid organic matter in the chalk beds leads to the evolution of liquids and gas of higher volume, cracking the chalk (Grabowski, 1981, 1984; Hunt and McNichol, 1984; Hinds and Berg, 1990). The loss of volume due to expulsion of hydrocarbons would lead to uniform shrinking, producing the same end result as stretching. Without further paleostrain and stress measurements, it is impossible to identify where each mechanism applies.

4) With the exception of Waco, the longest fractures trend parallel to the Gulf Coast Basin edge, suggesting the dominant control on the fracturing was the basin configuration.

## ACKNOWLEDGEMENTS

Field work was supported by Department of Energy contract No. DE-FG07-89BC14444 and the Center for Energy and Mineral Resources, Texas A&M University, State of Texas. We are indebted to Mr. Alan Walsh, Alamo Cement Company, San Antonio; Mr. C. B. Leos, Mr. Charlie Moore, and Mr. Dave Groman of Lehigh Portland Cement Company, Waco; and Mr. Jim Melead and Mr. John S. Wittmayer, Lafarge Corporation, Dallas for allowing us repeated access to their respective quarries. Mike Howell assisted with data collection from fracture maps. Jack Magouirk expertly performed the strength tests on the Waco samples for Table 1. Robin McNeely provided considerable, efficient, editorial help with the manuscript. Thanks to all of these

individuals for their support.

REFERENCE CITED


1 Barnes, V. E., 1977, Geologic Atlas of Texas, Del Rio Sheet, Scale 1:250,000, The University of Texas at Austin, Bureau of Economic Geology.

2 Barnes, V. E., 1976, Geologic Atlas of Texas, Crystal City-Eagle Pass Sheet, Scale 1:250,000, The University of Texas at Austin, Bureau of Economic Geology.

3 Barnes, V. E., 1974, Geologic Atlas of Texas, San Antonio Sheet, Scale 1:250,000, The University of Texas at Austin, Bureau of Economic Geology.

4 Barnes, V. E., 1990, Geologic Atlas of Texas, Waco Sheet, Scale 1:250,000, The University of Texas at Austin, Bureau of Economic Geology.

5 Barnes, V. E., 1972, Geologic Atlas of Texas, Dallas Sheet, Scale 1:250,000, The University of Texas at Austin, Bureau of Economic Geology.

6 Barton, C. C. and E. Larsen, 1985, Fractal geometry of two dimensional fracture networks at Yucca Mountain, southwestern Nevada: Proceedings International Symposium on Fundamentals of Rock Joints, pp. 77-84, Bjorkliden, Sweden.

7 Barton, C.C. and Hsieh, P.A., 1989, Physical and hydrologic-flow properties of fractures: American Geophysical Union Field Trip Guidebook T385, 35 p.

8 Bogdanov, A. A., 1947, The intensity of cleavage as related to the thickness of the Bed (Russian Text): Soviet Geology, v. 16, p. 147.

9 Brace, W. F., 1961, Dependence of fracture strength of rocks on grain size: Pennsylvania State University Mineral Export Station Bulletin, v. 79, p. 99-103.

10 Cloud, K. W., 1975, The diagenesis of the Austin Chalk: M.S. Thesis, University of Texas at Dallas, Dallas, Texas, 70 p.

11 Corbett, K. P., 1982, Structural stratigraphy of the Austin Chalk: M.S. Thesis, Texas A&M University, College Station, Texas, 111 p.

12 Corbett, K. P., M. Friedman, and J. Spang, 1987, Fracture development and mechanical stratigraphy of Austin Chalk, Texas: AAPG Bull., v. 71, p. 17-28.

13 Corbett, K. P., Friedman, M., Wiltschko, D.V., and Hung, J.H., 1991, Controls on fracture development, spacing, and geometry in the Austin Chalk Formation, central Texas: considerations for exploration and production: Dallas Geological Society, Field Trip #4, 49 p.

14 Dravis, J. J., 1979, Sedimentology and diagenesis of the Upper Cretaceous Austin Chalk formation, south Texas and northern Mexico: Ph.D. Dissertation, Rice University, Houston, Texas, 513 p.

15 Dunn, D. E., L. J. LaFountain, and R. E. Jackson, 1973, Porosity dependence and mechanism of brittle fracture in sandstones: Journal of Geophysical Research, v. 78, p. 2403.

16 Durham, C. O., Jr., 1957, The Austin Group in central Texas: Ph.D. Dissertation, Columbia University, New York, New York, 130 p.

17 Friedman, M., 1975, Fracture in Rock: Reviews of Geophysics and Space Physics, v. 13, #3, U.S. National Report 1971-1974, 16th General Assembly, International Union of Geology and Geophysics, p. 352-358.

18 Grabowski, G. J. Jr., 1981, Origin, distribution and alteration of organic matter and generation and migration of hydrocarbons in Austin Chalk, Upper Cretaceous, southeastern Texas: Ph.D. Dissertation, Rice University, Houston, Texas, 276 p.

19 Grabowski, G. J., Jr., 1984, Generation and migration of hydrocarbons in Upper Cretaceous Austin Chalk, south-central Texas, *in* J. G. Palacas, ed., Petroleum geochemistry and source rock potential of carbonate rocks: AAPG Studies in Geology, v. 18, p. 97-115.

20 Harris, J. F., G. L. Taylor, and J. L. Walper, 1960, Relations of deformational fractures of sedimentary rocks to regional and local structure: AAPG Bull., v. 44, p. 1853-1873.

21 Hinds, G.S. and Berg, R.R., 1990, Estimating organic maturity from well logs,

Upper Cretaceous Austin Chalk, Texas Gulf Coast: GCAGS Trans., v. 40, p. 295-300.

22 Holifield, R., 1982, Austin Chalk trend Upper Gulf Coast, Texas--keynote address: *in* Austin Chalk Oil Recovery Conference, Texas Petroleum Research Committee, Bulletin 256, p. 1-27.

23 Hunt, J. M., and A. P. McNichol, 1984, The Cretaceous Austin Chalk of South Texas—a petroleum source rock, *in* J. G. Palacas, ed., Petroleum geochemistry and source-rock potential of carbonate rocks: AAPG Studies in Geology, v. 18, p. 117-125.

24 Kuich, N., 1989, Seismic fracture identification and horizontal drilling: keys to optimizing productivity in a fractured reservoir, Giddings field, Texas: GCAGS Trans., v. 39, p. 153-158.

25 Ladiera, F. L., and N. J. Price, 1981, Relationship between fracture spacing and bed thickness: Journal Structural Geology, v. 3, no. 2, p. 179-183.

26 LaPointe, P. R., 1988, A method to characterize fracture density and connectivity through fractal geometry: International Journal of Rock Mechanics Mineral Sciences and Geomechanical Abstracts, v. 25, p. 421-429.

27 La Pointe, P. R., and J. A. Hudson, 1985, Characterization and interpretation of rock mass joint patterns: GSA, Special Paper 199, 37 p.

28 Long, J. C. S., and P. A. Witherspoon, 1985, The relationship of the degree of interconnection to permeability in fracture networks: Journal of Geophysical Research, v. 90, p. 3087-3099.

29 Mandelbrot, B. B., 1983, The Fractal Geometry of Nature (Updated and Augmented): Freeman, New York, 468 p.

30 Marshak, S. and Engelder, T., 1985, Development of cleavage in limestones of a fold-thrust belt in eastern New York: Journal of Structural Geology, v. 7, p. 345-359.

31 Nelson, R.A., 1985, Geologic analysis of naturally fractured reservoirs: Contributions in Petroleum Geology and Engineering, Gulf Publishing Co., Houston, 320 p.

32 Olson, J. and Pollard, D.D., 1989, Inferring paleostresses from natural fracture patterns: A new method: Geology, v. 17, p. 345-348.

33 Pessagno, E. A., Jr., 1969, Upper Cretaceous planktonic foraminifera from the western Gulf coastal plain: Paleontographica Americana, v. 5, p. 245-445.

34 Price, N. J., 1966, Fault and Joint Development in Brittle and Semi-Brittle Rock: Pergammon Press, London, 176 p.

35 Pollard, D. D., and A. Aydin, 1988, Progress in understanding jointing over the past century: GSA Bulletin, v. 100, p. 1181-1204.

36 Ramez, M. R. H. and F. H. Mosalamy, 1969, The deformed nature of various size fractions of some clastic sands: Jour. Sed. Petro., v. 39, no. 3, p. 1181-1197.

37 Reaser, D. F., and E. W. Collins, 1988, Style of faults and associated fractures in Austin Chalk, northern extension of the Balcones Fault Zone, Central Texas: GCAGS Trans., v. 38, p. 267-277.

38 Segall, P. and D.D. Pollard, 1983, Joint formation in granitic rock of the Sierra Nevada: GSA Bull., v. 94, p. 563-575.

39 Sinclair, S.W., 1980, Analysis of macroscopic fractures on Teton Anticline, northwestern Montana: M.S. Thesis, Dept. of Geology, Texas A&M University, College Station, TX, May 1980, 102 p.

40 Snyder, R. H., and M. Craft, 1977, Evaluation of Austin and Buda Formations from core and fracture analysis: GCAGS Trans., v. 27, p. 376-385.

41 Sowers, G. M., 1972, Theory of spacing of extension fractures: *in* Geologic Fractures of Rapid Excavation, Geological Society of America Engineering

Geology Case History No. 9, p 27-53.
42 Stapp, W. L., 1977, The geology of the fractured Austin and Buda Formations in the subsurface of south Texas: Gulf Coast Association of Geological Societies Transactions, v. 27, p. 208-229.
43 Weaks, A. W., 1945, Balcones, Luling, and Mexia fault zones in Texas: AAPG Bulletin, v. 29, p. 1733-1737.

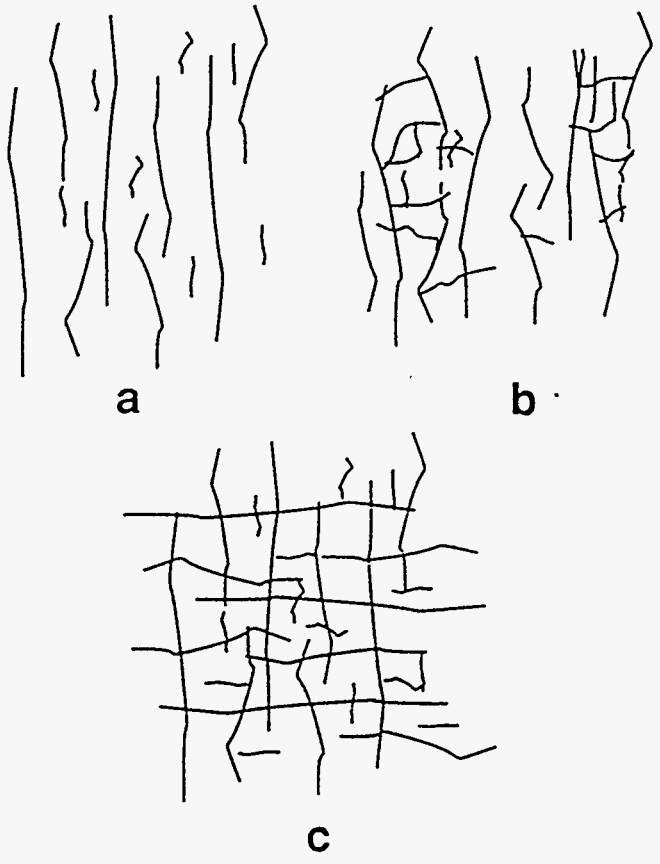


Figure 1. Three types of fracture connectivity: a) No connection among fractures—optimum reservoir drainage is achieved by intersecting the most fractures possible by horizontally drilling normal to the fracture trend; b) Patchy connectivity—best drainage is achieved by drilling through patches of connected fractures; c) High connectivity—direction of drilling unimportant.

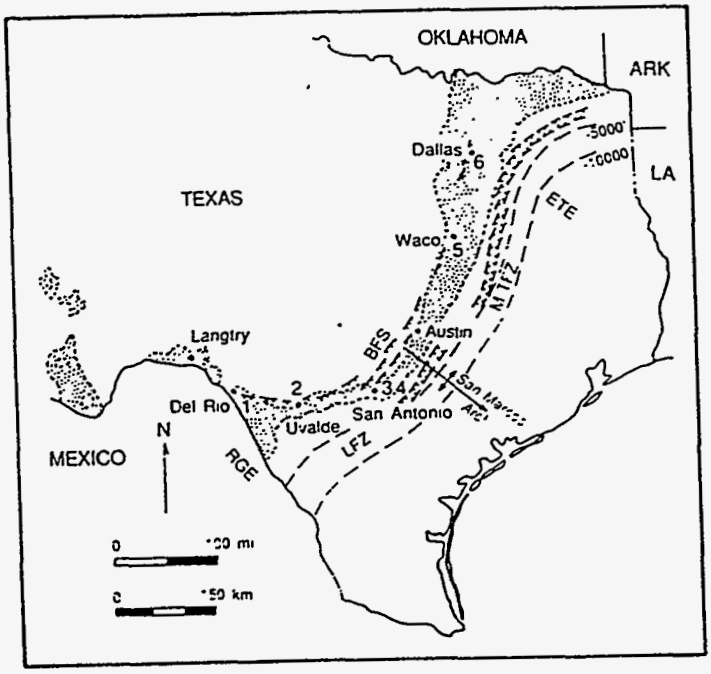


Figure 2. Location map for study sites, after Corbett *et al.* (1987). Upper Cretaceous outcrop trend is shown stippled and subsurface structural contours on top of the Austin Chalk are dashed lines. Symbols: RGE, Rio Grande embayment; LFZ, Luling fault zone; BFS, Balcones fault system; M-TFZ, Mexia-Talco fault zones; ETE, East Texas embayment. Numbers refer to study locations: 1) Tequequite Creek; 2) Uvalde (not reported on in this paper); 3, 4) Quarries in San Antonio, only one of which (Old Alamo Cement Quarry) was mapped; 5), Waco; 6) Dallas.

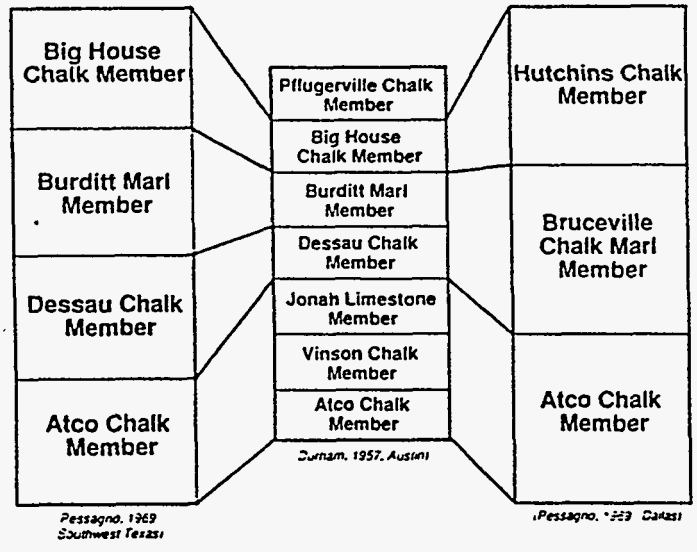


Figure 3. Lithostratigraphic correlation of units of the Austin Chalk, after Corbett *et al.* (1987). Maps reported on in this paper were made in the shaded units.

Figure 4. Geology in the vicinity of the Tequesquite Creek study area, simplified from the Del Rio and Crystal City-Eagle Pass sheets, Geologic Atlas of Texas (Barnes, 1977, 1976).

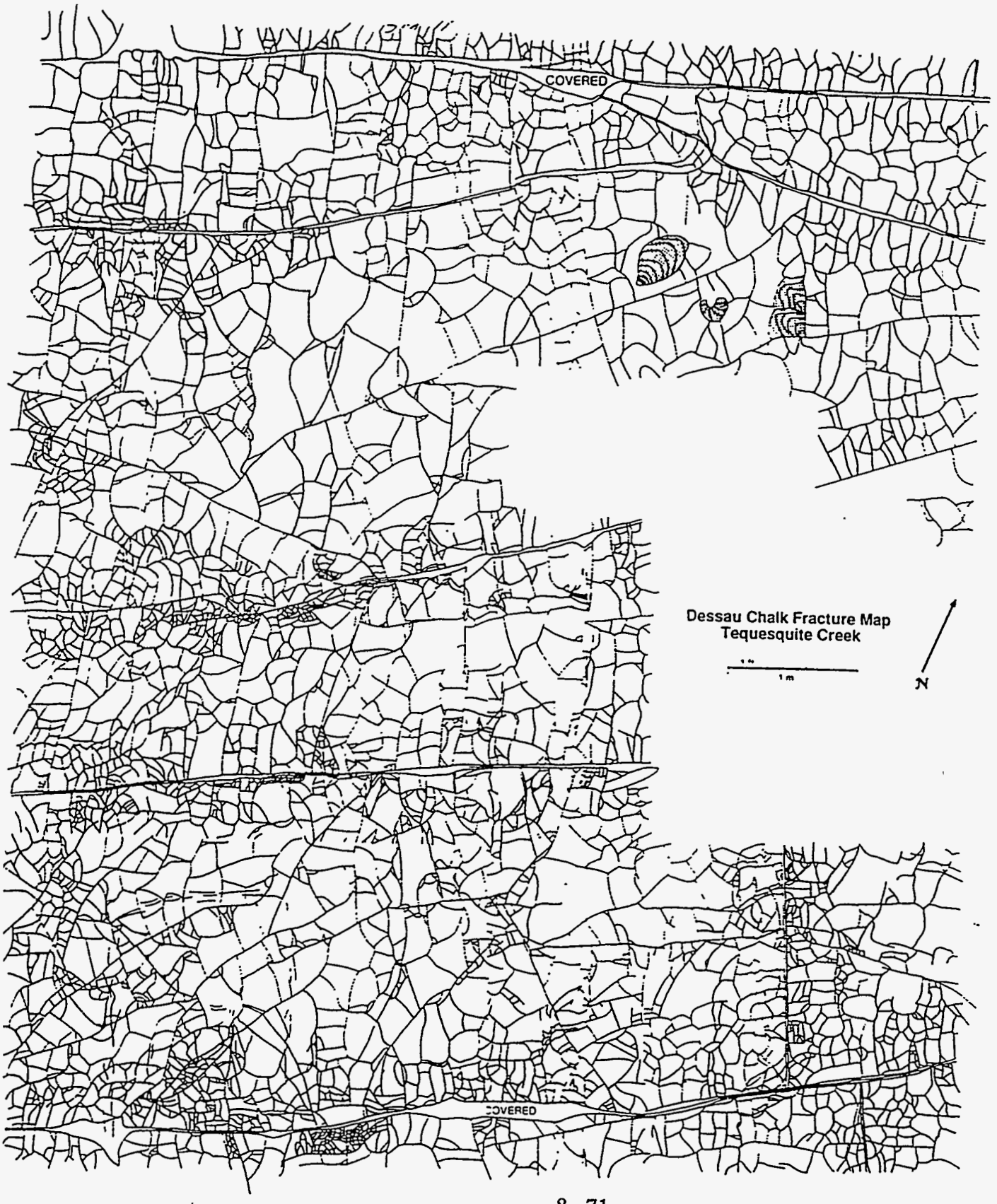
COVERED
Dessau Chalk Fracture Map
Tequesquite Creek
1 m
N
COVERED

Figure 5. Fracture map along Tequesquite Creek. Stippled areas are fossils; blank areas are covered. See text for further discussion.

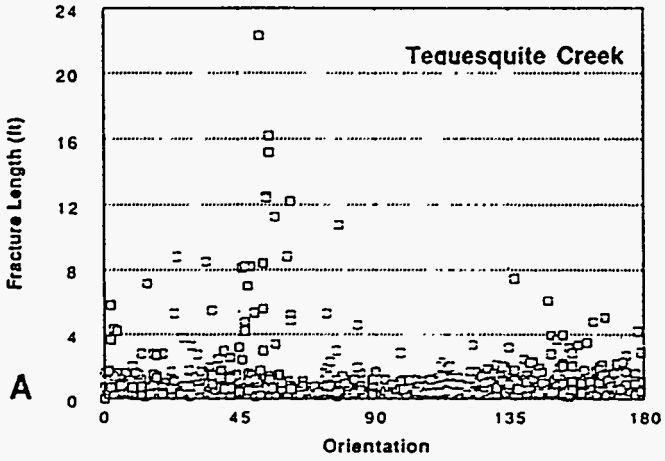
Tequesquite Creek
Fracture Length (ft)
24
20
16
12
8
4
0
A
0
45
90
135
180
Orientation

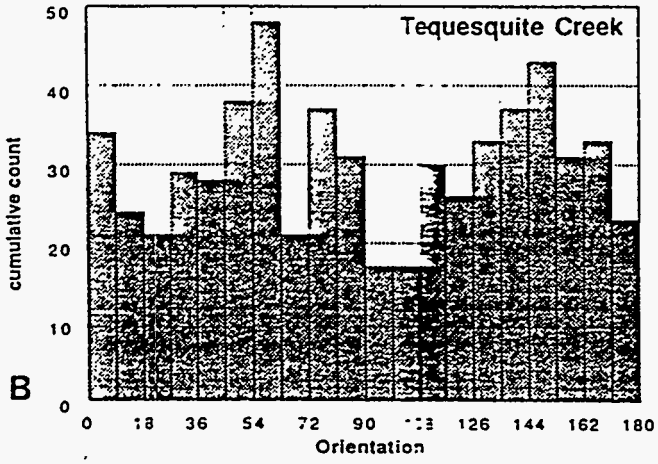
Tequesquite Creek
cumulative count
50
40
30
20
10
0
B
0
18
36
54
72
90
126
144
162
180
Orientation

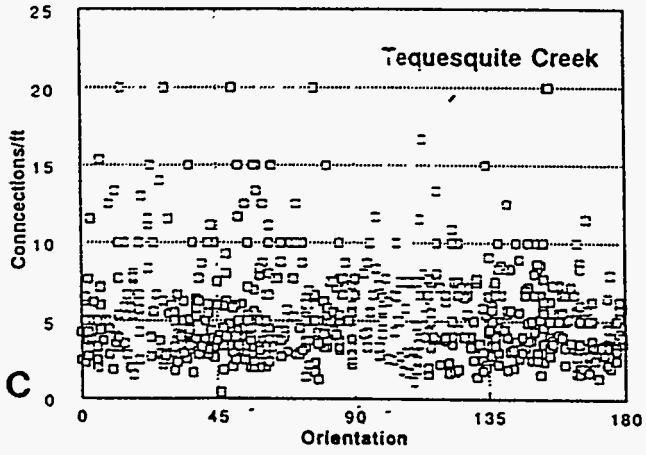
Tequesquite Creek
Connections/ft
25
20
15
10
5
0
C
0
45
90
135
180
Orientation

Figure 6. Data plots from map shown in Figure 5. Data were collected along sampling lines as described in the text. a) Fracture length vs orientation; fractures trending N50-60E are longest; b) Histogram of fracture orientation azimuth, 0=north; the most abundant fracture trends are about N60E and N30W; c) Intersections with other fractures (connections) per foot of fracture length versus orientation of the fracture; fracture connectivity is nearly randomly distributed with orientation.

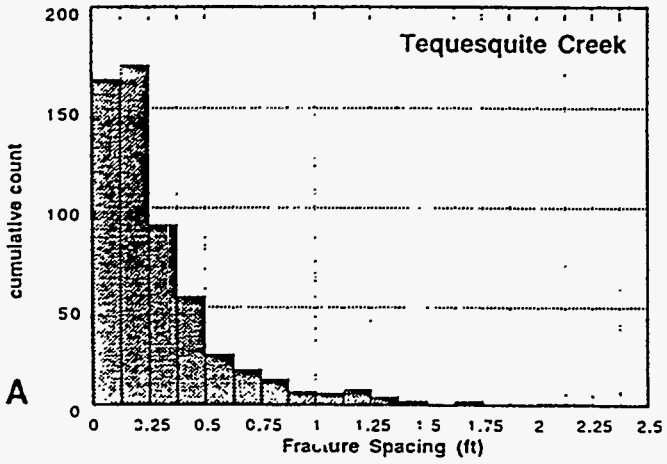


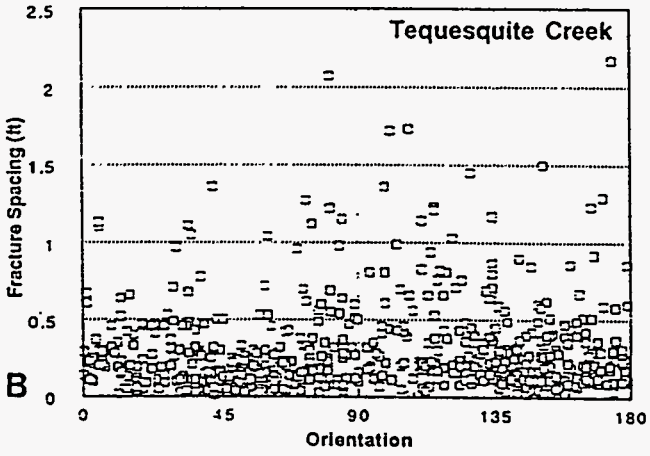


Figure 7. Plots of fracture spacing for the map shown in Figure 5. a) The frequency of fracture spacing closely follows a negative exponential distribution, as has been found for fracture length (Corbett *et al.*, 1991); b) Fracture spacing is nearly randomly distributed with respect to fracture orientation.

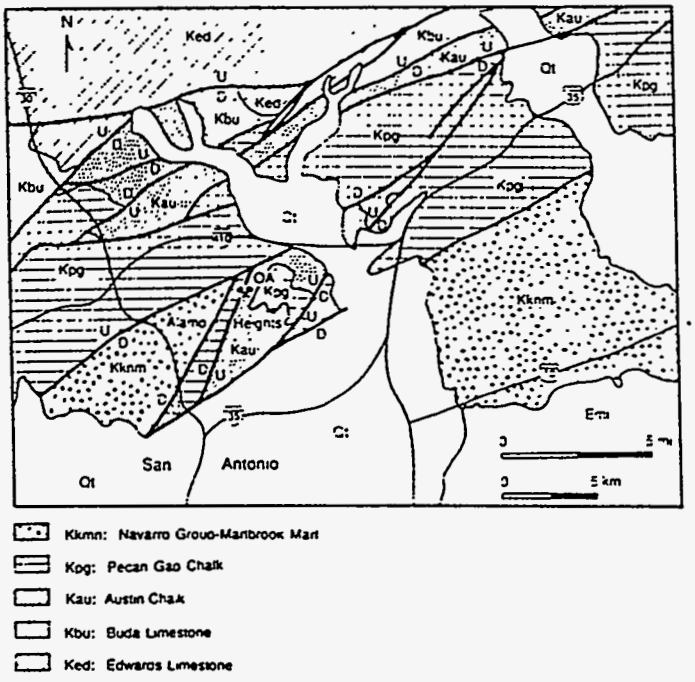


Figure 8. Geology in the vicinity of the San Antonio study areas, simplified from the San Antonio Sheet, Geologic Atlas of Texas, Barnes (1974). OA: Old Alamo Cement Quarry.


Atco Chalk Fracture Map
Old Alamo Quarry
N
COVERED
COVERED
COVERED
COVERED
COVERED
COVERED
COVERED
COVERED
COVERED
COVERED
COVERED
COVERED

Figure 9. Fracture map in the Old Alamo Cement Quarry, San Antonio. Cross-hatched fractures are vein filled. See text for further discussion.

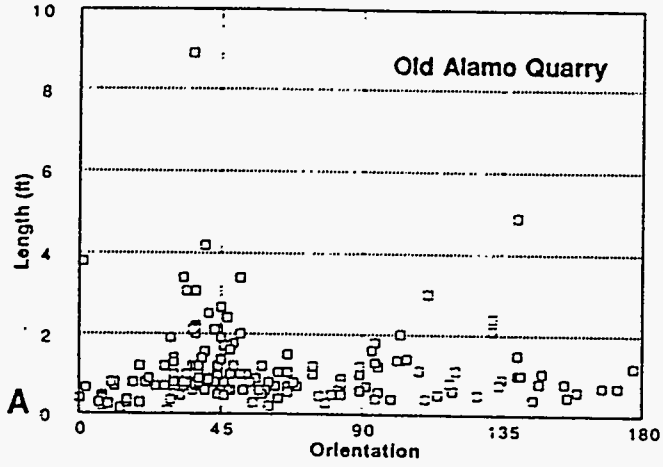
Old Alamo Quarry
Length (ft)
10
8
6
4
2
0
A
0
45
90
135
180
Orientation

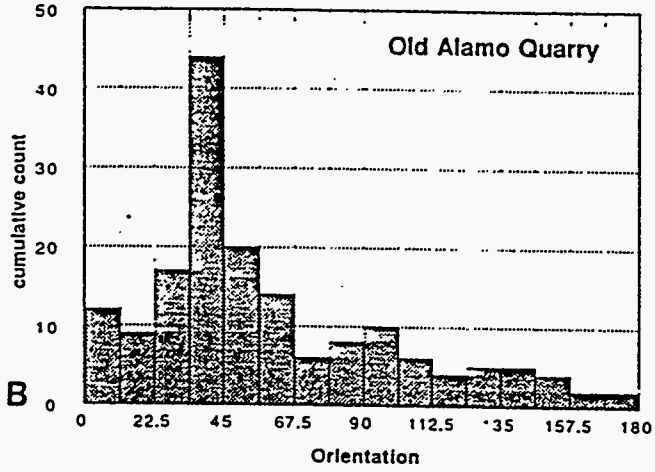
Old Alamo Quarry
cumulative count
50
40
30
20
10
0
B
0
22.5
45
67.5
90
112.5
135
157.5
180
Orientation

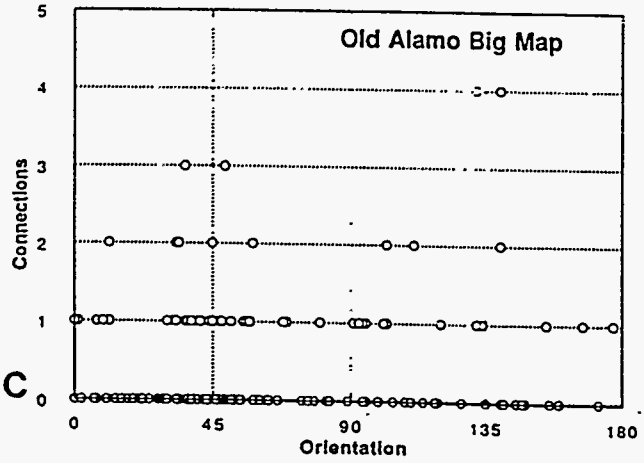
Old Alamo Big Map
Connections
5
4
3
2
1
0
C
0
45
90
135
180
Orientation

Figure 10. Data plots from map shown in Figure 9. Data were collected along sampling lines as described in the text. a) Fracture length vs orientation of the fracture; fractures trending N45E and N45W are longest; b) Histogram of fracture orientation azimuth, 0=north; the most abundant fractures trend N40E; in addition, the dispersion in fracture orientation is low, *i.e.*, there is a strong preferred orientation; c) Intersections with other fractures (connections) per foot of fracture length versus orientation of the fracture; fracture connectivity is, in general, low (compare figs. 6, 14 and 18).

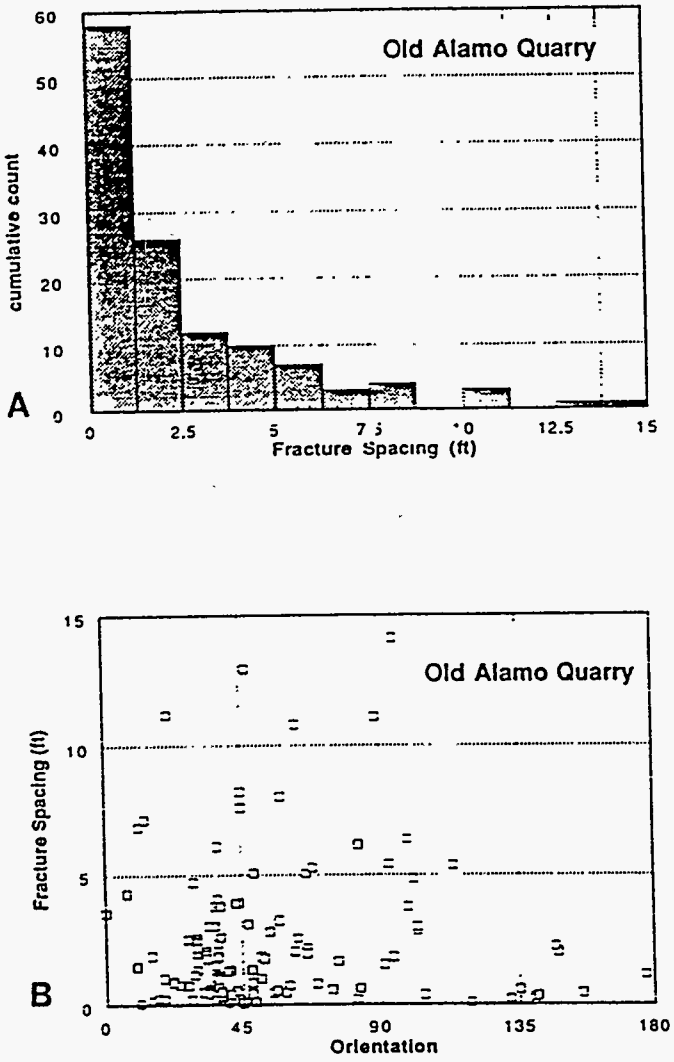


Figure 11. Plots of fracture spacing for the map shown in Figure 9. a) The frequency of fracture spacing follows a negative exponential distribution, as has been found for fracture length (Corbett *et al.*, 1991); b) Fracture spacing vs fracture orientation. See text for discussion.

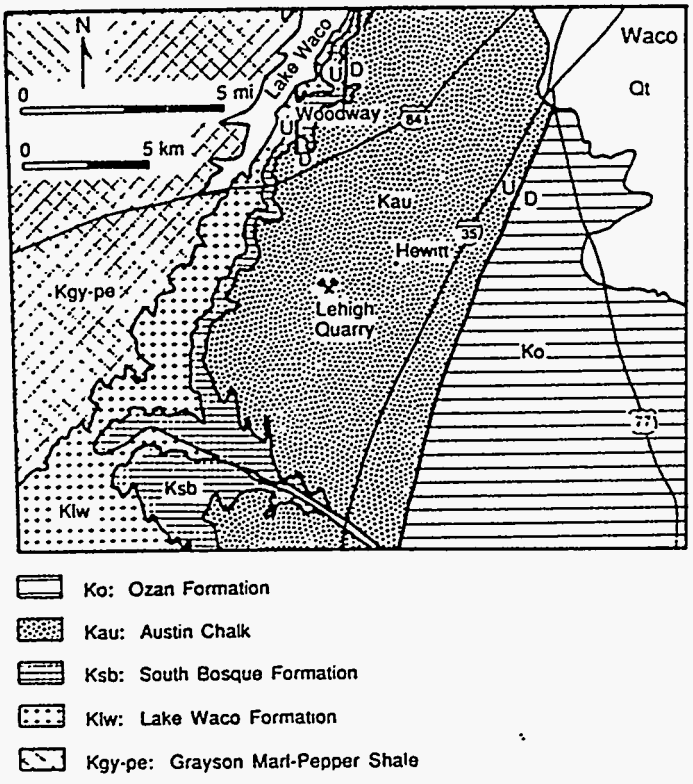


Figure 12. Geology in the vicinity of the Waco study site, simplified from the Waco Sheet, Geologic Atlas of Texas, Barnes (1990). Note north-south faults north of the quarry studied.

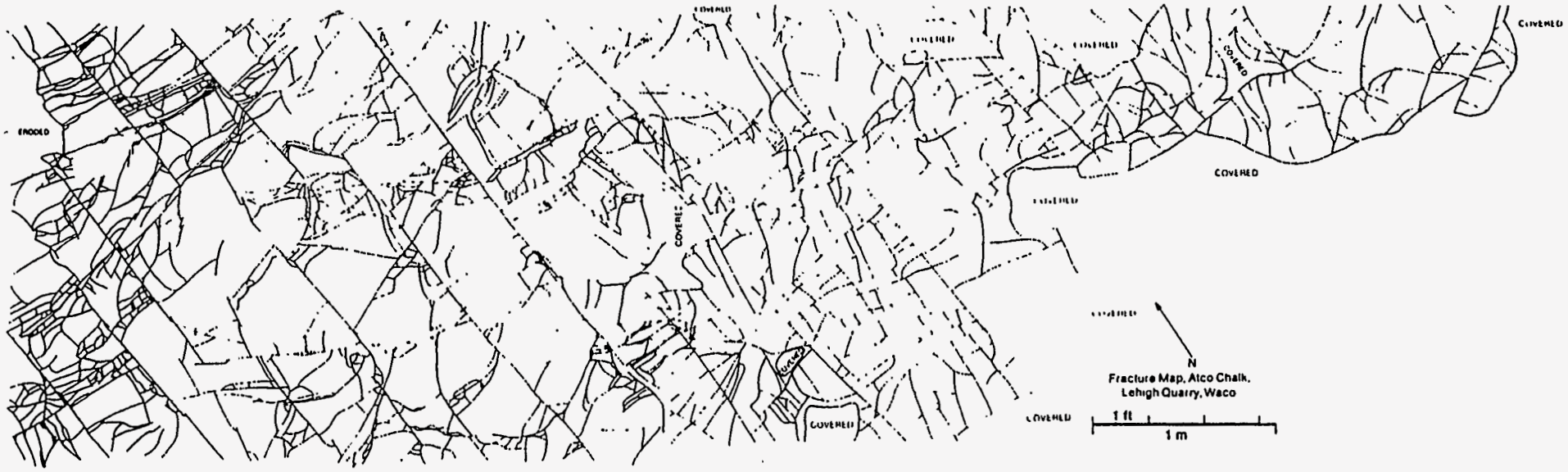
ERODED
COVERED
COVERED
COVERED
COVERED
COVERED
COVERED
COVERED
COVERED
COVERED
N
Fracture Map, Alco Chalk,
Lehigh Quarry, Waco
1 ft
1 m

Figure 13. Fracture map in the Lehigh Cement Quarry, Waco. See text for discussion.

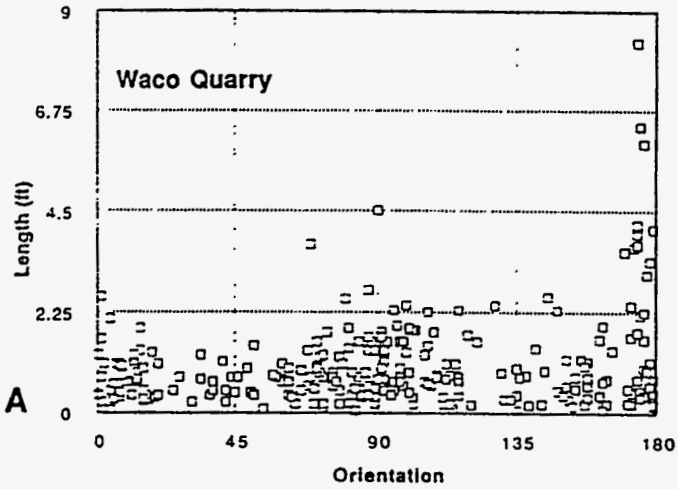
Waco Quarry
Length (ft)
9
6.75
4.5
2.25
0
A
0
45
90
135
180
Orientation

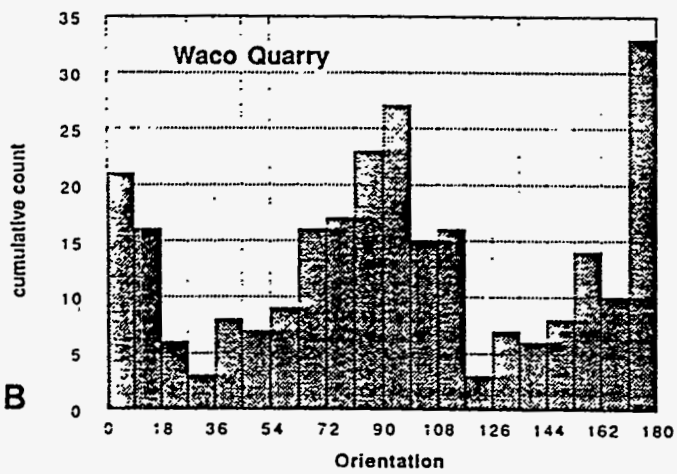
Waco Quarry
cumulative count
35
30
25
20
15
10
5
0
B
0
18
36
54
72
90
108
126
144
162
180
Orientation

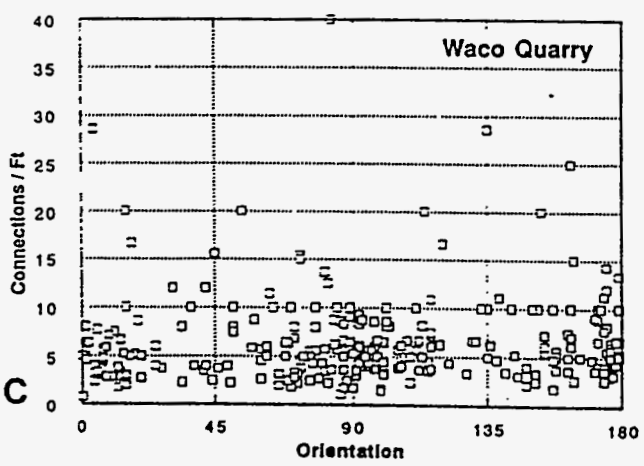
Waco Quarry
Connections / Ft
40
35
30
25
20
15
10
5
0
C
0
45
90
135
180
Orientation

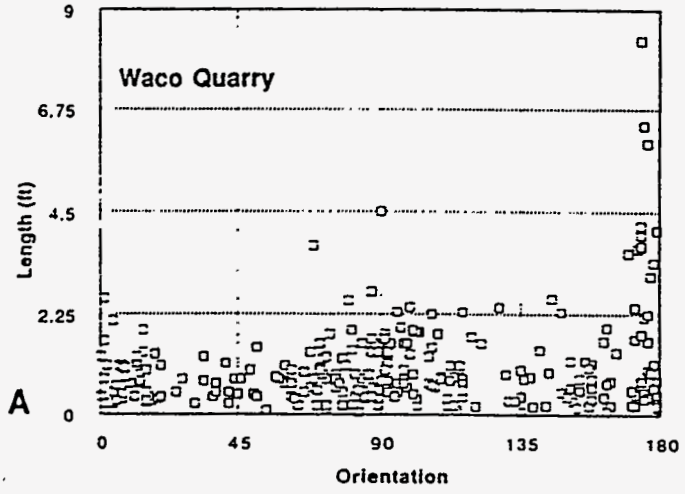
Waco Quarry
Length (ft)
9
6.75
4.5
2.25
0
A
0
45
90
135
180
Orientation

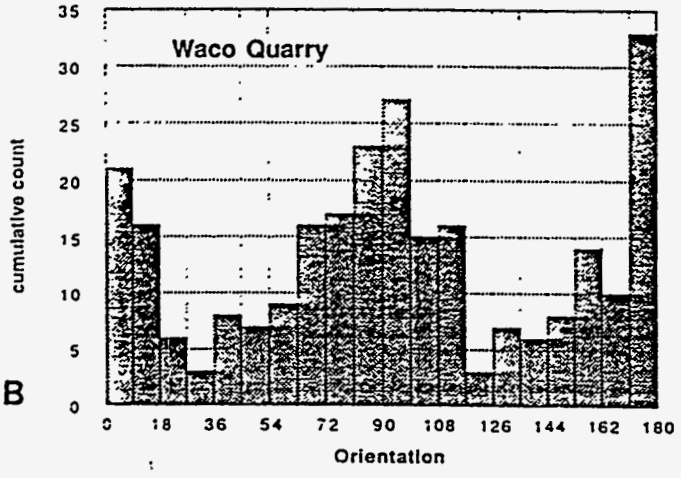
Waco Quarry
cumulative count
35
30
25
20
15
10
5
0
B
0
18
36
54
72
90
108
126
144
162
180
Orientation

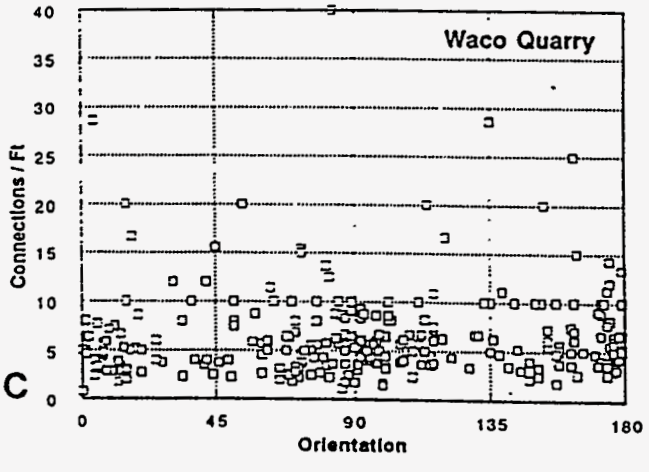
Waco Quarry
Connections / Ft
40
35
30
25
20
15
10
5
0
C
0
45
90
135
180
Orientation

Figure 14. Data plots from map shown in Figure 13. Data were collected along sampling lines as described in the text. a) Fracture length vs orientation of the fracture; fractures trending North-South and perhaps East-West are longest; b) Histogram of fracture orientation azimuth, 0=north; the most abundant fractures trend at about North-South and East-West; c) Intersections with other fractures (connections) per foot of fracture length versus orientation of the fracture; fracture connectivity is, in general, high.

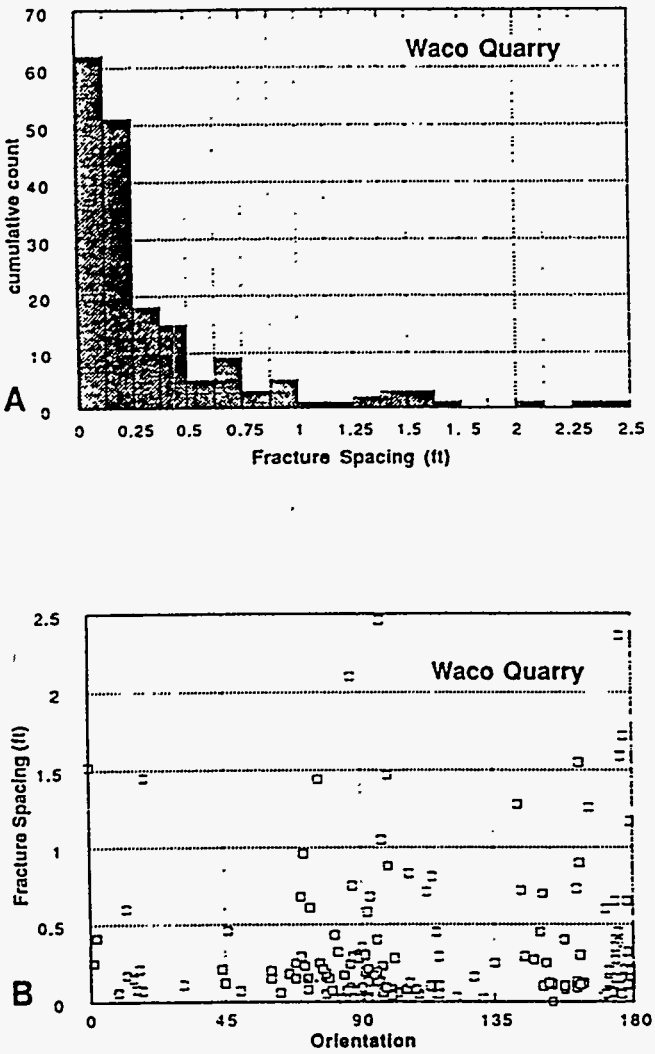


Figure 15. Plots of fracture spacing for the map shown in Figure 13. a) The frequency of fracture spacing follows a negative exponential distribution, as has been found for fracture length (Corbett *et al.*, 1991); b) Fracture spacing; spacing is greatest among North-South and East-West fractures. See text for discussion.

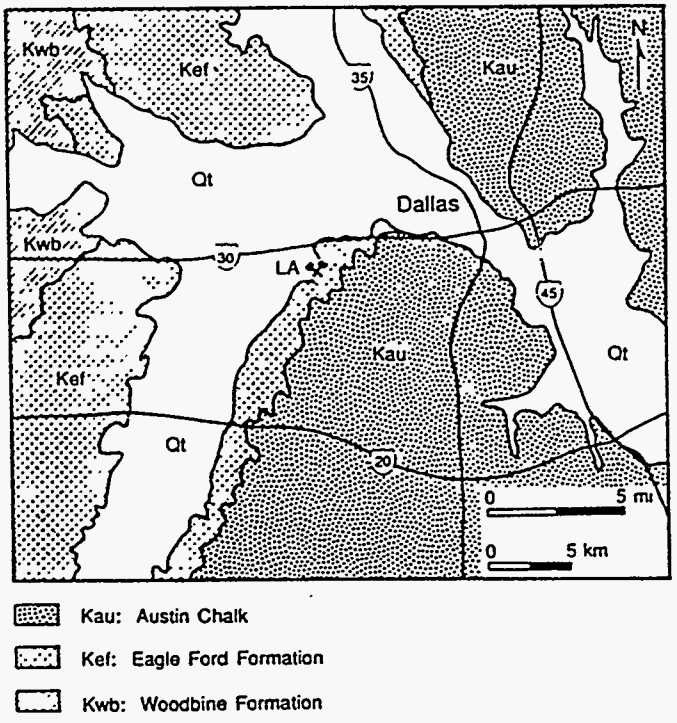


Figure 16. Geology in the vicinity of the Dallas study site, simplified from the Dallas Sheet, Geologic Atlas of Texas, Barnes (1972). The west boundary of the quarry is marked on the map (quarry symbol at LA); the quarry extends to the east into the Austin Chalk, where the map of Figure 17 was made.

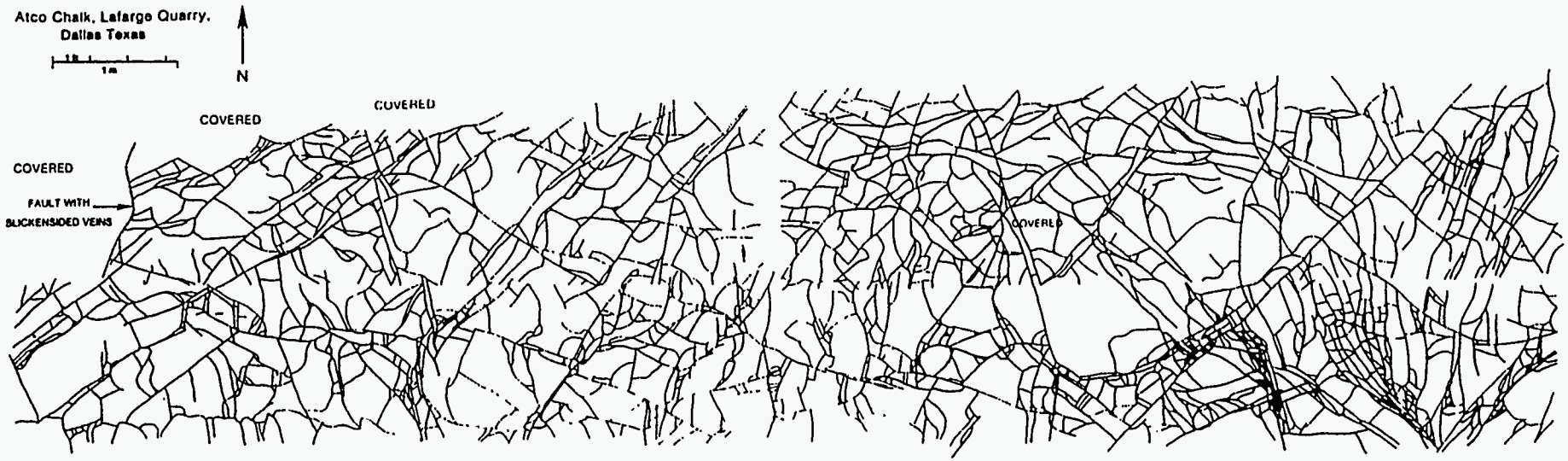
Atco Chalk, Lafarge Quarry,
Dallas Texas
1m
N
COVERED
COVERED
COVERED
COVERED
FAULT WITH
SLICKENSIDED VEINS

Figure 17. Fracture map in the LaFarge Cement Quarry, Dallas. See text for discussion.

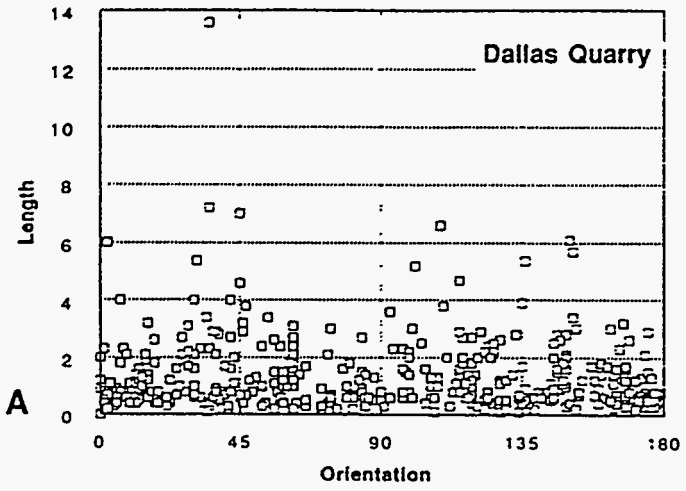
Dallas Quarry
Length
Orientation
A
0
2
4
6
8
10
12
14
0
45
90
135
180

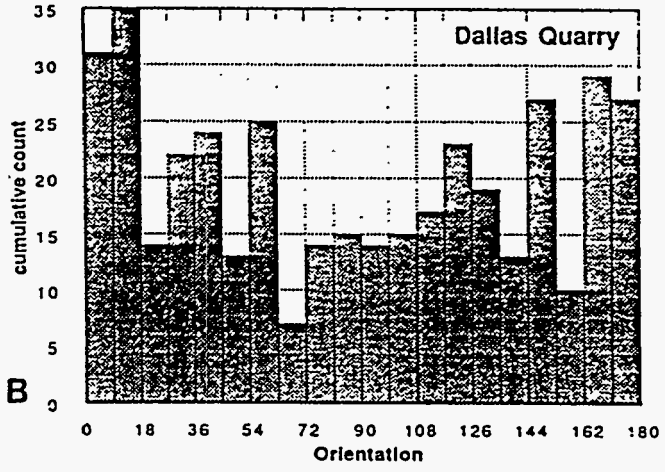
Dallas Quarry
cumulative count
Orientation
B
0
5
10
15
20
25
30
35
0
18
36
54
72
90
108
126
144
162
180

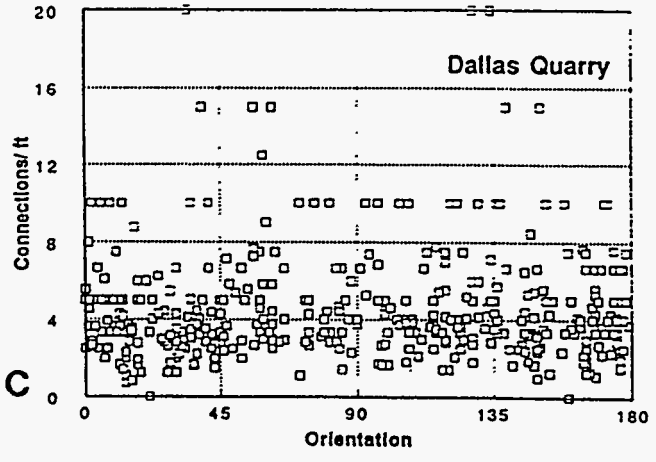
Dallas Quarry
Connections/ ft
Orientation
C
0
4
8
12
16
20
0
45
90
135
180

Figure 18. Data plots from map shown in Figure 17. Data were collected along sampling lines as described in the text. a) Fracture length vs orientation of the fracture; there is no strong pattern to fracture length; b) Histogram of fracture orientation azimuth, 0=north; there is no strong pattern to preferred orientation of fractures; c) Intersections with other fractures (connections) per foot of fracture length versus orientation of the fracture; fracture connectivity is, in general, high.

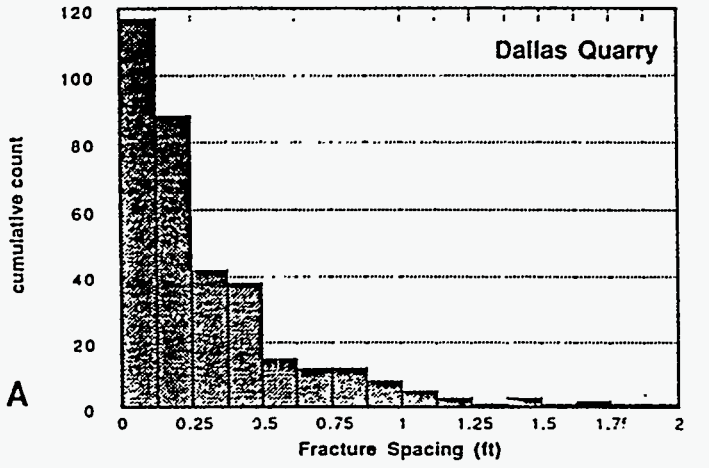


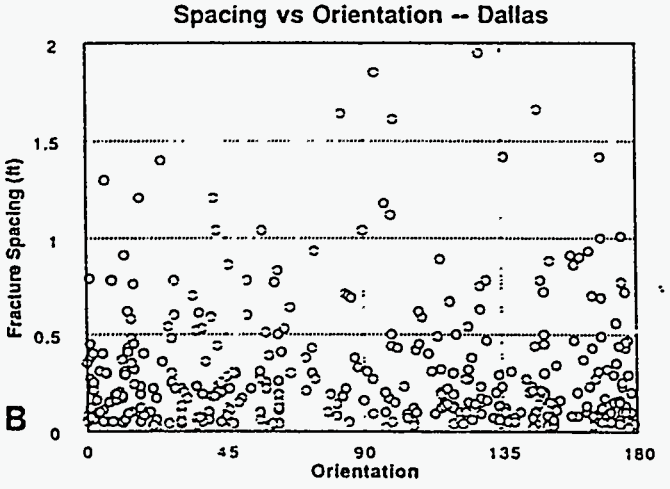


Figure 19. Plots of fracture spacing for the map shown in Figure 17. a) The frequency of fracture spacing follows a negative exponential distribution, as has been found for fracture length (Corbett *et al.*, 1991); b) Fracture spacing. Spacing is small and not preferentially oriented. See text for discussion.

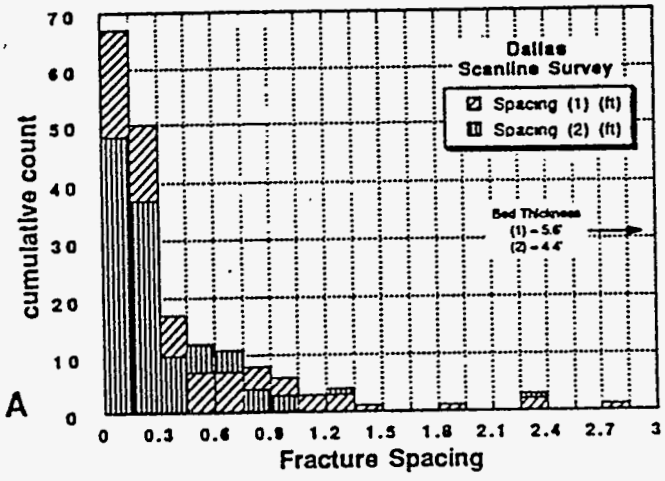
Dallas
Scanline Survey
Spacing (1) (ft)
Spacing (2) (ft)
Bed Thickness
(1) = 5.6'
(2) = 4.4'
cumulative count
Fracture Spacing
A

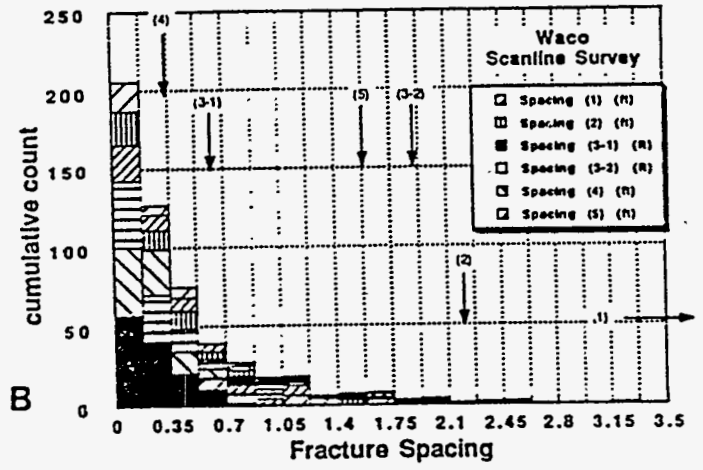
Waco
Scanline Survey
Spacing (1) (ft)
Spacing (2) (ft)
Spacing (3-1) (ft)
Spacing (3-2) (ft)
Spacing (4) (ft)
Spacing (5) (ft)
cumulative count
Fracture Spacing
B

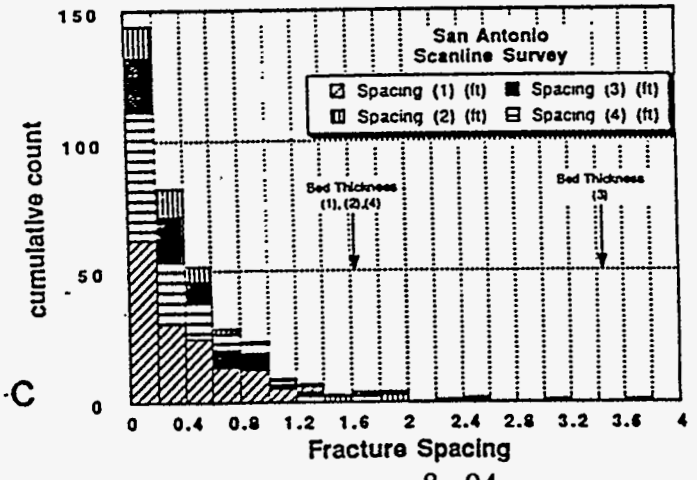
San Antonio
Scanline Survey
Spacing (1) (ft)
Spacing (2) (ft)
Spacing (3) (ft)
Spacing (4) (ft)
Bed Thickness
(1), (2), (4)
Bed Thickness
(3)
cumulative count
Fracture Spacing
C

Figure 20. Plots of fracture spacing from scanline surveys. Individual pars of each histogram bar represent contributions from each scanline; scanlines are indicated in the legend by numbers in parentheses. Arrows point to values on the horizontal axes for the thickness of the beds along which each particular scanline (parenthetical numbers) was made.

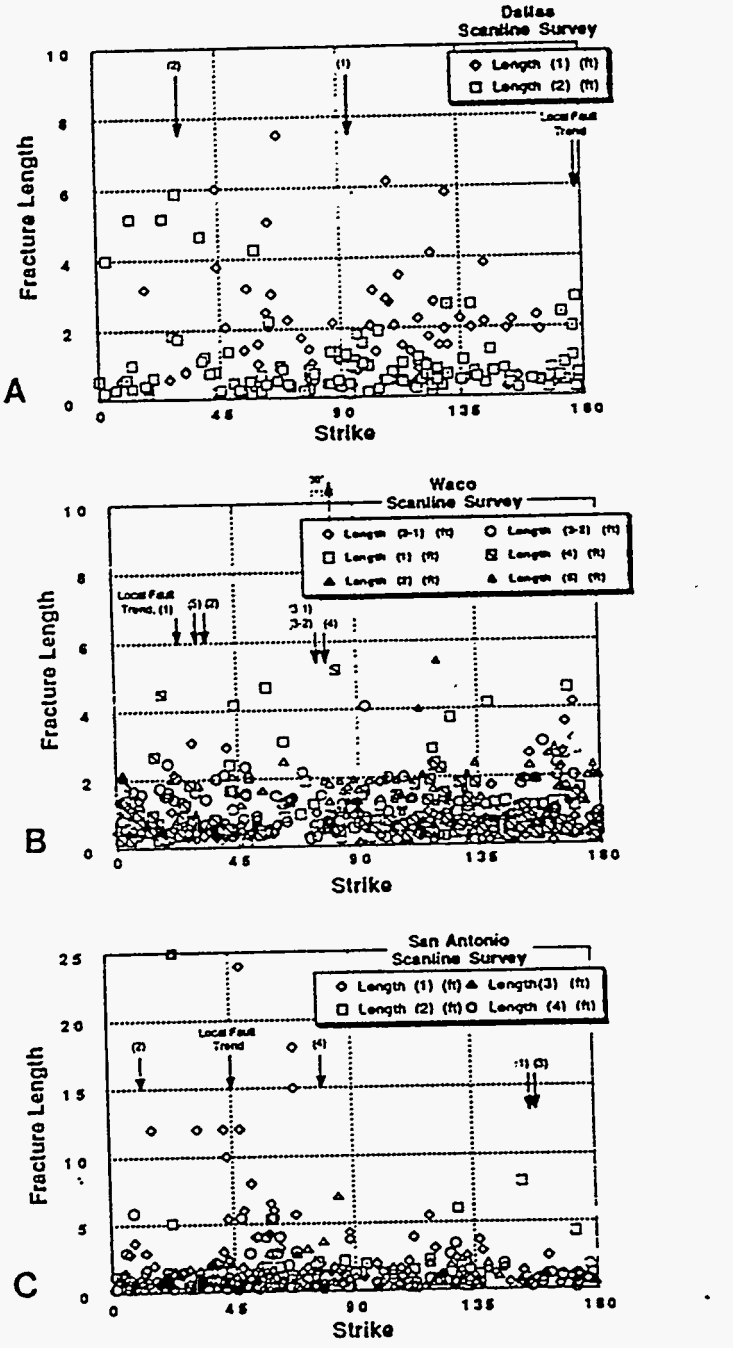


Figure 21. Plots of fracture length versus orientation from scanline surveys. The legend matches plot symbols with particular scanline surveys (parenthetical numbers). Arrows point to the orientations of each scanline (parenthetical numbers). The trend of the nearest segment of the Balcones fault is indicated as "Local Fault Trend".